New Electrolytic Media and Methods for Energy Storage and Conversion

Thesis by

Brendon James McNicholas

In Partial Fulfillment of the Requirements for the degree of

Doctor of Philosophy in Chemistry

CALIFORNIA INSTITUTE OF TECHNOLOGY

Pasadena, California

2020

(Defended May 22, 2020)

Brendon James McNicholas
ORCID: [0000-0002-3654-681X]

ACKNOWLEDGEMENTS

I would like to start this section by first thanking the two people responsible for raising me and for helping me become the man I am today: my mother, Caron McNicholas, and my father, Thomas McNicholas. Your undying love and support and nurturing of my education, especially through my adolescent years, helped shape the course of my future. Words cannot express the love I have for you.

To my advisors, Harry Gray and Bob Grubbs, you are both forces to be reckoned with. Your staunch support of my education and my growth as a scientist have propelled me forward in ways in which I never thought possible. You always lift me up when I continue to put myself down, something I will always be grateful for. Harry, your love for teaching and support for my teaching career have made me a better speaker, writer, and researcher. Your honesty, curiosity, and generosity inspire me to be a better man every day. Bob, you allowed me to carve my own path in graduate school, which is the reason for my independence as a scientist. Thank you for supporting me during my most uncertain times and for your incredible enthusiasm for chemistry. I will be forever grateful for both of you and your unwavering support.

Jay Winkler, your never-ending pursuit of knowledge, willingness to help, and love for spectroscopy have dramatically advanced my understanding and prowess as a scientist. I will forever be in your debt for always helping me in lab and teaching me to do experimental research with confidence and precision.

To the other members of my committee, Kimberly See and Mitchio Okumura, thank you for your guidance during my time at Caltech. Kim, your love for electrochemistry and battery technology is a constant inspiration, and I thank you for being such a wonderful Chair. I would also like to thank Ryan Hadt. Your happiness and commitment to theoretical chemistry and spectroscopy are undeniable, and I look forward to continuing my educational journey with you as my advisor.

I am very fortunate to have my Aunt Lee here in Southern California with me. Your bubbly personality, generosity, and love throughout my life and, most importantly, during graduate school, including holidays and vacations, have been instrumental in my success and happiness in life. Grammy, you are the kindest human being I know, and I thank you for always being there for me since I was born. I love you both so much!

To James McNicholas and Hilary McNicholas, being your brother has been such a blessing, and I thank you from the bottom of my heart for all of your support and love during my entire education. Ella McNicholas and Leighton McNicholas, your love and enthusiasm inspire Uncle Bean on a daily basis. I love all of you. And to my entire family: You are all an integral and indispensable part of my life, and I am so blessed to have each and every one of you.

A guy like me could not imagine having friends as special as Brian Sanders, Jill Clinton, and Wes Kramer. The three of you are shining lights in the world of science, and I thank you for the parties, binge-watching of TV shows, lunchtime conversations, video games, and all of the kindness and generosity you have shown me. I love you!

Emmanuelle Despagnet-Ayoub, without your incredible synthetic skills and support, I would not have become the synthetic chemist I am today. You are the reason for me overcoming significant hurdles in my studies, and I will always consider you my big sister in chemistry! I am so fortunate to be able to witness your continued success at Occidental and JPL.

Javier Fajardo, we have gone on this journey together, and I want to thank you for being such a great friend and for always having a smile on your face. Josef Schwan, you have been such a wonderful friend, and I am so happy to have you in my life. Alex Barth, I am so happy that our friendship and collaboration have blossomed into tangible scientific contributions, and I look forward to working with you for the next few years!

James Blakemore, thank you for your mentorship and guidance during my first year of graduate studies. Your commitment to starting me off on the right foot in lab was the catalyst for my success in graduate school, and it warms my heart to see your continued success at KU.

I have had the wonderful opportunity of interacting with the incredible group known as the "Gray Nation". To all of the graduate and undergraduate students, postdoctoral scholars, and visiting professors and researchers, including Bradley Brennan, Katharina Brinkert, Tania Darnton, Sarah Del Ciello, Shabnam Hematian, Bryan Hunter, Patrycja Kielb, Yan Choi Lam, Astrid Müller, Julius Oppenheim, Raheleh Rafanvar, Chris Roske, Aaron Sattler, Wes Sattler, Yuling Shen, Tom Sheridan, Oliver Shafaat, Jieun Shin, Kana Takematsu, Tony Vlcek, Sara Wehlin, Julian West, I thank you for all of the insightful discussions, wonderful group parties, and sense of community all of you made me feel

during my time at Caltech. I would like to also thank Siddharth Dasgupta: your commitment to CCI Solar and supporting all of us in the Solar Army inspired a new generation of young scientists. Rick Jackson, your friendship and skilled organization of all of our events, wonderful parties, snacks, and group lunches were an indispensable part of graduate school.

I want to also thank the "Grubbs Nation", including Tonia Ahmed, Zainab Al-Saihati, Christopher Bates, Kerry Betz, Alice Chang, Crystal Chu, Peter Dornan, Keary Engle, Aidan Fenwick, Quan Gan, Michael Haibach, Pablo Guzman, John Hartung, JK Ko, Sankar Krishnamoorthy, Eunseng Lee, Juneyoung Lee, Jiaming Li, Allegra Liberman-Martin, TP Lin, Robert Macfarlane, Shane Mangold, Chris Marotta, Karthish Manthiram, Vanessa Marx, Patrick Montgomery, Noah Nathel, Brendan Quigley, Lauren Rosebrugh, Shunsuke Sato, Michael Schulz, Nicholas Swisher, Anton Toutov, JC Wang, Raymond Weitekamp, Zachary Wickens, William Wolf, Yan Xu, Melanie Yen, Ki-Young Yoon, for friendship, research and life advice, and an amazing time in lab. Linda Syme, thank you for your kindness and helpfulness during my entire graduate school career.

Other members of the Caltech community who have contributed to my success and happiness during graduate school include Ethan Simonoff, Annelise Thompson, Hsiang-Yun Chen, Simon Jones, Jeffrey Mendez, Ethan Simonoff, Annelise Thompson, and Agnes Tong. Ethan Simonoff and Annelise Thompson have been wonderful friends and have contributed to my love for teaching. Jeff Mendez, you propelled my love for teaching during my first year of graduate school, and I thank you for your advice and support. Hsiang-Yun Chen, thank you for all of your help during my time in JCAP. Simon Jones, you were an incredible mentor to me at JPL. Agnes Tong, your commitment to CCE and friendship and support during my early years of graduate school were a huge reason for my success.

Paul Oyala, thank you so much for your friendship and mentorship and sharing your love of EPR spectroscopy with the Caltech community. David Vander Velde, thank you for maintaining an incredible NMR facility for everyone at Caltech. Mike Takase and Larry Henling, your commitment to the art of X-ray crystallography, your willingness to help, and your mentorship are another reason my time at Caltech has been so special. You are all an integral part of this institute.

To my undergraduates, Alessio Amaolo, Angel Elizondo, Anita Chen, Cherish Nie, Danh Ngo, Lucille Wells, and Jayce Miller, thank you for teaching me how to be a better mentor and scientist, and I am so impressed and ecstatic to see your continued success beyond Caltech.

To all of my students from Chem 3X, Chem 153a and Chem 213a, teaching all of you taught me the importance of being a mentor in truly understanding and mastering concepts, and it has been an absolute pleasure in guiding all of you towards success.

To my love, I did not begin this journey with you, but completing it with you has been the biggest blessing I could ever imagine. Your courage and love for your work continually inspires me, and I cannot wait for our bright future. I hope I can do as much for you as you have already done for me.

ABSTRACT

New electrolytic media and methods for energy storage and conversion are needed to fully realize the sustained use of renewable energy and complete removal of dependence on fossil fuels. Motivated by this urgency, researchers today are heavily invested in developing new electrocatalytic systems for carbon dioxide sequestration to reduce greenhouse gas emissions and new battery architectures, such as non-aqueous redox flow batteries, to keep solar energy at our disposal during peak times of energy consumption. **Chapter 1** provides an overview of the conceptual frameworks for these two alternative energy technologies and a literature review of relevant work and inspiration in these fields. **Chapter 2** demonstrates one of the first examples of ionic liquid voltammetry of a molecular species, namely (tpfc)Mn, and its electron transfer reactivity in ionic liquids with varying solvent viscosity, effective electrolyte concentration, and donor strength. As well as showing the non-unity diffusional properties of molecular species in ionic liquids and the capability of ionic liquid anions to coordinate to molecular species, these studies suggest the viability of ionic liquids as conductive media for energy storage and conversion. **Chapter 3** introduces methods for immobilization of molecular catalysts in polymeric ion gels, a general strategy that bridges the divide between homogeneous solution-state catalysis and heterogeneous solid-state catalysis. These results provide insight into how environment, catalyst concentration, catalyst mobility, substrate availability, and dielectric properties of a medium all affect the catalytic response and overpotential for CO_2 reduction. Further implementation of these ion gel composites in solid-state devices, in aqueous environments, and in gas diffusion electrodes is also discussed. In **Chapter 4**, a brief overview of the use of boranes as capping ligands for cyanide is provided. The synthesis, electronic properties, and theoretical calculations of homoleptic, boronated Fe(II) hexacyanoferrates are reported. Addition of borane to cyanometallates dramatically alters electronic structures and is a novel method for permanent modification of formal potentials while

simultaneously maintaining or improving electrochemical reversibility and ambient stability. These complexes are characterized and studied by cyclic and differential pulse voltammetry, UV-vis, IR, and Raman spectroscopy, and flash-quench photolysis. **Chapter 5** extends the unique reactivity of borane adducts to the characterization of a full series of hexaisocyanoboratometallates (Cr, Mn, Fe, Ru, Os), compounds which demonstrate the concept of cyanide as a "variable-field" ligand, including magnetic circular dichroism spectroscopy, electron paramagnetic resonance spectroscopy, luminescence studies, excited-state lifetime studies, and electrochemistry. As electrolytes for non-aqueous redox flow batteries, these species exhibit excellent Coulombic and voltage efficiencies and fast electron transfer rates. The highly oxidizing species will also find use as reversible oxidants for chemical oxidations. **Chapter 6** extends the concept of modifying formal potentials to heteroleptic cyanometallates (M = Fe, Ru) with diimine ligands (L = bipyridine, phenanthroline, 4,4'-trifluoromethylbipyridine). These species are shown to be potent excited-state reductants and oxidants, strong and long-lived phosphors, and promising electrolytes for symmetric, non-aqueous redox flow batteries. These data also demonstrate improved excited-state lifetimes for borane-appended species, likely due to inhibition of non-radiative decay pathways. **Chapter 7** focuses on the generation of a solution stable, square pyramidal Co(II) species, which is studied by electrochemistry, UV-vis-NIR spectroscopy, X-band and Q-band CW EPR, and pulsed EPR techniques (HYSCORE, ENDOR). These studies demonstrate that boronation of cyanide differentially affects the energies of ligand field transitions based on π backbonding ability.

PUBLISHED CONTENT AND CONTRIBUTIONS

Chapter 2:
Adapted with permission from **McNicholas, B. J.**; Blumenfeld, C.; Kramer, W. W.; Grubbs, R. H.; Winkler, J. R.; Gray, H. B. Electrochemistry in Ionic Liquids: Case Study of a Manganese Corrole. *Russ. J. Electrochem.* **2017**, *53*, 1189-1193. DOI: 10.1134/S1023193517100068. Copyright 2017 Pleiades Publishing, Ltd.

- B.J.M. contributed to the conception of the project, acquired all voltammetry data, acquired all spectroscopic data, contributed to data analysis, and along with the other authors, wrote the manuscript.

Chapter 3:
Adapted with permission from **McNicholas, B. J**.; Blakemore, J. D.; Chang, A. B.; Kramer, W. W.; Grubbs, R. H.; Gray, H. B. Electrocatalysis of CO_2 Reduction in Brush Polymer Ion Gels. *J. Am. Chem. Soc.* **2016**, *138*, 11160-11163. DOI: 10.1021/jacs.6b08795. Copyright 2016 American Chemical Society.

- B.J.M. contributed to the conception of the project, acquired all electrochemistry data, acquired all spectroscopic data, performed the majority of synthesis, analyzed the data, and along with the other authors, wrote the manuscript.

Chapter 4:
Adapted with permission from **McNicholas, B. J.**; Winkler, J. R.; Grubbs, R. H.; Gray, H. B.; Despagnet-Ayoub, E. Tuning the Formal Potential of Ferrocyanide over a 2.1 V Range. *Chem. Sci.* **2019**, *10*, 3623-3626. DOI: 10.1134/S1023193517100068. Copyright 2019 Royal Society of Chemistry.

- B.J.M. contributed to the conception of the project, acquired all electrochemistry data, acquired all UV-visible, IR, and Raman data, and along with the other authors, wrote the manuscript.

Chapter 5:
McNicholas, B. J.; Nie, C.; Barth, A. T.; Oyala, P. H.; Amaolo, A.; Hadt, R. G.; Grubbs, R. H.; Winkler, J. R.; Despagnet-Ayoub, E.; Gray, H. B. Borane Adducts of Homoleptic Cyanometallates: Electronic Structure, Energy Level Inversion, and Applications in Non-Aqueous Redox Flow Batteries., **2020**, in preparation.

- B.J.M. conceived the idea for this paper, synthesized most of the compounds, acquired most of the electrochemistry data, acquired some of the UV-visible data, acquired all luminescence and vibrational data, performed flow battery characterization, participated in collection of crystal structures, MCD, and EPR spectra, analyzed most of the data, and along with the other authors, wrote the manuscript.

Chapter 6:
Ngo, D. X.; Del Ciello, S. A.; Barth, A. T.; Hadt, R. G.; Grubbs, R. H.; Gray, H. B.; **McNicholas, B. J.** Electronic Structures, Spectroscopy, and Electrochemistry of $[M(diimine)(CN\text{-}BR_3)_4]^{2-}$ (M = Fe, Ru; R = Ph, C_6F_5) Complexes. *Inorg. Chem.* **2020**, submitted.

- B.J.M mentored D.X.N. and contributed to the idea for this project, acquired about half of the electrochemistry data, performed all theoretical calculations, analyzed much of the data, and along with the other authors, wrote the manuscript.

Adapted with permission from Ngo, D.; Del Ciello, S. A.; **McNicholas, B. J.**; Sanders, B. C.; Fajardo Jr., J.; Gray, H. B.; Winkler, J. R. Cyano-Ambivalence: Spectroscopy and Photophysics of $[Ru(diimine)(CN\text{-}BR_3)_4]^{2-}$. *Polyhedron* **2020**, accepted, invited contribution.

- B.J.M. mentored D.X.N., acquired some of the luminescence spectra, performed some of the data analysis, and assisted J.R.W. in writing the manuscript.

Chapter 7:

McNicholas, B. J.; Oyala, P. H.; Nie, C.; Grubbs, R. H.; Gray, H. B. Cobalt(II) and Cobalt(III) Boronated Cyanometallates: Synthesis, Electronic Structure, and EPR Spectroscopy. **2020**, in preparation.

- B.J.M. conceived the idea for the project, synthesized the complexes, acquired all electrochemistry data, participated in collection of EPR data, acquired all other spectroscopic data, performed all theoretical calculations, performed half of the data analysis, and in collaboration with P.H.O., wrote the manuscript.

TABLE OF CONTENTS

LIST OF FIGURES

Chapter 1

Chapter 2

Chapter 3

Chapter 4

Chapter 5

Chapter 6

Chapter 7

LIST OF TABLES

Chapter 1

Chapter 2

Chapter 3

Chapter 4

Chapter 5

Chapter 6

Chapter 7

NOMENCLATURE

(2,4,6-$F_3C_6H_2$)$_3$B Tris(*2,4,6*-trifluorophenyl)borane

2-MeTHF. 2-methyltetrahydrofuran

$AsPh_4$. Tetraphenylarsonium

BCF / $B(C_6F_5)_3$. Tris(pentafluorophenyl)borane

BMIm-TFSI. 1-Butyl-3-methylimidazolium bis(trifluoromethyl)sulfonylimide

BPh_3. Triphenylborane

bpy. 2,2'-bipyridine

BuCN. Butyronitrile

CASSCF. Complete active space self-consistent field

$CoCp_2^+$

DFT. Density functional theory

DMF Dimethylformamide

DMSO. Dimethylsulfoxide

***$E^{0'}$*/*E^0*.** Formal potential

E^0. Standard reduction potential

***$E_{1/2}$*.** Half-wave potential

EMIm-$EtOSO_3$. 1-Ethyl-3-methylimidazolium ethylsulfate

EMIm-OTf. 1-Ethyl-3-methylimidazolium trifluoromethylsulfonate

EMIm-TCB. 1-Ethyl-3-methylimidazolium tetracyanoborate

Fc. Ferrocene

flpy 4,4'-bis(trifluoromethyl)bipyridine

HOMO. Highest occupied molecular orbital

IL Ionic liquid

LMCT. Ligand-to-metal charge transfer

LUMO. Lowest unoccupied molecular orbital

MCD. Magnetic circular dichroism

MeCN. Acetonitrile

MLCT. Metal-to-ligand charge transfer

NEVPT2. N-electron valence state perturbation theory, second order

phen. 1,10-Phenanothroline

PPh_4. Tetraphenylphosphonium

PPN. Bis(triphenylphosphine)iminium

TBA. Tetrabutylammonium

TEA. Tetraethylammonium

(tpfc)Mn 5,10,15-tri(pentafluorophenylcorrole)Mn(III)

Chapter I

INTRODUCTION: AN OVERVIEW OF RELEVANT TECHNIQUES AND CONCEPTS

1.1 Overview

Given the scope and breadth of information covered in this thesis, this introduction is intended to give an overview of relevant concepts, techniques, and fields of chemistry that are discussed or employed throughout this document. The unifying theme throughout this thesis is the generation of novel electrolytic media which are capable of either electrochemical conversion or storage of energy as viewed through the lens of a physical inorganic chemist. The following sections provide succinct overviews of the benefits and challenges associated with use of ionic liquids as an alternative solvent, the current progress in electroreduction of CO_2 to produce value-added chemicals using heterogenized molecular electrocatalysts, the use of Lewis acids as modifiers of the ground-state and excited-state properties of transition metal cyanometallates, and the current thrust to develop highly-soluble, long-lived molecular species for non-aqueous redox flow batteries.

1.2 Ionic Liquids: Extreme Electrolyte Concentrations

Ionic liquids are molten salts which demonstrate high electrolyte concentrations due to the electrolyte being the solvent itself. The physical properties of ionic liquids have been extensively studied, with conductivity and stability studies demonstrating that ionic liquids exhibit comparable conductivity and polarity as non-aqueous solvents, suggesting their utility for a variety of electrochemical reactions. One of the first studies which demonstrated the ability of ionic liquids to act as viable solvents for electrochemical reactions was performed by Compton et al.[1] This publication demonstrated the diffusion-controlled voltammetry and electrochemical reversibility for cobaltocenium and ferrocene

when dissolved in a number of ionic liquids, including 1-butyl-3-methylimidazolium with bis(trifluoromethyl)sulfonylimide, triflate, nitrate, hexafluorophosphate, and tetrafluoroborate as anions and 1-ethyl-3-methylimidazolium with bis(trifluoromethyl)sulfonylimide as an anion. This study also established the non-additivity of Faradaic current and clear disparity in diffusion coefficients between oxidized and reduced species, a consequence of the high ionic concentration of ionic liquids.[2]

Analytical studies of a number of ionic liquids have also established the generally large electrochemical window available in ionic liquids.[3] One publication demonstrated the dramatic effect that water has on the electrochemical window, as shown in **Table 1.1**, an important aspect of these solvents for demanding catalytic reductions and oxidations.[4,5] In general, if water content is kept to a minimum, the electrochemical windows of these solvents exceed those of water and many non-aqueous solvents.

Table 1.1. Water content of atmospheric and vacuum-dried, room-temperature ionic liquids, as well as their Gutmann donor numbers and electrochemical solvent windows when vacuum-dried. Table adapted from Reference 3.

Solvent	Atmospheric Water Content (ppm)	Vacuum-Dried Water Content (ppm)	Donor Number	Solvent Window (V vs. $Fc^{+/0}$)
$[C_4mpyrr][NTf_2]$	406	133	---	−2.8-1.4
[HMIm][FAP]	417	203	---	−2.6-2.0
$[BMIm][NTf_2]$	491	144	10.2	−2.5-1.8
$[C_4dmim][NTf_2]$	504	295	---	−2.5-2.2
$[N_{6,2,2,2}][NTf_2]$	1150	167	---	−2.6-2.1
$[BMIm][PF_6]$	2119	268	---	−2.7-2.1
$[EMIm][NTf_2]$	3385	105	11.2	−2.2-2.0
$[BMIm][BF_4]$	5083	119	---	−2.6-2.0
[BMIm][I]	11349	1050	---	−2.0-0.0
[BMIm][OTf]	15227	250	20.5	−2.6-1.6

Aside from fundamental electrochemical and conductive properties, ionic liquids have also exhibited high solubilities for non-polar gases such as CO_2, which has been exploited for the electrocatalytic reduction of CO_2 by a variety of surfaces typically used in aqueous solution.[5,6,7,8,9,10] For example, the electrochemical reduction of CO_2 to CO occurred at an overpotential as low as 40 mV when catalyzed by MoO_2 in a mixture of MeCN and imidazolium-based ionic liquids, which the authors ascribe to the ionic liquid acting as a cocatalyst.[11] Another study demonstrated complexation of the CO_2^- intermediate by imidazolium cations in ionic liquids to lower the overpotential of ultimate reduction by a silver cathode.[10] Finally, an important study was published in 2014 on the electrocatalytic reduction of CO_2 in BMIm-TCB using $Re(bpy)(CO)_3Cl$, the prototypical molecular CO_2 reduction catalyst. This advance demonstrated the role of ionic liquids in minimizing the overpotential of reduction through cation stabilization.[12]

1.3 CO_2 Reduction: Current Status and Trends

Solar fuels continue to dominate the vast majority of alternative energy research due to the possibility of mitigating emissions from fossil fuel resources and generating energy-dense molecules using sunlight.[13] The ultimate goal is to design a spectroelectrochemical cathode capable of harnessing sunlight as a source of energy and pairing it with a photoanode to create a solar cell with the ability to run without an applied potential bias with a high solar to chemical energy conversion efficiency.[14] The photoanode facilitates solar excitation and oxidation of H_2O. The generated protons and electrons travel through a permeable membrane and circuity, respectively, to combine with CO_2 to generate liquid fuels and H_2O. Both processes are facilitated by semiconductor or metal electrodes, or heterogeneous molecular catalysts.

Molecular catalysis of reactions pertinent to the synthesis of liquid fuels and other single-carbon (C_1) building blocks from carbon dioxide (CO_2) is one of the most challenging problems in sustainable energy research today.[15,16,17,18,19] Though capable of producing small amounts of C_2 and C_3 products, heterogeneous catalysis at metal surfaces has been consistently plagued by a lack of selectivity in the carbon containing products.[20] For example, sixteen different products of CO_2 reduction by copper surfaces have been identified.[21] Some promising modifications, such as the use of copper nanoparticles on carbon, have increased the selectivity for methane to 80% of the total Faradaic efficiency.[22] Headway using Ni-Ga alloys has also been made, with generation of C_2 products occurring at lower overpotential than that required for Cu foil. Molecular electrocatalysts are more selective, but their use is precluded by issues of product stability and product separation.[23] Additionally, CO_2 reduction beyond 2 e^-, carbon monoxide (CO) and formic acid (HCO_2H), processes has been a challenge.[24] Many of the challenges associated with finding an efficient, inexpensive catalyst for CO_2 reduction arise as a result of the reactions and formal reduction potentials presented in **Table 1.2**.[25] The one-electron reduction of CO_2 is quite negative compared to the potentials for C_1 products. However, finding a catalyst which combines, for example, six protons and six electrons to selectively reduce CO_2 to methanol at low overpotential (η) is a formidable challenge. Selectivity is often diminished due to hydrogen production, which has a competitive reduction potential in neutral (pH = 7) media.

Another difficulty in the study of CO_2 reduction to higher order products is that the intermediates and mechanistic information involved in, for example, a six-to-twelve step mechanism are quite difficult to elucidate, hindering the rational design of catalysts for CO_2 reduction. To gain mechanistic insight, current efforts are focused on *operando* techniques, such as transient infrared absorption spectroscopy, differential electrochemical mass spectrometry, and surface Raman spectroscopy.[26]

Table 1.2. Reactions and standard reduction potentials of CO_2 to C_1 products. The formal potential of hydrogen production is shown for comparison.

Reaction	Formal Potential (V vs. NHE)
$CO_2 + e^- \rightarrow CO_2^{\bullet -}$	−1.90 V (in H_2O), -2.21 V (in aprotic media)
$CO_2 + 2H^+ + 2e^- \rightarrow CO + H_2O$	−0.53 V
$CO_2 + 2H^+ + 2e^- \rightarrow HCO_2H$	−0.61 V
$CO_2 + 4H^+ + 4e^- \rightarrow CH_2O + H_2O$	−0.48 V
$CO_2 + 6H^+ + 6e^- \rightarrow CH_3OH + H_2O$	−0.38 V
$CO_2 + 8H^+ + 8e^- \rightarrow CH_4 + 2H_2O$	−0.24 V
$2H^+ + 2e^- \rightarrow H_2$	−0.41 V

The electrolytic medium for CO_2 reduction catalysis can also present challenges. Due to the low solubility of CO_2 in H_2O ($H^{\phi} = 0.034$ M atm^{-1} at 298 K), constraints exist on limiting current densities obtainable for CO_2 reduction in aqueous media.[27] It is estimated that the maximum current density achievable in neutral, aqueous media is approximately 10 mA cm^{-2}. Therefore, it is necessary to find alternative strategies to improve current densities, and thus rates of product formation. One method for achieving higher rates of reduction is to use a medium with a greater concentration of CO_2.

While using Fischer-Tröpsch to reduce CO_2 to mixtures of CO and H_2 might increase the utility of catalysts that perform these reactions efficiently,[28] past discoveries of molecular and heterogeneous, polymerized catalysts with selectivity for formaldehyde and systems with stoichiometric selectivity for methane using "pre-activated" CO_2 and a supporting molecule have generated interest in leveraging inorganic complexes for molecular CO_2 reduction.[29,30] To date, use of these molecular catalysts in industry has often been precluded by implementation difficulties.

Attempts at heterogenization of molecular catalysts on electrode surfaces by covalent or non-covalent interactions have achieved some success, with many systems producing stable catalysis for only hours to days. Blakemore et al. demonstrated non-covalent immobilization of a pyrene-appended analogue of $Re(bpy)(CO)_3Cl$ on highly-ordered pyrolytic graphite. Stable current density for reduction of CO_2 to CO was maintained for multiple hours.[31] However, as with many other immobilized catalysts, loss in activity occurred due to dissociation of catalyst from the electrode surface. Alternative strategies are therefore required for stabilizing molecular catalysts in the solid state to maximize efficiency and prevent catalyst decomposition.

$Re(bpy)(CO)_3Cl$ is one of the most studied molecular CO_2 reduction catalysts. It is selective for the production of CO over H_2, stable under catalytic conditions, and has a well-characterized mechanism. Additionally, previous reports have demonstrated enhanced activity of **1** in IL media.[12] Since the discovery of its activity for CO_2 reduction in 1984, numerous studies have been conducted on **1** and its analogues to elucidate the mechanism of CO_2 reduction and the reason for improved activity in the presence of a proton source.[32,33,34] It has been shown through X-ray crystallography, computational methods, and EXAFS that the active form of the catalyst is the doubly-reduced $Re^0(bpy^{\bullet-})(CO)_3$. X-ray crystallographic studies of $[Re(bpy\text{-}t\text{Bu})(CO)_3Cl][K(18\text{-crown-}6)(THF)]$ show significant lengthening of the C-C and C-N bonds in the bipyridine ligand, suggesting the presence of a ligand radical in the π^* orbital of the bpy ligand.[35] Stopped-flow kinetic studies have provided evidence that the five-coordinate complex binds CO_2 approximately 35 times faster than H^+. This selectivity can be justified by the qualitative orbital interactions shown in **Figure 1.1**,

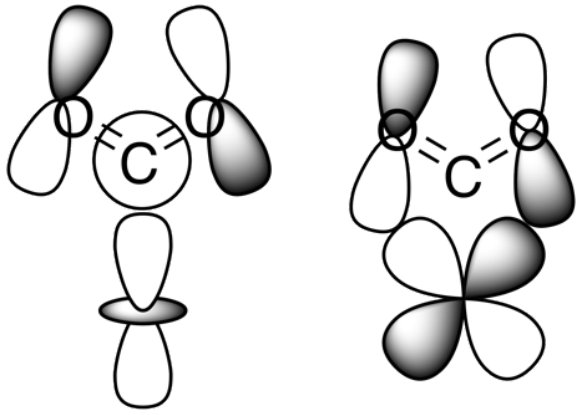

Figure 1.1. Orbital interactions for CO_2 with $Re^0(bpy^{\bullet-})(CO)_3$.

where the five-coordinate Re complex can participate in sigma and pi bonding with CO_2 versus sigma-only bonding with H^+, leading to a lower activation energy for CO_2 binding to $Re^0(bpy^{\bullet-})(CO)_3$.[35]

The currently accepted mechanism of CO_2 reduction by **1** is shown in **Figure 1.2**. The intermediates of this mechanism have been observed by stopped-flow kinetic studies, calculated using density functional theory (DFT), and supported with proton concentration dependence studies.[35,36]

In this mechanism, two-electron reduction of **1** and loss of chloride is followed by binding of CO_2 and a proton. An analogue to **1** is $Mn(bpy)(CO)_3Br$, and mechanistic studies of both catalysts have shown that $Mn(bpy)(CO)_3Br$ follows a protonation-first pathway, while **1** follows a reduction-first pathway. Upon reduction, an additional proton binds to the hydroxyl moiety, which then undergoes C-O bond cleavage to generate bound CO. An additional reduction causes CO to dissociate and regenerates the catalytically active form of the complex.[36] It has also been shown that CO_2 reduction by **1** does not require a discrete proton source, which is suggested to be due to sufficient stabilization of the carboxylate intermediate. In the absence of an added proton source, solvent or electrolyte can act as an oxide ion acceptor.[33] Many studies have also utilized secondary coordination sphere

interactions to tune the metal center towards higher activities, better selectivity, and/or longer lifetimes.

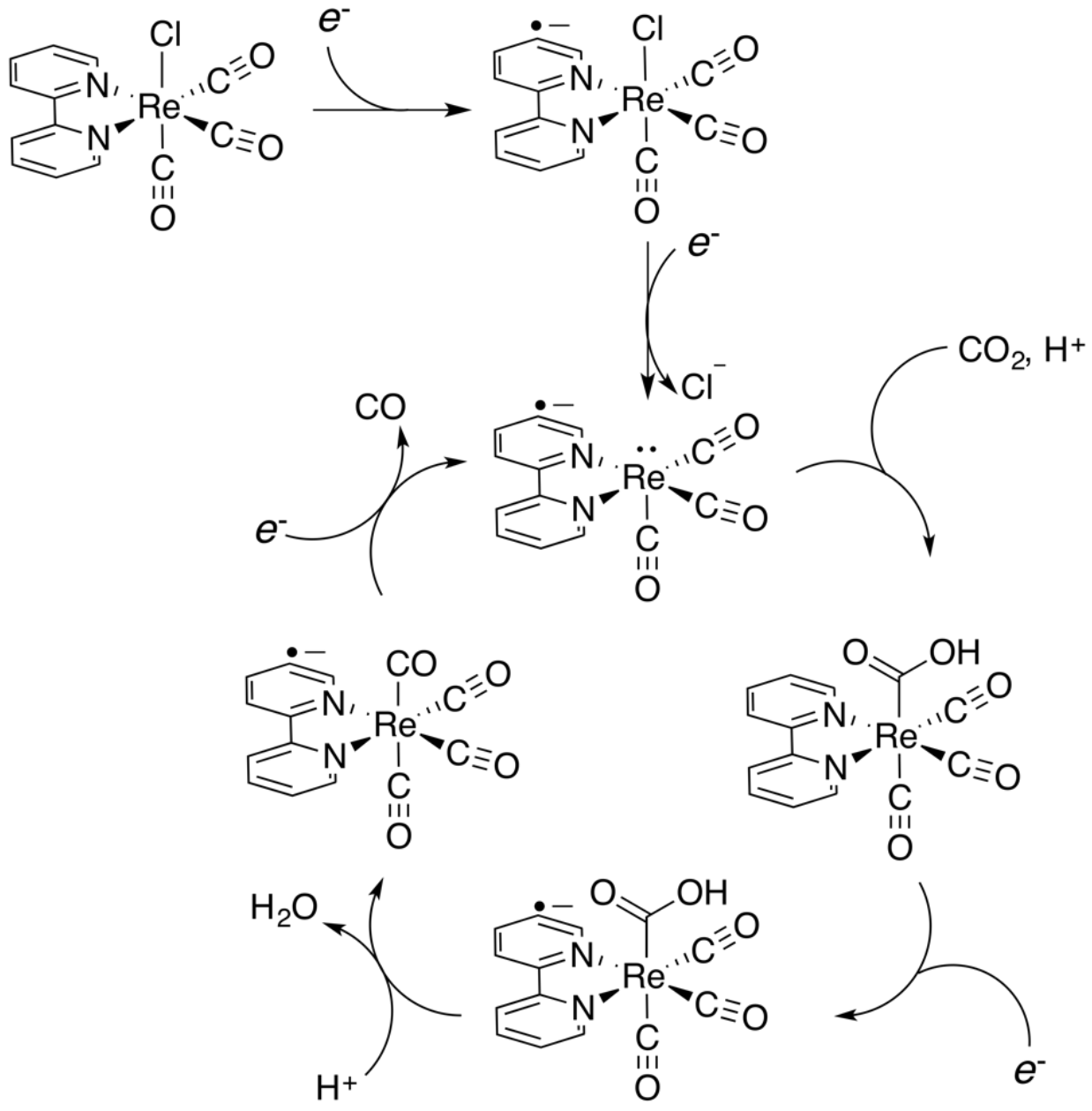

Figure 1.2. Currently accepted mechanism for the electrocatalytic reduction of CO_2 by $Re(bpy)(CO)_3Cl$. The mechanism follows a reduction-first pathway, where electron transfer to the complex occurs prior to C-O bond cleavage to generate H_2O.

1.4 Lewis Acid-Base Interactions in Organometallic Chemistry: History and Fundamentals

"We are inclined to think of substances as possessing acid or basic properties, without having a particular solvent in mind. It seems to me that with complete generality we may say that a basic substance is one which has a lone pair of electrons which may be used to complete the stable group of another atom, and that an acid substance is one which can employ a lone pair from another molecule in completing the stable group of one of its own atoms. In other words, the basic substance furnishes a pair of electrons for a chemical bond, the acid substance accepts such a pair."

Lewis, G. N. *Valence and the Structure of Atoms and Molecules*, 1st edition; The Chemical Catalog Company, Inc.: New York, 1923; p. 142.

A spectrum of Lewis acid-base interactions, ranging from frustrated Lewis pairs to solvent interactions to full dative bond formation, have been exploited in the literature for a number of different applications. The first example of boranes as Lewis acids for dative bond formation with cyanometallates was reported by Duward Shriver in 1962. Since then, the Lewis acid modification of electrophilic ligands as secondary sphere modifications of transition metal complexes has become a standard in the field. For example, the use of secondary sphere proton shuttles and modifiers of reduction and oxidation potentials for small molecule electrocatalysts has become standard practice.[37,38,39]

Boranes as neutral Lewis acids for dative bonds with cyanometallates were pioneered by Duward Shriver in the early 1960s. In his original study from 1962, he provided evidence for BF_3 coordination with $K_2Ni(CN)_4$, $K_4Fe(CN)_6$, and $K_4Mo(CN)_8$ by IR spectroscopy.[40] However, these bridge adducts displayed great instability to a number of both aprotic and protic solvents, suggesting the relative instability of B-F bonds and/or dative interactions of BF_3 to a number of conditions. However, the strength of bond to vacuum was purported to be quite strong, as evidenced by low-pressure experiments.[40] Another

important conclusion demonstrated from this work was the blueshift in the CN stretching frequency observed in infrared spectra. Soon after, in 1963, Shriver extended the concept of BF_3 coordination to cyanometallates with $Fe(phen)_2(CN)_2$. With the compounds originally studied, Shriver demonstrated by UV-Vis reflectance, absorption by mass, and IR spectroscopy the stoichiometry and characteristics of borane-appended cyanometallates. One particularly salient point made in this publication is the discussion of the charge-transfer spectrum of $Fe(phen)_2(CN)_2$, which displays a dramatic color change as a result of adduct formation with BF_3 that is consistent with a significant blueshift in the metal-to-ligand charge transfer spectra of the complex.[41] Extending these studies even further, in 1966, Shriver and Posner demonstrated the variable shift in IR frequencies and charge-transfer bands in borane adducts of $Fe(phen)_2(CN)_2$ depending on the Lewis acidity of the borane.[42] This study reported the first example of the effects of neutral Lewis acids on the formal potential of transition metal complexes, with BBr_3 exerting a more dramatic shift on the formal potential relative to BF_3, demonstrating the stronger Lewis acidity of BBr_3.

The Gutmann Donor and Acceptor model for solvents, first delineated in the 1970s, rationalizes the relative Lewis acid and Lewis base strengths of solvents towards dissolved substrates. Acceptor number values are measured by finding the ^{31}P-NMR shift of triethylphosphine oxide (Et_3PO with $SbCl_5$ in 1,2-dichloroethane is arbitrarily set to AN = 100), where solvents with greater electrophilicity will inductively withdraw a greater amount of electron density through oxygen.[43]

In the 1970s, Gutmann published detailed studies on the formal potential of both hexacyanoferrate(III/II) and hexacyanomanganate(IV/III/II) in a variety of protic and aprotic solvents.[44,45,46] His studies demonstrated that the formal potentials for both hexacyanoferrate and

hexacyanomanganate could be tuned over a 1.9 V range simply through judicious choice of solvent, as shown in **Table 1.3**. An approximately linear correlation is found for the formal potential of the Fe(III/II) redox couple and the acceptor number of the solvent, with small variations due to dielectric constant and solvation effects. These studies laid the groundwork for a more definitive understanding of the effects of both dielectric constant and donor-acceptor interactions on the ground-state electronic properties of cyanometallates and provided a unifying theory for the effects of donor-acceptor interactions of solvents on the reactivity of small molecules. The Gutmann donor-acceptor has since been verified by a variety of solvent-dependence studies for both chemical and electrochemical reactions. One interesting comment made in the original publications by Gutmann mentioned the inability to boronate $[Fe(CN)_6]^{3-}$ with BF_3, despite the success that Shriver experienced with $[Fe(CN)_6]^{4-}$.

Table 1.3. Formal potentials for $(TBA)_3[Fe(CN)_6]$ in aprotic and protic solvents with varying dielectric constants and acceptor numbers. All voltammetry was acquired with 0.1 M $TBAClO_4$ as the electrolyte. Table adapted from References [46,44,47,48]

Solvent	Formal Potential (V vs. $Fc^{+/0}$)	Dielectric Constant	Acceptor Number
N-Methylpyrrolidinone (NMP)	−1.75	32.0	13.3
N,N-Dimethylformamide	−1.72	36.1	16.0
Acetonitrile	−1.54	38.0	18.9
Dimethylsulfoxide	−1.51	45.0	19.3
N,N-Dimethylthioformamide	−1.48	51.2	18.8
1,2-Dichloroethane	−1.43	10.1	16.7
Propylene carbonate	−1.32	69.0	18.3
Nitromethane	−1.26	35.9	20.5
Ethanol	−0.88	24.3	37.9
Methanol	−0.74	32.6	41.5
Acetic Acid	0.15	6.2	52.9

In the 1980s, Woodcock and Shriver extended the concept of Lewis acid coordination to heteroleptic cyanometallates ($CpFe(CO)_2CN$ and $Fe(phen)_2(CN)_2$) through solvation in an acidic molten salts.[49] These studies also preface the use of ionic liquids for electrochemical and energy-related applications. In the $AlCl_3$ melt, $Fe(phen)_2(CN)_2$ demonstrates dramatic color changes and blueshifted MLCT transition maxima and CN stretching frequencies.

Following the studies by Shriver, little research was reported on the incorporation of boranes with cyanometallates. In 2001, Bochmann et al. reported the use of tris(pentafluorophenyl)borane as a Lewis acid with tetracyanonickelate and tetracyanopallidate to generate non-coordinating anions for dramatically improved metallocene polymerization catalysts.[50] These studies demonstrate the greatly improved activity of polymerization catalysts as a result of stabilizing the negative charge of the counterion.

Beyond non-coordinating anions and fundamental Lewis acid coordination and its effect on spectroscopic properties, other studies have demonstrated that boranes can induce the structural rearrangement of cyanometallate species to generate the thermodynamically favored product. In 2005, Dunbar et al. demonstrated that coordination of BPh_3 to $[Cr(CN)_6]^{3-}$ at elevated temperatures results in isomerization of the cyanometallate complex to a nitrile complex, suggesting the variable ligand field strength of cyanide.

Since 2014, multiple studies by Ko et al. have demonstrated the utility of Lewis acid coordination on the modification of formal potentials and luminescence spectroscopy for heteroleptic cyanometallates to generate longer-lived phosphorescent species and modified electronic structures. In 2014, Ko et al.

characterized derivatives of $Re(phen)(CO)_3(CN)$ appended with $B(C_6F_5)_3$, which exhibited improved quantum yields and electrochemical properties as a result of boronation.[51] These reports were followed up by characterization of $Os(bpy)_2(CN)_2$ and its derivatives with BPh_3 and $B(C_6F_5)_3$.[52] These complexes also extended the concept of blueshifting MLCTs and increasing lifetimes in heteroleptic cyanometallate complexes through boronation. Other studies have shown this effect in heteroleptic Ir(III) and Cu(I) diimine complexes, demonstrating the universality of modification of cyanometallates using boranes.[53,54]

Despite multiple studies demonstrating borane coordination to cyanometallates, the field is underdeveloped, and previous research provides significant fodder for the utilization of boranes to modify the ground- and excited-state electronic properties of both homoleptic and heteroleptic cyanometallates.

1.5 Redox Flow Batteries: From Aqueous to Non-Aqueous

Flow batteries are batteries in which the charge carriers, the catholyte and anolyte, are dissolved in solution, thereby decoupling the power output and capacity of the battery. The catholyte and anolyte are flowed over polarized electrodes and oxidized or reduced while electrolyte migrates across either an ion-

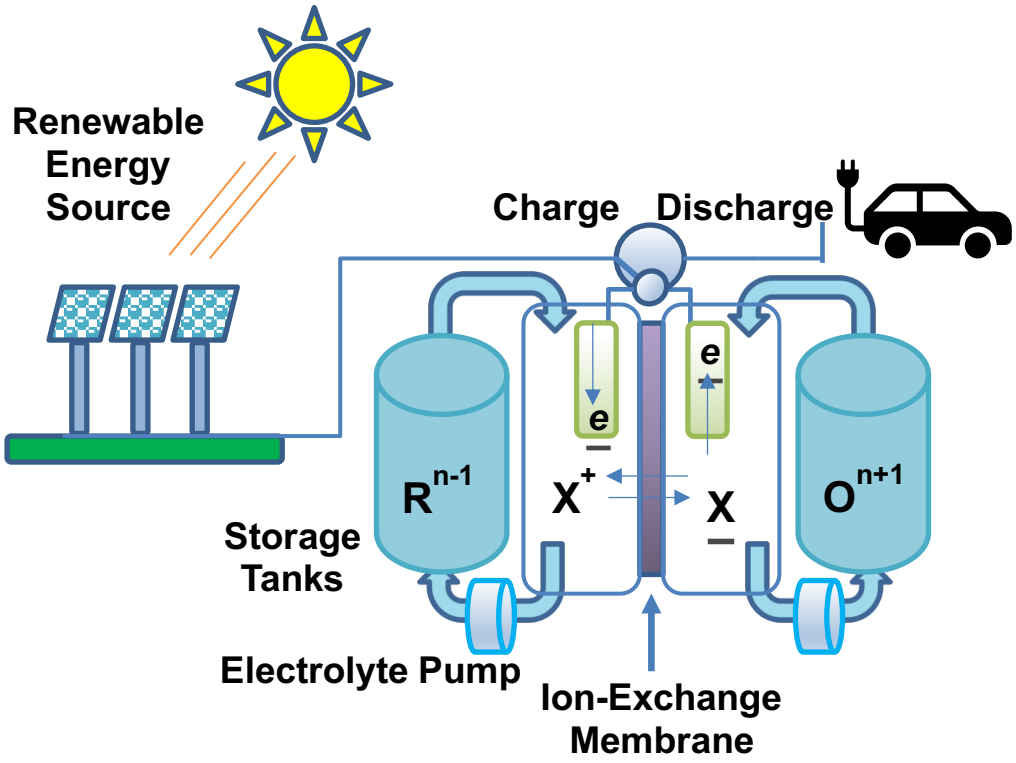

Figure 1.3. Operating principle of a redox flow battery. Light energy from the sun is captured by a photovoltaic array, converted to electrical energy, and used to charge the flowing catholyte and anolyte, which is then stored in large chambers and allowed to discharge when energy is needed.

exchange or a porous membrane to balance charge. The electrodes are connected to bipolar plates and current collectors that connect to an external circuit. The Department of Energy's Office of Electricity has identified flow batteries as key technology for grid scale energy storage. Flow batteries comprise less than 5% of today's battery market due to low energy density systems and higher $/kWh costs for the

current state of the art, primarily aqueous all-vanadium or zinc-bromine flow batteries.[55] However, these systems exhibit low volumetric energy densities and require expensive ion-exchange membranes.[56] Despite great strides in flow battery technology, greater energy densities and improved lifetimes are required to make these batteries commercially viable.

One way to move towards this goal is to use non-aqueous media, which benefit from greater voltage windows, thus increasing theoretical energy densities. Current non-aqueous redox flow battery technology is plagued with a variety of problems, including charge carrier decomposition (ligand dissociation, reaction with solvent),[57] speciation at the electrode surface due to a mismatch in solubility in the charged or discharged state of the battery, species crossover at the membrane,[58] and low voltage efficiencies due to high overpotentials stemming from resistance at ion-exchange membrane interfaces.[59] Aside from technical challenges of stability and scalability, there are a limited number of non-aqueous solvents that are useful for flow batteries due to flammability, recyclability, and ecotoxicity.[60,61]

Some particularly noteworthy examples of non-aqueous redox flow batteries have been reported in the literature in the past few years. One study utilized cobalt and vanadium trimetaphosphate complexes which demonstrated excellent cycling stability and high Coulombic and voltage efficiencies.[62] Other studies have used tris(bipyridine) complexes, polymeric ferrocene complexes, and phthalocyanines and porphyrins as redox-active species.[63,64,65] One of the particularly exciting aspects of the porphyrin-based redox flow battery in dichloromethane is the relatively high efficiency of the battery even at incredibly low temperatures.[64]

1.6 Chapter Summaries

Chapter 2 demonstrates one of the first examples of ionic liquid voltammetry of a molecular species, namely (tpfc)Mn, and its electron transfer reactivity in ionic liquids with varying solvent viscosity, effective electrolyte concentration, and donor strength. As well as showing the non-unity diffusional properties of molecular species in ionic liquids and the capability of ionic liquid anions to coordinate to molecular species, these studies suggest the viability of ionic liquids as conductive media for energy storage and conversion.

Chapter 3 introduces methods for immobilization of molecular catalysts in polymeric ion gels, a general strategy that bridges the divide between homogeneous solution-state catalysis and heterogeneous solid-state catalysis. These results provide insight into how environment, catalyst concentration, catalyst mobility, substrate availability, and dielectric properties of a medium all affect the catalytic response and overpotential for CO_2 reduction. Further implementation of these ion gel composites in solid-state devices, in aqueous environments, and in gas diffusion electrodes is also discussed.

In **Chapter 4**, a brief overview of the use of boranes as capping ligands for cyanide is provided. The synthesis, electronic properties, and theoretical calculations of homoleptic, boronated Fe(II) hexacyanoferrates are reported. Addition of borane to cyanometallates dramatically alters electronic structures and is a novel method for permanent modification of formal potentials while simultaneously maintaining or improving electrochemical reversibility and ambient stability. These complexes are characterized and studied by cyclic and differential pulse voltammetry, UV-vis, IR, and Raman spectroscopy, and flash-quench photolysis.

Chapter 5 extends the unique reactivity of borane adducts to the characterization of a full series of hexaisocyanoboratometallates (Cr, Mn, Fe, Ru, Os), compounds which demonstrate the concept of cyanide as a "variable-field" ligand, including magnetic circular dichroism spectroscopy, electron paramagnetic spectroscopy, luminescence studies, excited-state lifetime studies, and electrochemistry. As electrolytes for non-aqueous redox flow batteries, these species exhibit excellent Coulombic and voltage efficiencies and fast electron transfer rates. The highly oxidizing species will also find use as reversible oxidants for chemical oxidations.

Chapter 6 extends the concept of modifying formal potentials to heteroleptic cyanometallates (M = Fe, Ru) with diimine ligands (L = bipyridine, phenanthroline, 4,4'-trifluoromethylbipyridine). These species are shown to be potent excited-state reductants and oxidants, strong and long-lived phosphors, and promising electrolytes for symmetric, non-aqueous redox flow batteries. CASSCF+NEVPT2 calculations corroborate general trends in both ligand field and MLCT transition energies based on the Gutmann-Beckett acceptor number of the solvent or the borane. These data also demonstrate improved excited-state lifetimes for borane-appended species, likely due to inhibition of non-radiative decay pathways.

Chapter 7 focuses on the generation of a solution stable, square pyramidal Co(II) species, which is studied by electrochemistry, UV-vis-NIR spectroscopy, X-band and Q-band CW EPR, and pulsed EPR techniques (HYSCORE, ENDOR). These studies demonstrate that boronation of cyanide differentially affects the energies of ligand field transitions based on π backbonding ability.

1.7 References

(1) Rogers, E. I.; Silvester, D. S.; Poole, D. L.; Aldous, L.; Hardacre, C.; Compton, R. G. Voltammetric Characterization of the Ferrocene|Ferrocenium and Cobaltocenium|Cobaltocene Redox Couples in RTILs. *J. Phys. Chem. C* **2008**, *112* (7), 2729–2735. https://doi.org/10.1021/jp710134e.

(2) Barrosse-Antle, L. E.; Bond, A. M.; Compton, R. G.; O'Mahony, A. M.; Rogers, E. I.; Silvester, D. S. Voltammetry in Room Temperature Ionic Liquids: Comparisons and Contrasts with Conventional Electrochemical Solvents. *Chem. Asian J.* **2010**, *5* (2), 202–230. https://doi.org/10.1002/asia.200900191.

(3) O'Mahony, A. M.; Silvester, D. S.; Aldous, L.; Hardacre, C.; Compton, R. G. Effect of Water on the Electrochemical Window and Potential Limits of Room-Temperature Ionic Liquids. *J. Chem. Eng. Data* **2008**, *53* (12), 2884–2891. https://doi.org/10.1021/je800678e.

(4) Alvarez-Guerra, M.; Albo, J.; Alvarez-Guerra, E.; Irabien, A. Ionic Liquids in the Electrochemical Valorisation of CO_2. *Energy Environ. Sci.* **2015**, *8* (9), 2574–2599. https://doi.org/10.1039/C5EE01486G.

(5) Cadena, C.; Anthony, J. L.; Shah, J. K.; Morrow, T. I.; Brennecke, J. F.; Maginn, E. J. Why Is CO_2 So Soluble in Imidazolium-Based Ionic Liquids? *J. Am. Chem. Soc.* **2004**, *126* (16), 5300–5308. https://doi.org/10.1021/ja039615x.

(6) Lei, Z.; Dai, C.; Chen, B. Gas Solubility in Ionic Liquids. *Chem. Rev.* **2014**, *114* (2), 1289–1326. https://doi.org/10.1021/cr300497a.

(7) Mahurin, S. M.; Hillesheim, P. C.; Yeary, J. S.; Jiang, D.; Dai, S. High CO_2 Solubility, Permeability and Selectivity in Ionic Liquids with the Tetracyanoborate Anion. *RSC Adv.* **2012**, *2* (31), 11813. https://doi.org/10.1039/c2ra22342b.

(8) Sun, L.; Ramesha, G. K.; Kamat, P. V.; Brennecke, J. F. Switching the Reaction Course of Electrochemical CO_2 Reduction with Ionic Liquids. *Langmuir* **2014**, *30* (21), 6302–6308. https://doi.org/10.1021/la5009076.

(9) Makino, T.; Kanakubo, M.; Masuda, Y.; Mukaiyama, H. Physical and CO_2-Absorption Properties of Imidazolium Ionic Liquids with Tetracyanoborate and Bis(Trifluoromethanesulfonyl)Amide Anions. *J. Solut. Chem.* **2014**, *43* (9–10), 1601–1613. https://doi.org/10.1007/s10953-014-0232-x.

(10) Rosen, B. A.; Salehi-Khojin, A.; Thorson, M. R.; Zhu, W.; Whipple, D. T.; Kenis, P. J. A.; Masel, R. I. Ionic Liquid-Mediated Selective Conversion of CO_2 to CO at Low Overpotentials. *Science* **2011**, *334* (6056), 643–644. https://doi.org/10.1126/science.1209786.

(11) Oh, Y.; Hu, X. Ionic Liquids Enhance the Electrochemical CO_2 Reduction Catalyzed by MoO_2. *Chem. Commun.* **2015**, *51* (71), 13698–13701. https://doi.org/10.1039/C5CC05263G.

(12) Grills, D. C.; Matsubara, Y.; Kuwahara, Y.; Golisz, S. R.; Kurtz, D. A.; Mello, B. A. Electrocatalytic CO_2 Reduction with a Homogeneous Catalyst in Ionic Liquid: High Catalytic Activity at Low Overpotential. *J. Phys. Chem. Lett.* **2014**, *5* (11), 2033–2038. https://doi.org/10.1021/jz500759x.

(13) Gray, H. B. Powering the Planet with Solar Fuel. *Nat. Chem.* **2009**, *1* (1), 7–7. https://doi.org/10.1038/nchem.141.

(14) Berardi, S.; Drouet, S.; Francàs, L.; Gimbert-Suriñach, C.; Guttentag, M.; Richmond, C.; Stoll, T.; Llobet, A. Molecular Artificial Photosynthesis. *Chem. Soc. Rev.* **2014**, *43* (22), 7501–7519. https://doi.org/10.1039/C3CS60405E.

(15) Savéant, J.-M. Molecular Catalysis of Electrochemical Reactions. Mechanistic Aspects. *Chem. Rev.* **2008**, *108* (7), 2348–2378. https://doi.org/10.1021/cr068079z.

(16) Benson, E. E.; Kubiak, C. P.; Sathrum, A. J.; Smieja, J. M. Electrocatalytic and Homogeneous Approaches to Conversion of CO_2 to Liquid Fuels. *Chem. Soc. Rev.* **2009**, *38* (1), 89–99. https://doi.org/10.1039/B804323J.

(17) Appel, A. M.; Bercaw, J. E.; Bocarsly, A. B.; Dobbek, H.; DuBois, D. L.; Dupuis, M.; Ferry, J. G.; Fujita, E.; Hille, R.; Kenis, P. J. A.; Kerfeld, C. A.; Morris, R. H.; Peden, C. H. F.; Portis, A. R.; Ragsdale, S. W.; Rauchfuss, T. B.; Reek, J. N. H.; Seefeldt, L. C.; Thauer, R. K.; Waldrop, G. L. Frontiers, Opportunities, and Challenges in Biochemical and Chemical Catalysis of CO_2 Fixation. *Chem. Rev.* **2013**, *113* (8), 6621–6658. https://doi.org/10.1021/cr300463y.

(18) Costentin, C.; Robert, M.; Savéant, J.-M. Catalysis of the Electrochemical Reduction of Carbon Dioxide. *Chem. Soc. Rev.* **2013**, *42* (6), 2423–2436. https://doi.org/10.1039/C2CS35360A.

(19) Sampson, M. D.; Froehlich, J. D.; Smieja, J. M.; Benson, E. E.; Sharp, I. D.; Kubiak, C. P. Direct Observation of the Reduction of Carbon Dioxide by Rhenium Bipyridine Catalysts. *Energy Environ. Sci.* **2013**, *6* (12), 3748. https://doi.org/10.1039/c3ee42186d.

(20) Yoshio, H.; Katsuhei, K.; Shin, S. Production of CO and CH_4 in Electrochemical Reduction of CO_2 at Metal Electrodes in Aqueous Hydrogencarbonate Solution. *Chem. Lett.* **1985**, *14* (11), 1695-1698.

(21) Kuhl, K. P.; Cave, E. R.; Abram, D. N.; Jaramillo, T. F. New Insights into the Electrochemical Reduction of Carbon Dioxide on Metallic Copper Surfaces. *Energy Environ. Sci.* **2012**, *5*, 7050-7059.

(22) Manthiram, K.; Beberwyck, B. J.; Alivisatos, A. P. Enhanced Electrochemical Methanation of Carbon Dioxide with a Dispersible Nanoscale Copper Catalyst. *J. Am. Chem. Soc.* **2014**, *136* (38), 13319–13325. https://doi.org/10.1021/ja5065284.

(23) Torelli, D. A.; Francis, S. A.; Crompton, J. C.; Javier, A.; Thompson, J. R.; Brunschwig, B. S.; Soriaga, M. P.; Lewis, N. S. Nickel–Gallium-Catalyzed Electrochemical Reduction of CO_2 to Highly Reduced Products at Low Overpotentials. *ACS Catal.* **2016**, *6* (3), 2100–2104. https://doi.org/10.1021/acscatal.5b02888.

(24) Kumar, B.; Asadi, M.; Pisasale, D.; Sinha-Ray, S.; Rosen, B. A.; Haasch, R.; Abiade, J.; Yarin, A. L.; Salehi-Khojin, A. Renewable and Metal-Free Carbon Nanofibre Catalysts for Carbon Dioxide Reduction. *Nat. Commun.* **2013**, *4* (1), 2819. https://doi.org/10.1038/ncomms3819.

(25) Reaction Mechanisms in Carbon Dioxide Conversion. 10.1007/978-3-662-46831-9.

(26) Grills, D. C.; Farrington, J. A.; Layne, B. H.; Lymar, S. V.; Mello, B. A.; Preses, J. M.; Wishart, J. F. Mechanism of the Formation of a Mn-Based CO_2 Reduction Catalyst Revealed by Pulse Radiolysis with Time-Resolved Infrared Detection. *J. Am. Chem. Soc.* **2014**, *136* (15), 5563–5566. https://doi.org/10.1021/ja501051s.

(27) Chen, Y.; Lewis, N. S.; Xiang, C. Operational Constraints and Strategies for Systems to Effect the Sustainable, Solar-Driven Reduction of Atmospheric CO_2. *Energy Environ. Sci.* **2015**, *8* (12), 3663–3674. https://doi.org/10.1039/C5EE02908B.

(28) Underwood, A. J. V. Industrial Synthesis of Hydrocarbons from Hydrogen and Carbon Monoxide. *Ind. Eng. Chem.* **1940**, *32* (4), 449–454. https://doi.org/10.1021/ie50364a002.

(29) Luca, O. R.; McCrory, C. C. L.; Dalleska, N. F.; Koval, C. A. The Selective Electrochemical Conversion of Preactivated CO_2 to Methane. *J. Electrochem. Soc.* **2015**, *162* (7), H473–H476. https://doi.org/10.1149/2.0371507jes.

(30) Bontemps, S.; Vendier, L.; Sabo-Etienne, S. Ruthenium-Catalyzed Reduction of Carbon Dioxide to Formaldehyde. *J. Am. Chem. Soc.* **2014**, *136* (11), 4419–4425. https://doi.org/10.1021/ja500708w.

(31) Blakemore, J. D.; Gupta, A.; Warren, J. J.; Brunschwig, B. S.; Gray, H. B. Noncovalent Immobilization of Electrocatalysts on Carbon Electrodes for Fuel Production. *J. Am. Chem. Soc.* **2013**, *135* (49), 18288–18291. https://doi.org/10.1021/ja4099609.

(32) Hawecker, J.; Lehn, J.-M.; Ziessel, R. Photochemical and Electrochemical Reduction of Carbon Dioxide to Carbon Monoxide Mediated by (2, 2'-Bipyridine)Tricarbonylchlororhenium(I) and Related Complexes as Homogeneous Catalysts. *Helv. Chim. Acta* **1986**, *69*, 1990-2012.

(33) Sullivan, B. P.; Bolinger, C. M.; Conrad, D.; Vining, W. J.; Meyer, T. J. One- and Two-Electron Pathways in the Electrocatalytic Reduction of CO_2 by fac-Re(bpy)$(CO)_3$Cl (bpy = 2,2'-Bipyridine). *J. Chem. Soc., Chem. Commun.* **1985**, *20*, 1414-1416.

(34) Hawecker, J.; Lehn, J.-M.; Ziessel, R. Electrocatalytic Reduction of Carbon Dioxide Mediated by Re(bipy)$(CO)_3$Cl (bipy = 2,2'-Bipyridine). *J Chem. Soc., Chem. Commun.* **1984**, *6*, 328-330.

(35) Grice, K. A.; Kubiak, C. P. In *Advances in Inorganic Chemistry;* Aresta, M.; van Eldik, R. Elsevier: Oxford, U. K., 2014; 66, 163.

(36) Riplinger, C.; Sampson, M. D.; Ritzmann, A. M.; Kubiak, C. P.; Carter, E. A. Mechanistic Contrasts between Manganese and Rhenium Bipyridine Electrocatalysts for the Reduction of Carbon Dioxide. *J. Am. Chem. Soc.* **2014**, *136* (46), 16285–16298. https://doi.org/10.1021/ja508192y.

(37) Nichols, A. W.; Machan, C. W. Secondary-Sphere Effects in Molecular Electrocatalytic CO_2 Reduction. *Front. Chem.* **2019**, *7*, 397. https://doi.org/10.3389/fchem.2019.00397.

(38) Schmeier, T. J.; Dobereiner, G. E.; Crabtree, R. H.; Hazari, N. Secondary Coordination Sphere Interactions Facilitate the Insertion Step in an Iridium(III) CO_2 Reduction Catalyst. *J. Am. Chem. Soc.* **2011**, *133* (24), 9274–9277. https://doi.org/10.1021/ja2035514.

(39) Khosrowabadi Kotyk, J. F.; Hanna, C. M.; Combs, R. L.; Ziller, J. W.; Yang, J. Y. Intramolecular Hydrogen-Bonding in a Cobalt Aqua Complex and Electrochemical Water Oxidation Activity. *Chem. Sci.* **2018**, *9* (10), 2750–2755. https://doi.org/10.1039/C7SC04960A.

(40) Shriver, D. F. Bridge Adducts-the Interaction of BF_3 with Transition Metal Cyanide Complexes. *J. Am. Chem. Soc.* **1962**, *84* (23), 4610–4611. https://doi.org/10.1021/ja00882a061.

(41) Shriver, D. F. Preparation and Structures of Metal Cyanide-Lewis Acid Bridge Compounds. *J. Am. Chem. Soc.* **1963**, *85* (10), 1405–1408. https://doi.org/10.1021/ja00893a011.

(42) Shriver, D. F.; Posner, J. Bridge Addition Compounds. III. The Influence of Boron-Containing Lewis Acids on Electronic Spectra, Vibrational Spectra, and Oxidation Potentials of Some Iron-Cynanide Complexes. *J. Am. Chem. Soc.* **1966**, *88* (8), 1672–1677. https://doi.org/10.1021/ja00960a018.

(43) Gutmann, V. Solvent Effects on the reactivities of organometallic compounds. *Coord. Chem. Rev.* **1976**, *18*, 225-255.

(44) Gutmann, V.; Gritzner, G.; Danksagmüller, K. Solvent Effects on the Redox Potential of Hexacyanoferrate(III)-Hexacyanoferrate(II) *Inorganica Chim. Acta* **1976**, *17*, 81-86.

(45) Gritzner, G.; Danksagmüller, K. Gutmann, V. Solvent Effects on the Redox Potentials of Tetraethylammonium Hexacyanomanganate(III) and Hexacyanoferrate(III). *J. Electroanal. Chem. Interf. Electrochem.* **1978**, *90* (2), 203-210.

(46) Gritzner, G.; Danksagmüller, K. Gutmann, V. Outer-sphere coordination effects on the redox behaviour of the $Fe(CN)_6^{3-}$/ $Fe(CN)_6^{4-}$ couple in non-aqueous solvents. *J. Electroanal. Chem. Interf. Electrochem.* **1976**, *72* (2), 177-185.

(47) Gutmann, V. *The Donor Acceptor Approach to Molecular Interactions*; Springer US: New York, 1978.

(48) Mayer, U., Gutmann, V.; Gerger, W. The acceptor number — A quantitative empirical parameter for the electrophilic properties of solvents. *Monatshefte für Chemie* **1975**, *106*, 1235–1257. https://doi.org/10.1007/BF00913599

(49) Woodcock, C.; Shriver, D. F. Electrochemistry and Spectroscopy of Dicyanobis(Phenanthroline)Iron, Tetracarbonyltetrakis(Cyclopentadienyl)Tetrairon and Dicarbonylcyano(Cyclopentadienyl)Iron in an Acidic Molten Salt. *Inorg. Chem.* **1986**, *25* (13), 2137–2142. https://doi.org/10.1021/ic00233a008.

(50) Zhou, J.; Lancaster, S. J.; Walker, D. A.; Beck, S.; Thornton-Pett, M.; Bochmann, M. Synthesis, Structures, and Reactivity of Weakly Coordinating Anions with Delocalized Borate Structure: The Assessment of Anion Effects in Metallocene Polymerization Catalysts. *J. Am. Chem. Soc.* **2001**, *123* (2), 223–237. https://doi.org/10.1021/ja002820h.

(51) Chu, W.-K.; Ko, C.-C.; Chan, K.-C.; Yiu, S.-M.; Wong, F.-L.; Lee, C.-S.; Roy, V. A. L. A Simple Design for Strongly Emissive Sky-Blue Phosphorescent Neutral Rhenium Complexes: Synthesis,

Photophysics, and Electroluminescent Devices. *Chem. Mater.* **2014**, *26* (8), 2544–2550. https://doi.org/10.1021/cm4038654.

(52) Chu, W.-K.; Yiu, S.-M.; Ko, C.-C. Neutral Luminescent Bis(Bipyridyl) Osmium(II) Complexes with Improved Phosphorescent Properties. *Organometallics* **2014**, *33* (23), 6771–6777. https://doi.org/10.1021/om500630c.

(53) Chan, K.-C.; Chu, W.-K.; Yiu, S.-M.; Ko, C.-C. Synthesis, Characterization, Photophysics and Electrochemical Study of Luminescent Iridium(III) Complexes with Isocyanoborate Ligands. *Dalton Trans.* **2015**, *44* (34), 15135–15144. https://doi.org/10.1039/C5DT00904A.

(54) Chan, K.-C.; Cheng, S.-C.; Lo, L. T.-L.; Yiu, S.-M.; Ko, C.-C. Luminescent Charge-Neutral Copper(I) Phenanthroline Complexes with Isocyanoborate Ligand: Luminescent Charge-Neutral Copper(I) Phenanthroline Complexes with Isocyanoborate Ligand. *Eur. J. Inorg. Chem.* **2018**, *2018* (7), 897–903. https://doi.org/10.1002/ejic.201701205.

(55) Environmental Energy and Study Institute. Fact Sheet: Energy Storage (2019). https://www.eesi.Org/Papers/View/Energy-Storage-2019.

(56) Yang, Z.; Zhang, J.; Kintner-Meyer, M. C. W.; Lu, X.; Choi, D.; Lemmon, J. P.; Liu, J. Electrochemical Energy Storage for Green Grid. *Chem. Rev.* **2011**, *111*, 3577−3613.

(57) Saraidaridis, J. D.; Bartlett, B. M.; Monroe, C. W. Spectroelectrochemistry of Vanadium Acetylacetonate and Chromium Acetylacetonate for Symmetric Nonaqueous Flow Batteries. *J. Electrochem. Soc.* **2016**, *163*, A1239-A1246.

(58) Odom, S. Preventing Crossover in Redox Flow Batteries through Active Material Oligomerization. *ACS Cent. Sci.* **2018**, *4*, 140-141.

(59) Soloveichik, G. L. Flow Batteries: Current Status and Trends. *Chem. Rev.* **2015**, *115* (20), 11533–11558. https://doi.org/10.1021/cr500720t.

(60) Yu, I. K. M.; Tsang, D. C. W.; Yip, A. C. K.; Hunt, A. J.; Sherwood, J.; Shang, J.; Song, H.; Ok, Y. S.; Poon, C. S. Propylene carbonate and γ-valerolactone as green solvents enhance Sn(IV)-catalysed hydroxymethylfurfural (HMF) production from bread waste. *Green Chem.* **2018**, *20*, 2064-2074.

(61) Tang, S.; Zhao, H. Glymes as versatile solvents for chemical reactions and processes: from the laboratory to industry. *RSC Adv.* **2014**, *4*, 11251-11287.

(62) Stauber, J. M.; Zhang, S.; Gvozdik, N.; Jiang, Y.; Avena, L.; Stevenson, K. J.; Cummins, C. C. Cobalt and Vanadium Trimetaphosphate Polyanions: Synthesis, Characterization, and Electrochemical Evaluation for Non-Aqueous Redox-Flow Battery Applications. *J. Am. Chem. Soc.* **2018**, *140* (2), 538–541. https://doi.org/10.1021/jacs.7b08751.

(63) Hunt, C.; Mattejat, M.; Anderson, C.; Sepunaru, L.; Ménard, G. Symmetric Phthalocyanine Charge Carrier for Dual Redox Flow Battery/Capacitor Applications. *ACS Appl. Energy Mater.* **2019**, *2* (8), 5391–5396. https://doi.org/10.1021/acsaem.9b01317.

(64) Ma, T.; Pan, Z.; Miao, L.; Chen, C.; Han, M.; Shang, Z.; Chen, J. Porphyrin-Based Symmetric Redox-Flow Batteries towards Cold-Climate Energy Storage. *Angew. Chem. Int. Ed.* **2018**, 5.

(65) Lai, Y. Y.; Li, X.; Zhu, Y. Polymeric Active Materials for Redox Flow Battery Application. *ACS Appl. Polym. Mater.* **2020**, *2* (2), 113–128. https://doi.org/10.1021/acsapm.9b00864.

C h a p t e r I I

ELECTROCHEMISTRY IN IONIC LIQUIDS: CASE STUDY OF A MANGANESE CORROLE

Adapted with permission from McNicholas, B. J.; Blumenfeld, C.; Kramer, W. W.; Grubbs, R. H.; Winkler, J. R.; Gray, H. B. Electrochemistry in Ionic Liquids: Case Study of a Manganese Corrole. *Russ. J. Electrochem.* **2017**, *53*, 1189-1193. DOI: 10.1134/S1023193517100068.

2.1. Summary

Voltammetry of [5,10,15-tris(pentafluorophenylcorrole)]Mn(III) was investigated in four different ionic liquids (ILs): 1-butyl-3-methylimidazolium bis(trifluoromethylsulfonyl)imide (BMIm-TFSI); 1-ethyl-3-methylimidazolium ethylsulfate (EMIm-$EtOSO_3$); 1-ethyl-3-methylimidazolium triflate (EMIm-OTf); and 1-ethyl-3-methylimidazolium tetracyanoborate (EMIm-TCB). We found that $Mn^{IV/III}$ formal potentials depend on IL counter anion: $OTf^- < EtOSO_3^- < TFSI^- < TCB^-$. In EMIm-TCB and BMIm-TFSI, reversible, diffusion-controlled $Mn^{IV/III}$ reactions occurred, as evidenced in each case by the ratio of anodic to cathodic diffusion coefficients over a range of scan rates. Axial coordination was evidenced by a cathodic to anodic diffusion coefficient ratio greater than one, an increasing cathodic to anodic peak current ratio with increasing scan rate, and a split Soret band in the UV-vis spectrum of the complex.

2.2. Introduction

Ionic liquids (ILs) are green solvents that possess a wide range of tunable properties.[1] Owing to high viscosities, ILs retard diffusion of dissolved molecular species; and as salts, they typically have smaller diffusion coefficients than uncharged species.[2-4] Other IL properties include wide electrochemical potential windows and high conductivity, which contribute to the current interest in pursuing electrocatalytic and battery applications.[5] Of particular note is the high solubility of CO_2 in ILs, which has motivated research aimed at increasing their use as media for electrocatalytic CO_2 reduction.[6-8] With the exception of ferrocene and cobaltocenium, the electrochemical properties of metal complexes in neat ILs have not been investigated in depth.[3,9] **Figure 2.1** depicts the ionic liquids relevant to this study.

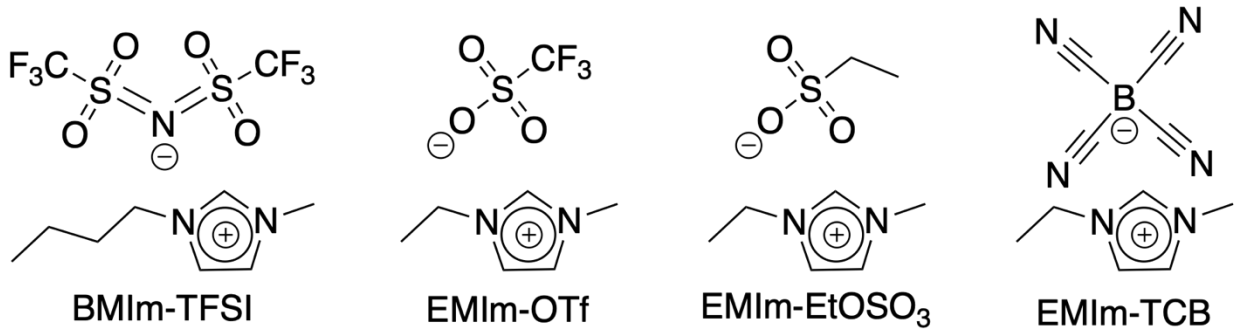

Figure 2.1. Chemical structures of the various ionic liquids used as redox-inactive electrolytes in this work.

Corroles are organic macrocycles that are structurally similar to porphyrins. As corroles are trianionic ligands, they stabilize higher valent metal centers than do porphyrin analogues.[10] The corrole cavity that the metal occupies is smaller than that of porphyrins, which likely has a role in reactivity pattern differences with substrates.[11] Importantly, metallocorroles are versatile oxygen and imido transfer reagents, as well as active electrocatalysts for CO_2, O_2, and H_2O_2 reduction reactions.[12-16]

Manganese corroles exhibit a wide range of accessible oxidation states.[17] The manganese metal center readily binds axial ligands, especially in higher oxidation states, a property that has been exploited in the catalysis of epoxidation, oxo-transfer, and nitride-transfer reactions.[18] In this tribute to Veniamin Grigorievich Levich, we report the results of our work on the voltammetry and UV-vis spectroscopy of (5,10,15-trispentafluorophenylcorrole)Mn(III) ((tpfc)Mn) in four different ILs.

2.3. Results and Discussion

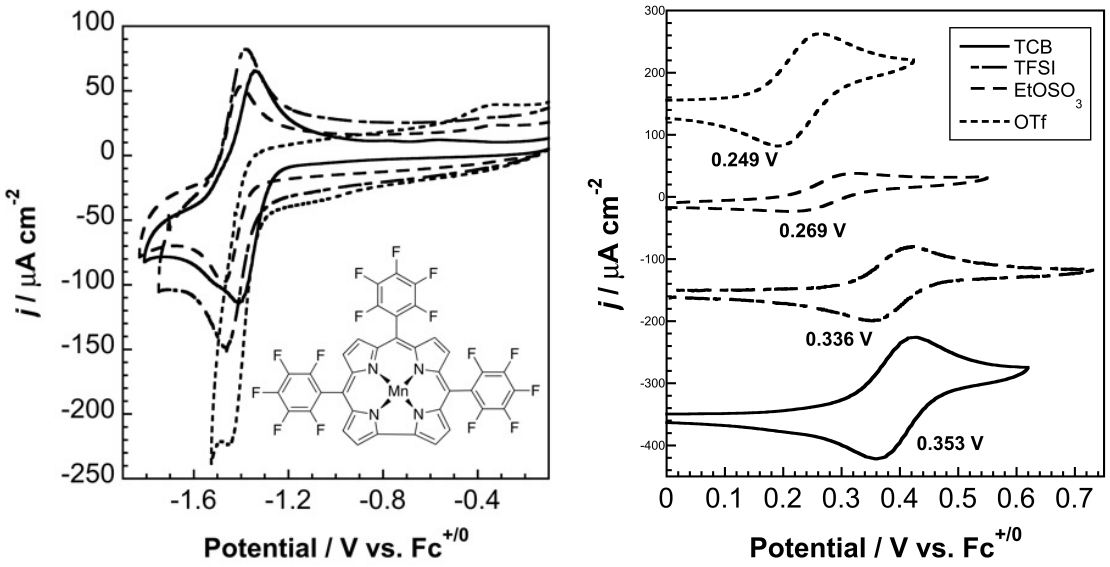

Figure 2.2. (Left) $Mn^{III/II}$ and (Right) $Mn^{IV/III}$ redox processes in ionic liquids with different anions. Inset: Structure of (tpfc)Mn. All scan rates were 100 mV s^{-1}. All potentials were referenced to $Fc^{+/0}$

We investigated four ionic liquids as solvents (EMIm-$EtOSO_3$, EMIm-OTf, EMIm-TCB, BMIm-TFSI). We thought it likely that IL anions would play a role in tuning (tpfc)$Mn^{IV/III}$ formal potentials, as there was an earlier report of $Mn^{IV/III}$ cathodic shifts upon addition of OAc^-, Cl^-, OH^-, and CN^-.[17] Additionally, axial coordination of Br^- to a Mn(III) corrole has been established by X-ray analysis.[19] Of interest is that the electronic ground states of five-coordinate Mn(III) corroles are high-spin (S = 2): in the case of a prototypal complex, (tfpc)Mn($OPPh_3$), the magnetic moment is 4.88 μ_B.[19,20]

Cyclic voltammograms of the $Mn^{IV/III}$ and $Mn^{III/II}$ redox couples of (tpfc)Mn are shown in **Figure 2.2** (formal potential values for the $Mn^{IV/III}$ oxidation and $Mn^{III/II}$ reduction of (tpfc)Mn in the four ILs are given in **Table 2.1**). Complete scan rate dependence data for all three redox events for (tpfc)Mn in BMIm-TFSI are given in **Figure 2.3**. We found that $Mn^{IV/III}$ formal potentials decrease in the order $OTf^- < EtOSO_3^- < TFSI^- < TCB^-$. It was surprising that (tpfc)Mn oxidation in EMIm-OTf occurred at lower potential than that in EMIm-EtOSO as, according to Schmeisser et al., ethylsulfate is a stronger donor than triflate (in ILs).[21]

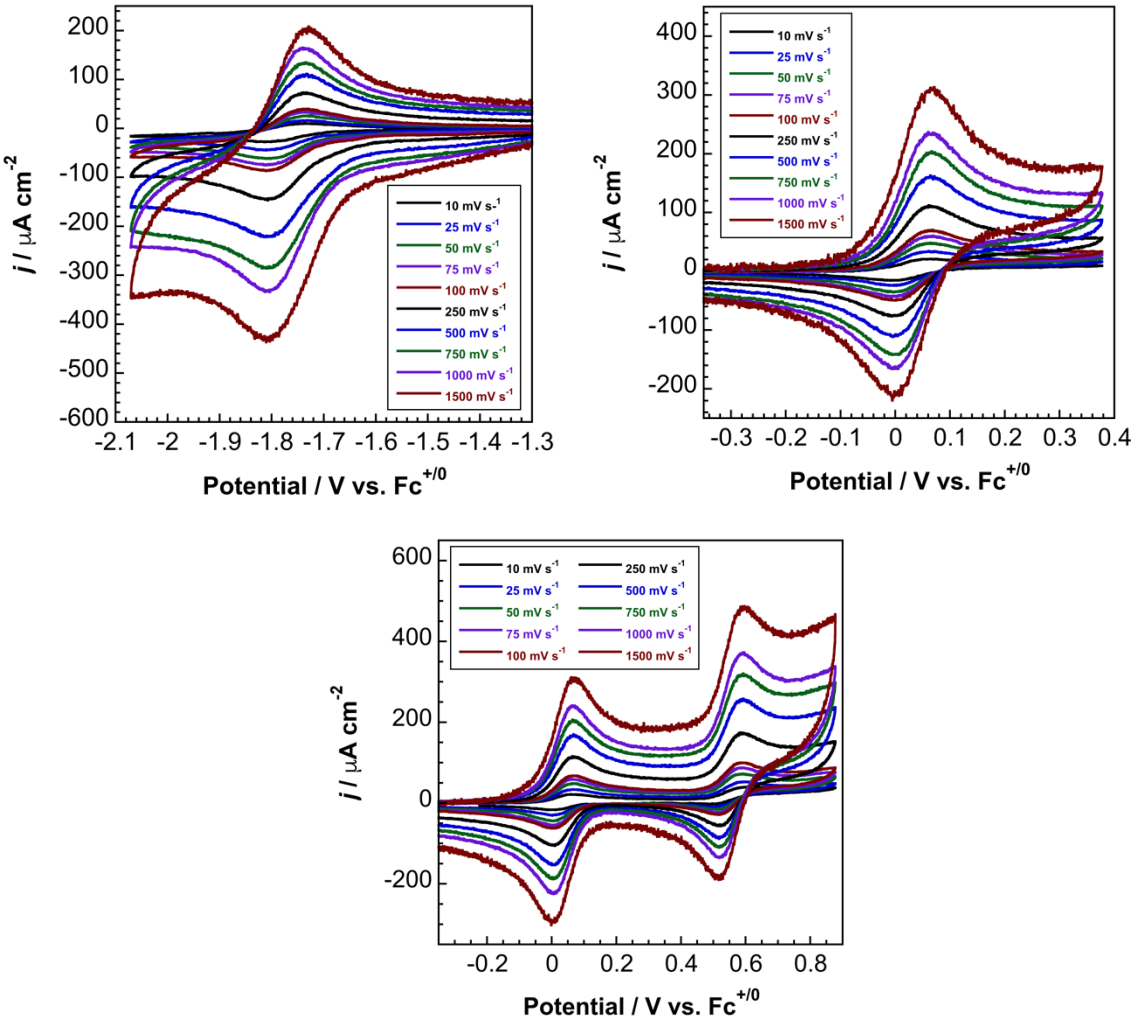

Figure 2.3. Scan rate dependence of the three redox couples of (tpfc)Mn in BMIm-TFSI. All potentials referenced to $Fc^{+/0}$.

Table 2.2 presents the peak-to-peak separations for each redox process, calculated by subtracting the peak anodic potential from the peak cathodic potential, and potential separations between the peak oxidation and reduction potentials, calculated by subtracting the formal reduction potential (or peak potential obtained from differential pulse voltammetry) from the formal oxidation potential, of (tpfc)Mn for each IL.

Redox Process	EMIm-TCB	EMIm-$EtOSO_3$	BMIm-TFSI	EMIm-OTf	MeCN
Reduction	−1.375 V	−1.423 V	−1.422 V	−1.458 V	−1.48 V
Oxidation	0.353 V	0.269 V	0.336 V	0.249 V	0.24 V

[a]Peak cathodic potential.

Table 2.1. Formal potentials for (tpfc)Mn in different ionic liquids. All potentials referenced to $Fc^{+/0}$.

Ionic Liquid	$\Delta E_{Reduction}$	$\Delta E_{Oxidation}$	ΔE_{Ox-Red}	Donor Strength (kcal mol^{-1})
EMIm-TCB	66 mV	69 mV	1.728 V	20.8
BMIm-TFSI	80 mV	68 mV	1.758 V	10.2
EMIm-$EtOSO_3$	72 mV	106 mV	1.692 V	22.3
EMIm-OTf	---	76 mV	1.630 V[a]	20.4

[a]Calculated using the peak potential obtained from differential pulse voltammetry.
[b]Reference 21.

Table 2.2. Peak-to-peak separations at 100 mV s^{-1} for (tpfc)Mn and donor strength of each ionic liquid.

The separations can be attributed to IL uncompensated resistance and/or viscosity, rather than electrochemical irreversibility of the electron transfer process, with $Mn^{IV/III}$ in EMIm-$EtOSO_3$ exhibiting the largest peak-to-peak difference. For reference, the peak-to-peak separation for $Fc^{+/0}$ in EMIm-$EtOSO_3$ is 85 mV at a scan rate of 0.1 V s^{-1}. The separation between the first oxidation and reduction peaks of (tpfc)Mn was found to depend on the extent of axial anion coordination to the complex, with smaller values an indication of stronger binding.[17,21]

The $Mn^{IV/III}$ redox couple has been shown to be electrochemically reversible.[17] To probe the effects of IL viscosity and anion binding strength on the electrochemical behavior of this couple, voltammetry at a range of scan rates was conducted; the Randles-Ševćik plots for (tpfc)Mn in each IL are displayed in **Figure 2.4**.[22] Diffusion coefficients were calculated using the Randles-Ševćik equation (**Equation 2.1**),

$$i_p = 0.4463 n^{3/2} F^{3/2} A C \sqrt{\frac{\nu D}{RT}} \quad (2.1)$$

where n is the number of electrons (n = 1 e^-), A is the electrode surface area (A = 0.0707 cm^2), D is the diffusion coefficient of the electroactive species ($cm^2\ s^{-1}$), ν is the scan rate ($V\ s^{-1}$), and C is the bulk concentration of analyte ($mol\ cm^{-3}$).[22] **Table 2.3** lists the anodic and cathodic diffusion coefficients for (tpfc)Mn in each IL.

Ionic Liquid	$D_{O,a}$ (10^{-12} $m^2\ s^{-1}$)	$D_{O,c}$ (10^{-12} $m^2\ s^{-1}$)	$D_{O,c}/D_{O,a}$	Ionic Liquid Viscosity (cP)
EMIm-TCB	7.9 ± 0.2	5.7 ± 0.2	0.7	20[a]
BMIm-TFSI	3.9 ± 0.2	3.2 ± 0.2	0.8	52[b]
EMIm-$EtOSO_3$	0.88 ± 0.1	1.1 ± 0.1	1.3	131[c]
EMIm-OTf	1.9 ± 0.7	3.8 ± 0.1	2.0	43[d]

[a]Reference 23 [b]Reference 24 [c]Reference 25 [d]Reference 26

Table 2.3 Anodic and cathodic diffusion coefficients of the $Mn^{IV/III}$ redox couple in each ionic liquid and their ratios. Values obtained from the first oxidation of the complex.

The diffusion coefficients obtained for the first oxidation of (tpfc)Mn vary substantially, owing to charge effects and viscosities of the ionic liquids.[23-26] Diffusion-controlled, electrochemically reversible electron transfer behavior was displayed by (tpfc)Mn in EMIm-TCB and BMIm-TFSI. In these ILs, the diffusion coefficient ratio was found to depend on the net charge and size of the complex as well as on the IL dynamic viscosity. The diffusion coefficient ratios for (tpfc)Mn(IV) for ILs EMIm-TCB and BMIm-

TFSI are very different from those for EMIm-$EtOSO_3$ and EMIm-OTf, suggesting that the latter complexes are axially ligated prior to oxidation.

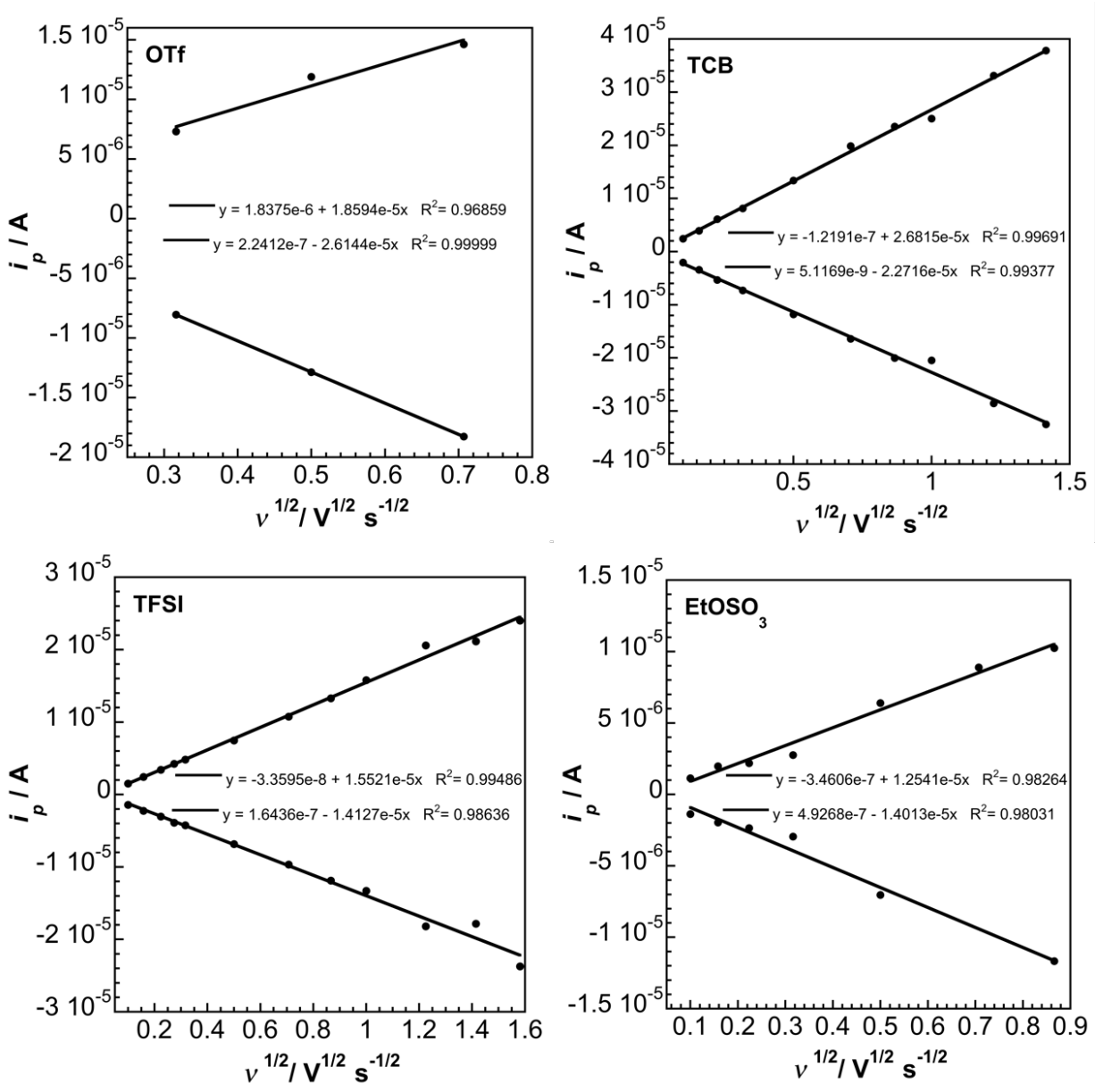

Figure 2.4. Peak current versus square root of scan rate plots for anodic and cathodic components of the $Mn^{IV/III}$ redox couple in various ionic liquids.

One question of interest is whether the metal center is singly- or doubly-coordinated to an IL anion. To address this question, UV-vis absorption spectra for (tpfc)Mn in the four different ionic liquids were obtained and are displayed in **Figure 2.5**. It is well established that the LMCT band in the 470–500 nm region is a reporter of Mn(III) coordination environment.[27] The proposal is that the ratio of Soret and LMCT band intensities distinguish single versus double axial anion coordination (the extinction coefficient of the LMCT band being greater than that of the Soret when Mn(III) is six-coordinate).[17] For $EtOSO_3^-$, splitting of the Soret and lower LMCT intensity suggests that Mn(III) is five-coordinate.[17] In contrast, the higher LMCT extinction coefficient (relative to the Soret) of (tpfc)Mn in EMIm-OTf indicates that two triflates could be bound to Mn(III) in that IL. We suspect that the nature of axial coordination to Mn(III) in these ILs is not as clear cut as this "single vs double" proposal, although these tentative assignments are consistent with our finding that the EMIm-OTf diffusion coefficient ratio is higher than the one in EMIm-$EtOSO_3$.

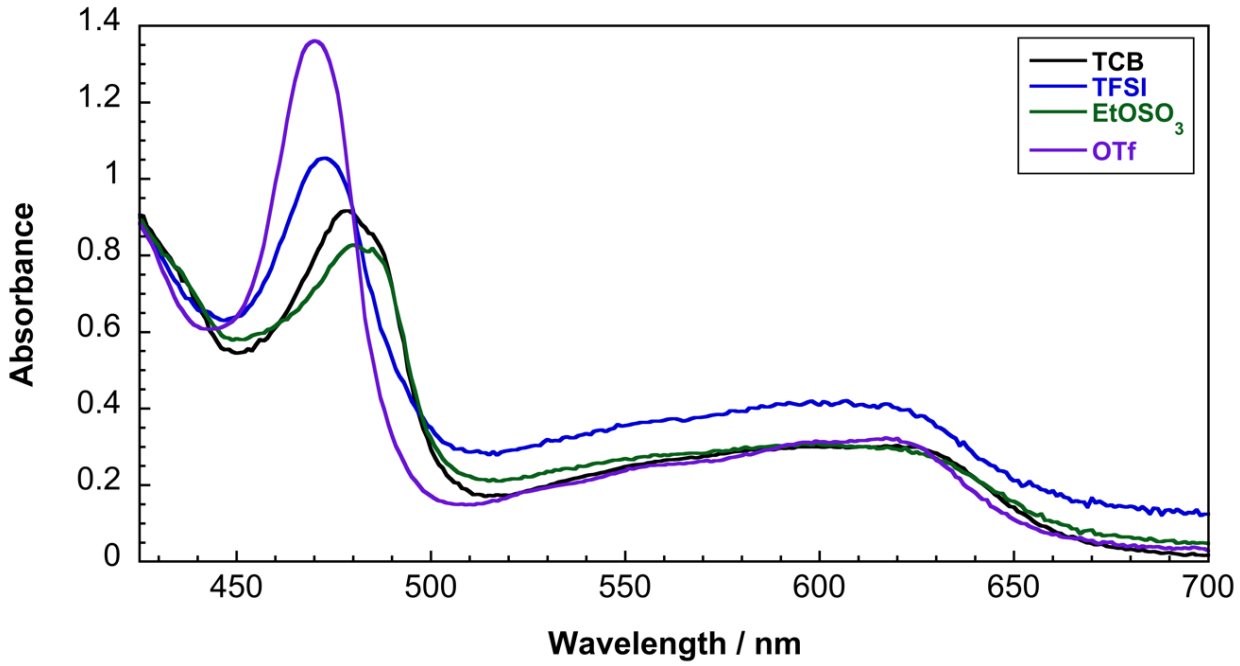

Figure 2.5. UV-visible absorption spectra for (tpfc)Mn in four different ionic liquids.

2.4. Conclusions

The redox behavior of (tpfc)Mn in ionic liquids depends on the nature of the counter anion: formal potential values for oxidations in ILs containing TCB^- and $TFSI^-$ are greater than those in EMIm-OTf and EMIm-$EtOSO_3$, thereby indicating that each of the latter two anions is more strongly coordinated to (tpfc)Mn. What is more, UV-vis data suggest that axial coordination to Mn(III) is tighter in EMIm-OTf than in EMIm-$EtOSO_3$. In looking ahead, we predict that ILs will find increasing use as solvents in many electrochemical processes.

2.5 Experimental

General

1-butyl-3-methylimidazolium bis(trifluoromethylsulfonyl)imide (99%, Iolitec, Inc.), 1-ethyl-3-methylimidazolium ethylsulfate (99% Iolitec, Inc.), 1-ethyl-3-methylimidazolium triflate (99%, Iolitec, Inc.), and 1-ethyl-3-methylimidazolium tetracyanoborate (99.95%, Merck KGaA) were dried under vacuum for 24 h at 333 K prior to electrochemical studies. Ferrocene (Sigma-Aldrich) was used as received. Water content of ionic liquids vacuum-dried under these conditions contain on the order of 100 ppm water. Exact values of water in vacuum-dried ILs have been previously measured by Karl Fischer titration.[5] Ferrocene (Sigma-Aldrich) was used as received.

Synthesis

H_3(tpfc) and [(5,10,15-pentafluorophenyl)corrole]Mn(III) were synthesized according to literature procedures.[19]

Electrochemistry:

Electrochemistry of (tpfc)Mn in ionic liquids was performed with a Bio-Logic VSP-300 potentiostat by transferring dried ionic liquid to a nitrogen-purged, oven-dried three-electrode cell containing a 3

mm diameter glassy carbon electrode (CH Instruments) working electrode, a 0.01 M $Ag^{+/0}$ in 0.1 M $TBAPF_6$ in MeCN quasi-reference electrode (BAS Inc.), and a platinum wire counter electrode (K. J. Lesker). Microelectrode experiments were performed with an 11 μm carbon fiber disk electrode, a 0.01 M $Ag^{+/0}$ in 0.1 M $TBAPF_6$ in MeCN quasi-reference electrode (BAS, Inc.), and platinum wire counter electrode. All 3 mm disk and electrolysis experiments were compensated for 85% of the measured uncompensated resistance (R_u) value. All measured potentials are reported relative to the ferrocene formal potential.

2.6 References

(1) Earle, M. J. and Seddon, K. R., *Pure Appl. Chem.*, **2000**, vol. 72, p. 1391.

(2) Evans, R. G., Klymenko, O. V., Price, P. D., *ChemPhysChem*, **2005**, vol. 6, p. 526.

(3) Rogers, E. I., Silvester, D. S., and Poole, D. L., *J. Phys. Chem. C*, **2008**, vol. 112, p. 2729.

(4) Cabral, D., Howlett, P. C., and Pringle, J. M., *Electrochim. Act.*, **2015**, vol. 180, p. 419.

(5) O'Mahony, A. M., Silvester, D. S., and Aldous, L., *J. Chem. Eng. Data*, **2008**, vol. 53, p. 2884.

(6) Klähn, M. and Seduraman, A. *J. Phys. Chem. B*, **2015**, vol. 119, p. 10066.

(7) Oh, Y. and Hu, X., *Chem. Commun.*, **2015**, vol. 51, p. 13698.

(8) Zeng, G., Qiu, J., and Hou, B., *Chem. Eur. J.*, 2015, vol. 21, p. 13502.

(9) Fu, C., Aldous, L., and Dickinson, E. J. F., *Chem. Commun.,* 2011, vol. 47, p. 7083.

(10) Aviv-Harel, I. and Gross, Z. *Chem. Eur. J.*, 2009, vol. 15, p. 8382.

(11) Aviv, I. and Gross, Z., *Chem. Commun.*, 2007, p. 1987.

(12) Meier-Callahan, A. E., di Bilio, A. J., and Simkhovich, L., *Inorg. Chem.*, 2001, vol. 40, p. 6788.

(13) Grodkowski, J., Neta, P., and Fujita, E., *J. Phys. Chem. A*, 2002, vol. 106, p. 4772.

(14) Zdilla, M. J. and Abu-Omar, M. M., *J. Am. Chem. Soc.*, 2006, vol. 128, p. 16971.

(15) Gao, Y., Liu, J., and Wang, M., *Tetrahedron*, 2007, vol. 63, p. 1987.

(16) Schechter, A., Stanevsky, M., and Mahammed, A., *Inorg. Chem.*, 2012, vol. 51, p. 22.

(17) Shen, J., El Ojaimi, M., and Chkounda, M., *Inorg. Chem.*, 2008, vol. 47, p. 7717.

(18) Liu, H-Y., Mahmood, M. H., and Qiu, S-X. S., *Coord. Chem. Rev.*, 2013, vol. 257, p. 1306.

(19) Golubkov, G., Bendix, J., and Gray, H. B., *Angew. Chem. Int. Ed. Engl.*, 2001, vol. 40, p. 2132.

(20) Mingos, D. M. P., Day, P., and Dahl, J. P., *Molecular Electronic Structures of Transition Metal Complexes I. Structure and Bonding*, New York: Springer, 2012, p. 49.

(21) Schmeisser, M., Illner, P., and Puchta, R., *Chem. Eur. J.*, 2012, vol. 18, p. 10969.

(22) Bard, A. J. and Faulkner, L. R., *Electrochemical Methods: Fundamentals and Applications*, New York: Wiley, 2001.

(23) Ohno, H., *Electrochemical Aspects of Ionic Liquids*, New York: Wiley, 2011.

(24) Fröba, A. P., Wasserscheid, P., and Gerhard, D., *J. Phys. Chem. B*, 2007, vol. 111, p. 12817.

(25) Barrosse-Antle, L. E., Bond, A. M., and Compton, R. G., *Chem. Asian J.*, 2010, vol. 5, p. 202.

(26) Yan, P-F., Yang, M., and Liu, X., *J. Chem. Thermodyn.*, 2010, vol. 42, p. 817.

(27) Edwards, N. Y., Elkey, R. A., and Loring, M. I., *Inorg. Chem.*, 2005, vol. 44, p. 3700.

Chapter III

ELECTROCATALYSIS OF CO_2 REDUCTION IN BRUSH POLYMER ION GELS

Adapted with permission from McNicholas, B. J.; Blakemore, J. D.; Chang, A. B.; Kramer, W. W.; Grubbs, R. H.; Gray, H. B. Electrocatalysis of CO_2 Reduction in Brush Polymer Ion Gels. *J. Am. Chem. Soc.* **2016**, *138*, 11160-11163. DOI: 10.1021/jacs.6b08795.

3.1. Summary

The electrochemical characterization of brush polymer ion gels comprised of polystyrene-polyethyleneoxide-polystyrene (PS-PEO-PS) triblock brush polymer, 1-butyl-3-methylimidazolium bis(trifluoromethylsulfonyl)imide (BMIm-TFSI), and some combination of ferrocene (Fc), cobaltocenium ($CoCp_2^+$) and $Re(bpy)(CO)_3Cl$ is reported. Gels were characterized by ^1H NMR, small-angle X-ray scattering, and cyclic voltammetry. Characterization suggests that gels are disordered micellar spheres of polystyrene bridged by polyethyleneoxide chains which interact with the ionic liquid. The small-angle X-ray scattering results suggest that no change in gel morphology occurs on the microscopic length scale between blank gels and gels with added redox-active species. The gel electrolytes exhibit diffusion-controlled redox processes with diffusion coefficients approximately one-fifth of those observed in neat BMIm-TFSI. Notably, **1** dissolves homogeneously in the interpenetrating matrix domain of the ion gel, and displays electrocatalytic CO_2 reduction to CO in the gel. The catalytic wave exhibits a positive shift vs. $Fc^{+/0}$ compared to analogous non-aqueous solvents, such as acetonitrile and dichloromethane, with a reduction potential 450 mV positive of onset and a 90% Faradaic efficiency for CO production. These materials appear to be a promising and alternative approach to immobilized electrocatalysis, creating numerous opportunities for application in solid-state devices, such as CO_2 gas diffusion electrodes and flow cells.

3.2. Introduction

To circumvent common drawbacks of heterogenized molecular catalysts and leverage the selectivity of a molecular catalyst, physically cross-linked polymer networks can be utilized to provide the interactions and diffusion-control of a dissolved molecular catalyst in a medium that exhibits macroscopic solid-like mechanical properties. This design captures the benefits of a solid support without requiring catalyst redesign and/or addition of membranes to surface attach molecular catalysts.[23-27] This advance is afforded by the use of ABA triblock brush polymers, specifically polystyrene-polyethyleneoxide-polystyrene (PS-PEO-PS), infused with ionic liquid (IL) as the matrix, which preferentially interacts with the hydrophilic PEO block. The blend forms physically cross-linked A-block micelles that are surrounded by a continuous PEO-IL phase.[28-30] **Figure 3.1** depicts the previously reported synthesis of the living ring opening metathesis polymerization (ROMP) used to synthesize PS-PEO-PS from PS and PEO macromonomers.[29] Living ROMP is a reliable method for obtaining narrowly dispersed multiblock polymers. Also, it has been shown that the solubility of CO_2 in BMIm-TFSI (H^{cp} = 0.13 M atm^{-1}) is higher than aqueous media by almost an order of magnitude. This solubility is advantageous for CO_2R and minimizes the drawbacks associated with slower diffusion coefficients for redox-active species in IL media. Little precedent exists for catalysis in a solid-state medium with facile catalyst diffusion through the structure. Specifically, reversible voltammetry of redox-active species has not been observed for IL-polymer gel electrolytes, aside from one report of a reversible $Fc^{+/0}$ wave when a gel was still wet with casting solvent.[31]

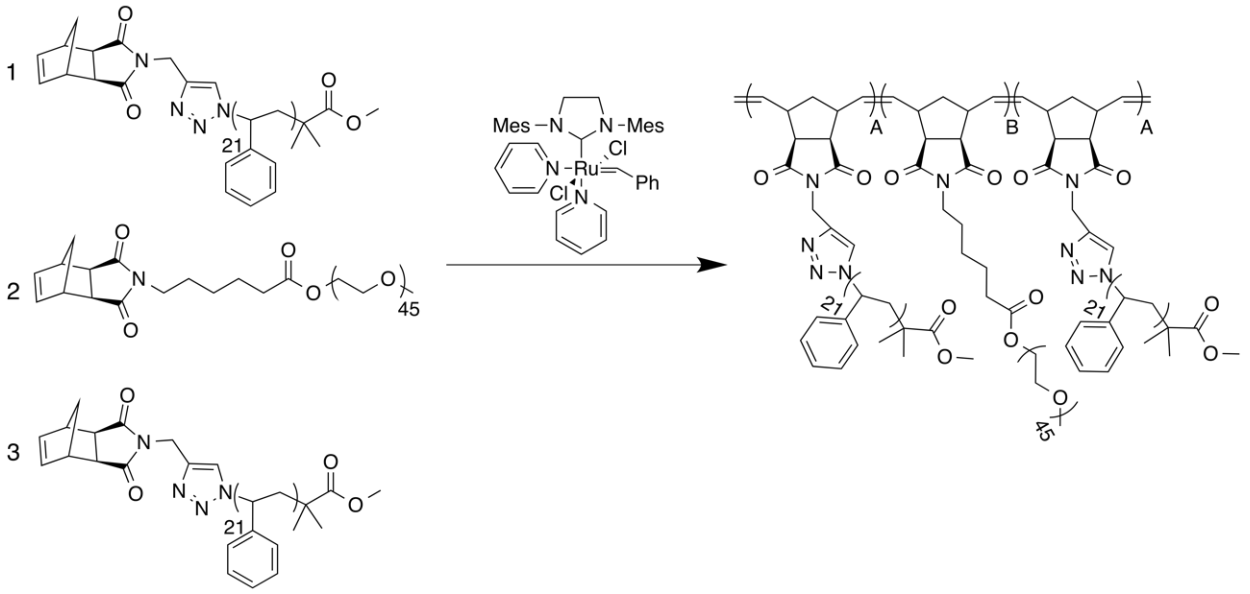

Figure 3.1. Macromonomers and general structure of polystyrene-polyethyleneoxide-polystyrene ABA brush triblock polymer after living ROMP with Grubbs 3rd generation catalyst.

3.3 Significance

The research herein demonstrates that electroactive small molecules dissolved in the matrix domain are capable of undergoing redox reactions due to the high ionic conductivity and polarizability of the IL medium. Incorporation of the well-established CO_2 reduction catalyst **1** provides evidence that this system is a robust method for performing useful electrochemical reactions with homogenous catalysts in a medium that exhibits macroscopic solid-like properties. These pseudo solid-state media have the potential for use in water as stabilizing media for typically less stable and/or non-aqueous CO_2 reduction catalysts. Additionally, they exhibit promise as thin layers for immobilization of CO_2 reduction catalysts for gas diffusion cells.

3.4 Results and Discussion

3.4.1 Characterization and Electrochemistry of Ferrocene (Fc) and Cobaltocenium ($CoCp_2^+$) in Ion Gel Electrolyte

Ion gels were prepared by stirring PS-PEO-PS triblock brush polymer (N_A:N_B:N_A = 15:119:15, where N is the degree of polymerization of each block) with vacuum-dried 1-butyl-3-methylimidazolium bis(trifluoromethyl-sulfonyl)imide (BMIm-TFSI) and dichloromethane (DCM) as co-solvent. Fc and/or $CoCp_2^+$ were added to the pre-cast solution to determine if reversible redox couples could be observed in the gel. The mixtures were stirred for 20 minutes, then allowed to dry in a nitrogen-filled glove box for over 24 hours. ^{1}H NMR of the gels dissolved after synthesis in $CDCl_3$ confirmed complete removal of DCM, and small-angle X-ray scattering, shown in **Figure 3.2**, suggests little change compared to neat gel in the structure with incorporation of electroactive species. Based on literature precedent for these ion gel electrolytes, the data are consistent with a network of disordered spherical micelles of PS brushes with bridging, hydrophilic PEO brushes.[29]

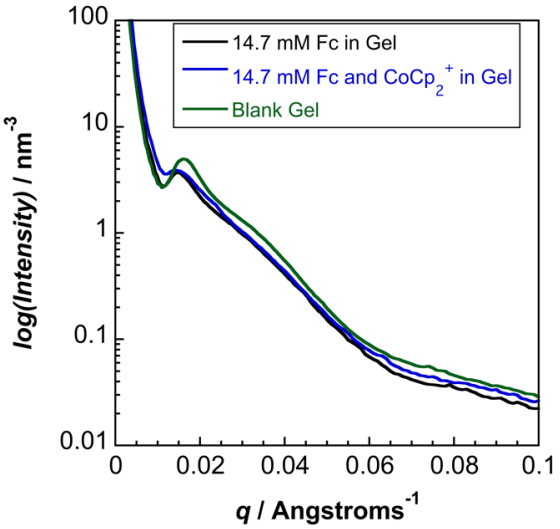

Figure 3.2. Small angle X-ray scattering (SAXS) of ion gel electrolytes without and with redox-active molecule loadings.

Figure 3.3 depicts macroscopic and molecular views of ion gel electrolytes with $Re(bpy)(CO)_3Cl$. The inverted vial test indicates that static equilibrium by the von Mises yield criterion, shown in **Equation 3.1**,

$$\sigma_y = \rho \times g \times L \tag{3.1}$$

is satisfied, where ρ is the density of the material, g is the gravitational constant, and L is the length of the vertical column of the material.[38] Though the gel is a stable solid under ambient conditions, the physical cross-links can be disrupted by addition of a solvent or an increase in temperature, allowing the incorporation of more charged species. The gel can reversibly be recast by evaporation of the solvent or lowering the temperature, which restores physical cross-links, making these gels renewable media.

Electrochemical characterization was conducted in a nitrogen-filled glove box by resting a glassy carbon working electrode on the surface of the gel and inserting a Pt-wire counter electrode and a silver pseudo-reference electrode into the gel. **Figure 3.4** displays potential sweeps of blank gel,

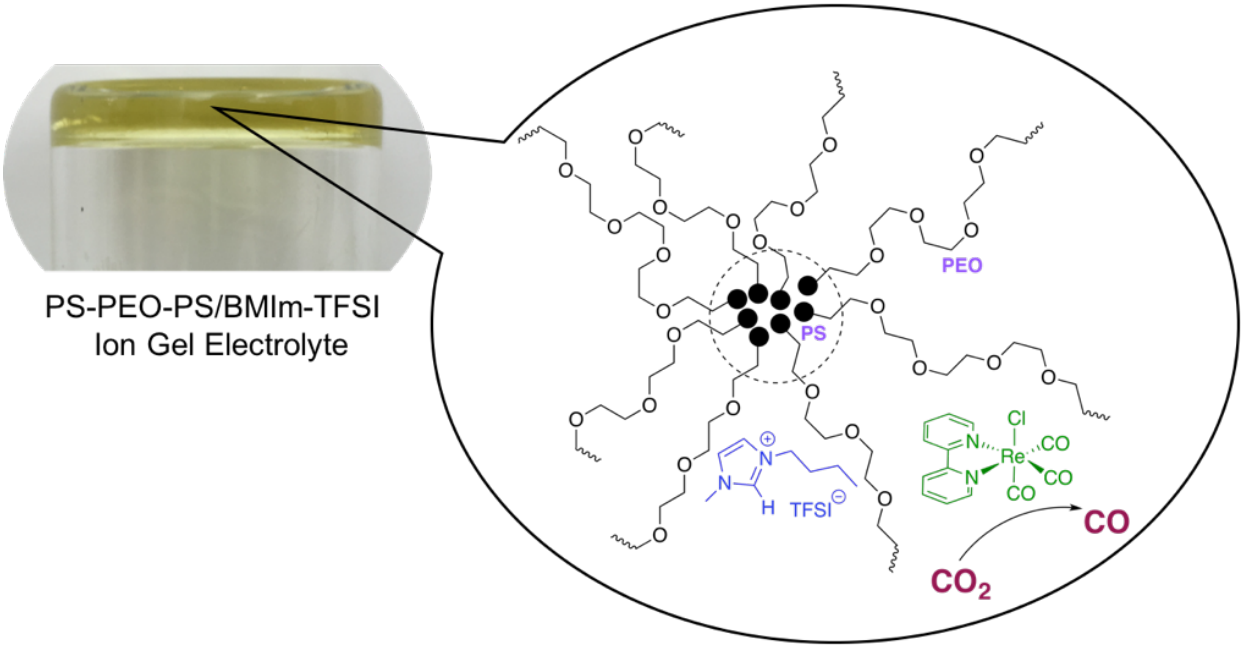

Figure 3.3. Macroscopic and molecular views of ion gel electrolytes with Re(bpy)(CO)$_3$Cl. The inverted vial test indicates that static equilibrium is satisfied.

gel with Fc, and gel with both Fc and $CoCp_2^+$. The thermodynamic separation between two redox standards, i.e. $CoCp_2^+$ and Fc, should be independent of the solvating medium. The formal potential ($E^{0'}$) for $CoCp_2^{+/0}$ of −1.33 V vs. $Fc^{+/0}$ in ion gel is consistent with reported values for $CoCp_2^{+/0}$ in ILs as well as non-aqueous electrolytes.[39]

To confirm that the redox behavior of the $Fc^{+/0}$ and $CoCp_2^{+/0}$ redox couples in ion gel is consistent with non-aqueous behavior, diagnostic plots were obtained using Nicholson and Shain metrics. These relationships confirmed that the redox behavior of both couples can be classified as "Case I," which corresponds to an electrochemically reversible redox process.[40] A deviation from one was observed for the $Fc^{+/0}$ peak current ratio. This could be attributed to unequal diffusion coefficients for corresponding neutral and oxidized species in ILs due to the charge effect of the medium.[41,42]

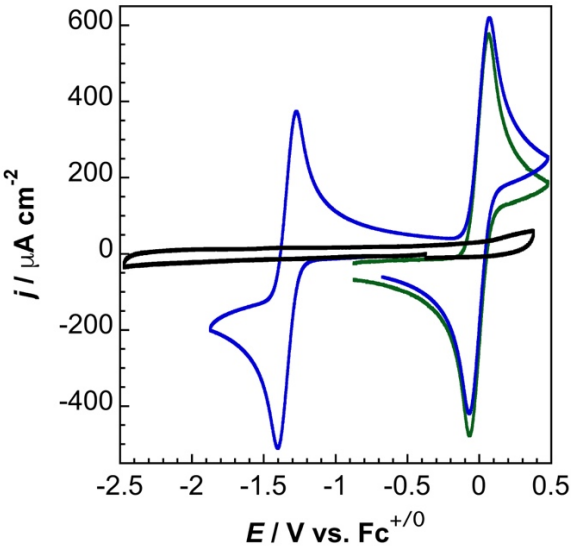

Figure 3.4. Cyclic voltammetry of blank ion gel electrolyte (black), with ferrocene (14.3 mM) (green), and with ferrocene (14.3 mM) and cobaltocenium (15.3 mM) (blue).

The diffusion coefficient can be obtained from a plot of peak current vs. $v^{1/2}$.[43] To determine the diffusion coefficient of a reversible electron transfer, the peak current, i_p, in homogeneous electrochemistry is given in **Equation 3.2**,

$$i_p = 0.4463n^{3/2}F^{3/2}AC_0^*\sqrt{\frac{D_0 v}{RT}} \qquad (3.2)$$

where n is the number of electrons ($n = 1e^-$ for Fc oxidation and $CoCp_2^+$ reduction), D_0 is the diffusion coefficient of the electroactive species ($cm^2\ s^{-1}$), v is the scan rate ($V\ s^{-1}$), A is the electrode surface area (A = 0.0707 cm^2), and C_0^* is the bulk concentration of analyte ($mol\ L^{-1}$). Good reproducibility was found in the values obtained from triplicate samples, and the diffusion coefficient of Fc in ion gel is roughly one-fifth that for Fc in neat BMIm-TFSI.[39] **Figure 3.5** displays the scan-rate dependence for the $Fc^{+/0}$ redox couple and the corresponding linear fits.

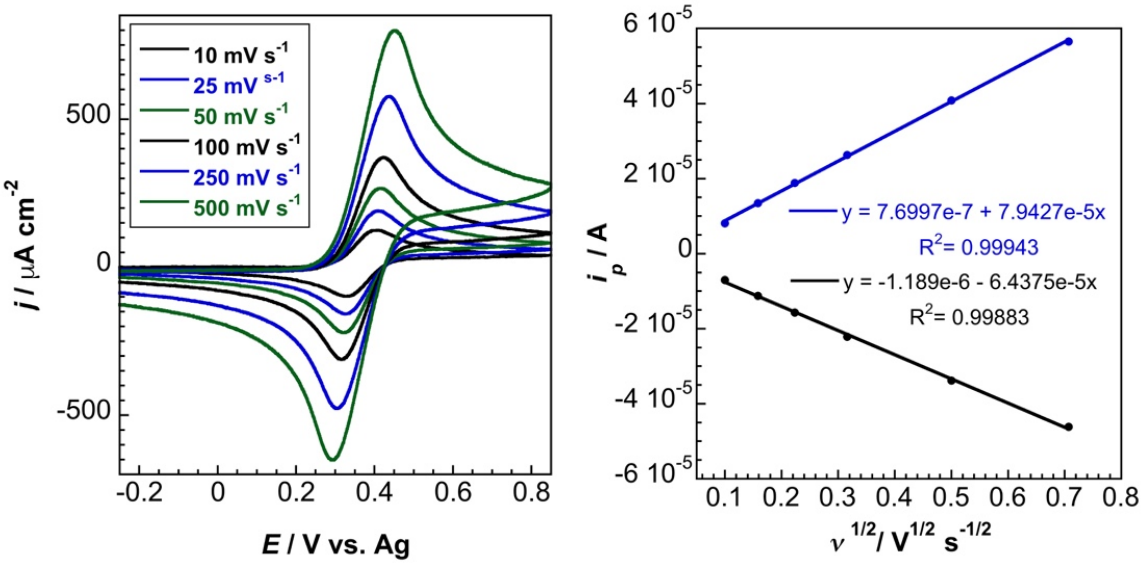

Figure 3.5. Randles-Sevcik plots and scan rate dependence for $Fc^{+/0}$ in ion gel electrolyte (14.3 mM ferrocene).

Table 3.1 gives average values for the diffusion coefficients of Fc and $CoCp_2^+$ in both ion gel electrolyte and neat BMIm-TFSI.[39] **Figure 3.6** and **Figure 3.7** give all of the plots for the triplicate measurements of diffusion coefficients for $Fc^{+/0}$ and $CoCp_2^{+/0}$.

Table 3.1. Diffusion coefficients obtained by Randles-Sevcik analysis and literature data for ferrocene, cobaltocenium, and $Re(bpy)(CO)_3Cl$ in BMIm-TFSI and in ion gel electrolyte.

Species	D_0 in Gel (10^{-11} m^2 s^{-1})	D_0 in BMIm-TFSI (10^{-11} m^2 s^{-1})
Fc	0.81 ± 0.04	3.89[a] ± 0.05
$CoCp_2^+$	0.53 ± 0.04	2.22 ± 0.03
$Re(bpy)(CO)_3Cl$	0.42[b] ± 0.01	1.94 ± 0.02

[a]Literature values
[b]Calculated by multiplying the diffusion coefficient in BMIm-TFSI with the change in peak current ratio observed for ferrocene

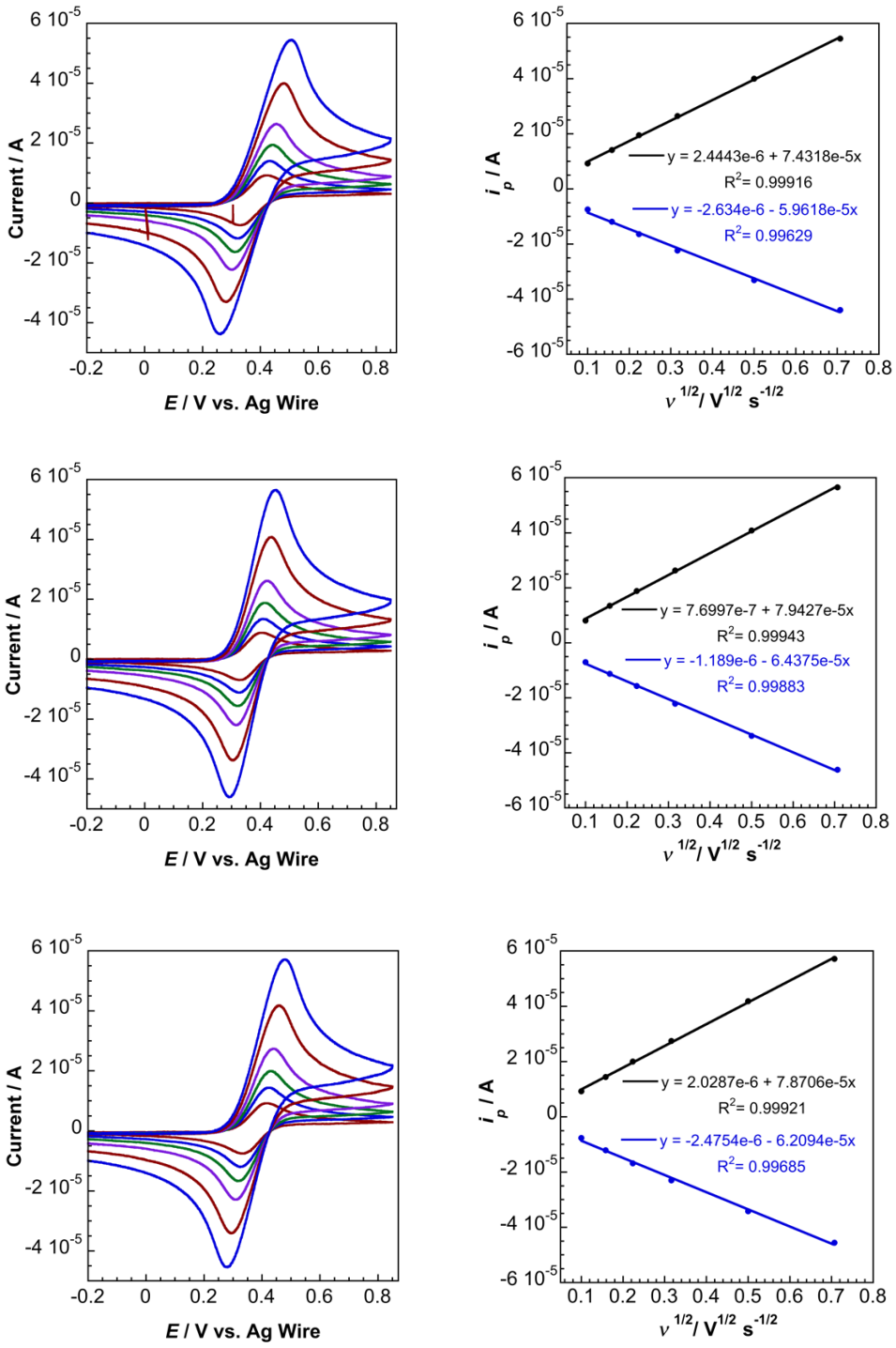

Figure 3.6. Scan rate dependence plots and Randles-Sevcik plots for ferrocene in ion gel electrolyte.

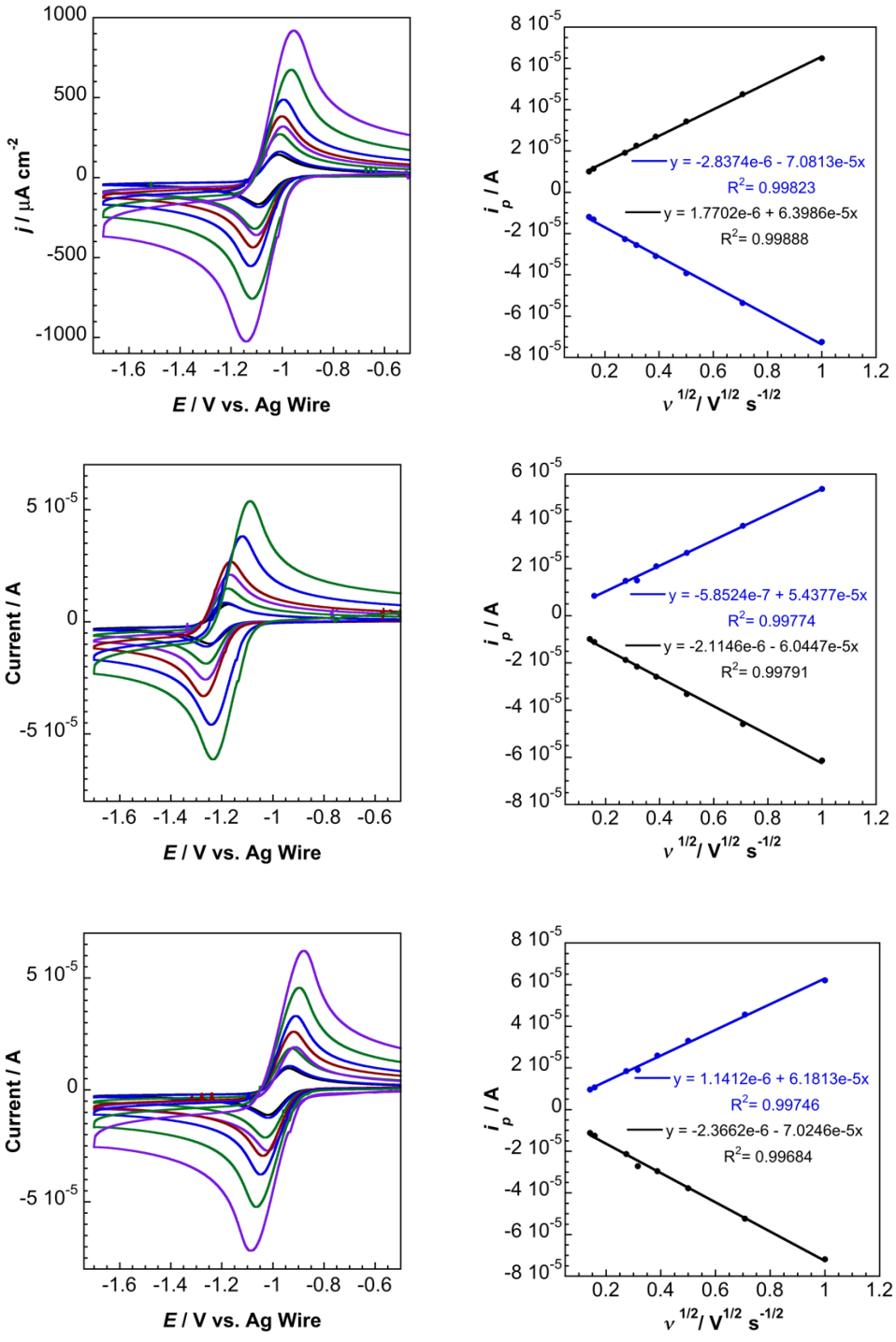

Figure 3.7. Scan rate dependence plots and Randles-Sevcik plots for cobaltocenium in ion gel electrolyte.

3.4.2. Electrochemistry of $Re(bpy)(CO)_3Cl$ in BMIm-TFSI and Ion Gel Electrolyte.

Having confirmed their ability to serve as an electrochemical medium, polymer ion gels were subsequently investigated as media capable of supporting homogeneous electrocatalytic reactions.[44-46] CO_2 reduction studies were pursued with **1** due to its selectivity for production of CO and well-characterized mechanism in non-aqueous electrolytes.[35,47,48] The redox behavior of **1** in ion gel electrolyte, shown in **Figure 3.8**, is more complex than in organic solvents. Rather than two one-electron reductions corresponding to bipyridine-centered and metal-centered reductions, as observed in acetonitrile, the electrochemistry in both gel and neat BMIm-TFSI exhibits four reduction waves, tentatively assigned as a 2 e^- wave with $E_{p,c} = -1.72$ V, two 1 e^- waves with $E_{p,c} = -1.94$ V, which overlap, and an additional reversible redox process near the edge of the electrochemical window with $E_{p,c} = -2.23$ V. This reversible redox process near the solvent window is proposed to correspond to a second bipyridine reduction, which has been observed for analogous complexes.[49]

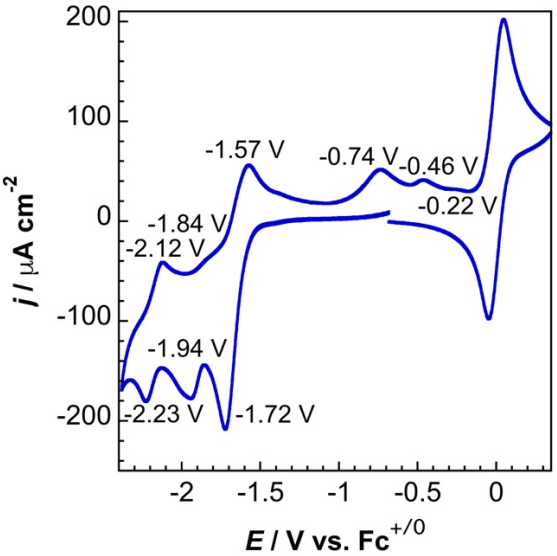

Figure 3.8. Voltammetry of ion gel electrolyte with $Re(bpy)(CO)_3Cl$ (14.3 mM) and ferrocene (5.0 mM). Potentials were shifted relative to the formal potential of $Fc^{+/0}$. Peak potential shown for each process.

Previous research has suggested that coalescence of the two sequential reductions observed for Re(bpy)(CO)$_3$Cl in IL media occurs and is a result of $2e^-$ transfer to the complex through an $E_r + E_qC_i$ mechanism, where the complex undergoes an electrochemically reversible electron transfer, followed by an electrochemically quasireversible electron transfer coupled to an irreversible chemical reaction.[32] This mechanism has been suggested by analysis of Re(bpy)(CO)$_3$Cl in 1-ethyl-3-methylimidazolium tetracyanoborate (EMIm-TCB).[32] To confirm the validity of this interpretation, scan rate dependence studies of **1** in 1-ethyl-3-methylimidazolium ethylsulfate (EMIm-EtSO$_4$) were performed. **Figure 3.9** displays the voltammetry at a range of scan rates, and at scan rates above 250 mV s^{-1}, the first redox process separates into two, discrete waves, as observed in acetonitrile. The first redox event does not shift to more negative potentials at any of the tested scan rates, suggesting it is an

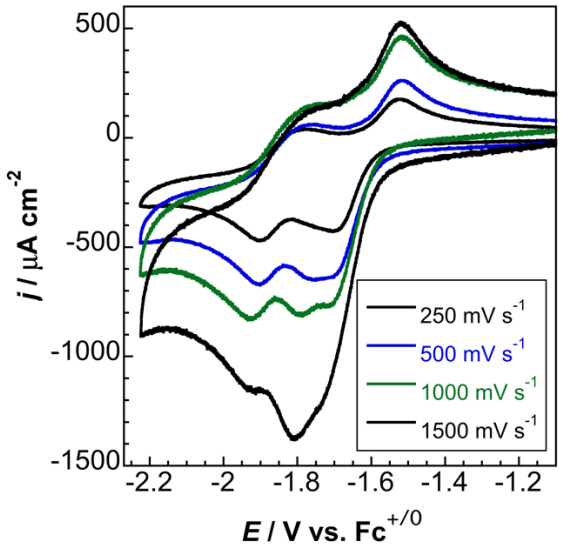

Figure 3.9. Scan rate dependence of Re(bpy)(CO)$_3$Cl (10.0 mM) in EMIm-EtSO$_4$ under N$_2$.

electrochemically reversible electron transfer. The shift in potential of an electrochemically quasireversible electron transfer with a coupled, irreversible chemical reaction is given by **Equation 3.3**,[43]

$$-\left(\frac{\partial E_p}{\partial log v}\right) = 59.1\ mV \qquad (3.3)$$

with the plot of E_p versus $log(v)$ of the second reduction wave given in **Figure 3.10**, where the slope, $\Delta E_p/\Delta log(v)$, of 65 mV is in good agreement with the relationship given by Equation 3. This suggests that the second wave can be described by an E_qC_i mechanism.

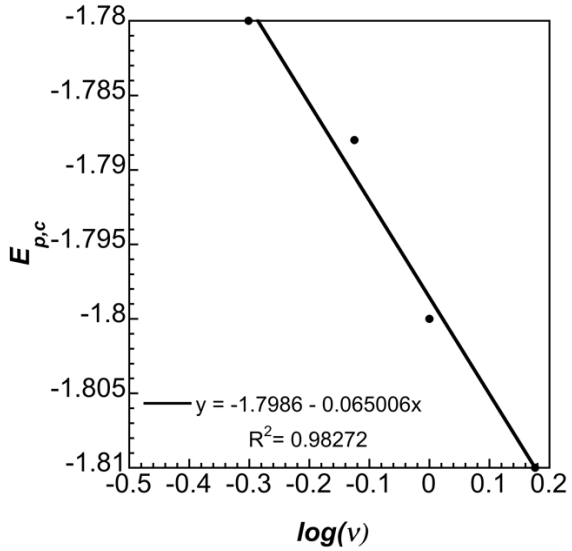

Figure 3.10. Peak cathodic potential versus the logarithm of the scan rate in EMIm-$EtSO_4$ for the proposed E_qC_i redox process of $Re(bpy)(CO)_3Cl$.

Additional analysis of **1** in BMIm-TFSI by Nicholson and Shain metrics, shown in **Figure 3.11**, resulted in diagnostic plots which further suggests that the second wave is E_qC_i, with a quasireversible electron transfer followed by an irreversible, chemical step corresponding to loss of chloride and generation of the catalytically active form of the complex.[40] First, the plot of $i_{p,c}/i_{p,a}$ vs. $log(v)$ should tend towards one at higher scan rates for an EC_i mechanism. Second, the plot of current function versus $log(v)$ should gradually decrease as scan rate is increased for an EC_i mechanism. Third, the plot of shift in half-peak potential versus $log(v)$ should increase rapidly towards zero at slower scan rates and flatten out near 0 for an EC_i mechanism. All three criteria support the assignment of the separated

and shifting reduction wave as EC_i. Thus, the previously reported mechanism, $E_r + E_qC_i$, is in line with independent data taken in two different, imidazolium based ILs.

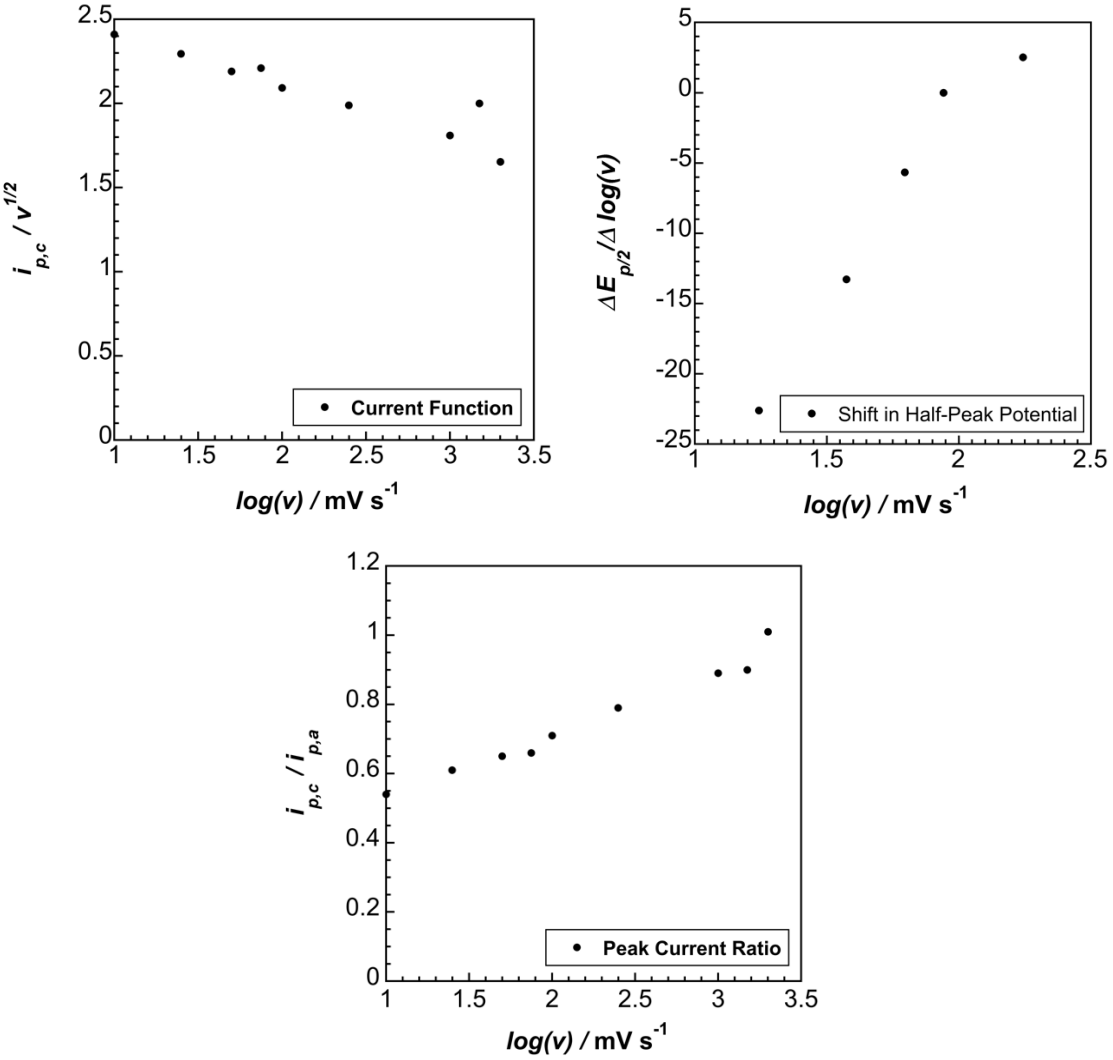

Figure 3.11. Nicholson and Shain plots for the second reduction wave (E_qC_i) of Re(bpy)(CO)$_3$Cl in BMIm-TFSI.

To gain insight about the number of electrons transferred and the mechanism that causes additional reduction waves to be observed for Re(bpy)(CO)$_3$Cl, microelectrode voltammetry of Re(bpy)(CO)$_3$Cl

was performed with an 11-micrometer carbon-fiber disk microelectrode. **Figure 3.12** displays the steady-state voltammetry observed, and three separate redox processes are visible. **Table 3.2** gives the corrected limiting current values and the potential reached at steady state obtained from this plot. The values obtained at $E_{1/2}$ in microelectrode experiments correlate well with the values obtained in 3 mm glassy carbon disk experiments.

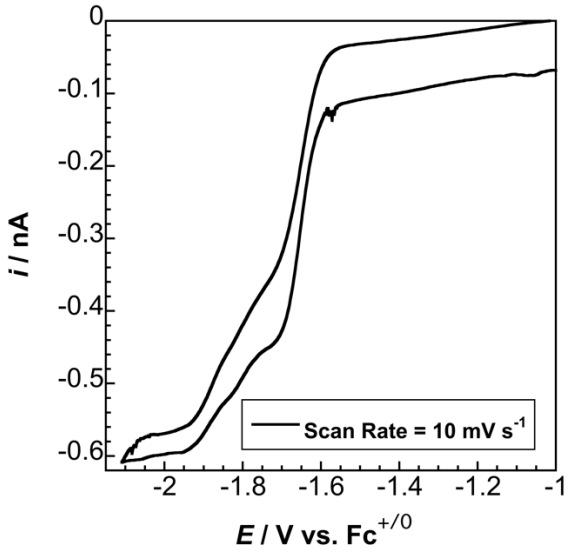

Figure 3.12. Microelectrode voltammetry of Re(bpy)$(CO)_3$Cl (5.9 mM) in BMIm-TFSI under N_2.

Table 3.2. Data for redox processes observed for Re(bpy)$(CO)_3$Cl at an 11-micrometer carbon fiber microdisk electrode. Currents at steady state were normalized by extrapolation of baseline currents.

Species	Potential at $i_{1/2}$ (V vs. $Fc^{+/0}$)	$E_{p,c}$ at 3 mm GC disk (V vs. $Fc^{+/0}$)	I_{ss} (pA)
1	−1.66	−1.67	−243.2
2	−1.82	−1.83	−44.6
3	−1.91	−1.91	−35.0

The steady state current at a disk microelectrode is given by **Equation 3.4**,

$$i_{ss} = 4nFDC_0r_0 \quad (3.4)$$

where n is the number of electrons transferred, F is Faraday's constant, D is the diffusion coefficient of the redox-active species, C_0 is the bulk concentration of redox-active species, and r_0 is the radius of the disk microelectrode. Using Equation 4, a steady state reduction current in BMIm-TFSI for a one-electron process with a diffusion coefficient of 10^{-11} $m^2\,s^{-1}$ is −0.126 nA.[4] Based on the currents obtained for the three redox processes, approximately two electrons are transferred for the first reduction, and the other two waves most likely correspond to two consecutive reductions of a different species, which is present in a smaller concentration. This behavior may arise from ligand exchange of the chloride for the TFSI anion. TFSI is present in high concentration and is a weak, π-donor ligand like Cl^-, which makes ligand exchange at negative potentials feasible.[50] These data contrast with the previous report studying the microelectrode voltammetry of $Re(bpy)(CO)_3Cl$ in EMIm-TCB, which exhibits a single reduction wave.[5] Adding together the currents of all redox processes in the absence of CO_2 gives a total current of −0.314 nA. If the total current at steady state is used to find the diffusion coefficient for a two-electron transfer to all electroactive species, $D = 1.8 \times 10^{-11}$ $m^2\,s^{-1}$, which correlates well with the coefficient obtained in 3 mm glassy carbon disk electrochemistry.

To further support the occurrence of ligand exchange for $Re(bpy)(CO)_3Cl$, other complexes with axial ligands were characterized by voltammetry in neat BMIm-TFSI. Scan rate dependence studies in BMIm-TFSI of Co(5,10,15-trisperfluorophenyl)corrole(pyridine)$_2$, shown in **Figure 3.13**, revealed a

doubling of redox events compared to its electrochemical behavior in dichloromethane, suggesting two redox-active forms of the complex.[51]

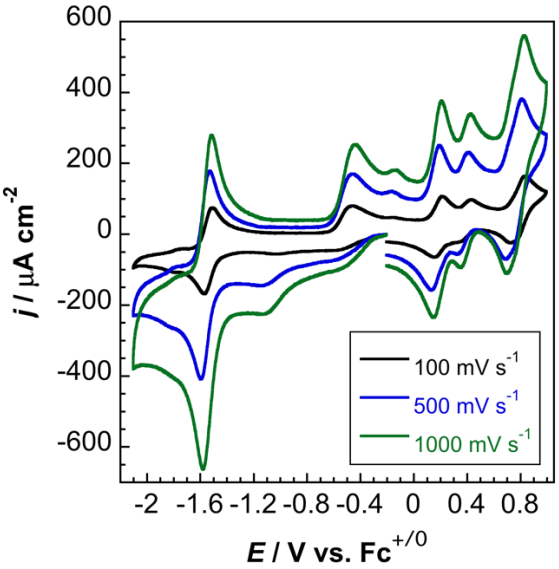

Figure 3.13. Scan rate dependence of Co(5,10,15-tris(pentafluorophenyl)corrole(pyridine)$_2$ (5.6 mM) in BMIm-TFSI under N_2.

3.4.3. CO_2 Reduction by Re(bpy)(CO)$_3$Cl in BMIm-TFSI and Ion Gel Electrolyte

With an understanding of the electrochemical behavior of Re(bpy)(CO)$_3$Cl in IL media, CO_2 reduction studies were carried out to determine if Re(bpy)(CO)$_3$Cl exhibited catalytic behavior in ion gel electrolytes. Since all studies were performed in vacuum-dried IL or ion gel electrolyte, no discrete proton source other than adventitious water or imidazolium cation from the IL is present. A recent report of Re(bpy)(CO)$_3$Cl has shown dramatic improvement in catalytic activity and positive shift in onset potential of Re(bpy)(CO)$_3$Cl in EMIm-TCB, a low-viscosity IL.[32] The increased CO_2 reduction activity observed in ILs was attributed to a hydrogen-bonding effect, where the imidazolium of the IL hydrogen bonds to the halide ligand to generate the catalytically active form of the complex at a more positive potential, shown in **Figure 3.14**.[52] The cation of the IL has also been posited to stabilize the carboxylate intermediate during CO_2 reduction, as shown in **Figure 3.14**.[32] To qualitatively support

these claims, $Re(bpy)(CO)_3Cl$ was characterized by voltammetry in both EMIm-$EtSO_4$ and 1-ethyl-3-methylimidazolium triflate with added CO_2. Both ILs caused similar enhancement in CO_2 reduction by $Re(bpy)(CO)_3Cl$, which suggests that the cation is the reason for this behavior.

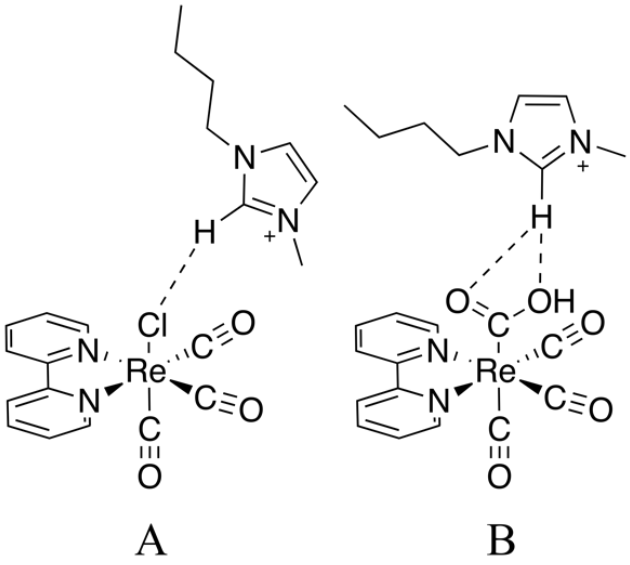

Figure 3.14. Proposed stabilization of ligand dissociation by imidazolium cation of BMIm-TFSI (A). Stabilization of Re-carboxylate intermediate by imidazolium cation of BMIm-TFSI (B).

To further support these claims, the bromide analogue of **1**, $Re(bpy)(CO)_3Br$ (**2**), was synthesized to probe the effect of the axial ligand on activity and onset potential for catalysis. **Figure 3.15** compares the CO_2 reduction observed for both complexes. The peak cathodic current ($E_{p,c}$) for $Re(bpy)(CO)_3Cl$ is −1.91 V, while $E_{p,c}$ for $Re(bpy)(CO)_3Br$ is −2.06 V, suggesting that the catalytically active form of the complex is generated at a less negative potential for $Re(bpy)(CO)_3Cl$. **Figure 3.15** suggests that the imidazolium cation more effectively stabilizes the dissociation and solvation of chloride compared to bromide. This trend can also be explained with hard-soft acid base theory. Halides become increasingly soft bases from fluoride to iodide, and Re(I) is a soft acid that will form a stronger bond to bromide, which increases the energy of the LUMO + 1. This results in a more negative second

reduction potential for the complex, thereby making the onset potential for CO_2 reduction for $Re(bpy)(CO)_3Br$ more negative relative to $Re(bpy)(CO)_3Cl$.

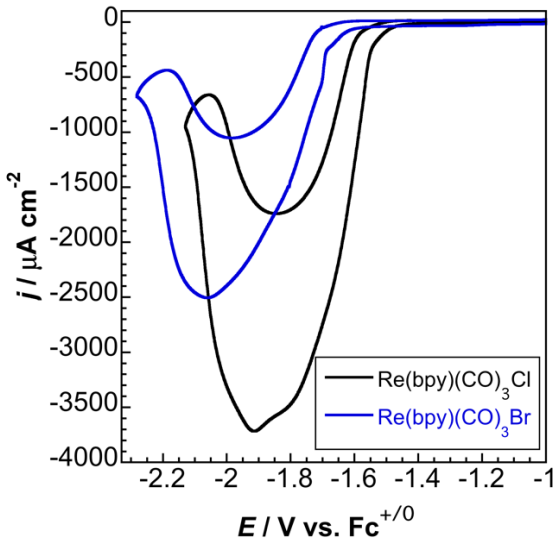

Figure 3.15. Voltammetry of $Re(bpy)(CO)_3Cl$ (5.0 mM) and $Re(bpy)(CO)_3Br$ (5.0 mM) in BMIm-TFSI under CO_2 (1 atm), showing the effect of X-type ligand on catalysis. Potentials were shifted relative to the formal potential of $Fc^{+/0}$.

Microelectrode voltammetry was also used to characterize the catalytic response of $Re(bpy)(CO)_3Cl$ in the presence of CO_2. **Figure 3.16** gives the current response of the system in the absence and in the presence of CO_2, with a large catalytic wave peaking at −2.08 V vs. $Fc^{+/0}$. Since a change in the slope of the current response occurs over the course of catalysis, either the two analogues of the catalyst present in solution are both catalytically active, or a change in the mechanism of CO_2RR occurs as the overpotential increases. The catalytic peak current ratio, i_{cat}/i_{ss}, is equal to 30.8, which agrees with the ratio of 29.9 obtained at 10 mV s^{-1} in the 3 mm glassy carbon disk experiment.

The electrochemistry of (1) ion gel with Fc under CO_2 (1 atm), (2) ion gel with $Re(bpy)(CO)_3Cl$ and Fc under inert atmosphere, and (3) ion gel with Fc and $Re(bpy)(CO)_3Cl$ under CO_2 (1 atm) is shown

in **Figure 3.16**. Under CO_2, a catalytic wave is observed for reduction of CO_2 to CO. Based on thermodynamic cycles and solvation energies for all species involved in the 2 e^- reduction of CO_2 to CO, $E(CO_2/CO) = -0.13$ V vs. $Fc^{+/0}$ in dry MeCN, and $E(CO_2/CO) = -0.146$ V vs. $Fc^{+/0}$ in BMIm-TFSI.[32] The formal potential of $Fc^{+/0}$ in BMIm-TFSI is approximately equal to the formal potential of $Fc^{+/0}$ in dry MeCN, as measured by voltammetry, meaning an approximate comparison of catalytic onset potentials for $Re(bpy)(CO)_3Cl$ in both media can be made. Thus, analogous to neat BMIm-TFSI, the potential needed for reduction of CO_2 with $Re(bpy)(CO)_3Cl$ is shifted 450 mV positive of its value in acetonitrile.

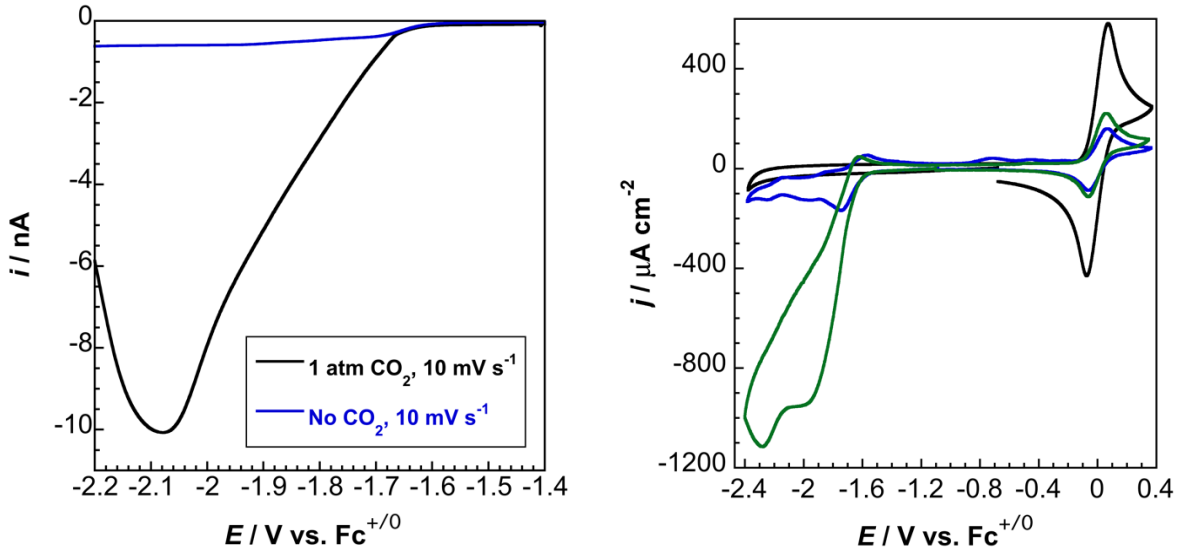

Figure 3.16. (Left) Carbon disk microelectrode voltammetry of $Re(bpy)(CO)_3Cl$ (5.9 mM) in BMIm-TFSI without and with CO_2 (1 atm). (Right) Cyclic voltammetry of ion gel electrolyte with ferrocene (14.3 mM) and CO_2 (1 atm) (black trace), with ferrocene (5.0 mM) and $Re(bpy)(CO)_3Cl$ (10.0 mM) (blue trace), and with ferrocene (7.1 mM), $Re(bpy)(CO)_3Cl$ (14.3 mM), and CO_2 (1 atm) (green).

To determine the product distribution and Faradaic efficiencies for CO_2 reduction, controlled potential electrolysis of $Re(bpy)(CO)_3Cl$ in both BMIm-TFSI and ion gel electrolyte was performed. **Figure 3.17** shows the current versus time trace for controlled potential electrolysis of the ion gel with

$Re(bpy)(CO)_3Cl$ using a glassy carbon plate working electrode in a three-electrode, gas-tight cell; results for both the ion gel and BMIm-TFSI control are summarized in **Table 3.4**. The electrolysis for the gel was diffusion-controlled, while the electrolysis for BMIm-TFSI was mass-transport controlled through rapid stirring. Onset of CO_2 reduction by $Re(bpy)(CO)_3Cl$ is similar in both the gel electrolyte and BMIm-TFSI. The onset potentials were determined by obtaining the inflection point where non-Faradaic charging current is no longer the only contribution to current density.

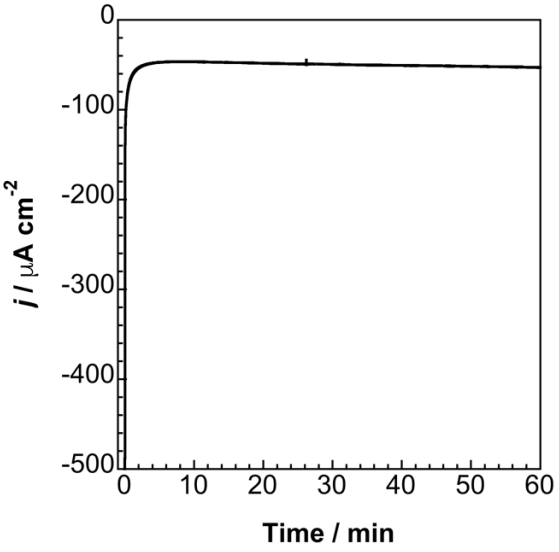

Figure 3.17. Controlled potential electrolysis of ion gel electrolyte with ferrocene (7.1 mM) and $Re(bpy)(CO)_3Cl$ (1.0 mM) under CO_2 (1 atm).

Table 3.3. Controlled potential electrolysis of $Re(bpy)(CO)_3Cl$ in BMIm-TFSI and in ion gel electrolyte. Results averaged from triplicate measurements.

Medium	Onset Potential (V vs. $Fc^{+/0}$)	Electrolysis Potential (V vs. $Fc^{+/0}$)	Faradaic Efficiency for CO	Charge Passed in One Hour (C)
BMIm-TFSI	–1.55	–1.90	92 % ± 5 %	–2.70 C
Ion Gel Electrolyte	–1.60	–2.10	90 % ± 5 %	–0.450 C

The potentials for electrolysis were selected based on the peak catalytic current of CO_2 reduction from voltammetry experiments in the two different media. The more negative peak current for CO_2 reduction in the ion gel electrolyte compared to BMIm-TFSI could be due to diffusion limitations of the ion gel. 10.0 mL of headspace was sampled after one hour of electrolysis and injected into a gas chromatograph-thermal conductivity detector (GC-TCD). Based on the area of the CO peak in the GC trace and the charge passed during electrolysis, the Faradaic efficiencies were calculated. In both BMIm-TFSI and ion gel electrolyte, the CO produced corresponds to nearly quantitative conversion of CO_2 to CO. Any loss in product can be ascribed to the viscosity of both neat IL and gel electrolyte, which prevents complete product escape (time limitation) before sampling of the headspace. Additionally, the solubility of CO in ion gel electrolyte could prevent complete product escape. Due to the diffusion limitations of the gel, the thickness of the gel, and the lack of stirring for the gel, the amount of charge passed for CO_2 reduction in the gel electrolyte is smaller than in BMIm-TFSI.

3.5. Conclusions

The materials described herein reflect a general strategy to bridge the divide between homogenous, solution-state catalysis and heterogeneous, solid-state catalysis. Decoupling the timescales associated with macroscopic flow and local molecular reorganization enables the formulation of materials with solid-like properties containing small molecules that respond to electrochemical stimuli in a diffusion-controlled manner with near liquid-like kinetics. It was demonstrated that this new class of materials is capable of electrocatalytically reducing CO_2 to CO with a well-defined, small-molecule catalyst historically used in homogenous solutions. The catalytic enhancement imparted by the IL results in a significant decrease in CO_2 reduction potential compared to typical non-aqueous electrolytes. The high solubility of CO_2 in the ion gel electrolyte attenuates the drawbacks of slow diffusion. The physical cross-links imbue mechanical properties, such as rigidity and tensile strength, to the gel.

However, reversible gelation is thermally accessible with an appropriately tuned upper critical solution temperature or through good solvent addition, providing a means for renewing catalytic activity. Extraction of electrochemical reaction products, reformulation of the composition, and macroscopic shape adjustment should thus be possible, making this a promising medium for CO_2 reduction and other electrocatalytic transformations.

3.6 Future Directions

Further implementation of these ion gel composites in solid-state devices is currently underway. Because the aforementioned ion gel electrolytes degrade in the presence of water, a modified ion gel scaffold is needed to carry out CO_2 reduction in aqueous media. **Figure 3.18** displays the synthesis of chemically cross-linked, PEO homopolymer ion gel electrolytes. Using a hydrophobic IL (BMIm-TFSI), the chemically cross-linked gels are both elastic and mechanically robust in aqueous media. Additionally, a discrete proton source, such as phenol or trifluoroethanol, can be incorporated in gel electrolytes, suggesting greater rates of reduction, and hence current densities can be achieved.

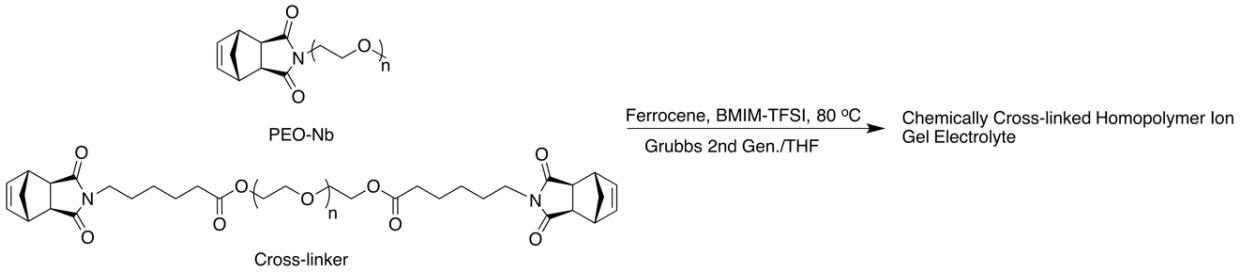

Figure 3.18. Synthesis of chemically crosslinked, PEO homopolymer ion gel electrolytes. In addition to greater elasticity and mechanical integrity, these gel electrolytes do not degrade in aqueous media, making them a promising solid-state medium for aqueous CO_2 reduction.

Characterization of these gel electrolytes by voltammetry was performed. **Figure 3.19** depicts the scan rate dependence of $Fc^{+/0}$ in homopolymer gel electrolytes. Analogous to the physically cross-linked

gels, diffusion-controlled voltammetry was observed in this medium. Additionally, great control over mechanical toughness and elasticity of the gel is achieved by varying the amount of cross-linker added to the reaction, with more cross-linker producing a less elastic gel.

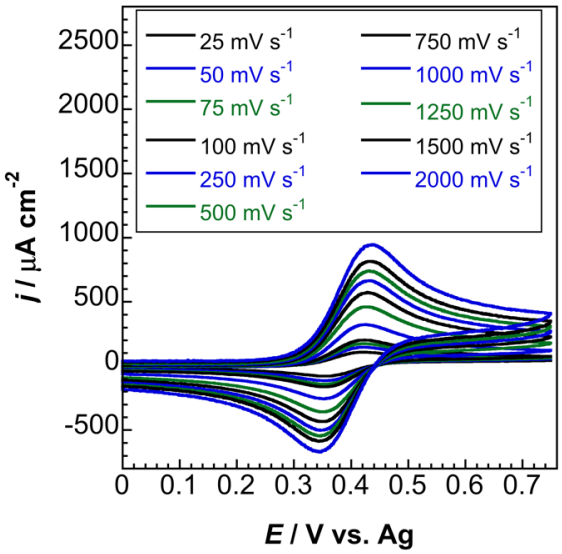

Figure 3.19. Scan rate dependence of Fc (8.4 mM) in chemically cross-linked, PEO-homopolymer ion gel electrolyte.

While CO_2 reduction at less negative potentials has been shown with polymer gel electrolytes, one drawback is the diffusion limitation of this medium. As shown with triblock brush copolymers, diffusion through gel media is approximately an order of magnitude slower than diffusion in the corresponding IL and approximately three orders of magnitude slower than diffusion in non-aqueous media.[53] While the solubility of CO_2 in ion gel electrolytes (H^{cp} = 0.13 M atm^{-1}, where H^{cp} is the Henry solubility constant) is approximately three times greater than that for neutral, aqueous media (H^{cp} = 0.034 M atm^{-1}) at 298 K, alternative methods are necessary to leverage the benefits of ion gel electrolytes and eliminate drawbacks associated with slow diffusion that inhibit greater current densities.[18,54]

To improve performance, one possible method is to make use of a thin-layer, polymer electrolyte on the cathode to circumvent the mass-transport limit associated with heterogeneous catalysis in aqueous media.[18] Rather than being controlled by diffusion or mass-transport, CO_2 reduction in a thin-layer membrane is limited by the permeability of CO_2 through the layer.[18] If the permeability of CO_2 through a thin film of gel electrolyte is fast enough, limiting current densities of 20 mA cm^{-2} could theoretically be achieved. Making use of the concept of permeability, two possible cell designs arise from this type of heterogeneous catalysis. First, as depicted in **Figure 3.20**, the triblock brush polymer ion gel electrolyte could be used as a thin layer scaffold to generate CO or CH_4 in air or with a positive pressure of CO_2 transported over the surface of the gel, provided a suitable catalyst is found to selectively carry out these transformations. Second, the water-tolerant, chemically cross-linked gel could be used as a thin layer in aqueous medium coupled to a gas diffusion electrode, which has been shown to sustain current densities greater than 50 mA cm^{-2}.[55] Presuming the gel is stable to liquid products such as CH_3OH, the constant flow of CO_2 would facilitate removal of the methanol from the polymer diffusion layer, thus preventing buildup of product that could block active sites for catalysis. The incorporation of these ion gel electrolytes into practical devices is an exciting prospect that will be pursued.

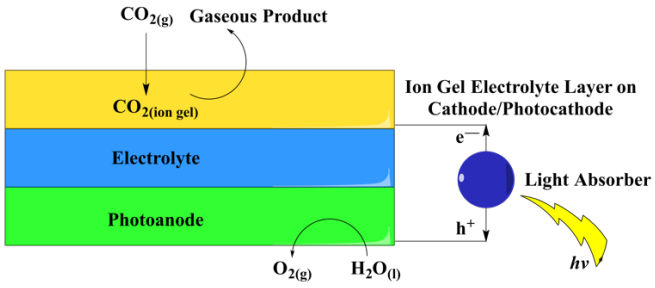

Figure 3.20. Cell schematic of a thin membrane ion gel electrolyte layer employed to surpass diffusion limitations of CO_2 reduction in aqueous media. Figure adapted from Reference 17.

3.7 Experimental

General

Pentacarbonylrhenium(I) chloride (Sigma-Aldrich), pentacarbonylrhenium(I) bromide (Sigma-Aldrich), and 2,2'-bipyridyl (Sigma-Aldrich) were used without further purification. 1,3-butylmethylimidazolium bis(trifluoromethylsulfonyl)imide, 1,3-ethylmethylimidazolium ethylsulfate, and 1,3-ethylmethylimidazolium triflate (Iolitec, Inc.) were dried under vacuum at 65 degrees Celsius for 24 hours prior to use. Anhydrous DCM was used for all syntheses. $Re(bpy)(CO)_3Cl$ and $Re(bpy)(CO)_3Br$ were prepared according to literature precedent.[36] 15:119:15 Polystyrene-polyethyleneoxide-polystyrene brush-block copolymer was synthesized according to literature precedent.[22] The gel phase chromatography of the final copolymer indicated that the polymer had a polydispersity close to 1, suggesting a narrowly dispersed polymer weight distribution.

15:119:15 PS:PEO:PS-BMIm-TFSI Ion Gel Electrolyte

In a glove box atmosphere, 15:119:15 polystyrene-polyethyleneoxide-polystyrene (100 mg) was dissolved in anhydrous dichloromethane (1.0 mL) and stirred for ten minutes. Additional dichloromethane (1.0 mL) and 1,3-butylmethylimidazolium bis(trifluoromethylsulfonyl)imide (0.70 mL) were added, and the mixture was stirred for an additional ten minutes. The stir bar was removed from the reaction, and the solution was allowed to sit for 36 hours to evaporate the dichloromethane and cast the gel electrolyte. Gels were confirmed dry by NMR.

Electrochemical Measurements

All electrochemical characterization of IL-polymer gel electrolytes was performed in an inert, argon atmosphere. Electrochemical characterization of ILs was performed with a Gamry Reference 600 or Bio-Logic VSP-300 potentiostat by transferring dried IL into a nitrogen-purged standard three-

electrode cell containing a 3 mm diameter glassy carbon working electrode (CH Instruments), silver wire pseudo-reference electrode (CH Instruments), and platinum wire counter electrode (Kurt J. Lesker). Bulk electrolysis measurements were performed in a gas-tight cell with a glassy carbon plate with a 1.35 cm^2 working area, a 0.01 M $Ag^{+/0}$ quasireference electrode (BMIm-TFSI) or Ag wire pseudoreference electrode (ion gel), and a platinum mesh counter electrode separated by a glass frit. The cell was purged with CO_2 for 2 hours prior to being sealed. Prior to gel electrolysis, gels were vacuum-dried for 4 days. Ultramicroelectrode experiments were performed with an 11 μm carbon fiber disk microelectrode, Ag pseudoreference electrode, and platinum wire counter electrode. All 3 mm glassy carbon disk experiments were compensated for 80-85% of the measured uncompensated resistance (R_u) value. Due to the small surface area of the working electrode, PEIS methods for determination of R_u are valid.

Gas Chromatography

After 1 hour of electrolysis, 10 mL of headspace were sampled with a gas-tight syringe and injected into an Agilent 7890a gas chromatograph. Calibration curve was obtained using mixtures of different percent volumes of CO in CO_2. For experiments with BMIm-TFSI, the headspace was measured to be 52.5 mL. For ion gel experiments, the headspace was measured to be 62 mL. **Figure 3.21** displays the calibration curve used to determine the Faradaic efficiency for all experiments.

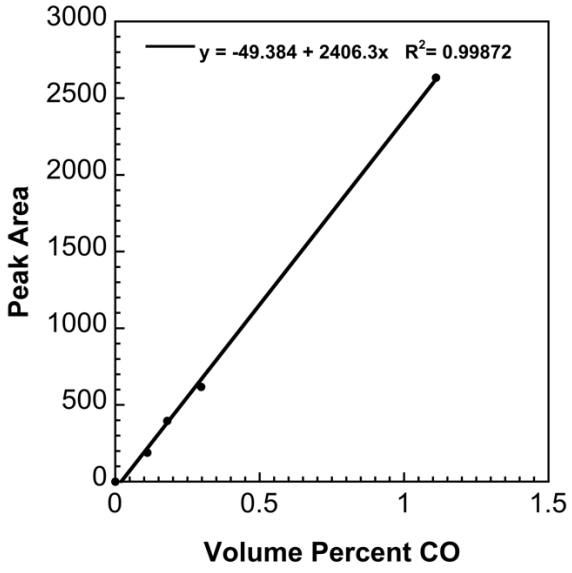

Figure 3.21. Calibration curve for CO detection on Agilent 7890a gas chromatograph. The curve was obtained by injecting different ratios of CO_2 to CO with a gas-tight syringe.

3.8 References

1. Grubbs, R. H.; Bates, C. M.; Chang, A. B.; McNicholas, B. J.; Jones, S. C. Brush Block Copolymer Electrolytes and Electrocatalyst Compositions. 15065317, 2016.
2. Grubbs, R. H.; Bates, C. M.; Chang, A. B.; McNicholas, B. J.; Jones, S. C. Triblock Brush Block Copolymers. 15065291, 2016.
3. McNicholas, B. J.; Blakemore, J. D.; Chang, A. B.; Bates, C. M.; Kramer, W. W.; Grubbs, R. H.; Gray, H. B. *J. Am. Chem. Soc.* **2016**, Submitted.
4. Gray, H. B. *Nat. Chem.* **2009**, *1*, 7.
5. Berardi, S.; Drouet, S.; Francàs, L.; Gimbert-Suriñach, C.; Guttentag, M.; Richmond, C.; Stoll, T.; Llobet, A. *Chem. Soc. Rev.* **2014**, *43*, 7501.
6. Savéant, J. M. *Chem. Rev.* **2008**, *108*, 2348.
7. Benson, E. E.; Kubiak, C. P.; Sathrum, A. J.; Smieja, J. M. *Chem. Soc. Rev.* **2009**, *38*, 89.
8. Appel, A. M.; Bercaw, J. E.; Bocarsly, A. B.; Dobbek, H.; DuBois, D. L.; Dupuis, M.; Ferry, J. G.; Fujita, E.; Hille, R.; Kenis, P. J. A.; Kerfeld, C. A.; Morris, R. H.; Peden, C. H. F.; Portis, A. R.; Ragsdale, S. W.; Rauchfuss, T. B.; Reek, J. N. H.; Seefeldt, L. C.; Thauer, R. K.; Waldrop, G. L. *Chem. Rev.* **2013**, *113*, 6621.
9. Costentin, C.; Robert, M.; Savéant, J.-M. *Chem. Soc. Rev.* **2013**, *42*, 2423.
10. Sampson, M. D.; Froehlich, J. D.; Smieja, J. M.; Benson, E. E.; Sharp, I. D.; Kubiak, C. P. *Energy Environ. Sci.* **2013**, *6*, 3748.
11. Hori, Y.; Kikuchi, K.; Suzuki, S. *Chem. Lett.* **1985**, 1695.
12. Kuhl, K. P.; Cave, E. R.; Abram, D. N.; Jaramillo, T. F. *Energy Environ. Sci.* **2012**, *5*, 7050.

13. Manthiram, K.; Beberwyck, B. J.; Alivisatos, A. P. *J. Am. Chem. Soc.* **2014**, *136*, 13319.

14. Torelli, D. A.; Francis, S. A.; Crompton, J. C.; Javier, A.; Thompson, J. R.; Brunschwig, B. S.; Soriaga, M. P.; Lewis, N. S. *ACS Catal.* **2016**, *6*, 2100.

15. Kumar, B.; Asadi, M.; Pisasale, D.; Sinha-Ray, S.; Rosen, B. A.; Haasch, R.; Abiade, J.; Yarin, A. L.; Salehi-Khojin, A. *Nat. Commun.* **2013**, *4*, 1.

16. Aresta, M.; Dibenedetto, A.; Quaranta, E. In *Reaction Mechanisms in Carbon Dioxide Conversion*; 1 ed.; Springer Berlin Heidelberg: Berlin, Germany, 2016, p 311.

17. Grills, D. C.; Farrington, J. A.; Layne, B. H.; Lymar, S. V.; Mello, B. A.; Preses, J. M.; Wishart, J. F. *J. Am. Chem. Soc.* **2014**, *136*, 5563.

18. Chen, Y.; Lewis, N. S.; Xiang, C. *Energy Environ. Sci.* **2015**, *8*, 3663.

19. Underwood, A. J. V. *Ind. Eng. Chem. Res.* **1940**, *32*, 449.

20. Bontemps, S.; Vendier, L.; Sabo-Etienne, S. *J. Am. Chem. Soc.* **2014**, *136*, 4419.

21. Luca, O. R.; McCrory, C. C. L.; Dalleska, N. F.; Koval, C. A. *J. Electrochem. Soc.* **2015**, *162*, H473.

22. Blakemore, J. D.; Gupta, A.; Warren, J. J.; Brunschwig, B. S.; Gray, H. B. *J. Am. Chem. Soc.* **2013**, *135*, 18288.

23. Kinning, D. J.; Thomas, E. L. *Macromolecules* **1984**.

24. Bates, F. S.; Fredrickson, G. H. *Phys. Today* **1999**, *52*, 32.

25. He, Y.; Boswell, P. G.; Bühlmann, P.; Lodge, T. P. *J. Phys. Chem. B* **2007**, *111*, 4645.

26. Lodge, T. P. *Science* **2008**, *321*, 50.

27. Gu, Y.; Zhang, S.; Martinetti, L.; Lee, K. H.; McIntosh, L. D.; Frisbie, C. D.; Lodge, T. P. *J. Am. Chem. Soc.* **2013**, *135*, 9652.

28. Xia, Y.; Kornfield, J. A.; Grubbs, R. H. *Macromolecules* **2009**; *42*, 3761.

29. Bates, C. M.; Chang, A. B.; Schulze, M. W.; Momcilovic, N.; Jones, S. C.; Grubbs, R. H. *J. Polym. Sci. B Polym. Phys.* **2015**, *54*, 292.

30. Bates, C. M.; Chang, A. B.; Momčilović, N.; Jones, S. C. *Macromolecules* **2016**, *48*, 4967.

31. Fuller, J.; Breda, A. C.; Carlin, R. T. *J. Electrochem. Soc.* **1997**, *144*, L67.

32. Grills, D. C.; Matsubara, Y.; Kuwahara, Y.; Golisz, S. R.; Kurtz, D. A.; Mello, B. A. *J. Phys. Chem. Lett.* **2014**, *5*, 2033.

33. Hawecker, J.; Lehn, J. M.; Ziessel, R. In *J. Chem. Soc., Chem. Commun.* **1984**, 328.

34. Sullivan, B. P.; Bolinger, C. M.; Conrad, D.; Vining, W. J.; Meyer, T. J. *J. Chem. Soc., Chem. Commun.* **1985**, 1414.

35. Hawecker, J.; Lehn, J. M.; Ziessel, R. *Helv. Chim. Acta.* **1986**, *69*, 1990.

36. Grice, K. A.; Kubiak, C. P. In *Advances in Inorganic Chemistry*; Aresta, M.; van Eldik, R. Elsevier: Oxford, U. K., 2014; Vol. 66, p 163.

37. Riplinger, C.; Sampson, M. D.; Ritzmann, A. M.; Kubiak, C. P.; Carter, E. A. *J. Am. Chem. Soc.* **2014**, *136*, 16285.

38. Raghavan, S. R.; Cipriano, B. H. In *Molecular Gels*; Weiss, R. G.; Pierre, T. Springer Netherlands: Dordrecht, The Netherlands, 2006, p 241.

39. Rogers, E. I.; Silvester, D. S.; Poole, D. L.; Aldous, L.; Hardacre, C.; Compton, R. G. *J. Phys. Chem. C* **2008**, *112*, 2729.

40. Nicholson, R. S.; Shain, I. *Anal. Chem.* **1964**, *36*, 706.

41. Hapiot, P.; Lagrost, C. *Chem. Rev.* **2008**, *108*, 2238.

42. Barrosse-Antle, L. E.; Bond, A. M.; Compton, R. G.; O'Mahony, A. M.; Rogers, E. I.; Silvester, D. S. *Chem. Asian J.* **2010**, *5*, 202.

43. Bard, A. J.; Faulkner, L. R. In *Electrochemical Methods*; Wiley: 2000.

44. Sun, L.; Ramesha, G. K.; Kamat, P. V.; Brennecke, J. F. *Langmuir* **2014**, *30*, 6302.

45. Alvarez-Guerra, M.; Albo, J.; Alvarez-Guerra, E.; Irabien, A. *Energy Environ. Sci.* **2015**, *8*, 2574.

46. Oh, Y.; Hu, X. *Chem. Commun.* **2015**, *51*, 13698.

47. Juris, A.; Campagna, S.; Bidd, I.; Lehn, J.-M.; Ziessel, R. *Inorg. Chem.* **1988**, *27*, 4007.

48. Smieja, J. M.; Kubiak, C. P. *Inorg. Chem.* **2010**, *49*, 9283.

49. Erhard, H.; Jaenicke, W. *J. Electroanal. Chem. Interfacial Electrochem.* **1977**, *81*, 79.

50. Tsurumaki, A.; Kagimoto, J.; Ohno, H. *Polymer. Adv. Tech.* **2011**, *22*, 1223.

51. Kadish, K. M.; Shen, J.; Frémond, L.; Chen, P.; Ojaimi, M. E.; Chkounda, M.; Gros, C. P.; Barbe, J. M.; Ohkubo, K.; Fukuzumi, S.; Guilard, R. *Inorg. Chem.* **2008**, *47*, 6726.

52. Matsubara, Y.; Grills, D. C.; Kuwahara, Y. *ACS Catal.* **2015**, *5*, 6440.

53. Wang, Y.; Rogers, E. I.; Compton, R. G. *J. Electroanal. Chem.* **2010**, *648*, 15.

54. Lei, Z.; Dai, C.; Chen, B. *Chem. Rev.* **2014**, *114*, 1289.

55. Hara, K.; Sakata, T. *J. Electrochem. Soc.* **1997**, *144*, 539.

Chapter IV

TUNING THE FORMAL POTENTIAL OF FERROCYANIDE OVER A >2.1 V RANGE

Adapted with permission from McNicholas, B. J.; Grubbs, R. H.; Winkler, J. R.; Grubbs, R. H.; Gray, H. B.; Despagnet-Ayoub, E. Tuning the Formal Potential of Ferrocyanide over a 2.1 V Range. *Chem. Sci.* **2019**, *10*, 3623-3626. DOI: 10.1134/S1023193517100068. Copyright 2019 Royal Society of Chemistry.

4.1 Summary

We report the synthesis and characterization of homoleptic borane adducts of hexacyanoferrate(II). Borane coordination blueshifts d–d transitions, metal-to-ligand charge transfer, and cyanide IR and Raman frequencies. Control over redox properties is established with respect to borane Lewis acidity, reflected in peak anodic potential shifts per borane of +250 mV for triphenylborane (BPh_3) and +380 mV for tris(pentafluorophenyl)borane (BCF). Differential pulse voltammetry, scan rate dependence, and chemical oxidation of $[Fe(CN\text{-}BPh_3)_6]^{4-}$ demonstrate the lability of CN-BPh_3 linkages upon oxidation from Fe(II) to Fe(III). Electron transfer from $[Fe(CN\text{-}BCF)_6]^{4-}$ to photogenerated $[Ru(2,2'\text{-bipyridine})_3]^{3+}$ is very rapid, consistent with electrochemically reversible voltammetry data. Coordination by Lewis acids provides an avenue for selective modification of the electronic structures and electrochemical properties of cyanometallates. While previous studies have hinted at the effects of Lewis acids on the electronic structure of homoleptic cyanometallates, the studies presented herein unambiguously identify the effects of boronation on the energies of both ligand field and metal-to-ligand charge transfer transitions, as well as the ground state electronic structure, as evidenced by the electrochemical responses of iron-based cyanometallates.

4.2 Introduction

Duward Shriver pioneered the study of borane adducts of cyanometallates.[1a-d] Although he established from analysis of vibrational spectroscopic data that borane coordination (CN-BR_3) enhanced M(d^6)-CN π backbonding, surprisingly, to the best of our knowledge, no structures of d^6 low-spin borane adducts have been hitherto reported.[2] Indeed, only three homoleptic borane adducts have been crystallographically characterized, $(TEA)_3[Cr(NC\text{-}BPh_3)_6]$ (TEA = tetraethylammonium, BPh_3 = triphenylborane), $(CPh_3)_2[Ni(CN\text{-}B(C_6F_5)_3)_4]$, and $(CPh_3)_2[Ni(CN\text{-}B(C_6F_5)_3)_4]$ (CPh_3 = trityl cation, $B(C_6F_5)_3$ = tris(pentafluorophenyl)borane).[3,4] Also surprising is that very little is known about the electrochemistry of coordinatively-saturated borane adducts of hexacyanometallates, with the majority of previous work focused on the solvent dependence of cyanometallate redox potentials or the effects on MLCT transition energies.[1d,5-8]

4.3 Significance

Our work unambiguously quantifies the effects of Lewis acids on both the ground state and excited state electronic structures of closed shell cyanometallates. We demonstrate the effects of boronation on the energies of both ligand field states and metal-to-ligand charge transfer (MLCT) states. We also show herein that the formal potentials (the use of formal potential as a term is valid since we are considering the $E_{1/2}$ of a species in a specific solvent referenced to a standard redox couple) of these boronated adducts span an unusually wide range (approximately 2.3 V), making these complexes useful oxidants and reductants in energy storage devices, reversible chemical oxidants and reductants, and excited state quenching reagents. We also demonstrate that the strength of Lewis acidity dramatically affects the electrochemical response of these complexes, with weaker Lewis acids exhibiting electrochemically irreversible voltammetry that is coupled to chemical reactions associated with dissociation of cyanide or isocyanoborate ligands. This electrochemical irreversibility stems from

the lack of π-backdonation from the metal center, which results in instability of lesser d electron configurations.

4.4 Results and Discussion

Tetrabutylammonium (TBA) and TEA hexacyanoferrate(II) compounds were prepared using a modified literature procedure.[9] Neutralization of $H_4[Fe(CN)_6]$ with TBAOH (or TEAOH) in water generated the alkylammonium salt in quantitative yield. Bis(triphenylphosphine)iminium (PPN) hexacyanoferrate(II) (**1c**) was prepared by combining four equivalents of PPNCl with one equivalent of $K_4[Fe(CN)_6]$ in water. ^{1}H NMR, $^{13}C\{^1H\}$ NMR, UV-vis, solid-state IR, and voltammetry confirmed the purity of $[Fe(CN)_6]^{4-}$, with a single, electrochemically reversible redox couple with a formal potential equal to −1.45 V vs. $Fc^{+/0}$ in MeCN.

The borane adducts of hexacyanoferrate(II) were synthesized by combining six equivalents of borane with one equivalent of hexacyanoferrate(II) dissolved in DCM in a nitrogen-filled glove box. Coordination of borane generated $(TEA)_4[Fe(CN\text{-}BPh_3)_6]$ and $(PPN/TBA)_4[Fe(CN\text{-}B(C_6F_5)_3)_6]$. Both complexes were purified and subsequently analyzed by ^{11}B and ^{13}C NMR spectroscopy, X-ray crystallography, UV-vis spectroscopy, elemental analysis, and voltammetry.

Full borane coordination for all species was confirmed by analysis of X-ray crystallographic data, with representative structures depicted in **Figure 4.1**. The average M-CN (1.91 Å) and C-N (1.17 Å) bond lengths for $(TEA)_4[Fe(CN\text{-}BPh_3)_6]$ compared to the base complex, 1.93 Å and 1.17 Å, respectively, are consistent with competing σ and π interactions, where σ donation from nitrogen to boron weakens the M-CN bond, while π backbonding strengthens it. Thus, the contraction of the M-CN bond in $(TEA)_4[Fe(CN\text{-}BPh_3)_6]$ is negligibly small. The average M-C-N (174.6°) and C-N-B (172.3°) bond

angles in complex $[Fe(CN\text{-}BPh_3)_6]^{4-}$ are not perfectly linear, likely due to the effects of steric clash among the aryl groups. The average M-C-N (176.9°) and C-N-B (173.9°) bond angles for complex **3** are similarly perturbed. There are slight contractions in average M-CN (1.90 Å) and C-N (1.15 Å) bond lengths for $(PPN)_4[Fe(CN\text{-}B(C_6F_5)_3)_6]$ compared to those in $(TEA)_4[Fe(CN\text{-}BPh_3)_6]$.

In the $^{13}C\{^1H\}$ NMR spectra, the cyanide carbon exhibits only one peak, indicating that boranes are bound to all six cyanides (δ_{CN}: 159 ppm for $[Fe(CN\text{-}BPh_3)_6]^{4-}$ and 162 ppm for $[Fe(CN\text{-}B(C_6F_5)_3)_6]^{4-}$).

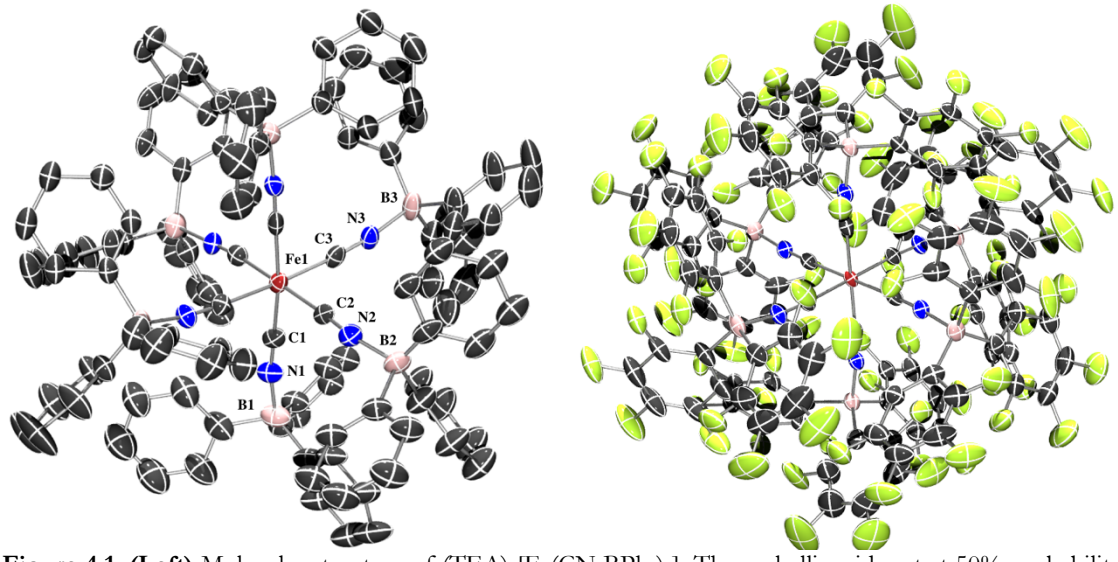

Figure 4.1. **(Left)** Molecular structure of $(TEA)_4[Fe(CN\text{-}BPh_3)_6]$. Thermal ellipsoids set at 50% probability. Cations and protons omitted for clarity. Selected bond distances and angles: Fe1-C1: 1.908(7) Å, Fe1-C3: 1.913(8) Å, Fe1-C4: 1.908(8) Å, C1-N1: 1.170(9) Å, C3-N3: 1.164(10) Å, C4-N4: 1.166(10) Å, N1-B1: 1.559(9) Å, N3-B3: 1.573(10) Å, N4-B4: 1.557(10) Å, Fe1-C1-N1: 174.0(7), Fe1-C3-N3: 174.0(7), Fe4-C4-N4: 179.6(8), C1-N1-B1: 172.0(8), C3-N3-B3: 173.5(8), C4-N4-B4: 176.3(7), **(Right)** Molecular structure of $(PPN)_4[Fe(CN\text{-}B(C_6F_5)_3)_6]$. Thermal ellipsoids set at 50% probability. Cations omitted for clarity. Selected bond distances and angles (labels as in **Left**): Fe1-C1: 1.899(4) Å, Fe1-C3: 1.904(3) Å, Fe1-C4: 1.897(3) Å, C1-N1: 1.146(4) Å, C3-N3: 1.152(4) Å, C4-N4: 1.160(4) Å, N1-B1: 1.545(5) Å, N3-B3: 1.550(5) Å, N4-B4: 1.551(4) Å, Fe1-C1-N1: 176.9(3), Fe1-C3-N3: 177.9(3), Fe1-C4-N4: 175.9(3), C1-N1-B1: 173.2(3), C3-N3-B3: 175.1(3), C4-N4-B4: 173.3(4).

The carbon chemical shift follows the expected downfield trend for a Lewis acid inductively withdrawing electron density through the terminal nitrogen. The change in shift between the BPh_3

and $B(C_6F_5)_3$ adducts is small due to cooperative σ donation from the nitrogen and π backdonation from the metal center. It is well understood that isocyanoborate complexes experience decreased σ-bonding relative to cyano parents due to reduced electron density on carbon. Conversely, isocyanoborate complexes experience greater π-backbonding relative to cyanide complexes due to lower π^*(CN) energies. The ^{11}B NMR spectra of $(TEA)_4[Fe(CN\text{-}BPh_3)_6]$ and $(PPN)_4[Fe(CN\text{-}B(C_6F_5)_3)_6]$ are in line with increased electron-withdrawing by $B(C_6F_5)_3$ relative to BPh_3, with the ^{11}B signal for $B(C_6F_5)_3$ more upfield versus BPh_3 (δ = −5.3 ppm for $(TEA)_4[Fe(CN\text{-}BPh_3)_6]$ and −14.4 ppm for $(PPN)_4[Fe(CN\text{-}B(C_6F_5)_3)_6]$).

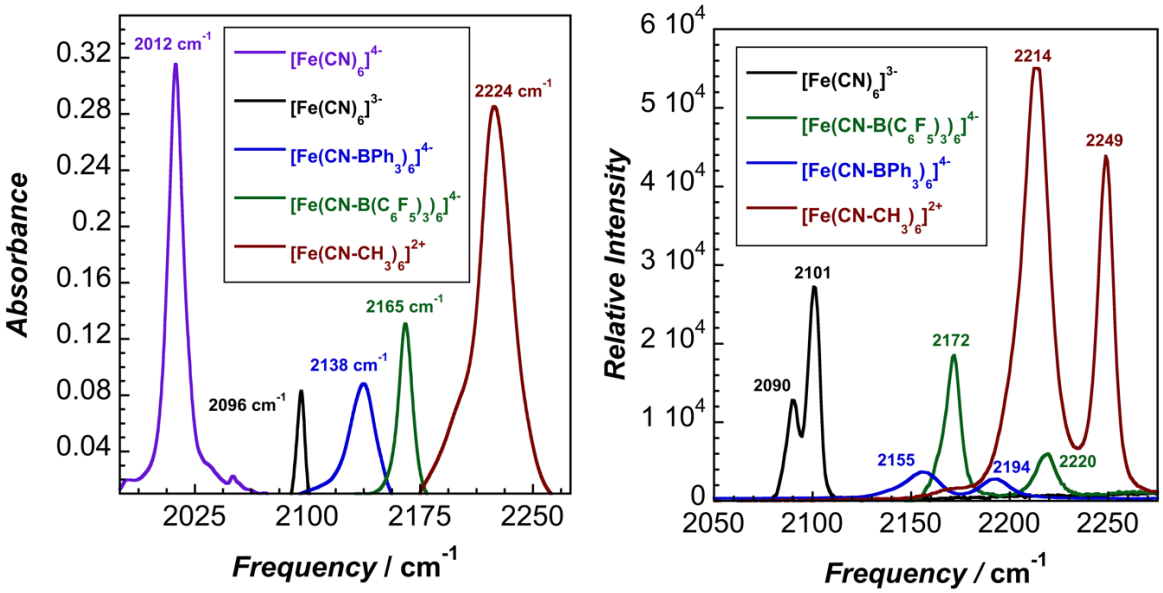

Figure 4.2. (**Left**) Infrared spectra of hexacyanoferrate derivatives. (**Right**) Raman spectra of hexacyanoferrate derivatives.

The solid-state IR and Raman spectra of $[Fe(CN)_6]^{4-}$ and its various adducts are shown in **Figure 4.2**. As expected, the CN stretching frequency increases as the Lewis acidity of the borane or the oxidation state of the metal increases. Increased Lewis acidity causes increased stretching frequency, a result of

lowering the absolute energies of the cyanide-based π-bonding orbitals.[10] To complete the trend, the methylated adduct of hexacyanoferrate was synthesized, and this species exhibits the most blue shifted IR and Raman stretching frequencies. However, this is likely a combination of both the increased Lewis acidity and increased net positive charge of the species.

The lowest energy absorption band in the UV-vis spectra (**Figure 4.3**) of the adducts is attributable to an electric dipole-forbidden, spin-allowed d-d transition ($^1A_{1g} \rightarrow {}^1T_{1g}$).[9] This band, 323 nm in water, redshifts to 357 nm in MeCN (29,060 cm^{-1} based on Gaussian deconvolution). Upon coordination of BPh_3 and $B(C_6F_5)_3$, $(TEA)_4[Fe(CN\text{-}BPh_3]$ and $(TBA)_4[Fe(CN\text{-}B(C_6F_5)_3)_6]$ exhibit blueshifted absorbance maxima, indicating that increased backbonding outweighs decreased σ bonding in the octahedral ligand field.[9] For $[Fe(CN\text{-}BPh_3)_6]^{4-}$ and $[Fe(CN\text{-}B(C_6F_5)_3)_6]^{4-}$, bands below 270 nm are attributable to either borane $\pi\text{-}\pi^*$ transitions or metal-to-ligand charge transfer transitions of $[Fe(CN\text{-}BPh_3)_6]^{4-}$ or $[Fe(CN\text{-}B(C_6F_5)_3)_6]^{4-}$ (**Figure 4.4**).

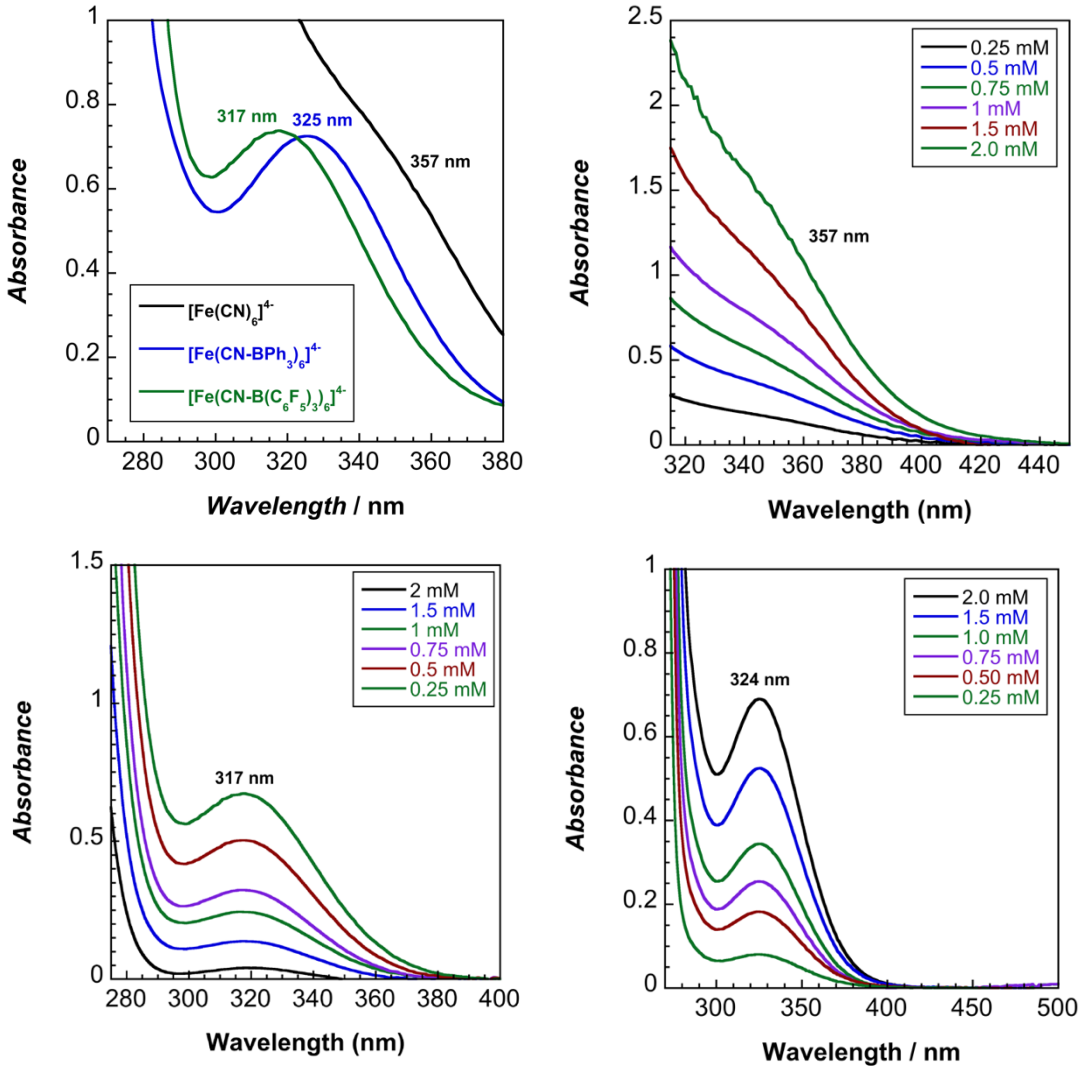

Figure 4.3. Comparison of the $^1A_{1g} \rightarrow {}^1T_{1g}$ absorption bands in borane adducts of hexacyanoferrate in dichloromethane, emphasizing the blue shifted absorbance of boronated cyanometallates. (Top Right) $^1A_{1g} \rightarrow {}^1T_{1g}$ absorption of $[Fe(CN)_6]^{4-}$. (Bottom Left) $^1A_{1g} \rightarrow {}^1T_{1g}$ absorption of $[Fe(CN\text{-}BPh_3)_6]^{4-}$. (Bottom Right) $^1A_{1g} \rightarrow {}^1T_{1g}$ absorption of $[Fe(CN\text{-}BCF)_6]^{4-}$.

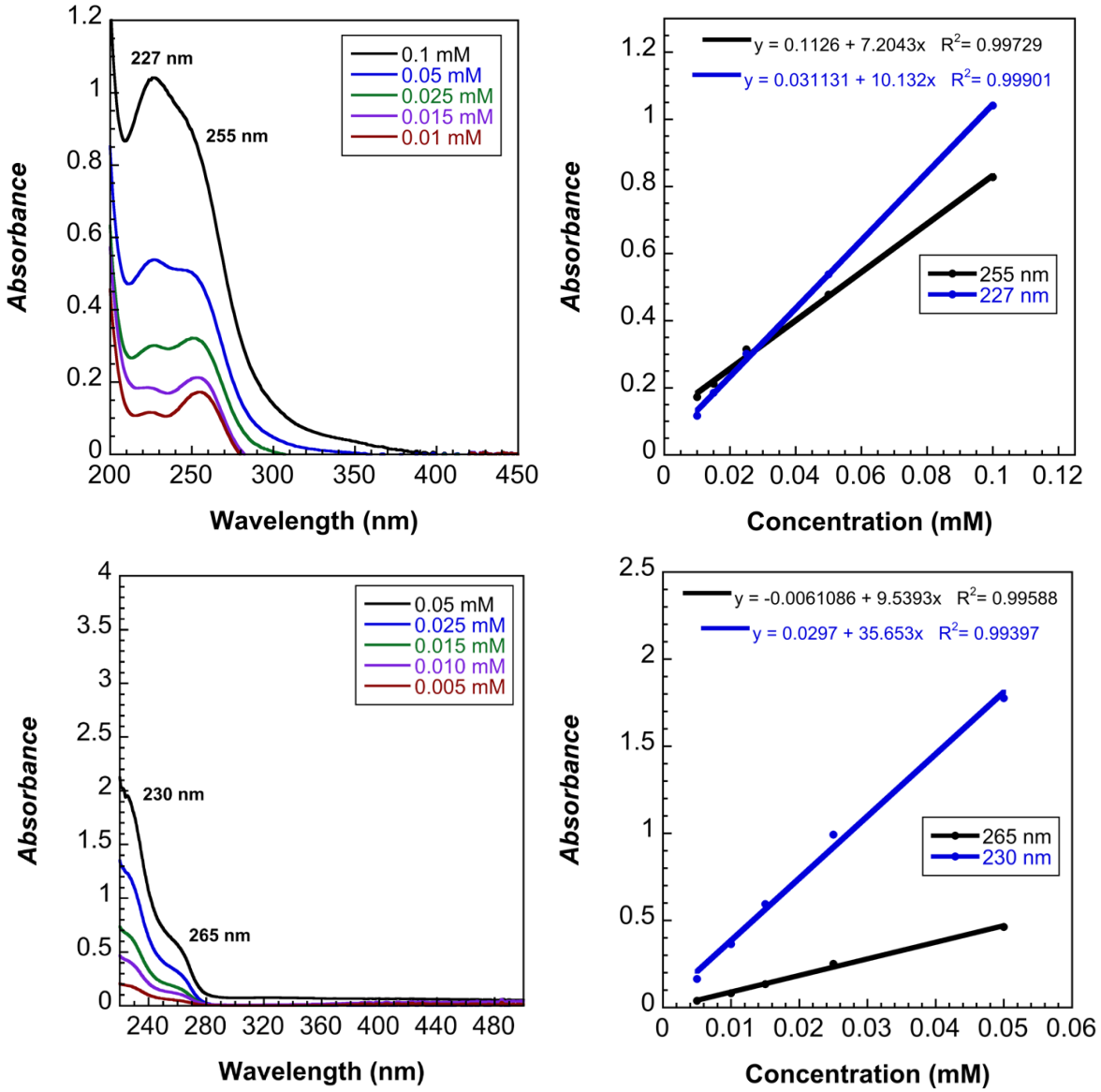

Figure 4.4. Comparison of the charge transfer transitions in bare hexacyanoferrate and borane adducts of hexacyanoferrate in dichloromethane, emphasizing the blue shifted absorbance of MLCT transitions in boronated cyanometallates. (Top) MLCT transitions in $(TBA)_4[Fe(CN)_6]$. (Bottom) π-π^* transitions in $(TBA)_4[Fe(CN\text{-}BCF)_6]$.

To more rigorously analyze and compare the charge transfer transitions in homoleptic Fe(II) complexes, the complexes' absorbance spectra were deconvoluted using a series of Gaussian curves. **Figure 4.5** displays the curves extracted from both $(TEA)_4[Fe(CN)_6]$ and $(TBA)_4[Fe(CN\text{-}BCF)_6]$. To

our knowledge, this is the first demonstration of the solvation-dependent red-shifting of the MLCT bands of $[Fe(CN)_6]^{4-}$. Previous studies have used MCD spectroscopy to analyze the selection rules and transition intensities of d^6, closed shell hexacyanometallates (M = Ru, Os, Fe) and metal hexacarbonyl complexes. Based on group theory, the dipole allowed MLCT transitions in homoleptic hexacyanoferrates are $t_{2g} \rightarrow t_{2u}$ and $t_{2g} \rightarrow t_{1u}$. However, the allowedness of each transition, which dictates the observed oscillator strength and extinction coefficient, is mitigated by orbital overlap of the transition.

Based on UV-vis spectroscopy of neat $B(C_6F_5)_3$ in MeCN, the first two transitions in $[Fe(CN\text{-}B(C_6F_5)_3)_6]^{4-}$ corresponds to $\pi \rightarrow \pi^*$ transitions of $B(C_6F_5)_3$, with extinction coefficients of approximately 10,300 M^{-1} cm^{-1} and 27,360 M^{-1} cm^{-1}. This is in contrast to the observed spectroscopy of $[Fe(CN)_6]^{4-}$, where UV-vis spectroscopy display two transitions at 38,700 cm^{-1} and 44,190 cm^{-1}, both of which are assigned to MLCT transitions. The Gaussian deconvolution of both $[Fe(CN)_6]^{4-}$ and $[Fe(CN\text{-}B(C_6F_5)_3)_6]^{4-}$ is shown in **Figure 4.5**. For $[Fe(CN\text{-}B(C_6F_5)_3)_6]^{4-}$, the first MLCT transition occurs at 48,100 cm^{-1}, approximately 600 cm^{-1} blue shifted of the first MLCT in $H_4[Fe(CN)_6]$. This trend is intuitive based on the interplay between backbonding and sigma donation afforded by six boranes versus four protons. **Table 4.1** delineates the ligand field and MLCT energies of Fe(II) hexacyanometallates based on both Gaussian deconvolution and previous studies. Further studies of the higher-energy UV region of the spectrum will provide more conclusive diagnosis of the $t_{2g} \rightarrow t_{2u}$ transition in $[Fe(CN\text{-}B(C_6F_5)_3)_6]^{4-}$ and identification of the $t_{2g} \rightarrow t_{2u}$ and $t_{2g} \rightarrow t_{1u}$ transitions in $[Fe(CN\text{-}BPh_3)_6]^{4-}$.

Table 4.1. MLCT transitions and ligand field transitions observed for Fe(II) cyanometallate derivatives.

Complex / Transition (cm^{-1})	$t_{2g}(\pi) \rightarrow t_{1u}(\pi^*)$	$t_{2g}(\pi) \rightarrow t_{2u}(\pi^*)$	$t_{2g}(\pi) \rightarrow e_g(\sigma^*)$ $^1A_{1g} \rightarrow {}^1T_{1g}$	$t_{2g}(\pi) \rightarrow e_g(\sigma^*)$ $^1A_{1g} \rightarrow {}^1T_{2g}$
$K_4[Fe(CN)_6]$[a]	45,870	50,000	31,000	37,040
$(TBA)_4[Fe(CN)_6]$	38,700	44,190	29,060	33,510
$H_4[Fe(CN)_6]$[a]	47,500	---	32,800	---
$(TBA)_4[Fe(CN\text{-}BCF)_6]$	48,380	52,230	31,550	---
$(TEA)_4[Fe(CN\text{-}BPh_3)_6]$	---	---	30,960	---

[a]Reference 10

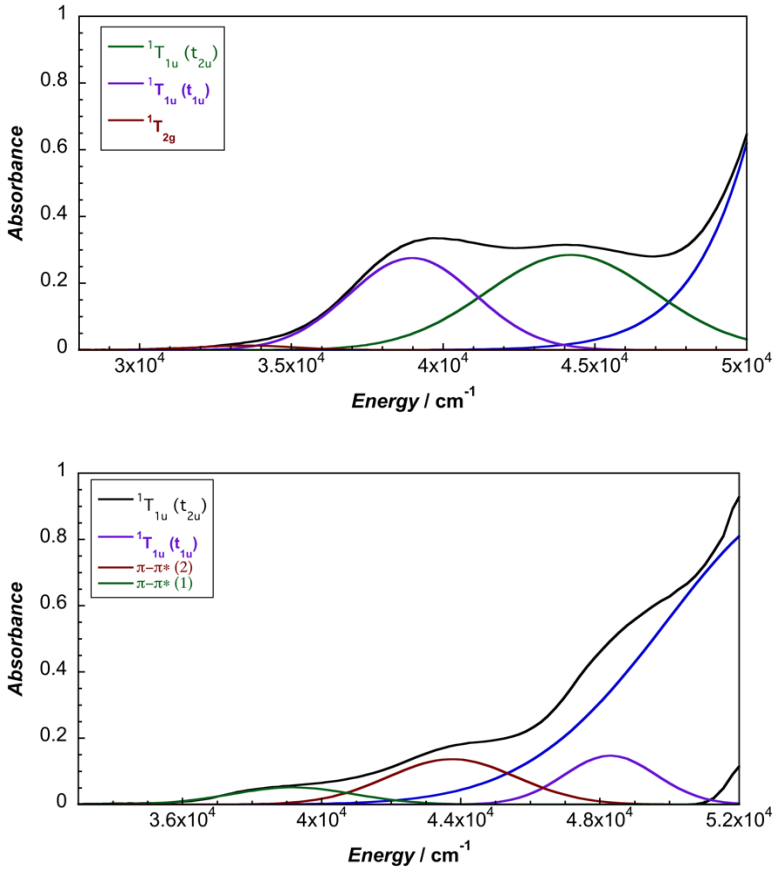

Figure 4.5. Gaussian deconvolution of the MLCT and LLCT transitions in $[Fe(CN)_6]^{4-}$ (upper) and $[Fe(CN\text{-}B(C_6F_5)_3)_6]^{4-}$ in MeCN.

Cyclic voltammograms of pure $(TBA)_4[Fe(CN)_6]$ in DCM solution and one with two equivalents of BPh_3 added are shown in **Figure 4.6**. Both voltammograms were corrected for the non-Faradaic charging current and integrated to ensure that the anodic charge passed was equal for both, suggesting

that the only redox reaction taking place is the one of interest ($Fe^{III/II}$). By adding two equivalents of BPh_3, seven anodic peaks are visible, corresponding to an equilibrium distribution of all possible numbers of boranes coordinated to hexacyanoferrate(II). The seven anodic peaks corresponding to different coordination numbers are clearly seen in differential pulse voltammetry (**Figure 4.6**). The differential current responses for the two- and three-coordinate species are broader, likely due to the existence of isomers being oxidized at slightly different potentials, which decreases the intensity and broadens the observed differential wave for these adducts.[11] As expected, the addition of borane results in a more positive peak anodic potential, likely due to lowering the absolute energies of the metal-based orbitals. The trend in peak anodic potential shift (from cyclic voltammetry) per borane added to hexacyanoferrate(II) is linear (**Figure 4.6**), suggesting an electron withdrawing effect that is solely dependent on the Lewis acidity of the borane, with little to no attenuating effects as more boranes are added to the secondary coordination sphere.[12] Assuming the peak anodic potential correlates with the formal potential for each borane species, the linear behavior is consistent with **Equation 4.1**,

$$E_n^o - E_{n-1}^o = \frac{RT}{F} \ln \frac{K_n^{II}}{K_n^{III}} \tag{4.1}$$

where the change in formal potential upon coordination of an additional borane is proportional to the ratio of binding constants of BPh_3 to the Fe(II) and Fe(III) states of the complex.[12] The approximate $E_{1/2}$ value in DCM for $(TEA)_4[Fe(CN\text{-}BPh_3)_6]$ is 0.32 V vs. $Fc^{+/0}$.

Although full coordination of borane in $(TEA)_4[Fe(CN\text{-}BPh_3)_6]$ was confirmed by both X-ray crystallography and ^{13}C NMR, the voltammetry of $(TEA)_4[Fe(CN\text{-}BPh_3)_6]$ in both DCM and MeCN is not electrochemically reversible (**Figure 4.6**).

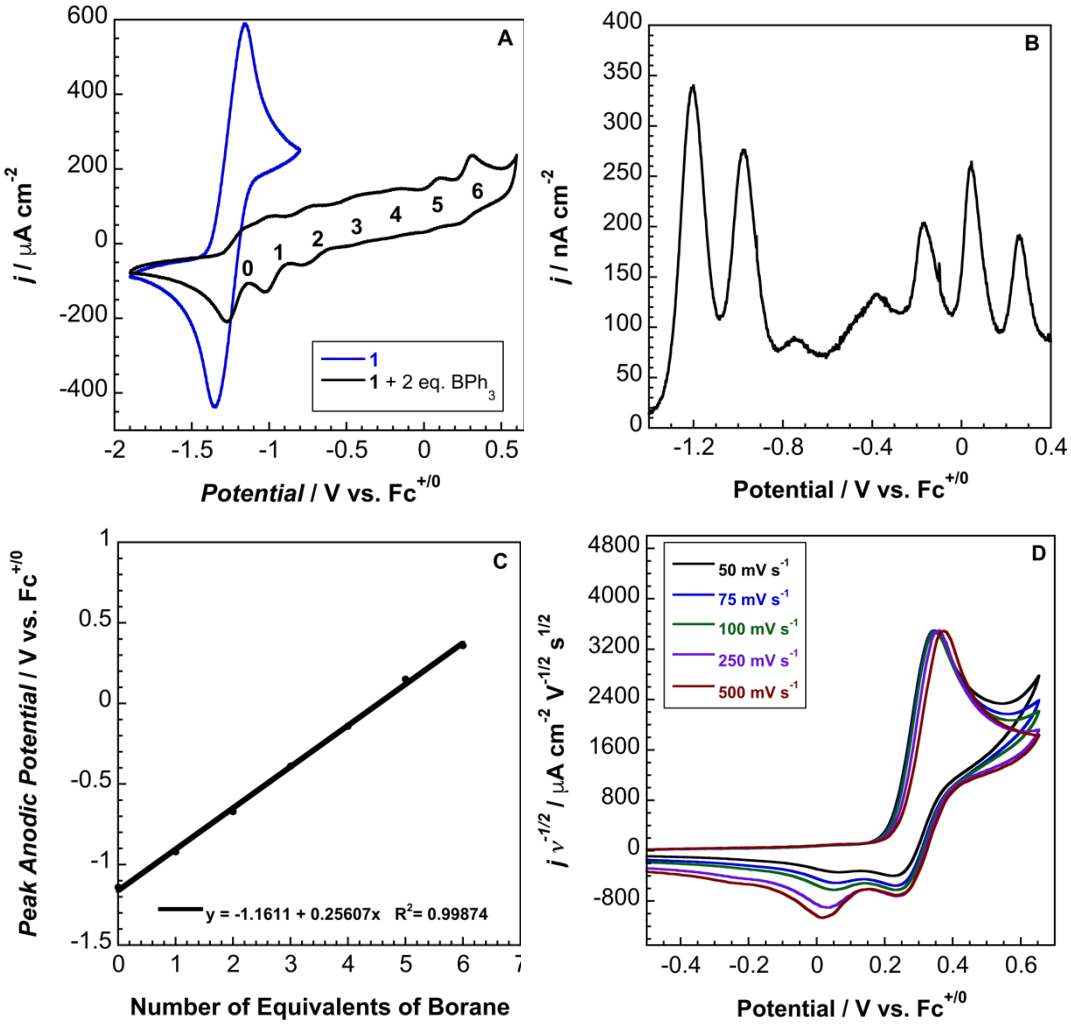

Figure 4.6. (**A**) Cyclic voltammograms of 5 mM $(TBA)_4[Fe(CN)_6]$ with two equivalents of BPh_3 (black) at 100 mV s^{-1} in dichloromethane with 0.1 M $TBAPF_6$, (**B**) Differential pulse voltammetry of $(TBA)_4[Fe(CN)_6]$ with two equivalents of BPh_3, (**C**) Linear regression of peak anodic potential versus number of BPh_3 coordinated to $(TBA)_4[Fe(CN)_6]$, (**D**) Scan rate dependence of $(TEA)_4[Fe(CN\text{-}BPh_3)_6]$ in MeCN with 0.2 M $TBAPF_6$.

Cyclic voltammetry suggests that the complex undergoes electron transfer followed by a borane dissociation, with the metalloproduct undergoing reduction and subsequent re-oxidation (EC mechanism).[13] The proposed mechanism is supported by a peak current ratio that is less than one for the six-coordinate species and by the presence of cathodic waves that correspond to reduction of the four-, five-, and six-coordinate species (**Figure 4.7**).[13] We observe a 28 mV shift in peak anodic potential with a ten-fold increase in scan rate, consistent with the theoretical value of 30 mV for a purely kinetic EC mechanism.[13] This mechanism is also supported by the appearance of anodic waves for the four- and five-coordinate species as a result of sweeping through multiple cycles at fast scan rates and by the decrease in anodic current for the six-coordinate species after the first scan (**Figure 4.7**). The peak cathodic current does not increase with increasing scan rate, consistent with very rapid BPh_3 dissociation.[13] Additionally, $(TEA)_4[Fe(CN\text{-}BPh_3)_6]$ was oxidized with dibenzo-1,4-dioxin radical cation in MeCN, and ^1H NMR in CD_3CN confirmed the presence of $Ph_3B\text{-}NCMe$ (**Figure 4.8**). Based on changes in peak current ratio with scan rate (**Figure 4.9**), current densities, and peak potentials, a square scheme mechanism (**Figure 4.9**) can be derived for sequential dissociations of BPh_3 from the complex.

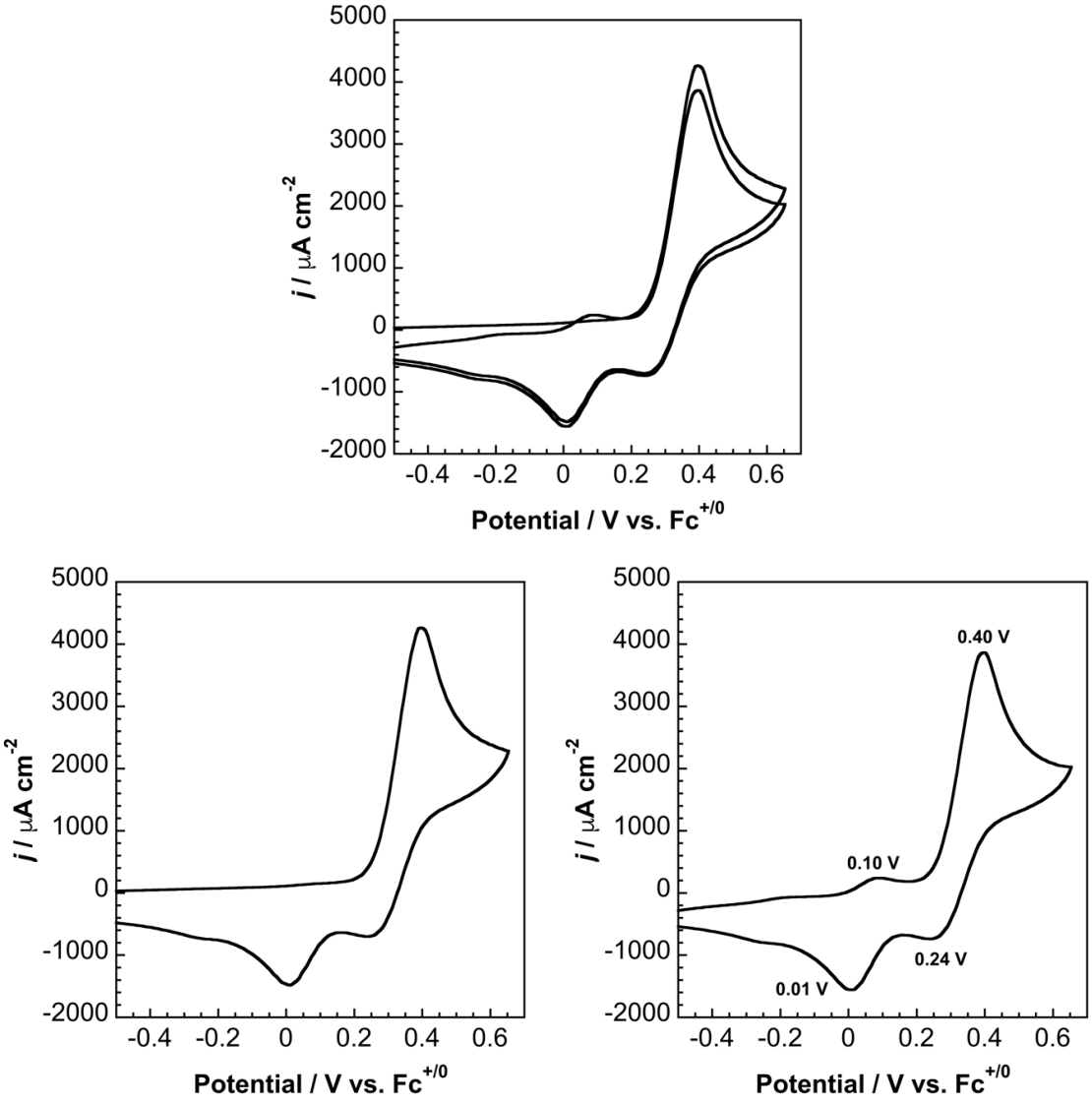

Figure 4.7. (Top) Voltammetry of $(TEA)_4[Fe(CN\text{-}BPh_3)_6]$ in acetonitrile with 0.2 M $TBAPF_6$ at 5 V s^{-1}. (Left) First scan at 5 V s^{-1}, showing three cathodic peaks. (Right) Second scan at 5 V s^{-1}, showing reoxidation of the electrochemically generated four- and five-coordinate species. Peak anodic potentials match the peak anodic potentials observed in the voltammetry of $(TEA)_4[Fe(CN)_6]$ with different equivalents of BPh_3.

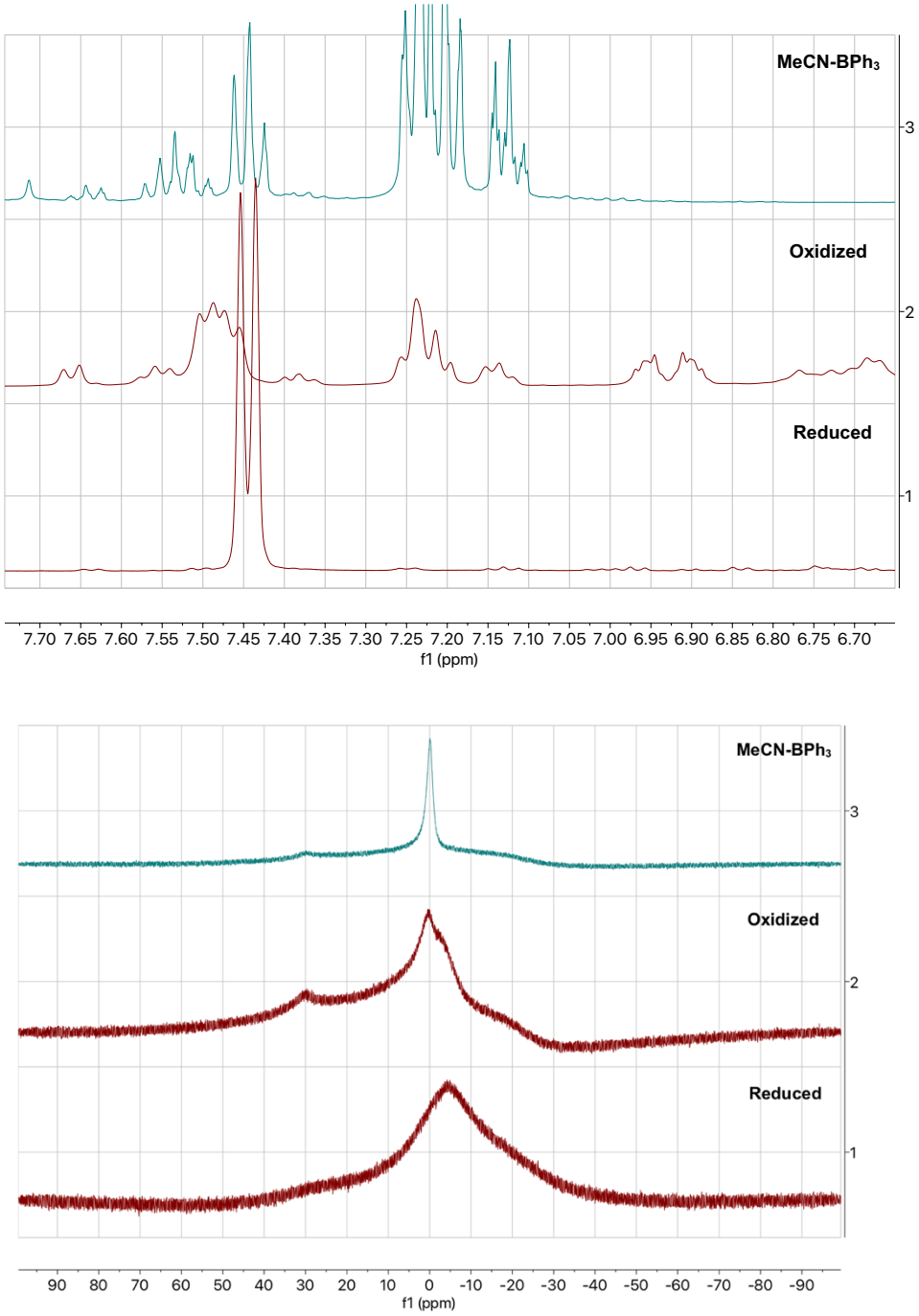

Figure 4.8. ^{1}H (top) and ^{11}B (bottom) NMR in CD_3CN of free MeCN-BPh_3, oxidized $(TEA)_4[Fe(CN\text{-}BPh_3)_6]$, and $(TEA)_4[Fe(CN\text{-}BPh_3)_6]$, showing the liberation of BPh_3 upon oxidation of $(TEA)_4[Fe(CN\text{-}BPh_3)_6]$. ^{1}H peaks upfield of 7.00 ppm in the oxidized NMR are due to benzo-1,4-dioxin. Additional ^{11}B peaks are due to background signal from borosilicate glass.

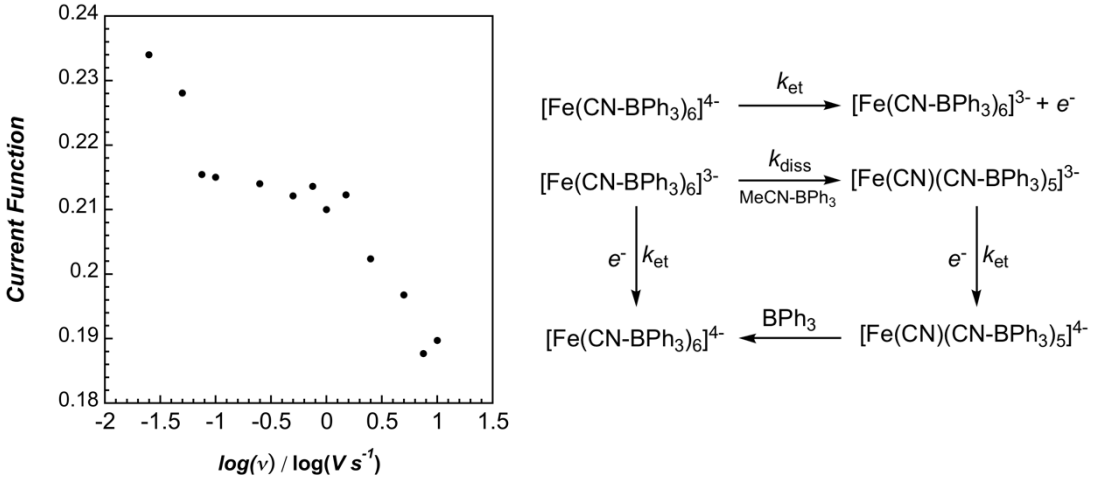

Figure 4.9. (**Left**) Current function versus logarithm of the scan rate for $(TEA)_4[Fe(CN\text{-}BPh_3)_6]$, (**Right**) Square scheme mechanism for dissociation of BPh_3 as a result of oxidation of $(TEA)_4[Fe(CN\text{-}BPh_3)_6]$.

In contrast to $(TEA)_4[Fe(CN\text{-}BPh_3)_6]$, $(TBA)_4[Fe(CN\text{-}B(C_6F_5)_3)_6]$ displays a single, electrochemically reversible redox event with a formal potential equal to 0.85 V vs. $Fc^{+/0}$ (**Figure 4.10**), corresponding to a 2.3 V anodic shift in the $Fe^{III/II}$ couple, which is a 380 mV anodic shift per $B(C_6F_5)_3$ added to hexacyanoferrate(II). Our results initially suggested a 2.1 V shift in formal potential for $(TBA)_4[Fe(CN)_6]$ as a result of BCF coordination. However, the shift was underestimated due to the unrecognized difficulty in fully dehydrating ferrocyanide. Many publications which report formal potentials for cyanometallates have experienced similar issues. Analogous to $(TEA)_4[Fe(CN\text{-}BPh_3)_6]$, a linear potential shift per borane added to hexacyanoferrate(II) was observed for $(TBA)_4[Fe(CN\text{-}B(C_6F_5)_3)_6]$. Borane adducts of $Fe(phen)_2(CN)_2$ in dichloromethane showed an approximately 300 mV increase in half-wave potential per borane, with BBr_3 (the strongest Lewis acid in the study) producing the largest shift.[1d] Cyanorhenate(I) complexes, $Re(R_2phen)(CO)_3[CN\text{-}B(C_6F_5)_3]$, where R = H, Me, displayed a ~320 mV shift in peak anodic potential ($E_{p,a}$) in acetonitrile compared to the parent.[12] Cyanoosmate(II) complexes, $[Os(4,4'\text{-}R_2(bpy))_2(CNBL_3)_2]$, where R = H, Me, showed ~420 and ~290

mV anodic shifts per borane for L = $B(C_6F_5)_3$ and BPh_3 in MeCN, respectively.[13] As the $Fe^{III/II}$ potential shifts are very near those observed for Re(I) and Os(II) complexes, there is minimal dependence on metal identity or oxidation state. As a note, we observed no shift in formal potential

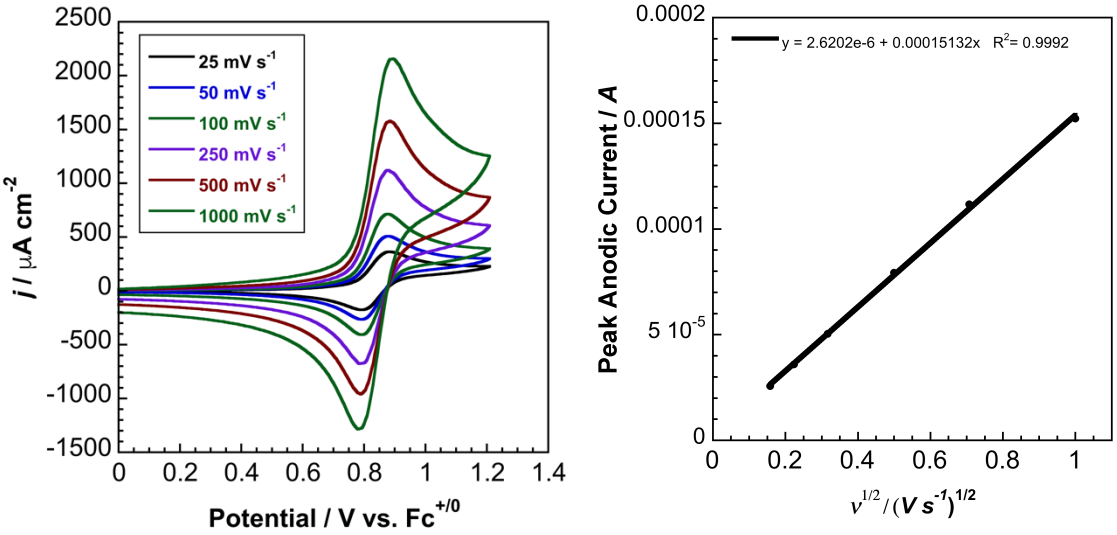

Figure 4.10. (Left) Cyclic voltammetry (scan rates from 25 mV s^{-1} to 1000 mV s^{-1} of 3.6 mM $[Fe(CN\text{-}B(C_6F_5)_3)_6]^{4-}$ in acetonitrile with 0.2 M $TBAPF_6$. Potentials referenced to $Fc^{+/0}$. (Right) Randles-Sevcik plot of the voltammetry data.

by voltammetry for $[Fe(CN)_6]^{4-}$ upon addition trimesitylborane in DCM electrolyte solution, reflecting the weak Lewis acidity coupled with the steric hindrance of this Lewis acid.

Oxidation of $(TBA)_4[Fe(CN\text{-}B(C_6F_5)_3)_6]$ by flash-quench-generated $[Ru(2,2'\text{-bipyridine})_3]^{3+}$ was very rapid. From a linear fit of electron transfer rate versus concentration (**Figure 4.11**), the apparent second order rate constant, k_{ex}, was found to be 8.4 x 10^8 M^{-1} s^{-1}. Using an ion-pair preequilibrium model, K_0, the ion-pair association constant, was found to be 0.19 M^{-1} with k_{et} estimated to be 4.5 x 10^9 s^{-1}.[17] We conclude that electron tunneling from Fe^{II} to Ru^{III} in the ion-paired precursor complex is not inhibited by the wall of 90 fluorine atoms in the boronated cyanide complex.

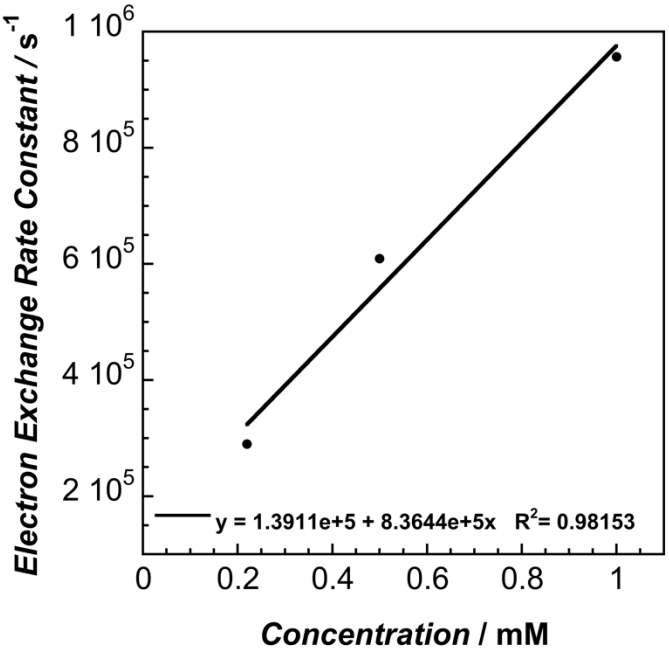

Figure 4.11. Linear fit of electron exchange rate versus concentration of $(PPN)_4[Fe(CN\text{-}B(C_6F_5)_3)_6]$.

4.5. Conclusions

We have demonstrated that boranes can tune the formal potentials of electrochemically reversible redox couples. As evidenced by the combined voltammetric and spectroscopic studies, we are able to rigorously quantify the effects of boronation on transition energies in closed-shell cyanometallates, where absolute energy levels are depressed, metal-to-ligand charge transfer states are blue shifted, and ligand field transitions are moderately blue shifted. Also, these findings allow researchers to selectively alter the formal potentials of cyanide-based inorganic complexes, providing opportunities for creating new quenchers, oxidants, and single-electron transfer reagents. Importantly, the fluorinated "cage" surrounding the iron center of $[Fe(CN\text{-}BCF)_6]^{4-}$ does not hinder outer-sphere electron transfer, indicating that boronated cyanide complexes will likely be useful as electrolytes in non-aqueous redox flow batteries.

4.6. Experimental

Synthesis

General

Tetrabutylammonium hydroxide (Sigma-Aldrich), tetraethylammonium hydroxide (Sigma-Aldrich), potassium hexacyanoferrate(II) (Sigma-Aldrich), bis(triphenylphosphine)iminium chloride (Sigma-Aldrich), methyl triflate (Sigma-Aldrich), tris(pentafluorophenyl)borane (Sigma-Aldrich), and triphenylborane (Sigma-Aldrich) were used as received. [dibenzo-1,4-dioxin][$SbCl_6$] was prepared according to literature precedent.[1] NMR spectra were collected on either a Varian 400 MHz spectrometer or Bruker 400 MHz spectrometer (δ in ppm, m: multiplet, s: singlet, d: doublet, t: triplet, pt: pseudo-triplet). ^{13}C NMR and ^{31}P NMR were ^{1}H decoupled. ^{31}P NMR spectra were externally referenced to 85% H_3PO_4, ^{19}F NMR spectra were externally referenced to neat $CFCl_3$, and ^{11}B NMR were internally referenced to 15% $BF_3{\cdot}Et_2O$. UV-visible spectroscopy were collected on an HP 8453 spectrometer. Solid-state infrared spectra were collected on a Thermo Scientific Nicolet iS5 FT-IR spectrometer with an iD5 ATR diamond. Solid-state Raman spectra were collected using a coherent Innova argon ion laser with a 488 nm line, a Spex 0.75 m spectrograph, and a Horiba thermoelectrically cooled CCD detector.

Tetrabutylammonium/tetraethylammonium hexacyanoferrate(II), (TBA/TEA)$_4$[Fe(CN)$_6$]

$H_4[Fe(CN)_6]$ was prepared according to literature procedure.[2] $H_4[Fe(CN)_6]$ (0.25 g, 1.16 mmol) was combined under nitrogen with a stoichiometric excess of 55% tetrabutylammonium hydroxide (TBAOH) in water (2.2 mL, 1.20 g, 4.64 mmol). The reaction was stirred for one hour and then immediately dried under vacuum. The product was then placed in a nitrogen-filled glove box, washed with ether to remove excess TBAOH, and dried under vacuum. To remove trace water, the desired

product was repeatedly redissolved in dicholoromethane and re-dried to obtain a colorless powder. UV-visible spectroscopy can be used to confirm the absence of ferricyanide (Fe(III)). **1a** ^{1}H NMR (400 MHz, CD_3CN) δ 2.94 (br s, 8H, CH_2), 1.56 (br s, 8H, CH_2), 1.31 (br s, 8H, CH_2), 0.95 (br s, 12H, CH_3); ^{13}C NMR (400 MHz, CD_3CN) δ 144.7 (CN) δ 59.7 (s, CH_2), 24.4 (s, CH_2), 20.4 (s, CH_2), 13.9 (s, CH_3). **1b** ^{1}H NMR (400 MHz, CD_3CN) δ 3.28 (q, 8H, CH_2), 1.20 (t, 12H, CH_3); ^{13}C NMR (400 MHz, CD_3CN) δ 143.4 (CN) δ 52.9 (s, CH_2), 7.9 (s, CH_3).

Bis(triphenylphosphine)iminium hexacyanoferrate(II), $(PPN)_4[Fe(CN)_6]$.

PPNCl (6.00 g, 0.010 mmol) was dissolved in approximately 3 L of water. $K_4[Fe(CN)_6]$ (0.822 g, 0.0022 mmol) was added, and a colorless precipitate immediately formed. The solution was filtered, and the precipitate was washed three times with water. The precipitate was placed on a vacuum line, dried, and immediately transferred to a nitrogen-filled glove box and redissolved in dichloromethane to remove trace water. The solution was dried, washed with ether to remove any remaining PPNCl, and re-dried to obtain a colorless powder. ^{31}P NMR (162 MHz, CD_3CN) δ 20.8; ^{1}H NMR (400 MHz, CD_3CN) δ 7.45-7.67 (m, 30H, CH_{Ph}); ^{13}C NMR (100 MHz, CD_3CN) δ 134.5 (m), 133.2 (m), 130.3 (m), 128.7 (dd, J_{CP} = 108 Hz, J_{CP} = 2 Hz), the CN peak was not observed.

Tetraethylammonium hexakisisocyanotris(triphenyl)boratoferrate(II) $(TEA)_4[Fe(CN\text{-}B(C_6H_5)_3)_6]$

Triphenylborane (BPh_3) was purified by washing repeatedly with diethyl ether to remove a yellow impurity until the washes and the borane were colorless. The purity of the BPh_3 was confirmed by ^{11}B NMR. $(TEA)_4[Fe(CN)_6]$ (0.20 g, 0.27 mmol) was combined with 6.1 equivalents of BPh_3 (0.40 g, 1.65 mmol) in DCM (5 mL). After one hour of stirring, the precipitate was filtered and washed with ether. The desired product was obtained as a white powder (0.4 g, 67 %). Elem. Anal. (%) found (calc'd) for $C_{146}H_{170}B_6FeN_{10}$ ($(TEA)_4[Fe(CN\text{-}B(C_6H_5)_3)_6]$): C, 78.67 (80.27); H, 7.71 (8.14); N, 6.88 (6.46). ^{11}B NMR

(128 MHz, CD_3CN) δ -5.3; ^1H NMR (400 MHz, CD_3CN) δ 7.45 (d, J_{HH} = 7.9 Hz, J_{HH} = 1.5 Hz, 36H, CH_{Ph}), 6.53 (t, J_{HH} = 7.3 Hz, 18H, CH_{Ph}), 6.35 (t, J_{HH} = 7.5 Hz, 36H, CH_{Ph}), 3.08 (q, J_{HH} = 7.4 Hz, 32H, CH_2), 1.16 (t, J_{HH} = 7.4 Hz, 48H, CH_3) ^{13}C NMR (100 MHz, CD_3CN) 134.4 (s, CH), 127.0 (s, CH), 123.1 (s, CH), 53.0 (s, CH_2), 7.7 (s, CH_3).

Bis(triphenylphosphine)iminium/Tetrabutylammonium Hexakisisocyanotris(pentafluorophenyl)boratoferrate(II) (PPN/TBA)$_4$[Fe(CN-B(C_6F_5)$_3$)$_6$]

$(PPN)_4[Fe(CN)_6]$ (0.45 g, 0.19 mmol) was combined with 6.2 equivalents of tris(pentafluorophenyl)borane (0.6 g, 1.17 mmol) in DCM (10 mL). After 30 minutes, ether was added to the reaction mixture and the vial was stored in the fridge yielding a white powder. The resulting precipitate was filtered and washed with ether. For further purification, the precipitate was dissolved in tetrahydrofuran and precipitated with ether. After drying under vacuum, the desired product was obtained as a white powder (0.62 g, 0.11 mmol, 57 %). The tetrabutylammonium salt of this compound was synthesized in an identical manner. Elem. Anal. (for TBA salt) (%) found (calc'd) for $C_{178}H_{144}B_6F_{90}FeN_{10}$ ($(TBA)_4[Fe(CN\text{-}B(C_6F_5)_3)_6]$): C, 50.18 (50.26); H, 3.67 (3.41); N, 3.28 (3.29). ^{11}B NMR (128 MHz, CD_3CN) δ -14.4; ^{31}P NMR (162 MHz, CD_3CN) δ 20.8; ^{19}F NMR (376 MHz, CD_3CN) δ -132.3 (d, J_{FF} = 20.7 Hz), -165.0 (pt, J_{FF} = 19.8 Hz), -169.0 (pt, J_{FF} = 18.1 Hz); ^1H NMR (400 MHz, CD_3CN) δ 7.43-7.66 (m, 30H, CH_{Ph}); ^{13}C NMR (100 MHz, CD_3CN) δ 161.5 (CN), 149.1 (d, J_{CF} = 242 Hz), 139.5 (d, J_{CF} = 245 Hz), 136.7 (d, J_{CF} = 248 Hz), 134.5 (s), 133.4 (m), 130.3 (m), 128.1 (dd, J_{CP} = 108 Hz, J_{CP} = 2 Hz), 122.1 (br. s, CB).

Hexamethylisocyanoiron(II) triflate [Fe(CN-CH_3)$_6$](OTf)$_2$

Tetrabutylammonium hexacyanoferrate(II) (0.2 g) was combined with 6.9 equivalents of methyl triflate (0.15 mL) in DCM. A white solid immediately precipitated from solution. The solution was stirred for one hour at room temperature. The reaction mixture was stored at 253 K for 48 hours. The precipitate

was collected, dissolved in acetonitrile, and re-filtered to obtain the methylated product. ^{1}H NMR (400 MHz, CD_3CN) 3.49, 1H, s).

Electrochemistry

All electrochemical characterization was performed in a nitrogen-filled glove box. Electrochemical characterization was performed with a Gamry Reference 600 potentiostat in a standard three-electrode cell containing a 3 mm diameter glassy carbon (CH Instruments) working electrode, a 0.01 M $Ag^{+/0}$ in 0.1 M $TBAPF_6$/MeCN quasireference electrode (CH Instruments), and a platinum wire counter electrode (Kurt J. Lesker). All voltammograms were compensated for 85% of the measured uncompensated resistance (R_u) value.

Laser Experiments, Flash Quench Electron Transfer, and Rate Derivation

Laser samples were composed of 20 μM $[Ru(bpy)_3]Cl_2$, 10 mM of oxidative quencher (methylviologen-2 PF_6) and different concentrations of $(PPN)_4[Fe(CN\text{-}B(C_6F_5)_3)_6]$ (0, 0.22, 0.5 and 1 mM) in 2 mL of acetonitrile. Laser samples were prepared in an inert atmosphere glove box and placed in a quartz fluorescence cuvette with high-vacuum Teflon valve, equipped with a small stir bar.

For nanosecond-to-millisecond transient luminescence and absorption experiments, excitation was provided by 460 nm pulses from a tunable optical parametric oscillator (Spectra Physics, Quanta-Ray MOPO-700) pumped by the third harmonic from a Spectra Physics Q-switched Nd:YAG laser (Spectra-Physics, Quanta-Ray PRO-Series, 8 ns pulse width) operated at 10 Hz. Probe light was provided by a 75-W arc lamp (PTI model A 1010) that could be operated in continuous or pulsed mode and passed through the sample collinearly with the excitation pulse. After rejection of scattered light by appropriate long- and short-pass filters, and intensity modulation by a neutral density filter, probe wavelengths were selected by a double monochromator (Instruments SA DH-10) with 1 mm

slits. Transmitted light was detected by a photomultiplier tube (PMT, Hamamatsu R928) and amplified by a 200 MHz wideband voltage amplifier DHPVA-200 (FEMTO). Luminescence decays were monitored at 630 nm. Single wavelength transient absorption kinetics were monitored at 440 nm, averaging approximately 500 shots. Data from three separate time scales (2 μs, 10 μs, and 100 μs) were collected, log-compressed, and spliced together to produce full kinetics traces using Matlab software (Mathworks).

Table 4.2. Rate constants of for the oxidative quenching of Ru(III) with different concentrations of $(TBA)_4[Fe(CN\text{-}BCF)_6]$ estimated from MatLab modeling.

Luminescence	k_{rate} ($\times 10^6$ s^{-1})	Lifetime ($\times 10^{-7}$ s)
No Fe	7.16	1.40
220 μM	7.64	1.31
500 μM	7.91	1.26
1 mM	8.40	1.19
Transient Absorption		
No Fe	7.16	1.40
	0.112	89.5
220 μM	7.64	1.31
	0.290	34.5
500 μM	7.91	1.26
	0.609	16.4
1 mM	8.40	1.19
	0.957	10.5

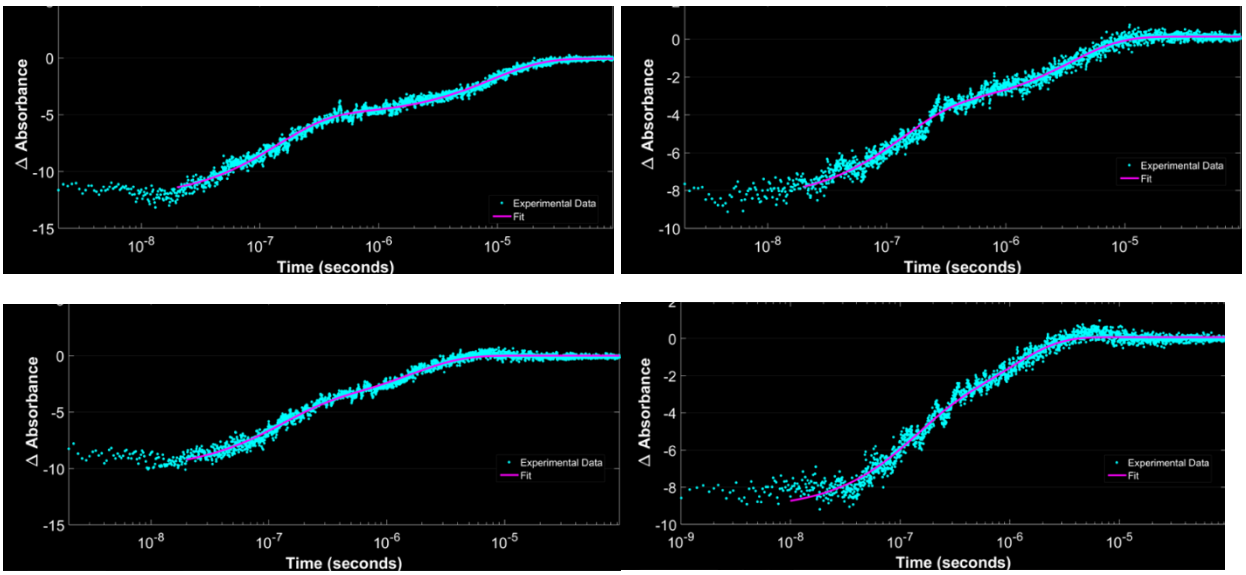

Figure 4.12. Transient absorption kinetics following reductive quenching of $[Ru(bpy)_3]^{3+}$ (λ_{ex} = 460 nm; λ_{obs} = 440 nm) at different concentrations of $[Fe(CN\text{-}B(C_6F_5)_3)_6]^{4-}$: (**Top Left**) without $[Fe(CN\text{-}B(C_6F_5)_3)_6]^{4-}$, (**Top Right**) 0.22 mM $[Fe(CN\text{-}B(C_6F_5)_3)_6]^{4-}$ (**Bottom Left**) 0.50 mM $[Fe(CN\text{-}B(C_6F_5)_3)_6]^{4-}$ (**Bottom Right**) 1.00 mM $[Fe(CN\text{-}B(C_6F_5)_3)_6]^{4-}$.

NMR Spectra:

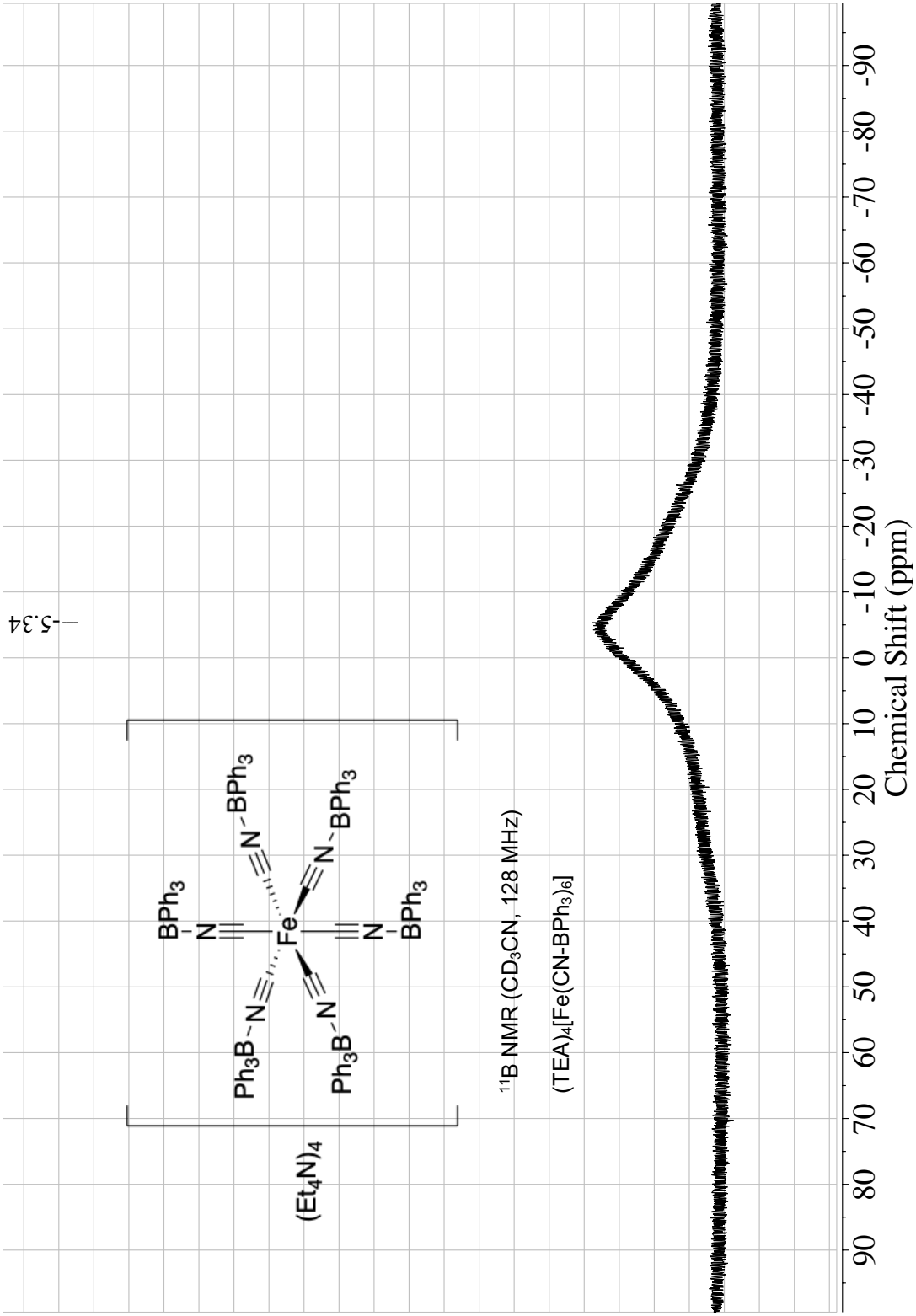

Figure 4.13. ^{11}B NMR spectrum of $(TEA)_4[Fe(CN\text{-}BPh_3)_6]$ in CD_3CN.

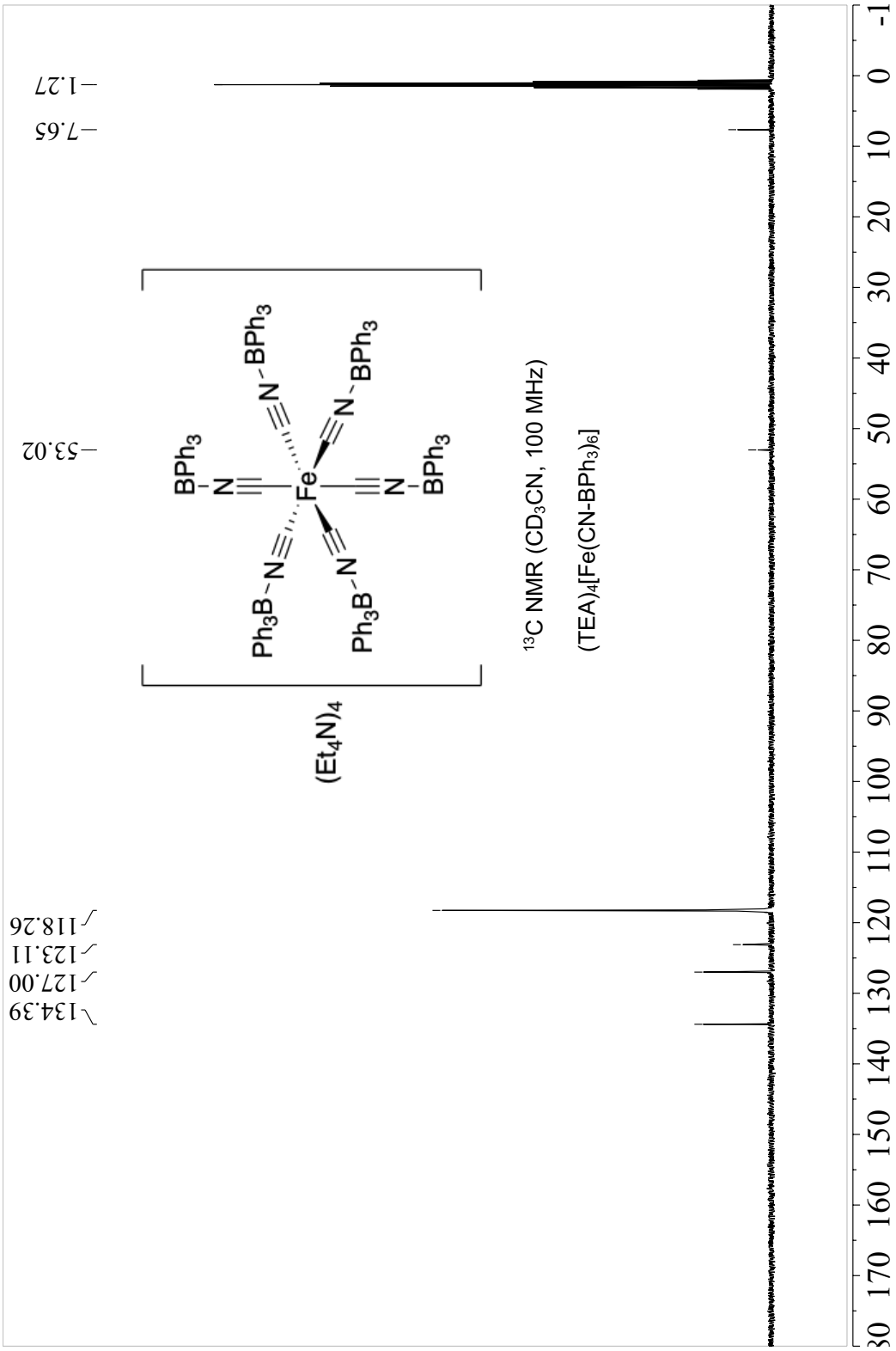

Figure 4.14. ^{13}C NMR spectrum of $(TEA)_4[Fe(CN\text{-}BPh_3)_6]$ in CD_3CN.

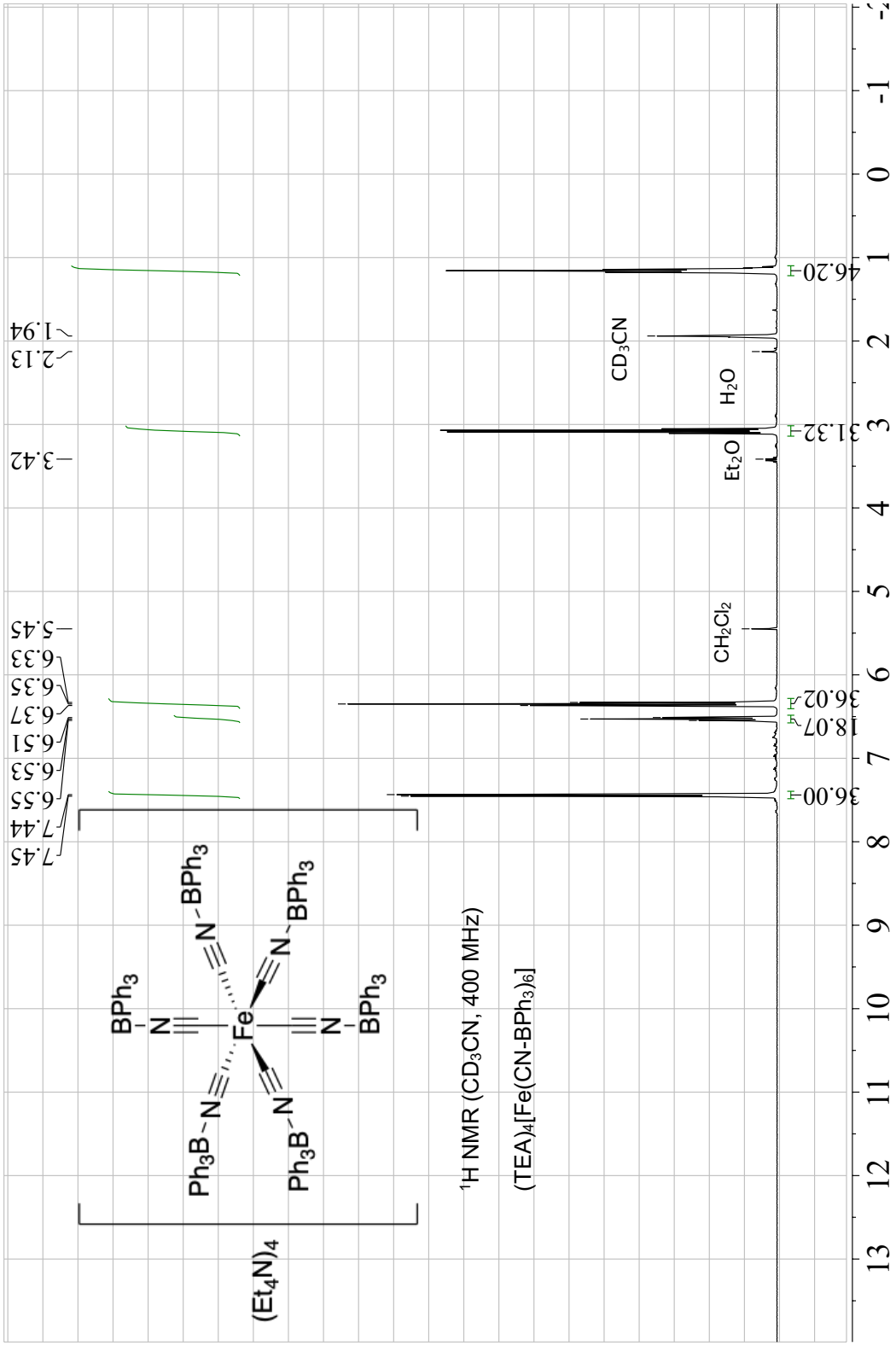

Figure 4.15. ^{1}H NMR spectrum of $(TEA)_4[Fe(CN\text{-}BPh_3)_6]$ in CD_3CN.

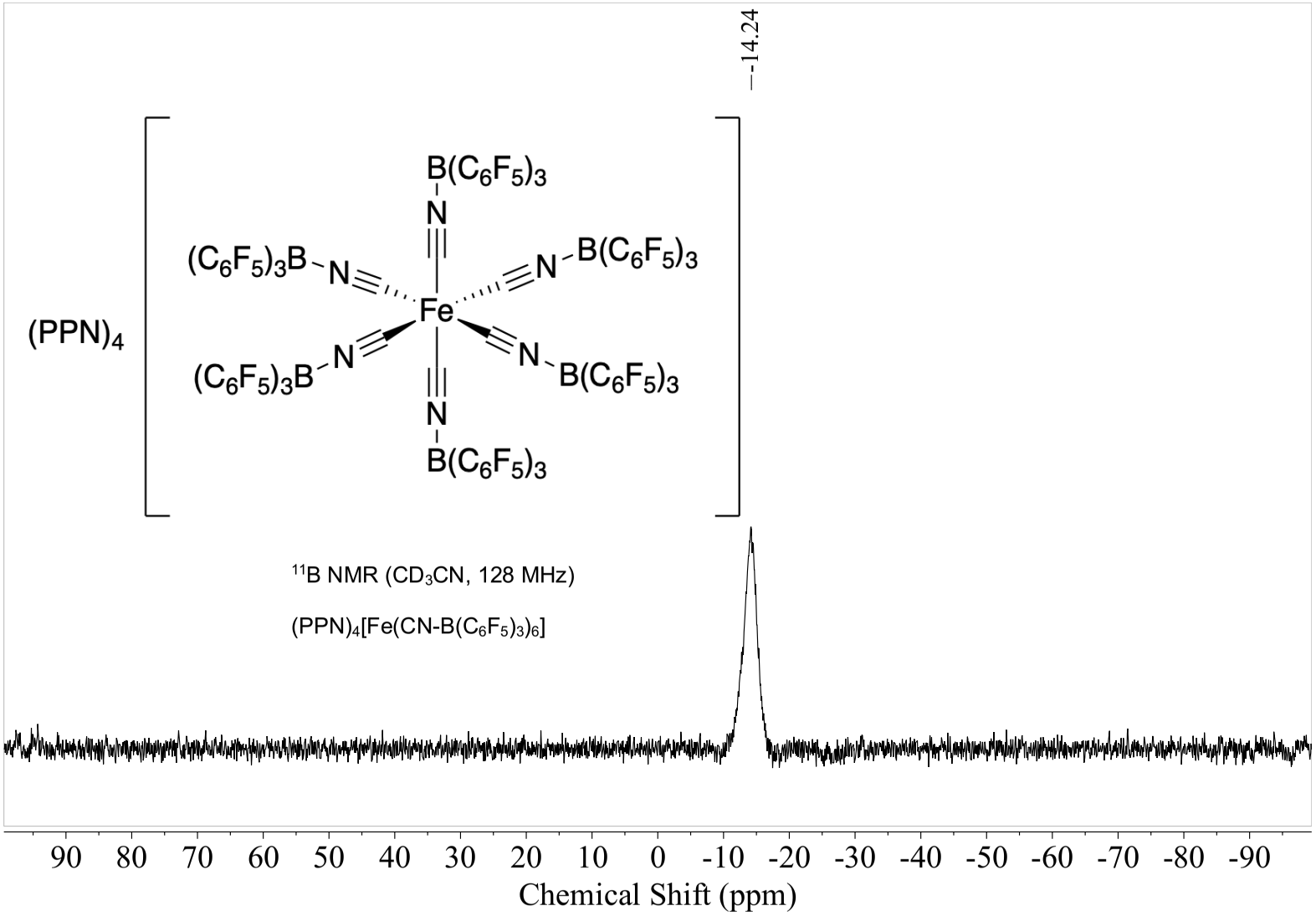

Figure 4.16. ^{11}B NMR spectrum of $(PPN)_4[Fe(CN\text{-}B(C_6F_5)_3)_6]$ in CD_3CN.

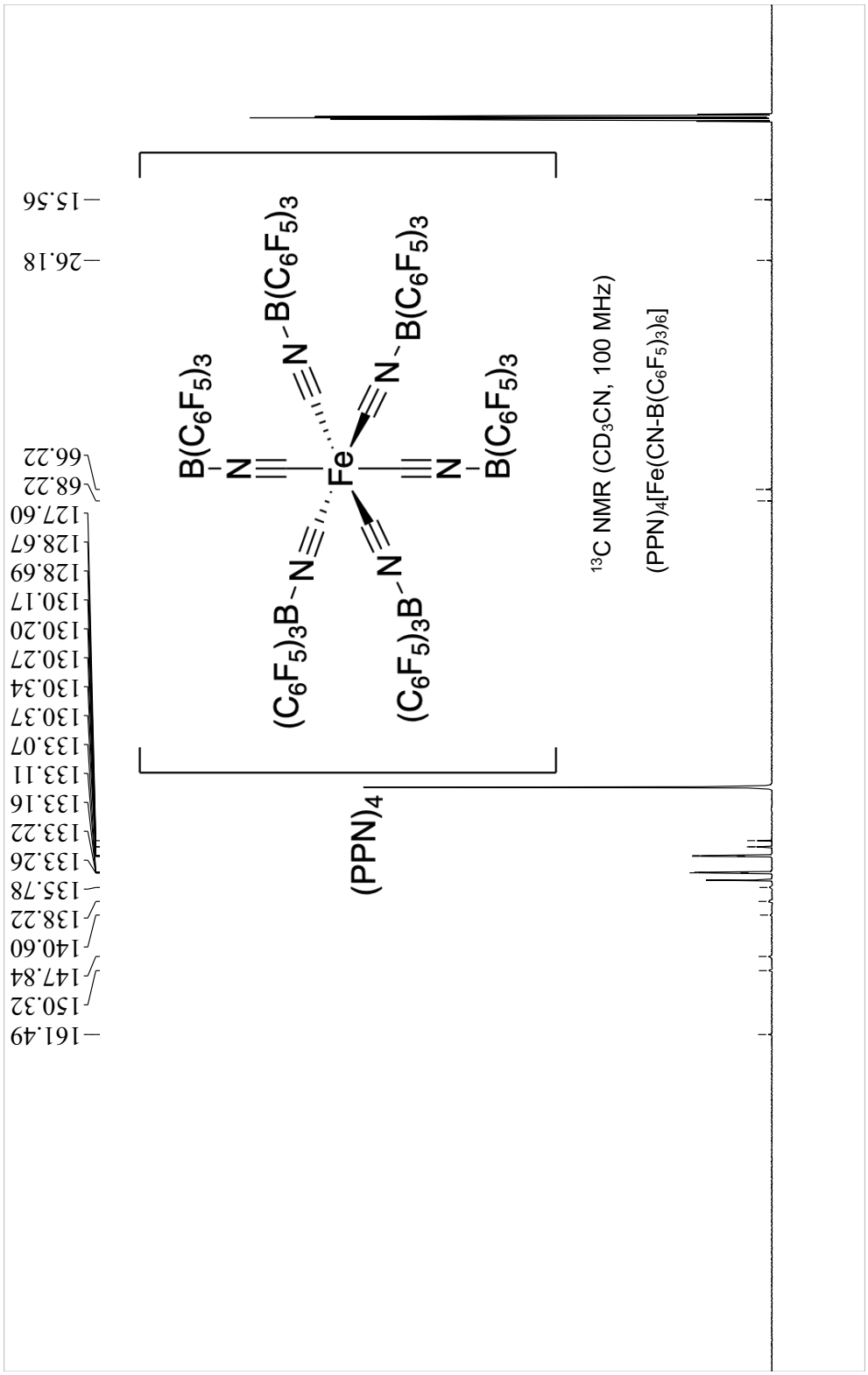

Figure 4.17. ^{13}C NMR spectrum of $(PPN)_4[Fe(CN\text{-}B(C_6F_5)_3)_6]$ in CD_3CN.

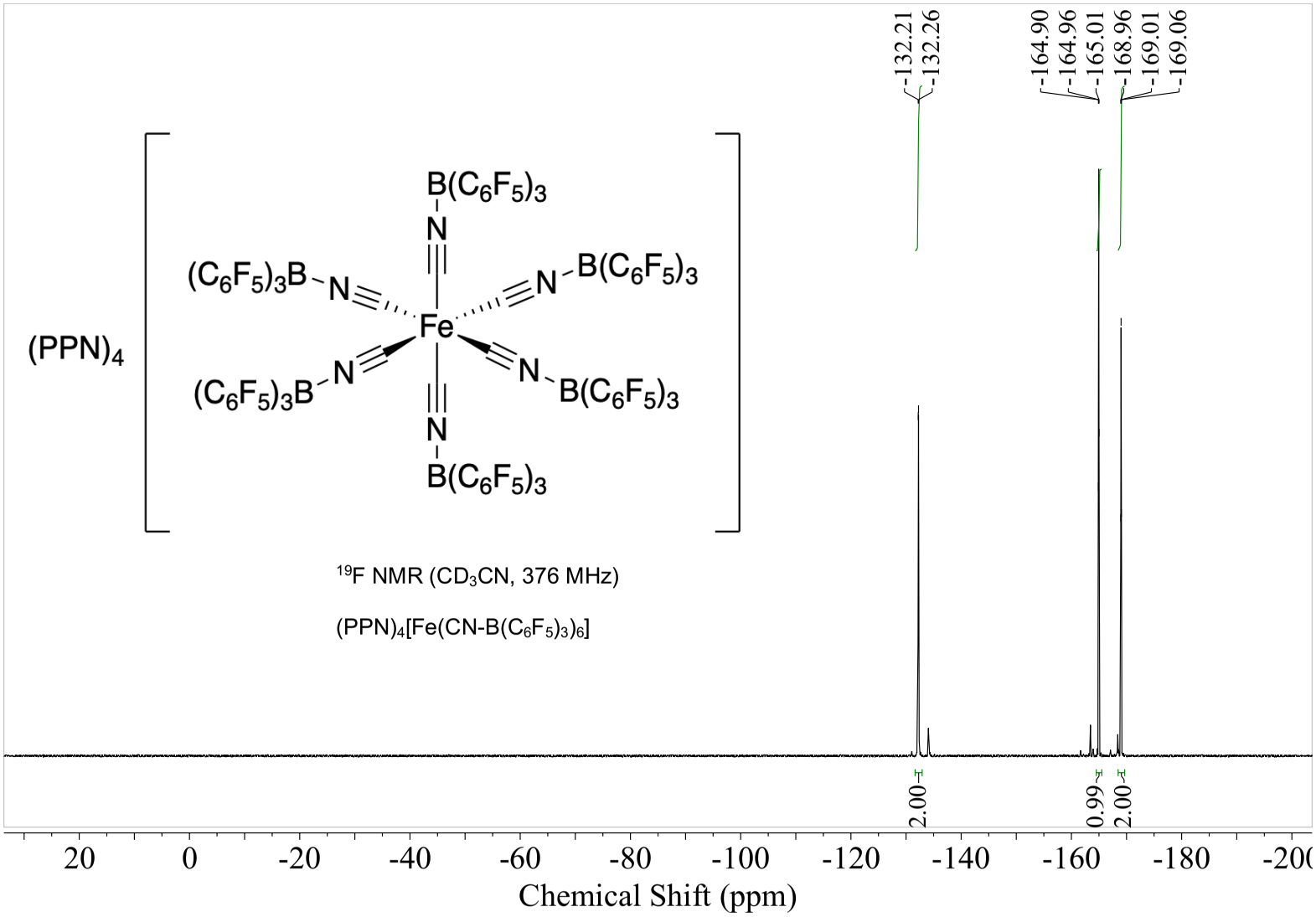

Figure 4.18. ^{19}F NMR spectrum of $(PPN)_4[Fe(CN\text{-}B(C_6F_5)_3)_6]$ in CD_3CN.

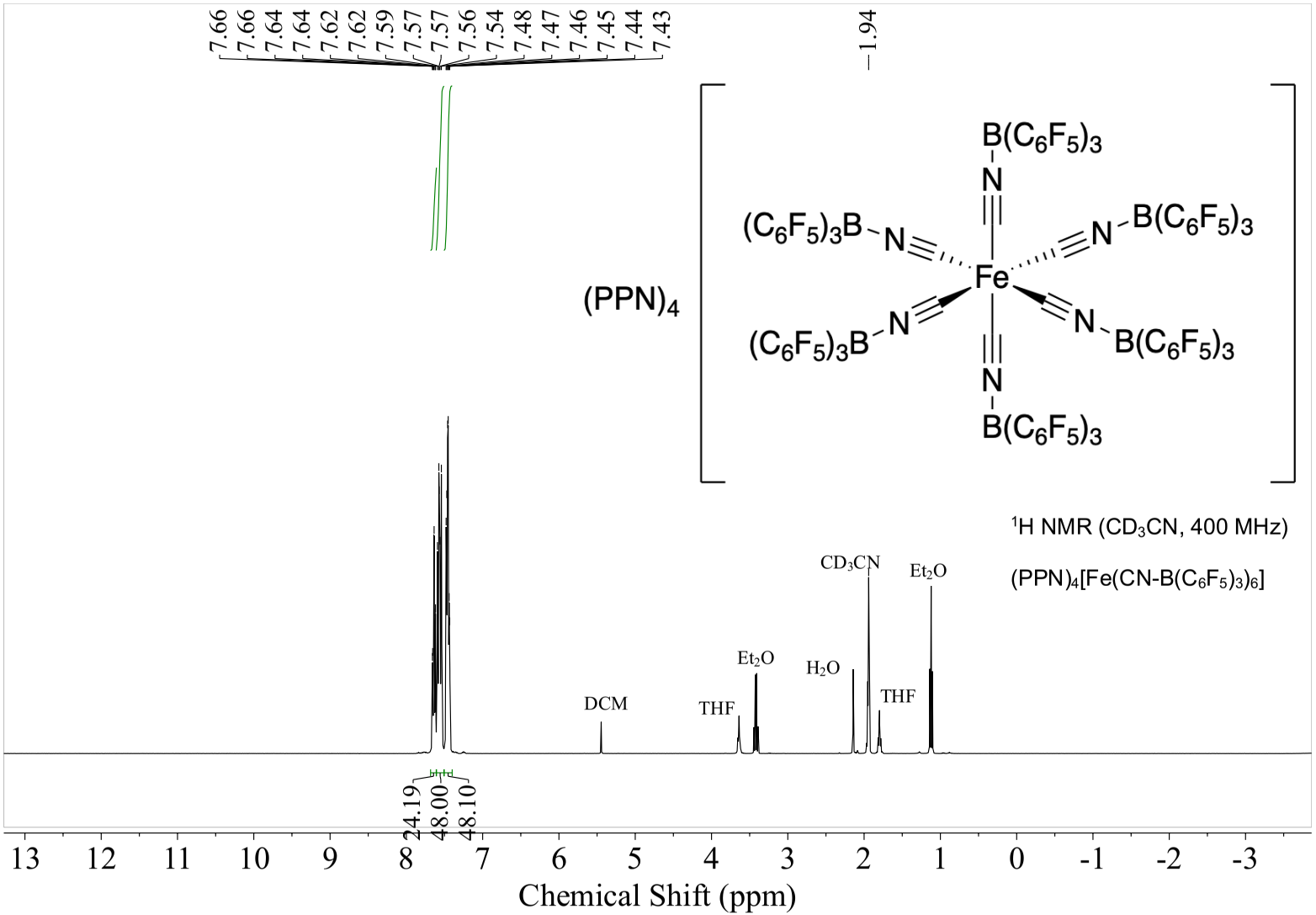

Figure 4.19. ^{1}H NMR spectrum of $(PPN)_4[Fe(CN\text{-}B(C_6F_5)_3)_6]$ in CD_3CN.

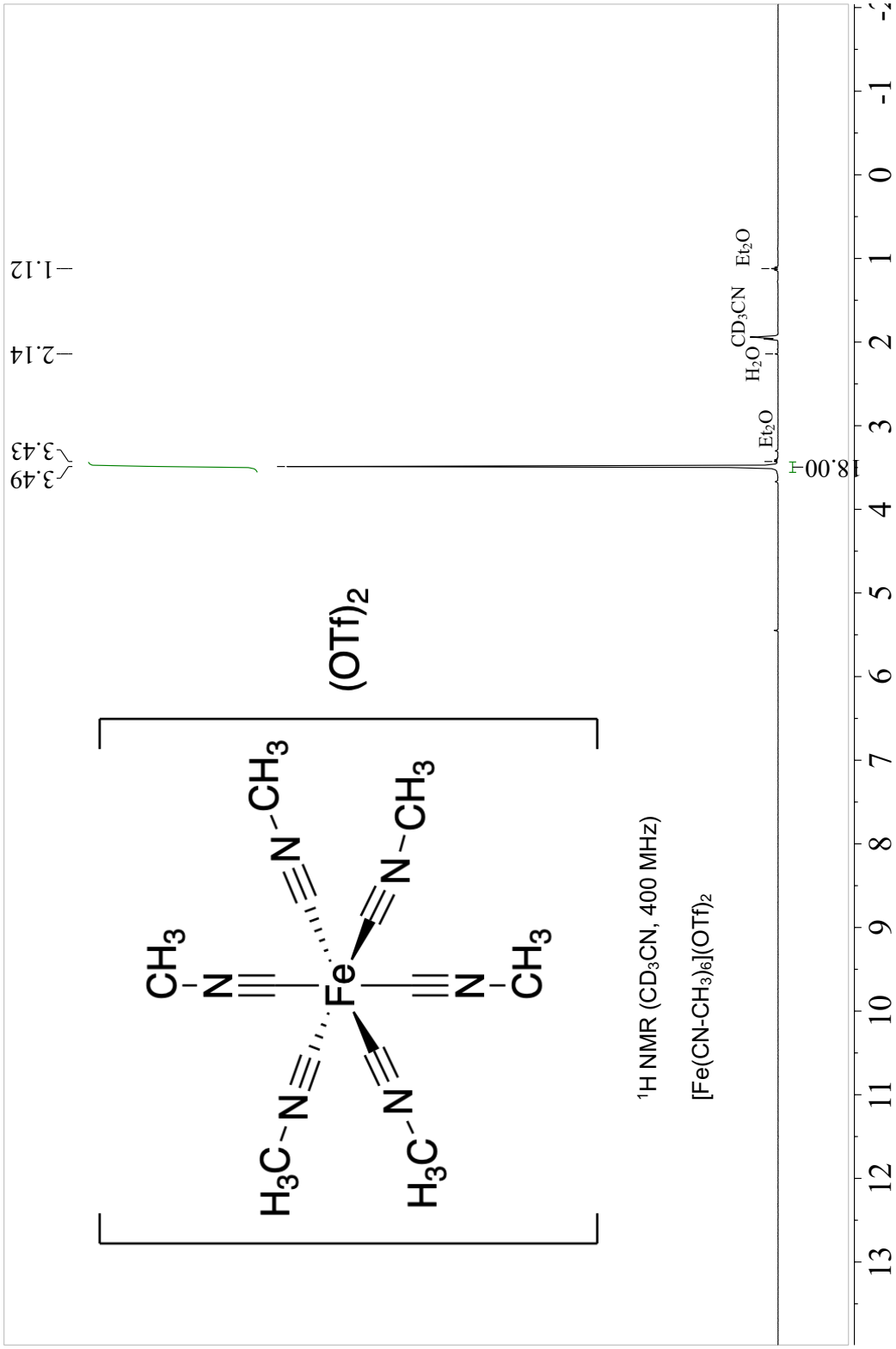

Figure 4.20. ^{1}H NMR spectrum of $[Fe(CN\text{-}CH_3)_6](OTf)_2$ in CD_3CN.

Crystallographic Data

Collection and Refinement of $(TEA)_4[Fe(CN)_6]$

Low-temperature diffraction data (φ-and ω-scans) were collected on a Bruker AXS D8 VENTURE KAPPA diffractometer coupled to a PHOTON 100 CMOS detector with Mo K_α radiation (λ = 0.71073 Å) from an IμS micro-source for the structure of compound $(TEA)_4[Fe(CN)_6]$. The structure was solved by direct methods using SHELXS[21] and refined against F^2 on all data by full-matrix least squares with SHELXL-2016[22] using established refinement techniques.[23] All non-hydrogen atoms were refined anisotropically. Unless otherwise noted, all hydrogen atoms were included into the model at geometrically calculated positions and refined using a riding model. The isotropic displacement parameters of all hydrogen atoms were fixed to 1.2 times the U value of the atoms they are linked to (1.5 times for methyl groups). All disordered atoms were refined with the help of similarity restraints on the 1,2- and 1,3-distances and displacement parameters as well as enhanced rigid bond restraints for anisotropic displacement parameters.

$(TEA)_4[Fe(CN)_6]$ crystallizes in the monoclinic space group Cc with one molecule in the asymmetric unit along with four tetraethyl ammonium cations, two molecules of acetonitrile, and five molecules of water. One of the tetraethyl ammonium cations and one of the acetonitrile molecules were disordered over two positions. The coordinates for the hydrogen atoms bound to O1S, O2S, O3S, O4S, and O5S were located in the difference Fourier synthesis and refined semi-freely with the help of restraints on the O-H distance (0.84(4) Å) and H-H distance (1.5(4) Å). In addition, the oxygen atom, hydrogen atoms, and hydrogen acceptors were restrained to be flat for all water molecules.

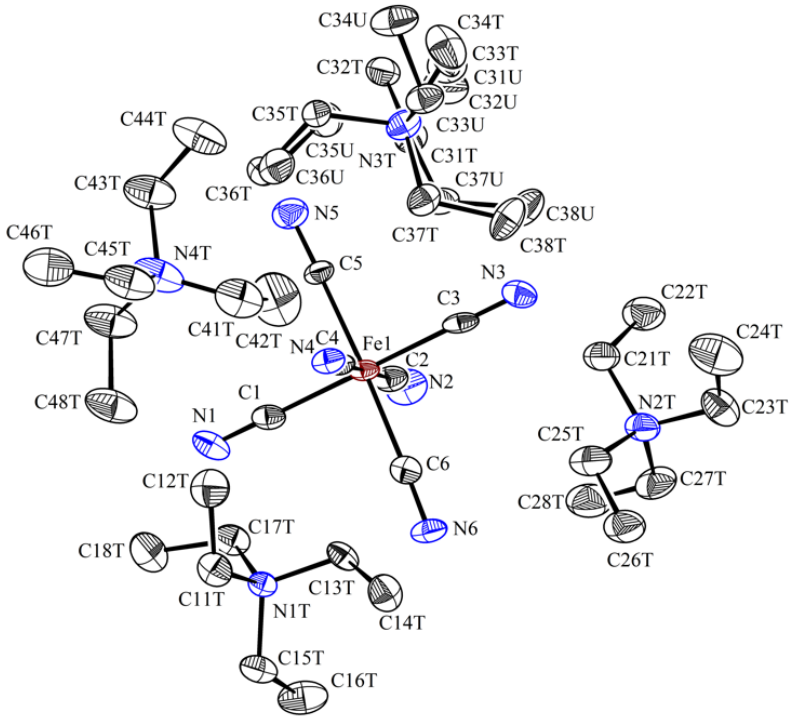

Figure 4.21. Crystal structure of $(TEA)_4[Fe(CN)_6]$. Thermal ellipsoids set at 50% probability. Solvent molecules omitted for clarity.

Table 4.3. Crystal data and structure refinement for complex $(TEA)_4[Fe(CN)_6]$.

Empirical formula	C44 H99 Fe N13 O5	
Formula weight	946.21	
Temperature	100(2) K	
Wavelength	0.71073 Å	
Crystal system	Monoclinic	
Space group	Cc	
Unit cell dimensions	a = 16.3801(6) Å	a= 90°.
	b = 15.2273(6) Å	b= 92.0316(14)°.
	c = 22.2072(9) Å	g = 90°.
Volume	5535.5(4) $Å^3$	
Z	4	
Density (calculated)	1.135 Mg/m^3	
Absorption coefficient	0.323 mm^{-1}	
F(000)	2080	
Crystal size	0.300 x 0.300 x 0.250 mm^3	
Theta range for data collection	2.488 to 30.581°.	
Index ranges	$-23 \le h \le 21$, $-20 \le k \le 21$, $-31 \le l \le 31$	
Reflections collected	36004	
Independent reflections	15251 [R(int) = 0.0369]	
Completeness to theta = 25.242°	99.9 %	
Absorption correction	Semi-empirical from equivalents	
Max. and min. transmission	0.7461 and 0.6757	
Refinement method	Full-matrix least-squares on F^2	
Data / restraints / parameters	15251 / 717 / 700	
Goodness-of-fit on F^2	1.041	
Final R indices [I>2sigma(I)]	R1 = 0.0621, wR2 = 0.1517	
R indices (all data)	R1 = 0.0767, wR2 = 0.1605	
Absolute structure parameter	0.050(18)	
Extinction coefficient	n/a	
Largest diff. peak and hole	0.792 and -0.537 $e.Å^{-3}$	

Collection and Refinement of Complex $(TEA)_4[Fe(CN\text{-}BPh_3)_6]$

Low-temperature diffraction data (ϕ-and ω-scans) were collected on Bruker AXS D8 VENTURE KAPPA diffractometer coupled to a PHOTON 100 CMOS detector with Cu K_α radiation (λ = 1.54178 Å) from an IμS micro-source for the structure of $(TEA)_4[Fe(CN\text{-}B(C_6H_5)_3)_6]$. The structure was solved by direct methods using SHELXS[21] and refined against F^2 on all data by full-matrix least squares with SHELXL-2014[22] using established refinement techniques.[23] All non-hydrogen atoms were refined anisotropically. All hydrogen atoms were included into the model at geometrically calculated positions and refined using a riding model. The isotropic displacement parameters of all hydrogen atoms were fixed to 1.2 times the U value of the atoms they are linked to (1.5 times for methyl groups). All disordered atoms were refined with the help of similarity restraints on the 1,2- and 1,3-distances and displacement parameters as well as rigid bond restraints for anisotropic displacement parameters.

$(TEA)_4[Fe(CN\text{-}B(C_6H_5)_3)_6]$ crystallizes in the orthorhombic space group $P2_12_12_1$ with one molecule in the asymmetric unit along with four molecules of tetraethylammonium and 2.58 molecules of dichloromethane. Two of the triphenyl borane groups and tetraethylammonium cations were disordered over two positions. One of the dichloromethane molecules was disordered over two positions. The remaining 1.58 molecules of dichloromethane were disordered over four positions.

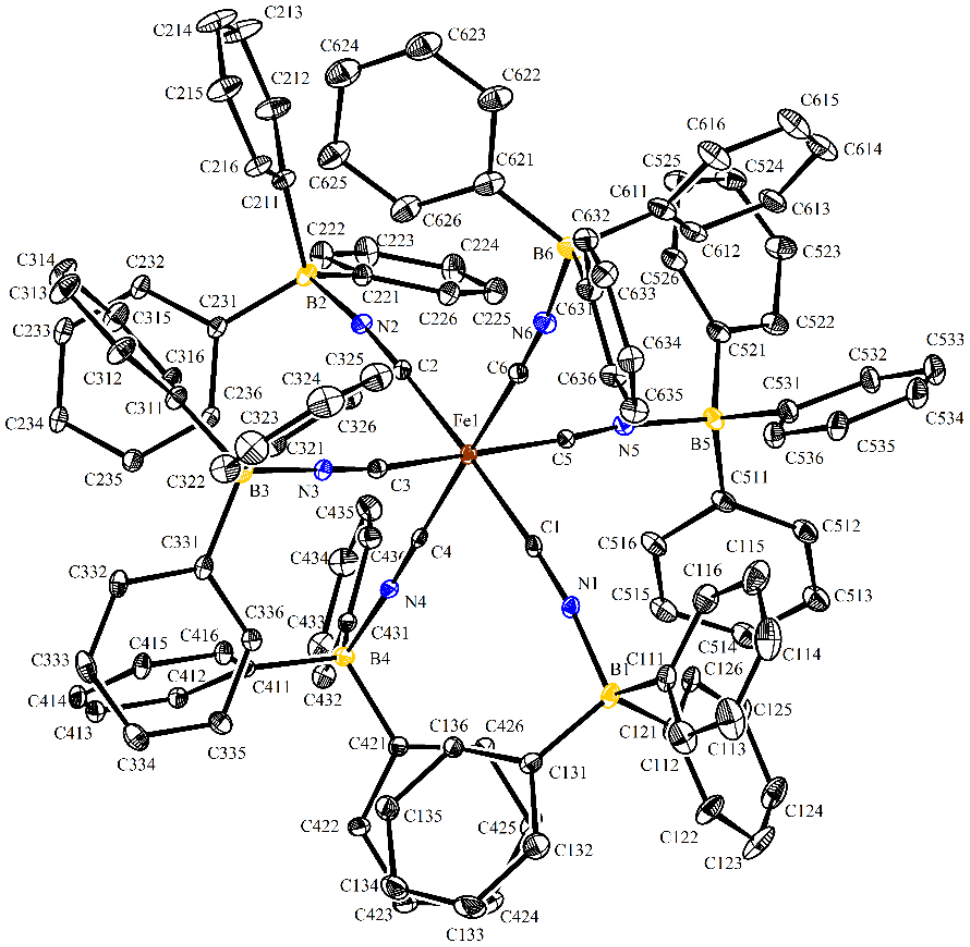

Figure 4.22. Crystal structure of $(TEA)_4[Fe(CN\text{-}BPh_3)_6]$. Thermal ellipsoids set at 50% probability. Solvent molecules, cations, and protons omitted for clarity.

Table 4.4 Crystal data and structure refinement for complex $(TEA)_4[Fe(CN\text{-}BPh_3)_6]$.

Empirical formula	C148.57 H175.16 B6 Cl5.16 Fe N10	
Formula weight	2404.67	
Temperature	100(2) K	
Wavelength	1.54178 Å	
Crystal system	Orthorhombic	
Space group	$P2_12_12_1$	
Unit cell dimensions	a = 17.5522(6) Å	a= 90°.
	b = 21.2914(7) Å	b= 90°.
	c = 35.9929(11) Å	g = 90°.
Volume	13450.9(8) $Å^3$	
Z	4	
Density (calculated)	1.187 Mg/m^3	
Absorption coefficient	2.250 mm^{-1}	
F(000)	5121	
Crystal size	0.200 x 0.150 x 0.050 mm^3	
Theta range for data collection	2.411 to 74.493°.	
Index ranges	$-21 \le h \le 21$, $-26 \le k \le 26$, $-44 \le l \le 44$	
Reflections collected	155470	
Independent reflections	27477 [R(int) = 0.1619]	
Completeness to theta = 67.679°	100.0 %	
Absorption correction	Semi-empirical from equivalents	
Max. and min. transmission	0.5953 and 0.4527	
Refinement method	Full-matrix least-squares on $^{43}F^2$	
Data / restraints / parameters	27477 / 8929 / 2341	
Goodness-of-fit on F^2	1.024	
Final R indices [I>2sigma(I)]	R1 = 0.1006, wR2 = 0.2528	
R indices (all data)	R1 = 0.1439, wR2 = 0.2890	
Absolute structure parameter	0.392(3)	
Extinction coefficient	n/a	
Largest diff. peak and hole	0.726 and -0.575 $e.Å^{-3}$	

Collection and Refinement of $(PPN)_4[Fe(CN\text{-}B(C_6F_5)_3]_6$

A crystal was mounted on a polyimide MiTeGen loop with STP Oil Treatment and placed under a nitrogen stream. Low temperature (100K) X-ray data were obtained on a Bruker AXS D8 VENTURE KAPPA diffractometer with an IμS micro-source (50 kV and 1mA; Cu K_α radiation, λ = 1.54178 Å), Helios focusing multilayer mirror optics, and a PHOTON II CPAD detector. All diffractometer manipulations, including data collection, integration, and scaling were carried out using the Bruker APEX3 software. An absorption correction was applied using SADABS. The space group was determined on the basis of systematic absences and intensity statistics; the structure was solved by intrinsic phasing using XT and refined by full-matrix least squares on F^2 using XL. All non-hydrogen atoms were refined using anisotropic displacement parameters. Hydrogen atoms were placed in idealized positions and refined using a riding model. The isotropic displacement parameters of all hydrogen atoms were fixed at 1.2 times the U_{eq} value of the bonded atom.

$(PPN)_4[Fe(CN\text{-}B(C_6F_5)_3)_6]$ crystallizes in the triclinic space group *P*-1 with half an anion (the Fe lies on a center of symmetry), two cations, and some CH_2Cl_2 in the asymmetric unit. Collecting data at temperatures above 100 K did not improve the structure. A large solvent region consists of disordered CH_2Cl_2 molecules. A few are modelled with restraints. Although difference peaks at the characteristic 2.9 Å separation indicated additional CH_2Cl_2, these would not behave during refinement and therefore an OLEX2 solvent mask was employed (617.8 $Å^3$; 242.8 e^-).

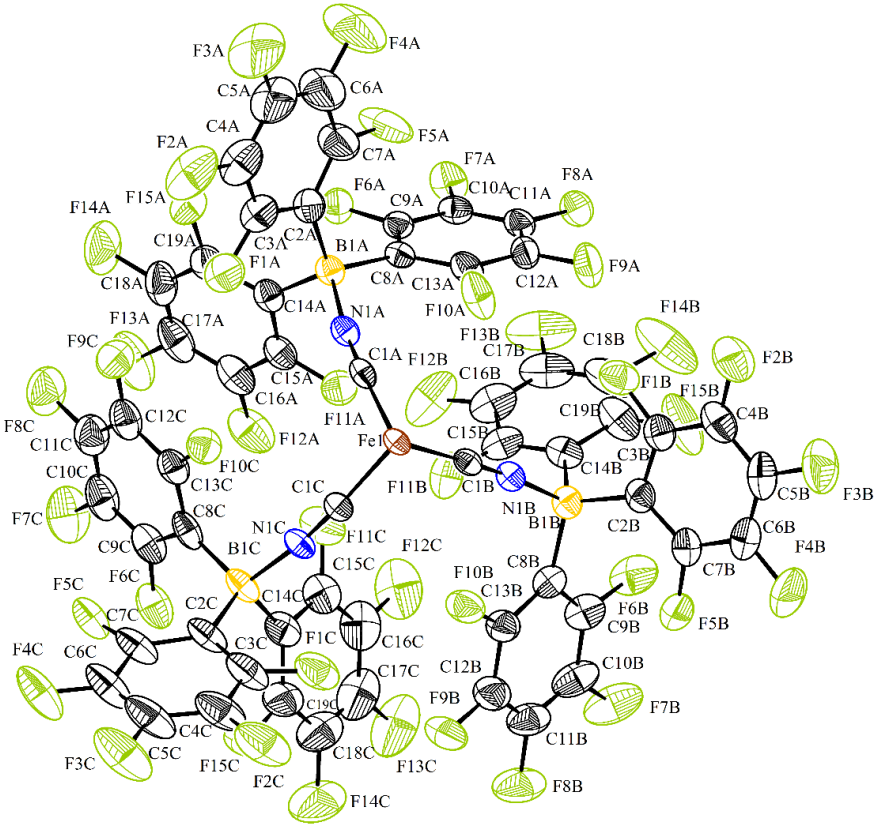

Figure 4.23. Crystal structure of the asymmetric unit of $(PPN)_4[Fe(CN\text{-}B(C_6F_5)_3)_6]$. Thermal ellipsoids set at 50% probability. Cations and solvent omitted for clarity.

Table 4.5 Crystal data and structure refinement for $(PPN)_4[Fe(CN\text{-}B(C_6F_5)_3)_6]$.

Empirical formula	C263.25 H130.49 B6 Cl10.49 F90 Fe N10 P8	
Moiety formula	C114 B6 F90 Fe N6, 4(C36 H30 N P2), 5.25(C H2 Cl2)	
Formula weight	5883.60	
Temperature	100 K	
Wavelength	1.54178 Å	
Crystal system	Triclinic	
Space group	P-1	
Unit cell dimensions	a = 19.290(4) Å	α= 65.073(6)°
	b = 19.912(4) Å	β= 68.449(19)°
	c = 20.432(4) Å	γ = 80.849(6)°
Volume	6619(2) $Å^3$	
Z	1	
Density (calculated)	1.476 g/cm^3	
Absorption coefficient	2.947 mm^{-1}	
F(000)	2944	
Crystal size	0.21 x 0.11 x 0.08 mm^3	
Theta range for data collection	2.447 to 70.367°.	
Index ranges	$-22 \le h \le 23$, $-23 \le k \le 24$, $-24 \le l \le 24$	
Reflections collected	158484	
Independent reflections	24649 [R(int) = 0.0483]	
Completeness to theta = 67.679°	99.1 %	
Absorption correction	Semi-empirical from equivalents	
Max. and min. transmission	1.0000 and 0.7413	
Refinement method	Full-matrix least-squares on F^2	
Data / restraints / parameters	24649 / 48 / 1839	
Goodness-of-fit on F^2	1.058	
Final R indices [I>2sigma(I)]	R1 = 0.0743, wR2 = 0.2117	
R indices (all data)	R1 = 0.0915, wR2 = 0.2272	
Extinction coefficient	n/a	
Largest diff. peak and hole	1.628 and -0.999 $e.Å^{-3}$	

Collection and Refinement of $[Fe(CN\text{-}CH_3)_6](OTf)_2$

Low-temperature diffraction data (ϕ-and ω-scans) were collected on a Bruker AXS D8 VENTURE KAPPA diffractometer coupled to a PHOTON 100 CMOS detector with Mo K_α radiation (λ = 0.71073 Å) from an IμS micro-source for the structure of $[Fe(CN\text{-}CH_3)_6](OTf)_2$. The structure was solved by direct methods using SHELXS[21] and refined against F^2 on all data by full-matrix least squares with SHELXL-2014[22] using established refinement techniques.[23] All non-hydrogen atoms were refined anisotropically. All hydrogen atoms were included into the model at geometrically calculated positions and refined using a riding model. The isotropic displacement parameters of all hydrogen atoms were fixed to 1.2 times the *U* value of the atoms they are linked to (1.5 times for methyl groups). All disordered atoms were refined with the help of similarity restraints on the 1,2- and 1,3-distances and displacement parameters as well as rigid bond restraints for anisotropic displacement parameters.

$[Fe(CN\text{-}CH_3)_6](OTf)_2$ crystallizes in the rhombohedral space group *R*-3. The iron compound is located in two independent positions, which add up to 2/3 of a molecule. Both of the molecules are located on crystallographic symmetry elements (-3 and inversion center). The structure also contains 4/3 triflate anions. One of the triflate anions is located near a crystallographic three-fold rotation axis and disordered over six positions, three of which are pairwise-related to the other three by the rotation axis.

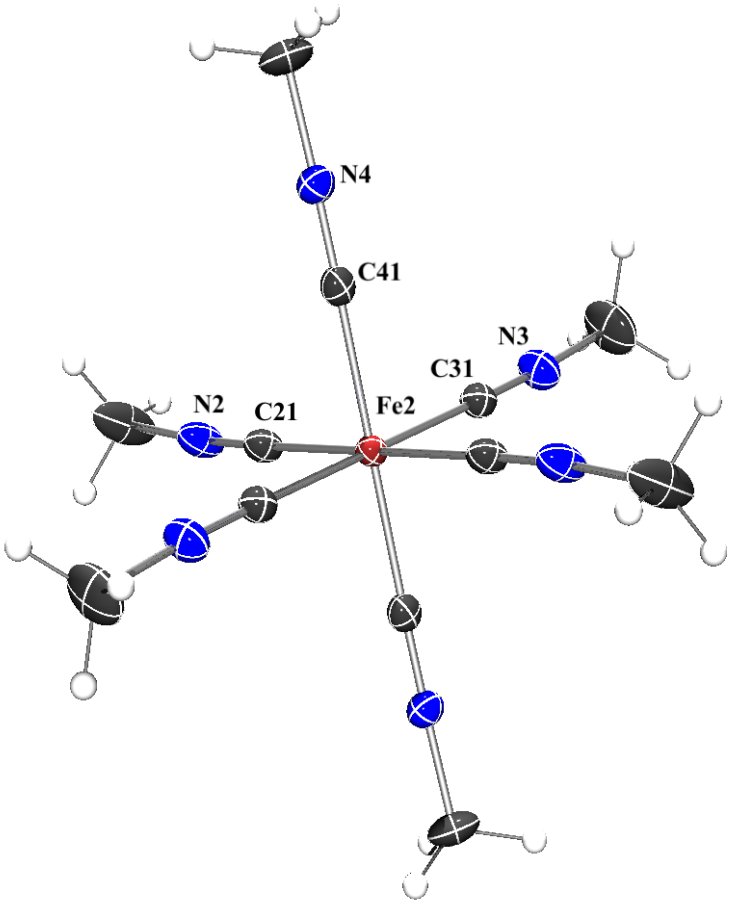

Figure 4.24. Crystal structure of $[Fe(CN\text{-}CH_3)_6](OTf)_2$. Thermal ellipsoids set at 50% probability. Cations and solvent omitted for clarity.

Table 4.5. Crystal data and structure refinement for $[Fe(CN\text{-}CH_3)_6](OTf)_2$.

Empirical formula	C14 H18 F6 Fe N6 O6 S2	
Formula weight	600.31	
Temperature	100(2) K	
Wavelength	0.71073 Å	
Crystal system	Trigonal	
Space group	R-3	
Unit cell dimensions	a = 21.9439(7) Å	a= 90°.
	b = 21.9439(7) Å	b= 90°.
	c = 16.8583(5) Å	g = 120°.
Volume	7030.3(5) $Å^3$	
Z	12	
Density (calculated)	1.702 Mg/m^3	
Absorption coefficient	0.913 mm^{-1}	
F(000)	3648	
Crystal size	0.150 x 0.100 x 0.100 mm^3	
Theta range for data collection	2.460 to 34.968°.	
Index ranges	$-35 \le h \le 35$, $-35 \le k \le 31$, $-26 \le l \le 27$	
Reflections collected	69954	
Independent reflections	6881 [R(int) = 0.0633]	
Completeness to theta = 25.242°	99.9 %	
Absorption correction	Semi-empirical from equivalents	
Max. and min. transmission	1.0000 and 0.9508	
Refinement method	Full-matrix least-squares on F^2	
Data / restraints / parameters	6881 / 579 / 338	
Goodness-of-fit on F^2	1.033	
Final R indices [I>2sigma(I)]	R1 = 0.0593, wR2 = 0.1234	
R indices (all data)	R1 = 0.1053, wR2 = 0.1429	
Extinction coefficient	n/a	
Largest diff. peak and hole	1.087 and -0.887 $e.Å^{-3}$	

4.6 References

(1) (a) D. F. Shriver, *J. Am. Chem. Soc.*, 1962, **84**, 4610-4611. (b) D. F. Shriver *J. Am. Chem. Soc.*, 1963, **85**, 1405-1408. (c) D. F. Shriver, The Ambident Nature of Cyanide. In *Structure and Bonding*. Springer: Berlin, Heidelberg, 1966; Vol. 1, p 32-58. (d) C. F. Woodcock and D. F. Shriver, *Inorg. Chem.*, 1986, **25**, 2137-2142.

(2) J. S. Kristoff and D. F. Shriver, *Inorg. Chem.*, 1973, **12**, 1788-1793.

(3) E. J. Schelter, M. Shatruk, R. A. Heintz, J. R. Galán-Mascarós, and K. R. Dunbar, *Chem. Commun.*, 2005, **11**, 1417-1419.

(4) J. Zhou, S. J. Lancaster, D. A. Walker, S. Beck, M. Thornton-Pett, and M., *J. Am. Chem. Soc.*, 2001, **123**, 223-237.

(5) V. Gutmann, G. Gritzner, and K. Danksagmuller, *Inorganica Chim. Acta*, 1976, **17**, 81-86.

(6) P. K. Mascharak, *Inorg. Chem.*, 1986, **25**, 245-247.

(7) H. E. Toma and M. S. Takasugi, *J. Solution Chem.*, 1989, **18**, 575-583.

(8) J. Jiang, A. Acunzo, and S. A. Koch, *J. Am. Chem. Soc.*, 2001, **123**, 12109-12110.

(9) D. F. Shriver, S. A. Shriver, and S. E. Anderson, *Inorg. Chem.*, 1965, **4**, 725-730.

(10) J. J. Alexander and H. B. Gray, *J. Am. Chem. Soc.*, 1968, **90**, 4260-4271.

(11) D. E. Richardson and H. Taube, *Inorg. Chem.*, 1981, **20**, 1278-1285.

(12) FD. Lexa, P. Rentien, J. M. Savéant and F. Xu, *J. Electroanal. Chem.,* 1985, **191**, 253-279.

(13) R. S. Nicholson and I. Shain, *Anal. Chem.*, 1964, **36**, 706.

(14) W. -K. Chu, C. -C. Ko, K. -C. Chan, S. -M. Yiu, F. -L. Wong, C. -S. Ling, and V. A. L. Roy, *Chem. Mater.*, 2014, **26**, 2544-2550.

(15) W. -K. Chu, S. -M. Yiu, and C. -C. Ko, *Organometallics*, 2014, **33**, 6771-6777.

(16) A. J. Bard and L. R. Faulkner, *Electrochemical Methods*, Wiley, 2000.

(17) S. J. Konopka and B. McDuffie, *Anal. Chem.*, 1970, **42**, 1741-1746.

(18) G. Gerhardt and R. N. Adams, *Anal. Chem.*, 1982, **54**, 2618-2620.

(19) G. M. Brown and N. Sutin, *J. Am. Chem. Soc.*, 1979, **101**, 883-892.

(20) J. M. Stauber, S. Zhang, N. Gvozdik, Y. Jiang, L. Avena, K. J. Stevenson, and C. C. Cummins, *J. Am. Chem. Soc.*, 2018, **140**, 538-541.

(21) Sheldrick, G. M. *Acta Crystallogr.* **1990**, *A46*, 467–473.

(22) Sheldrick, G. M. *Acta Crystallogr. C71*, 3–8.

(23) Müller, P. *Crystallogr Rev 15*, 57–83.

Chapter V

BORANE ADDUCTS OF HOMOLEPTIC CYANOMETALATES: ELECTRONIC STRUCTURE, ENERGY LEVEL INVERSION, AND APPLICATIONS IN NON-AQUEOUS REDOX FLOW BATTERIES

5.1. Summary

The synthesis and characterization of the oxidized and reduced forms of $[M(CN\text{-}B(C_6F_5)_3)_6]^{3/4-}$ (M = Cr, Mn, Fe, Ru, Os), of $[Mn(CN\text{-}B(2,4,6\text{-}F_3C_6H_2)_3)_6]^{3/4-}$, and of $[Cr(CN\text{-}BPh_3)_6]^{3-}$ are reported. The structural and spectroscopic data suggest the variable ligand field strength of cyanide, with greater d electron counts imparting shorter M-C bond lengths and greater stability. Boronation results in a 2.10-2.29 V anodic shift in the $M^{III/II}$ formal potential for all species while simultaneously maintaining or improving electrochemical reversibility. The formal potentials of all five species scale according to the first ligand to metal charge transfer (LMCT) observed in UV-vis spectroscopy. UV-vis spectroscopy, magnetic circular dichroism spectroscopy, and density functional theory calculations suggest that the first LMCT in all M(III) species is a $t_{2u} \rightarrow t_{2g}$ transition, meaning enhanced pi backbonding negligibly influences the t_{2u} ligand orbitals. Based on this assignment, the t_{2u} level energy shift is very near the shift in formal potential for all complexes. $t_{2u} \rightarrow t_{2g}$ energy versus formal potential is linear, suggesting weak coupling of these molecular orbitals to metal-centered levels. Initial theoretical studies using time-dependent density functional theory support the LMCT assignment. We also report the luminescence of M(II) and M(III) species, demonstrating that boronation blue shifts ligand field emission but red shifts LMCT emission.

5.2 Introduction

Since the 1950s, ligand field theory and SCF calculations in conjunction with UV-vis, IR, have been heavily exploited as a means for rationalizing the experimental spectra and ground-state properties of homoleptic cyanometallates. A periodic table of homoleptic cyanometallates have since been synthesized and characterized, almost entirely encompassing the transition metal block. In 1968, Alexander and Gray published the first comprehensive study of first-row and Group VIII transition metal cyanometallates that combined SCF calculations with variable temperature UV-vis spectroscopy.[1] **Figure 5.1** reproduces a contracted version of the one-electron molecular orbital energy diagram for hexacyanoferrate(II) calculated previously.[1]

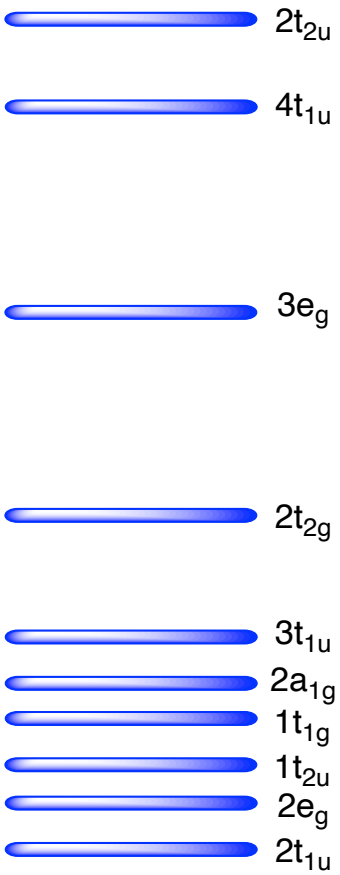

Figure 5.1. Contracted one-electron molecular orbital energy level diagram for hexacyanoferrate(II).

Unlike hexacyanoferrate(III), the electronic structure of both hexacyanoruthenate(III) and hexacyanoosmate(III) are understudied, with studies primarily focused on comparisons to reported spectra for hexacyanoferrate(III), theoretical calculations, magnetic circular dichroism studies, and applications as single-molecule/Prussian-Blue analogue magnetic materials. Given their paramagnetism and variable spin-orbit coupling, d^5 hexacyanometallates have also been probed as possible molecular qubits.[2]

Boranes are neutral Lewis acids which coordinate to the lone pair of nitrogen in a dative bond when the carbon lone pair is already coordinated to a metal. According to self-consistent field molecular orbital calculations, coordination of an electron-deficient species to nitrogen results in a lowering of all one-electron molecular orbital energy levels, but not by the same amount. The simultaneous increase in pi backbonding and decrease in sigma donation cause isocyanoborates to behave similarly to carbon monoxide. When solvation effects are minimized, anodic shifts in formal potentials are consistent with the relative Lewis acidity of electron acceptors, as evidenced by work on borane adducts of $Fe(phen)_2(CN)_2$.[3] An extreme example of an isocyanide ligand is methylisocyanide, whose ligand field behaves very similarly to carbon monoxide.[4] Methylation has been used as a means to dramatically alter the electronic structure of cyanometallates; however, this strategy does not retain the overall charge of the species. Additionally, many of these alterations shift charge transfer states so high in energy that the lowest energy transition is now ligand-centered.[5] The molecular orbital interpretation of boronation on cyanometallates is shown in **Figure 5.2**.

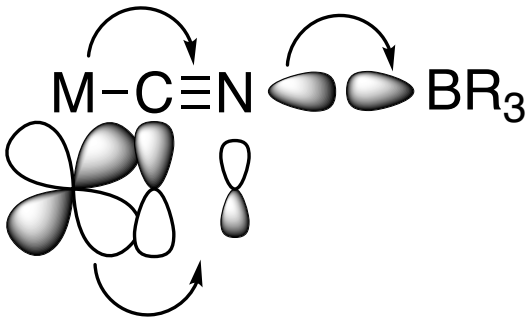

Figure 5.2 Effect of boronation on the electron density of metal isocyanoborates.

We have focused on transition metal ions with strong-field ligands, namely boronated hexacyanoferrates. We recently reported initial studies of these compounds, which exhibit high thermal, electrochemical, and photochemical stability when a strong Lewis acid, namely tris(pentafluorophenyl)borane (BCF) is coordinated to hexacyanoferrate. The stability results from enhanced pi backdonation by the metal center. Herein, we report a full electronic and structural characterization of a series of homoleptic, transition metal isocyanoborates. These species exhibit unique structural and electronic features which provide an avenue for enhancing our understanding of the electronic structure and energy levels of molecular materials. These studies will be of great importance in the systematic modulation of inorganic complexes for use in electrocatalysis, slurry-state or solution-state batteries, molecular wires and magnets, and qubits. Since boronation tends to blue shift ligand field transitions, we also hope that these modifications will provide an avenue for the realization of longer-lived luminescence in first row transition metals, a rare and sought-after property for Fe complexes.

5.3 Results and Discussion

Synthesis and X-Ray Crystallography

Tetrabutylammonium (TBA) hexacyanoferrate(III) was synthesized according to literature precedent. The bis(triphenylphosphine)iminium (PPN^+) salt of hexacyanoferrate (III) was synthesized by combining a slight stoichiometric excess of PPNCl with $K_3[Fe(CN)_6]$, filtering, washing with distilled water, and drying overnight under vacuum. Previous studies provided starting points for syntheses of potassium hexacyanoruthenate ($K_4[Ru(CN)_6]$) and hexacyanoosmate ($K_4[Os(CN)_6]$) from ruthenium(III) trichloride and hexachloroosmate(IV), respectively.[6,7] However, the yield of $K_4[Os(CN)_6]$ obtained can be improved to nearly 80% by refluxing the reaction in an inert atmosphere. $K_4[Os(CN)_6]$ was oxidized with ceric ammonium nitrate, and $K_4[Ru(CN)_6]$ was oxidized with cerium sulfate. Both oxidized solutions were then treated with excess tetraphenylarsonium chloride (Ph_4AsCl) or tetraphenylphosphonium chloride (Ph_4PCl) near 0 °C to precipitate the lipophilic salt, which was then washed with cold water and dried under vacuum.[8,9] An alternative synthetic route employed a biphasic mixture of the potassium salt of Os(II) or Ru(II) in H_2O and the chloride salt of TBA or PPh_4 in chloroform ($CHCl_3$), resulting in isolation of the lipophilic salt from CH_2Cl_2.[10] Both $(TBA/PPN)_3[Mn(CN)_6]$ and $(TBA/PPN)_3[Cr(CN)_6]$ were synthesized according to literature precedent.[11,12,13]

Boronation with $B(C_6F_5)_3$ of the Fe(III), Ru(III), Os(III), Cr(III), and Mn(III) salts in dichloromethane (DCM) resulted in dramatic color changes from yellow or orange to violet for Fe(III) (**4**), to green for Ru(III) (**5**), to indigo for Os(III) (**6**), to colorless for Cr(III) (**7**), to red-orange for Mn(III) (**8**), and to orange for Mn(III) (**9**). $[Ru(CN\text{-}B(C_6F_5)_3)_6]^{3-}$ and $[Os(CN\text{-}B(C_6F_5)_3)_6]^{3-}$ were then reduced by addition of diethyl ether (Et_2O) or tetrahydrofuran (THF) to a solution of the salt in DCM, followed by

precipitation of the colorless product by addition of more Et_2O (**2** and **3**). Alternatively, boronated TBA salts of Fe(II), Ru(II), and Os(II) were synthesized by generating the acid salts in HCl followed by titration with TBAOH and extensive drying of the resulting $(TBA)_4[M(CN)_6]$.[14] The non-aqueous salt was then boronated in a 1:1 mixture of DCM:toluene, precipitated as an oil with excess toluene, dried, and purified with $MeCN/Et_2O$ to ultimately obtain the boronated M(II) salt. X-ray quality crystals of all M(II) species were grown from a concentrated solution of the M(II) species in DCM with minimal Et_2O at −20 °C. All M(III) species were crystallized from a concentrated solution of the compound in DCM at −20 °C.

We were also inspired by previous studies by Dunbar et al., which demonstrated the linkage isomerism of hexacyanochromate with triphenylborane (BPh_3) to isolate both $[Cr(CN\text{-}BPh_3)_6]^{3-}$ and $[Cr(NC\text{-}BPh_3)_6]^{3-}$.[15,16] When hexacyanochromate is refluxed with BPh_3 in MeCN, a dramatic color change from yellow to orange occurs.[16] The study demonstrated that all six cyanide ligands had inverted, resulting in a borane-capped hexakisisoboratonitrile species. Analysis of the vibrational and UV-vis spectra and X-ray structural characterization supported assignment of the N-bound, octahedral complex. However, based on our experience with the $B(C_6F_5)_3$ adduct of hexacyanochromate and theoretical calculations that the thermodynamic and kinetic products are not energetically disparate, we attempted synthesis and crystallographic characterization of the isocyanoborate isomer $[Cr(CN\text{-}BPh_3)_6]^{3-}$. Addition of a stoichiometric excess of BPh_3 to a room-temperature solution of $(TBA)_3[Cr(CN)_6]$ in DCM resulted in an immediate color change from pale yellow to bright yellow. The solution was concentrated by evaporating solvent in vacuo, and the oil was placed in a freezer at −20 °C. X-ray crystallography of yellow crystals revealed with relative certainty that the species was $(Ph_4As)_3[Cr(CN\text{-}BPh_3)_6]$. We also note that after prolonged exposure to X-ray irradiation, the color of the crystal began to change to orange-

pink. Thus, early reflections were used for structure refinement. **Figure 5.3** summarizes the schemes used for synthesis of all boronated cyanometallates in these studies.

The bond lengths for all species are readily compared to literature values for the base complexes. **Tables 5.1**, **5.2**, **and 5.3** provide a summary of bond lengths for crystallographically characterized species and previously reported complexes. We previously showed that the M-C bond lengths showed slight decreases based on Lewis acid strength.[17] The M-C bond lengths for the complexes increase in the order,

$$\text{M(II)-BCF} < \text{M(III)-BCF} \approx \text{M(II)} < \text{M(III)}$$

which is an intuitive trend based on the interplay between the metal's oxidation state and the binding strength of the Lewis acid. Decreasing metal oxidation state increases the number of electrons available for π backbonding, thereby increasing M-C covalency. Increasing the dative interaction of N to a Lewis acid decreases M-C sigma covalency. These data conclusively show that pi backbonding interactions more dramatically affect M-C bonding than CN bonding in metal isocyanoborates. This result is consistent with Raman studies on boronated derivatives of hexacyanocobaltate, where the Co-C symmetric stretch observed in the Raman spectrum blue shifts by about 10 cm^{-1}. In contrast, the C-N bond length is very similar in all cases, suggesting that the competing pi/sigma effects of Lewis acids on cyanometallates are more equally balanced in the C-N bonding regime.

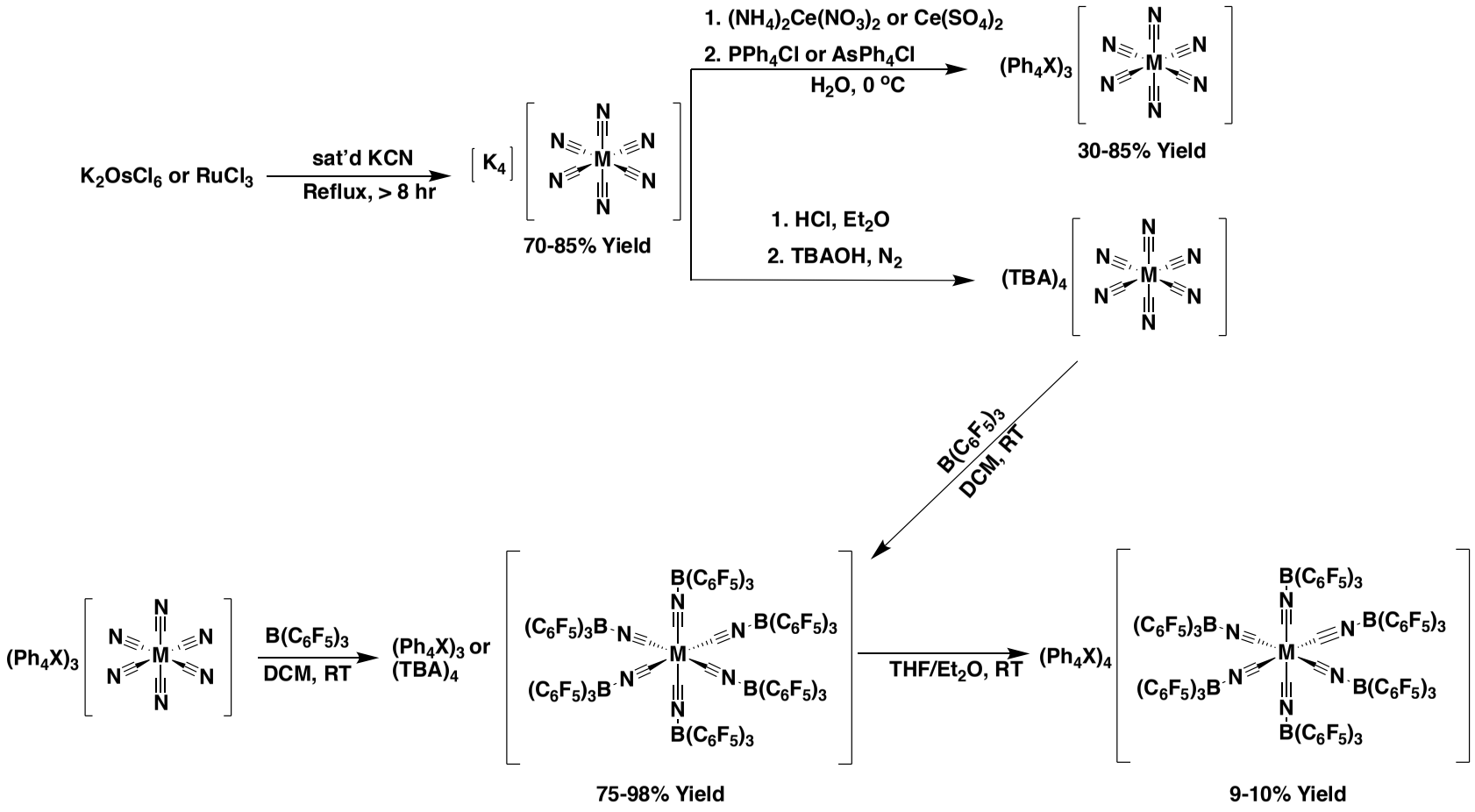

Figure 5.3. General synthetic scheme for M(II) and M(III) boronated cyanometallates.

Table 5.1. Relevant bond lengths and angles for M(II), Group VIII cyanometallate species.

Bond (Å) or Angle (°) / Compound	$[Fe(CN)_6]^{4-}$[a]	$[Ru(CN)_6]^{4-}$[b]	$[Os(CN)_6]^{4-}$[b]	$[Fe(CN\text{-}B(C_6F_5)_3)_6]^{4-}$ (1)[c]	$[Ru(CN\text{-}B(C_6F_5)_3)_6]^{4-}$ (2)	$[Os(CN\text{-}B(C_6F_5)_3)_6]^{4-}$ (3)
M-C_1 (or C_1#1)	1.926(5)	2.035(3)	2.068(7)	1.899(4)	2.0220(11)	2.023(5)
M-C_2 (or C_1#2)	1.920(4)	2.023(3)	2.044(7)	1.899(4)	2.0220(11)	2.023(5)
M-C_3 (or C_2#1)	1.922(5)	2.010(3)	2.013(6)	1.904(3)	2.0026(11)	2.037(5)
M-C_4 (or C_2#2)	1.924(4)	2.035(3)	2.068(7)	1.904(3)	2.0027(11)	2.037(5)
M-C_5 (or C_3#1)	1.919(4)	2.023(3)	2.044(7)	1.897(3)	2.0152(12)	2.036(5)
M-C_6 (or C_3#2)	1.918(4)	2.010(3)	2.013(6)	1.897(3)	2.0152(12)	2.036(5)
C-N_1	1.174(6)	1.151(4)	1.116(9)	1.146(4)	1.1546(13)	1.144(6)
C-N_2	1.164(6)	1.158(5)	1.156(9)	1.146(4)	1.1546(13)	1.144(6)
C-N_3	1.168(6)	1.161(4)	1.149(9)	1.152(4)	1.1551(13)	1.148(6)
C-N_4	1.170(6)	1.151(4)	1.116(9)	1.152(4)	1.1551(13)	1.148(6)
C-N_5	1.161(5)	1.158(5)	1.156(9)	1.160(4)	1.1530(14)	1.133(7)
C-N_6	1.156(6)	1.161(4)	1.149(9)	1.160(4)	1.1530(14)	1.133(7)
M-C_1-N_1 (or 1 #1)	176.4(4)	177.3(3)	176.2(4)	176.9(3)	177.62(9)	178.0(4)
M-C_2-N_2 (or 1 #2)	177.2(4)	178.8(2)	179.3(5)	177.9(3)	177.35(9)	177.8(4)
M-C_3-N_3 (or 1 #3)	179.1(4)	178.3(3)	179.1(6)	175.9(3)	176.99(9)	176.1(5)
M-C_4-N_4 (or 2 #1)	178.6(4)	177.3(3)	176.2(4)	176.9(3)	177.62(9)	178.0(4)
M-C_5-N_5 (or 2 #2)	179.0(4)	178.8(2)	179.3(5)	177.9(3)	177.35(9)	177.8(4)
M-C_6-N_6 (or 2 #3)	178.0(4)	178.3(3)	179.1(6)	175.9(3)	176.99(9)	176.1(5)

[a]Reference 17
[b]Reference 18

The X-ray structures of **4**, **5**, and **6** show minimal changes in M-C bonding as a result of one electron oxidation, allowing us to make comparisons between the electronic structure of both oxidation states. It is well known that d^5 and d^6 valence electron configurations are able to effect a strong ligand field for a cyanometallate due to significant π-backbonding. However, as valence electron counts become smaller, the effect of sigma donation is greater, and while counterintuitive to many preconceived notions about CN^-, this effectively converts CN^- into a weak field ligand.

Table 5.2. Relevant bond lengths and angles for M(III) cyanometallate species.

Bond (Å) or Angle (°) / Compound	$[Fe(CN)_6]^{3-}$[a] / $[Fe(CN\text{-}B(C_6F_5)_3)_6]^{3-}$ (4)	$[Ru(CN)_6]^{3-}$[b] / $[Ru(CN\text{-}B(C_6F_5)_3)_6]^{3-}$ (5)	$[Os(CN)_6]^{3-}$[c] / $[Os(CN\text{-}B(C_6F_5)_3)_6]^{3-}$ (6)	$[Mn(CN)_6]^{3-}$[d] / $[Mn(CN\text{-}B(C_6F_5)_3)_6]^{3-}$ (8)	$[Mn(CN\text{-}B(\textit{246}\text{-}F_3C_6H_2)_3)_6]^{3-}$ (9)
M-C_1 (or C_1#1)	1.935(5) / 1.918(8)	2.066(6) / 2.025(9)	2.063(5) / 2.066(11)	2.022(2) / 1.9989(19)	1.9749(13)
M-C_2 (or C_1#2)	1.959(5) / 1.918(8)	2.064(6) / 2.025(9)	2.063(5) / 2.043(9)	2.022(2) / 1.9900(19)	1.9750(13)
M-C_3 (or C_2#1)	1.946(8) / 1.944(9)	2.023(6) / 2.048(6)	2.070(5) / 2.060(11)	2.025(2) / 1.9768(18)	1.9794(13)
M-C_4 (or C_2#2)	1.965(8) / 1.944(9)	2.025(6) / 2.048(6)	2.070(5) / 2.051(9)	2.025(2) / 1.983(2)	1.9794(13)
M-C_5 (or C_3#1)	1.955(8) / 1.901(7)	2.054(6) / 2.017(8)	2.056(5) / 2.077(9)	2.013(2) / 2.0048(18)	1.9714(11)
M-C_6 (or C_3#2)	1.959(8) / 1.902(7)	2.064(6) / 2.017(8)	2.056(5) / 2.038(10)	2.013(2) / 1.9878(18)	1.9715(11)
C-N_1	1.156(7) / 1.152(10)	1.161(6) / 1.158(9)	1.137(6) / 1.117(14)	1.161(2) / 1.138(3)	1.1498(14)
C-N_2	1.136(7) / 1.152(10)	1.143(6) / 1.158(9)	1.141(6) / 1.140(13)	1.161(2) / 1.134(2)	1.1498(14)
C-N_3	1.141(11) / 1.130(11)	1.145(6) / 1.134(9)	1.139(6) / 1.136(14)	1.161(2) / 1.142(2)	1.1508(14)
C-N_4	1.134(11) / 1.130(11)	1.165(7) / 1.134(9)	1.154(6) / 1.125(13)	1.161(2) / 1.135(3)	1.1508(14)
C-N_5	1.131(11) / 1.185(10)	1.142(6) / 1.161(9)	1.145(6) / 1.102(13)	1.156(2) / 1.142(2)	1.1489(13)
C-N_6	1.140(10) / 1.185(10)	1.147(6) / 1.161(9)	1.157(6) / 1.145(14)	1.156(2) / 1.141(2)	1.1489(13)
M-C_1-N_1 (or 1 #1)	178.8(9) / 176.6(7)	175.9(5) / 178.5(6)	177.2(5) / 172.7(10)	178.6(2) / 175.54(17)	175.33(9)
M-C_2-N_2 (or 1 #2)	178.3(7) / 176.6(7)	175.4(5) / 178.5(6)	177.6(5) / 174.6(10)	178.6(2) / 177.46(18)	175.33(9)
M-C_3-N_3 (or 2 #1)	179.3(7) / 176.8(7)	173.7(5) / 176.1(6)	176.2(4) / 176.2(9)	178.9(2) / 176.02(17)	175.21(9)
M-C_4-N_4 (or 2 #2)	178.4(6) / 176.8(7)	178.3(5) / 176.1(6)	175.3(5) / 177.7(9)	178.9(2) / 176.99(17)	175.21(9)
M-C_5-N_5 (or 3 #1)	178.1(8) / 176.9(6)	178.9(5) / 177.8(6)	177.1(4) / 175.2(9)	177.2(2) / 173.99(17)	178.29(9)
M-C_6-N_6 (or 3 #2)	179.2(7) / 176.9(6)	177.7(5) / 177.8(6)	177.3(5) / 176.9(9)	177.2(2) / 175.10(17)	178.29(9)

[a] Reference 19
[b] Reference 20
[c] Reference 9
[d] Reference 21

Table 5.3. Relevant bond lengths and angles for Cr(III) cyanometallate species.

Bond (Å) or Angle (°) / Compound	$[Cr(CN)_6]^{3-}$[a] / $[Cr(CN\text{-}B(C_6F_5)_3)_6]^{3-}$ (7)	$[Cr(CN\text{-}BPh_3)_6]^{3-}$ (12)	$[Cr(NC\text{-}BPh_3)_6]^{3-}$ (13)
M-C_1 (or C_1#1)	2.0865(19) / 2.067(4)	2.081(3)	1.995(7)
M-C_2 (or C_1#2)	2.0768(19) / 2.055(4)	2.068(3)	2.009(7)
M-C_3 (or C_1#3)	2.0751(18) / 2.073(4)	2.052(3)	2.002(7)
M-C_4 (or C_2#1)	2.0854(18) / 2.067(4)	2.074(3)	2.011(7)
M-C_5 (or C_2#2)	2.0871(18) / 2.055(4)	2.054(3)	2.008(7)
M-C_6 (or C_2#3)	2.0823(18) / 2.073(4)	2.080(3)	2.003(7)
C-N_1	1.156(2) / 1.148(5)	1.145(3)	1.141(10)
C-N_2	1.149(3) / 1.143(5)	1.145(3)	1.137(10)
C-N_3	1.149(2) / 1.149(5)	1.145(4)	1.144(9)
C-N_4	1.152(2) / 1.148(5)	1.143(3)	1.152(10)
C-N_5	1.152(2) / 1.143(5)	1.150(4)	1.136(9)
C-N_6	1.154(2) / 1.149(5)	1.144(3)	1.152(10)
M-C_1-N_1 (or 1 #1)	173.28(16) / 173.9(3)	177.8(2)	176.4(6)
M-C_2-N_2 (or 1 #2)	177.18(16) / 174.7(3)	175.6(2)	169.2(6)
M-C_3-N_3 (or 1 #3)	179.09(17) / 172.3(3)	170.7(2)	172.1(6)
M-C_4-N_4 (or 2 #1)	172.79(16) / 173.6(3)	173.8(2)	170.5(6)
M-C_5-N_5 (or 2 #2)	173.73(15) / 175.6(3)	171.0(2)	174.1(6)
M-C_6-N_6 (or 2 #3)	172.43(16) / 175.7(3)	175.7(2)	172.5(6)

[a] Reference 22

Figure 5.4 provides molecular structure representations for **4**, **5**, **6**, **7**, **12**, and **13**. **Table 5.3** tabulates structural parameters for the various chromium species. These values support the assignment of **12** as the CN isomer and **13** as the NC isomer. The NC isomer exhibits contracted M-N bond lengths as a result of the improved sigma bonding from nitrogen relative to carbon, while the weak pi backbonding of Cr(III) coupled with weakened M-C bonding as a result of boronation results in a minimal decrease in M-C bond length in going from $[Cr(CN)_6]^{3-}$ to **12**. The IR spectra for all species support the structural parameters obtained from X-ray crystallography, with ν(CN) values tabulated in **Table 5.4**.

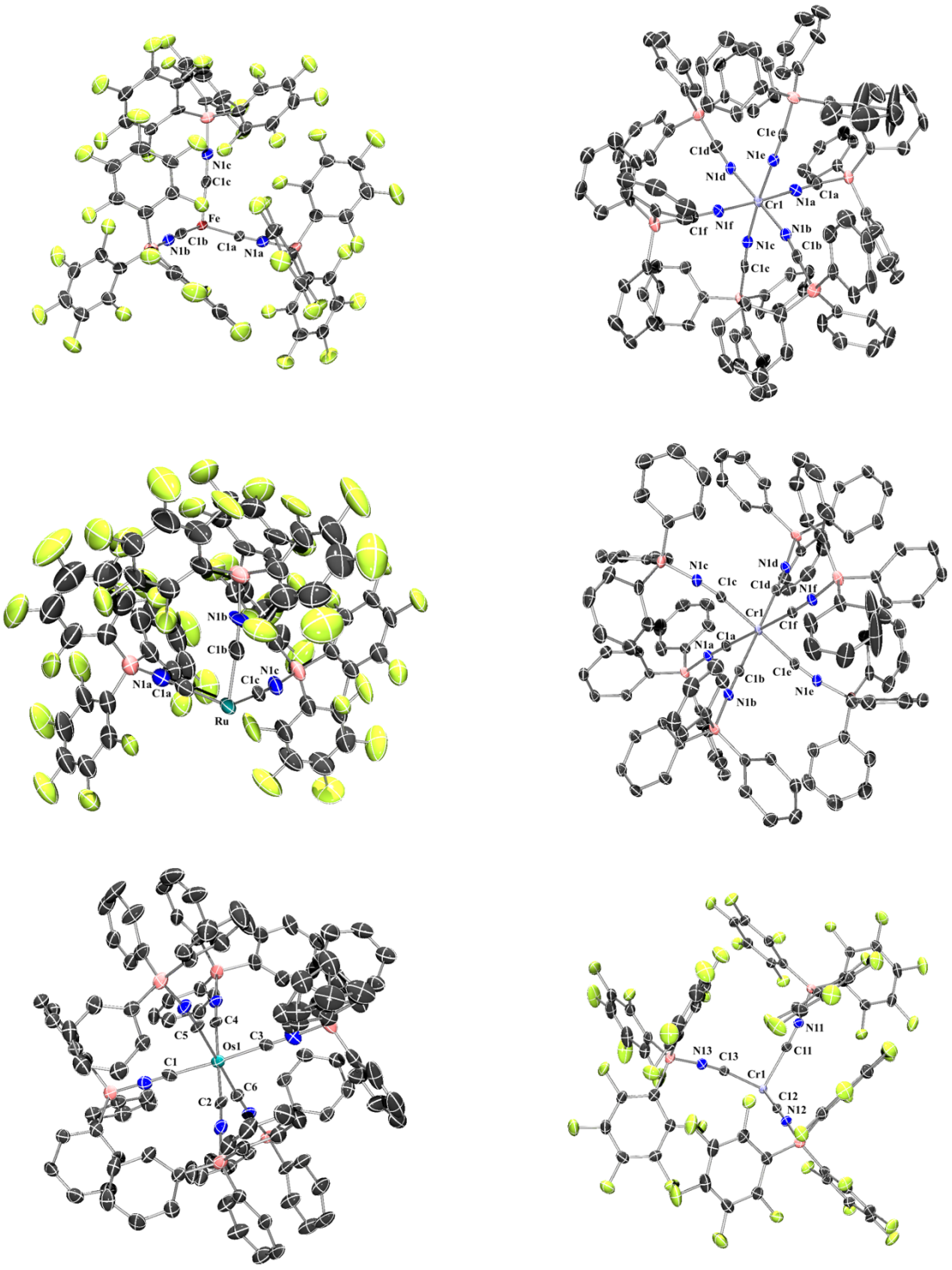

Figure 5.4. (**Left**) Molecular structures of Fe(III)-CN-BCF, Ru(III)-CN-BCF, and Os(III)-CN-BCF. (**Right**) Molecular structures of Cr(III)-NC-BPh_3, Cr(III)-CN-BPh_3, and Cr(III)-CN-BCF.

Table 5.4. CN stretching frequencies for hexacyanometallate derivatives with bulky cations (TBA^+, PPN^+, Ph_4As^+, or Ph_4P^+). The stretching frequency for $K_4[Os(CN)_6]$ is reported.

Species	ν_{CN} (cm^{-1})
$[Cr(CN\text{-}B(C_6F_5)_3)_6]^{3-}$	2229
$[Co(CN\text{-}B(C_6F_5)_3)_6]^{3-}$	2242
$[Mn(CN\text{-}B(2,4,6\text{-}C_6F_3H)_3)_6]^{3-}$	2226
$[Mn(CN\text{-}B(2,4,6\text{-}C_6F_3H)_3)_6]^{4-}$	2148
$[Mn(CN\text{-}B(C_6F_5)_3)_6]^{3-}$	2222
$[Mn(CN\text{-}B(C_6F_5)_3)_6]^{4-}$	2151
$[Fe(CN\text{-}B(C_6F_5)_3)_6]^{3-}$	2228
$[Ru(CN\text{-}B(C_6F_5)_3)_6]^{3-}$	2210
$[Os(CN\text{-}B(C_6F_5)_3)_6]^{3-}$	2204
$[Fe(CN\text{-}B(C_6F_5)_3)_6]^{4-}$	2165
$[Ru(CN\text{-}B(C_6F_5)_3)_6]^{4-}$	2172
$[Os(CN\text{-}B(C_6F_5)_3)_6]^{4-}$	2152
$[Cr(CN\text{-}BPh_3)_6]^{3-}$	2202
$[Cr(NC\text{-}BPh_3)_6]^{3-}$	2211
$[Cr(CN)_6]^{3-}$	2110
$[Mn(CN)_6]^{3-}$	2095
$[Mn(CN)_6]^{2-}$[a]	2132
$[Fe(CN)_6]^{3-}$	2096
$[Ru(CN)_6]^{3-}$[b]	2090
$[Os(CN)_6]^{3-}$[c]	2100
$[Fe(CN)_6]^{4-}$	2012
$[Ru(CN)_6]^{4-}$[b]	2060
$[Os(CN)_6]^{4-}$[d]	2032

[a]Reference 23
[b]Reference 8
[c]Reference 9
[d]Reference 24

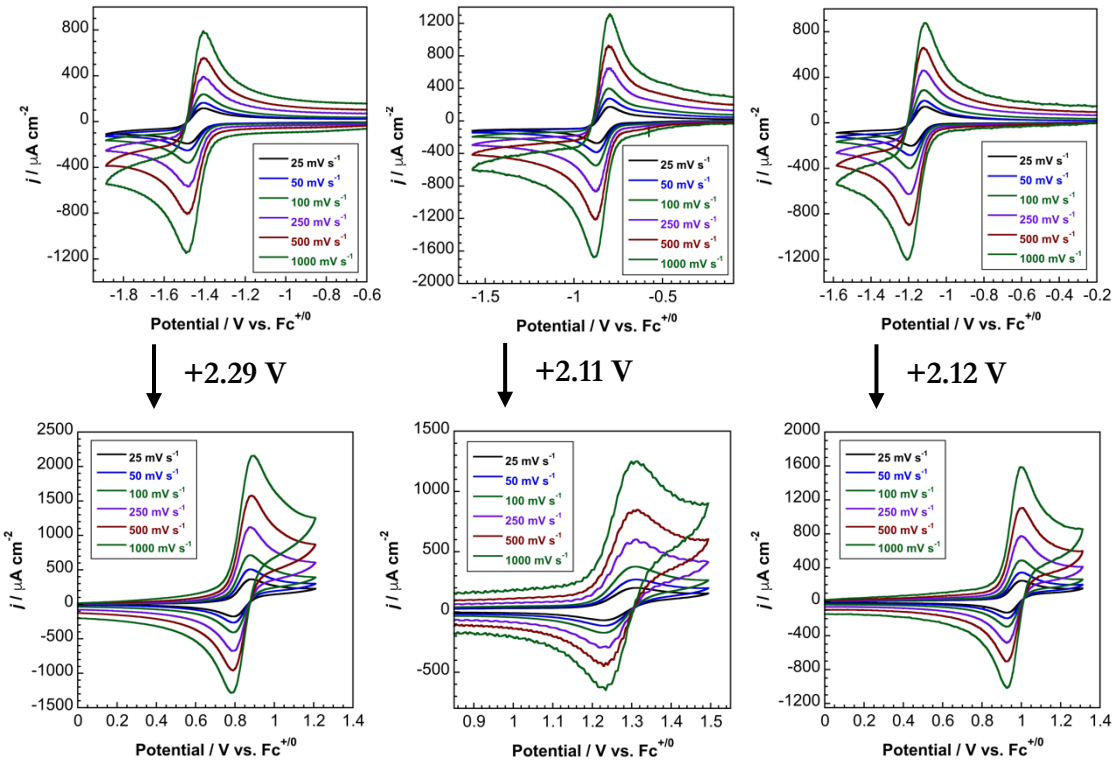

Figure 5.5. Voltammetry of $[Fe(CN)_6]^{3-}$ and $[Fe(CN\text{-}B(C_6F_5)_3)_6]^{4-}$ (**Left**), $[Ru(CN)_6]^{3-}$ and $[Ru(CN\text{-}B(C_6F_5)_3)_6]^{4-}$ (**Middle**), and $[Os(CN)_6]^{3-}$ and $[Os(CN\text{-}B(C_6F_5)_3)_6]^{4-}$ (**Right**) in MeCN with 0.1-0.2 M $TBAPF_6$.

Electrochemistry of $[M(CN\text{-}B(C_6F_5)_3)_6]^{3/4-}$

The voltammetry of **1**, **2**, **3**, **7**, **8**, and **9** were examined in acetonitrile (MeCN) with 0.1-0.2 M $TBAPF_6$ as the supporting electrolyte. Electrochemical impedance spectroscopy was used to obtain the uncompensated resistance of the cell via a Nyquist plot. 85% of the cell resistance was compensated for electronically. This step is important to ensure that peak-to-peak separations in voltammetry at fast scan rates are not broadened as a result of the resistance, but rather, as a result of convolution of the heterogeneous electron transfer rate constant with the diffusion coefficient of the complex.

Table 5.5. Electrochemical parameters for base and boronated cyanometallates in MeCN with 0.1-0.2 M $TBAPF_6$ electrolyte. All formal potentials taken from 100 mV s^{-1} scan rate data. Peak-to-peak separations taken from 25-1500 mV s^{-1} scan rate data. All formal potentials referenced to $Fc^{+/0}$.

Redox Process	$E_{p,a}$ (V vs. $Fc^{+/0}$)	$E_{p,c}$ (V vs. $Fc^{+/0}$)	E_0' (V vs. $Fc^{+/0}$)	ΔE_p (mV)
$[Cr(CN\text{-}B(C_6F_5)_3)_6]^{3/4-}$[a]	−0.82	−0.92	−0.87	100-162
$[Mn(CN\text{-}B(2,4,6\text{-}C_6F_3H)_3)_6]^{3/4-}$[b]	−0.93	−1.04	−0.99	85-175
$[Mn(CN\text{-}B(2,4,6\text{-}C_6F_3H)_3)_6]^{4/5-}$[b]	−2.64	−2.73	−2.68	79-118
$[Mn(CN\text{-}B(2,4,6\text{-}C_6F_3H)_3)_6]^{2/3-}$[c]	1.17	---	1.13[d]	---
$[Mn(CN\text{-}B(C_6F_5)_3)_6]^{3/4-}$	0.07	−0.01	0.03	79-80
$[Mn(CN\text{-}B(C_6F_5)_3)_6]^{4/5-}$	−1.61	−1.72	−1.67	95-138
$[Mn(CN\text{-}B(C_6F_5)_3)_6]^{2/3-}$	2.07	---	2.00[d]	---
$[Fe(CN\text{-}B(C_6F_5)_3)_6]^{3/4-}$	0.88	0.79	0.84	74-85
$[Ru(CN\text{-}B(C_6F_5)_3)_6]^{3/4-}$	1.31	1.23	1.27	85-85
$[Os(CN\text{-}B(C_6F_5)_3)_6]^{3/4-}$	1.00	0.93	0.96	72-83
$[Cr(CN)_6]^{3/4-}$[e]	---	---	−2.95	---
$[Mn(CN)_6]^{3/4-}$	---	−2.18	−2.11[d]	---
$[Mn(CN)_6]^{2/3-}$	−0.24	−0.32	−0.28	79-82
$[Fe(CN)_6]^{3/4-}$	−1.41	−1.49	−1.45	80-105
$[Ru(CN)_6]^{3/4-}$	−0.80	−0.88	−0.84	73-93
$[Os(CN)_6]^{3/4-}$	−1.12	−1.20	−1.16	75-107
$[Fe(CN)_6]^{3/4-}$[f]	---	---	0.361	---
$[Ru(CN)_6]^{3/4-}$[f]	---	---	0.926	---
$[Os(CN)_6]^{3/4-}$[f]	---	---	0.636	---

[a]Formal potential and peak-to-peak separation affected by a chemically coupled reaction
[b]Voltammetry acquired in THF
[c]Voltammetry acquired in DCM
[d]Taken from the inflection potential of the redox process, which approximates the formal potential. See Reference 25
[e]Taken from References 26 and 27 in 1.0 M KCN at a dropping mercury electrode. Derived by using the separation in aqueous formal potential between $[Fe(CN)_6]^{3-}$ and $[Cr(CN)_6]^{3-}$
[f]In neutral, aqueous media vs. NHE. Taken from References 28, 29, and 24

The formal potential shifts by over 2.1 V for all five complexes. **1** exhibits the largest shift (2.29 V), which was underestimated in our previous work due to incomplete removal of H_2O coordinated to bare hexacyanoferrate.[17] Many inaccurate formal potentials exist in the literature for hexacyanometallates due to the strong binding of H_2O to coordinated cyanide.[9,30] **2** and **3** exhibit nearly identical shifts in formal potential, 2.11 V and 2.12 V, respectively. The greater shift for **1** is likely due to a greater change in ionic radius between Fe(II) and Fe(III). It is gratifying to point out that the potential separation between the formal potential for **7** and the estimate of formal potential for $[Cr(CN)_6]^{3/4-}$ is consistent with other shifts in formal potential for the electrochemically reversible species. The potential separations among Fe, Ru, and Os are identical in both aqueous and non-aqueous media, with Os species exhibiting less positive formal potentials as a result of stronger spin-orbit coupling for third-row transition metals.[31]

The shift in formal potential for the redox couples correlates with the Gutamnn-Beckett acceptor number of the solvent, and by extension, the acceptor number of the borane. For $[Mn(CN)_6]^{3-}$, the potential shifts by 2.14 V anodically upon coordination of BCF, while for $(2,4,6\text{-}F_3C_6H_2)_3B$ the potential shifts about 1.1 V anodically. Per borane, this corresponds to approximately 350 mV per coordinated BCF (AN = 77.15 - 82)[32,33] and 180 mV per coordinated $(2,4,6\text{-}F_3C_6H_2)_3B$ (AN = 68.5).[34] **Figure 5.6** displays the scan rate dependence and Randles-Sevcik plots for $[Mn(CN\text{-}B(2,4,6\text{-}C_6F_3H_2)_3)_6]^{3-}$, which demonstrates the first example of a Mn(I) cyanometallate species that is only accessible as a result of boronation. **Figure 5.7** displays the scan rate dependence and Randles-Sevcik plots for $[Mn(CN\text{-}B(C_6F_5)_3)_6]^{3-}$. **Figure 5.8** displays the potential dependence and linear shift in potential for $[Mn(CN\text{-}B(C_6F_5)_3)_6]^{3-}$.

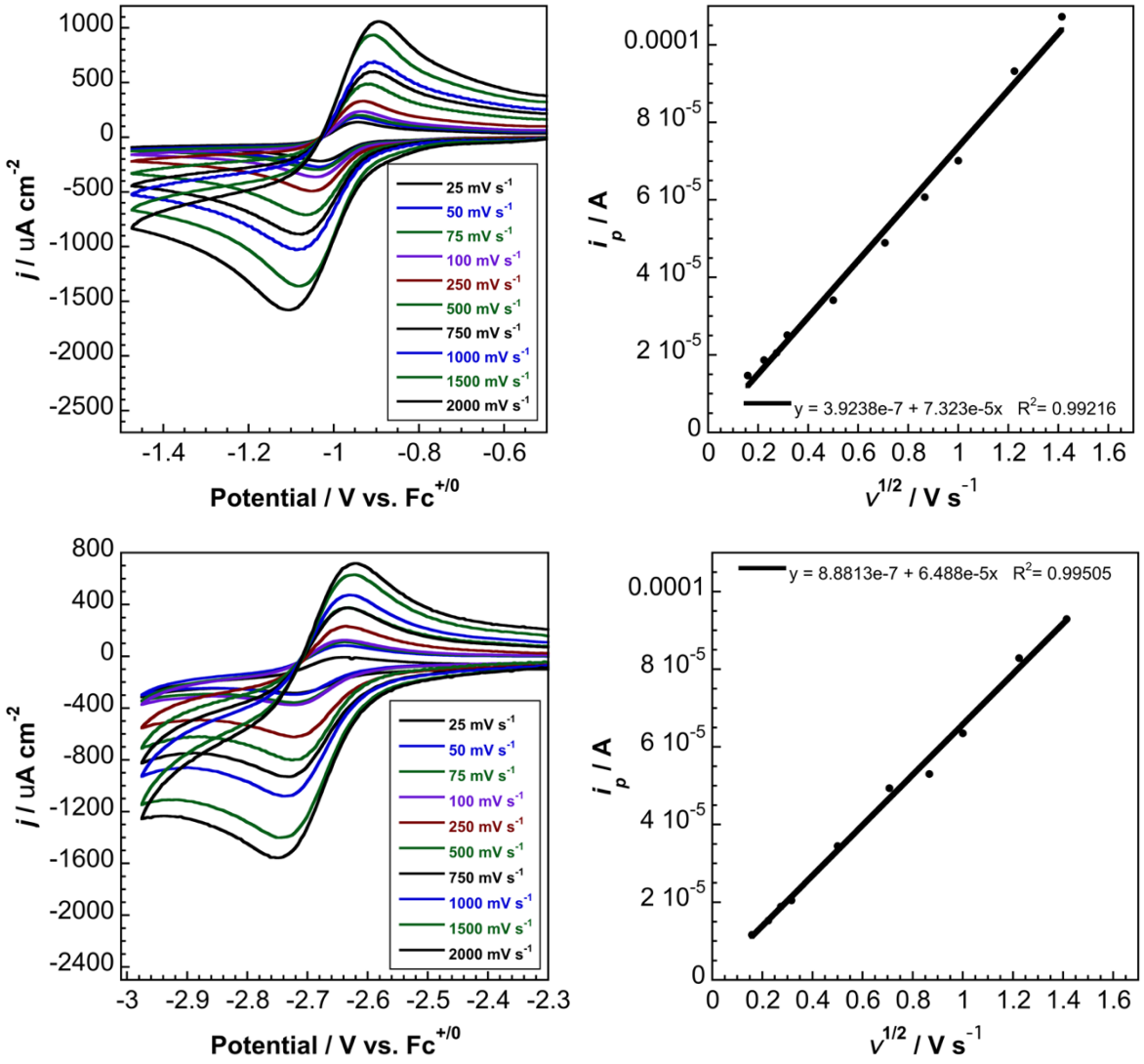

Figure 5.6. Scan rate dependence of $(TBA)_3[Mn(CN\text{-}B(C_6F_3H_2)_3)_6]$ in 0.2 M $TBAPF_6$ in THF. All potentials referenced to $Fc^{+/0}$. (**Upper**) $Mn^{III/II}$ redox couple. (**Lower**) $Mn^{II/I1}$ redox couple.

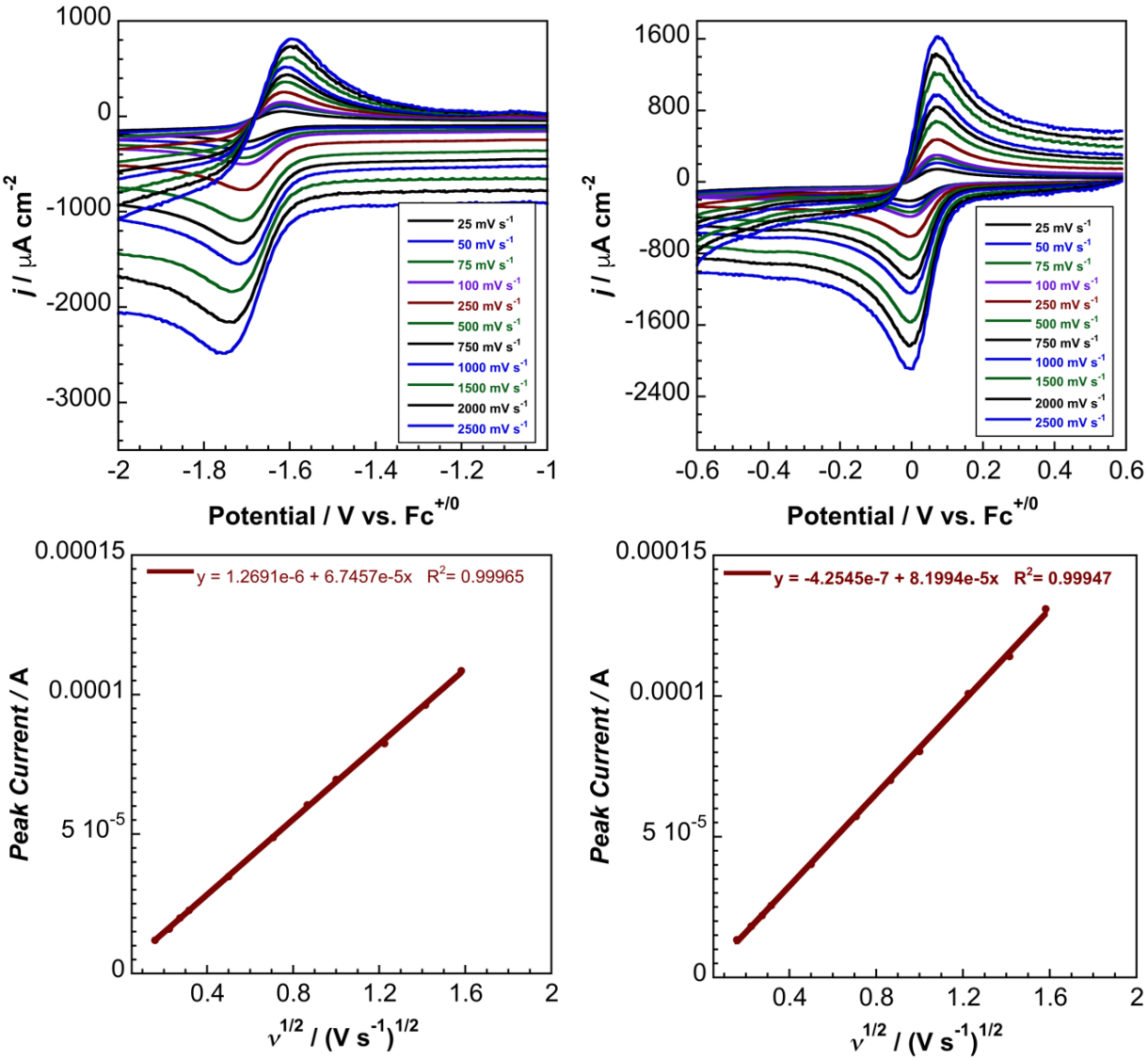

Figure 5.7. Scan rate dependence of $(TBA)_3[Mn(CN\text{-}B(C_6F_5)_3)_6]$ in 0.2 M $TBAPF_6$ in MeCN. All potentials referenced to $Fc^{+/0}$. (**Left**) $Mn^{II/I}$ redox couple. (**Right**) $Mn^{III/II}$ redox couple.

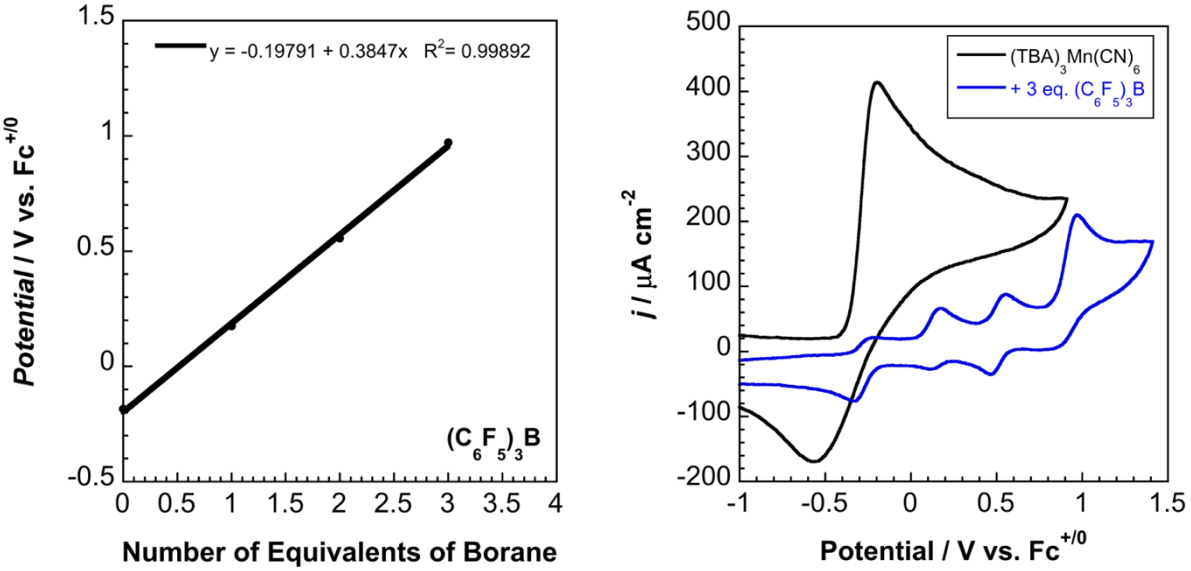

Figure 5.8. (**Left**) Linear shift in peak anodic potential per equivalent of $B(C_6F_5)_3$ added to $(TBA)_3[Mn(CN)_6]$. (**Right**) Voltammetry of $(TBA)_3[Mn(CN)_6]$ and $(TBA)_3[Mn(CN)_6]$ with three stoichiometric equivalents of $B(C_6F_5)_3$. All voltammetry taken in dichloromethane with 0.1 M $TBAPF_6$. All potentials referenced to $Fc^{+/0}$.

The peak current, i_p, of an electrochemically reversible electron transfer in homogeneous linear sweep voltammetry is given in **Equation 5.1**,

$$i_p = 0.4463n^{3/2}F^{3/2}AC_0^*\sqrt{\frac{D_0 v}{RT}} \tag{5.1}$$

where n is the number of electrons ($n = 1$ e^- for Fc oxidation and $CoCp_2^+$ reduction), D_0 is the diffusion coefficient of the electroactive species ($cm^2\ s^{-1}$), v is the scan rate ($V\ s^{-1}$), A is the electrode surface area ($A = 0.0707\ cm^2$) and C_0^* is the bulk concentration of analyte ($mol\ L^{-1}$). Randles-Sevcik plots of many of the boronated species and base complexes are linear, suggesting diffusion-controlled, electrochemically reversible electron transfers. However, the Randles-Sevcik equation does not provide conclusive evidence of electrochemical reversibility.

Given the anodic formal potentials for these species, peak current ratios were calculated using an empirical formula that deconvolutes the current at the reversal potential from the redox event, **Equation 5.2**,

$$\frac{i_{p,c}}{i_{p,a}} = \frac{i_{p,c,0}}{i_{p,a,0}} + \frac{i_{p,c,0}}{i_{sp}} + 0.0486 \tag{5.2}$$

where $i_{p,c}/i_{p,a}$ is the corrected peak current ratio, $i_{p,c,0}/i_{p,a,0}$ is the peak current ratio relative to zero current, and $i_{p,c,0}/i_{sp}$ is the ratio of the uncorrected peak cathodic current and the current at the switching potential.[35]

Peak-to-peak separations in cyclic voltammetry correlate with the heterogeneous rate constant of an outer-sphere electron transfer. All Group VIII complexes are highly electrochemically reversible, exhibiting faster electron transfer rates than their unboronated counterparts. The improved electron transfer rate likely stems from a decrease in outer-sphere reorganization energy upon boronation, spatially inhibiting solvent from interacting with the inner sphere. This phenomenon is quite evident from a space-filling model of each complex. Additionally, based on the changes in M-C-N bond lengths upon oxidation for bare and boronated species, the inner-sphere reorganization energy is likely comparable for bare and boronated species.

In addition to solubility and stability requirements, electron transfer reagents for non-aqueous redox flow batteries should have heterogeneous electron transfer rate constants greater than 10^{-5} cm s^{-1} and diffusion-controlled electron transfer behavior.[36] The standard rate constant k_0 is related to the dimensionless parameter ψ through **Equation 5.3**,

$$\psi = \frac{\left(\frac{D_0}{D_R}\right)^{\alpha/2} k_0}{\sqrt{\frac{D_0 \pi \nu n F}{RT}}} \quad (5.3)$$

where ψ is a dimensionless parameter, D_0 and D_R are the diffusion coefficients of the oxidized and reduced electroactive species ($cm^2\ s^{-1}$), ν is the scan rate ($V\ s^{-1}$), and α is the transfer coefficient for electron transfer. The rate constant can be derived from fitting values of ψ that are derived from a working curve and peak-to-peak separations. By interpolating the experimental working curve for ψ versus ΔE_p delineated by Nicholson and Shain, more exact values for ψ were obtained. As shown previously, these values are reliable for electron transfers with transfer coefficient values between 0.3 and 0.7. Diffusion coefficients for evaluation of kinetic parameters were obtained from either Randles-Sevcik plots or Cottrellian current decay fits. The Nicholson plots are displayed in **Figure 5.9**, and the heterogeneous charge transfer rate constants are given in **Table 5.6**. We observe more than an order of magnitude difference between $[Mn(CN\text{-}B(2,4,6\text{-}C_6F_3H)_3)_6]^{3-}$ and $[Mn(CN\text{-}B(C_6F_5)_3)_6]^{3-}$, possibly a result of decreased outer-sphere solvent reorganization for $[Mn(CN\text{-}B(C_6F_5)_3)_6]^{3-}$.

Table 5.6. Kinetic parameters derived from scan rate dependence voltammetry for boronated cyanometallates. k^0 derived from the Nicholson working curve assumes a transfer coefficient value of 0.5.

Species	k^0 (Nicholson) ($cm\ s^{-1}$)	k^0 (Literature) ($cm\ s^{-1}$)
$[Mn(CN\text{-}B(2,4,6\text{-}C_6F_3H)_3)_6]^{3/4-}$	0.0013	---
$[Mn(CN\text{-}B(2,4,6\text{-}C_6F_3H)_3)_6]^{4/5-}$	0.0041	---
$[Mn(CN\text{-}B(2,4,6\text{-}C_6F_3H)_3)_6]^{2/3-}$	Irreversible	---
$[Mn(CN\text{-}B(C_6F_5)_3)_6]^{3/4-}$[a]	0.085	---
$[Mn(CN\text{-}B(C_6F_5)_3)_6]^{4/5-}$	0.014	---
$[Mn(CN\text{-}B(C_6F_5)_3)_6]^{2/3-}$	Irreversible	---
$[Mn(CN)_6]^{3/4-}$	Irreversible	---
$[Fe(CN)_6]^{3/4-}$	0.017	0.023-0.100[ref]
$[Os(CN)_6]^{3/4-}$	0.014	---

[a]Derived from rotating disk voltammetry data

Based on the heterogeneous electron transfer rate constants derived from cyclic voltammetry, we can conclude that a wide variety of homoleptic cyanometallates will find use as electrochemically reversible redox couples for non-aqueous redox flow batteries. **Figure 5.10** and **Table 5.7**. display the scan rate dependence, Randles-Sevcik plot, and electrochemical parameters for $[Os(CN\text{-}B(C_6F_5)_3)_6]^{4-}$.

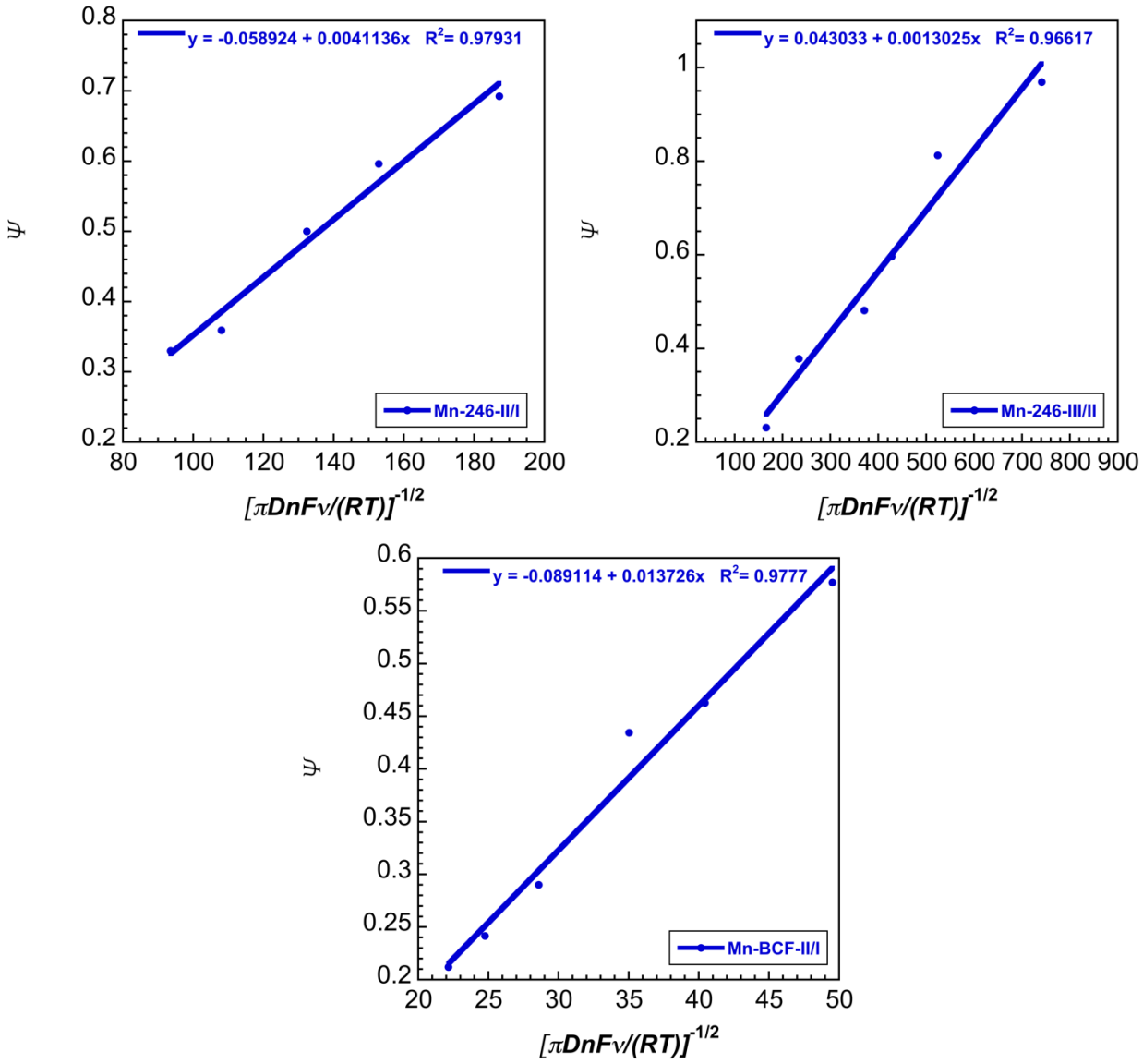

Figure 5.9. Nicholson plots for $[Mn(CN\text{-}B(2,4,6\text{-}C_6F_3H)_3)_6]^{3-}$ and $[Mn(CN\text{-}B(C_6F_5)_3)_6]^{3-}$.

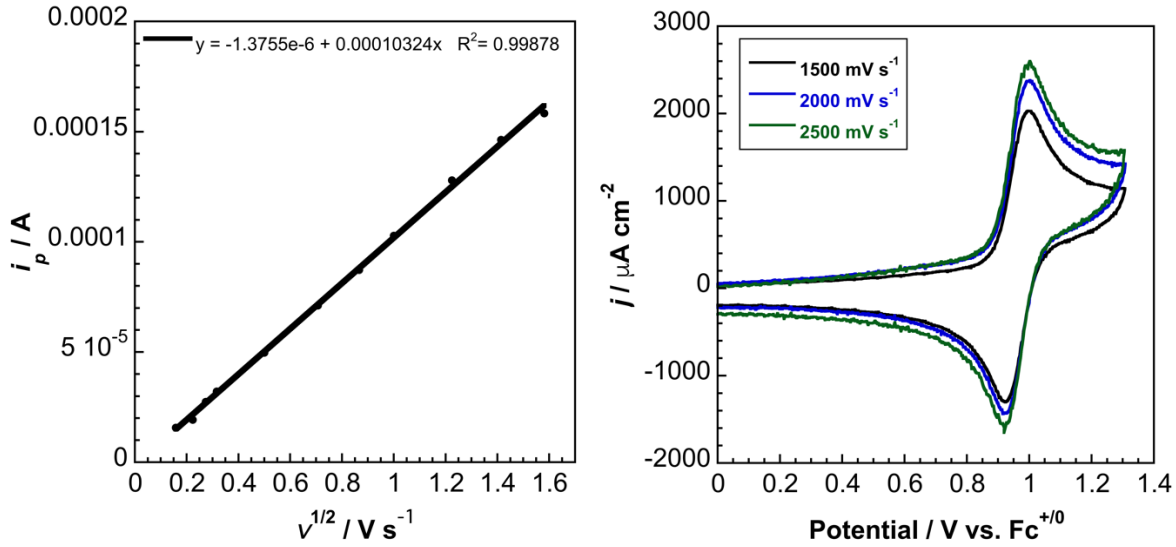

Figure 5.10. Fast scan rate data and Randles-Sevcik plot for the oxidation of 2.1 mM $[Os(CN\text{-}B(C_6F_5)_3)_6]^{4-}$ with 0.2 M $TBAPF_6$ in MeCN.

Table 5.7. Electrochemical parameters for 2.1 mM $[Os(CN\text{-}B(C_6F_5)_3)_6]^{4-}$ with 0.2 M $TBAPF_6$ in MeCN.

Scan Rate/Parameter	$i_{p,a}$	$i_{p,c}$	$i_{p,s}$	$E_{p,a}$	$E_{p,c}$	$i_{p,c}/i_{p,a}$	ΔE_p
25 mV s^{-1}	17.52 μA	−9.14 μA	11.19 μA	0.996 V	0.924 V	0.92	72.0 mV
50 mV s^{-1}	24.39 μA	−13.89 μA	14.31 μA	0.996 V	0.924 V	0.94	72.0 mV
75 mV s^{-1}	29.64 μA	−17.86 μA	16.64 μA	0.997 V	0.926 V	0.96	71.0 mV
100 mV s^{-1}	34.33 μA	−20.94 μA	21.30 μA	0.997 V	0.924 V	1.00	73.0 mV
250 mV s^{-1}	54.21 μA	−33.92 μA	29.23 μA	0.995 V	0.921 V	0.97	74.0 mV
500 mV s^{-1}	78.13 μA	−49.65 μA	42.12 μA	0.998 V	0.925 V	0.98	73.0 mV
750 mV s^{-1}	96.76 μA	−61.57 μA	51.98 μA	0.997 V	0.924 V	0.98	73.0 mV
1000 mV s^{-1}	112.00 μA	−71.70 μA	60.46 μA	0.995 V	0.922 V	0.99	73.0 mV
1500 mV s^{-1}	143.10 μA	−91.32 μA	80.67 μA	0.999 V	0.924 V	1.00	75.0 mV
2000 mV s^{-1}	167.60 μA	−101.50 μA	100.80 μA	0.998 V	0.923 V	0.98	75.0 mV
2500 mV s^{-1}	181.00 μA	−111.60 μA	113.40 μA	1.005 V	0.922 V	1.01	83.0 mV

Hexakisisocyanotris(pentafluorophenyl)boratoferrate(III/II) (1 and 4)

The UV-visible spectrum of $[Fe(CN)_6]^{3-}$ was first studied in detail in the early 1960s, with many orbital interpretations appearing based on SCF calculations, magnetic circular dichroism (MCD)

spectroscopy, magnetic optical rotary dispersion spectroscopy, and UV-vis spectroscopy.[1,37,38] In particular, the ordering of the ligand energy levels and thus the band assignments were of particular interest. The full low-energy spectrum of $[Fe(CN\text{-}B(C_6F_5)_3)_6]^{3-}$ in THF is presented in **Figure 5.11**. For **4**, the first electronic transition occurs at 18,830 cm^{-1}. This transition is dramatically red-shifted from the first transition in $(TBA)_3[Fe(CN)_6]$ in DCM, which is seen at 23,640 cm^{-1}. The lowest energy band in $(TBA)_3[Fe(CN)_6]$ has been previously assigned to a $t_{1u}(\sigma+\pi) \rightarrow t_{2g}(\pi)$ transition. We resisted the temptation of assigning the red-shifted band to the same electronic transition, instead obtaining room-temperature magnetic circular dichroism (MCD) spectroscopy of **4** to generate a more definitive assignment.

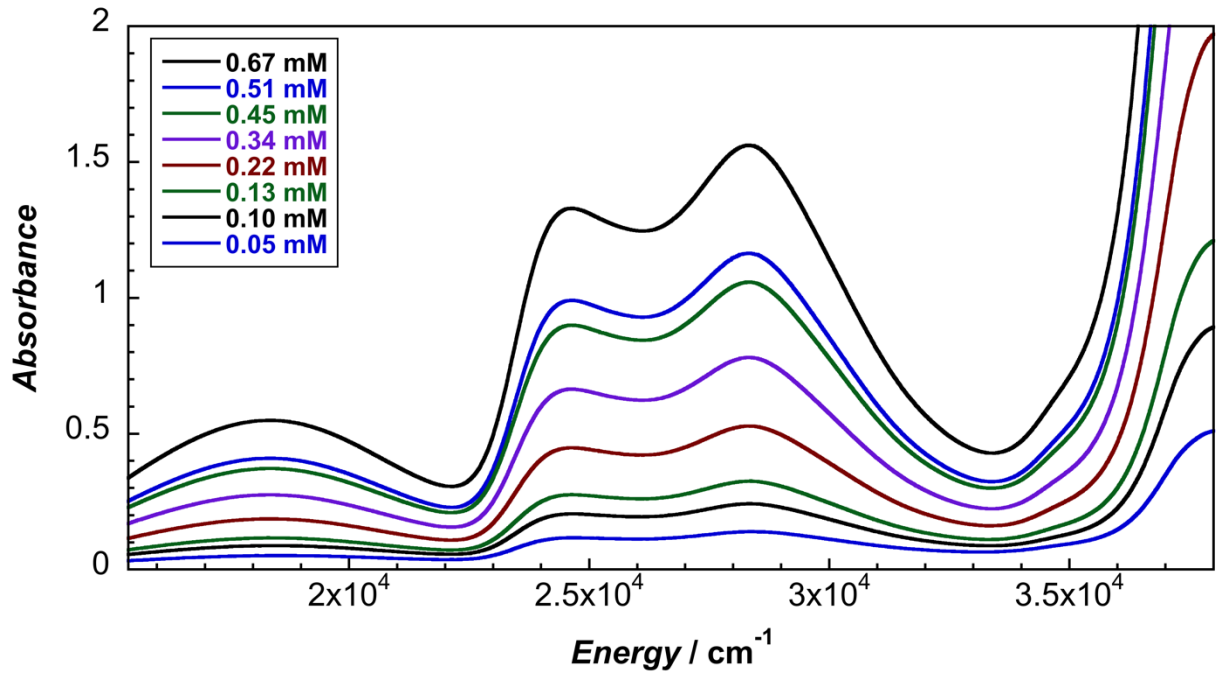

Figure 5.11. Absorption spectra for $[Fe(CN\text{-}B(C_6F_5)_3)_6]^{3-}$ in THF.

MCD spectroscopy uses a magnetic field oriented parallel to the direction of light to induce differential absorption of left circularly polarized and right circularly polarized light, a consequence

of the Faraday effect. The differential absorption of a sample due to a magnetic field **B** oriented in the direction of light propagation is given by **Equation 5.4**,

$$\Delta A = A_- - A_+ = \Delta\varepsilon_M clB \tag{5.4}$$

where $\Delta\varepsilon_M$ is the differential molar absorptivity per Tesla of applied magnetic field, **B**, c is the concentration, and l is the path length. Three different types of terms can contribute to the positive or negative intensity of an MCD band, A, B, and C terms.[39] A terms result from nondegenerate ground state transitions to degenerate excited states, which are different in energy as a result of Zeeman splitting.[39,40] A typical example of this MCD feature is seen in closed-shell cyanometallates and hexacarbonyl complexes, which exhibit singlet ground states with triply degenerate MLCT transitions.[40] B terms arise from mixing of two closely-spaced excited states, which result from the magnetic field. Both A and B terms are temperature independent. In contrast, C terms exhibit strong temperature dependence, and arise from a degenerate ground state that typically results from paramagnetism. Thus, most open shell cyanometallates will exhibit strong C terms. Usually, the experimental intensity varies with the inverse of temperature for C terms. The mechanism of intensity for different MCD bands is helpful in assigning the types of transitions observed in experimental spectra. Ferricyanide has been characterized by MCD in multiple studies, all of which debate the origin of intensity in the terms.[41,42]

MCD spectroscopy measures the differential absorption of a sample under circularly polarized light in the presence of a magnetic field. Three possible terms, *A*, *B*, and *C*, can contribute to the sign and magnitude of MCD profiles.[41] Numerous MCD studies have been performed on ferricyanide to elucidate the exact character of all transitions in its complex spectrum, and room-temperature and

low-temperature measurements[43,44,42] have demonstrated that the $[Fe(CN)_6]^{3-}$ spectrum is dominated by temperature-dependent *C* terms. The selection rules for *C* terms of orbitally-allowed LMCT transitions from a $^2T_{2g}$ ground state (neglecting spin-orbit coupling) are given by **Equation 5.5**,[39]

$$C_0(T_{2g} \rightarrow T_{1u}) = -1/9\sqrt{6}\,\langle T_{2g} \parallel L_z^{t_{1g}} \parallel T_{2g}\rangle\langle T_{2g} \parallel m^{t_{1u}} \parallel T_{1u}\rangle$$
$$C_0(T_{2g} \rightarrow T_{2u}) = +1/9\sqrt{6}\,\langle T_{2g} \parallel L_z^{t_{1g}} \parallel T_{2g}\rangle\langle T_{2g} \parallel m^{t_{1u}} \parallel T_{2u}\rangle \quad (5.5)$$

which results in values of $\frac{C_0}{D_0}$ of $+1$ for $T_{2g} \rightarrow T_{1u}$ and -1 for $T_{2g} \rightarrow T_{2u}$, where D_0 is the dipole strength of a given transition. Experimentally, this translates to a negative differential absorbance band for $T_{2g} \rightarrow T_{2u}$ and a positive differential absorbance band for $T_{2g} \rightarrow T_{1u}$. Armed with this information, we are able to interpret the UV-vis and MCD spectroscopy acquired for **4**.

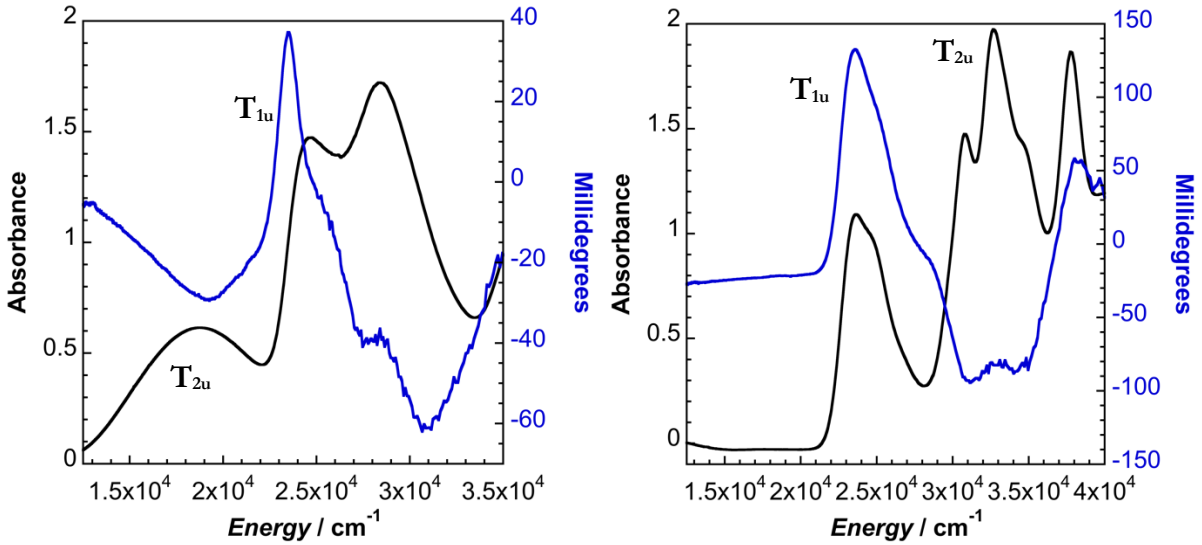

Figure 5.12. Room temperature UV-visible absorption spectrum (black) and magnetic circular dichroism (blue) spectroscopy of $[Fe(CN\text{-}B(C_6F_5)_3)_6]^{3-}$ (**4**) (Left) and $[Fe(CN)_6]^{3-}$. **4** acquired in neat tetrahydrofuran, and $[Fe(CN)_6]^{3-}$ acquired in MeCN.

As shown in **Figure 5.12**, the MCD responses for **4** and bare $Fe(CN)_6^{3-}$ are quite different. In bare ferricyanide, three peaks are evident in the UV-vis absorbance spectrum in the range 30,000-35,000

cm^{-1}, where the middle peak corresponds to the negative MCD response of the $t_{2u} \rightarrow t_{2g}$ transition. In contrast, the MCD response for **4** displays a prominent negative differential absorption peak at 18,830 cm^{-1}. Given the absence of this transition in the base complex and the same sign as that in bare ferricyanide, we ascribe this peak to the $^2T_{2g} \rightarrow {}^2T_{2u}$ transition for boronated ferricyanide.[45] The shift in this transition is approximately 1.8 eV, which is relatively close to the shift in formal potential for boronation of $[Fe(CN)_6]^{3-}$.

To obtain further insight into electronic assignments for $[Fe(CN\text{-}B(C_6F_5)_3)_6]^{3-}$, 16.7 K absorbance of the compound in a poly(methyl methacrylate) film (23.1 mM) was obtained, shown in **Figure 5.13**. Fortunately, we observed a well-defined vibrational progression for the first LMCT transition. The average separation among vibronic transitions is 2050 cm^{-1}, which is the CN stretching frequency in the LMCT excited state. This value is consistent with weakening of CN bonding and supports assignment of this band as the $t_{2u} \rightarrow t_{2g}$ transition (ν(CN)) for $[Fe(CN\text{-}B(C_6F_5)_3)_6]^{3-}$ is 2228 cm^{-1}).

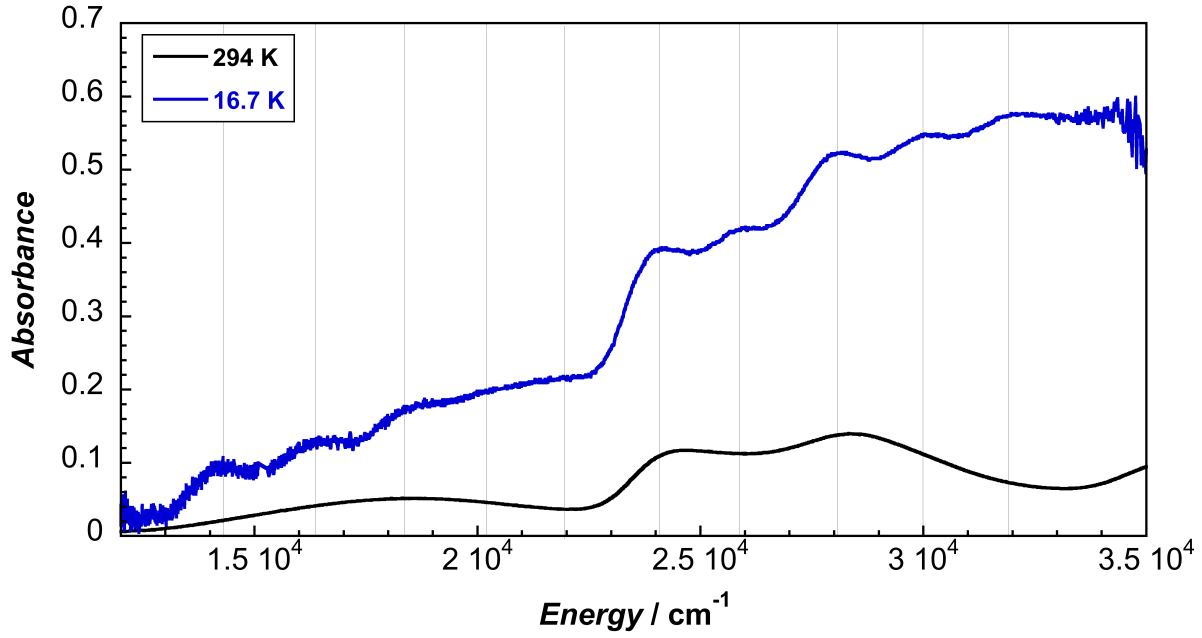

Figure 5.13. Absorption spectra for $[Fe(CN\text{-}B(C_6F_5)_3)_6]^{3-}$ at room temperature (solution-phase in THF) and at 16.7 K (23.1 mM, solid-state in poly(methyl methacrylate).

Additional transitions are resolved from the low temperature spectrum, including likely forbidden LMCT transitions centered at 26,000 cm^{-1}, 30,000 cm^{-1}, and 35,000 cm^{-1}, which are assigned to the $a_{1g} \rightarrow t_{2g}$, $t_{1g} \rightarrow t_{2g}$ and $e_g \rightarrow t_{2g}$ transitions, respectively. Alternatively, the band at 35,000 cm^{-1} could be ascribed to the $t_{2g} \rightarrow e_g$ ligand field transition. However, the extinction coefficient and presence of an identical band in $[Os(CN\text{-}B(C_6F_5)_3)_6]^{3-}$ supports assignment as a forbidden LMCT transition. Assignments for the various LMCT transitions observed in **4** are tabulated in **Table 5.8**.

Table 5.8. Electronic and vibrationally-coupled transitions observed for $[Fe(CN\text{-}B(C_6F_5)_3)_6]^{3-}$ in a PMMA film cast from THF at 16.7 K.

λ (nm)	$\tilde{\nu}$ (cm^{-1})	Type	Assignment	Transition
699	14,300	LMCT	$^2T_{2g} \rightarrow {}^2T_{2u}$	$t_{2u}\,\pi \rightarrow t_{2g}\,\pi$
614	16,300	LMCT	$^2T_{2g} \rightarrow {}^2T_{2u}$	$t_{2u}\,\pi \rightarrow t_{2g}\,\pi$
544	18,400	LMCT	$^2T_{2g} \rightarrow {}^2T_{2u}$	$t_{2u}\,\pi \rightarrow t_{2g}\,\pi$
417	24,000	LMCT	$^2T_{2g} \rightarrow {}^2T_{1u}$	$t_{1u}\,(\sigma+\pi) \rightarrow t_{2g}\,\pi$
388	25,770	LMCT	$^2T_{2g} \rightarrow {}^2A_{1g}$	$a_{1g}\,\sigma \rightarrow t_{2g}\,\pi$
356	28,100	LMCT	$^2T_{2g} \rightarrow {}^2A_{2g}, {}^2T_{1g}$	$t_{1g}\,\pi \rightarrow t_{2g}\,\pi$
336	30,100	LMCT	$^2T_{2g} \rightarrow {}^2A_{2g}, {}^2T_{1g}$	$t_{1g}\,\pi \rightarrow t_{2g}\,\pi$
313	32,000	LMCT	$^2T_{2g} \rightarrow {}^2A_{2g}, {}^2T_{1g}$	$t_{1g}\,\pi \rightarrow t_{2g}\,\pi$
286	35,000[a]	LMCT (d-d?)	$^2T_{2g} \rightarrow {}^2E_g$	$e_g\,\sigma \rightarrow t_{2g}\,\pi$

[a]Obtained from room temperature UV-visible Gaussian deconvolution

Based on the various spectroscopic data collected for **4**, we are capable of deriving a relative energy level diagram for the effects of boronation. The one-electron molecular orbital energy level diagram is shown in **Figure 5.14**. The formal potential of the $[Fe(CN\text{-}B(C_6F_5)_3)_6]^{3-/4-}$ redox couple was used to set the zero point of energy at the $t_{2g}(\pi)$ level. UV-vis spectroscopy of **1** and **4** provided the separation

of the $t_{2g}(\pi)$ and $e_g(\sigma^*)$ energy levels, with the energy corrected for electron-electron repulsion. The ligand field energy for the $^1A_{1g} \rightarrow {}^1T_{1g}$ transition is approximated by **Equation 5.6**,

$$E_{A_{1g} \rightarrow T_{1g}} = \Delta_o - C \tag{5.6}$$

where Δ_o is the octahedral splitting energy and C is an interelectronic repulsion parameter. MCD and low temperature spectroscopy support assignments, and MLCT transition energies were obtained from Gaussian deconvolution. The transition energy decreases by nearly 0.5 eV less than the $t_{2g}(\pi)$ level, likely due to the greater strengthening of boronation on π backdonation relative to the decrease in σ donation.

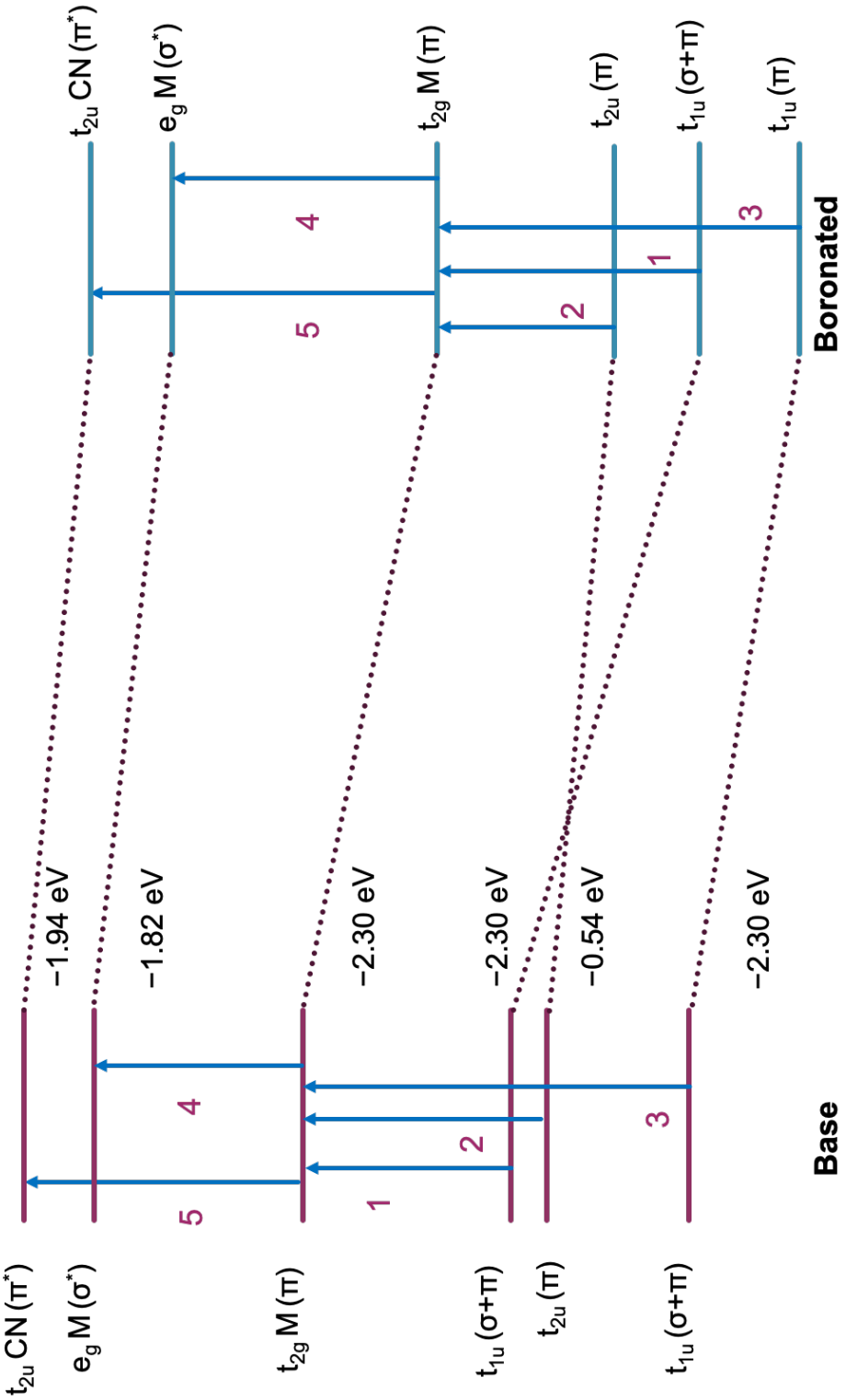

Figure 5.14. One-electron molecular orbital energy level diagram for $[Fe(CN)_6]^{3/4-}$ and $[Fe(CN\text{-}B(C_6F_5)_3)_6]^{3/4-}$.

Hexakisisocyanotris(pentafluorophenyl)boratoruthenate(III/II) (2 and 5)

Previous studies have shown that both the Ru(II) and Ru(III) oxidation states of hexacyanoruthenate are luminescent.[46] Based on emission maximum and lifetime measurements, previous studies have assigned the luminescence in Ru(III) to a rare LMCT fluorescence. Unsurprisingly, this emission is absent in both Fe(III) (lower energy ligand field states and a low-lying $^6A_1$ state) and Os(III) (higher energy LMCTs) analogues as a result of internal quenching by ligand field states.[47]

To provide further evidence of the identity of this emission, we recorded the powder emission spectrum of the TBA salt of **5** at 13.6 K after excitation with a 355 nm Nd:YAG laser. The emission maximum occurs at λ_{em} = 12,280 cm^{-1}, and a second emission line, presumably resulting from vibronic coupling, occurs at λ = 12,030 cm^{-1}. The peak spacing suggests vibronic coupling to a ligand bending mode of the complex. The dramatic red shift in this band relative to $[Ru(CN)_6]^{3-}$ (λ_{max} = 19,050 cm^{-1} at 77 K in EtOH)[46] is consistent with the red shift in the $^2T_{2g} \rightarrow {}^2T_{2u}$ transition, further supporting the assignment of this band as a LMCT emission. However, the dramatic reduction in FWHM for this band is concerning, necessitating us to confirm that this emission in fact originates from **5**.

In contrast, the only possible luminescence that can occur for **2** is from either MLCT or ligand field transitions. Emission of $[Ru(CN)_6]^{4-}$ was first reported in 1969, where a broad band at 22,650 cm^{-1} was observed as a result of excitation of a single crystal by a mercury arc lamp at 77 K.[48] These studies demonstrated that excitation at energies lower than the first spin-forbidden band result in no luminescence from the complex and that the lifetime of the emission is about 32 ms, leading the author to conclude that the band results from $^3T_{1g} \rightarrow {}^1A_{1g}$ phosphorescence. For **2**, excitation by

energies red of 366 nm do not result in emission, consistent with a blue-shifted $^3T_{1g}$ state relative to the base complex. The solid-state emission spectrum of **2** is shown in **Figure 5.15**.

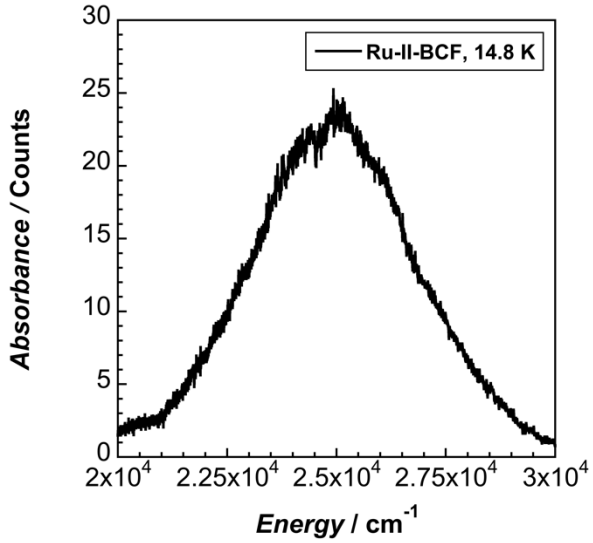

Figure 5.15. (**Left**) Corrected solid-state emission spectrum of $(TBA)_4[Ru(CN\text{-}B(C_6F_5)_3)_6]$ (**2**). The emission response was corrected by obtaining the spectral response as a function of wavelength using a standard lamp. (**Right**)

However, using 266 nm laser light, we observe a broad emission band centered at 24,930 cm^{-1}, a blue-shift of 2,300 cm^{-1} relative to the base complex. The magnitude of this shift is unsurprising, considering that the energy shift for the $^1A_{1g} \rightarrow {}^1T_{1g}$ ligand field transition in **1** is 2,400 cm^{-1} (based on Gaussian fitting, the maximum of $^1A_{1g} \rightarrow {}^1T_{1g}$ for **1** is 29,060 cm^{-1}). This shift suggests that boronation exerts a constant increase in ligand field strength, regardless of the identity of the metal center. We measured the lifetime of this emission at both 13.6 K in the solid state and at 77 K in a butyronitrile glass. As expected, the solid-state lifetime is significantly greater than the glass lifetime. In both cases, however, the lifetime is considerably shorter than that for $[Ru(CN)_6]^{4-}$ in 1:1:1 H_2O:MeOH:EtOH.[48] This is in contrast to the lifetime lengthening observed for **7**, which is consistent with the decrease in

non-radiative decay pathways associated with solvent interactions.[49] We are unsure of the discrepancy in lifetimes for this species.

Table 5.9. Electronic transitions observed for $[Ru(CN\text{-}B(C_6F_5)_3)_6]^{3-}$ in DCM at room temperature.

λ (nm)	$\tilde{\nu}$ (cm^{-1})	Type	Assignment	Transition
689	14,510	LMCT	$^2T_{2g} \rightarrow {}^2T_{2u}$	$t_{2u}\,\pi \rightarrow t_{2g}\,\pi$
451	22,170	LMCT	$^2T_{2g} \rightarrow {}^2T_{1u}$	$t_{1u}\,(\sigma+\pi) \rightarrow t_{2g}\,\pi$
401	24,950	LMCT	$^2T_{2g} \rightarrow {}^2A_{1g}$	$a_{1g}\,\sigma \rightarrow t_{2g}\,\pi$
333	30,000	LMCT	$^2T_{2g} \rightarrow {}^2A_{2g}, {}^2T_{1g}$	$t_{1g}\,\pi \rightarrow t_{2g}\,\pi$
312	32,500	LMCT	$^2T_{2g} \rightarrow {}^2E_g$	$e_g\,\sigma \rightarrow t_{2g}\,\pi$

Compared to $[Fe(CN)_6]^{3-}$, little research on $[Ru(CN)_6]^{3-}$ exists in the literature, a result of heavy debate on how to purify and properly synthesize the compound to avoid hydrolysis of the Ru(III) product. Initial attempts to oxidize $[Ru(CN)_6]^{4-}$ in the presence of various counter-cations occurred in 1951, with the UV-visible absorption spectrum possessing striking similarity to that of $[Fe(CN)_6]^{3-}$.[50] No attempts were made at assignment of bands. The first example of a well-established protocol for synthesis of $(TBA)_3[Ru(CN)_6]$ was reported in 1990.[8] A few years later, the magnetic circular dichroism of Os(III) and Ru(III) demonstrated similar band profiles as those observed for $[Fe(CN)_6]^{3-}$.

Table 5.9 presents transition assignments for $[Ru(CN\text{-}B(C_6F_5)_3)_6]^{3-}$. The assignments for bands in the boronated species are entirely consistent with those observed for $[Fe(CN\text{-}B(C_6F_5)_3)_6]^{3-}$. The band structure observed for $[Ru(CN\text{-}B(C_6F_5)_3)_6]^{3-}$ is quite similar to that for $[Fe(CN\text{-}B(C_6F_5)_3)_6]^{3-}$, allowing us to confidently assign these transitions based on data for $[Fe(CN\text{-}B(C_6F_5)_3)_6]^{3-}$. However, we note that the assignment of $^2T_{2g} \rightarrow {}^2A_{1g}$ is tentative due to our lack of low-temperature data for this species.

Hexakisisocyanotris(pentafluorophenyl)boratoosmate(III/II) (3 and 6)

Similarly to $[Ru(CN\text{-}B(C_6F_5)_3)_6]^{4-}$, $[Os(CN)_6]^{4-}$ has been shown to luminesce from a triplet ligand field state.[48] Emission of $[Os(CN)_6]^{4-}$ was first reported in 1969, where a broad band at 20,900 cm^{-1} was observed as a result of excitation of a single crystal by a mercury arc lamp at 77 K.[48] Analogous to **2**, a blue shift of the $^3T_{1g} \rightarrow {}^1A_{1g}$ emission band to 24,860 cm^{-1}, nearly 4,000 cm^{-1}, was observed. The spectrum is depicted in **Figure 5.16**. As we carried out for **2**, we still need to obtain the phosphorescence decay time at both 77 K in frozen solution and at <20 K; however, it will be interesting to see if this isoelectronic species exhibits a similar shortening in decay time compared to the base complex. In addition to the phosphorescence of **3**, we were hopeful that redshifting the lowest ligand to metal charge transfer of **6** would result in fluorescence. However, we were unable to observe any emission from **6** down to 13.0 K.

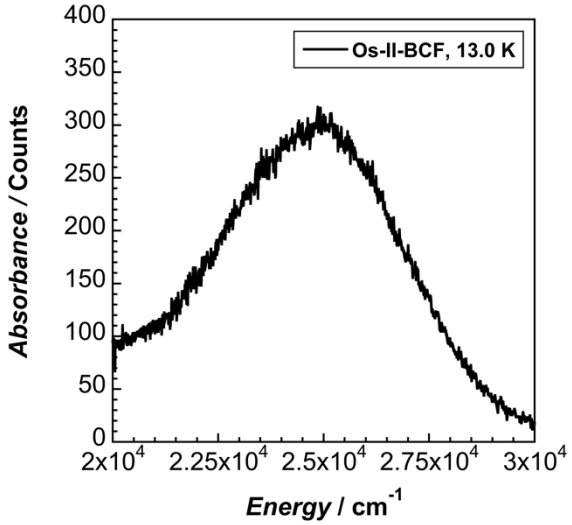

Figure 5.16. (Left) Corrected solid-state emission spectrum of $(TBA)_4[Os(CN\text{-}B(C_6F_5)_3)_6]$ (**3**). The emission response was corrected by obtaining the spectral response as a function of wavelength using a standard lamp. (Right)

Ambient and Low Temperature UV-visible and MCD Spectroscopy

The room- and low-temperature UV-vis absorption spectra of **6**, shown in **Figures 5.17** and **5.18**, are analogous to those observed for **4**. However, no vibronic coupling was observed for low-temperature absorbance. The lowest energy transition is ascribed to a $^2T_{2g} \rightarrow {}^2T_{2u}$ transition. We also obtained a room temperature MCD spectrum of **6** (**Figure 5.19**). However, the $^2T_{2g} \rightarrow {}^2T_{2u}$ transition does not give any appreciable intensity, consistent with the strong temperature dependence of *C* terms. Previous studies have shown the minimal intensity of C terms for Os(III) and Ru(III) at elevated temperatures.[47] The other differential maxima are nearly identical to those for $[Fe(CN\text{-}B(C_6F_5)_3)_6]^{3-}$, specifically absence of the higher energy t_{2u} transition.[47] Given the assignments in **4**, these results are consistent with assignment of the lowest-energy band to the $^2T_{2g} \rightarrow {}^2T_{2u}$ transition. Despite the increased spin-orbit coupling for 3rd row transition metals, which should necessitate the use of double groups for assignment of electronic transitions, the striking similarity in electronic transitions across all three Group VIII species supports our assignment of each band to similar transitions in all three complexes.

Similarly to $[Fe(CN\text{-}B(C_6F_5)_3)_6]^{3-}$, a number of allowed and forbidden LMCT transitions are resolved from the room- and low-temperature spectra for $[Os(CN\text{-}B(C_6F_5)_3)_6]^{3-}$. Forbidden LMCT transitions are likely centered at 26,000 cm^{-1}, 28,200 cm^{-1}, and 34,360 cm^{-1}, which are assigned to the $a_{1g} \rightarrow t_{2g}$, $t_{1g} \rightarrow t_{2g}$ and $e_g \rightarrow t_{2g}$ transitions, respectively. Assignments for the various LMCT transitions observed in $[Os(CN\text{-}B(C_6F_5)_3)_6]^{3-}$ are tabulated in **Table 5.10**. The increased number of bands observed in the low energy region of the spectrum is consistent with the increased spin-orbit coupling,

with small splitting of some LMCT transitions likely resulting from the SO coupling and high delocalization of the Os metal center with the ligands.

Table 5.10. Gaussian deconvolution of the ligand-to-metal charge transfer transitions in $[Os(CN\text{-}B(C_6F_5)_3)_6]^{3-}$. Spectra obtained at room temperature in DCM.

λ (nm)	$\tilde{\nu}$ (cm^{-1})	Type	Assignment	Transition
589	16,970	LMCT	$^{2r}T_{2g} \rightarrow {}^{2r}T_{2u}$	$t_{2u}\,\pi \rightarrow t_{2g}\,\pi$
420	23,830	LMCT	$^{2r}T_{2g} \rightarrow {}^{2r}T_{1u}$	$t_{1u}\,(\sigma+\pi) \rightarrow t_{2g}\,\pi$
408	24,490	LMCT	$^{2r}T_{2g} \rightarrow {}^{2r}T_{1u}$	$t_{1u}\,(\sigma+\pi) \rightarrow t_{2g}\,\pi$
377	26,500	LMCT	$^{2r}T_{2g} \rightarrow {}^{2}A_{1g}$	$a_{1g}\,\pi \rightarrow t_{2g}\,\pi$
357	28,050	LMCT	$^{2r}T_{2g} \rightarrow {}^{2}A_{2g}, {}^{2r}T_{1g}$	$t_{1g}\,\pi \rightarrow t_{2g}\,\pi$
350	28,570	LMCT	$^{2r}T_{2g} \rightarrow {}^{2}A_{2g}, {}^{2r}T_{1g}$	$t_{1g}\,\pi \rightarrow t_{2g}\,\pi$
291	34,360	LMCT	$^{2r}T_{2g} \rightarrow {}^{2}E_{g}$	$e_{g}\,\sigma \rightarrow t_{2g}\,\pi$

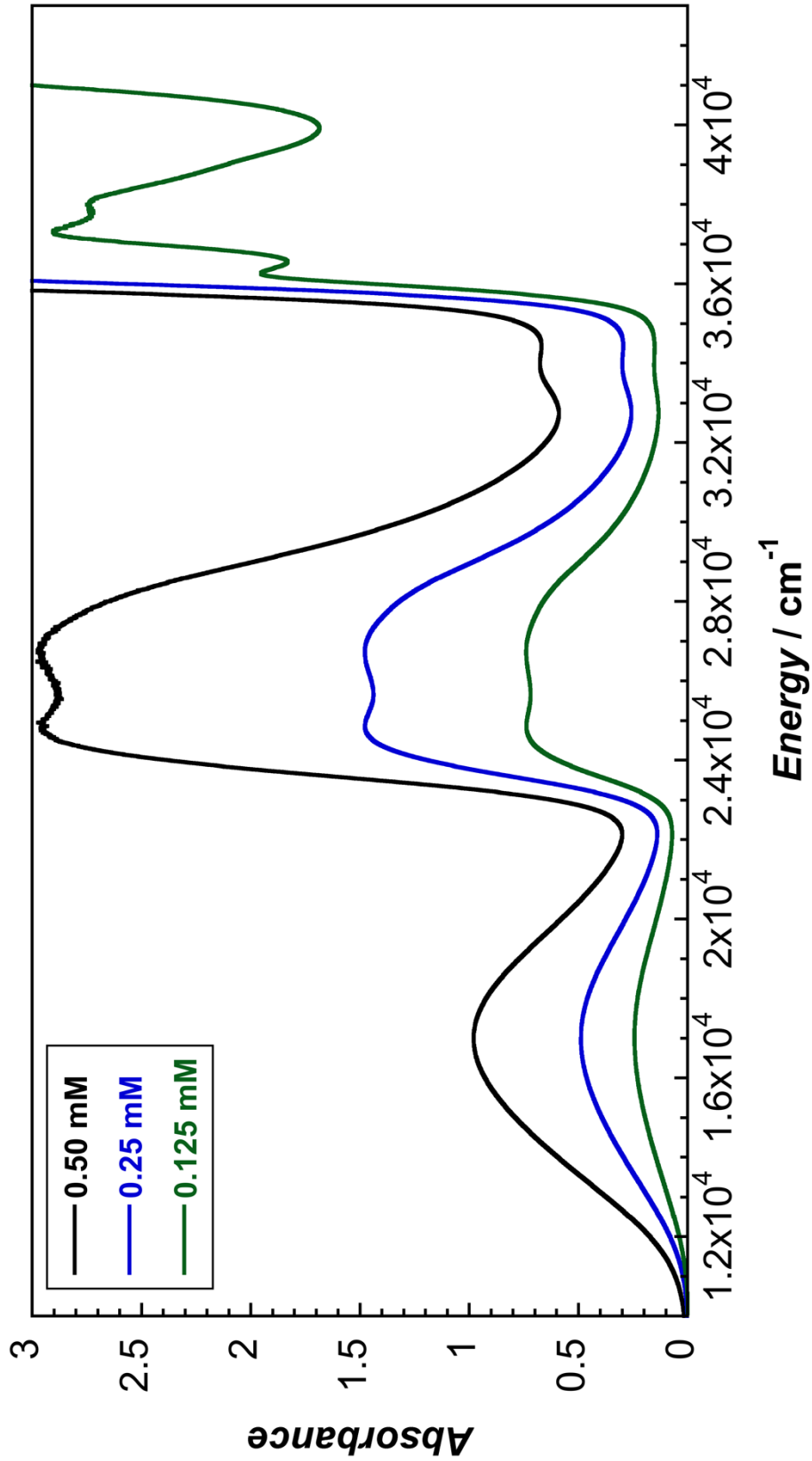

Figure 5.17. UV-visisble absorption spectrum of $(Ph_4P)_3[Os(CN\text{-}B(C_6F)_3)]$ in DCM.

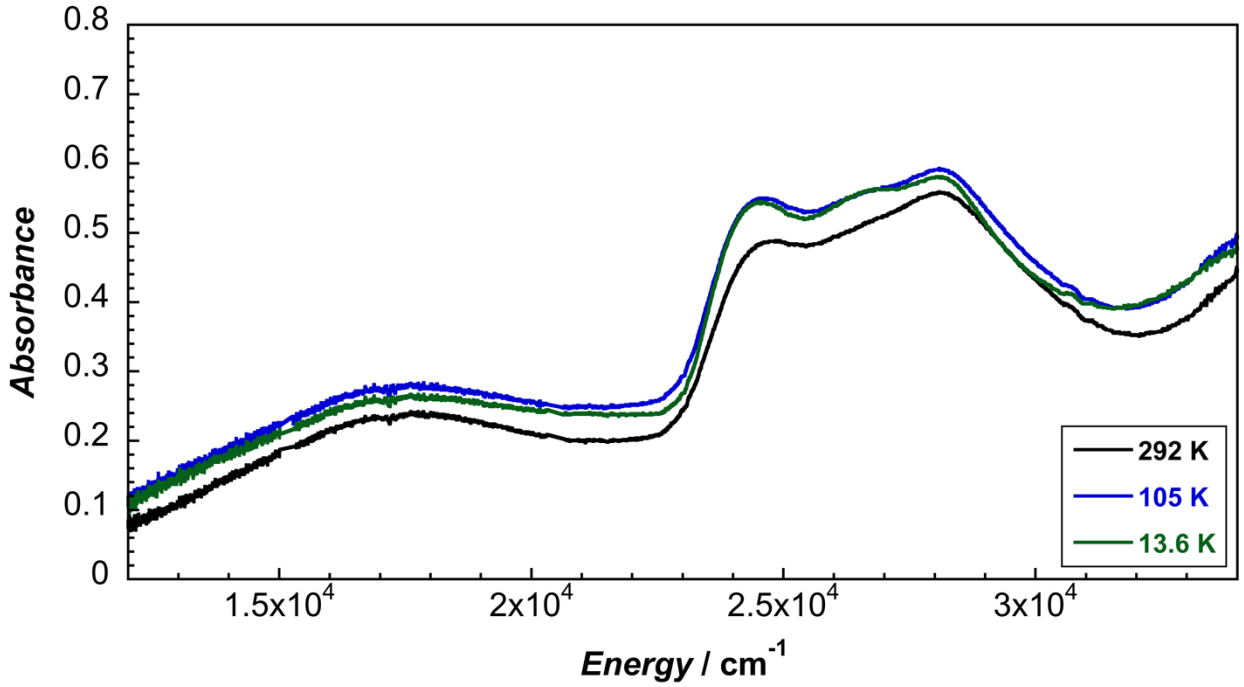

Figure 5.18. Variable temperature UV-vis spectrum of $(PPh_4)_3[Os(CN\text{-}B(C_6F_5)_3]$ in a PMMA film.

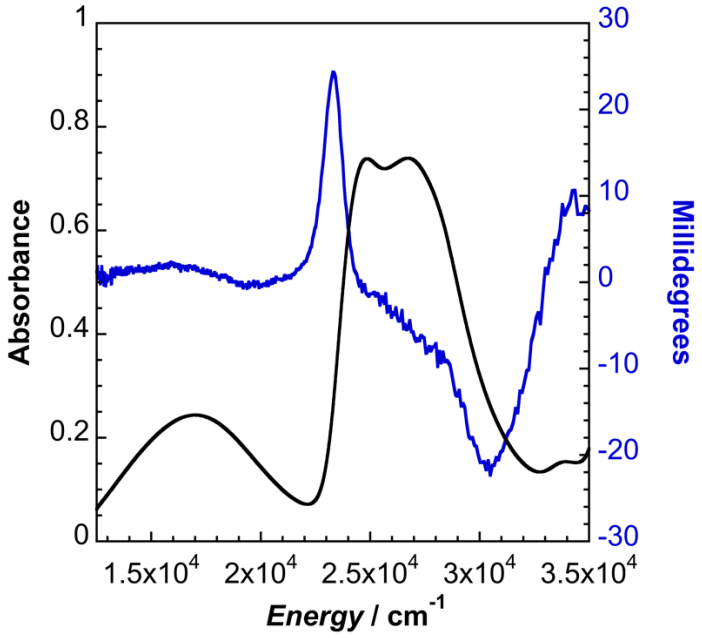

Figure 5.19. Room temperature magnetic circular dichroism spectroscopy of $[Os(CN\text{-}B(C_6F_5)_3)_6]^{3-}$ in dichloromethane.

One particularly unique feature of the electronic structure of Os(III) complexes is the intraconfigurational transitions observed in the NIR energy region of the spectrum. These transitions result from large spin-orbit coupling constants for third-row transition metals. The transitions observed in heavy metal complexes are best described using double groups. For Os(III), the octahedral $^{2r}T_{2g}$ state will split into Γ_7 and Γ_8 under the action of spin-orbit coupling, resulting in intraconfigurational (IC) $\Gamma_7 \rightarrow \Gamma_8$ transitions in the NIR region of the spectrum. Spectra were acquired in deuterated dichloromethane to minimize absorbance contributions from solvent vibrational overtones. A NIR spectrum of 60 mM tetraphenylphosphonium chloride showed no measurable absorbance in the NIR region of the spectrum. The $\Gamma_7 \rightarrow \Gamma_8$ transition of **6** is given in **Figure 5.20**. The spectrum is consistent with previous ligand field analysis.

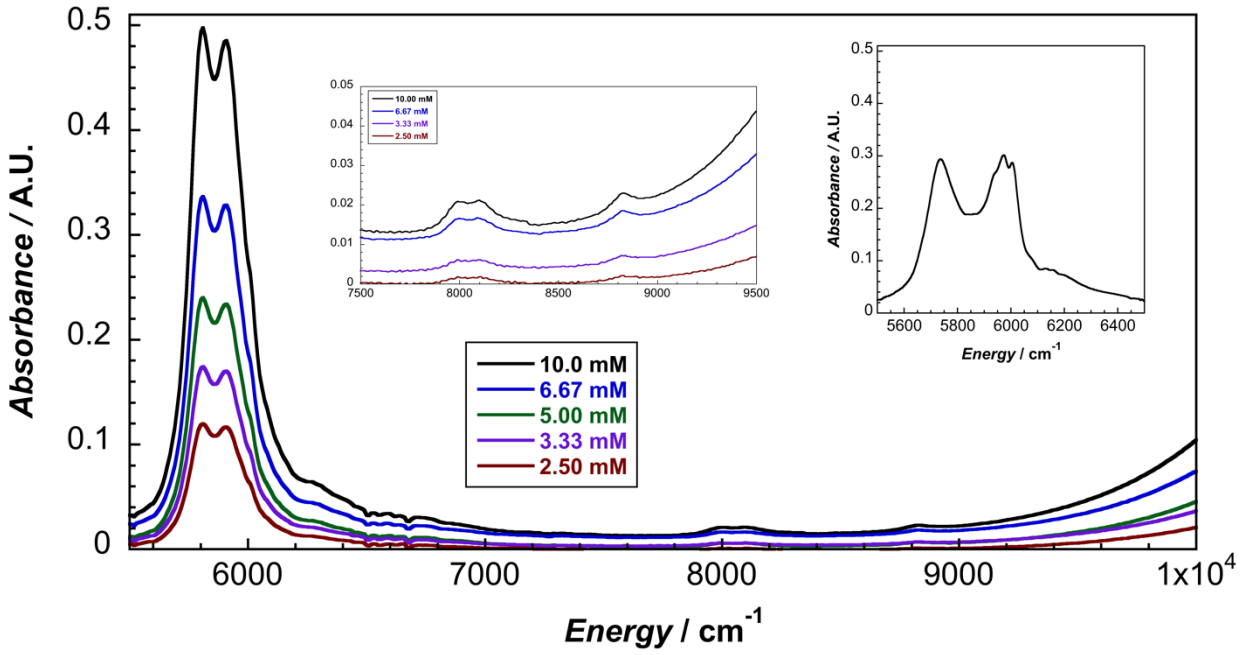

Figure 5.20. Near infrared spectrum of $(PPh_4)_3[Os(CN\text{-}B(C_6F_5)_3)_6]$ in CD_2Cl_2. (**Left Inset**) False origins stemming from vibronic coupling to a cyanide stretching mode. (**Right Inset**) NIR spectrum for $(PPh_4)_3[Os(CN)_6]$ in CD_2Cl_2.

IC transitions can also couple to asymmetric vibrational modes of the complex to produce false origins. The unresolved fine structure appearing on the high energy side of the NIR transition likely corresponds to a number of false origins due to vibronic coupling.[51] We also observe a NIR absorbance centered at 8,060 cm^{-1}, which is 2,210 cm^{-1} higher in energy than the center of the IC band. The coupled bands at higher energy peak at 7,990 cm^{-1} and 8,100 cm^{-1}. This energy difference (2190 cm^{-1}) is consistent with vibronic coupling to the stretching mode of the isocyanoborate ligand, which occurs at 2,204 cm^{-1}.

We also measured the NIR absorbance spectrum of $[Os(CN)_6]^{3-}$ in DCM and obtained a NIR spectrum that is consistent with previous studies. The two IC transitions for the base complex are separated by a greater value than those in **6**, suggesting a greater tetragonal distortion for $[Os(CN)_6]^{3-}$ (224 cm^{-1}) relative to **6** (100 cm^{-1}).[9] These results are summarized in **Figure 5.21**.

$[Os(CN\text{-}B(C_6F_5)_3)_6]^{3-}$	$[Os(CN)_6]^{3-}$
5810	5750
5910	5974
7990	7810
8100	7990

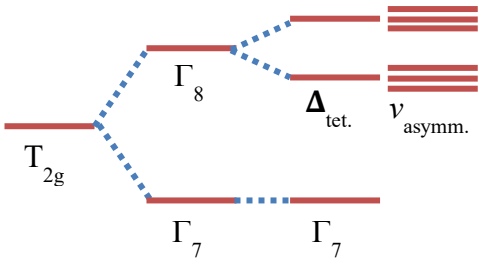

Figure 5.21. (**Left**) Intraconfigurational transitions observed for $[Os(CN\text{-}B(C_6F_5)_3)_6]^{3-}$ and $[Os(CN)_6]^{3-}$ in CD_2Cl_2. (**Right**) Splitting of the $^2T_{2g}$ ground state of $(Ph_4P)_3[Os(CN\text{-}B(C_6F_5)_3)_6]$ under the action of spin orbit coupling and additional transitions possible as a result of tetragonal distortion and vibronic coupling.

Hexakisisocyanotris(pentafluorophenyl)boratochromate(III) (7/10/11)

The lowest observable transition for $[Cr(CN)_6]^{3-}$ is a spin-forbidden band that has been previously assigned to the $^4A_{2g} \rightarrow {}^2T_{2g}(G)$ transition. A 10.0 mM spectrum of **7**, shown in **Figure 5.22**, is consistent with this interpretation. We observe a weak band centered at 21,500 cm^{-1} with an extinction coefficient of about 2 M^{-1} cm^{-1}.

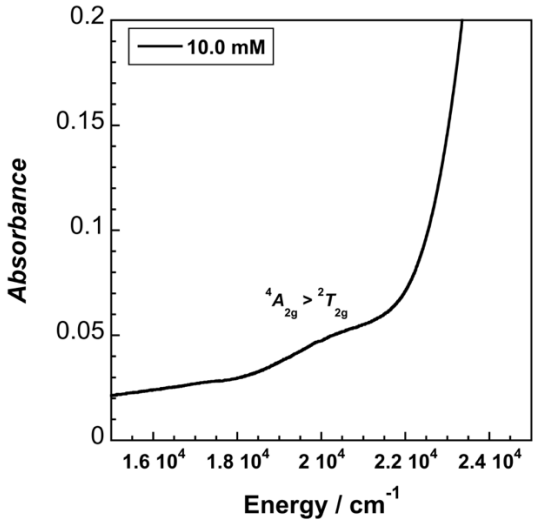

Figure 5.22. UV-vis absorption spectrum of 10.0 mM $(TBA)_3[Cr(CN\text{-}B(C_6F_5)_3)_6]$ in DCM.

The first LMCT for $[Cr(CN)_6]^{3-}$ is found at 38,600 cm^{-1} and is ascribed to a $^4A_{2g} \rightarrow {}^4T_{2u}$ transition.[1] For **7**, we observe a transition at 32,900 cm^{-1} with an extinction coefficient of 3,830 M^{-1} cm^{-1} and a FWHM of about 7200 cm^{-1}. Consistent with Fe, Os, and Ru, we assign this transition to a $^4A_{2g} \rightarrow {}^4T_{2u}$ transition.

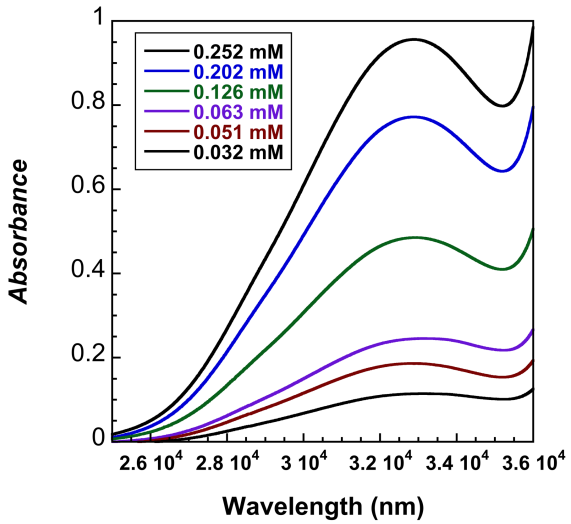

Figure 5.23. The first LMCT transition of $(TBA)_3[Cr(CN\text{-}B(C_6F_5)_3)_6]$ in DCM.

Few studies of the aqueous electrochemistry of $[Cr(CN)_6]^{3-}$ exist in the literature, though the studies that have been reported are particularly illuminating.[52,53,54] Previous electrochemical studies have suggested that $[Cr(CN)_6]^{3-}$ is reduced by an ECE mechanism, and previous photochemical studies have demonstrated the ligand field photolysis of $[Cr(CN)_6]^{3-}$ to produce $[Cr(CN)_5(MeCN)]^{2-}$.[53,55]

To our knowledge, the only non-aqueous voltammetry previously observed was recorded in a dimethylsulfoxide solution using a silver wire as a pseudo-reference electrode.[26] The $E_{1/2}$ for this process was −1.74 V vs. Ag wire. However, using a pseudo-reference electrode suggests that the formal potential associated with this reduction is ambiguous.[26] As a result of the anodic shift in potential that results from boronation, we performed scan rate dependence of **7** in MeCN electrolyte at both 22 °C and −20 °C, shown previously. At room-temperature, slow scan rates (v < 25 mV s^{-1}) result in minimal return oxidation current, suggesting a slow (on the time scale of the scan), irreversible chemical process coupled to reduction. This mechanism is consistent with generation of a S = 2, d^4 electron

configuration that ejects a $^{-}$CN-B(C_6F_5)$_3$ ligand upon reduction. A plot of the peak current ratio versus the logarithm of the scan rate supports this interpretation (**Figure 5.24**).

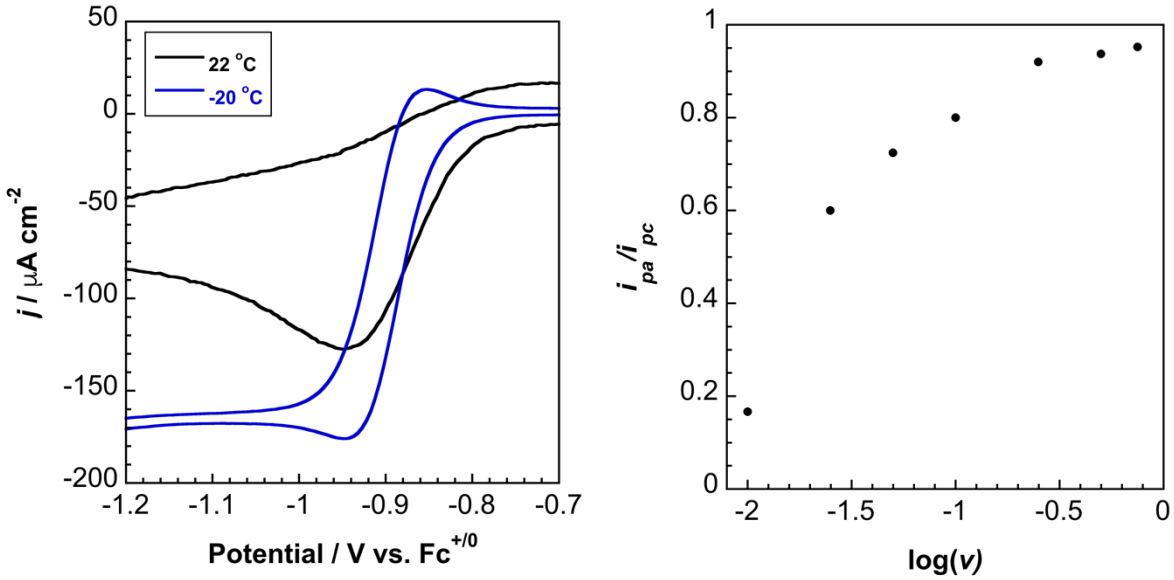

Figure 2.24. (**Left**) Room-temperature and low-temperature (−25 °C) voltammetry and peak current ratio versus the logarithm of the scan rate (**Right**) for [Cr(CN-B(C_6F_5)$_3$)$_6$]$^{3-}$.

Given the long-lived phosphorescence observed that has been previously reported for [Cr(CN)$_6$]$^{3-}$, we also measured the low-temperature luminescence and excited-state lifetimes for **7**, **12**, and **13**. Biexponential fits were used to determine average decay times at 77 K after excitation using the 3rd harmonic (355 nm) of a Nd:YAG laser. These values, along with others reported in the literature, are given in **Table 5.11**. In certain cases, it seems that an increase in average decay time is observed upon boronation, which likely results from the decrease in non-radiative decay pathways from solvent interactions.

Table 5.11. Phosphorescence lifetimes for hexacyanochromate derivatives.

Complex	Solvent	τ_{lum}, ms
$(TBA)_3[Cr(CN\text{-}B(C_6F_5)_3)_6]$	2-MeTHF (77 K)	46.7
$(TBA)_3[Cr(CN\text{-}BPh_3)_6]$	2-MeTHF (77 K)	9.4
$(TBA)_3[Cr(NC\text{-}BPh_3)_6]$	2-MeTHF (77 K)	22.9
$(TBA)_3[Cr(NC\text{-}BPh_3)_6]$[a]	Solid (77 K)	8.7
$(TBA)_3[Cr(NC\text{-}BPh_3)_6]$[b]	DMF (213 K)	15

[a] Reference 56
[b] Reference 57

Cyanide Isomerism in Hexacyanochromate

The ambident nucleophilicity of the cyanide ligand has been well known for many years, specifically in the context of Prussian blue and its analogues.[4] Resonance delocalization of the negative charge allows cyanide to bind through carbon or nitrogen both to electron-deficient and electron-rich metal centers. However, the nature of bonding is entirely different. In early transition metals and metals in high oxidation states, the nitrile species is thermodynamically stable, while in late transition metals and metals in low oxidation states, the cyanide compound is the thermodynamic product. This behavior stems from the capability of the metal center to participate in covalent interactions, namely, pi-backbonding. Additionally, extensive studies on the $^2E_g \rightarrow {}^4A_{2g}$ phosphorescence of hexacyanochromate have been performed, including solvent dependence and substitution reactions of excited-state species.[11,58,26,59]

Despite our confidence in assignment of the C-bound and N-bound isomers, **12** and **13**, by X-ray crystallography, we performed EPR studies to more unambiguously ascertain the bonding environment for chromium. Previous studies have demonstrated that neutron diffraction studies unambiguously assign the coordination environment for octahedral metal complexes. However, we decided to utilize pulsed EPR techniques, namely Q-band and X-band hyperfine sublevel correlation (HYSCORE), as

these measurements provide information about the hyperfine coupling and spin density of different ligands relative to the metal center.

The CW X-band and HYSCORE X-band and Q-band spectra for both $[Cr(CN\text{-}BPh_3)_6]^{3-}$ and $[Cr(NC\text{-}BPh_3)_6]^{3-}$ are displayed in **Figures 5.25-5.27**. For CW spectra, both isomers exhibit relatively isotropic doublets with values of g = 1.993 and g = 1.985 for $[Cr(CN\text{-}BPh_3)_6]^{3-}$ and $[Cr(NC\text{-}BPh_3)_6]^{3-}$, respectively. These values are consistent with previous studies of $[Cr(CN)_6]^{3-}$ in various matrices and under various conditions.[60,61] The HYSCORE spectra for these complexes support the identity of each isomer, with observation of hyperfine couplings to ^{14}N being greater in the N-bound isomer relative to the C-bound isomer. In both cases the weak hyperfine coupling to ^{11}B is consistent with the larger distance of boron relative to C/N to the metal center. To our knowledge, this is the first example of using HYSCORE spectroscopy for the identification of the primary ligand field surrounding Cr^{3+}.

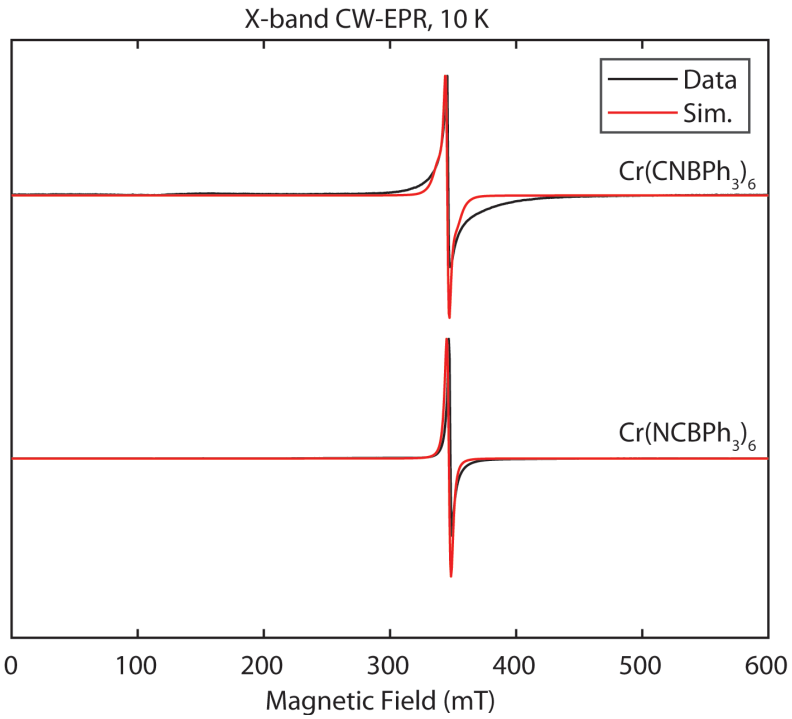

Figure 5.25. X-band CW-EPR spectrum (black) of frozen solution of $[Cr(CN\text{-}BPh_3)_6]^{3-}$ and $[Cr(CN\text{-}BPh_3)_6]^{3-}$ prepared in 2Me-THF with simulation overlaid in red. Acquisition parameters for $[Cr(CN\text{-}BPh_3)_6]^{3-}$: temperature = 10 K; MW freq. = 9.387 GHz; MW power = 2 mW; modulation amplitude = 0.8 mT; conversion time = 82 ms.

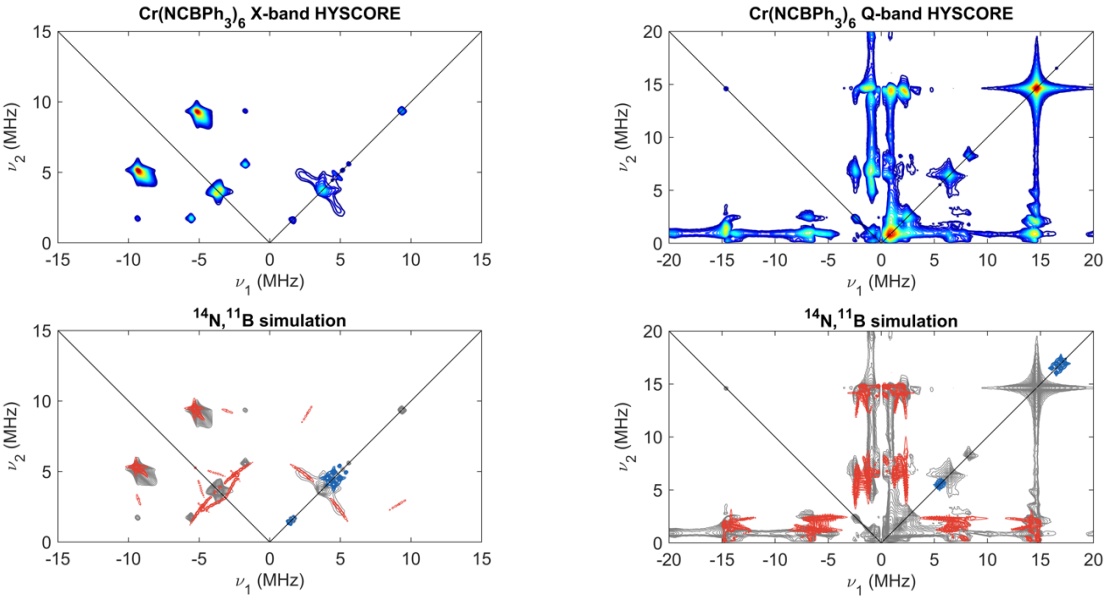

Figure 5.23. X-band and Q-band Hyperfine sublevel correlation (HYSCORE) spectrum of a 1:1 propionitrile/2-MeTHF frozen solution of 2.5 mM $(Ph_4As)_3[Cr(NC\text{-}BPh_3)_6]$ acquired at 1224 mT (Q-band) and 349 mT (X-band). The experimental data is plotted in color in the top panel, ranging from dark blue to red in increasing intensity. This same data is plotted in grey in the bottom panel, with simulations of coupling to six equivalent ^{14}N nuclei (red) and coupling to six equivalent ^{11}B nuclei (blue) overlaid. Simulation parameters: $A(^{14}N)$ = [7.2, 7.2, 6.2] MHz, $e^2qQ/h(^{14}N_a)$ = 2.4 MHz, $\eta(^{14}N)$ = 0; $A(^{11}B)$ = [0.4, 0.4, 0.5] MHz, $e^2qQ/h(^{11}B)$ = 0.3 MHz, $\eta(^{11}B)$ = 0.

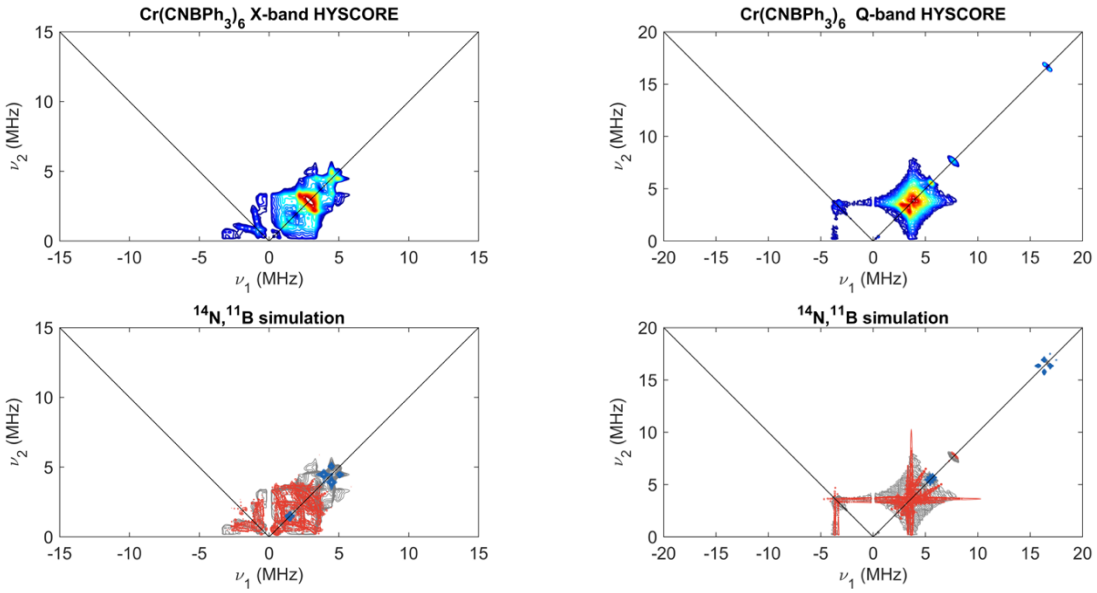

Figure 5.24. Q-band and X-band Hyperfine sublevel correlation (HYSCORE) spectrum of a 1:1 propionitrile/2-MeTHF frozen solution of 2.6 mM $(Ph_4As)_3[Cr(CN\text{-}BPh_3)_6]$ acquired at 1218 mT (Q-band) and 348 mT (X-band). The experimental data is plotted in color in the top panel, ranging from dark blue to red in increasing intensity. This same data is plotted in grey in the bottom panel, with simulations of coupling to six equivalent ^{14}N nuclei (red) and coupling to six equivalent ^{11}B nuclei (blue) overlaid. Simulation parameters: $A(^{14}N) = [-1.2, -1.2, 2.0]$ MHz, $e^2qQ/h(^{14}N_a) = 1.8$ MHz, $\eta(^{14}N_a) = 0$; $A(^{11}B) = [0.5, 0.5, 0.7]$ MHz, $e^2qQ/h(^{11}B) = <1$ MHz, $\eta(^{11}B) = 0$.

Hexakisisocyanotris(pentafluorophenyl/2,4,6-trifluorophenyl)boratomanganate(III) (8/9)

Previous studies of both $[Mn(CN)_6]^{2-}$ and $[Mn(CN)_6]^{3-}$ have assigned both the UV-vis spectrum and oxidation states that are accessible by electrochemical methods.[21,23] Both the Mn(III) and Mn(IV) oxidation states have been isolated and characterized. As a result of this previous research, we decided to boronate and characterize $[Mn(CN\text{-}B(C_6F_5)_3)_6]^{3-}$ (**8**) and $[Mn(CN\text{-}B(2,4,6\text{-}F_3C_6H_2)_3)_6]^{3-}$ (**9**) to determine if lower valent states become accessible as a result of boronation and to further quantify the effect of Lewis acidity on the electronic and structural properties of boronated cyanometallates.

Three electrochemical events are observed for **8**, which contrasts with previous manganate electrochemistry. The first redox event occurs at $E_{1/2}$ = 0.03 V vs. $Fc^{+/0}$, which we assign to the $Mn^{III/II}$ formal potential. This reduction is 2.14 V positive of the formal potential for $Mn^{III/II}$ for $[Mn(CN)_6]^{3-}$, consistent with our previous studies on $[Fe(CN)_6]^{4-}$.

We observe eight discrete peaks in the absorbance spectrum, two corresponding to borane transitions and six corresponding to MCN-based transitions. We deconvoluted this spectrum into eight Gaussian peaks, all of which are consistent with our work on d^5, isostructural species. The assignments of these bands are tabulated in **Table 5.12**. **Figure 5.28** displays the low-temperature absorption spectrum of $[Mn(CN\text{-}B(C_6F_5)_3)_6]^{3-}$, while **Figure 5.30** gives the concentration dependence of the absorption spectrum of $[Mn(CN\text{-}B(C_6F_5)_3)_6]^{3-}$ at ambient temperature. Previous studies and our room-temperature MCD spectrum, shown in **Figure 5.29**, support assignment of the second band to the $t_{1u}(\sigma+\pi) \rightarrow t_{2g}\pi$ transition.[1,21,62,63]

Table 5.12. Transition assignments for $[Mn(CN\text{-}B(C_6F_5)_3)_6]^{3-}$ from Gaussian deconvolution of the absorption spectrum.

λ (nm)	$\tilde{\nu}$ (cm^{-1})	Type	Transition
202	49505	MLCT	$t_{2g}\pi \rightarrow t_{1u}\pi^*$
266	38023	LMCT	$e_g\sigma \rightarrow t_{2g}\pi$
283	35336	LMCT	$t_{1g}\pi \rightarrow t_{2g}\pi$
293	34130	LMCT	$a_{1g}\sigma \rightarrow t_{2g}\pi$
314	31847	LMCT	$t_{1u}(\sigma+\pi) \rightarrow t_{2g}\pi$
376	26596	LMCT	$t_{2u}\pi \rightarrow t_{2g}\pi$

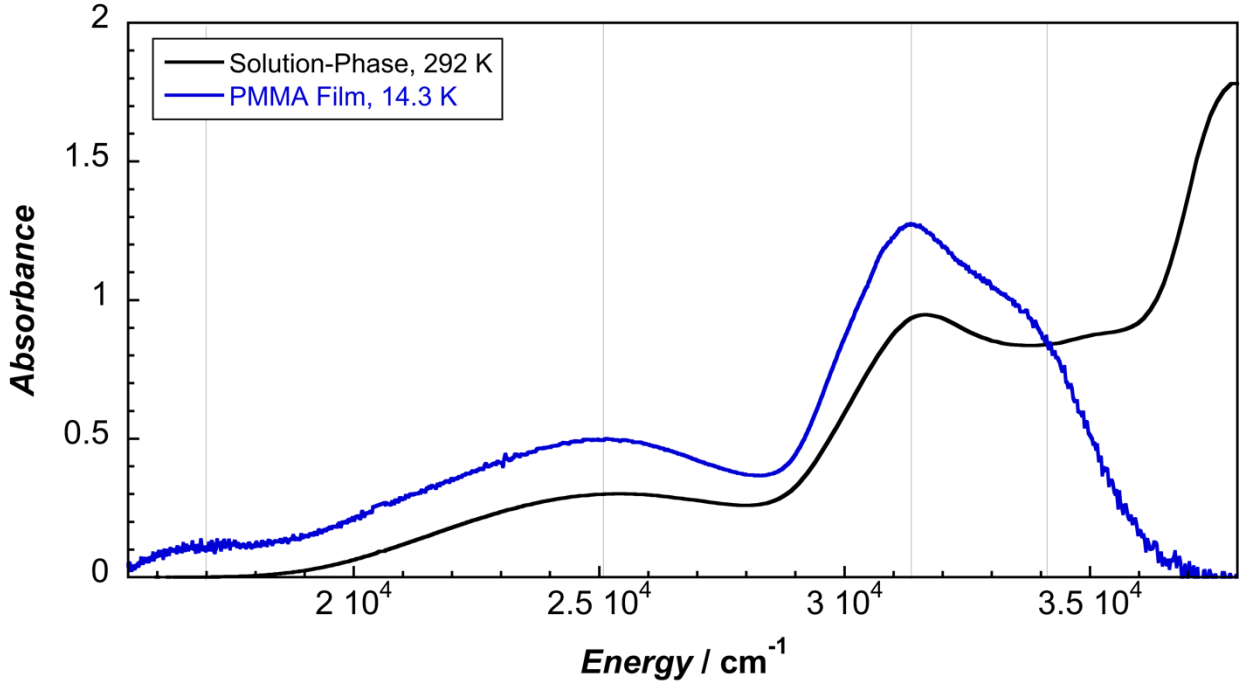

Figure 5.28. Comparison of room-temperature (MeCN) and low-temperature (14.3 K in poly(methyl methacrylate) film) absorption of $[Mn(CN\text{-}B(C_6F_5)_3)_6]^{3-}$.

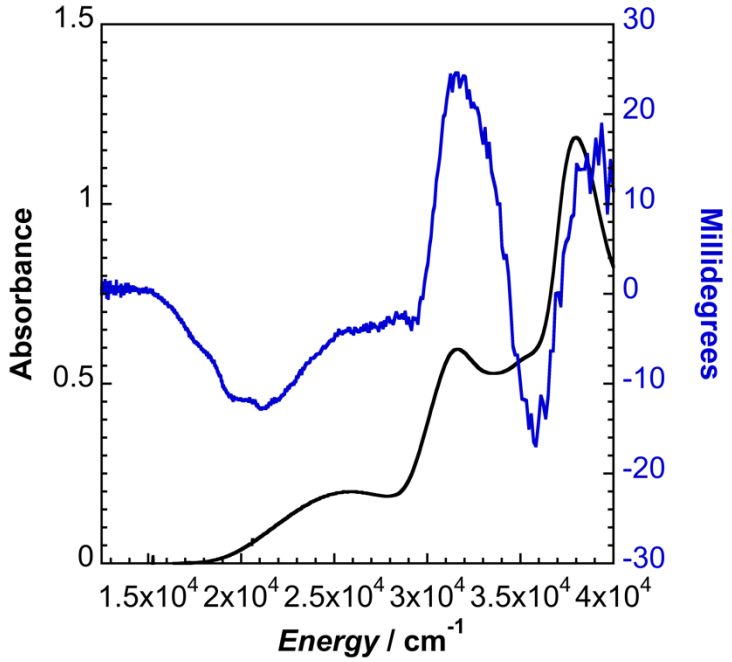

Figure 5.29. Room-temperature MCD absorption spectrum of $[Mn(CN\text{-}B(C_6F_5)_3)_6]^{3-}$ in MeCN.

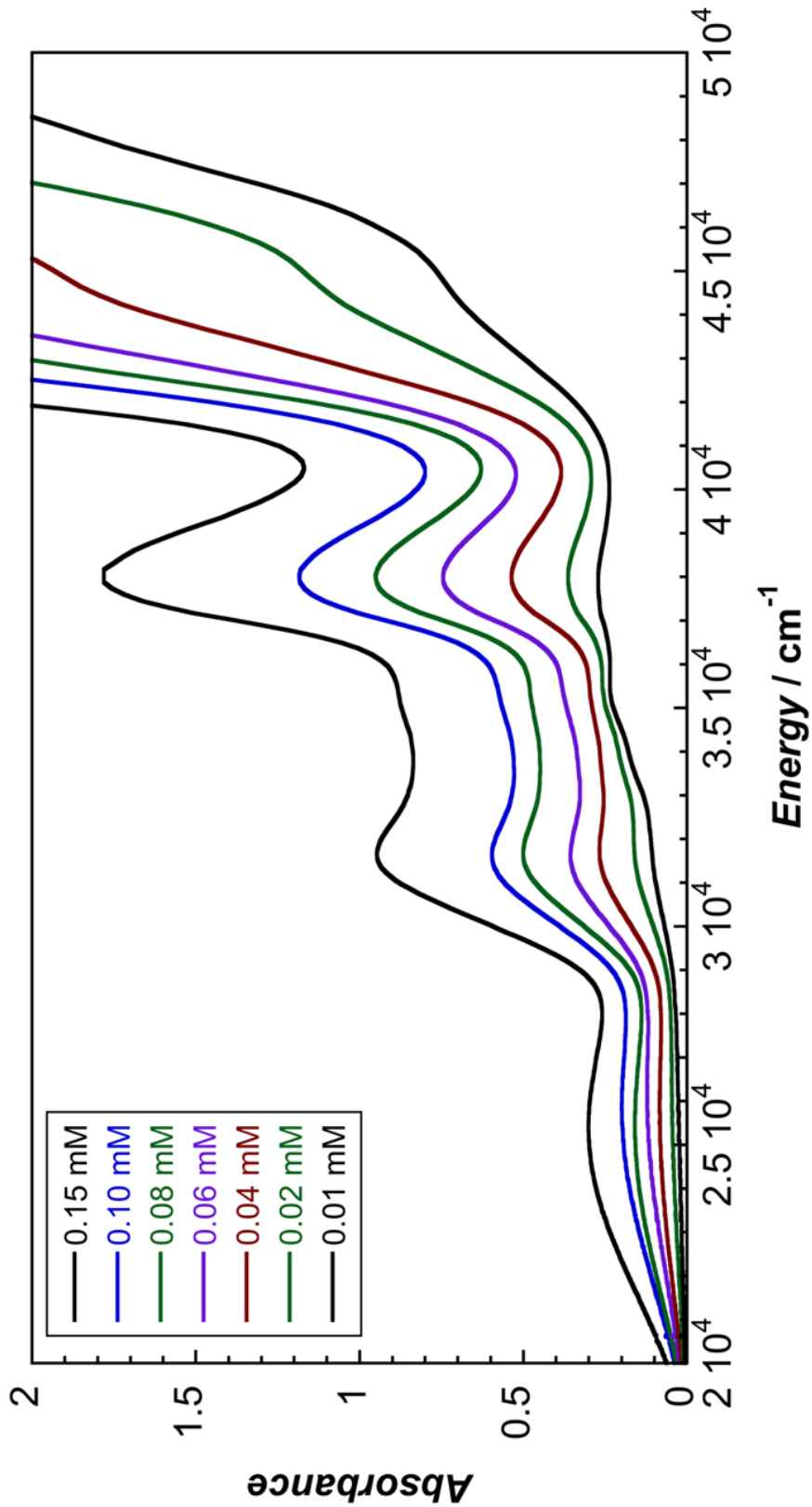

Figure 5.30. UV-vis absorbance spectrum of $(TBA)_3[Mn(CN\text{-}B(C_6F_5)_3)_6]$.

General Discussion

When the first LMCT of all five M(III) species is plotted versus the formal potential of each compound, the result is a line with a slope near unity, as shown in **Figure 5.31**. This value is consistent with this transition being a pure charge transfer from ligand to metal, with little mixing from other orbitals. This behavior supports the assignment of this band as arising from a $t_{2u} \rightarrow t_{2g}$ transition since the t_{2u} level is essentially nonbonding with respect to the metal, resulting in a strong correlation between spectroscopic and electrochemical reduction. **Table 5.13** demonstrates the minimal changes in $t_{1u} \rightarrow t_{2g}$ transition energy and dramatic change in $t_{2u} \rightarrow t_{2g}$ transition energy from base to boronated species.

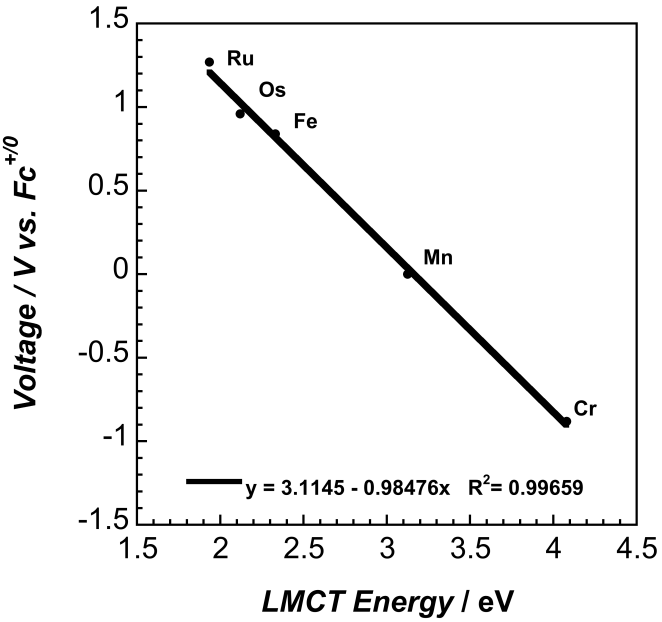

Figure 5.31. Formal potential versus first ligand-to-metal charge transfer energy for boronated, homoleptic cyanometallates.

Table 5.13. Comparison of the first two LMCT transitions in boronated cyanometallates and changes in energy upon boronation.

Complex	$t_{2u}(\pi) \rightarrow t_{2g}(\pi)$ (cm^{-1})	$t_{1u}(\sigma+\pi) \rightarrow t_{2g}(\pi)$ (cm^{-1})	$\Delta E_{Transition}$ (t_{2u}/ t_{1u}) (eV)
$[Fe(CN\text{-}BCF)_6]^{3-}$	18,400	24,000	(1.81 / 0.06)
$[Ru(CN\text{-}BCF)_6]^{3-}$	14,510	22,170	(1.69 / 0.08)
$[Os(CN\text{-}BCF)_6]^{3-}$	16,970	23,830	(1.60 / 0.03)
$[Cr(CN\text{-}BCF)_6]^{3-}$	32,900	37,700	(--- / 0.11)
$[Mn(CN\text{-}BCF)_6]^{3-}$	26,596	31,847	(1.25 / 0.09)
$[Fe(CN)_6]^{3-}$	33,000	23,500	---
$[Ru(CN)_6]^{3-}$	28,100	21,500	---
$[Os(CN)_6]^{3-}$	29,900	24,100	---
$[Cr(CN)_6]^{3-}$	---	38,600	---
$[Mn(CN)_6]^{3-}$	36,700	31,100	---

[a] Reference 1
[b] Reference 8

We also measured the X-band CW EPR spectra for the d^5 boronated cyanometallates in frozen solutions of either THF or DCM (**Figure 5.32**). For $[Fe(CN)_6]^{3-}$, the g tensor has been previously found to be axial with significant rhombicity, with g = [2.35, 2.10, 0.91].[64] The g-tensor for $[Fe(CN\text{-}B(C_6F_5)_3)_6]^{3-}$ exhibits enhanced rhombicity relative to the base compound, with g = [2.47, 1.92, 1.35], which likely results from the high steric crowding and small MC bond lengths for the Fe(III) species, causing greater distortions in geometry. In contrast, for $[Os(CN\text{-}B(C_6F_5)_3)_6]^{3-}$, g = [1.863, 1.790, 1.690], which is much closer to isotropic than the previously reported values of g = [1.79, 1.79, 1.21].[9] The decreased anisotropy is consistent with the decreased tetragonal distortion calculated from the NIR spectra.

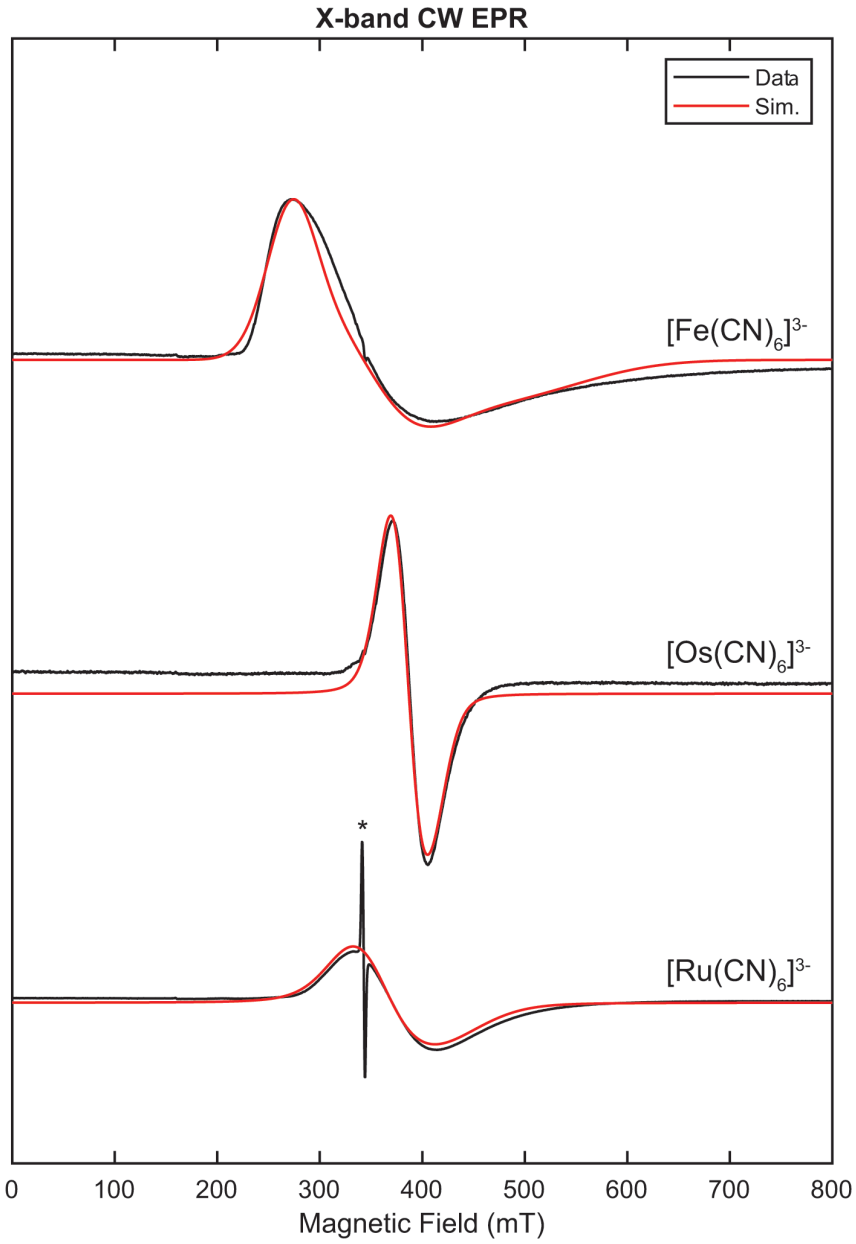

Figure 5.32. X-band CW-EPR spectrum (black) of frozen solution of complex **4**, **5**, and **6** prepared in 2Me-THF (Fe) or DCM (Ru and Os) with simulation overlaid in red. Acquisition parameters: temperature = 5 K; MW freq. = 9.638 GHz (Fe), 9.636 GHz (Ru), 9.636 GHz (Os); MW power = 2 mW (Fe and Os), 8 mW (Ru); modulation amplitude = 0.8 mT; conversion time = 81.92 ms.
Simulation parameters: Fe: g = [2.47, 1.92, 1.35]; H-strain = [1600, 1500, 1500] MHz; g-strain = [0.2, 0.45, 0.4] MHz; Ru: g = [1.985, 1.896, 1.616]; H-strain = [60, 40, 30] MHz; lw = 60; g-strain = [0.19, 0.35, 0.3] MHz; Os: g = [1.863, 1.790, 1.690]; lw = 20; g-strain = [0.2, 0.12, 0.15] MHz.

Asymmetric, Non-Aqueous Flow Battery Studies of $[Fe(CN)_6]^{3/4-}$ and $[Fe(CN\text{-}B(C_6F_5)_3)_6]^{3/4-}$

Based on the electrochemical reversibility of group VIII cyanometallates and previously published voltammetry of **3**,[64] a non-aqueous redox flow battery was constructed. 6 (0.85 V vs. $Fc^{+/0}$) was used as the anolyte, and $[Fe(CN)_6]^{3-}$ (−1.45 V vs. $Fc^{+/0}$) was used as the catholyte, giving a theoretical cell voltage of 2.3 V. The cell was charged to 80% SOC at C/2 to demonstrate fast-charging capability, and the cell was discharged at C/4 to display cell stability and minimal charge recombination across the membrane. The charge voltage was pinned at 2.6 V, which is within the electrochemical window of MeCN. The discharge voltage was pinned at 0.3 V.

Our initial attempts at this system used a Nafion 115 cation exchange membrane. Figure X shows the charge-discharge profile for the model battery using a Nafion 115 membrane after soaking for 48 hours in MeCN with 1.0 M $TBAPF_6$. The voltage, coulombic, and energy efficiencies over fourteen charge-discharge cycles are given in **Figure 5.33**. An average discharge voltage of 2.1 V was observed, one of the highest ever obtained for a homogeneous, non-aqueous redox flow battery.[64] The coulombic efficiency (*CE*), voltage efficiency (*VE*), and energy efficiency (*EE*) for a redox flow battery are given by **Equations 5.7-5.9**,

$$CE = \eta_C = \frac{Q_D}{Q_C} \times 100\% \tag{5.7}$$

$$VE = \eta_v = \frac{\frac{\int_0^{t_D} E_D(t)dt}{t_D}}{\frac{\int_0^{t_C} E_C(t)dt}{t_C}} \times 100\% \tag{5.8}$$

$$EE = \eta_{EE} = \eta_v \times \eta_C \tag{5.9}$$

where Q is the charge passed during charging or discharging, $E(t)$ is the voltage as a function of time during charging or discharging, and t is the total time of charging or discharging.

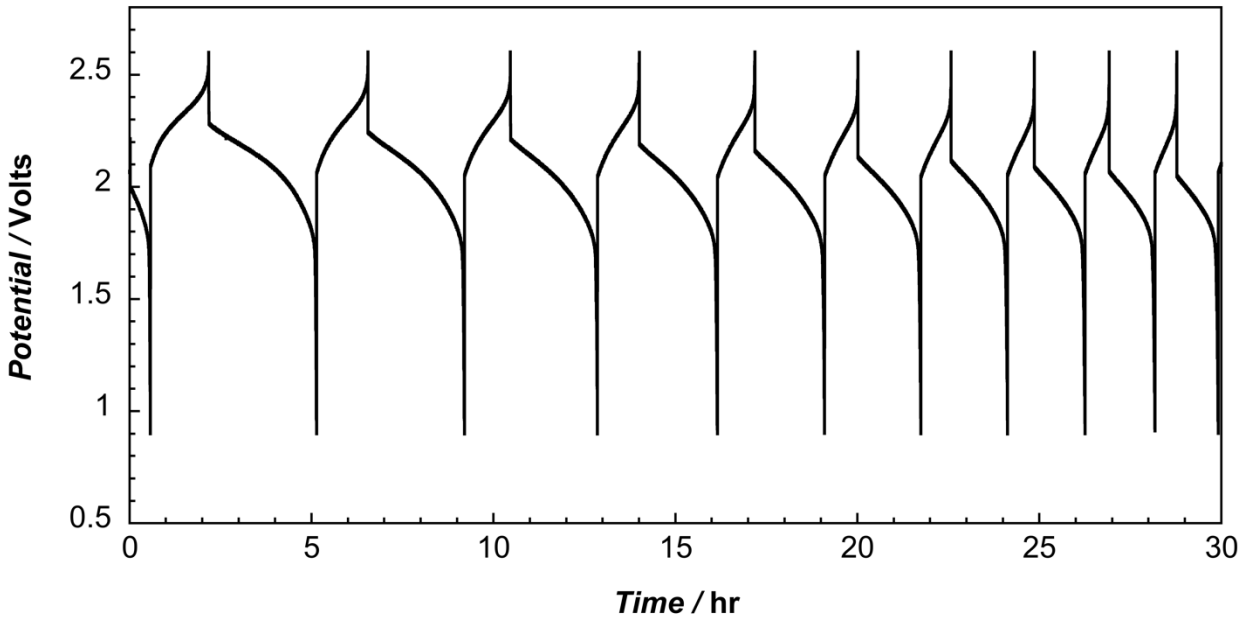

Figure 5.33. Charge discharge cycles for the $[Fe(CN)_6]^{3-}$/ Nafion 115 / $[Fe(CN\text{-}B(C_6F_5)_3)_6]^{3-}$ non-aqueous redox flow battery.

Figure 5.34 displays the efficiencies for $[Fe(CN)_6]^{3-}$/Nafion 115/$[Fe(CN\text{-}B(C_6F_5)_3)_6]^{4-}$ cell. No fade in Coulombic efficiency occurred; however, a noticeable decline in voltage efficiency (7% decay) occurred throughout repeated cycling. The capacity fade and decrease in voltage efficiency stem from two possible issues: precipitation that was observed at the membrane and/or crossover at the membrane. Nafion 115 is impregnated with Na^+ and is likely still present despite membrane soaking. This cation likely causes precipitation of the electrolytes employed in this study, which decreases cell capacity and increases the resistance across the membrane, thereby increasing the overpotential for charging. Additionally, voltammetry of the catholyte and anolyte solutions after cycling revealed significant crossover of **1**, thereby decreasing overall cell capacity.

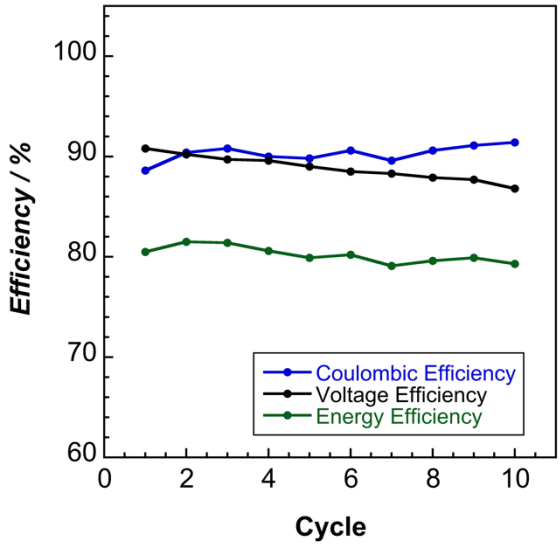

Figure 5.34. Voltage, Coulombic, and energy efficiencies for the $[Fe(CN)_6]^{3-}$/ Nafion 115 / $[Fe(CN\text{-}B(C_6F_5)_3)_6]^{3-}$ non-aqueous redox flow battery.

5.4 Conclusions

We have performed a systematic investigation of different hexaisocyanoboratometallates using a strong Lewis acid, $B(C_6F_5)_3$. Boronation effects structural and electronic changes which provide further insight into the nature of metal-ligand bonding in these species. In general, all ligand field excited states of these complexes blueshift slightly as a result of boronation due to unequal depression in the t_{2g} and e_g molecular orbital energy levels. Though a similar increase in energy for MLCTs is observed, this phenomenon likely results from enhanced pi backbonding, which pushes ligand orbitals to higher energies. Furthermore, the energies of most LMCT states are approximately constant between bare and boronated species.

Voltammetry, UV-vis spectroscopy, and MCD spectroscopy provide evidence that the first electronic transition in all M(III) complexes is $t_{2u}(\pi) \rightarrow t_{2g}(\pi)$. From a molecular orbital standpoint, this assignment is consistent with the t_{2u} symmetry molecular orbitals being formally non-bonding with respect to the metal. The correspondence between the potential shift from voltammetry and the energy shift of the electronic transition is striking. The strength of Lewis acid is consistent with the shift observed in the first LMCT. For **9**, the LMCT energy is blueshifted relative to **8**, consistent with decreased suppression of the t_{2g} energy level by a weaker Lewis acid. However, predictions about increasing or decreasing lifetimes for emission processes with boronation are not completely tenable, as the phosphorescence for **2** is shortened dramatically, while the phosphorescence for **7** is lengthened moderately. Preliminary non-aqueous redox flow battery studies demonstrate the high Coulombic and voltage efficiencies that are attainable with boronated cyanometallates.

These results demonstrate that boronated cyanometallates are a general class of molecules which are now well-characterized and available to spectroscopists and electrochemists for further study on the nuances between bare cyanometallates and boronated cyanometallates.

5.5 Synthesis and Experimental

General

Potassium hexacyanoferrate(III) ($K_3[Fe(CN)_6]$) (Sigma-Aldrich), bis(triphenylphosphine)iminium chloride (PPNCl) (Sigma-Aldrich), potassium hexacyanoferrate(II) ($K_4[Fe(CN)_6]$) (Sigma-Aldrich), potassium hexacyanomanganate(III) (Sigma-Aldrich), potassium hexachloroosmate(IV) (Sigma-Aldrich), potassium cyanide (Sigma-Aldrich), ruthenium trichloride (Sigma-Aldrich), elemental bromine, tris(pentafluorophenyl)borane (TCI Chemicals), tetraphenylarsonium chloride (Sigma-Aldrich/Strem Chemicals), and tetraphenylphosphonium chloride (Sigma-Aldrich) were used as received. Solvents were obtained from degassed, dry solvent systems. All boronations were performed in a nitrogen-filled glove box. $K_4[Os(CN)_6]$,[7] $K_4[Ru(CN)_6]$,[6] $(TBA)_3[Fe(CN)_6]$,[65] $(Ph_4P)_3[Os(CN)_6]$,[10] $(Ph_4As/Ph_4P)_3[Ru(CN)_6]$,[10] $(PPN)_4[Fe(CN)_6]$,[17] $(TBA)_3[Ru(CN)_6]$,[10] $(TBA)_4[Ru(CN)_6]$,[6] $(TBA)_3[Os(CN)_6]$,[10] $(TBA)_4[Os(CN)_6]$,[66,8] $(TBA)_3[Cr(CN)_6]$,[12] $(Ph_4As)_3[Cr(CN)_6]$,[12] $(TBA)_3[Mn(CN)_6]$,[13] $(PPN)_3[Mn(CN)_6]$,[13] and $(TBA)_4[Fe(CN\text{-}B(C_6F_5)_3)_6]$ (**1**)[17] were synthesized according to literature precedent. $(Ph_4As)_3[Cr(NC\text{-}BPh_3)_6]$ was synthesized according to literature precedent,[16] beginning with $(Ph_4As)_3[Cr(CN)_6]$ instead of $(TEA)_3[Cr(CN)_6]$. Butyronitrile and propionitrile (Sigma-Aldrich) were dried over 3 Å molecular sieves and stored in a dry room or in a nitrogen-filled glove box. Deuterated solvents were dried and stored over activated 3 Å molecular sieves in a nitrogen-filled glove box. All NMR spectra were collected on a Varian 400 MHz spectrometer or Bruker 400 MHz spectrometer (δ in ppm, m: multiplet, s: singlet, d: doublet, t: triplet, pt: pseudo- triplet). ^{13}C NMR and ^{31}P NMR were ^{1}H decoupled. ^{31}P NMR spectra were externally referenced to 85% H_3PO_4, ^{19}F NMR spectra were externally referenced to neat $CFCl_3$, and ^{11}B NMR were internally referenced to 15% $BF_3{\cdot}Et_2O$. Elemental Analyses were performed on a PerkinElmer 2400 Series II CHN Elemental Analyzer. UV-visible-NIR spectra were recorded on either a Cary 500 UV-Vis-NIR or HP 8453 spectrophotometer.

Magnetic Circular Dichroism Spectroscopy

Circular dichroism data in the UV-vis region (300-800 nm) were collected on an Olis DSM 172 spectrophotometer operating with a 9798B series S20 PMT detector and 150 W xenon lamp power supply. The CD spectra were recorded at 293 K in a 1 cm path length borosilicate cuvette. Magnetic circular dichroism data were collected in a 1.490 T max field (1.2 to 1.4 T range) sample holder. Measurements were recorded over 16 scans, with an 8 nm measurement bandwidth.

Luminescence Spectroscopy

Low temperature luminescence spectra were recorded on an OceanOptics spectrometer. Low temperature luminescence spectra were recorded on a Melles-Griot 13 FOS 200 spectrometer coupled to a fiber optic cable which collected sample luminescence. Samples were excited with a 365 nm Thorlabs, Inc. UV LED (M365L1) and Thorlabs, Inc. LED driver (LEDD1) or the 3rd (355 nm) or 4th (266 nm) harmonic of a Nd:YAG laser. Long pass filters were used to isolate luminescence signals from LED light. An Edwards T-Station turbo pump coupled to a radiation-shielded cold head were used to mount the sample and apply dynamic vacuum. The sample was cooled using a CTI-Cryogenics compressor. Samples were allowed to evacuate for at least fifteen minutes prior to cooling.

Electron Paramagnetic Resonance Spectroscopy

Continuous wave X-band EPR spectra were obtained on a Bruker EMX spectrometer on 1.0-3.0 mM solutions prepared as frozen solutions in 2-MeTHF, THF, or dichloromethane. Pulse EPR spectroscopy: All pulse X- and Q-band (9.4-9.7 and 34 GHz, respectively) EPR and hyperfine sublevel correlation spectroscopy (HYSCORE) experiments were acquired using a Bruker ELEXSYS E580 pulse EPR spectrometer. All Q-band experiments were performed using a Bruker D2 pulse ENDOR

resonator. X-band HYSCORE experiments were performed using a Bruker MS-5 resonator. Temperature control was achieved using an ER 4118HV-CF5-L Flexline Cryogen-Free VT cryostat manufactured by ColdEdge equipped with an Oxford Instruments Mercury ITC temperature controller.

X-band and Q-band Pulse HYSCORE spectra were acquired using the 4-pulse sequence ($\pi/2-\tau-\pi/2-t_1-\pi-t_2-\pi/2-$ echo), where τ is a fixed delay, while t_1 and t_2 are independently incremented by Δ_{t_1} and Δ_{t_2}, respectively. The time domain data was baseline-corrected (third-order polynomial) to eliminate the exponential decay in the echo intensity, apodized with a Hamming window function, zero-filled to eight-fold points, and fast Fourier-transformed to yield the 2-dimensional frequency domain.

In general, the ENDOR spectrum for a given nucleus with spin I= 1⁄2 (^{19}F) coupled to the S = 1⁄2 electron spin exhibits a doublet at frequencies,

$$\nu_{\pm} = \left|\frac{A}{2} \pm \nu_N\right| \tag{5.10}$$

where $\nu_{\pm}$ is the nuclear Larmor frequency and A is the hyperfine coupling. For nuclei with $I \geq 1$ (^{14}N, ^{11}B), an additional splitting of the $\nu_{\pm}$ manifolds is produced by the nuclear quadrupole interaction (P).

$$\nu_{\pm,m_I} = \left|\nu_N \pm \frac{3P(2m_I-1)}{2}\right| \tag{5.11}$$

In HYSCORE spectra, these signals manifest as cross-peaks or ridges in the 2-D frequency spectrum which are generally symmetric about the diagonal of a given quadrant. This technique allows hyperfine levels corresponding to the same electron-nuclear submanifold to be differentiated, as well as separating features from hyperfine couplings in the weak-coupling regime ($|A| < 2|\nu_I|$) in the (+,+) quadrant from those in the strong coupling regime ($|A| > 2|\nu_I|$) in the (−,+) quadrant. The (−,−) and (+,−) quadrants of these frequency spectra are symmetric to the (+,+) and (−,+) quadrants, thus typically only two of the quadrants are typically displayed in literature. For systems with appreciable hyperfine anisotropy in frozen solutions or solids, HYSCORE spectra typically do not exhibit sharp cross peaks, but show ridges that represent the sum of cross peaks from selected orientations at the magnetic field position at which the spectrum is collected. The length and curvature of these correlation ridges allow for the separation and estimation of the magnitude of the isotropic and dipolar components of the hyperfine tensor, as shown in **Figure 5.35**.

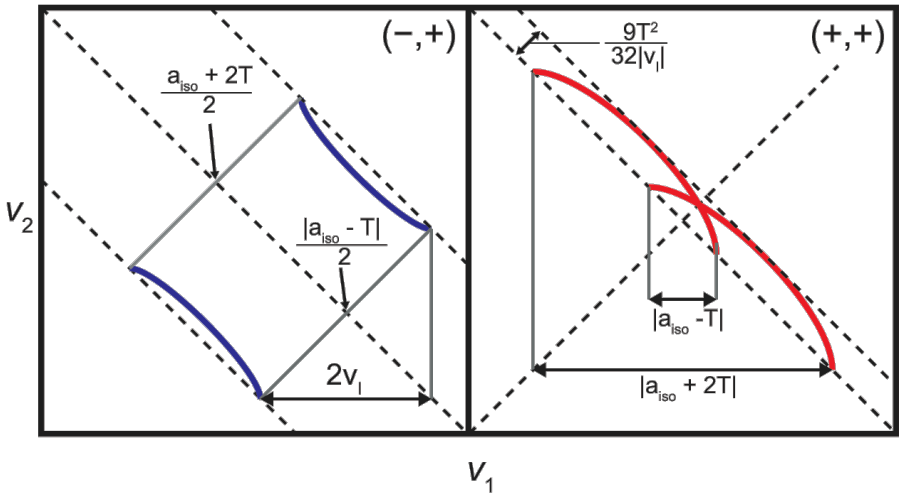

Figure 5.35. HYSCORE patterns for an $S = 1/2$, $I = 1/2$ spin system with an axial hyperfine tensor which contains isotropic (a_{iso}) and dipolar (T) contributions. Blue correlation ridges represent the strong coupling case; red correlation ridges represent the weak coupling case.

For systems coupled to nuclei with $I = 1$, such as ^{14}N, the double-quantum peaks are often the most intense feature. These cross-peaks are defined by the following equations,

$$\nu_\alpha = \pm 2\sqrt{(\upsilon_I + A/2)^2 + K^2(3+\eta^2)}$$
$$\nu_\beta = \pm 2\sqrt{(\upsilon_I - A/2)^2 + K^2(3+\eta^2)} \quad (5.12)$$

where $K = e^2qQ/4\hbar$. For weakly coupled nuclei ($A < 2\upsilon_I$) ν_α and ν_β are both positive, appearing in the (+,+) quadrant, while for strongly coupled nuclei ($A < 2\upsilon_I$) they will show up in the (−,+) quadrant. In the intermediate coupling regime where $A \approx 2\upsilon_I$, peaks will often appear in both the (+,+) and (−,+) quadrants of the HYSCORE spectrum.

All EPR spectra (CW, ENDOR, HYSCORE) were simulated using the EasySpin simulation toolbox (version 5.2.28)[67] with Matlab 2019 using the following Hamiltonian,

$$\hat{H} = \mu_B \vec{B}_0 g \hat{S} + \mu_N g_N \vec{B}_0 \hat{I} + h\hat{S} \cdot \boldsymbol{A} \cdot \hat{I} + h\hat{I} \cdot \boldsymbol{P} \cdot \hat{I} \quad (5.13)$$

In this expression, the first term corresponds to the electron Zeeman interaction term where μ_B is the Bohr magneton, g is the electron spin g-value matrix with principle components g = [gxx gyy gzz], and $\hat{S}$ is the electron spin operator; the second term corresponds to the nuclear Zeeman interaction term where μ_N is the nuclear magneton, g_N is the characteristic nuclear g-value for each nucleus (e.g. ^{19}F, ^{14}N, ^{11}B) and $\hat{I}$ is the nuclear spin operator; the third term corresponds to the electron-nuclear hyperfine term, where $\boldsymbol{A}$ is the hyperfine coupling tensor with principle components $\boldsymbol{A}$ = [Axx, Ayy, Azz]; and for nuclei with $I \geq 1$, the final term corresponds to the nuclear quadrupole (NQI) term

which arises from the interaction of the nuclear quadrupole moment with the local electric field gradient (efg) at the nucleus, where $\boldsymbol{P}$ is the quadrupole coupling tensor. In the principle axis system (PAS), $\boldsymbol{P}$ is traceless and parametrized by the quadrupole coupling constant e^2Qq/h and the asymmetry parameter η such that,

$$\boldsymbol{P} = \begin{pmatrix} P_{xx} & 0 & 0 \\ 0 & P_{yy} & 0 \\ 0 & 0 & P_{zz} \end{pmatrix} = \frac{e^2Qq/h}{4I(2I-1)} \begin{pmatrix} -(1-\eta) & 0 & 0 \\ 0 & -(1+\eta) & 0 \\ 0 & 0 & 2 \end{pmatrix} \qquad (5.14)$$

where $\frac{e^2Qq}{h} = 2I(2I-1)P_{zz}$ and $\eta = \frac{P_{xx}-P_{yy}}{P_{zz}}$. The asymmetry parameter may have values between 0 and 1, with 0 corresponding to an electric field gradient with axial symmetry and 1 corresponding to a fully rhombic efg.

The orientations between the hyperfine and NQI tensor principle axis systems and the g- matrix reference frame are defined by the Euler angles (α, β, γ), with rotations performed within the zyz convention where α rotates xyz counterclockwise about the z-axis to give x'y'z', β rotates x'y'z counterclockwise about the y'-axis to give x",y",z", γ rotates xyz counterclockwise about the z"- axis to give the final frame orientation.

Synthesis

Tetrabutylammonium/Tetraphenylphosphonium/Tetraphenylarsonium hexakisisocyanotris(pentafluorophenyl)boratoruthenate(II) (TBA/Ph_4P/Ph_4As)$_4$[Ru(CN-B(C_6F_5)$_3$)$_6$] (2)

Note: After titration with tetrabutylammonium hydroxide, (TBA)$_4$[Ru(CN)$_6$] must be dried in vacuo at an elevated temperature (about 60 °C) for about 36 hours to eliminate as much coordinated water as possible prior to further use. The starting material must be stored and handled under an inert atmosphere to prevent oxidation to the yellow Ru(III) salt and/or decomposition to a green solid, especially when dissolved in non-aqueous/aprotic solvents. A solution of (TBA)4[Ru(CN)6] (51.5 mg, 0.042 mmol) in DCM was added dropwise to a solution of 6.6 equivalents of B(C_6F_5)$_3$ (142.7 mg, 0.28 mmol) in 1:1 DCM:toluene (about five mL total). Additional toluene was added after stirring, and the solution was shaken vigorously to precipitate the crude product as a pseudo-crystalline gel-like material. The solvent was decanted, and the solid was dried in vacuo. The material was then dissolved in minimum acetonitrile, and a large excess of Et_2O was added to precipitate a colorless powder. The solvent was decanted, and the solid was again dried in vacuo. Finally, DCM was added, and the mixture was stirred to remove additional impurities. The solution was decanted to isolate the powder, and the powder was dried in vacuo to yield a colorless powder (0.040 g, 22.8 % yield). The impurities that need to be removed are likely borane-water and borane-hydroxide adducts, which are both removed by washing with toluene and/or DCM. The other salts of this compound were synthesized in a similar manner. Elem. Anal. (for TBA salt) (%) found (calc'd) for $C_{178}H_{144}B_6F_{90}N_{10}$ ((TBA)$_4$[Ru(CN-B(C_6F_5)$_3$)$_6$]): C, 49.50 (49.78); H, 3.40 (3.38); N, 3.40 (3.26). ^{11}B NMR (128 MHz, CD_3CN) δ -14.7; ^{19}F NMR (376 MHz, CD_3CN) δ -132.9 (d, J_{FF} = 18.0 Hz), -164.8 (pt, J_{FF} = 19.6 Hz), -169.1 (pt, J_{FF} = 18.0 Hz); ^{1}H NMR (400 MHz, CD_3CN) δ 3.07 (t, 2H, CH_{but}, J_{HH} = 8.5 Hz), 1.59 (pquint, 2H, CH_{but}),

1.33 (psextet, 2H, CH_{but}), 0.95 (t, 3H, CH_{but}, J_{HH} = 7.3 Hz); ^{13}C NMR (100 MHz, CD_3CN) δ 159.6 (CN), 149.1 (d, J_{CF} = 242 Hz), 139.5 (d, J_{CF} = 247 Hz), 137.1 (d, J_{CF} = 242 Hz), 59.3 (s), 24.2 (s), 20.3 (s), 13.7 (s). ATR-IR, ν: 2172 cm^{-1}.

Tetrabutylammonium/Tetraphenylphosphonium hexakisisocyanotris(pentafluorophenyl)boratoosmate(II) $(TBA/PPh_4)_4[Os(CN\text{-}B(C_6F_5)_3)_6]$ (3)

Note: After titration with tetrabutylammonium hydroxide, $(TBA)_4[Os(CN)_6]$ must be dried in vacuo at an elevated temperature (about 70 °C) for about 8 hours to eliminate as much coordinated water as possible prior to further use. The starting material must be stored and handled under an inert atmosphere to prevent oxidation to the yellow Os(III) salt. $(TBA)_4[Os(CN)_6]$ (0.203 g, 0.15 mmol) was combined with 7.2 equivalents of tris(pentafluorophenyl)borane (0.568 g, 1.11 mmol) in 1:1 DCM:toluene (5 mL). Additional toluene was added after stirring, and the solution was shaken vigorously to precipitate the crude product as a pseudo-crystalline gel-like material. The solid was allowed to settle, and the solvent was decanted. The solid was then dried in vacuo. The material was redissolved in a minimum of acetonitrile, and a large excess of Et_2O was added to precipitate a colorless powder. The mixture was filtered, and the solid was washed three times with 1:1 DCM:Et_2O (3 x 5 mL). This process was then repeated. The powder was dried in vacuo (0.211 g, 0.048 mmol, 31.2 %). Elem. Anal. (%) found (calc'd) for $C_{210}H_{80}B_6F_{90}N_6OsP_4$ ($(Ph_4P)_4[Os(CN\text{-}B(C_6F_5)_3)_6]$): C, 52.21 (52.81); H, 1.61 (1.69); N, 1.89 (1.76). ^{11}B NMR (128 MHz, CD_3CN) δ -14.4; ^{19}F NMR (376 MHz, CD_3CN) δ -132.8 (d, J_{FF} = 18.8 Hz), -164.8 (pt, J_{FF} = 20.7 Hz), -169.1 (pt, J_{FF} = 18.8 Hz); ^1H NMR (400 MHz, CD_3CN) δ 3.07 (t, 2H, CH_{but}, J_{HH} = 8.5 Hz), 1.59 (pquint, 2H, CH_{but}), 1.34 (psextet, 2H, CH_{but}), 0.95 (t, 3H, CH_{but}, J_{HH} = 7.3 Hz); ^{13}C NMR (100 MHz, CD_3CN) δ 59.3 (s), 24.2 (s), 20.2 (s), 13.7 (s). ATR-IR, ν: 2152 cm^{-1} (CN stretch).

Tetrabutylammonium/Bis(triphenylphosphine)iminium hexakisisocyanotris(pentafluorophenyl)boratoferrate(III) (TBA/PPN)$_3$[Fe(CN-B(C$_6$F$_5$)$_3$)$_6$] (4)

(TBA)$_3$[Fe(CN)$_6$] (0.101 g, 0.11 mmol) was dissolved in DCM and added dropwise to a stoichiometric excess of B(C$_6$F$_5$)$_3$ (0.380 g, 0.74 mmol) dissolved in DCM. An immediate color change from yellow to purple was observed. The solution was placed in a freezer at -20 °C, and the product was allowed to precipitate. The solution was decanted. Because of the limited solubility of the product in DCM, the solid was again washed with a small amount of DCM to remove additional impurities. The solvent was decanted, and the violet product was dried in vacuo to yield (TBA)$_3$[Fe(CN-B(C$_6$F$_5$)$_3$)$_6$] (0.165 g, 38.7% yield). The PPN salt of this complex was synthesized in an identical manner. Elem. Anal. (for TBA salt) (%) found (calc'd) for $C_{162}H_{108}B_6F_{90}FeN_9$ ((TBA)$_3$[Fe(CN-B(C$_6$F$_5$)$_3$)$_6$]): C, 48.89 (48.51); H, 2.64 (2.71); N, 3.34 (3.14). ^{11}B NMR (128 MHz, CD_2Cl_2) δ -54.2; ^{19}F NMR (376 MHz, CD_2Cl_2) δ -127.7 (d, J_{FF} = 15.0 Hz), -158.4 (pt, J_{FF} = 19.5 Hz), -163.8 (pt, J_{FF} = 17.8 Hz); ^{1}H NMR (400 MHz, CD_2Cl_2) δ 3.03 (t, 2H, CH_{but}, J_{HH} = 8.5 Hz), 1.57 (pquint, 2H, CH_{but}), 1.37 (psextet, 2H, CH_{but}), 0.98 (t, 3H, CH_{but}, J_{HH} = 7.3 Hz); ^{13}C NMR (100 MHz, CD_2Cl_2) δ 59.3 (s), 24.1 (s), 19.9 (s), 13.5 (s). ATR-IR, ν: 2228 cm^{-1} (CN stretch).

Tetraphenylarsonium/Tetrabutylammonium hexakisisocyanotris(pentafluorophenyl)boratoruthenate(III) (Ph$_4$As/TBA)$_3$[Ru(CN-B(C$_6$F$_5$)$_3$)$_6$] (5)

(TBA)$_3$[Ru(CN)$_6$] (0.035 mmol, 0.050 g) was dissolved in DCM and added dropwise to a stirred solution of B(C$_6$F$_5$)$_3$ (0.25 mmol, 0.129 g) in DCM. An immediate color change from orange to green was observed. A small amount of hexanes was added, and the solution was placed in the freezer. The product precipitated, and the solution was decanted. The solid was dried in vacuo and washed with hexanes (3 x 5 mL) to remove unreacted B(C$_6$F$_5$)$_3$. The product was then dried at 50 °C in vacuo to

yield $(TBA)_3[Ru(CN\text{-}B(C_6F_5)_3)_6]$ as a powder (0.122 g, 76.9% yield). Elem. Anal. (for Ph_4As salt) (%) found (calc'd) for $C_{188}H_{64}B_6Cl_4F_{90}N_6P_3Ru$ ($(Ph_4P)_3[Ru(CN\text{-}B(C_6F_5)_3)_6]\cdot 2CH_2Cl_2$): C, 49.72 (49.99); H, 1.58 (1.43); N, 1.63 (1.86). ^{11}B NMR (128 MHz, CD_2Cl_2) δ −62.3; ^{19}F NMR (376 MHz, CD_2Cl_2) δ -130.1 (d, J_{FF} = 18.4 Hz), −160.9 (pt, J_{FF} = 20.4 Hz), −166.8 (pt, J_{FF} = 19.0 Hz); ^1H NMR (400 MHz, CD_2Cl_2) δ 3.02 (t, 2H, CH_{but}, J_{HH} = 7.0 Hz), 1.57 (pquint, 2H, CH_{but}), 1.15 (psextet, 2H, CH_{but}), 0.98 (t, 3H, CH_{but}, J_{HH} = 7.3 Hz) ATR-IR, ν: 2210 cm^{-1} (CN stretch).

Tetraphenylphosphonium hexakisisocyanotris(pentafluorophenyl)boratoosmate(III) $(Ph_4P)_3[Os(CN\text{-}B(C_6F_5)_3)_6]$ (6):

$(Ph_4P)_3[Os(CN)_6]$ (0.049 g, 0.036 mmol) was dissolved in DCM and added dropwise to a stirred solution of $B(C_6F_5)_3$ (0.129 g, 0.25 mmol) in DCM. An immediate color change from yellow to indigo was observed. The solvent was removed in vacuo, and the resulting indigo solid was dispersed in chloroform and placed in a freezer at -20 °C for one hour. The solvent was decanted, and more chloroform was added. The mixture was again placed in the freezer for one hour, after which the solvent was decanted. The solid was dried in vacuo to yield $(Ph_4P)_3[Os(CN\text{-}B(C_6F_5)_3)_6]$ as an indigo, microcrystalline solid (0.156 g, 98.0% yield). Elem. Anal. (for Ph_4P salt) (%) found (calc'd) for $C_{186}H_{60}B_6F_{90}N_6OsP_3$: C, 50.12 (50.36); H, 1.66 (1.36); N, 1.41 (1.89). ^{11}B NMR (128 MHz, CD_2Cl_2) δ -37.6; ^{31}P NMR (162 MHz, CD_2Cl_2) δ 23.3; ^{19}F NMR (376 MHz, CD_2Cl_2) δ -132.9 (ps), -161.2 (pt, J_{FF} = 19.9 Hz), -167.1 (pt); ^1H NMR (400 MHz, CD_2Cl_2) δ 7.55-7.87 (m, 60H, CH_{Ph}); ^{13}C NMR (100 MHz, CD_3CN) δ 136.1 (d, C_{Ph}, J_{CP} = 3.1 Hz), 134.7 (d, C_{Ph}, J_{CP} = 10.3 Hz), 130.9 (d, C_{Ph}, J_{CP} = 89.8 Hz), 117.9 (d, C_{Ph}, J_{CP} = 8.5 Hz). ATR-IR, ν: 2204 cm^{-1} (CN stretch).

Tetrabutylammonium/Bis(triphenylphosphine)iminium hexakisisocyanotris(pentafluorophenyl)boratochromate(III) (TBA/PPN)$_3$[Cr(CN-B(C$_6$F$_5$)$_3$)$_6$] (7)

(TBA)$_3$[Cr(CN)$_6$] (0.134 g, 0.143 mmol) was dissolved in DCM and added dropwise to a stirred solution of 7.0 equivalents of B(C$_6$F$_5$)$_3$ (0.464 g, 0.906 mmol) in DCM. An immediate color change from pale yellow to nearly colorless was observed. The solvent was evaporated in vacuo, during which the product crystallized from solution. The colorless solid was washed with Et$_2$O (3 x 5 mL), followed by hexanes (3 x 5 mL), and the product was dried in vacuo to yield (TBA)$_3$[Cr(CN-B(C$_6$F$_5$)$_3$)$_6$] as a colorless, microcrystalline solid (0.518 g, 90.3% yield). The PPN salt of this complex was synthesized in an identical manner. Elem. Anal. (for TBA salt) (%) found (calc'd) for $C_{162}H_{108}B_6CrF_{90}N_9$: C, 48.06 (48.55); H, 2.47 (2.72); N, 3.13 (3.15). ^{19}F NMR (376 MHz, CD_2Cl_2) δ -132.6 (bs), -164.8 (bs) -167.4 (bs); ^{1}H NMR (400 MHz, CD_2Cl_2) δ 3.05 (bs, 2H, CH_{but}), 1.59 (bs, 2H, CH_{but}), 1.38 (bs, 2H, CH_{but}), 0.98 (bs, 3H, CH_{but}). ATR-IR, ν: 2229 cm^{-1} (CN stretch).

Tetrabutylammonium/Bis(triphenylphosphine)iminium hexakisisocyanotris(pentafluorophenyl)boratomanganate(III) (TBA/PPN)$_3$[Mn(CN-B(C$_6$F$_5$)$_3$)$_6$] (8)

(TBA)$_3$[Mn(CN)$_6$] (0.100 g, 0.11 mmol) was dissolved in DCM and added dropwise to a stirred solution of 6.1 equivalents of B(C$_6$F$_5$)$_3$ (0.344 g, 0.67 mmol) in DCM. An immediate color change from yellow to red-orange was observed, and the mixture was shaken. A crystalline red-orange material grew readily at room temperature. The solution was placed in a refrigerator at -20 °C and allowed to crystallize overnight. The resulting brown supernatant was decanted, and the orange solid was washed Et$_2$O (3 x 5 mL) to remove excess borane and other impurities. The solid was dried to obtain orange crystals (0.216 g, 50.4% yield). The PPN salt of this complex was synthesized in an identical manner. Elem. Anal. (for TBA salt) (%) found (calc'd) for $C_{162}H_{108}B_6F_{90}MnN_9$: C, 48.02 (48.52); H, 2.42 (2.71);

N, 3.15 (3.14). ^{11}B NMR (128 MHz, CD_2Cl_2) δ -136.1; ^{19}F NMR (376 MHz, CD_2Cl_2) δ -127.5 (ps), -161.7 (pt, J_{FF} = 19.7 Hz), -165.7 (ps); ^{1}H NMR (400 MHz, CD_2Cl_2) δ 3.05 (bs, 2H, CH_{but}), 1.59 (bs, 2H, CH_{but}), 1.39 (bs, 2H, CH_{but}), 0.99 (bs, 3H, CH_{but}).; ^{13}C NMR (100 MHz, CD_2Cl_2) δ 59.4 (s), 24.1 (s), 20.0 (s), 13.5 (s).. ATR-IR, ν: 2222 cm^{-1} (CN stretch).

Tetrabutylammonium/Bis(triphenylphosphine)iminium hexakisisocyanotris(2,4,6-trifluorophenyl)boratomanganate(III) (TBA/PPN)$_3$[Mn(CN-B($C_6F_3H_2$)$_3$)$_6$] (9)

(TBA)$_3$[Mn(CN)$_6$] (0.100 g, 0.11 mmol) was dissolved in DCM and added dropwise to a solution of 6.1 equivalents of tris(2,4,6-trifluorophenyl)borane (0.271 g, 0.67 mmol) in DCM. The solution was shaken to give a brown solution. The solution was left at room temperature overnight and became more viscous. The solution was filtered to remove a green impurity, leaving an orange solution. The solution was concentrated *in vacuo*, and Et_2O was added to precipitate a yellow powder. The yellow solid was dried and washed 3 x 5 ml with Et_2O to remove excess borane and other impurities. The solid was dried in vacuo to give a yellow powder (0.116 g, 46.1% yield). Elem. Anal. (for TBA salt) (%) found (calc'd) for $C_{162}H_{144}B_6F_{54}MnN_9$: C, 57.37 (57.86); H, 4.38 (4.32); N, 3.66 (3.75). ^{11}B NMR (128 MHz, CD_2Cl_2) δ -113.7; ^{19}F NMR (376 MHz, CD_2Cl_2) δ -94.1 (m, 2F), -117.2 (ps, 1F); ^{1}H NMR (400 MHz, CD_2Cl_2) δ 6.64 (m, 36H, CH_{Ph}), 3.00 (bs, 24H, CH_{but}), 1.56 (bs, 24H, CH_{but}), 1.39 (bs, 24H, CH_{but}), 1.01 (bs, 36H, CH_{but}). ATR-IR, ν: 2226 cm^{-1} (CN stretch).

Tetrabutylammonium/Bis(triphenylphosphine)iminium hexakisisocyanotris(pentafluorophenyl)boratomanganate(II) (TBA/PPN)$_4$[Mn(CN-B(C_6F_5)$_3$)$_6$] (10)

(TBA)$_3$[Mn(CN-B(C_6F_5)$_3$)$_6$] (50 mg, 0.0125 mmol), 1.2 equivalents of $TBAPF_6$ (2.8 mg, 0.0150 mmol), and 1.2 equivalents of $CoCp_2$ (5.8 mg, 0.0125 mmol) were dissolved separately in minimum DCM. The solution of $TBAPF_6$ was added to the solution of (TBA)$_3$[Mn(CN-B(C_6F_5)$_3$)$_6$], then the solution was

added dropwise to the $CoCp_2$ solution. An immediate color change from orange to brown was observed, and a pale yellow precipitate began to form. The solution was placed in a refrigerator at −20 °C and allowed to crystallize overnight. The supernatant was decanted, and the pale yellow solid was washed 3 x 5 mL with DCM and 3 x 5 mL with diethyl ether to remove excess borane and other impurities. The solid was dried *in vacuo* to obtain yellow crystals (49.1 mg, 92.6 %). Note that this product is sparingly soluble in DCM. The PPN salt of this complex was synthesized in an identical manner. ^{11}B NMR (128 MHz, MeCN) δ −60.4; ^{19}F NMR (376 MHz, MeCN) δ −131.52 (d, J = 18.3 Hz, 1F), −165.17 (t, J = 19.1 Hz, 2F), −168.86 (pt, J = 18.1 Hz, 2F); ^{1}H NMR (400 MHz, MeCN) δ 3.07 (t, J = 8.3 Hz, 2H, CH_{but}), 1.59 (p, J = 7.8 Hz, 2H, CH_{but}), 1.34 (pp, J = 7.5 Hz, 2H, CH_{but}), 0.96 (pt, J = 7.4 Hz, 3H, CH_{but}). ATR-IR, ν: 2151 cm^{-1} (CN stretch).

Tetrabutylammonium/Bis(triphenylphosphine)iminium hexakisisocyanotris(2,4,6-trifluorophenyl)boratomanganate(II) (TBA/PPN)$_3$[Mn(CN-B($C_6F_3H_2$)$_3$)$_6$] (11)

$(TBA)_3[Mn(CN\text{-}B(2,4,6\text{-}F_3C_6H_2)_3)_6]$ (50 mg), 1.2 equivalents of $TBAPF_6$, and 1.2 equivalents of $CoCp_2$ were dissolved separately in minimum DCM. The solution of $TBAPF_6$ was added to the solution of $(TBA)_3[Mn(CN\text{-}B(2,4,6\text{-}F_3C_6H_2)_3)_6]$, then the combined solution was added dropwise to the $CoCp_2$ solution. An immediate color change from yellow to light brown and appearance of yellow crystalline precipitate was observed. The solution was placed in a refrigerator at −20 °C and allowed to crystallize overnight. The supernatant was decanted, and the yellow solid was washed with 3 x 5 mL diethyl ether and 3 x 5 mL chloroform to remove excess borane and other impurities. The solid was dried in vacuo to obtain yellow crystals. Note that this compound is soluble in DCM and decomposes in MeCN. The PPN salt of this complex was synthesized in an identical manner. ^{11}B NMR (128 MHz, CD_2Cl_2) δ −19.6; ^{19}F NMR (376 MHz, CD_2Cl_2) δ −99.84 (d, J = 289.8 Hz), −115.65; ^{1}H NMR (400 MHz, CD_2Cl_2) δ 6.65 (s, 3H), 3.01 (s, 2H), 1.51 and 1.10 (m, 7H). ATR-IR, ν: 2148 cm^{-1} (CN stretch).

Tetrabutylammonium/Bis(triphenylphosphine)iminium/Tetraphenylarsonium hexakisisocyanotriphenylboratochromate(III) (TBA/PPN/$Ph_4As)_3$[Cr(CN-$BPh_3)_6$] (12)

$(TBA)_3[Cr(CN)_6]$ (0.114 g, 0.144 mmol) was dissolved in DCM and added dropwise to a stirred solution of 6.8 equivalents of BPh_{33} (0.202 g, 0.834 mmol) in DCM. An immediate color change from pale yellow to bright yellow was observed. The solvent was evaporated in vacuo. The yellow solid was washed 3 x 5 mL with Et_2O, followed by 3 x 5 mL with hexanes, and the product was dried in vacuo to yield $(TBA)_3[Cr(CN\text{-}BPh_3)_6]$ as a yellow solid (0.259 g, 85.6% yield). The PPN salt of this complex was synthesized in an identical manner. Elem. Anal. (for TBA salt) (%) found (calc'd) for $C_{162}H_{198}B_6CrN_9$: C, 79.72 (81.47); H, 7.87 (8.36); N, 5.01 (5.28). ATR-IR, ν: 2202 cm^{-1} (CN stretch).

Electrochemistry

Room temperature cyclic voltammetry was performed in a nitrogen-filled glove box with a Gamry Reference 600 potentiostat using a three-electrode cell. The working electrode was a 3 mm diameter glassy carbon (CH Instruments) working electrode, a 0.01 M $Ag^{+/0}$ in 0.1 M $TBAPF_6$/MeCN quasireference electrode (Bioanalytical Systems, Inc.), and a platinum wire counter electrode (Kurt J. Lesker). Potentiostatic electrochemical impedance spectra (PEIS) were recorded to obtain Nyquist plots to determine the uncompensated resistance. 85% of the uncompensated resistance was accounted for using electronic compensation. 0.1-0.2 M $TBAPF_6$ was used as the electrolyte for all experiments.

Low temperature voltammetry experiments were performed using either a 50:50 ethylene glycol:water temperature bath with a minimum temperature of −25 °C and a Gamry Reference 600 potentiostat, a 3 mm diameter glassy carbon (CH Instruments) working electrode, a 0.01 M $Ag^{+/0}$ in 0.1 M $TBAPF_6$/MeCN quasireference electrode (Bioanalytical Systems, Inc.), and a platinum wire counter electrode in acetonitrile with 0.2 M $TBAPF_6$ or a Tenney TUJR thermal chamber (minimum temperature of −70 °C) in butyronitrile with 0.5 M $TBAClO_4$, a Princeton Applied Research PARSTAT MC potentiostat, a 3 mm diameter glassy carbon working electrode, a Ag pseudoreference electrode, and a platinum counter electrode. Potentiostatic electrochemical impedance spectra (PEIS) were recorded to obtain Nyquist plots to electronically correct for at least 85% of the uncompensated resistance. The cell was degassed with nitrogen or argon for fifteen minutes prior to taking measurements.

NMR Spectra

Figure 5.36. ^{11}B NMR spectrum of $(TBA)_4[Ru(CN\text{-}B(C_6F_5)_3)_6]$ (**2**) in CD_3CN.

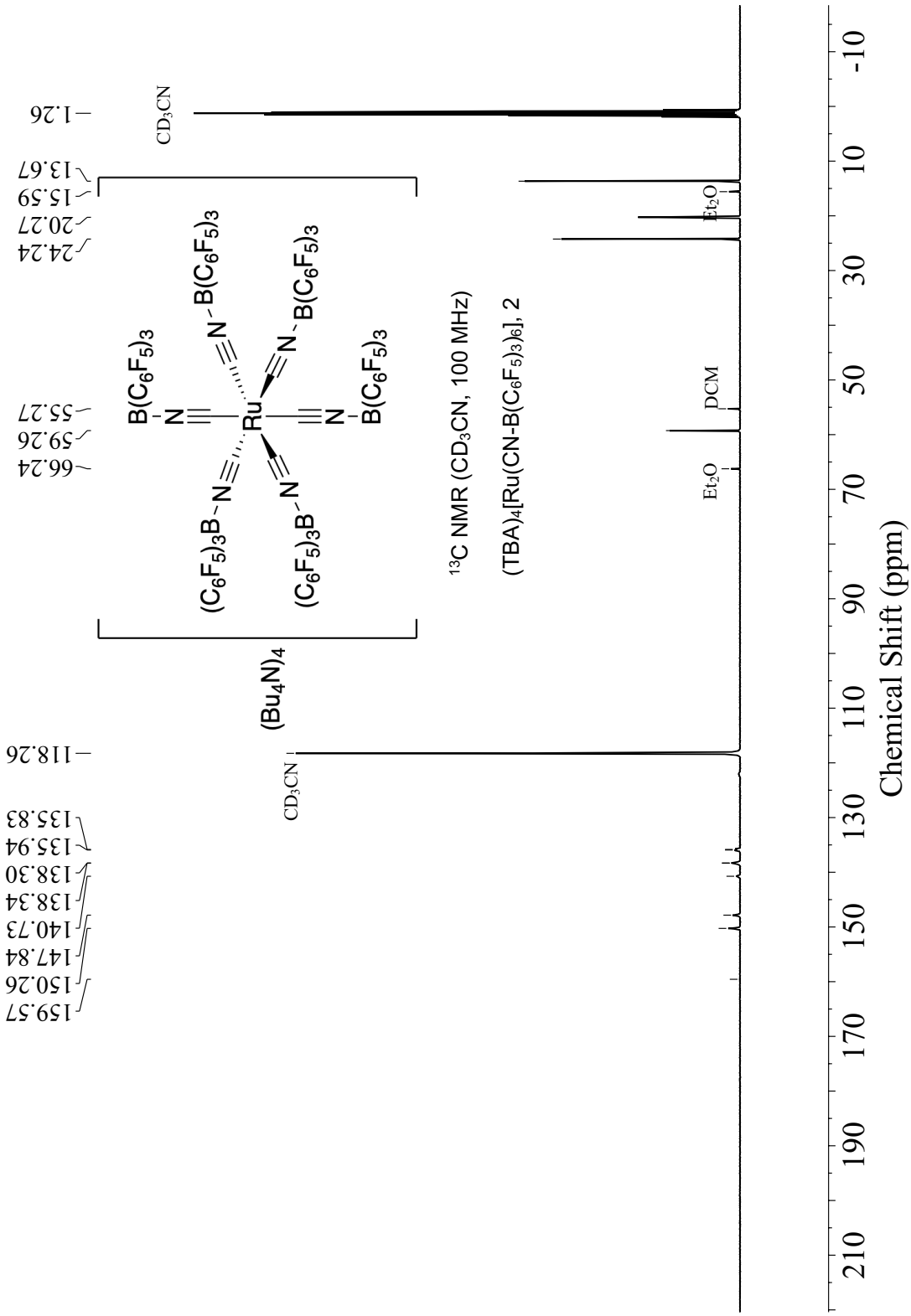

Figure 5.37. ^{13}C NMR spectrum of $(TBA)_4[Ru(CN\text{-}B(C_6F_5)_3)_6]$ (**2**) in CD_3CN.

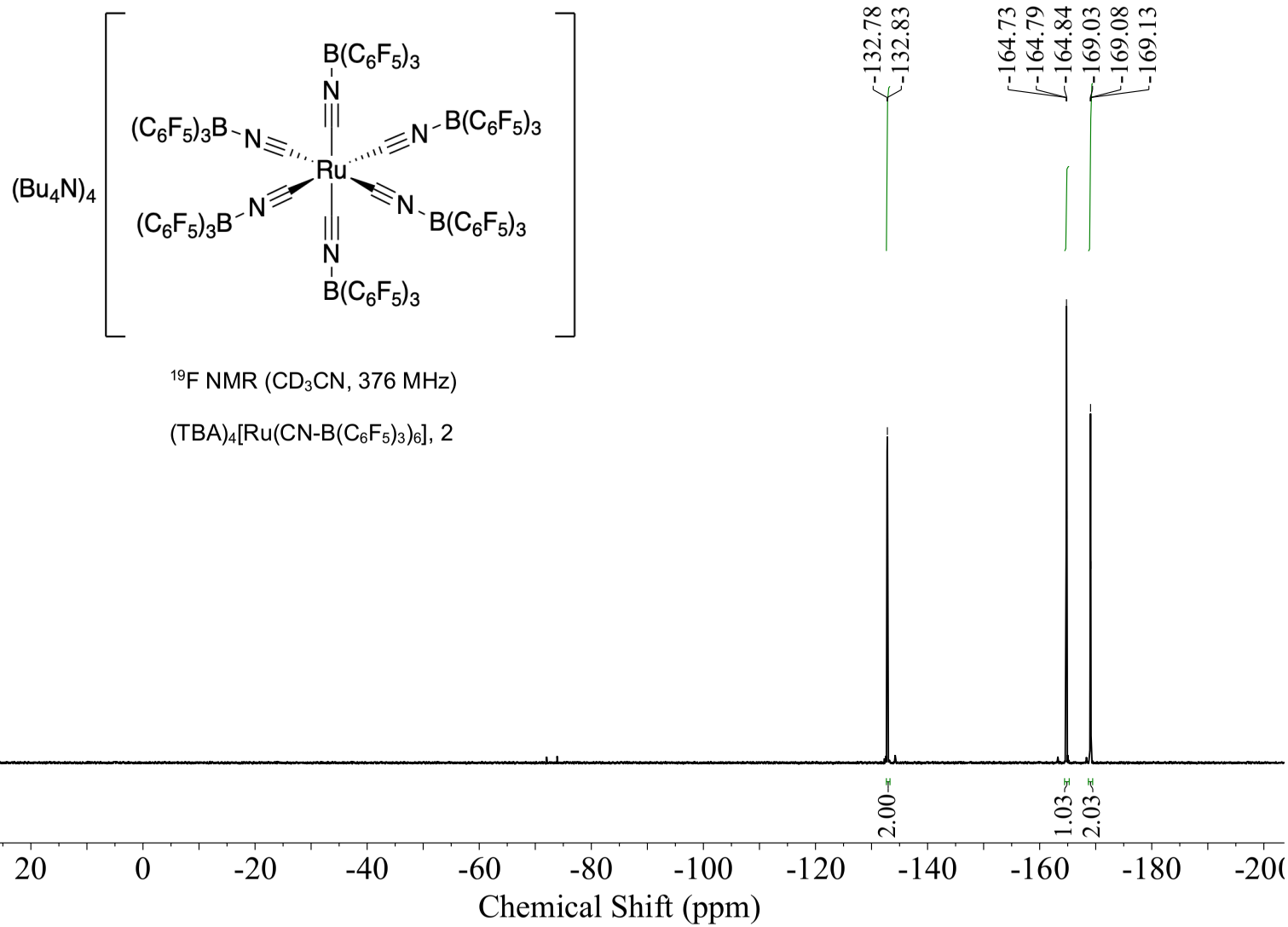

Figure 5.38. ^{19}F NMR spectrum of $(TBA)_4[Ru(CN\text{-}B(C_6F_5)_3)_6]$ (**2**) in CD_3CN.

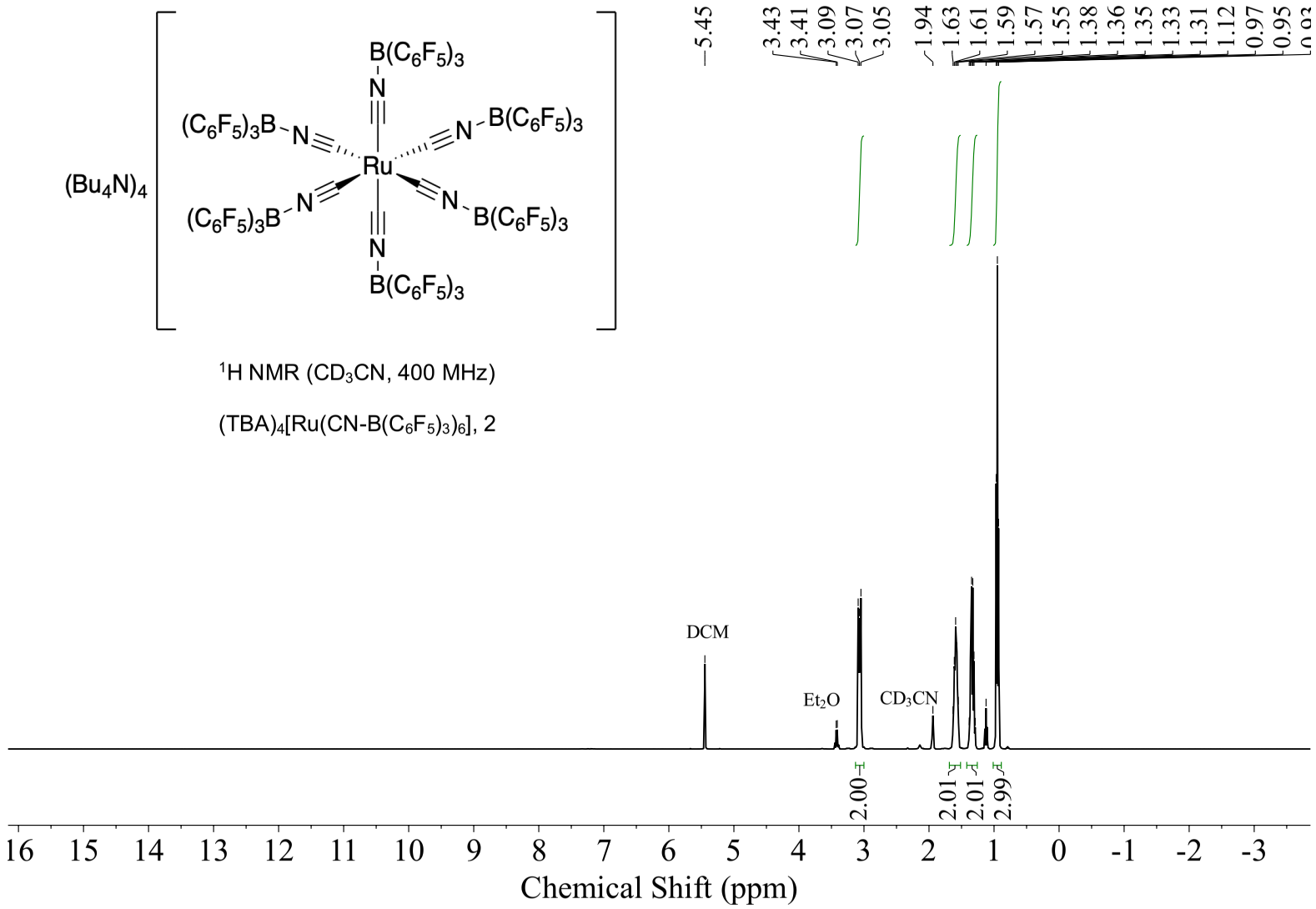

Figure 5.39. ^{1}H NMR spectrum of $(TBA)_4[Ru(CN\text{-}B(C_6F_5)_3)_6]$ (**2**) in CD_3CN.

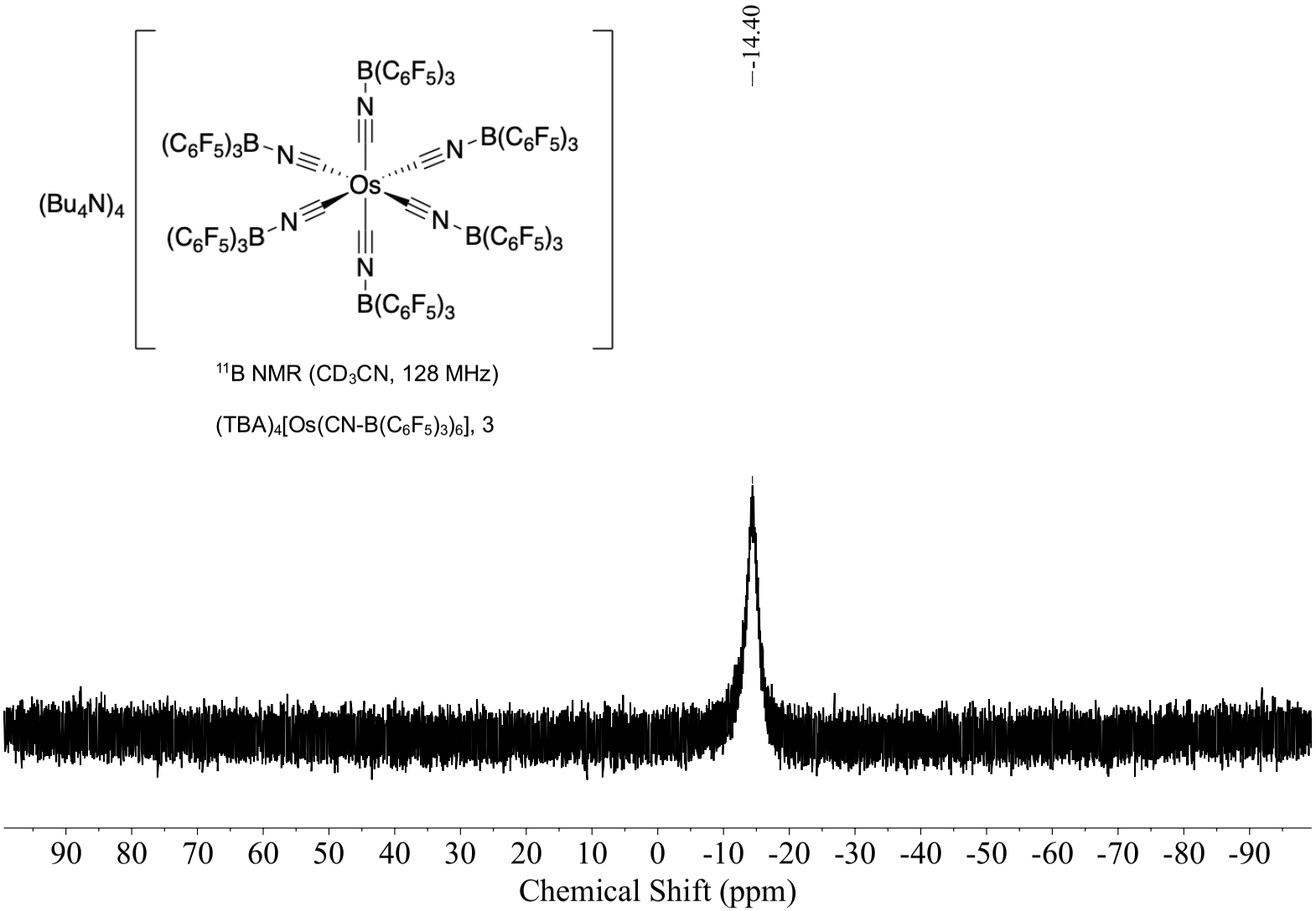

Figure 5.40. ^{11}B NMR spectrum of (TBA)$_4$[Os(CN-B(C$_6$F$_5$)$_3$)$_6$] (**3**) in CD$_3$CN.

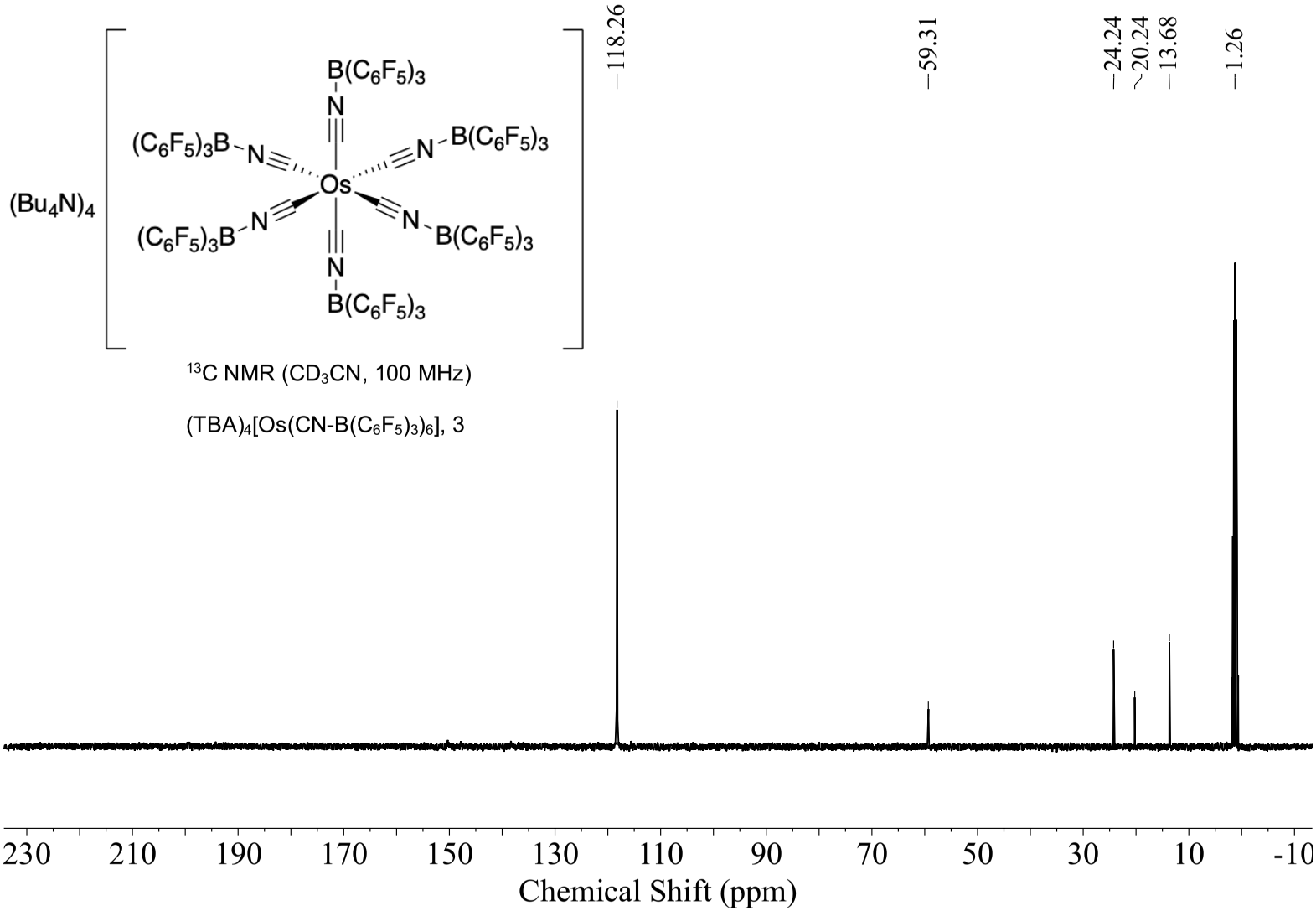

Figure 5.41. ^{13}C NMR spectrum of $(TBA)_4[Os(CN\text{-}B(C_6F_5)_3)_6]$ (**3**) in CD_3CN.

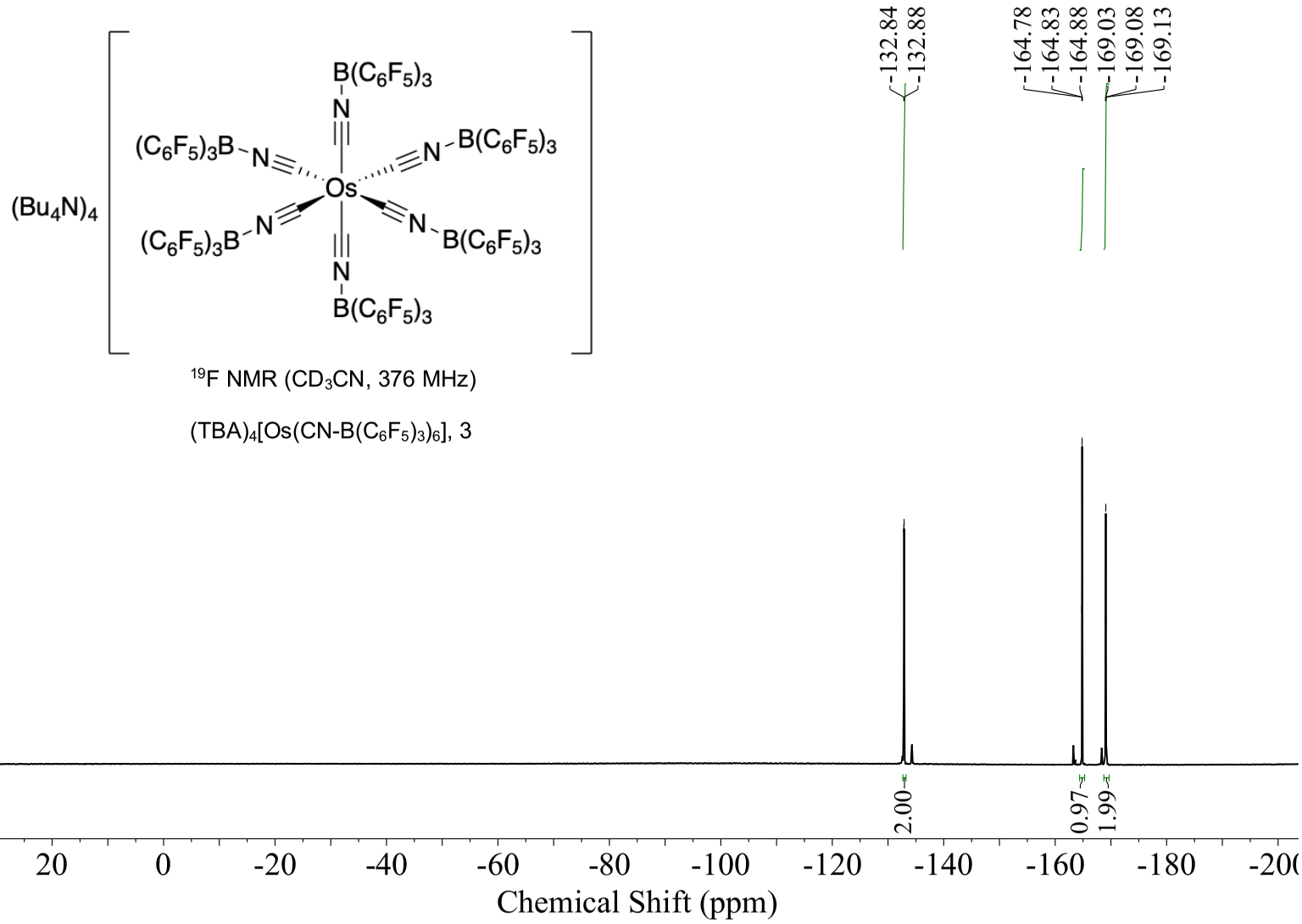

Figure 5.42. ^{19}F NMR spectrum of $(TBA)_4[Os(CN\text{-}B(C_6F_5)_3)_6]$ (**3**) in CD_3CN.

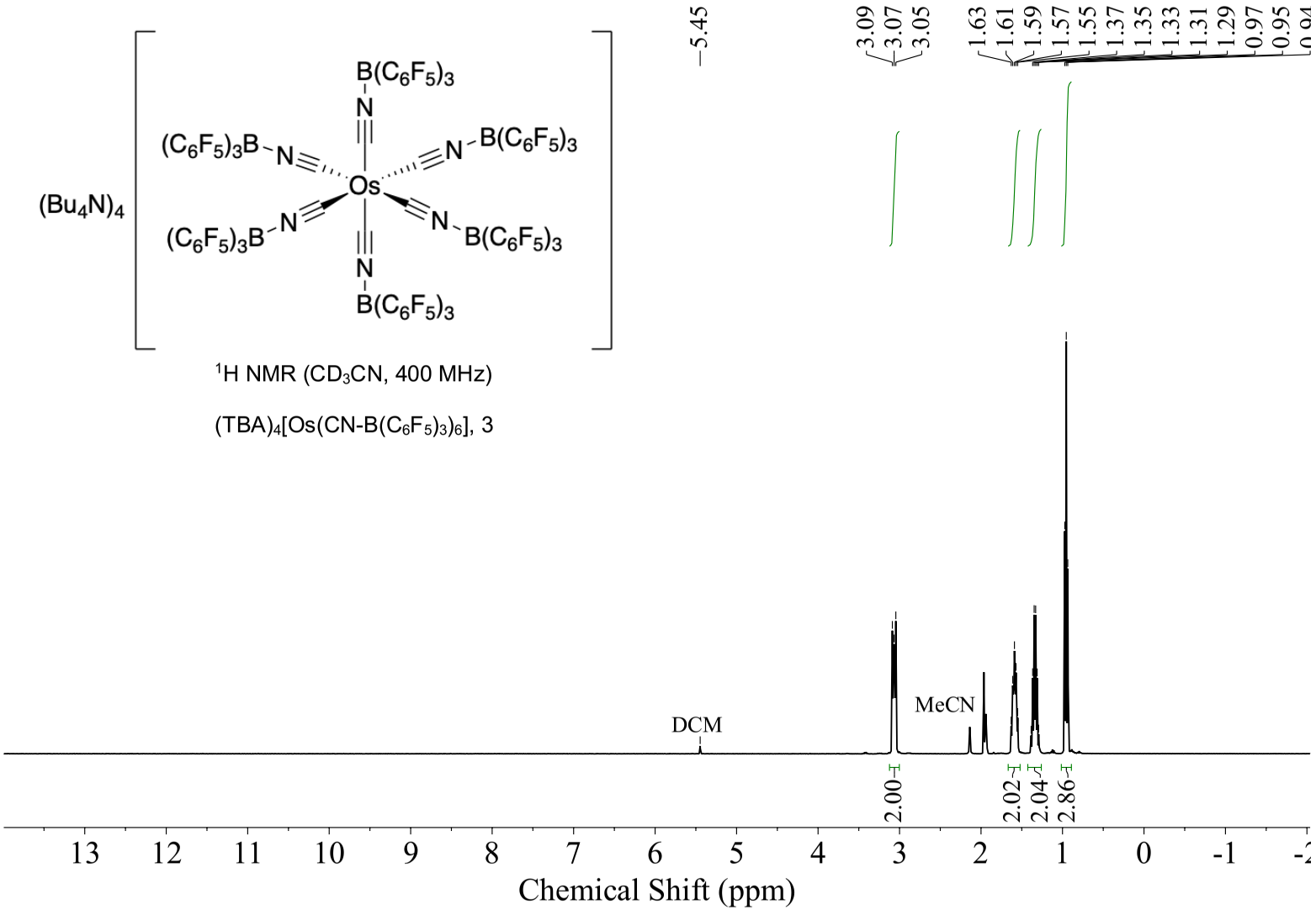

Figure 5.43. ^{1}H NMR spectrum of (TBA)$_4$[Os(CN-B(C$_6$F$_5$)$_3$)$_6$] (**3**) in CD$_3$CN.

^{11}B NMR (CD_2Cl_2, 128 MHz)

$(TBA)_3[Fe(CN\text{-}B(C_6F_5)_3)_6]$, 4

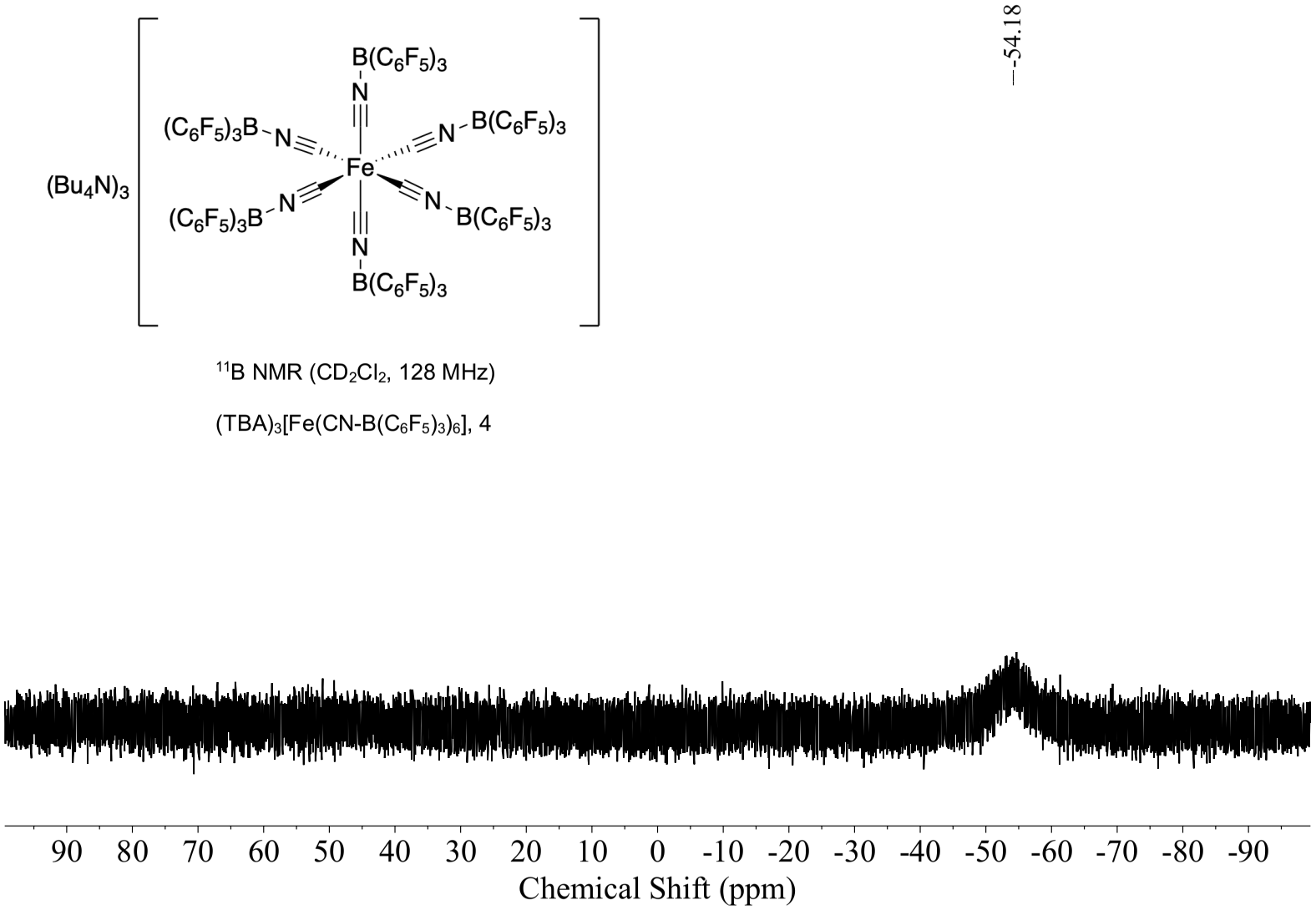

Figure 5.44. ^{11}B NMR spectrum of $(TBA)_3[Fe(CN\text{-}B(C_6F_5)_3)_6]$ (**4**) in CD_2Cl_2.

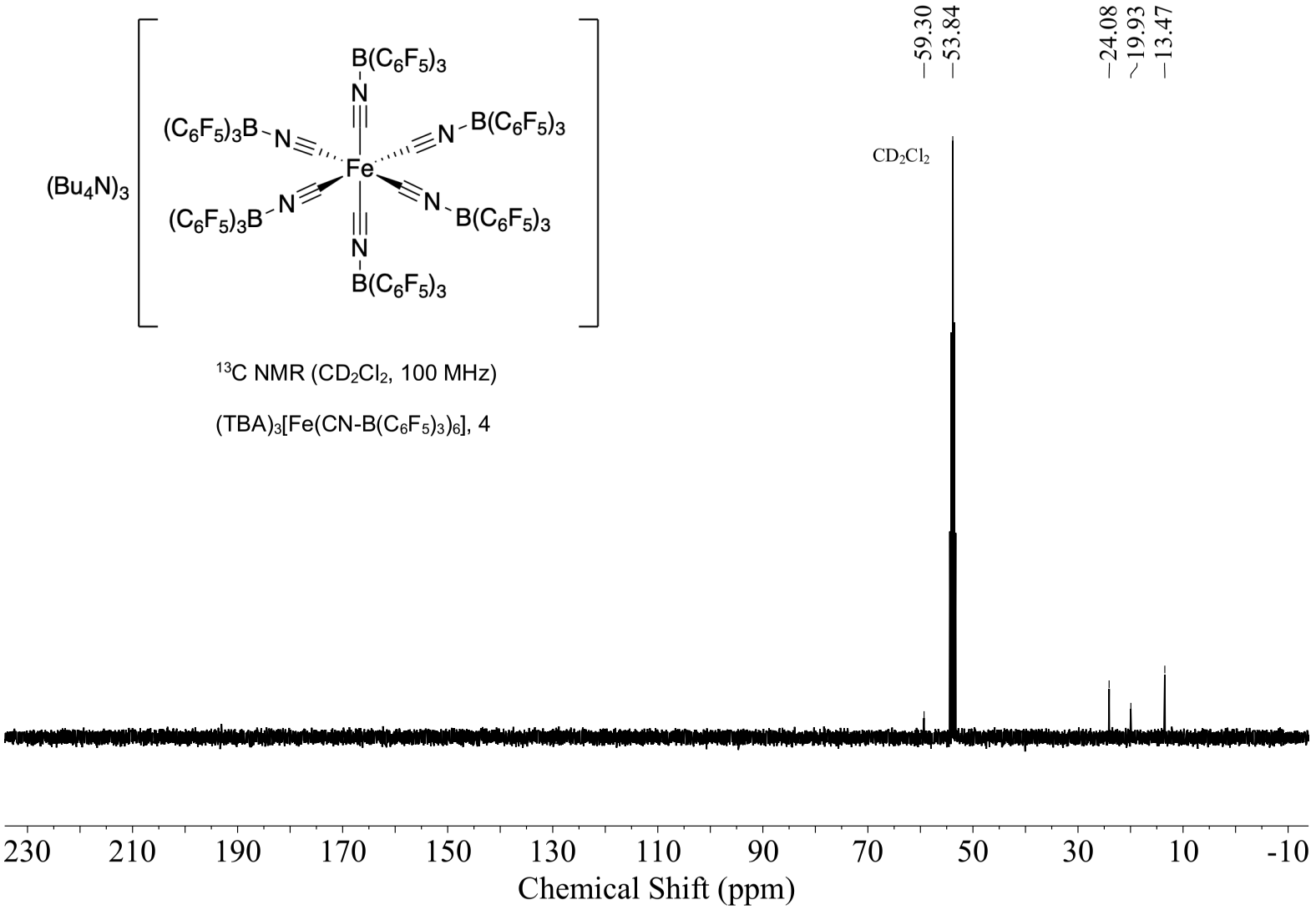

Figure 5.45. ^{13}C NMR spectrum of $(TBA)_3[Fe(CN\text{-}B(C_6F_5)_3)_6]$ (**4**) in CD_2Cl_2.

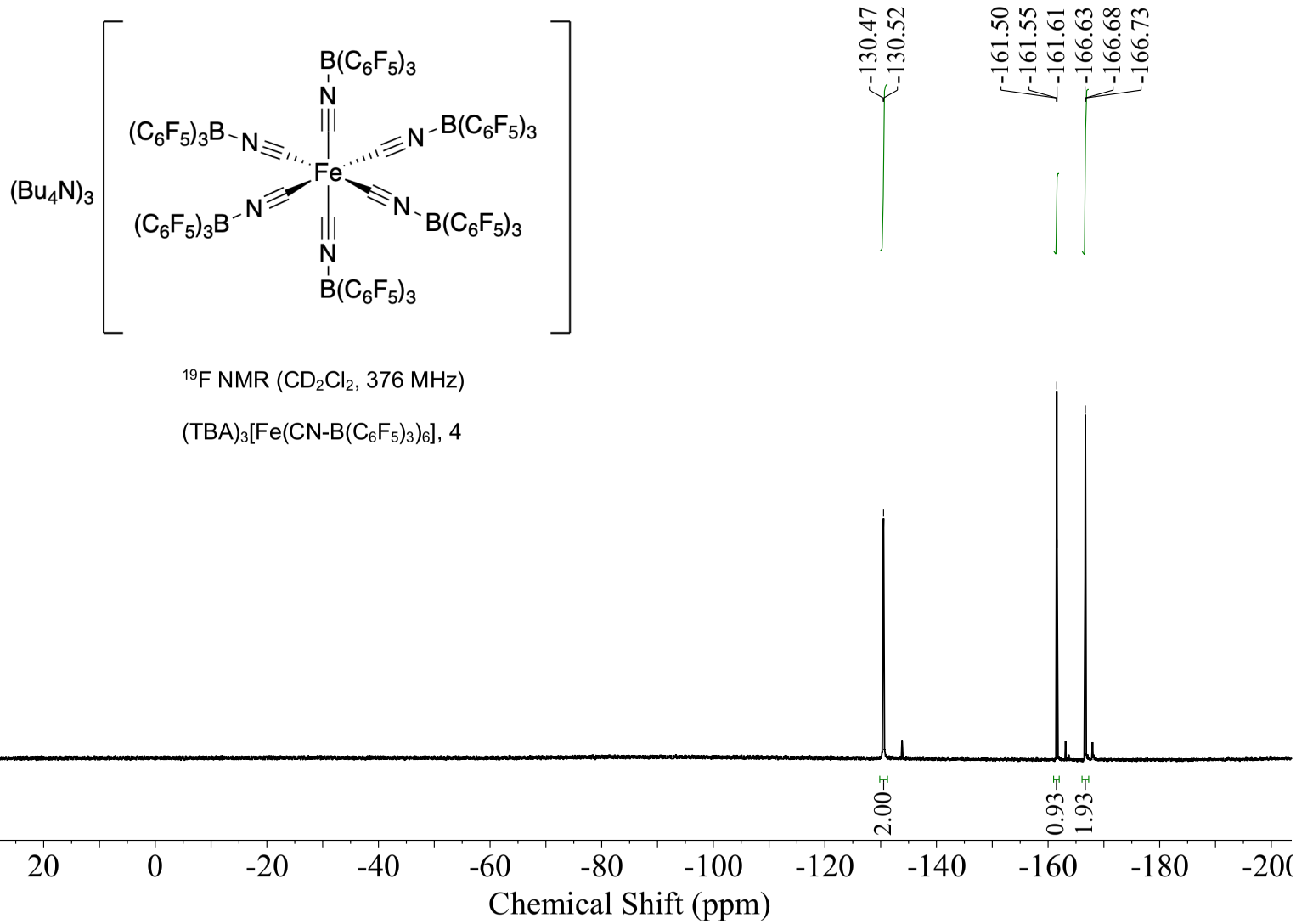

Figure 5.46. ^{19}F NMR spectrum of $(TBA)_3[Fe(CN\text{-}B(C_6F_5)_3)_6]$ (**4**) in CD_2Cl_2.

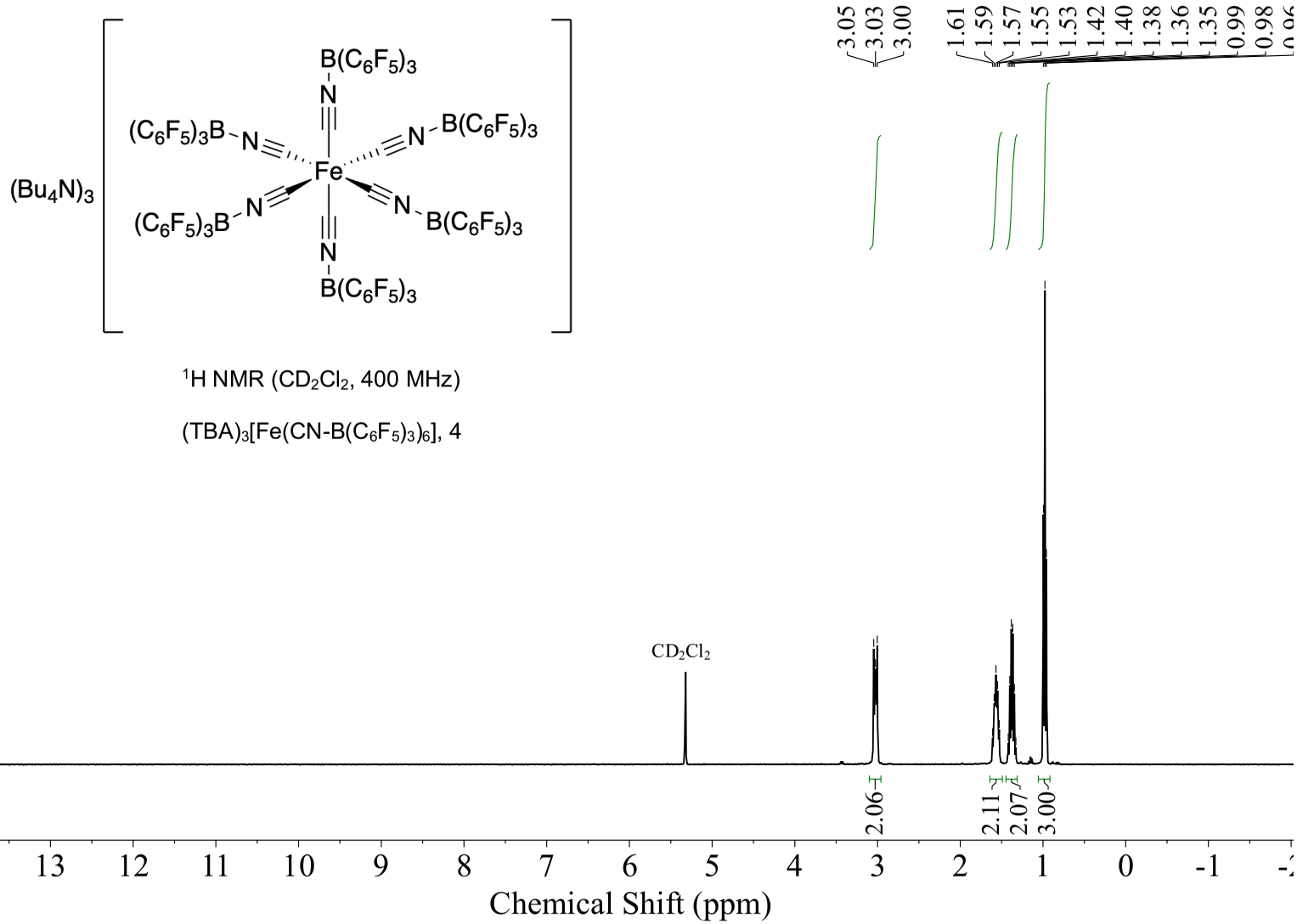

Figure 5.47. ^{1}H NMR spectrum of $(TBA)_3[Fe(CN\text{-}B(C_6F_5)_3)_6]$ (**4**) in CD_2Cl_2.

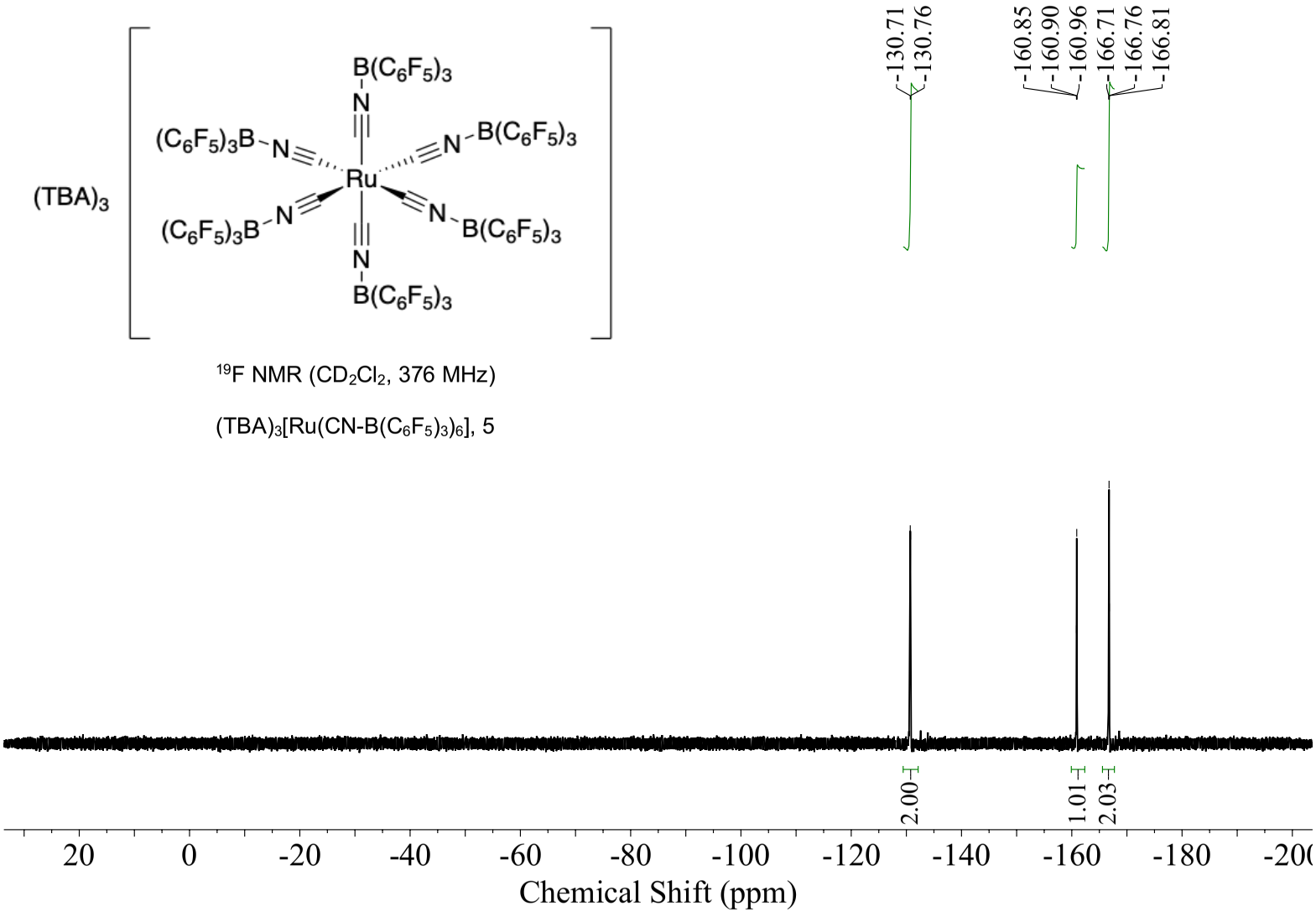

^{19}F NMR (CD_2Cl_2, 376 MHz)

$(TBA)_3[Ru(CN\text{-}B(C_6F_5)_3)_6]$, 5

Figure 5.48. ^{19}F NMR spectrum of $(TBA)_3[Ru(CN\text{-}B(C_6F_5)_3)_6]$ (**5**) in CD_2Cl_2.

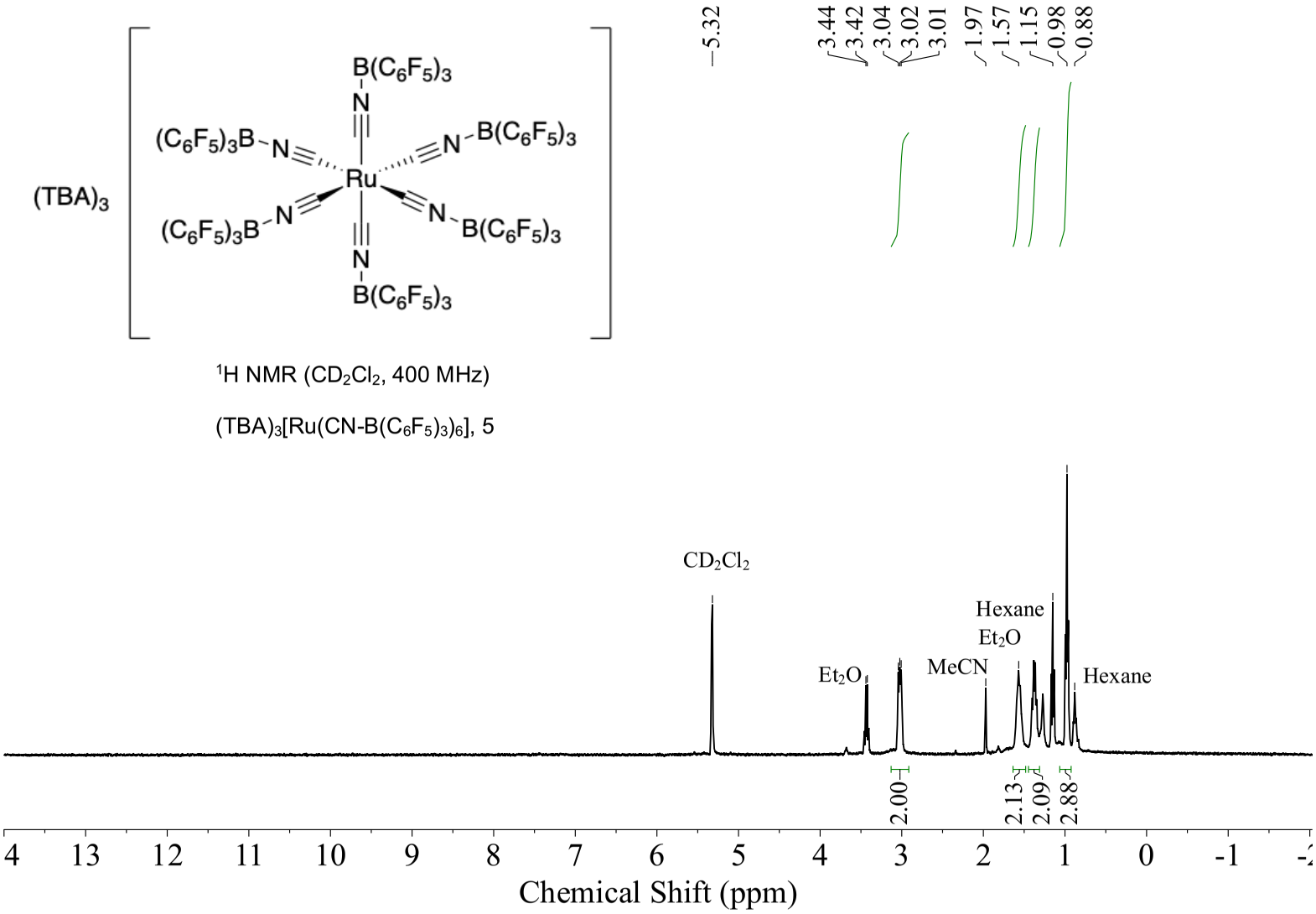

Figure 5.49. ^{1}H NMR spectrum of $(TBA)_3[Ru(CN\text{-}B(C_6F_5)_3)_6]$ (**5**) in CD_2Cl_2.

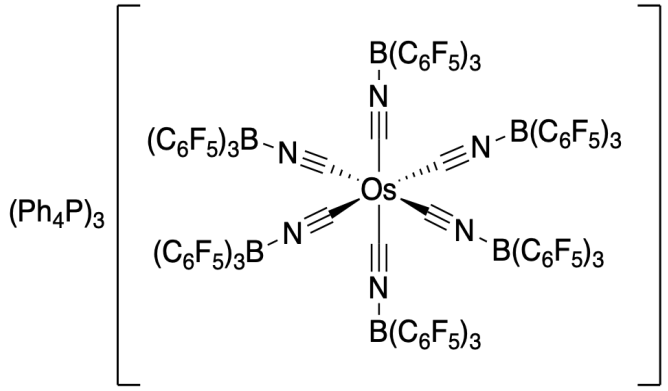

^{11}B NMR (CD_2Cl_2, 128 MHz)

$(Ph_4P)_3[Os(CN\text{-}B(C_6F_5)_3)_6]$, 6

-37.62

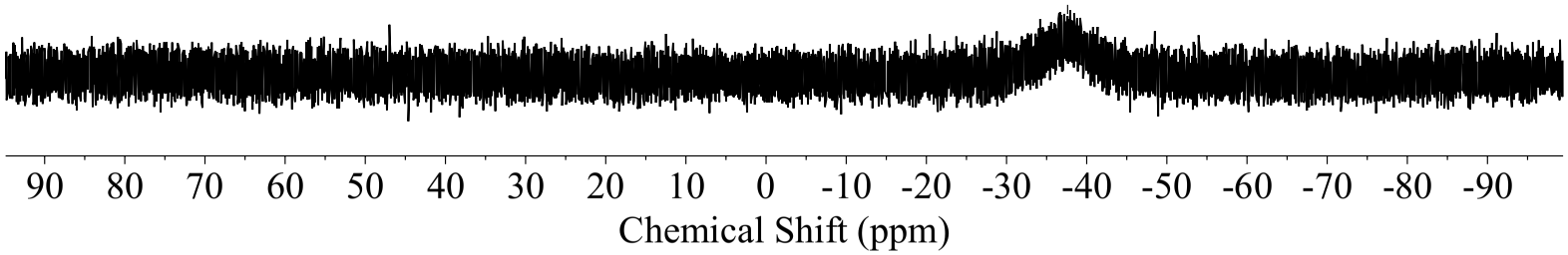

Figure 5.50. ^{11}B NMR spectrum of $(PPh_4)_3[Os(CN\text{-}B(C_6F_5)_3)_6]$ (**6**) in CD_2Cl_2.

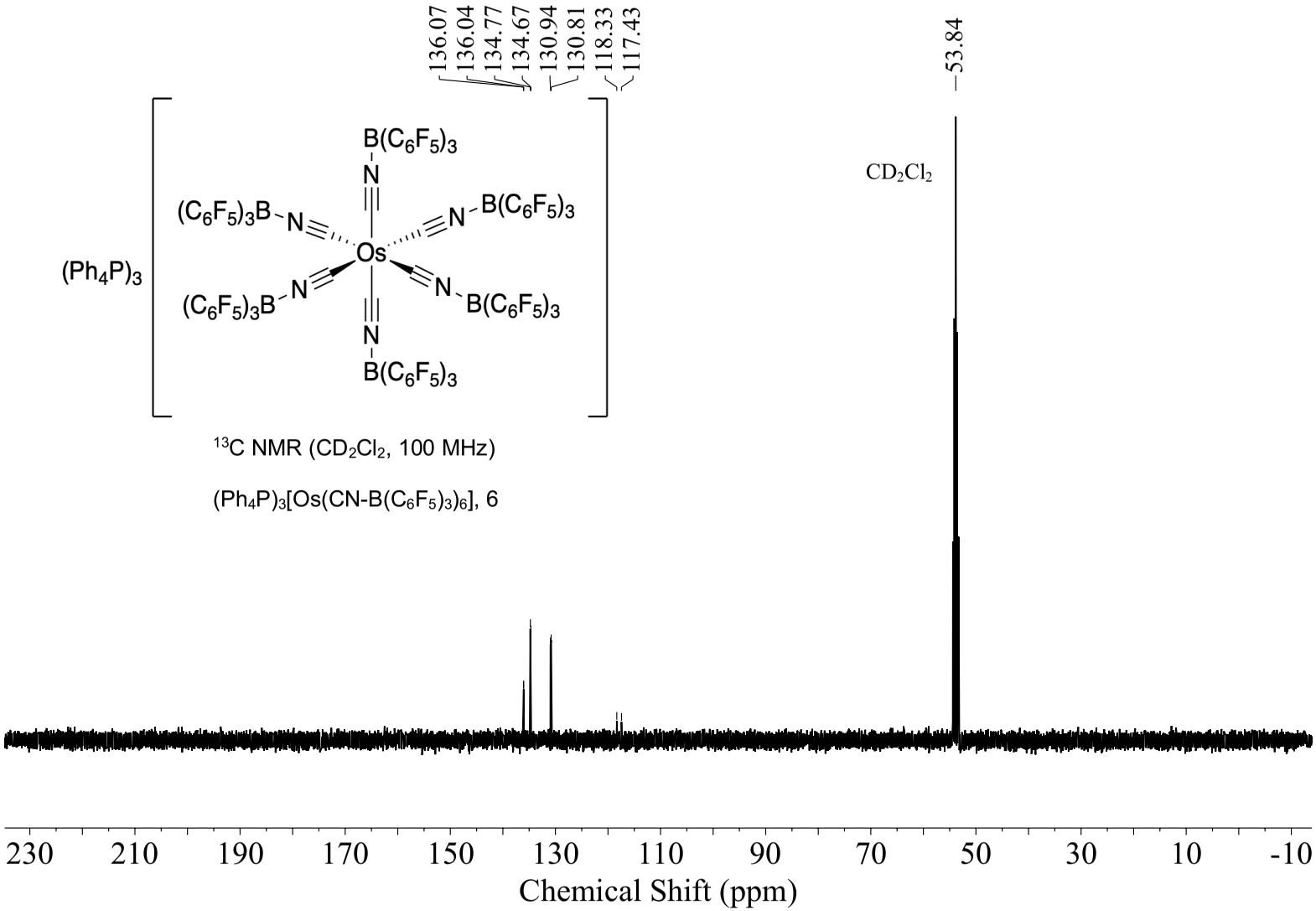

Figure 5.51. ^{13}C NMR spectrum of $(PPh_4)_3[Os(CN\text{-}B(C_6F_5)_3)_6]$ (**6**) in CD_2Cl_2.

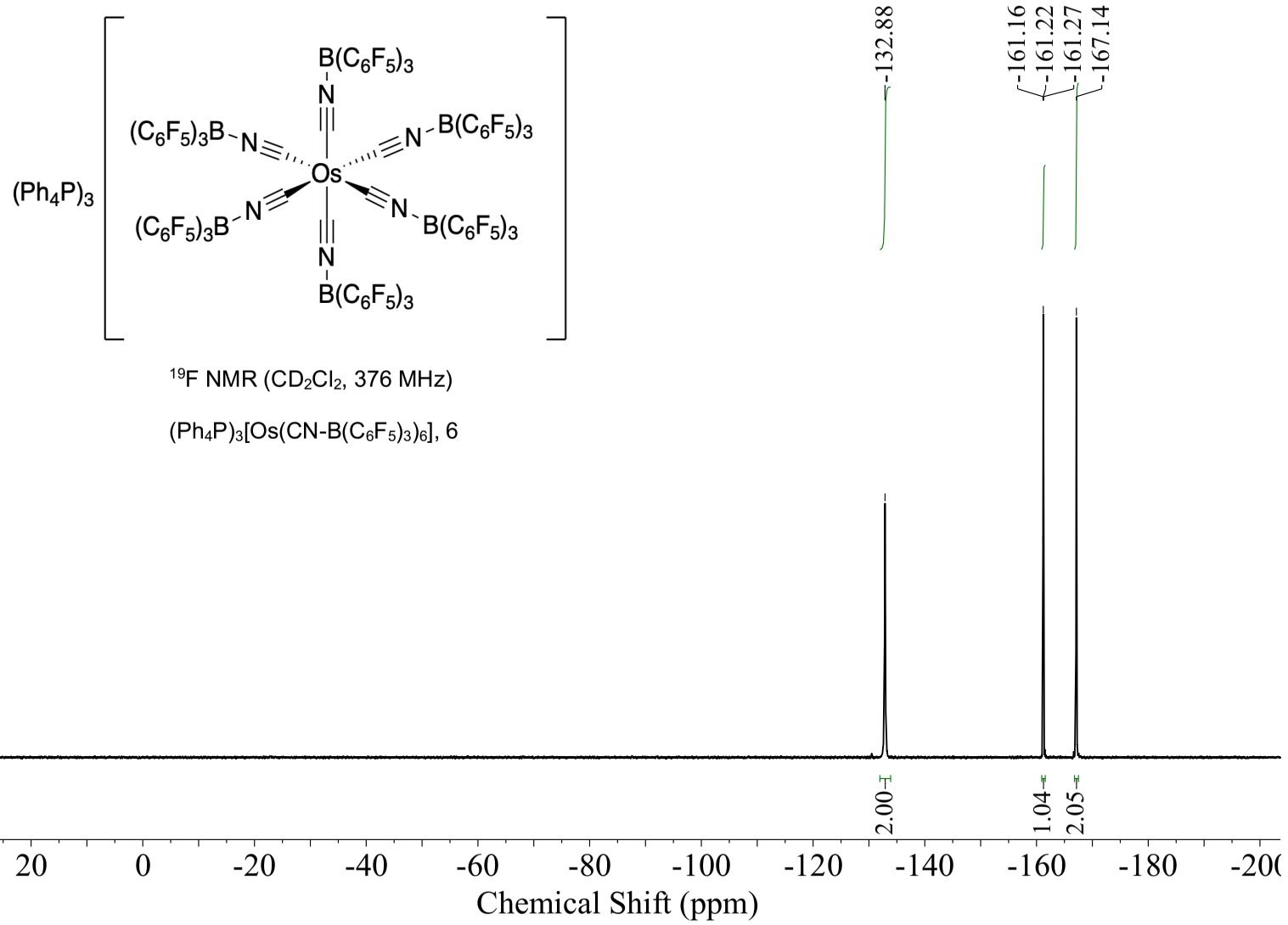

Figure 5.52. ^{19}F NMR spectrum of $(PPh_4)_3[Os(CN\text{-}B(C_6F_5)_3)_6]$ (**6**) in CD_2Cl_2.

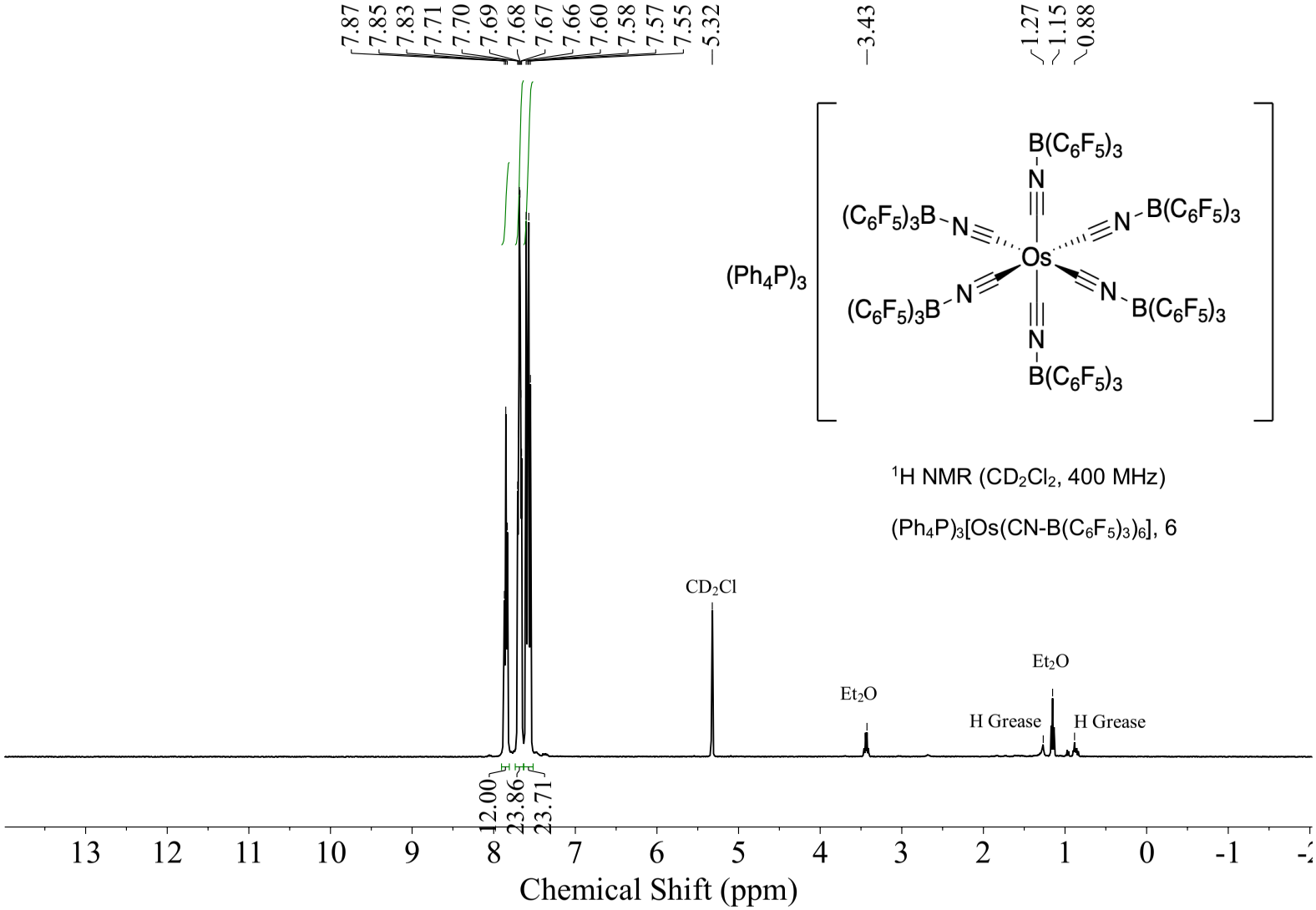

Figure 5.53. ^{1}H NMR spectrum of $(PPh_4)_3[Os(CN\text{-}B(C_6F_5)_3)_6]$ (**6**) in CD_2Cl_2.

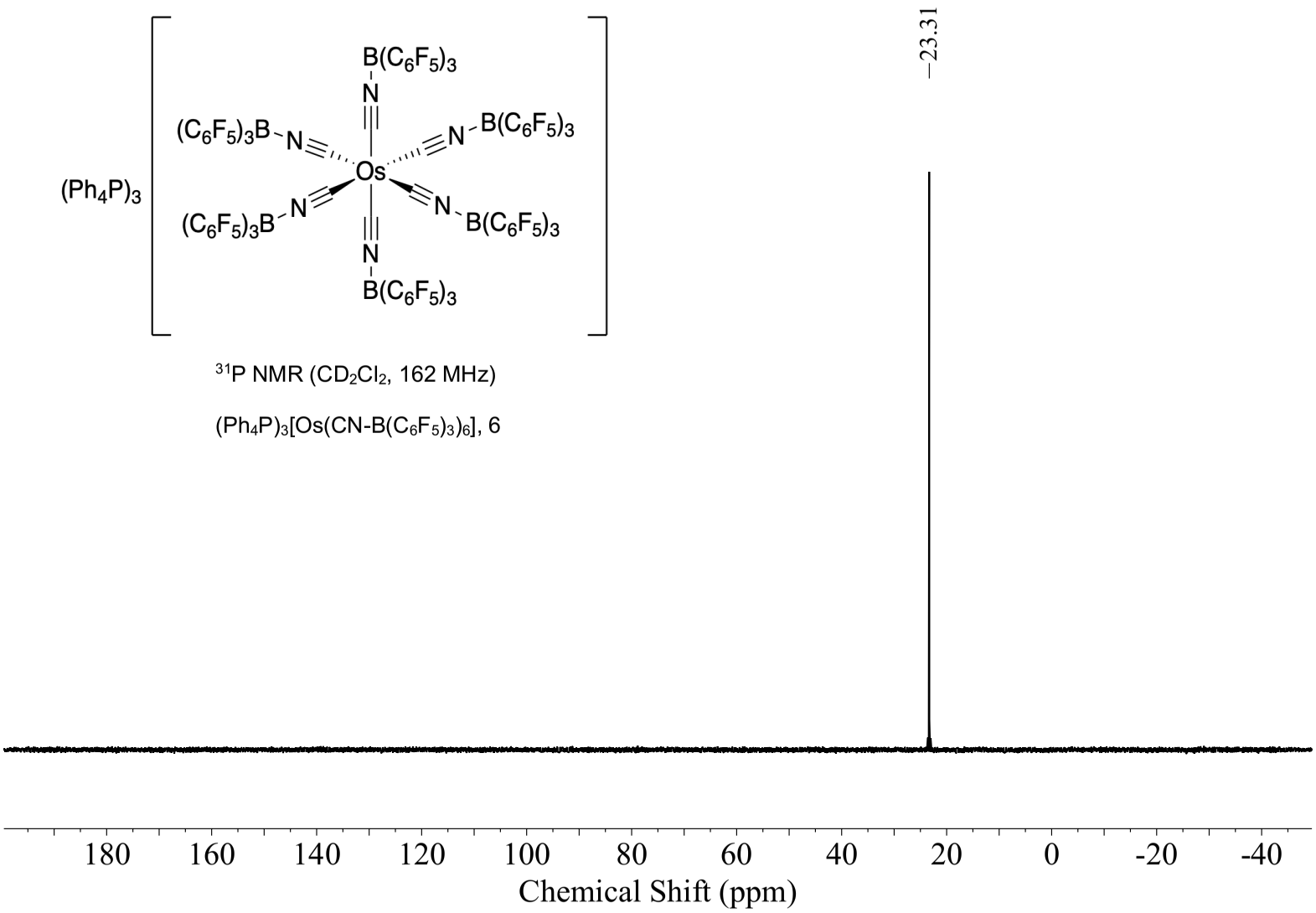

Figure 5.54. ^{31}P NMR spectrum of $(PPh_4)_3[Os(CN\text{-}B(C_6F_5)_3)_6]$ (**6**) in CD_2Cl_2.

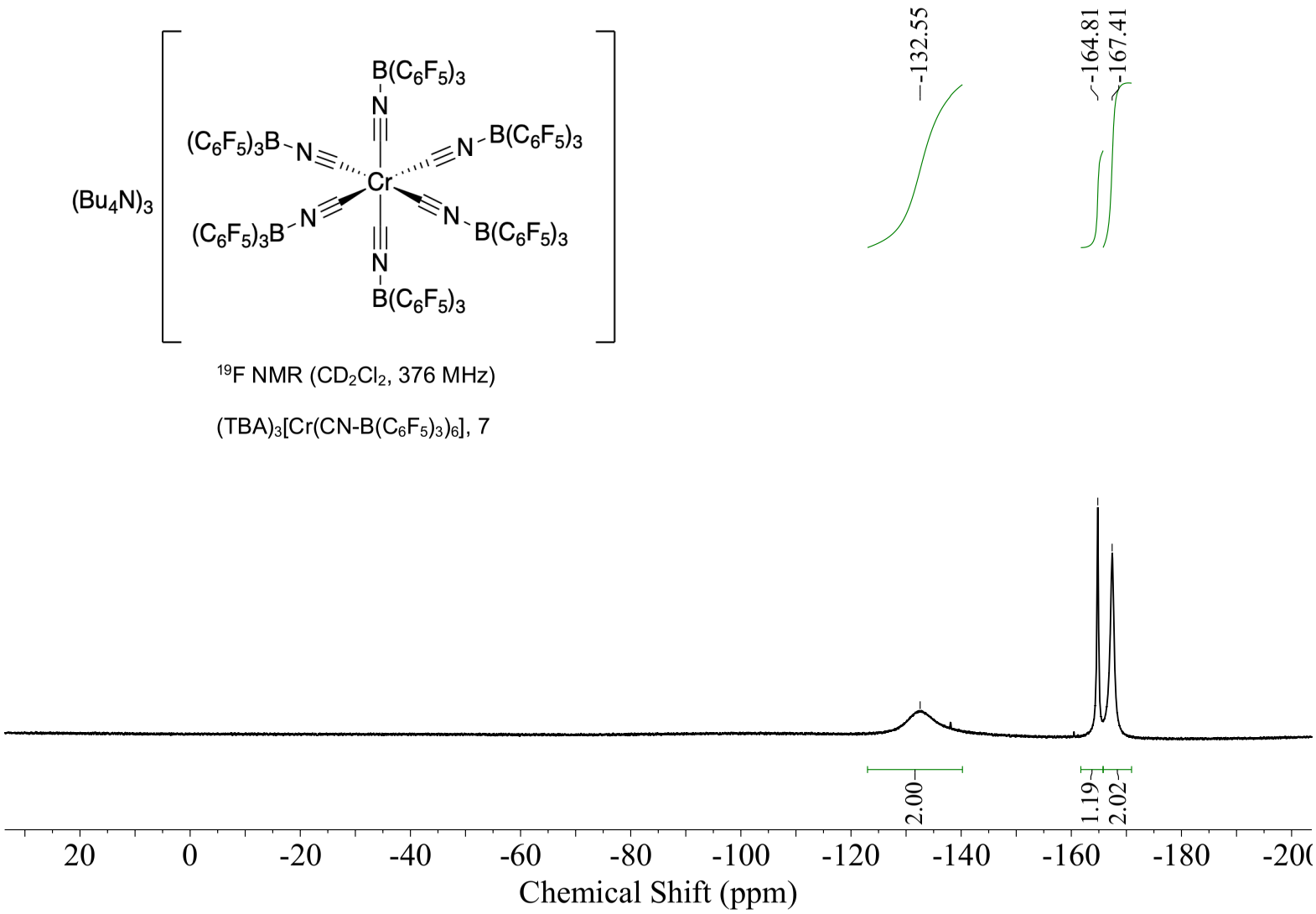

Figure 5.55. ^{19}F NMR spectrum of (TBA)$_3$[Cr(CN-B(C$_6$F$_5$)$_3$)$_6$] (**7**) in CD_2Cl_2.

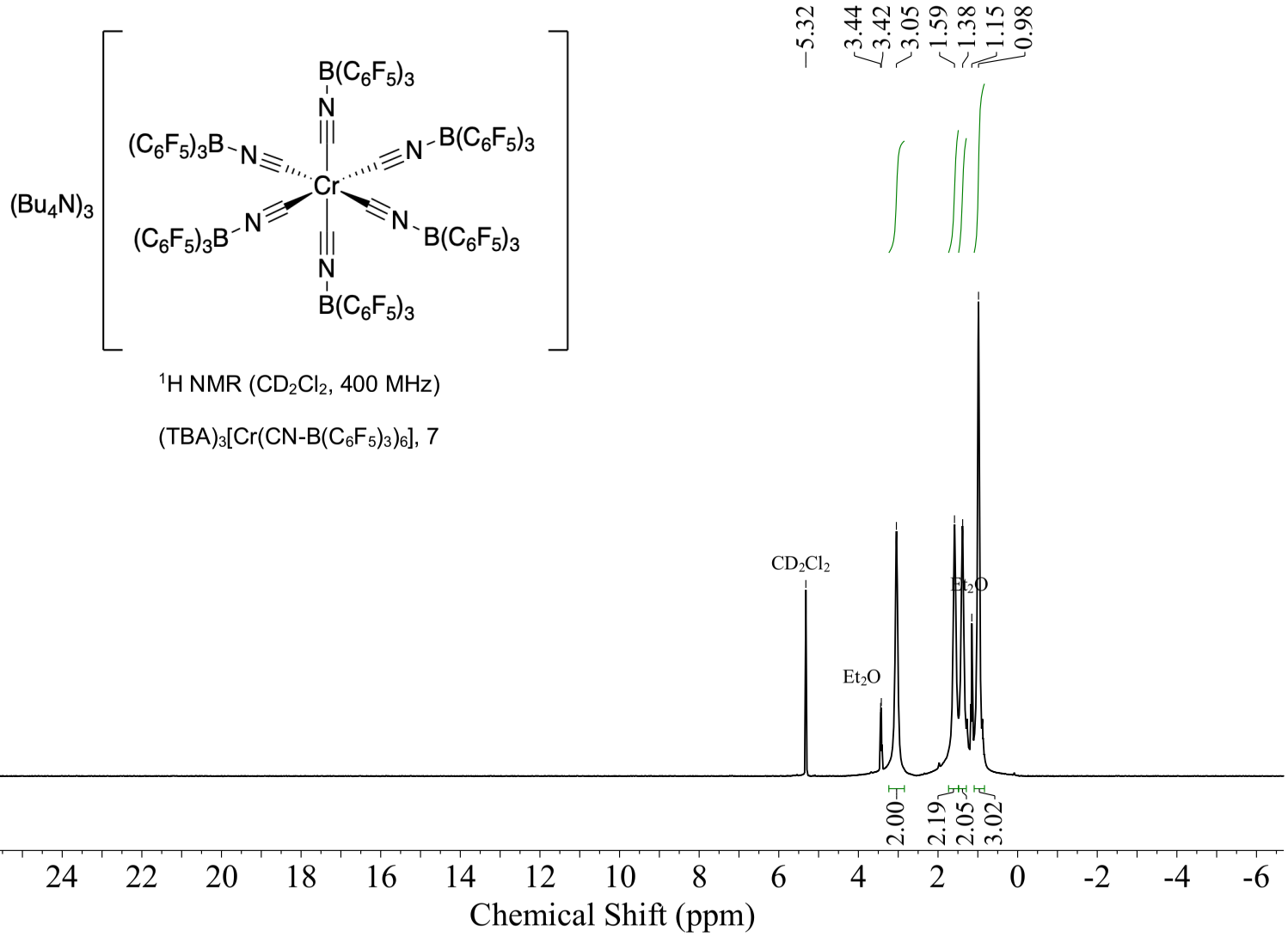

Figure 5.56. ^{1}H NMR spectrum of $(TBA)_3[Cr(CN\text{-}B(C_6F_5)_3)_6]$ (**7**) in CD_2Cl_2.

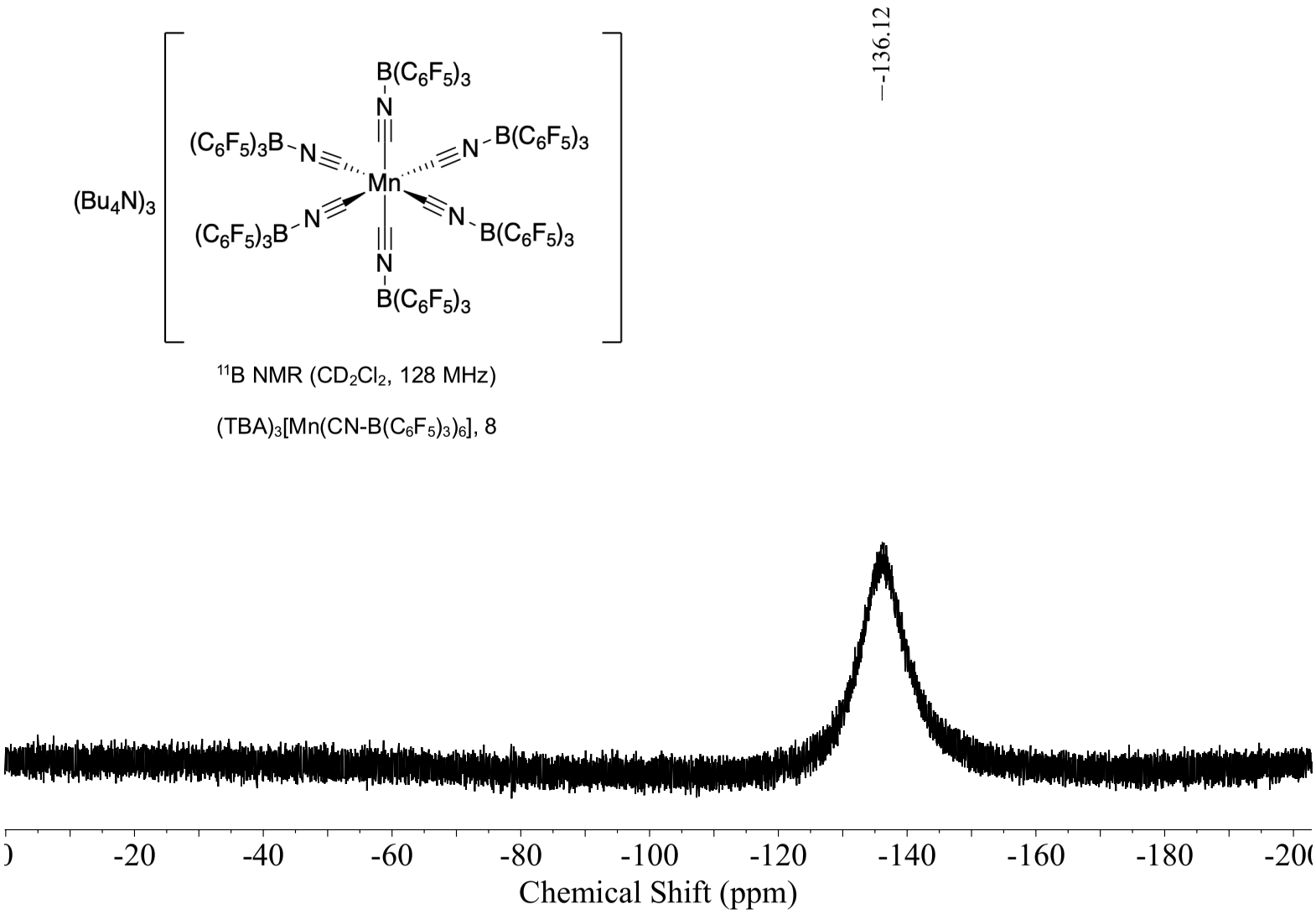

Figure 5.57. ^{11}B NMR spectrum of $(TBA)_3[Mn(CN\text{-}B(C_6F_5)_3)_6]$ (**8**) in CD_2Cl_2.

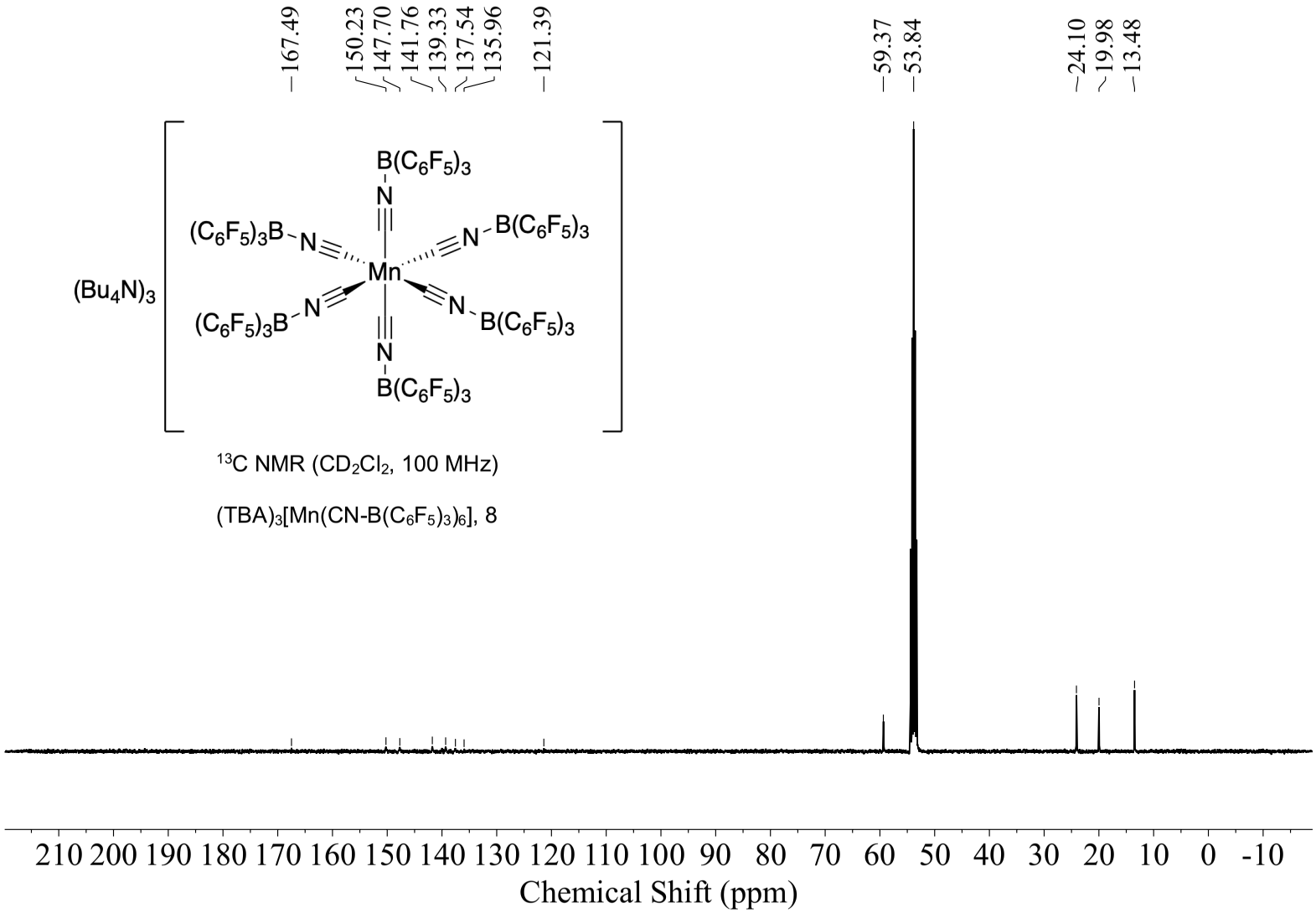

Figure 5.58. ^{13}C NMR spectrum of $(TBA)_3[Mn(CN\text{-}B(C_6F_5)_3)_6]$ (**8**) in CD_2Cl_2.

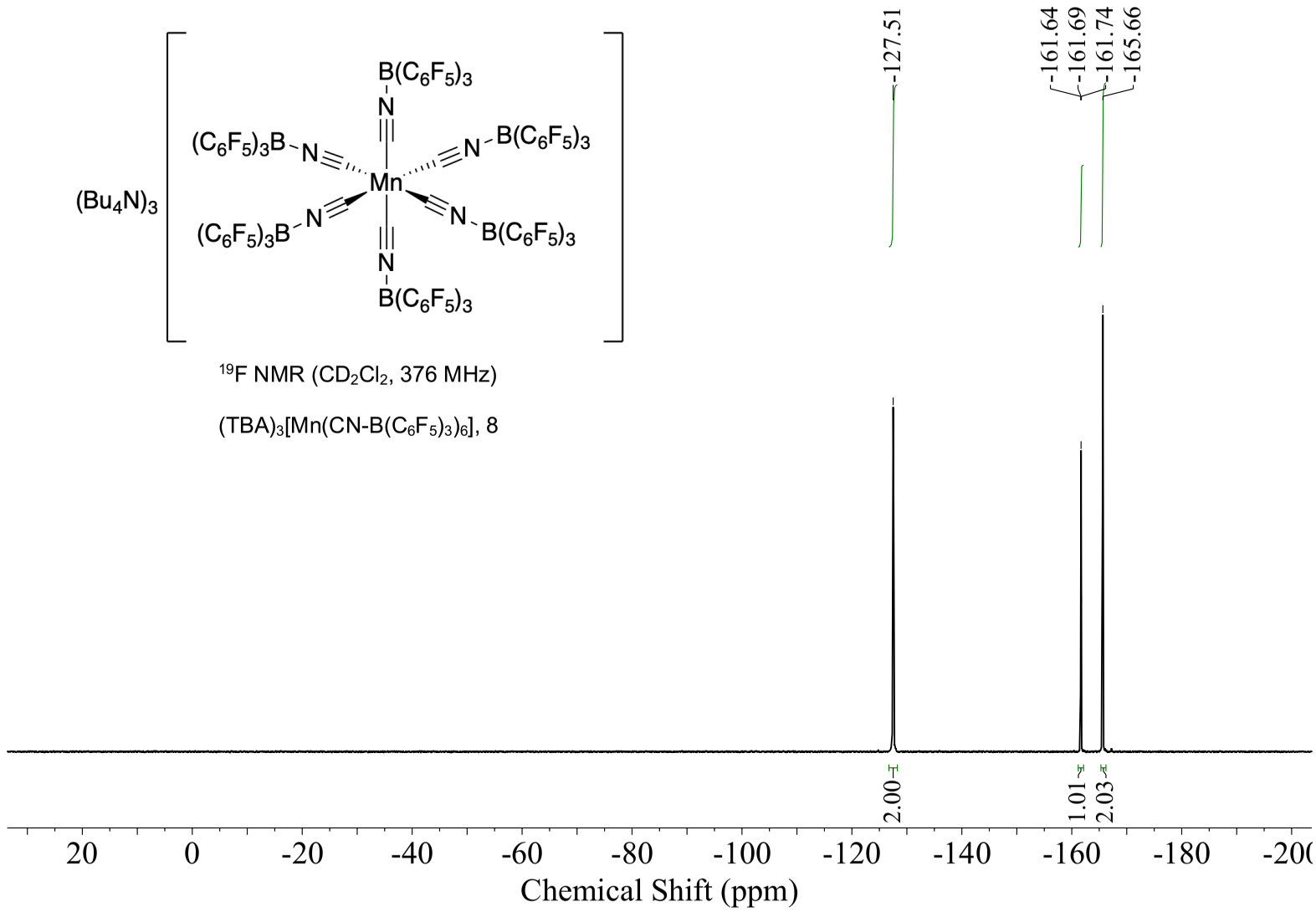

Figure 5.59. ^{19}F NMR spectrum of $(TBA)_3[Mn(CN\text{-}B(C_6F_5)_3)_6]$ (**8**) in CD_2Cl_2.

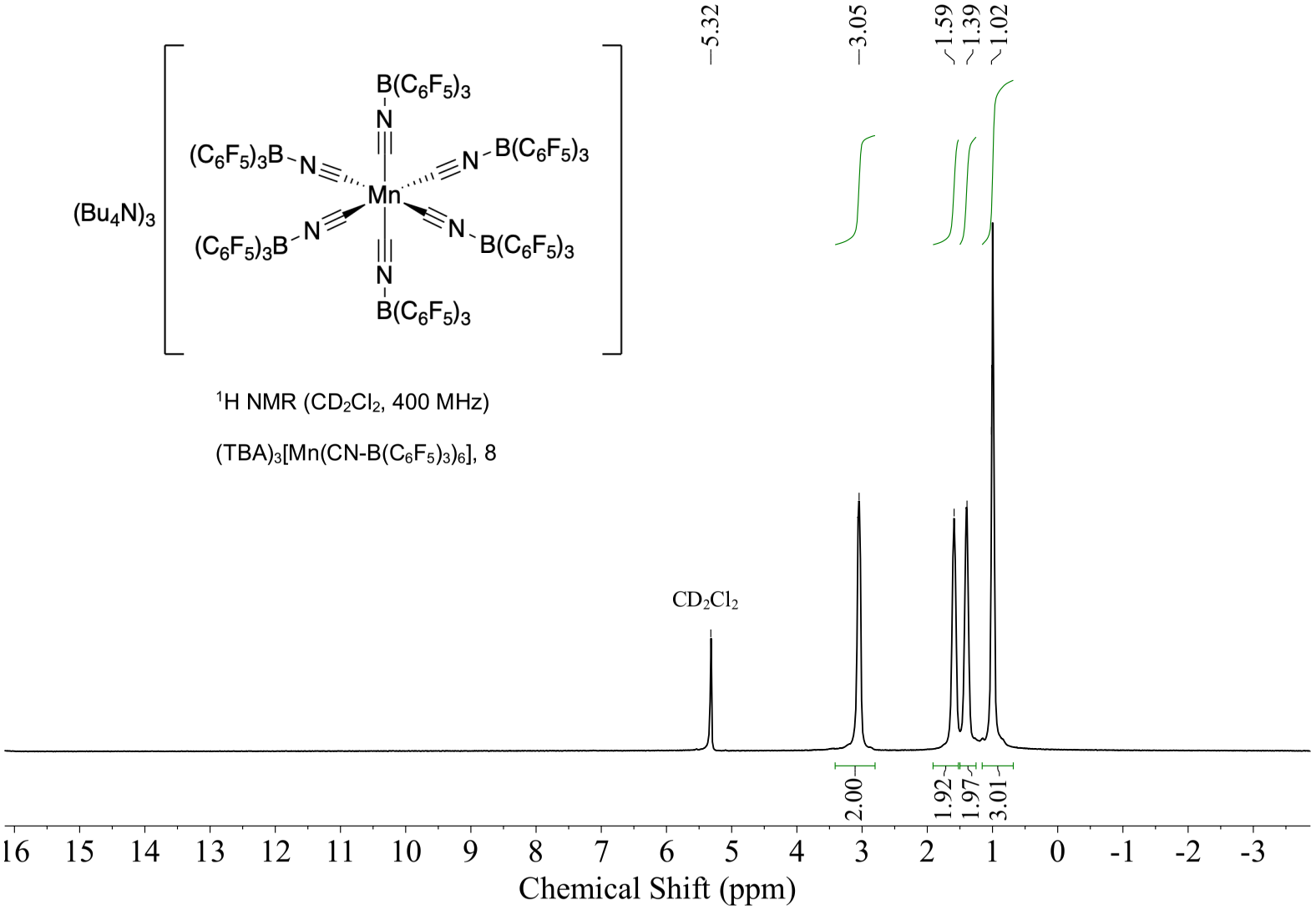

Figure 5.60. ^{1}H NMR spectrum of (TBA)$_3$[Mn(CN-B(C$_6$F$_5$)$_3$)$_6$] (**8**) in CD_2Cl_2.

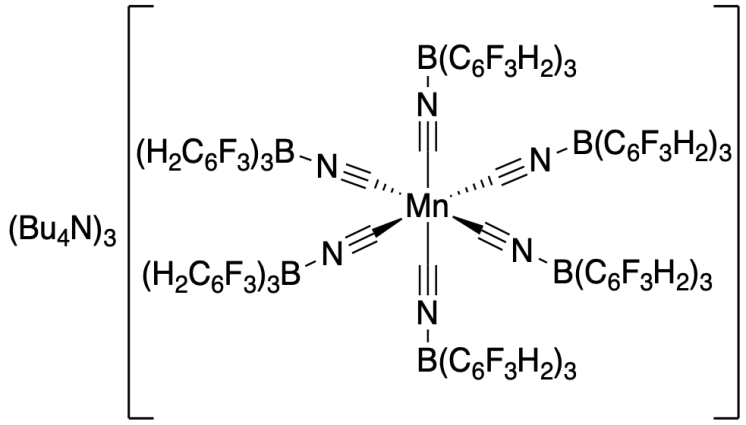

^{11}B NMR (CD_2Cl_2, 128 MHz)

$(TBA)_3[Mn(CN\text{-}B(C_6F_3H_2)_3)_6]$, 9

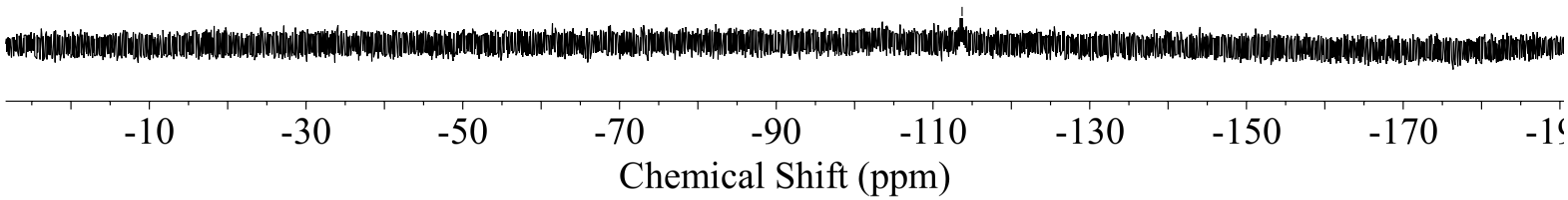

Figure 5.61. ^{11}B NMR spectrum of $(TBA)_3[Mn(CN\text{-}B(C_6F_3H_2)_3)_6]$ (**9**) in CD_2Cl_2.

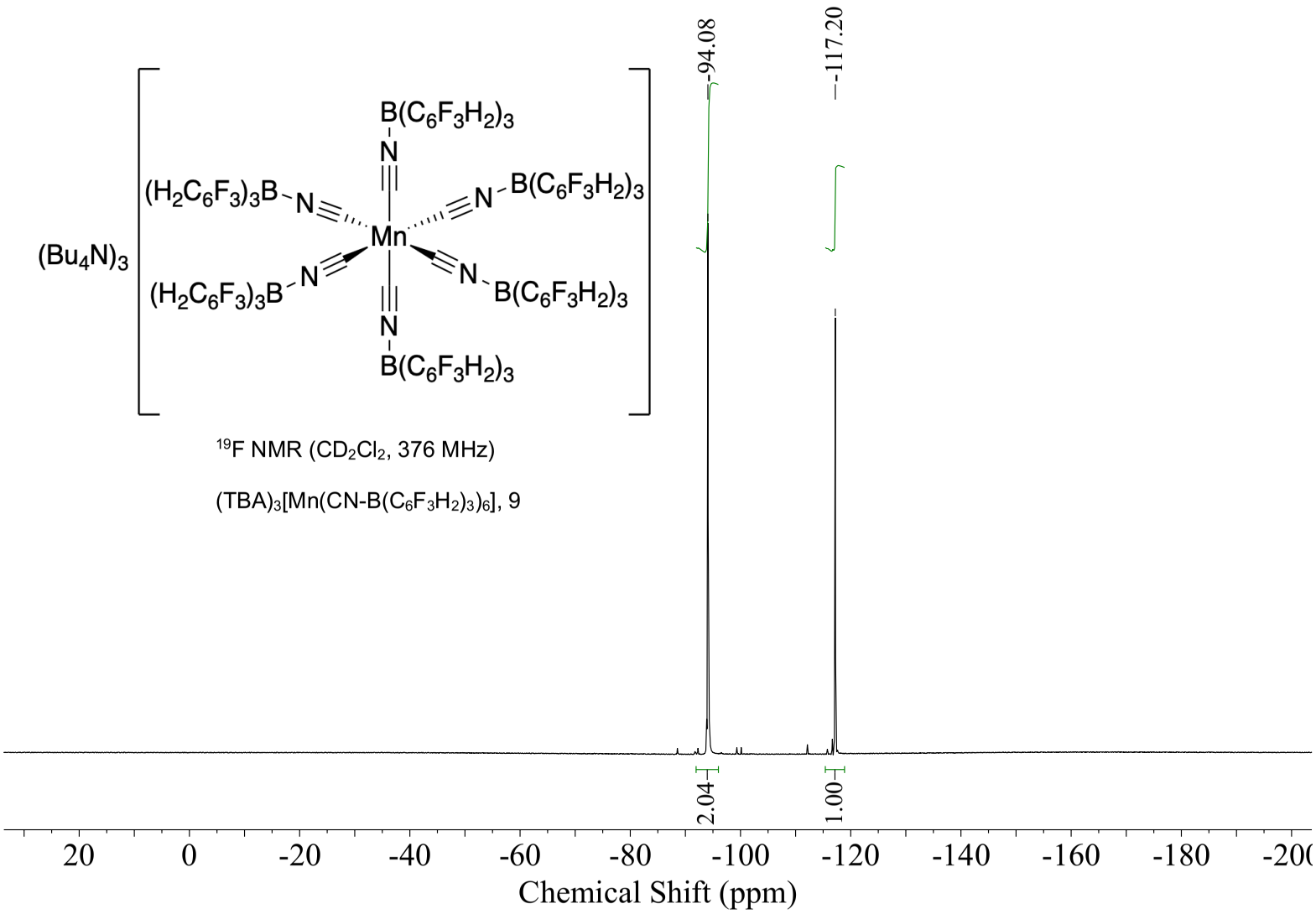

Figure 5.62. ^{19}F NMR spectrum of $(TBA)_3[Mn(CN\text{-}B(C_6F_3H_2)_3)_6]$ (**9**) in CD_2Cl_2.

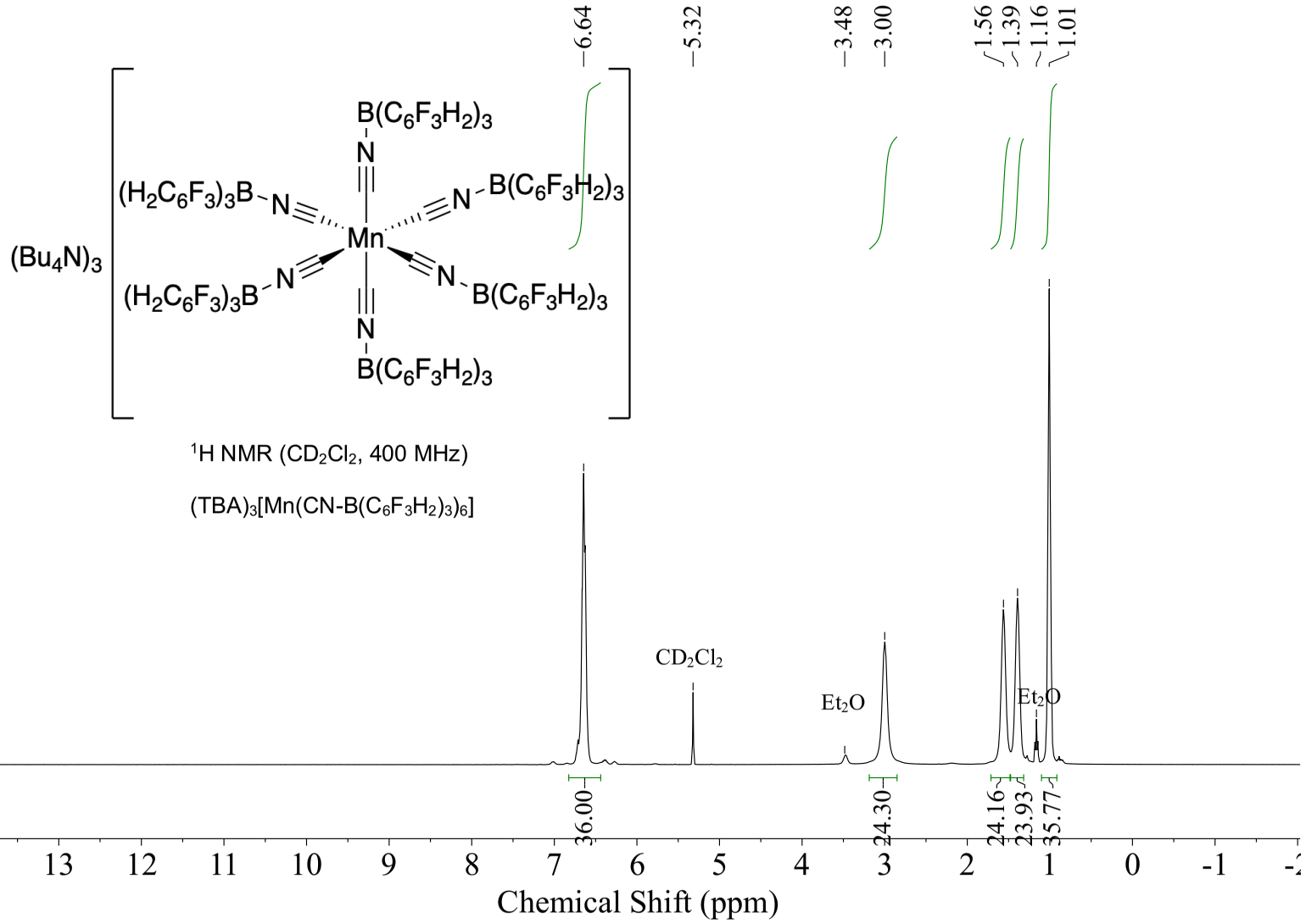

Figure 5.63. ^{1}H NMR spectrum of $(TBA)_3[Mn(CN\text{-}B(C_6F_3H_2)_3)_6]$ (**9**) in CD_2Cl_2.

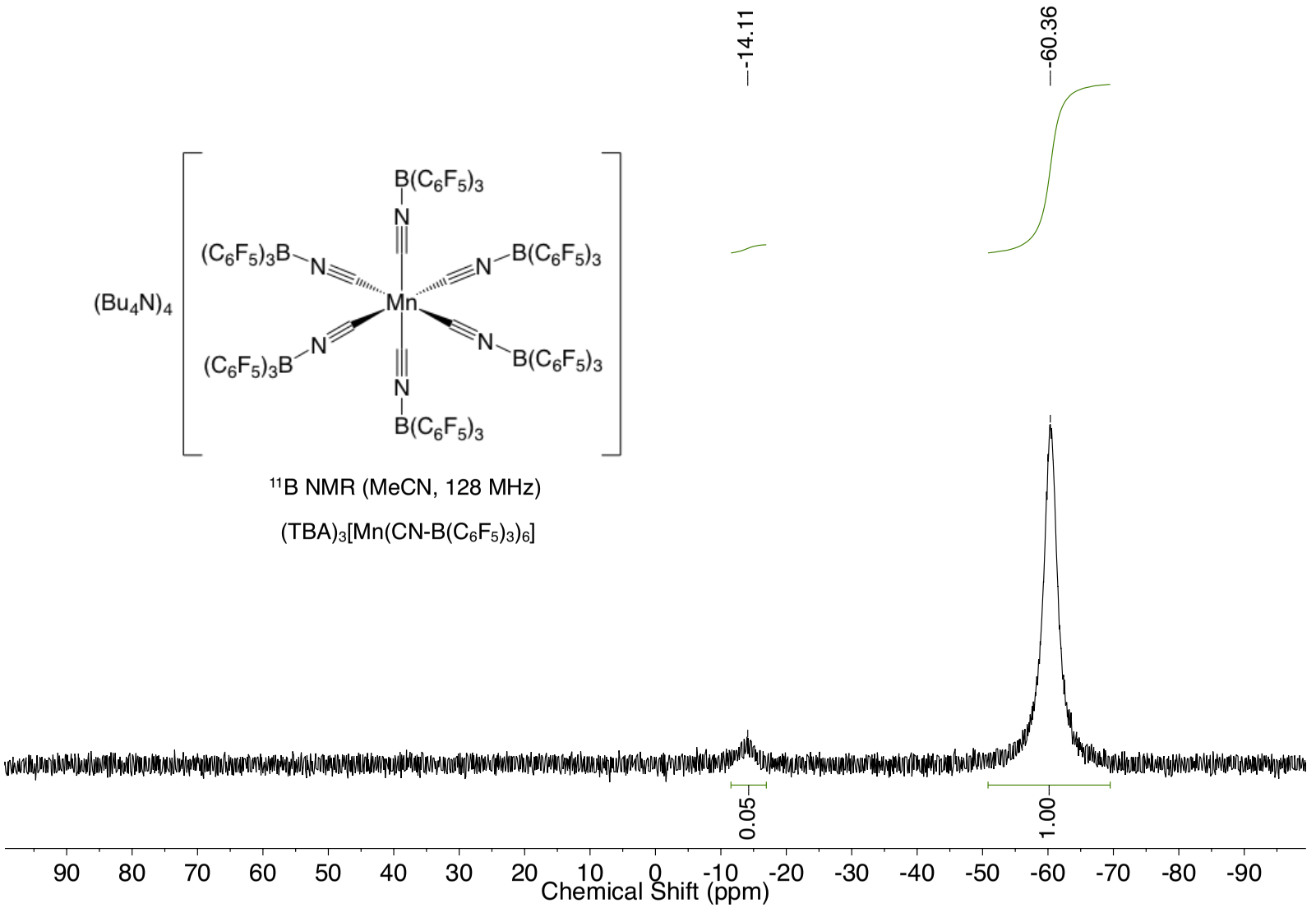

Figure 5.64. ^{11}B NMR spectrum of $(TBA)_4[Mn(CN\text{-}B(C_6F_5)_3)_6]$ (**10**) in CD_3CN.

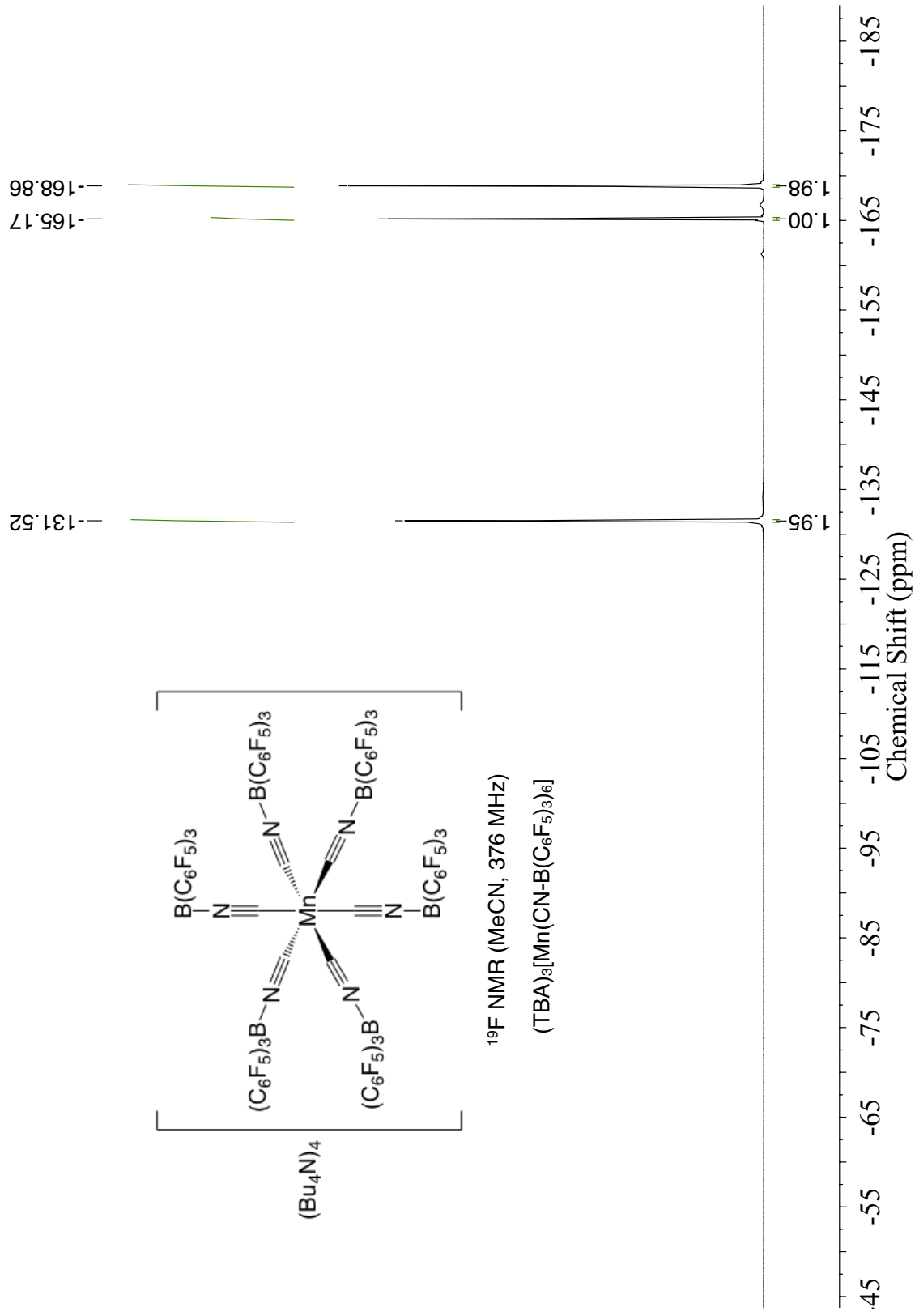

Figure 5.65. ^{19}F NMR spectrum of $(TBA)_4[Mn(CN\text{-}B(C_6F_5)_3)_6]$ (**10**) in CD_3CN.

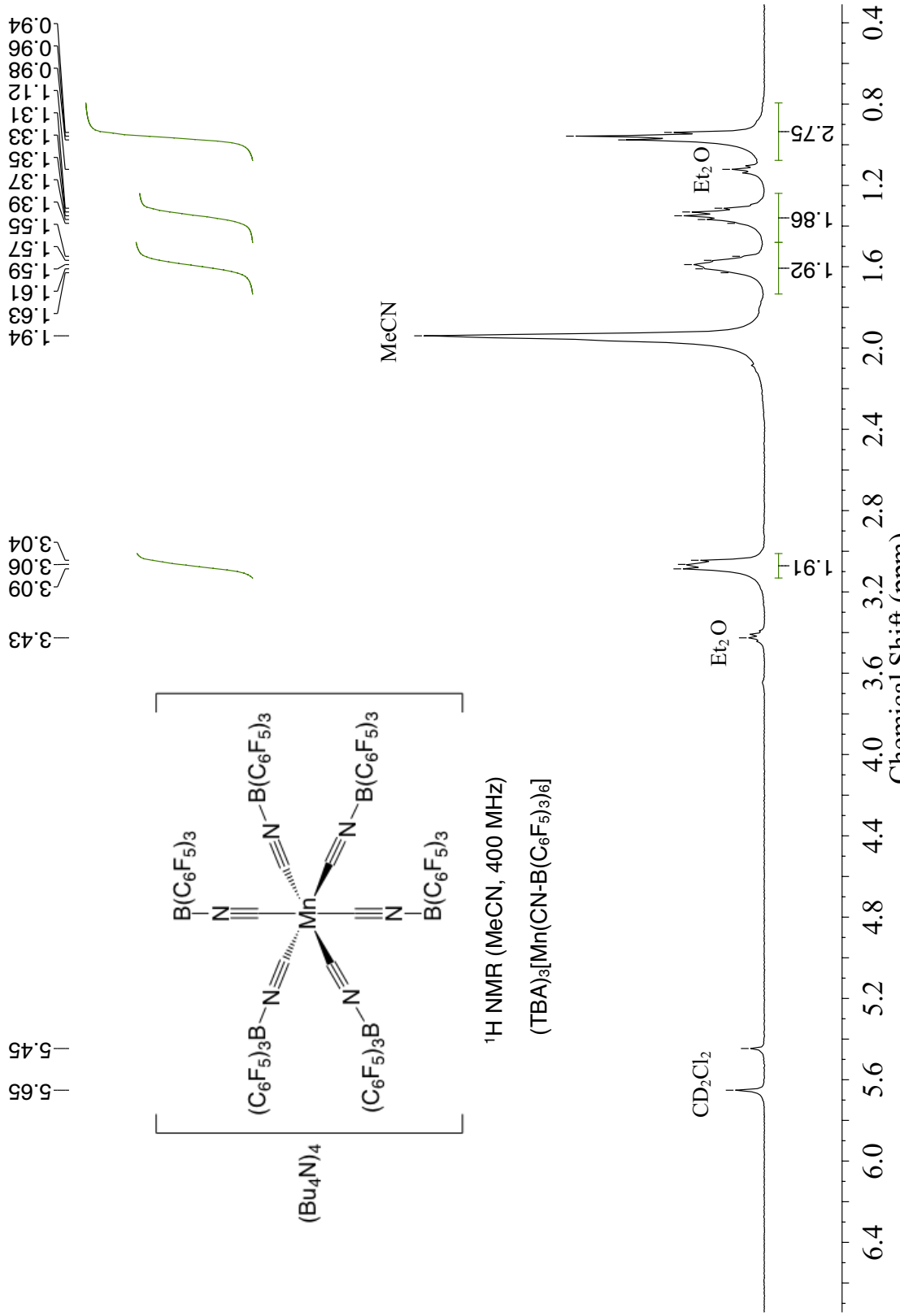

Figure 5.66. ^{1}H NMR spectrum of (TBA)$_4$[Mn(CN-B(C$_6$F$_5$)$_3$)$_6$] (**10**) in CD$_3$CN.

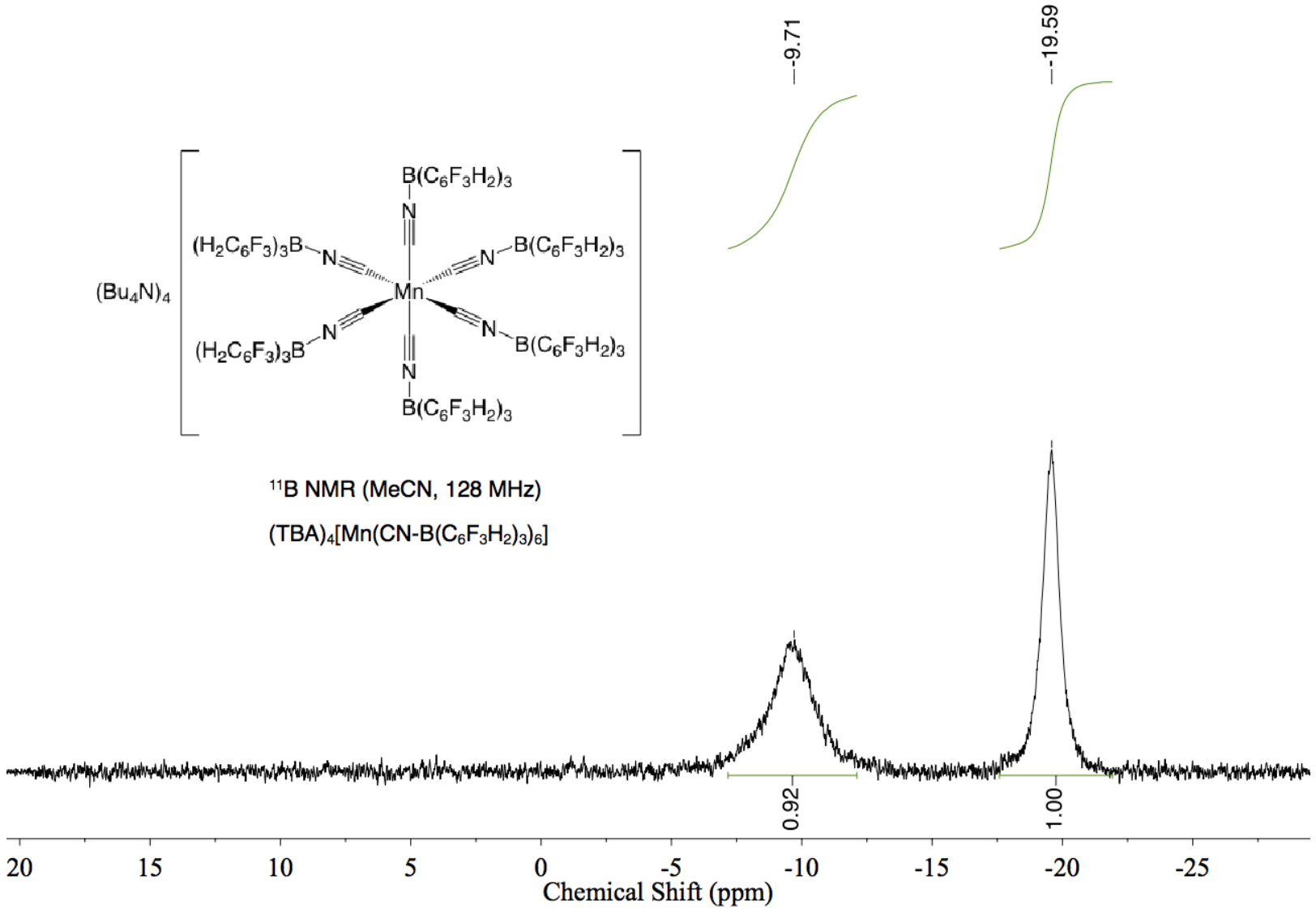

Figure 5.67. ^{11}B NMR spectrum of $(TBA)_4[Mn(CN\text{-}B(C_6F_3H_2)_3)_6]$ (**11**) in CD_3CN.

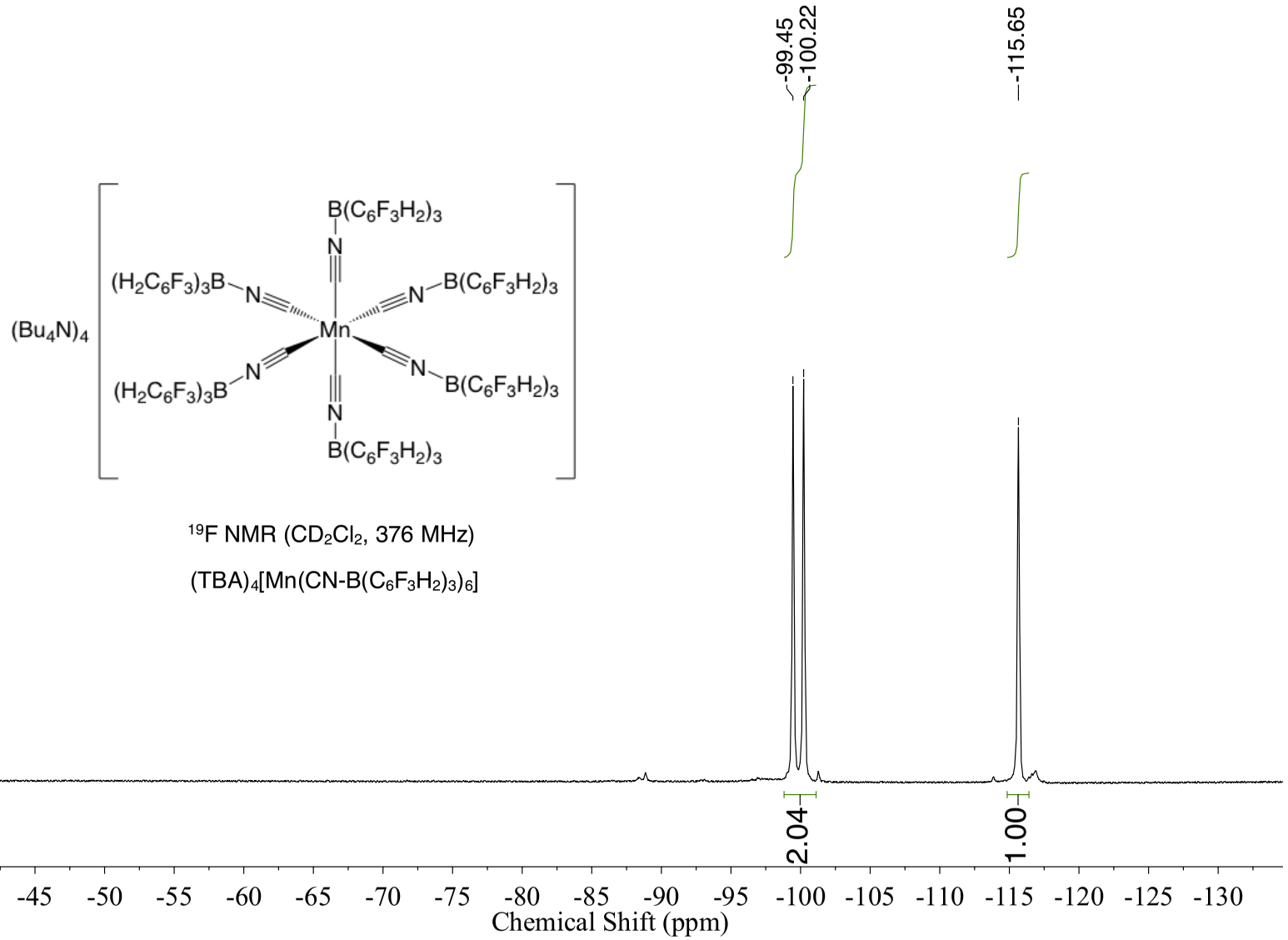

Figure 5.68. ^{19}F NMR spectrum of $(TBA)_4[Mn(CN\text{-}B(C_6F_3H_2)_3)_6]$ (**11**) in CD_3CN.

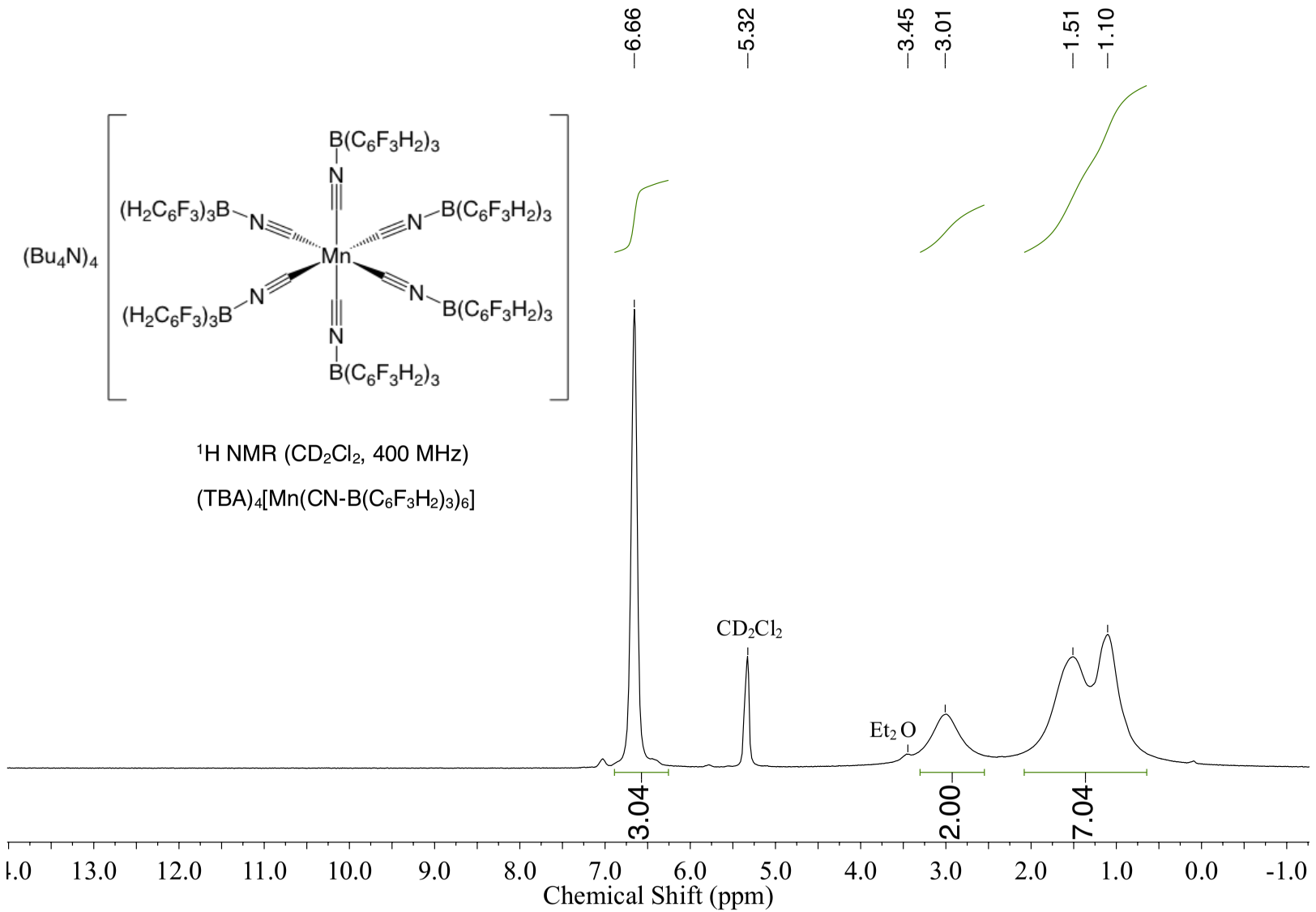

Figure 5.69. ^{1}H NMR spectrum of $(TBA)_4[Mn(CN\text{-}B(C_6F_3H_2)_3)_6]$ (**11**) in CD_3CN.

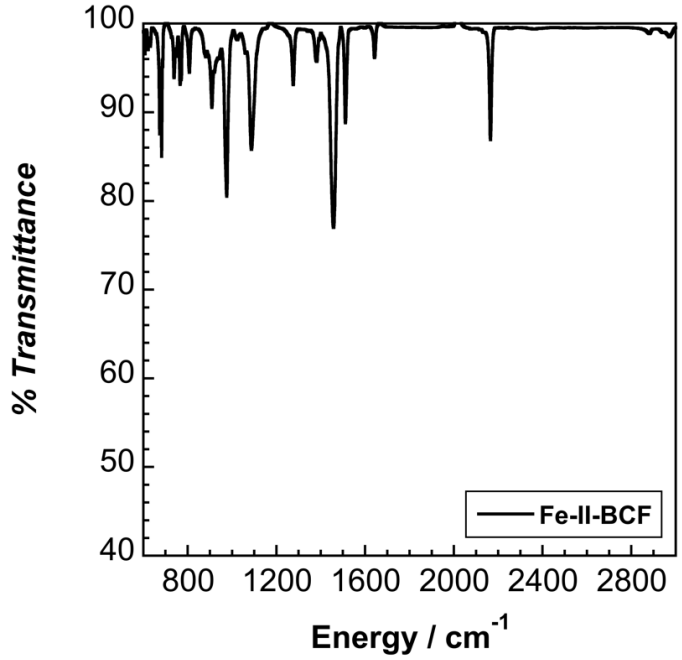

Figure 5.70. Solid-state ATR-IR spectrum of $(TBA)_4[Fe(CN\text{-}B(C_6F_5)_3)_6]$.

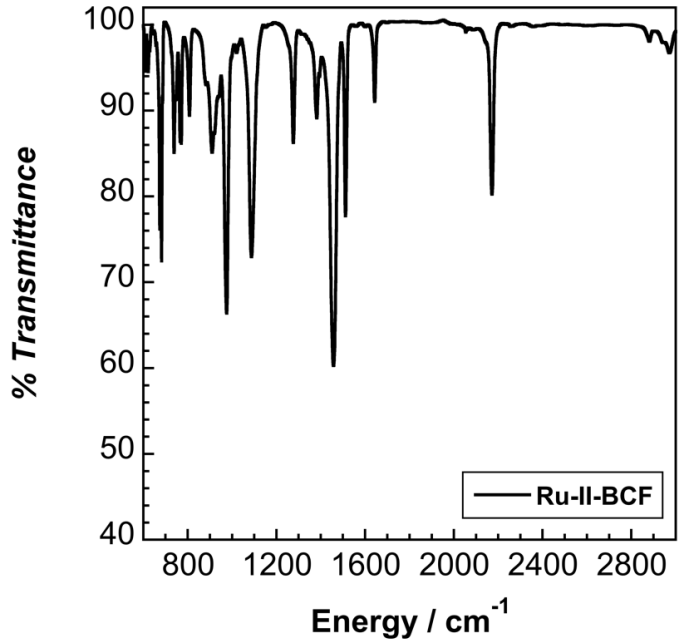

Figure 5.71. Solid-state ATR-IR spectrum of $(TBA)_4[Ru(CN\text{-}B(C_6F_5)_3)_6]$.

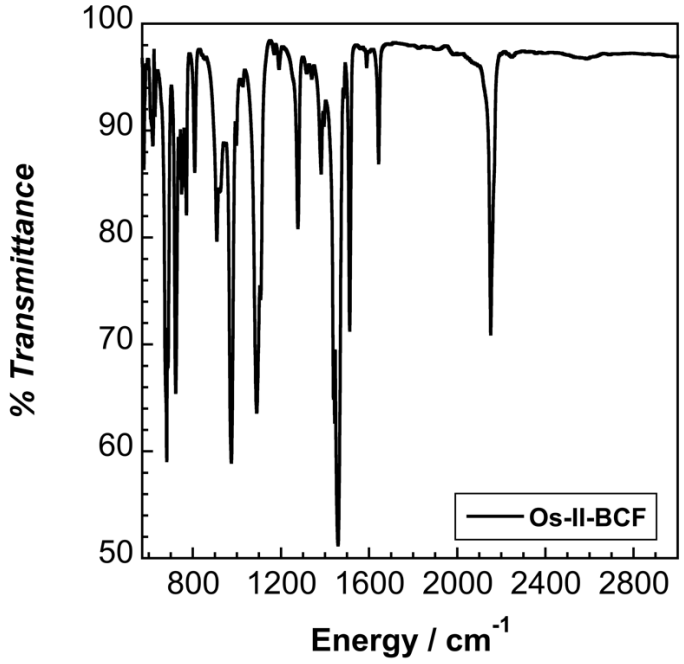

Figure 5.72. Solid-state ATR-IR spectrum of $(PPh_4)_4[Os(CN\text{-}B(C_6F_5)_3)_6]$.

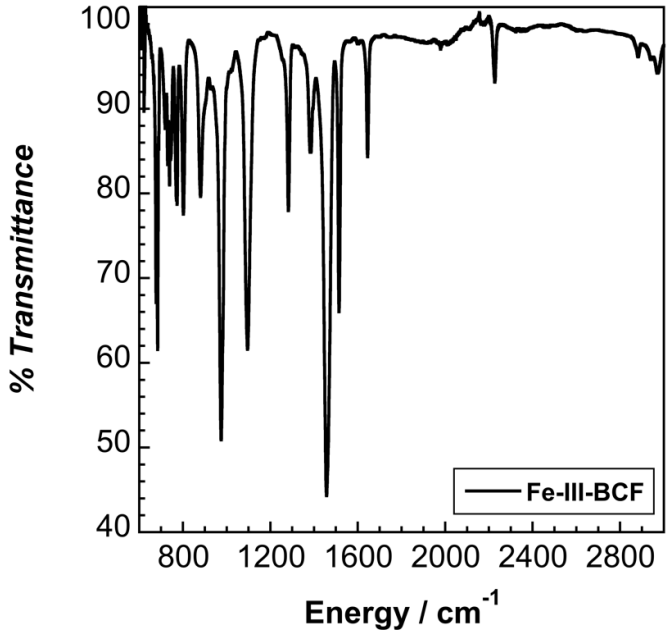

Figure 5.73. Solid-state ATR-IR spectrum of $(TBA)_3[Fe(CN\text{-}B(C_6F_5)_3)_6]$.

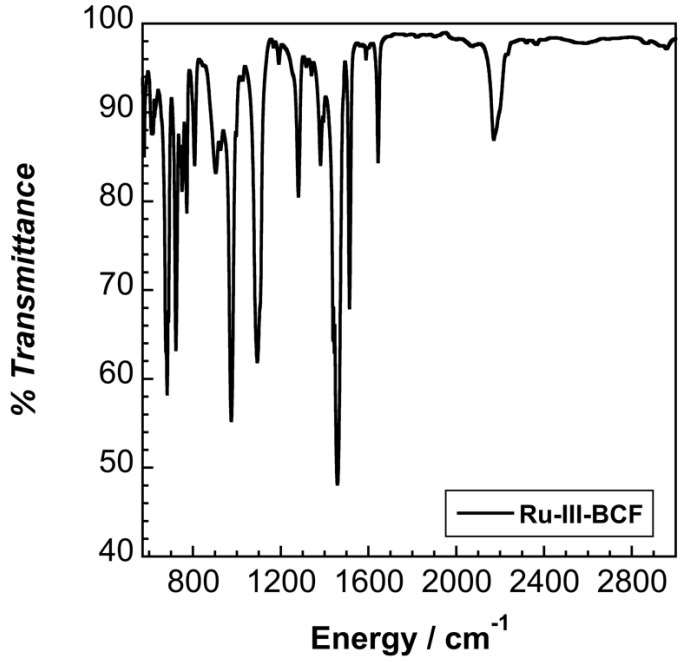

Figure 5.74. Solid-state ATR-IR spectrum of $(TBA)_3[Ru(CN\text{-}B(C_6F_5)_3)_6]$.

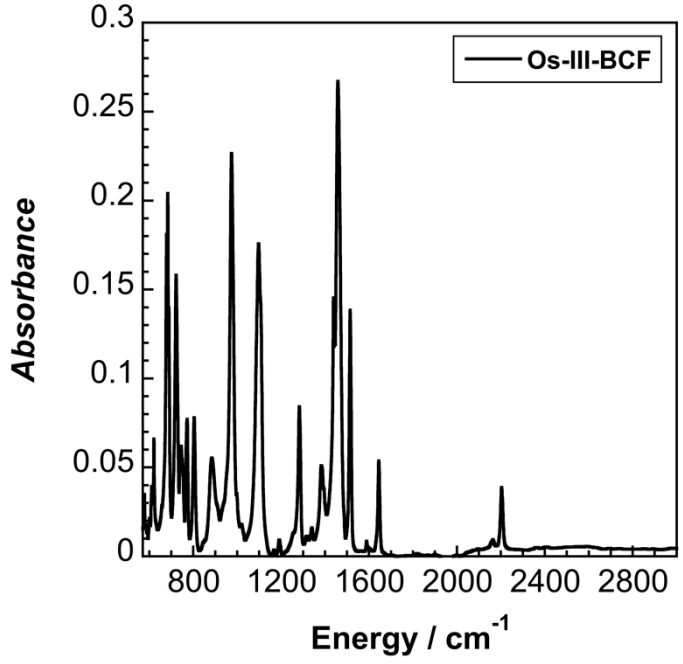

Figure 5.75. Solid-state ATR-IR spectrum of $(PPh_4)_3[Os(CN\text{-}B(C_6F_5)_3)_6]$.

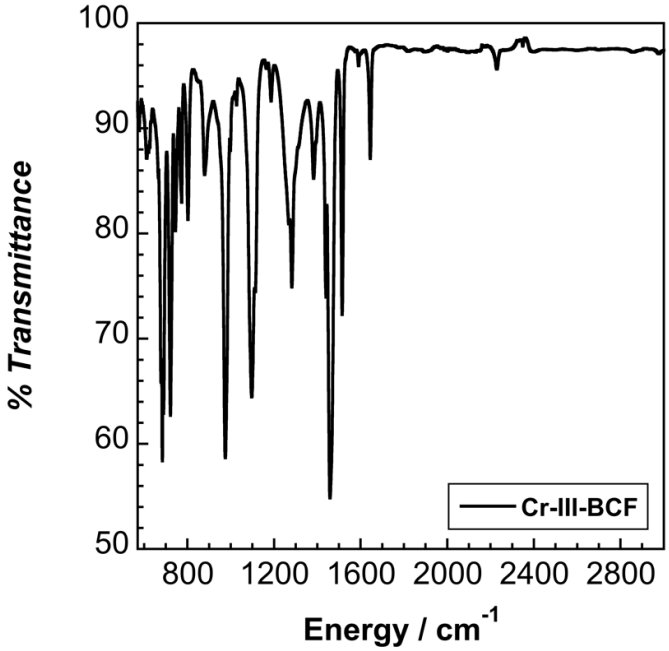

Figure 5.76. Solid-state ATR-IR spectrum of $(TBA)_3[Cr(CN\text{-}B(C_6F_5)_3)_6]$.

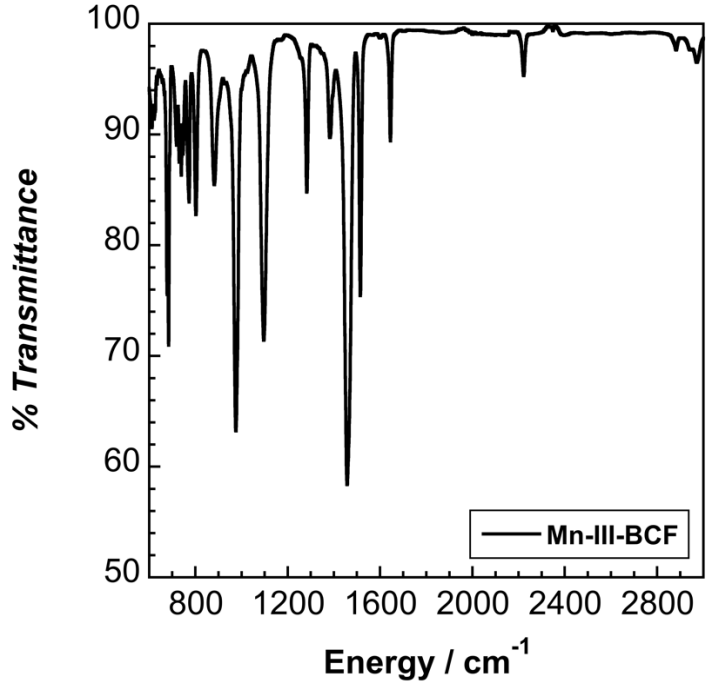

Figure 5.77. Solid-state ATR-IR spectrum of $(TBA)_3[Mn(CN\text{-}B(C_6F_5)_3)_6]$.

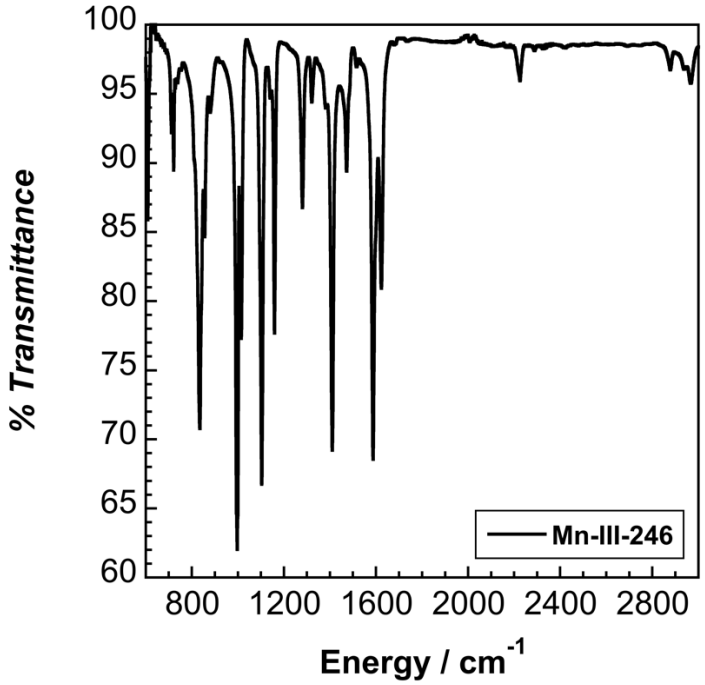

Figure 5.78. Solid-state ATR-IR spectrum of $(TBA)_3[Mn(CN\text{-}B(C_6F_3H_2)_3)_6]$.

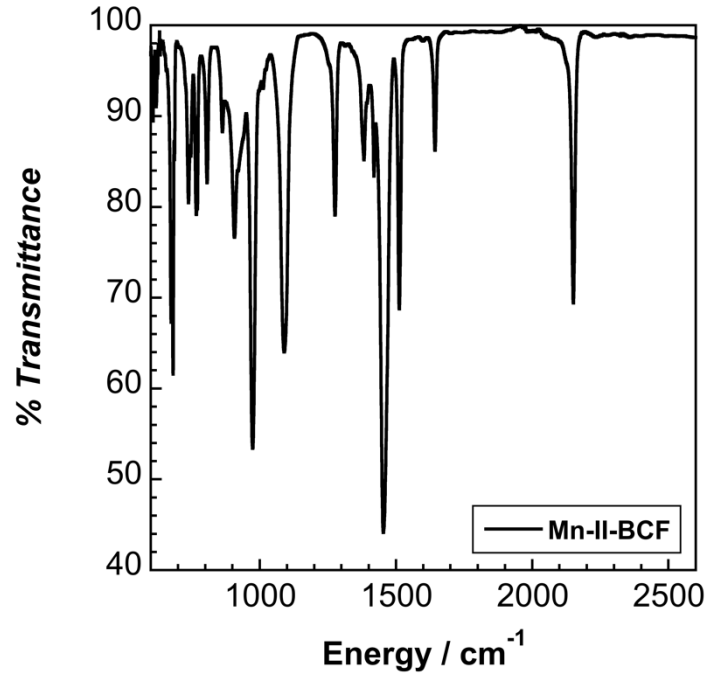

Figure 5.79. Solid-state ATR-IR spectrum of $(TBA)_4[Mn(CN\text{-}B(C_6F_5)_3)_6]$.

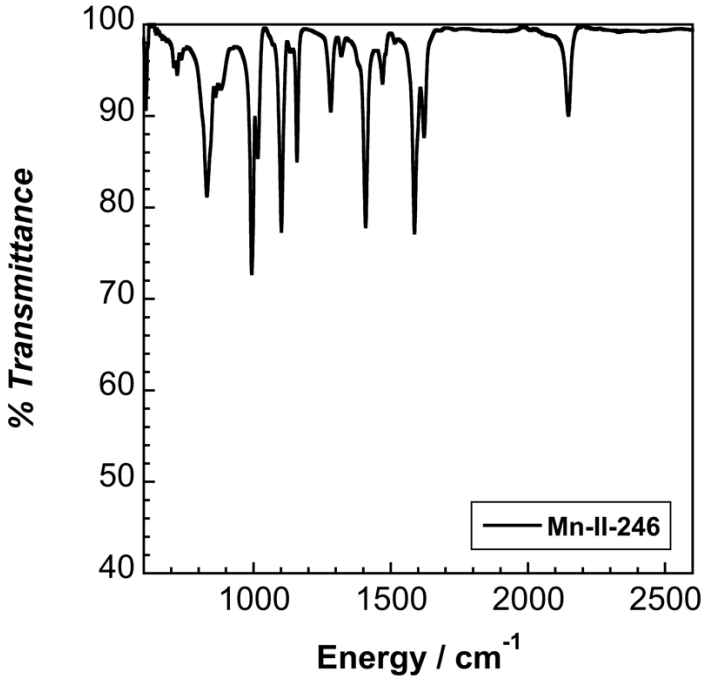

Figure 5.80. Solid state ATR-IR spectrum of $(TBA)_4[Mn(CN\text{-}B(2,4,6\text{-}F_3C_6H_2)_6]$.

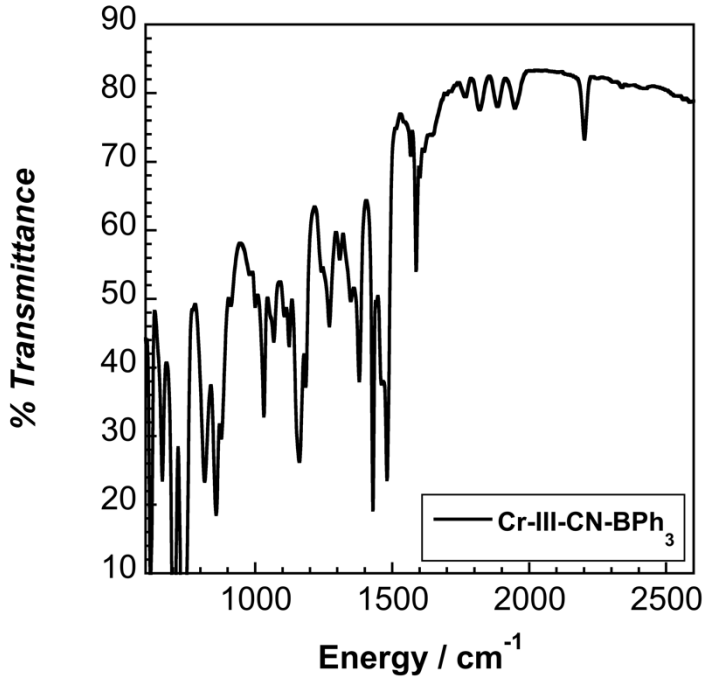

Figure 5.81. Solid state FTIR spectrum of $(Ph_4As)_3[Cr(CN\text{-}BPh_3)_6]$ in KBr.

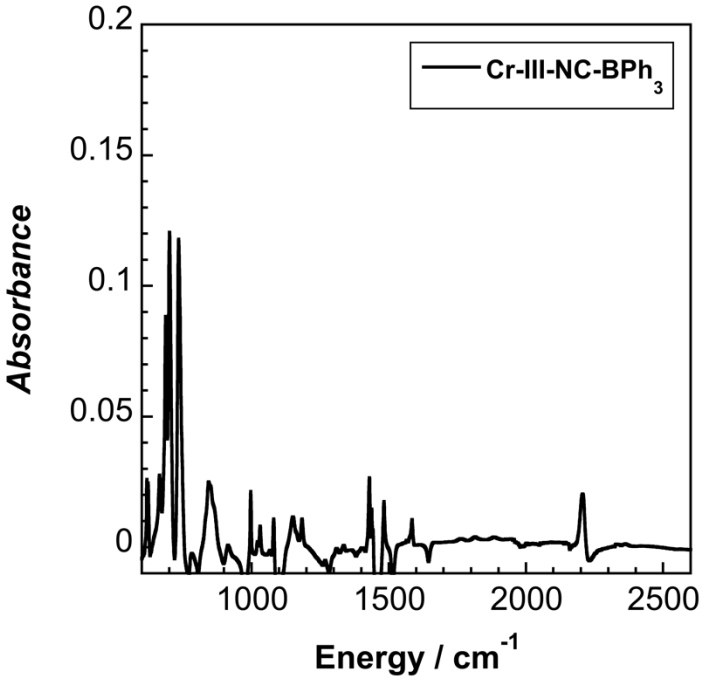

Figure 5.82. Solid state ATR-IR spectrum of $(Ph_4As)_3[Cr(NC\text{-}BPh_3)_6]$.

Collection and Refinement of $(Ph_4P)_4[Ru(CN\text{-}B(C_6F_5)_3)_6]$ (2)

A crystal was mounted on a polyimide MiTeGen loop with STP Oil Treatment and placed under a nitrogen stream. Low temperature (100K) X-ray data were collected with a Bruker AXS KAPPA APEX II diffractometer running at 50 kV and 30 mA (Mo K_α = 0.71073 Å; PHOTON 100 CMOS detector with TRIUMPH graphite monochromator). All diffractometer manipulations, including data collection, integration, and scaling were carried out using the Bruker APEX3 software. An absorption correction was applied using SADABS. The space group was determined, and the structure was solved by intrinsic phasing using XT. Refinement was full-matrix least squares on F^2 using XL. All non-hydrogen atoms were refined using anisotropic displacement parameters. Hydrogen atoms were placed in idealized positions and the coordinates refined. The isotropic displacement parameters of all hydrogen atoms were fixed at 1.2 times the U_{eq} value of the bonded atom.

$(Ph_4P)_4[Ru(CN\text{-}B(C_6F_5)_3)_6]$ crystallizes in the monoclinic space group $P2_1/n$ (#14) with ½ anion (on a center of symmetry), two tetraphenyl phosphonium cations, and one dichloromethane in the asymmetric unit. One pentafluorophenyl group is disordered 54:46; RIGU restraints were used on these atoms.

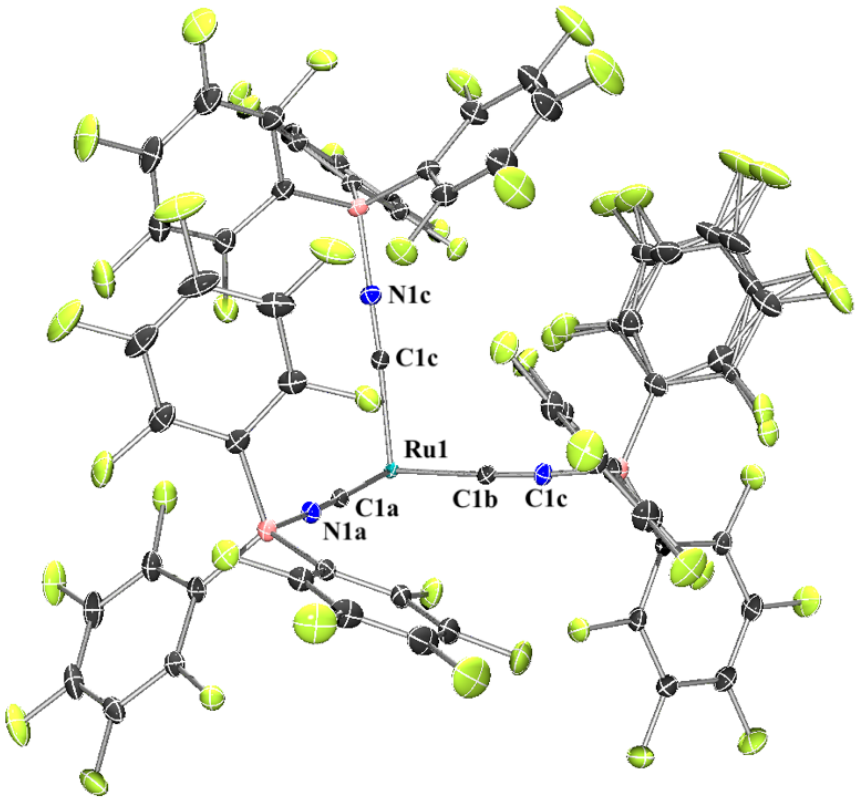

Figure 5.83. Crystal structure of the asymmetric unit of $(Ph_4P)_4[Ru(CN\text{-}B(C_6F_5)_3)_6]$. Thermal ellipsoids set at 50% probability. Solvent and cations omitted for clarity.

Table 5.14. Crystal data and structure refinement for $(Ph_4P)_4[Ru(CN\text{-}B(C_6F_5)_3)_6]$ (**2**).

Empirical formula	C212 H84 B6 Cl4 F90 N6 P4 Ru	
Formula weight	4856.46	
Temperature	100 K	
Wavelength	0.71073 Å	
Crystal system	Monoclinic	
Space group	P 1 21/n 1	
Unit cell dimensions	a = 17.267(5) Å	a= 90°
	b = 31.366(9) Å	b= 115.262(10)°
	c = 19.697(5) Å	g = 90°
Volume	9647(5) $Å^3$	
Z	2	
Density (calculated)	1.672 g/cm^3	
Absorption coefficient	0.317 mm^{-1}	
F(000)	4820	
Crystal size	0.37 x 0.31 x 0.28 mm^3	
Theta range for data collection	1.468 to 34.794°.	
Index ranges	$-27 \leq h \leq 27$, $-49 \leq k \leq 49$, $-30 \leq l \leq 31$	
Reflections collected	333950	
Independent reflections	40030 [R(int) = 0.0340]	
Completeness to theta = 25.242°	100.0 %	
Absorption correction	Semi-empirical from equivalents	
Max. and min. transmission	1.0000 and 0.9591	
Refinement method	Full-matrix least-squares on F^2	
Data / restraints / parameters	40030 / 42 / 1547	
Goodness-of-fit on F^2	1.034	
Final R indices [I>2sigma(I)]	R1 = 0.0369, wR2 = 0.0897	
R indices (all data)	R1 = 0.0506, wR2 = 0.0971	
Extinction coefficient	n/a	
Largest diff. peak and hole	0.506 and -1.336 $e.Å^{-3}$	

Collection and Refinement of $(Ph_4As)_4[Os(CN\text{-}B(C_6F_5)_3)_6]$ (3)

A crystal was mounted on a polyimide MiTeGen loop with STP Oil Treatment and placed under a nitrogen stream. Low temperature (100K) X-ray data were collected with a Bruker AXS KAPPA APEX II diffractometer running at 50 kV and 30 mA (Mo K_α = 0.71073 Å; PHOTON 100 CMOS detector with TRIUMPH graphite monochromator). All diffractometer manipulations, including data collection, integration, and scaling were carried out using the Bruker APEX3 software. An absorption correction was applied using SADABS. The space group was determined, and the structure was solved by intrinsic phasing using XT. Refinement was full-matrix least squares on F^2 using XL. All non-hydrogen atoms (except for 6 disordered solvent atoms) were refined using anisotropic displacement parameters. Hydrogen atoms were placed in idealized positions and the coordinates refined. The isotropic displacement parameters of all hydrogen atoms were fixed at 1.2 times the U_{eq} value of the bonded atom.

$(Ph_4As)_4[Os(CN\text{-}B(C_6F_5)_3)_6]$ crystallizes in the monoclinic space group $P2_1/n$ (#14) with ½ anion (on a center of symmetry), two tetraphenyl arsenate cations, and 1.66 dichloromethanes in the asymmetric unit. A phenyl group on one arsenate is disordered 59:41; two carbons on a phenyl on the other arsenate are disordered 54:46. One dichloromethane is partially disordered 58:14; another 60:16; and a third has a 0.17 occupancy. SUMP commands were used to constrain the populations of two of the disordered dichloromethanes. SADI and RIGU restraints were used on the solvent molecules and SADI restraints on the disordered phenyls.

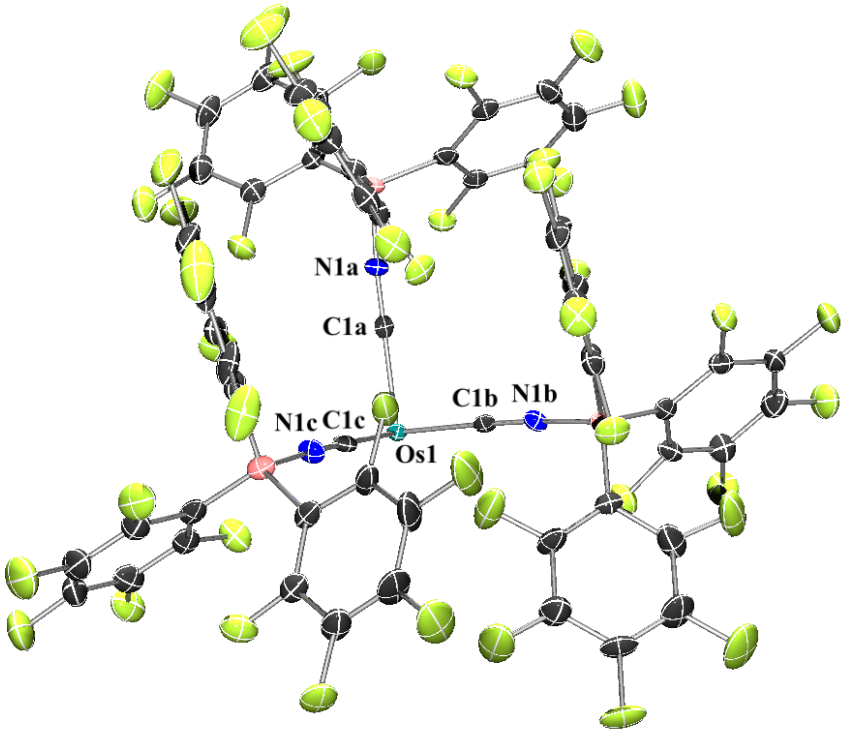

Figure 5.84. Crystal structure of the asymmetric unit of $(Ph_4As)_4[Os(CN\text{-}B(C_6F_5)_3)_6]$. Thermal ellipsoids set at 50% probability. Solvent and cations omitted for clarity.

Table 5.15. Crystal data and structure refinement for $(Ph_4As)_4[Os(CN\text{-}B(C_6F_5)_3)_6)]$ (**3**).

Empirical formula	C213.32 H86.64 As4 B6 Cl6.64 F90 N6 Os	
Formula weight	5233.49	
Temperature	100 K	
Wavelength	0.71073 Å	
Crystal system	Monoclinic	
Space group	P 1 21/n 1	
Unit cell dimensions	a = 17.511(6) Å	a= 90°
	b = 33.967(15) Å	b= 107.374(12)°
	c = 17.823(6) Å	g = 90°
Volume	10118(7) $Å^3$	
Z	2	
Density (calculated)	1.718 g/cm^3	
Absorption coefficient	1.508 mm^{-1}	
F(000)	5139	
Crystal size	0.32 x 0.12 x 0.02 mm^3	
Theta range for data collection	1.551 to 28.664°.	
Index ranges	$-22 \leq h \leq 23$, $-41 \leq k \leq 45$, $-22 \leq l \leq 21$	
Reflections collected	154695	
Independent reflections	23478 [R(int) = 0.0774]	
Completeness to theta = 25.242°	100.0 %	
Absorption correction	Semi-empirical from equivalents	
Max. and min. transmission	1.0000 and 0.8694	
Refinement method	Full-matrix least-squares on F^2	
Data / restraints / parameters	23478 / 72 / 1588	
Goodness-of-fit on F^2	1.081	
Final R indices [I>2sigma(I)]	R1 = 0.0720, wR2 = 0.1291	
R indices (all data)	R1 = 0.1220, wR2 = 0.1464	
Extinction coefficient	n/a	
Largest diff. peak and hole	1.282 and -1.068 $e.Å^{-3}$	

Collection and Refinement of $(PPN)_3[Fe(CN\text{-}B(C_6F_5)_3)_6]$ (4)

Low-temperature diffraction data (ϕ-and ω-scans) were collected on a Bruker AXS D8 VENTURE KAPPA diffractometer coupled to a PHOTON II CPAD detector with Cu K_α radiation (λ = 1.54178 Å) from an IμS micro-source for the structure of compound V18462. The structure was solved by direct methods using SHELXS[69] and refined against F^2 on all data by full-matrix least squares with SHELXL-2017[70] using established refinement techniques.[71] All non-hydrogen atoms were refined anisotropically. All hydrogen atoms were included into the model at geometrically calculated positions and refined using a riding model. The isotropic displacement parameters of all hydrogen atoms were fixed to 1.2 times the *U* value of the atoms they are linked to (1.5 times for methyl groups). All disordered atoms were refined with the help of similarity restraints on the 1,2- and 1,3-distances and displacement parameters as well as enhanced rigid bond restraints for anisotropic displacement parameters.

$(PPN)_3[Fe(CN\text{-}B(C_6F_5)_3)_6]$ crystallizes in the triclinic space group *P*-1 with one molecule in the asymmetric unit along with 6.46 molecules of dichloromethane. The dichloromethane was disordered in a large solvent accessible void and was disordered over 12 positions.

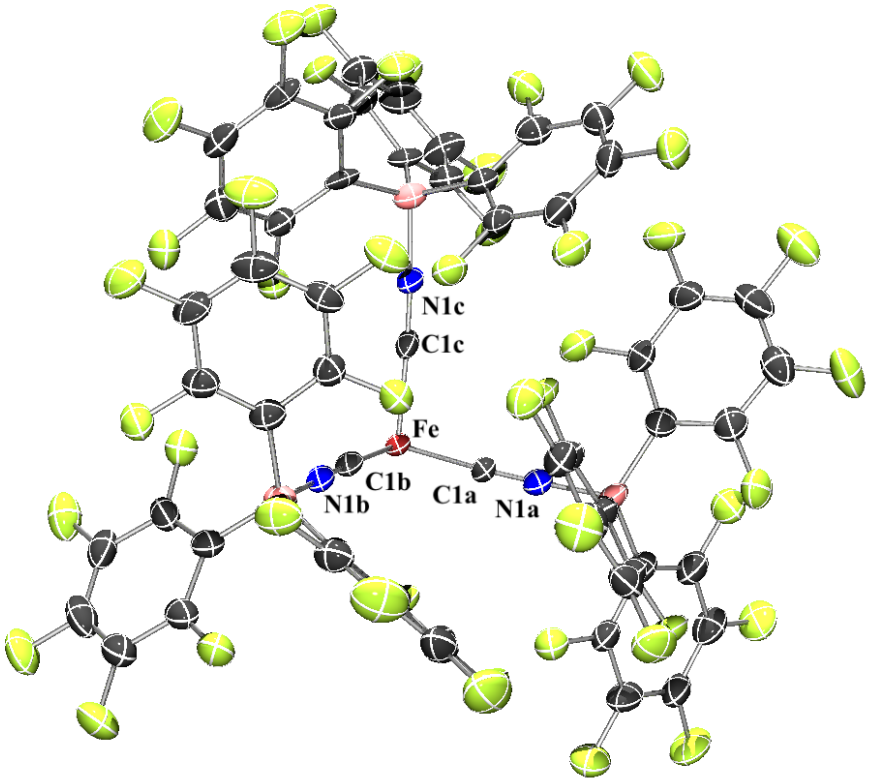

Figure 5.85. Crystal structure of one half of the asymmetric unit of $(PPN)_3[Fe(CN\text{-}B(C_6F_5)_3)_6]$. Thermal ellipsoids set at 50% probability. Solvent and cations omitted for clarity.

Table 5.16. Crystal data and structure refinement for $(PPN)_3[Fe(CN\text{-}B(C_6F_5)_3)_6]$ (**4**).

Empirical formula	C228.46 H102.93 B6 Cl12.92 F90 Fe N9 P6	
Formula weight	5448.36	
Temperature	100(2) K	
Wavelength	1.54178 Å	
Crystal system	Triclinic	
Space group	P-1	
Unit cell dimensions	a = 19.1416(9) Å	a= 85.871(3)°.
	b = 20.1699(10) Å	b= 80.885(3)°.
	c = 31.6515(14) Å	g = 67.381(3)°.
Volume	11136.9(9) $Å^3$	
Z	2	
Density (calculated)	1.625 Mg/m^3	
Absorption coefficient	3.577 mm^{-1}	
F(000)	5425	
Crystal size	0.100 x 0.050 x 0.050 mm^3	
Theta range for data collection	2.714 to 58.409°.	
Index ranges	$-21 \leq h \leq 20$, $-22 \leq k \leq 22$, $-34 \leq l \leq 34$	
Reflections collected	90663	
Independent reflections	30059 [R(int) = 0.1486]	
Completeness to theta = 58.409°	95.6 %	
Absorption correction	Semi-empirical from equivalents	
Max. and min. transmission	1.0000 and 0.8324	
Refinement method	Full-matrix least-squares on F^2	
Data / restraints / parameters	30059 / 696 / 3339	
Goodness-of-fit on F^2	1.019	
Final R indices [I>2sigma(I)]	R1 = 0.0979, wR2 = 0.2257	
R indices (all data)	R1 = 0.1625, wR2 = 0.2651	
Extinction coefficient	n/a	
Largest diff. peak and hole	0.813 and -0.877 $e.Å^{-3}$	

Collection and Refinement of $(Ph_4P)_3[Ru(CN\text{-}B(C_6F_5)_3)_6]$ (5)

A crystal was mounted on a polyimide MiTeGen loop with STP Oil Treatment and placed under a nitrogen stream. Low temperature (100K) X-ray data were collected with a Bruker AXS D8 VENTURE KAPPA diffractometer running at 50 kV and 1mA (Cu K_α = 1.54178 Å; PHOTON II CPAD detector and Helios focusing multilayer mirror optics). All diffractometer manipulations, including data collection, integration, and scaling were carried out using the Bruker APEX3 software. An absorption correction was applied using SADABS. The space group was determined, and the structure was solved by intrinsic phasing using XT. Refinement was full-matrix least squares on F^2 using XL. All non-hydrogen atoms were refined using anisotropic displacement parameters. Hydrogen atoms were placed in idealized positions and the coordinates refined. The isotropic displacement parameters of all hydrogen atoms were fixed at 1.2 times the U_{eq} value of the bonded atom.

$(Ph_4P)_3[Ru(CN\text{-}B(C_6F_5)_3)_6]$ crystallizes in the monoclinic space group *C2/c* (#15) with one half of the anion, cations, and solvent in the asymmetric unit. Only one PPh_4 cation in the asymmetric unit could be located (there was no evidence of a second phosphorus atom). One partially present (0.63 population) dichloromethane was included in the model. A large cavity (780 $Å^3$ representing ~ 284 electrons in the asymmetric unit was masked with the OLEX2 implementation of SQUEEZE.

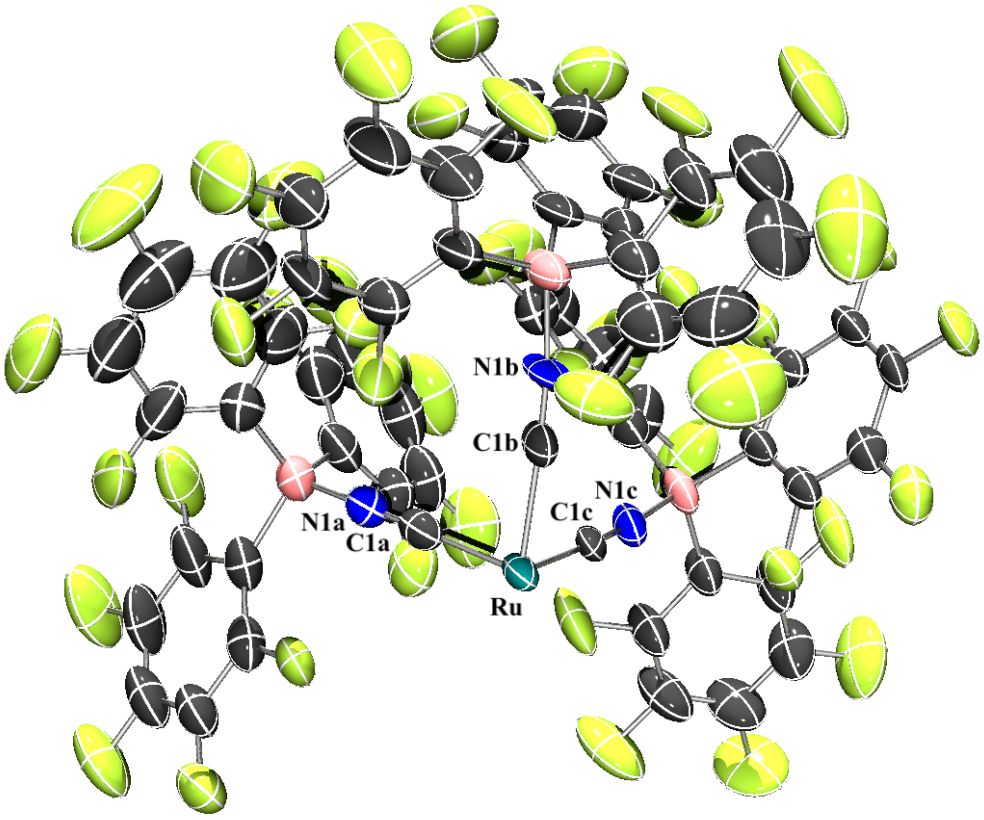

Figure 5.86. Crystal structure of the asymmetric unit of $(Ph_4P)_3[Ru(CN\text{-}B(C_6F_5)_3)_6]$. Thermal ellipsoids set at 50% probability. Solvent and cations omitted for clarity.

Table 5.17. Crystal data and structure refinement for $(Ph_4P)_3[Ru(CN\text{-}B(C_6F_5)_3)_6]$ (**5**).

Empirical formula	C163.27 H42.53 B6 Cl2.54 F90 N6 P2 Ru	
Formula weight	4115.51	
Moiety formula	B6 C114 F90 N6 Ru, 2(C24 H20 P), 1.268(C H2 Cl2)	
Temperature	100 K	
Wavelength	1.54178 Å	
Crystal system	Monoclinic	
Space group	C 1 2/c 1 (# 15)	
Unit cell dimensions	a = 30.558(5) Å	α= 90°
	b = 21.526(4) Å	β= 98.509(11)°
	c = 31.646(7) Å	γ = 90°
Volume	20587(7) $Å^3$	
Z	4	
Density (calculated)	1.328 g/cm^3	
Absorption coefficient	2.213 mm^{-1}	
F(000)	8085	
Crystal size	0.06 x 0.21 x 0.33 mm^3	
Theta range for data collection	2.52 to 67.94°	
Index ranges	$-29 \leq h \leq 36$, $-25 \leq k \leq 25$, $-37 \leq l \leq 34$	
Reflections collected	181419	
Independent reflections	18538 [R(int) = 0.0894]	
Completeness to theta = 67.679°	99.4 %	
Absorption correction	Semi-empirical from equivalents	
Max. and min. transmission	1.000 and 0.690	
Refinement method	Full-matrix least-squares on F^2	
Data / restraints / parameters	18538 / 36 / 1232	
Goodness-of-fit on F^2	1.033	
Final R indices [I>2sigma(I)]	R1 = 0.1038, wR2 = 0.2674	
R indices (all data)	R1 = 0.1441, wR2 = 0.2991	
Extinction coefficient	n/a	
Largest diff. peak and hole	1.30 and -1.33 $e.Å^{-3}$	

Collection and Refinement of $(Ph_4P)_3[Os(CN\text{-}B(C_6F_5)_3)_6]$ (6)

Low-temperature diffraction data (ϕ-and ω-scans) were collected on a Bruker AXS D8 VENTURE KAPPA diffractometer coupled to a PHOTON II CPAD detector with Cu K_α radiation (λ = 1.54178 Å) from an IμS micro-source for the structure of compound V19445. The structure was solved by direct methods using SHELXS[69] and refined against F^2 on all data by full-matrix least squares with SHELXL-2017[70] using established refinement techniques.[71] All non-hydrogen atoms were refined anisotropically. All hydrogen atoms were included into the model at geometrically calculated positions and refined using a riding model. The isotropic displacement parameters of all hydrogen atoms were fixed to 1.2 times the *U* value of the atoms they are linked to (1.5 times for methyl groups). All atoms were refined with the help of similarity restraints on the 1,2- and 1,3-distances and displacement parameters as well as enhanced rigid bond restraints for anisotropic displacement parameters.

$(Ph_4P)_3[Os(CN\text{-}B(C_6F_5)_3)_6]$ crystallizes in the triclinic space group *P*-1 with two molecules in the asymmetric unit along with 6.1 molecules of dichloromethane. The highest electron density maxima are located near the Os atoms. One of the C_6F_5 moieties was disordered over two positions. The osmium atoms are related by a crystallographic inversion center, however, the remaining atoms are not.

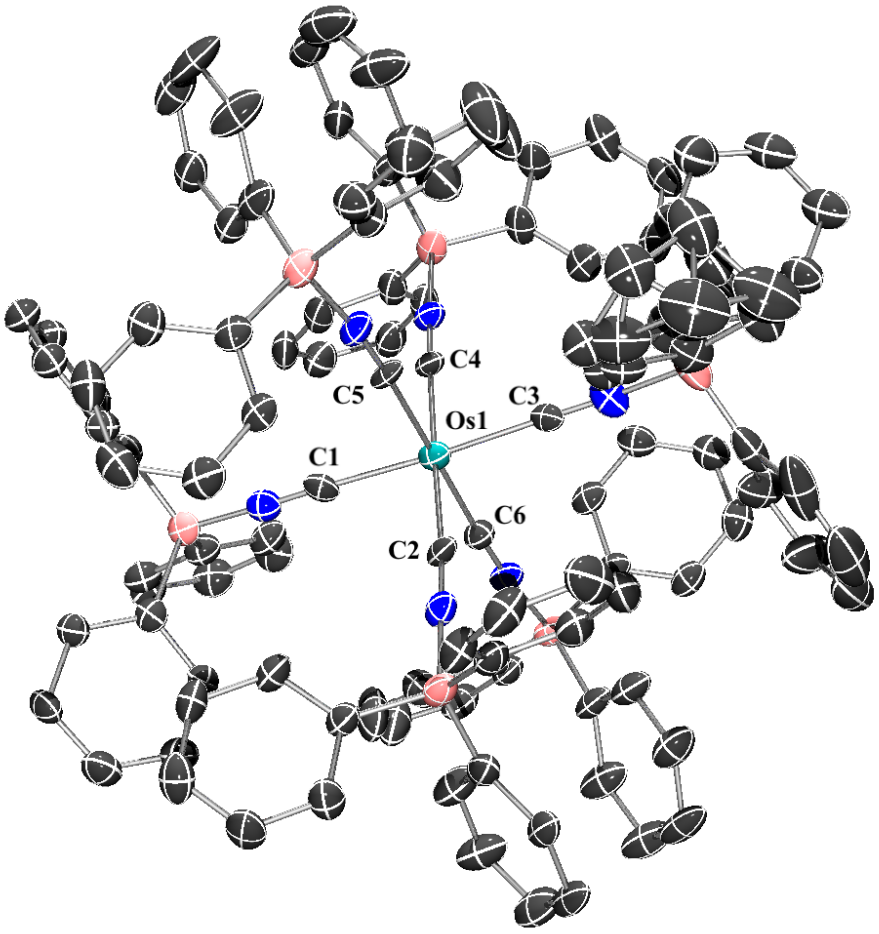

Figure 5.87. Crystal structure of one half of the asymmetric unit of $(Ph_4P)_3[Os(CN\text{-}B(C_6F_5)_3)_6]$. Thermal ellipsoids set at 50% probability. Solvent, fluorine atoms, and cations omitted for clarity.

Table 5.18 Crystal data and structure refinement for $(Ph_4P)_3[Os(CN\text{-}B(C_6F_5)_3)_6]$ (**6**).

Empirical formula	C189.07 H66.14 B6 Cl6.14 F90 N6 Os P3	
Formula weight	4697.33	
Temperature	100(2) K	
Wavelength	1.54178 Å	
Crystal system	Triclinic	
Space group	P1	
Unit cell dimensions	a = 18.2776(15) Å	a= 75.123(5)°.
	b = 18.348(3) Å	b= 86.984(6)°.
	c = 31.665(4) Å	g = 61.422(8)°.
Volume	8982(2) $Å^3$	
Z	2	
Density (calculated)	1.737 Mg/m^3	
Absorption coefficient	3.811 mm^{-1}	
F(000)	4616	
Crystal size	0.350 x 0.200 x 0.100 mm^3	
Theta range for data collection	2.762 to 74.846°.	
Index ranges	$-22 \leq h \leq 22$, $-19 \leq k \leq 22$, $-39 \leq l \leq 39$	
Reflections collected	223730	
Independent reflections	67423 [R(int) = 0.0629]	
Completeness to theta = 67.679°	99.9 %	
Absorption correction	Semi-empirical from equivalents	
Max. and min. transmission	0.3260 and 0.1820	
Refinement method	Full-matrix least-squares on F^2	
Data / restraints / parameters	67423 / 9493 / 5631	
Goodness-of-fit on F^2	1.034	
Final R indices [I>2sigma(I)]	R1 = 0.0676, wR2 = 0.1703	
R indices (all data)	R1 = 0.0792, wR2 = 0.1818	
Absolute structure parameter	0.454(6)	
Extinction coefficient	n/a	
Largest diff. peak and hole	3.561 and -0.873 e.$Å^{-3}$	

Collection and Refinement of $(PPN)_3[Cr(CN\text{-}B(C_6F_5)_3)_6]$ (7)

Low-temperature diffraction data (ϕ-and ω-scans) were collected on a Bruker AXS D8 VENTURE KAPPA diffractometer coupled to a PHOTON II CPAD detector with Mo K_α radiation (λ = 0.71073 Å) from an IμS micro-source for the structure of compound V18104_sq. The structure was solved by direct methods using SHELXS[69] and refined against F^2 on all data by full-matrix least squares with SHELXL-2016[70] using established refinement techniques.[71] All non-hydrogen atoms were refined anisotropically. All hydrogen atoms were included into the model at geometrically calculated positions and refined using a riding model. The isotropic displacement parameters of all hydrogen atoms were fixed to 1.2 times the *U* value of the atoms they are linked to (1.5 times for methyl groups). All disordered atoms were refined with the help of similarity restraints on the 1,2- and 1,3-distances and displacement parameters as well as rigid bond restraints for anisotropic displacement parameters.

$(PPN)_3[Cr(CN\text{-}B(C_6F_5)_3)_6]$ crystallizes in the triclinic space group *P*-1 with two half molecules in the asymmetric unit along with four molecules of dichloromethane and a large solvent accessible void. The highest electron density maxima are located near the Cr atoms. A void analysis with the program PLATON[72] revealed the presence of one large void and the program SQUEEZE[73] was used to remove the contribution of the disordered electron density inside this void from the structure factors. SQUEEZE removed the contribution of 292 electrons from the void with a volume of 840 Å^3, respectively.

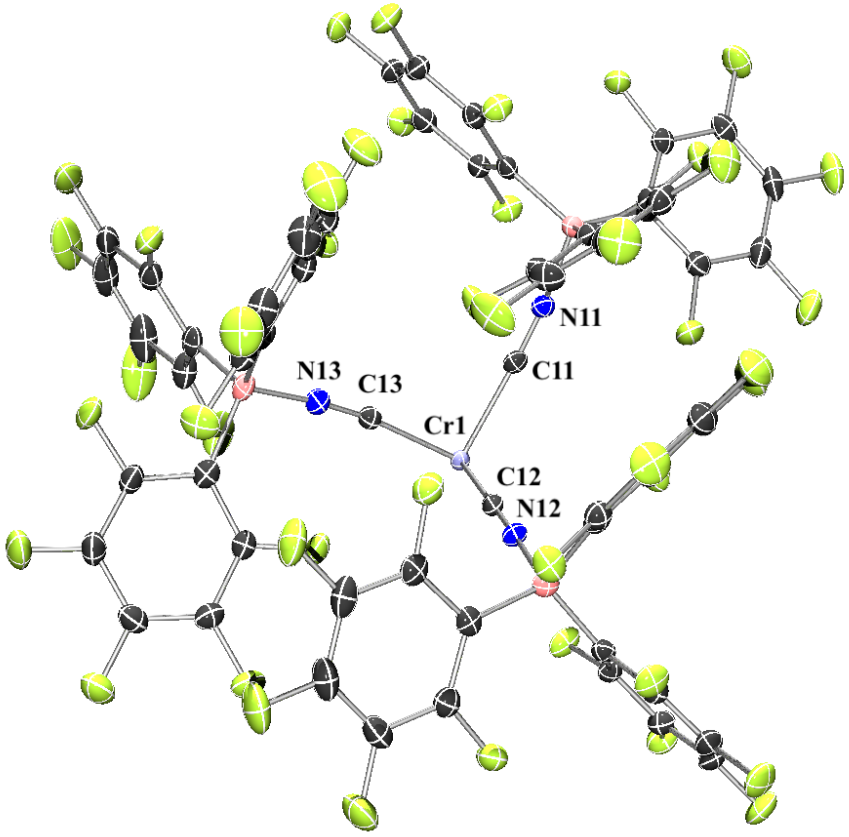

Figure 5.88. Crystal structure of one half of the asymmetric unit of $(PPN)_3[Cr(CN\text{-}B(C_6F_5)_3)_6]$. Thermal ellipsoids set at 50% probability. Solvent and cations omitted for clarity.

Table 5.19. Crystal data and structure refinement for $(PPN)_3[Cr(CN\text{-}B(C_6F_5)_3)_6]$ (**7**).

Empirical formula	C226 H98 B6 Cl8 Cr F90 N9 P6	
Formula weight	5235.41	
Temperature	100(2) K	
Wavelength	0.71073 Å	
Crystal system	Triclinic	
Space group	P-1	
Unit cell dimensions	a = 19.2145(12) Å	a= 85.517(2)°.
	b = 20.3541(12) Å	b= 80.371(2)°.
	c = 31.7571(19) Å	g = 67.296(2)°.
Volume	11294.9(12) $Å^3$	
Z	2	
Density (calculated)	1.539 Mg/m^3	
Absorption coefficient	0.318 mm^{-1}	
F(000)	5214	
Crystal size	0.400 x 0.300 x 0.200 mm^3	
Theta range for data collection	2.160 to 26.372°.	
Index ranges	$-24 \leq h \leq 24, -25 \leq k \leq 25, -39 \leq l \leq 39$	
Reflections collected	134659	
Independent reflections	46033 [R(int) = 0.0440]	
Completeness to theta = 25.242°	99.8 %	
Absorption correction	Semi-empirical from equivalents	
Max. and min. transmission	0.7461 and 0.6875	
Refinement method	Full-matrix least-squares on F^2	
Data / restraints / parameters	46033 / 0 / 3118	
Goodness-of-fit on F^2	1.012	
Final R indices [I>2sigma(I)]	R1 = 0.0689, wR2 = 0.1817	
R indices (all data)	R1 = 0.1019, wR2 = 0.2078	
Extinction coefficient	n/a	
Largest diff. peak and hole.	3.202 and -1.665 $e.Å^{-3}$	

Collection and Refinement of $(PPN)_3[Mn(CN\text{-}B(C_6F_5)_3)_6]$ (8)

Low-temperature diffraction data (ϕ-and ω-scans) were collected on a Bruker AXS D8 VENTURE KAPPA diffractometer coupled to a PHOTON II CPAD detector with Mo K_α radiation (λ = 0.71073 Å) from an IμS micro-source for the structure of compound V18154. The structure was solved by direct methods using SHELXS[69] and refined against F^2 on all data by full-matrix least squares with SHELXL-2017[70] using established refinement techniques.[71] All non-hydrogen atoms were refined anisotropically. All hydrogen atoms were included into the model at geometrically calculated positions and refined using a riding model. The isotropic displacement parameters of all hydrogen atoms were fixed to 1.2 times the *U* value of the atoms they are linked to (1.5 times for methyl groups). All disordered atoms were refined with the help of similarity restraints on the 1,2- and 1,3-distances and displacement parameters as well as rigid bond restraints for anisotropic displacement parameters.

$(PPN)_3[Mn(CN\text{-}B(C_6F_5)_3)_6]$ crystallizes in the triclinic space group *P*-1 with two half-molecules in the asymmetric unit along with eight molecules of dichloromethane. All of the dichloromethane molecules were disordered over two positions.

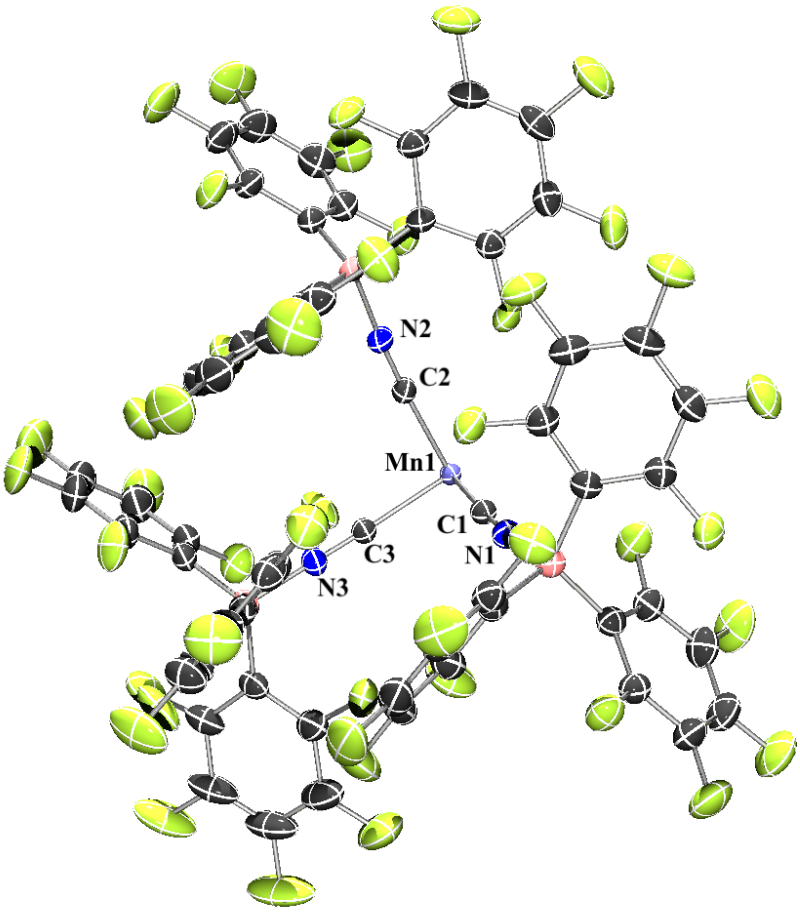

Figure 5.89. Crystal structure of one half of the asymmetric unit of $(PPN)_3[Mn(CN\text{-}B(C_6F_5)_3)_6]$. Thermal ellipsoids set at 50% probability. Solvent and cations omitted for clarity.

Table 5.20 Crystal data and structure refinement for $(PPN)_3[Mn(CN\text{-}B(C_6F_5)_3)_6]$ (**8**).

Empirical formula	C230 H106 B6 Cl16 F90 Mn N9 P6	
Formula weight	5578.05	
Temperature	200(2) K	
Wavelength	0.71073 Å	
Crystal system	Triclinic	
Space group	P-1	
Unit cell dimensions	a = 19.4633(5) Å	a= 85.5557(9)°.
	b = 20.4151(5) Å	b= 80.6484(10)°.
	c = 31.8444(7) Å	g = 66.5556(9)°.
Volume	11453.2(5) $Å^3$	
Z	2	
Density (calculated)	1.617 Mg/m^3	
Absorption coefficient	0.417 mm^{-1}	
F(000)	5552	
Crystal size	0.600 x 0.350 x 0.300 mm^3	
Theta range for data collection	2.146 to 30.508°.	
Index ranges	$-27 \le h \le 27, -29 \le k \le 29, -45 \le l \le 45$	
Reflections collected	286520	
Independent reflections	69885 [R(int) = 0.0397]	
Completeness to theta = 25.242°	99.9 %	
Absorption correction	Semi-empirical from equivalents	
Max. and min. transmission	0.7471 and 0.6963	
Refinement method	Full-matrix least-squares on F^2	
Data / restraints / parameters	69885 / 1210 / 3449	
Goodness-of-fit on F^2	1.014	
Final R indices [I>2sigma(I)]	R1 = 0.0588, wR2 = 0.1602	
R indices (all data)	R1 = 0.0914, wR2 = 0.1841	
Extinction coefficient	n/a	
Largest diff. peak and hole	1.269 and -0.646 $e.Å^{-3}$	

Collection and Refinement of $(PPN)_3[Mn(CN\text{-}B(2,4,6\text{-}F_3C_6H_2)_3)_6]$ (9)

Low-temperature diffraction data (ϕ-and ω-scans) were collected on a Bruker AXS KAPPA APEX II diffractometer coupled to an PHOTON 100 CMOS detector with graphite monochromated Mo K_α radiation (λ = 0.71073 Å) for the structure of compound D19022. The structure was solved by direct methods using SHELXS[69] and refined against F^2 on all data by full-matrix least squares with SHELXL-2017[70] using established refinement techniques.[71] All non-hydrogen atoms were refined anisotropically. All hydrogen atoms were included into the model at geometrically calculated positions and refined using a riding model. The isotropic displacement parameters of all hydrogen atoms were fixed to 1.2 times the *U* value of the atoms they are linked to (1.5 times for methyl groups). Where necessary, disordered atoms were refined with the help of similarity restraints on the 1,2- and 1,3-distances and displacement parameters as well as rigid bond restraints for anisotropic displacement parameters.

$(PPN)_3[Mn(CN\text{-}B(2,4,6\text{-}F_3C_6H_2)_3)_6]$ crystallizes in the triclinic space group *P*-1 with half a molecule in the asymmetric unit along with a mixture of tetrahydrofuran and diethyl ether located in three solvent accessible voids. One void contains tetrahydrofuran. One void contains tetrahydrofuran and diethyl ether disordered over two positions. The third void contains a five-component disorder, with three tetrahydrofuran and two diethyl ether positions. One of the diethyl ether molecules was refined with a constraint on the anisotropic displacement parameters.

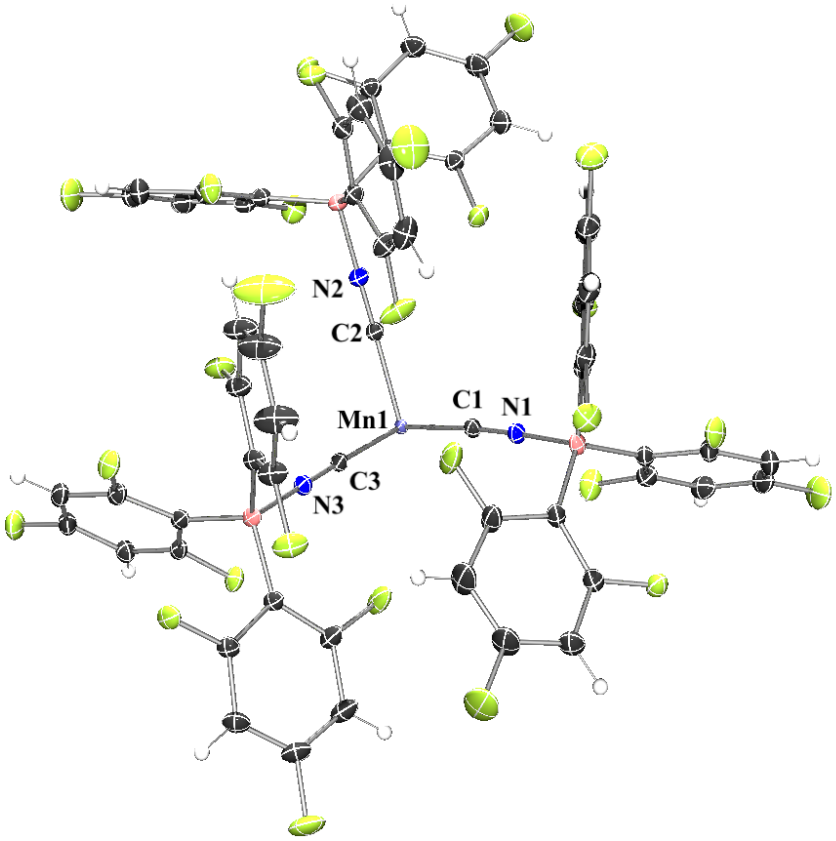

Figure 5.90. Crystal structure of the asymmetric unit of $(PPN)_3[Mn(CN\text{-}B(2,4,6\text{-}F_3C_6H_2)_3)_6]$. Thermal ellipsoids set at 50% probability. Solvent and cations omitted for clarity.

Table 5.21 Crystal data and structure refinement for $(PPN)_3[Mn(CN\text{-}B(2,4,6\text{-}F_3C_6H_2)_3)_6]$ (**9**).

Empirical formula	C125.14 H93.38 B3 F27 Mn0.50 N4.50 O3.54 P3	
Formula weight	2382.52	
Temperature	100(2) K	
Wavelength	0.71073 Å	
Crystal system	Triclinic	
Space group	P-1	
Unit cell dimensions	a = 19.032(8) Å	a= 117.244(11)°.
	b = 19.187(9) Å	b= 101.895(8)°.
	c = 19.644(9) Å	g = 107.363(15)°.
Volume	5569(4) $Å^3$	
Z	2	
Density (calculated)	1.421 Mg/m^3	
Absorption coefficient	0.210 mm^{-1}	
F(000)	2439	
Crystal size	0.800 x 0.400 x 0.300 mm^3	
Theta range for data collection	2.095 to 36.319°.	
Index ranges	$-31 \leq h \leq 31, -31 \leq k \leq 31, -32 \leq l \leq 32$	
Reflections collected	328543	
Independent reflections	53853 [R(int) = 0.0428]	
Completeness to theta = 25.242°	99.5 %	
Absorption correction	Semi-empirical from equivalents	
Max. and min. transmission	0.7475 and 0.6979	
Refinement method	Full-matrix least-squares on F^2	
Data / restraints / parameters	53853 / 1185 / 1817	
Goodness-of-fit on F^2	1.054	
Final R indices [I>2sigma(I)]	R1 = 0.0532, wR2 = 0.1295	
R indices (all data)	R1 = 0.0746, wR2 = 0.1464	
Extinction coefficient	n/a	
Largest diff. peak and hole	1.292 and -0.940 $e.Å^{-3}$	

Collection and Refinement of $(TBA)_4[Mn(CN\text{-}B(C_6F_5)_3)_6]$ (10)

Low-temperature diffraction data (ϕ-and ω-scans) were collected on a Bruker AXS D8 VENTURE KAPPA diffractometer coupled to a PHOTON II CPAD detector with Cu K_α radiation (λ = 1.54178 Å) from an IμS micro-source for the structure of compound V19273. The structure was solved by direct methods using SHELXS[69] and refined against F^2 on all data by full-matrix least squares with SHELXL-2017[70] using established refinement techniques.[71] All non-hydrogen atoms were refined anisotropically. All hydrogen atoms were included into the model at geometrically calculated positions and refined using a riding model. The isotropic displacement parameters of all hydrogen atoms were fixed to 1.2 times the U value of the atoms they are linked to (1.5 times for methyl groups). All disordered atoms were refined with the help of similarity restraints on the 1,2- and 1,3-distances and displacement parameters as well as enhanced rigid bond restraints for anisotropic displacement parameters.

$(TBA)_4[Mn(CN\text{-}B(C_6F_5)_3)_6]$ crystallizes in the monoclinic space group $P2_1/n$ with half a molecule in the asymmetric unit along with one molecule of dichloromethane. The dichloromethane and one of the tetrabutylammonium anions were disordered over two positions.

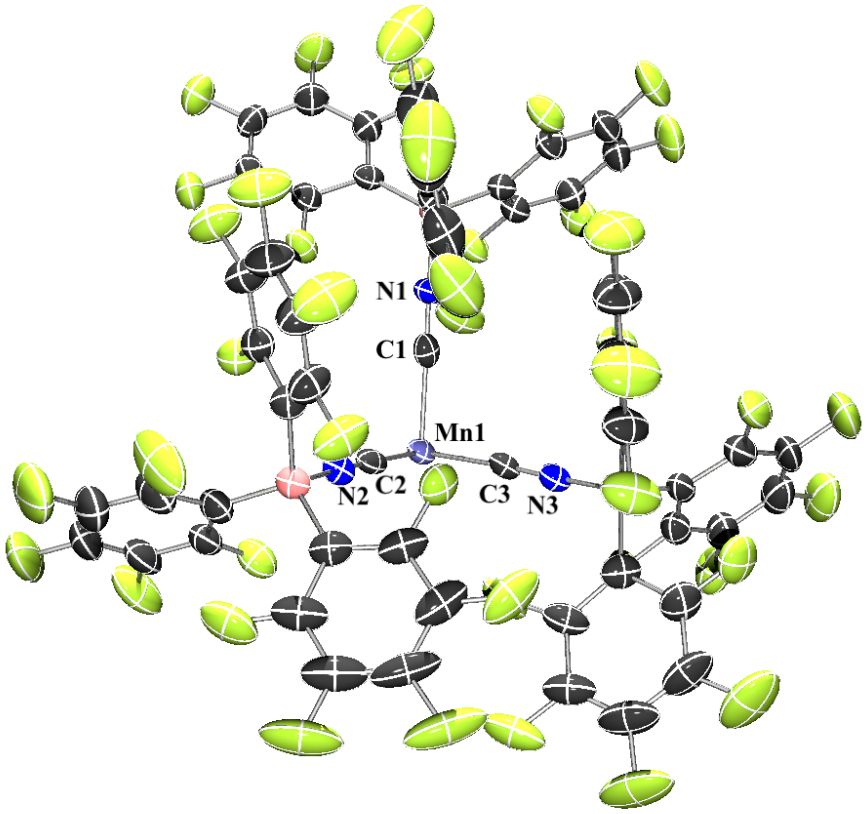

Figure 5.91. Crystal structure of the asymmetric unit of $(TBA)_4[Mn(CN\text{-}B(C_6F_5)_3)_6]$. Thermal ellipsoids set at 50% probability. Solvent and cations omitted for clarity.

Table 5.22. Crystal data and structure refinement for $(TBA)_4[Mn(CN\text{-}B(C_6F_5)_3)_6]$ (**10**).

Empirical formula	C180 H148 B6 Cl4 F90 Mn N10	
Formula weight	4422.68	
Temperature	100(2) K	
Wavelength	1.54178 Å	
Crystal system	Monoclinic	
Space group	$P2_1/n$	
Unit cell dimensions	a = 19.607(3) Å	a= 90°.
	b = 19.033(3) Å	b= 97.070(11)°.
	c = 24.982(5) Å	g = 90°.
Volume	9252(2) $Å^3$	
Z	2	
Density (calculated)	1.588 Mg/m^3	
Absorption coefficient	2.435 mm^{-1}	
F(000)	4462	
Crystal size	0.200 x 0.150 x 0.100 mm^3	
Theta range for data collection	2.709 to 63.686°.	
Index ranges	$-20 \le h \le 22$, $-21 \le k \le 22$, $-29 \le l \le 29$	
Reflections collected	120799	
Independent reflections	15208 [R(int) = 0.0894]	
Completeness to theta = 63.686°	99.9 %	
Absorption correction	Semi-empirical from equivalents	
Max. and min. transmission	0.7494 and 0.5971	
Refinement method	Full-matrix least-squares on F^2	
Data / restraints / parameters	15208 / 1272 / 1493	
Goodness-of-fit on F^2	1.017	
Final R indices [I>2sigma(I)]	R1 = 0.0902, wR2 = 0.2400	
R indices (all data)	R1 = 0.1255, wR2 = 0.2676	
Extinction coefficient	n/a	
Largest diff. peak and hole	1.050 and -0.790 $e.Å^{-3}$	

Collection and Refinement of $(PPN)_4[Mn(CN\text{-}B(2,4,6\text{-}F_3C_6H_2)_3)_6]$ (11)

A crystal was mounted on a polyimide MiTeGen loop with STP Oil Treatment and placed under a nitrogen stream. Low temperature (100K) X-ray data were collected with a Bruker AXS D8 KAPPA diffractometer diffractometer running at 50 kV and 30 mA (Mo K_α = 0.71073 Å; PHOTON 100 CMOS detector with TRIUMPH graphite monochromator. All diffractometer manipulations, including data collection, integration, and scaling were carried out using the Bruker APEX3 software. An absorption correction was applied using SADABS. The space group was determined, and the structure was solved by intrinsic phasing using XT. Refinement was full-matrix least squares on F^2 using XL. All non-hydrogen atoms were refined using anisotropic displacement parameters. Hydrogen atoms were placed in idealized positions and the coordinates refined. The isotropic displacement parameters of all hydrogen atoms were fixed at 1.2 times the U_{eq} value of the bonded atom.

$(PPN)_4[Mn(CN\text{-}B(2,4,6\text{-}F_3C_6H_2)_3)_6]$ crystallizes in the triclinic space group *P-1* (#2) with one half of an anion, two bis(triphenylphosphine)iminium cations, and 7.71 THF solvent molecules in the asymmetric unit. One of the cations was modelled at two slightly shifted positions; a number of geometry restraints and a few same-displacement-ellipsoid constraints for overlapping atoms were used. Some of the disordered solvent molecules were also restrained.

The Bruker D8 Kappa X-ray diffractometer was purchased via an NSF CRIF:MU award to the California Institute of Technology (CHE-0639094) and upgraded with a Dow Next Generation Instrumentation Grant. This work was performed by the X-Ray Crystallography Facility (XRCF) in the Beckman Institute (BI) at Caltech.

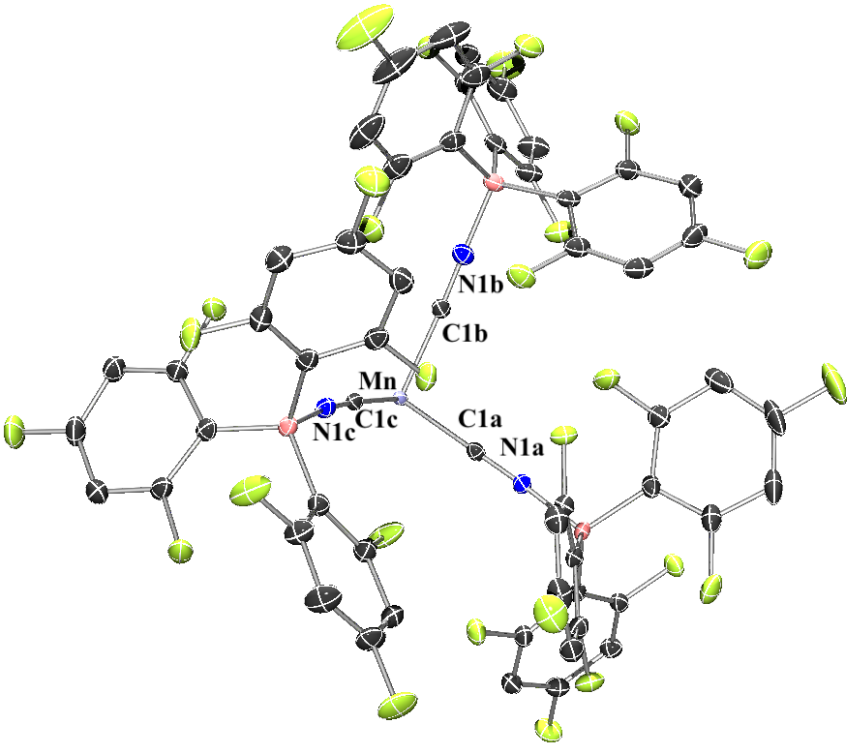

Figure 5.92. Crystal structure of the asymmetric unit of $(PPN)_4[Mn(CN\text{-}B(2,4,6\text{-}F_3C_6H_2)_3)_6]$. Thermal ellipsoids set at 50% probability. Solvent and cations omitted for clarity.

Table 5.23. Crystal data and structure refinement for $(TBA)_4[Mn(CN\text{-}B(C_6F_5)_3)_6]$ (**10**).

Empirical formula	C319.67 H279.34 B6 F54 Mn N10 O15.42 P8	
Formula weight	5901.17	
Temperature	100 K	
Wavelength	0.71073 Å	
Crystal system	Triclinic	
Space group	P-1 (# 2)	
Unit cell dimensions	a = 20.560(4) Å	α= 104.706(6)°
	b = 20.800(6) Å	β= 101.126(15)°
	c = 20.944(4) Å	γ = 118.363(7)°
Volume	7087(3) $Å^3$	
Z	1	
Density (calculated)	1.383 g/cm^3	
Absorption coefficient	0.193 mm^{-1}	
F(000)	3052	
Crystal size	0.16 x 0.34 x 0.40 mm^3	
Theta range for data collection	1.26 to 29.71°	
Index ranges	$-28 \leq h \leq 28$, $-28 \leq k \leq 28$, $-26 \leq l \leq 28$	
Reflections collected	359921	
Independent reflections	36255 [R(int) = 0.0387]	
Completeness to theta = 25.242°	99.8 %	
Absorption correction	None	
Max. and min. transmission	1.000 and 0.958	
Refinement method	Full-matrix least-squares on F^2	
Data / restraints / parameters	36255 / 371 / 2326	
Goodness-of-fit on F^2	1.133	
Final R indices [I>2sigma(I)]	R1 = 0.0645, wR2 = 0.1442	
R indices (all data)	R1 = 0.0877, wR2 = 0.1550	
Extinction coefficient	n/a	
Largest diff. peak and hole	0.68 and -0.54 $e.Å^{-3}$	

Collection and Refinement of $(Ph_4As)_3[Cr(CN\text{-}BPh_3)_6]$ (12)

A crystal was mounted on a polyimide MiTeGen loop with STP Oil Treatment and placed under a nitrogen stream. Low temperature (100K) X-ray data were collected with a Bruker AXS D8 VENTURE KAPPA diffractometer running at 50 kV and 1 mA (Cu K_α = 1.54178 Å; PHOTON II CPAD detector and Helios focusing multilayer mirror optics). All diffractometer manipulations, including data collection, integration, and scaling were carried out using the Bruker APEX3 software. An absorption correction was applied using SADABS. The space group was determined and the structure solved by intrinsic phasing using XT. Refinement was full-matrix least squares on F^2 using XL. All non-hydrogen atoms were refined using anisotropic displacement parameters. Hydrogen atoms were placed in idealized positions and refined using a riding model. The isotropic displacement parameters of all hydrogen atoms were fixed at 1.2 times (1.5 times for methyl groups) the U_{eq} value of the bonded atom.

$(Ph_4As)_3[Cr(CN\text{-}BPh_3)_6]$ crystallizes in the triclinic space group *P-1* (#2) with the asymmetric unit consisting of one full and two half anions (on inversion centers), six tetraphenyl arsenate cations, along with 3.96 restrained, partially occupied dichloromethanes over 5 sites with populations ranging from 0.44 to 0.92. An additional 3.5 dichlomethane molecules per asymmetric unit were squeezed out with OLEX2. One phenyl group on a cation is disordered 55:45. There is pseudo-symmetry relating the coordinates. One Cr is at (~1/4, ~1/2, ~3/4), not a special position in *P-1*. Many paired coordinates of other atoms sum to about twice the Cr coordinates (~1/2, ~1, ~3/2). Some pairs are Cr2 & Cr3, As1A & As1D, As1C & As1E. As1F and As1B do not have matches, but instead pair with Q1 and Q2 (coarsely). These difference peaks correspond to ~6% disorder of the As atoms about the pseudo-center. However, the phenyl group atoms could not be located, and this disorder was not modelled. The solvent populations allow this disorder.

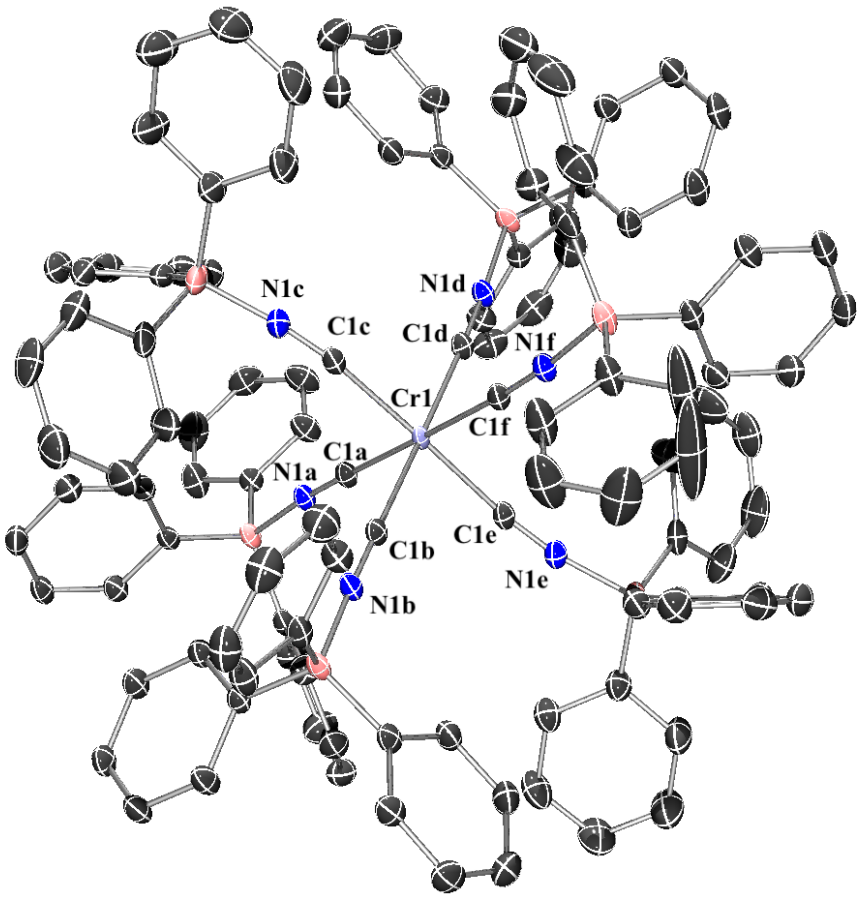

Figure 5.93. Crystal structure of one half of the asymmetric unit of $(Ph_4As)_3[Cr(CN\text{-}BPh_3)_6]$. Thermal ellipsoids set at 50% probability. Solvent, hydrogens, and cations omitted for clarity.

Table 5.24. Crystal data and structure refinement for $(Ph_4As)_3[Cr(CN\text{-}BPh_3)_6]$ (**12**).

Empirical formula	C189.73 H157.46 As3 B6 Cl7.46 Cr N6	
Formula weight	3127.50	
Temperature	100 K	
Wavelength	1.54178 Å	
Crystal system	Triclinic	
Space group	P-1	
Unit cell dimensions	a = 17.3319(13) Å	a= 86.388(6)°
	b = 30.692(3) Å	b= 88.480(5)°
	c = 30.844(3) Å	g = 79.123(6)°
Volume	16079(2) $Å^3$	
Z	4	
Density (calculated)	1.290 g/cm^3	
Absorption coefficient	2.741 mm^{-1}	
F(000)	6463	
Crystal size	0.28 x 0.14 x 0.09 mm^3	
Theta range for data collection	1.992 to 79.505°.	
Index ranges	$-22 \leq h \leq 22, -32 \leq k \leq 36, -38 \leq l \leq 39$	
Reflections collected	597130	
Independent reflections	68467 [R(int) = 0.0613]	
Completeness to theta = 67.679°	99.9 %	
Absorption correction	Semi-empirical from equivalents	
Max. and min. transmission	1.0000 and 0.7854	
Refinement method	Full-matrix least-squares on F^2	
Data / restraints / parameters	68467 / 61 / 3835	
Goodness-of-fit on F^2	1.016	
Final R indices [I>2sigma(I)]	R1 = 0.0612, wR2 = 0.1583	
R indices (all data)	R1 = 0.0726, wR2 = 0.1698	
Extinction coefficient	n/a	
Largest diff. peak and hole	4.065 and -1.321 $e.Å^{-3}$	

Collection and Refinement of $(Ph_4As)_3[Cr(NC\text{-}BPh_3)_6]$ (13)

A crystal was mounted on a polyimide MiTeGen loop with STP Oil Treatment and placed under a nitrogen stream. Low temperature (100K) X-ray data were collected with a Bruker AXS D8 VENTURE KAPPA diffractometer running at 50 kV and 1mA (Cu K_α = 1.54178 Å; PHOTON II CPAD detector and Helios focusing multilayer mirror optics). All diffractometer manipulations, including data collection, integration, and scaling were carried out using the Bruker APEX3 software. An absorption correction was applied using SADABS. The space group was determined and the structure solved by intrinsic phasing using XT. Refinement was full-matrix least squares on F^2 using XL. All non-hydrogen atoms were refined using anisotropic displacement parameters. Hydrogen atoms were placed in idealized positions and the coordinates refined. The isotropic displacement parameters of all hydrogen atoms were fixed at 1.2 times the U_{eq} value of the bonded atom.

$(Ph_4As)_3[Cr(NC\text{-}BPh_3)_6]$ crystallizes in the monoclinic space group $P2_1/n$ (#14) with one anion, three $AsPh_4$ cations, two acetonitrile molecules, and 3.22 dichloromethane molecules in the asymmetric unit. A number of restraints were used on the disordered solvent molecules. The crystal was small and diffracted poorly. The structure confirms the ligands are N (rather than C) bound to the Cr atom.

A Dow Next Generation Instrumentation Grant supported this work performed by the X-Ray Crystallography Facility (XRCF) in the Beckman Institute (BI) at Caltech.

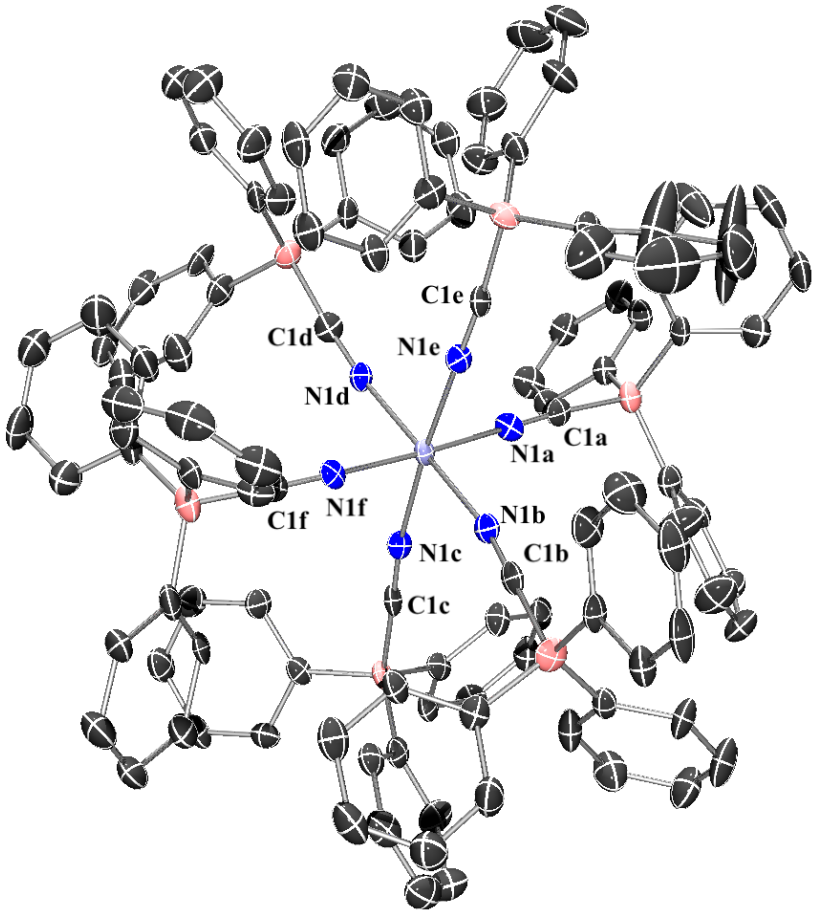

Figure 5.94. Crystal structure of the asymmetric unit of $(Ph_4As)_3[Cr(NC\text{-}BPh_3)_6]$. Thermal ellipsoids set at 50% probability. Solvent, hydrogens, and cations omitted for clarity.

Table 5.25. Crystal data and structure refinement for $(Ph_4As)_3[Cr(NC\text{-}BPh_3)_6]$ (**13**).

Empirical formula	C196.44 H168.89 As3 B6 Cl12.89 Cr N8	
Formula weight	3440.06	
Temperature	100 K	
Wavelength	1.54178 Å	
Crystal system	Monoclinic	
Space group	P 1 21/n 1 (# 14)	
Unit cell dimensions	a = 17.056(5) Å	a= 90°
	b = 35.966(9) Å	b= 93.153(15)°
	c = 29.134(10) Å	g = 90°
Volume	17845(9) $Å^3$	
Z	4	
Density (calculated)	1.280 g/cm^3	
Absorption coefficient	3.340 mm^{-1}	
F(000)	7103	
Crystal size	0.04 x 0.14 x 0.25 mm^3	
Theta range for data collection	1.95 to 64.22°	
Index ranges	$-12 \leq h \leq 19$, $-40 \leq k \leq 35$, $-28 \leq l \leq 33$	
Reflections collected	111126	
Independent reflections	26380 [R(int) = 0.0793]	
Completeness to theta = 64.217°	88.7 %	
Absorption correction	Semi-empirical from equivalents	
Max. and min. transmission	1.000 and 0.646	
Refinement method	Full-matrix least-squares on F^2	
Data / restraints / parameters	26380 / 98 / 2153	
Goodness-of-fit on F^2	1.060	
Final R indices [I>2sigma(I)]	R1 = 0.1057, wR2 = 0.2449	
R indices (all data)	R1 = 0.1470, wR2 = 0.2717	
Extinction coefficient	n/a	
Largest diff. peak and hole	4.065 and -1.321 $e.Å^{-3}$	

5.6 References

(1) Alexander, J. J.; Gray, H. B. Electronic Structures of Hexacyanometalate Complexes. *J. Am. Chem. Soc.* **1968**, *90* (16), 4260–4271. https://doi.org/10.1021/ja01018a013.

(2) Graham, M. J.; Zadrozny, J. M.; Shiddiq, M.; Anderson, J. S.; Fataftah, M. S.; Hill, S.; Freedman, D. E. Influence of Electronic Spin and Spin–Orbit Coupling on Decoherence in Mononuclear Transition Metal Complexes. *J. Am. Chem. Soc.* **2014**, *136* (21), 7623–7626. https://doi.org/10.1021/ja5037397.

(3) Woodcock, C.; Shriver, D. F. Electrochemistry and Spectroscopy of Dicyanobis(Phenanthroline)Iron, Tetracarbonyltetrakis(Cyclopentadienyl)Tetrairon and Dicarbonylcyano(Cyclopentadienyl)Iron in an Acidic Molten Salt. *Inorg. Chem.* **1986**, *25* (13), 2137–2142. https://doi.org/10.1021/ic00233a008.

(4) Shriver D.F. (1966) The ambident nature of cyanide. In: Structure And Bonding. Structure and Bonding, vol 1. Springer, Berlin, Heidelberg

(5) Indelli, M. Teresa.; Bignozzi, C. Alberto.; Marconi, Anna.; Scandola, Franco. Ruthenium(II) 2,2'-Bipyridine Complexes Containing Methyl Isocyanide Ligands. Extreme Effects of Nonchromophoric Ligands on Excited-State Properties. *J. Am. Chem. Soc.* **1988**, *110* (22), 7381–7386. https://doi.org/10.1021/ja00230a018.

(6) Krause, R. A.; Violette, C. An Improved Synthesis of Potassium Hexacyanoruthenate(II). *Inorganica Chim. Acta.* **1986**, *113* (2), 161-162.

(7) Curtis, J. C.; Meyer, T. J. Outer-Sphere Charge Transfer in Mixed-Metal Ion Pairs. *Inorg. Chem.* **1982**, *21* (4), 1562–1571. https://doi.org/10.1021/ic00134a059.

(8) Eller, S.; Fischer, R. D. Convenient Synthesis of Tris(Tetrabutylammonium) Hexacyanoruthenate(III): First Access to a Pure Salt of a Hexacyanoruthenate(III) Anion and to a Coordination Polymer Thereof. *Inorg. Chem.* **1990**, *29* (6), 1289–1290. https://doi.org/10.1021/ic00331a032.

(9) Albores, P.; Slep, L. D.; Baraldo, L. M.; Baggio, R.; Garland, M. T.; Rentschler, E. Crystal Structure and Electronic and Magnetic Properties of Hexacyanoosmate(III). *Inorg. Chem.* **2006**, *45* (6), 2361–2363. https://doi.org/10.1021/ic0516818.

(10) Samsonenko, D. G.; Vostrikova, K. E. Effective Preparation of a Variety of Ruthenium and Osmium Cyanides: Valuable Precursors for Molecular Nanomagnets. *Eur. J. Inorg. Chem.* **2016**, *2016* (9), 1369–1375. https://doi.org/10.1002/ejic.201501354.

(11) Dannöhl-Fickler, R.; Kelm, H.; Wasgestian, F. Solvent and Temperature Dependence of the Phosphorescence Decay Time of Hexacyanochromate (III). *J. Lumin.* **1975**, *10* (2), 103–112. https://doi.org/10.1016/0022-2313(75)90038-1.

(12) Schläfer, H. L.; Wagener, H.; Wasgestian, F.; Herzog, G.; Ludi, A. Elektronenspektren von Hexacyanochromaten. *Berichte Bunsenges. Für Phys. Chem.* **1971**, *75* (9), 878–883. https://doi.org/10.1002/bbpc.19710750904.

(13) Gritzner, G.; Danksagmüller, K.; Gutmann, V. Solvent Effects on the Redox Potentials of Tetraethylammonium Hexacyanomanganate(III) and Hexacyanoferrate(III). *J. Electroanal. Chem. Interf. Electrochem.* **1978**, *90* (2), 203-210.

(14) Ginsberg, A. P.; Koubek, E. Hydrogen Bonding in Ferrocyanic, Ruthenocyanic, and Osmocyanic Acids. *Inorg. Chem.* **1965**, *4* (8), 1186–1194. https://doi.org/10.1021/ic50030a022.

(15) Avendano, C.; Karadas, F.; Hilfiger, M.; Shatruk, M.; Dunbar, K. R. Cyanide Lability and Linkage Isomerism of Hexacyanochromate(III) Induced by the Co(II) Ion. *Inorg. Chem.* **2010**, *49* (2), 583–594. https://doi.org/10.1021/ic901681e.

(16) Schelter, E. J.; Shatruk, M.; Heintz, R. A.; Galán-Mascarós, J. R.; Dunbar, K. R. Unexpected Conversion of a Hexacyanometallate to a Homoleptic Nitrile Complex with Triphenylborane Substituents. *Chem. Commun.* **2005**, *11*, 1417–1419. https://doi.org/10.1039/B414262D.

(17) McNicholas, B. J.; Grubbs, R. H.; Winkler, J. R.; Gray, H. B.; Despagnet-Ayoub, E. Tuning the Formal Potential of Ferrocyanide over a 2.1 V Range. *Chem. Sci.* **2019**, *10* (12), 3623–3626. https://doi.org/10.1039/C8SC04972F.

(18) Gentil, L. A.; Navaza, A.; Olabe, J. A.; Rigotti, E. The crystal and molecular structure of sodium hexacyanoosmate(II) decahydrate and related hexacyanometalate complexes *Inorganica Chim. Acta* **1991**, *179* (1), 89-96.

(19) Ouahab, L.; Bouherour, S.; Auffredic, J.-P.; Grandjean, D. Tris-(tetraethylammonium) hexacyanoferrate (III): stability of its hydrates and X-ray structure of the pentahydrate *J. Solid. State Chem.* **1989**, *82* (1), 139-145.

(20) Bendix, J.; Steenberg, P.; Søtofte, I. Isolation and Molecular Structure of Hexacyanoruthenate(III). *Inorg. Chem.* **2003**, *42* (15), 4510–4512. https://doi.org/10.1021/ic034287n.

(21) Buschmann, W. E.; Liable-Sands, L.; Rheingold, A. L.; Miller, J. S. Structure and Physical Properties of Hexacyanomanganate(III), $[Mn^{III}(CN)_6]^{3-}$. *Inorganica Chim. Acta* **1999**, 5.

(22) Alborés, P.; Slep, L. D.; Weyhermüller, T.; Rentschler, E.; Baraldo, L. M. Exchange Coupling across the Cyanide Bridge: Structural and DFT Interpretation of the Magnetic Properties of a Binuclear Chromium(III) Complex. *Dalton. Trans.* **2006**, *7*, 948–954. https://doi.org/10.1039/B508386A.

(23) Buschmann, W. E.; Vazquez, C.; Ward, M. D.; Jones, N. C.; Miller, J. S. Structure and Physical Properties of Hexacyanomanganate(IV), $[Mn^{IV}(CN)_6]^{2-}$. *Chem. Commun.* **1997**, *4*, 409–410. https://doi.org/10.1039/a606979g.

(24) Opekar, F.; Beran, P. Electrochemical oxidation of $K_4[Os(CN)_6]$ on a platinum electrode. *J. Electroanal. Chem. Interf. Electrochem.* **1976**, *71* (1), 120-124.

(25) Espinoza, E. M.; Clark, J. A.; Soliman, J.; Derr, J. B.; Morales, M.; Vullev, V. I. Practical Aspects of Cyclic Voltammetry: How to Estimate Reduction Potentials When Irreversibility Prevails. *J. Electrochem. Soc.* **2019**, *166* (5), H3175–H3187. https://doi.org/10.1149/2.0241905jes.

(26) Kane-Maguire, N. A. P.; Guckert, J. A.; O'Neill, P. J. Electrogenerated Chemiluminescence of Hexacyanochromate(III) and Tris(2,2'-Bipyridine)Chromium(III) in Aprotic Solvents. *Inorg. Chem.* **1987**, *26* (14), 2340–2342. https://doi.org/10.1021/ic00261a036.

(27) Hume, D. N.; Kolthoff, I. M. The Oxidation Potential of the Chromocyanide—Chromicyanide Couple and the Polarography of the Chromium Cyanide Complexes. *J. Am. Chem. Soc.* **1943**, *65* (10), 1897–1901. https://doi.org/10.1021/ja01250a030.

(28) Murray, R. C.; Rock, P. A. The Determination of the Ferrocyanide—Ferricyanide Standard Electrode Potential at 25°C in Cells without Liquid Junction Using Cation-Sensitive Glass Electrodes. *Electrochimica Acta* **1968**, *13* (4), 969–975. https://doi.org/10.1016/0013-4686(68)85028-5.

(29) Crumbliss, A. L.; O. Hill, H. A.; Page, D. J. The Electrochemistry of Hexacyanoruthenate at Carbon Electrodes and the Use of Ruthenium Compounds as Mediators in the Glucose/Glucose Oxidase System. *J. Electroanal. Chem. Interfacial Electrochem.* **1986**, *206* (1–2), 327–331. https://doi.org/10.1016/0022-0728(86)90280-9.

(30) Mascharak, P. K. Convenient synthesis of tris(tetraethylammonium) hexacyanoferrate(III) and its use as an oxidant with tunable redox potential. *Inorg. Chem.* **1986**, *25* (3), 245-247.

(31) Srnec, M.; Chalupský, J.; Fojta, M.; Zendlová, L.; Havran, L.; Hocek, M.; Kývala, M.; Rulíšek, L. Effect of Spin−Orbit Coupling on Reduction Potentials of Octahedral Ruthenium(II/III) and Osmium(II/III) Complexes. *J. Am. Chem. Soc.* **2008**, *130* (33), 10947–10954. https://doi.org/10.1021/ja800616s.

(32) Beckett, M. A.; Brassington, D. S.; Coles, S. J.; Hursthouse, M. B. Lewis Acidity of tris(pentafluorophenyl)borane: crystal and molecular structure of $B(C_6F_5)_3{\cdot}OPEt_3$. *Inorg. Chem. Commun.* **2000**, *3* (10), 530-533.

(33) Blagg, R. J.; Simmons, T. R.; Hatton, G. R.; Courtney, J. M.; Bennett, E. L.; Lawrence, E. J.; Wildgoose, G. G. Novel $B(Ar')_2(Ar'')$ hetero-tri(aryl)boranes: a systematic study of lewis acidity. *Dalton Trans.* **2016**, *45* (14), 6032–6043. https://doi.org/10.1039/C5DT03854E.

(34) Soltani, Y.; Adams, S. J.; Börger, J.; Wilkins, L. C.; Newman, P. D.; Pope, S. J. A.; Melen, R. L. Synthesis and Photophysical Properties of Imine Borane Adducts towards Vapochromic Materials. *Dalton Trans.* **2018**, *47* (36), 12656–12660. https://doi.org/10.1039/C8DT03019G.

(35) Nicholson, R. S. Semiempirical Procedure for Measuring with Stationary Electrode Polarography Rates of Chemical Reactions Involving the Product of Electron Transfer *Anal. Chem.* **1966**, *38* (10), 1406.

(36) Weber, A. Z.; Mench, M. M.; Meyers, J. P.; Ross, P. N.; Gostick, J. T.; Liu, Q. Redox Flow Batteries: A Review. *J. Appl. Electrochem.* **2011**, *41* (10), 1137–1164. https://doi.org/10.1007/s10800-011-0348-2.

(37) Basu, G.; Belford, R. L. Nature of the Visible Charge-Transfer Bands of $K_3Fe(CN)_6$. *J. Chem. Phys.* **1962**, *37* (9), 1933–1935. https://doi.org/10.1063/1.1733408.

(38) Gray, H. B.; Beach, N. A. The Electronic Structures of Octahedral Metal Complexes. I. Metal Hexacarbonyls and Hexacyanides. *J. Am. Chem. Soc.* **1963**, *85* (19), 2922–2927. https://doi.org/10.1021/ja00902a014.

(39) Mason, W. R. *A Practical Guide to Magnetic Circular Dichroism Spectroscopy*; John Wiley & Sons, Inc.: Hoboken, NJ, USA, 2007. https://doi.org/10.1002/9780470139233.

(40) Chastain, S. K.; Mason, W. Roy. Magnetic Circular Dichroism of Metal-to-Ligand Charge-Transfer Spectra of Hexacarbonyl and Hexacyano Complexes of nd^6 Electron Configuration. *Inorg. Chem.* **1981**, *20* (5), 1395–1398. https://doi.org/10.1021/ic50219a013.

(41) Stephens, P. J. Magnetic Circular Dichroism. *Annu. Rev. Phys. Chem.* **1974**, *25*, 201-232.

(42) Stephens, P. J. The Faraday Rotation of Allowed Transitions: Charge-Transfer Transitions in $K_3Fe(CN)_6$. *Inorg. Chem.* **1965**, *4* (12), 1690–1692. https://doi.org/10.1021/ic50034a003.

(43) Upton, A. H. P.; Williamson, B. E. Magnetic Circular Dichroism and Absorption Spectra of Hexacyanoferrate(III) in a Poly(Vinyl Alcohol) Film. *J. Phys. Chem.* **1994**, *98* (1), 71–76. https://doi.org/10.1021/j100052a013.

(44) Gale, R.; McCaffery, A. J. Bonding Studies from Charge-Transfer Absorption and Magnetic Circular Dichroism Spectra. Part II. The Complex Hexacyanoferrate(III) and Pentacyanoferrate(III) Complexes of C_{4v} Symmetry. *J. Chem. Soc., Dalton Trans.* **1973**, 13, 1344-1351.

(45) Hahn, A. W.; Van Kuiken, B. E.; Chilkuri, V. G.; Levin, N.; Bill, E.; Weyhermüller, T.; Nicolaou, A.; Miyawaki, J.; Harada, Y.; DeBeer, S. Probing the Valence Electronic Structure of Low-Spin Ferrous and Ferric Complexes Using 2p3d Resonant Inelastic X-Ray Scattering (RIXS). *Inorg. Chem.* **2018**, *57* (15), 9515–9530. https://doi.org/10.1021/acs.inorgchem.8b01550.

(46) Vogler, A.; Kunkely, H. Luminescence from Hexacyanoruthenate(III). *Inorganica Chim. Acta* **1981**, *53*, L215-L216.

(47) Kang, H. W.; Moran, G.; Krausz, E. Magnetic Circular Dichroism Spectroscopy of the Hexacyano Complexes of Ru(III) and Os(III) *Inorganica Chim. Acta* **1996**, *249* (2), 231-235.

(48) Mingardi, M. A. P. Luminescence and Absorption Spectra of Some d^6 Complexes. Ph.D. Dissertation, The University of British Columbia, Vancouver, Canada, 1969.

(49) Englman, R.; Jortner, J. The Energy Gap Law for Radiationless Transitions in Large Molecules. *Mol. Phys.* **1970**, *18* (2), 145–164. https://doi.org/10.1080/00268977000100171.

(50) DeFord, D. D.; Davidson, A. W. Studies on the Oxidation of Potassium Ruthenocyanide. *J. Am. Chem. Soc.* **1951**, *73* (4), 1469–1474. https://doi.org/10.1021/ja01148a019.

(51) Buhr, J. D.; Winkler, J. R.; Taube, H. Characterization and Reactions of Osmium(IV) Ammines. *Inorg. Chem.* **1980**, *19*, 2416-2425.

(52) Giuliani, M. G. Effect of Some Tetraalkylammonium Hydroxides on the Electrode Kinetics of the Chromi-Chromocyanide Couple. *J. Electroanal. Chem.* **1959**, *11*, 313-315.

(53) Feldberg, S. W.; Jeftic, L. Nuances of the ECE Mechanism. IV. Theory of Cyclic Voltammetry and Chronoamperometry and the Electrochemical Reduction of Hexacyanochromate(III) *J. Phys. Chem.* **1972**, *76*, 2439-2446.

(54) Delahay, P.; Kleinerman, M. Structure of the Double Layer and Electrode Processes. II. Effect of the Nature of the Electrode and Application of the Thallium-Amalgam Electrode. *J. Am. Chem. Soc.* **1960**, *82* (17), 4509–4514. https://doi.org/10.1021/ja01502a016.

(55) Marchaj, A.; Wasgestian, F. Ligand Field Photolysis of $[Cr(CN)_6]^{3-}$ in Acetonitrile. *Inorganica Chim. Acta* **1985**, *102* (1), L13–L15. https://doi.org/10.1016/S0020-1693(00)89061-1.

(56) Castelli, F.; Forster, L. S. $^4T_2$ State Lifetimes and Intersystem Crossing Efficiencies in Chromium(III) Complexes. *J. Phys. Chem.* **1977**, *81* (5), 403–408. https://doi.org/10.1021/j100520a008.

(57) Wasgestian, H. F. Evidence against the Doublet Hypothesis. Photolysis of Hexacyanochromate(III) in Dimethylformamide. *J. Phys. Chem.* **1972**, *76* (14), 1947–1951. https://doi.org/10.1021/j100658a006.

(58) Castelli, F.; Forster, L. S. Absolute Quantum Yields of $^2E_g \rightarrow {}^4A_{2g}$ Luminescence in Potassium Hexacyano(Cobaltate, Chromate) Powders. *J. Phys. Chem.* **1974**, *78* (21), 2122–2127. https://doi.org/10.1021/j100614a012.

(59) Krishnamurthy, R.; Schaap, W. B. A Quartet-Doublet Transition in Hexacyanochromate(III) Anion. *Inorg. Chem.* **1963**, *2*, 605-608.

(60) Wolberg, A. Electron Paramagnetic Resonance Ligand Hyperfine Interactions in CrF_6^{3-} and $Cr(CN)_6^{3-}$ Complexes. *J. Chem. Phys.* **1971**, *54* (3), 1428–1430. https://doi.org/10.1063/1.1674998.

(61) Yang, Z.-Y. An Investigation of the EPR Zero-Field Splitting of Cr^{3+} Ions at the Tetragonal Site and the Cd^{2+} Vacancy in $RbCdF_3:Cr^{3+}$ Crystals. *J. Phys. Condens. Matter* **2000**, *12* (17), 4091–4096. https://doi.org/10.1088/0953-8984/12/17/314.

(62) Meyer, D. A.; Zhang, X.; Bergmann, U.; Gaffney, K. J. Characterization of Charge Transfer Excitations in Hexacyanomanganate(III) with Mn K-Edge Resonant Inelastic X-Ray Scattering. *J. Chem. Phys.* **2010**, *132* (13), 134502. https://doi.org/10.1063/1.3367958.

(63) Chawla, I. D.; Frank, M. J. Electronic Spectra of Hexacyanomanganate(III) and Hydroxopentacyanomanganate (III) Ions in Acidic Media. *J. Inorg. Nucl. Chem.* **1970**, *32* (2), 555–563. https://doi.org/10.1016/0022-1902(70)80265-2.

(64) DeSimone, R. E. Electron Paramagnetic Resonance Studies of Low-Spin d^5 Complexes. Trisbidentate Complexes of Iron(III), Ruthenium(III), and Osmium(III) with Sulfur-Donor Ligands. *J. Am. Chem. Soc.* **1973**, *95* (19), 6238–6244. https://doi.org/10.1021/ja00800a015.

(65) Stauber, J. M.; Zhang, S.; Gvozdik, N.; Jiang, Y.; Avena, L.; Stevenson, K. J.; Cummins, C. C. Cobalt and Vanadium Trimetaphosphate Polyanions: Synthesis, Characterization, and Electrochemical Evaluation for Non-Aqueous Redox-Flow Battery Applications. *J. Am. Chem. Soc.* **2018**, *140* (2), 538–541. https://doi.org/10.1021/jacs.7b08751.

(66) Das, B.; Carlin, R.; Osteryoung, R. A. The Ferro/Ferricyanide Couple in an Aluminum Chloride-1-Methyl-3-Ethylimidazolium Chloride Ambient-Temperature Molten Salt. *Inorg. Chem.* **1989**, *28* (3), 421–426. https://doi.org/10.1021/ic00302a011.

(67) Ginsberg, A. P.; Koubek, E. Hydrogen Bonding in Ferrocyanic, Ruthenocyanic, and Osmocyanic Acids. *Inorg. Chem.* **1965**, *4* (8), 1186–1194. https://doi.org/10.1021/ic50030a022.

(68) Stoll, S.; Schweiger, A. EasySpin, a Comprehensive Software Package for Spectral Simulation and Analysis in EPR. *J. Magn. Reson.* **2006**, *178* (1), 42–55. https://doi.org/10.1016/j.jmr.2005.08.013.

(69) Sheldrick, G. M. Phase annealing in *SHELX*-90: Direct Methods for Larger Structures. *Acta Crystallogr.* **1990**, *A46*, 467–473.

(70) Sheldrick, G. M. Crystal Structure Refinement with SHELXL. *Acta Crystallogr.* **2015**, *C71*, 3–8.

(71) Müller, P. Practical Suggestions for Better Crystal Structures. *Crystallogr. Rev.* **2009**, *15*, 57–83.

(72) Spek, A. L. Structural Validation in Chemical Crystallography. *Acta Cryst.* **2009**, D65, 148-155.

(73) Van der Sluis, P. and Spek, A. L. BYPASS: An Effective Method for the Refinement of Crystal Structures Containing Disordered Solvent Regions. *Acta Cryst.* **1990**, A46, 194-201.

Chapter VI

ELECTRONIC STRUCTURES, SPECTROSCOPY, AND ELECTROCHEMISTRY OF $[M(DIIMINE)(CN\text{-}BR_3)_4]^{2-}$ (M = FE, RU; R = PH, C_6F_5) COMPLEXES: A COMBINED EXPERIMENTAL AND COMPUTATIONAL STUDY

6.1. Summary

Complexes with the formula $[M(diimine)(CN\text{-}BR_3)_4]^{2-}$, where diimine = bipyridine (bpy), phenanthroline (phen), 3,5-trifluoromethylbipyridine (flpy), R = Ph, C_6F_5, and M = Fe^{II}, Ru^{II} were synthesized and characterized by X-ray crystal structure analysis, UV-visible spectroscopy, IR spectroscopy, and voltammetry. Three highly soluble complexes, $[Fe^{II}(bpy)(CN\text{-}B(C_6F_5)_3)_4]^{2-}$, $[Ru^{II}(bpy)(CN\text{-}B(C_6F_5)_3)_4]^{2-}$, and $[Ru^{II}(flpy)(CN\text{-}B(C_6F_5)_3)_4]^{2-}$ exhibit two electrochemically reversible redox couples, with large potential differences between the $bpy^{0/-}$ or $flpy^{0/-}$ and $M^{III/II}$ couples of 3.27, 3.52, and 3.19 V, respectively. The ruthenium complexes exhibit large excited state potentials, making these compounds viable photoredox agents. The UV-visible absorption and luminescence spectra of the $[M(diimine)(CN)_4]^{2-}$ derivatives are tuned over wide ranges through variations in solvent, substituents on the diimine ligand, and boronation of the cyanide ligands. Trifluoromethyl substitution at the 4 and 4' positions of the diimine induces red shifts in metal-to-ligand charge transfer (MLCT) transition absorption and luminescence bands. Boronation of the cyanide ligands produces substantial blue shifts in MLCT energies. The combination of diimine trifluoromethylation and cyanide boronation produces MLCT blue shifts that are about 75% as large as those produced by boronation alone. Subtle shifts in the energies of ligand field transitions and dramatic shifts in the energies of MLCT transitions are accurately reproduced using CASSCF+NEVPT2 calculations.

6.2. Introduction

Heteroleptic transition metal cyanide complexes with chelating diimine ligands of metals such as ruthenium,[1] iron,[2] copper,[3] iridium,[4] rhenium,[5] and osmium[6,7] have found use in a variety of applications, including as vapochromic agents,[8] electrochemically reversible oxidants and reductants,[7] phosphors for organic light-emitting diodes,[7,9,5] and photooxidants and photoreductants.[10] The electron transfer reactions of homoleptic and heteroleptic cyanometallates, such as the hexacyanoferrates, are electrochemically reversible and are uniquely sensitive to outer-sphere effects. The reduction potential of $[Fe(CN)_6]^{3-}$, for example, shifts anodically 1.3 V when N-methyl-2-pyrrolidone replaces water as a solvent,[11] and the metal-to-ligand charge transfer (MLCT) absorption band of $[Fe(bpy)(CN)_4]^{2-}$ (bpy = 2,2'-bipyridine) red shifts by 0.86 eV upon changing the solvent from water to acetone.[2] We and others have shown that octahedral metal cyanides bond with boranes such as boron trifluoride, lowering the σ and π* orbital energies of the cyanide ligand, which weakens metal-carbon bonding and strengthens CN bonding. Lowering the π* cyanide orbitals enhances π backbonding, thereby increasing overall ligand field strengths.[12,13,14] Consequently, formal potentials for $M^{(n+1)+}/M^{n+}$ couples are shifted anodically and metal-to-ligand charge transfer (MLCT) transitions are blue shifted, allowing resolution of ligand field (LF) absorptions, notably in hexacyanoferrate(II).[14] Heteroleptic analogues, such as $Os(bipyridine)_2(CN\text{-}B(C_6F_5)_3)_2$, also exhibit substantial anodic potential shifts for metal-centered redox events;[7] not surprising, shifts for diimine-localized redox processes are much smaller.[7] **Figure 6.1** depicts the general changes in one-electron energy levels that occur upon boronation of a heteroleptic tetracyanometallate that possesses an aromatic ligand.

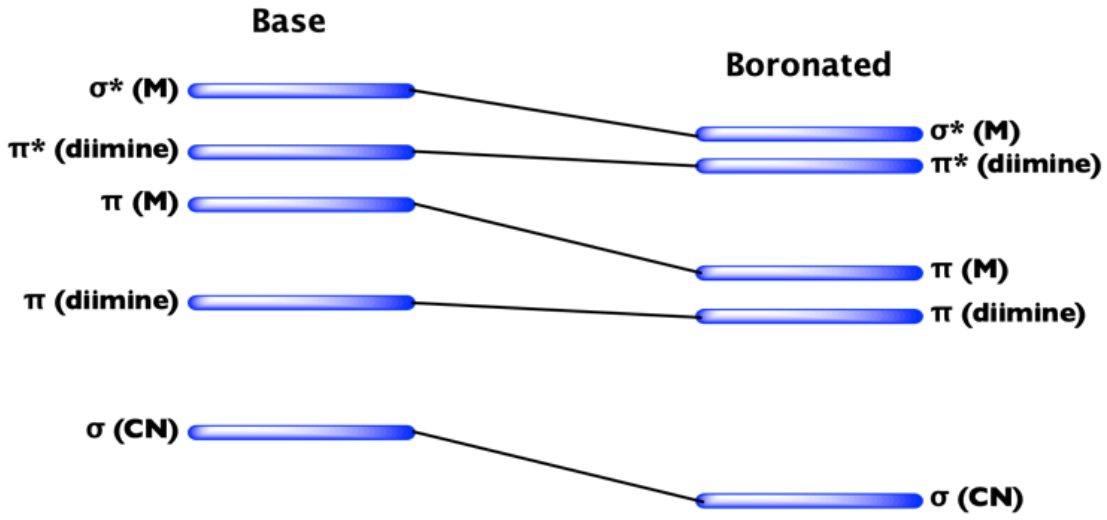

Figure 6.1. One-electron energy level changes resulting from boronation of $[M(diimine)(CN)_4]^{2-}$.

Outer-sphere effects also appear in the luminescence and photophysical properties of cyanometallates. The luminescence spectra and decay kinetics of $[Ru(diimine)(CN)_4]^{2-}$ complexes are tuned over wide ranges by the polarity, the presence of protons, and the isotopic composition of the surrounding solvent.[10,15,16,17,18] Electron-withdrawing substituents on the diimine and adduct formation with boranes induce similar perturbations.

Earlier reports demonstrated that the coordination of tris(pentafluorophenyl)borane (BCF) to $[Fe(CN)_6]^{4-}$ anodically shifts the formal $Fe^{III/II}$ potential by over 2.1 V.[19] Since complexes with two differently tunable redox centers are relatively rare, we have extended our investigations of boronated cyanometallates to include heteroleptic tetracyanometallates with bipyridine (bpy), 3,5-trifluoromethylbipyridine (flpy), or phenanthroline (phen). Boronation with BPh_3 or BCF afforded $([M(diimine)(CN\text{-}BR_3)])^{2-}$ (M = Fe^{II}, Ru^{II}; diimine = bpy, phen, flpy; and R = Ph, C_6F_5) complexes. In

addition to their utility as chromophores,[10,20,21,22] these complexes have impressive electrochemical properties.

To enhance our understanding of the effects of boronation on MLCT transitions, we performed *ab initio* calculations on trihydridoborane analogues of the heteroleptic cyanometallates using the complete active space self-consistent field (CASSCF) method coupled with n-electron valence state second-order perturbation theory (NEVPT2). Our calculations demonstrate the accuracy of CASSCF+NEVPT2 for both LF and MLCT transition states of boronated cyanoruthenates. We also probed the excited-state properties of Fe^{II} analogues, as we hoped boronation would extend the lifetimes of these typically short-lived states.

6.3. Results and Discussion

Synthesis and X-ray Crystallography

The potassium salts of the precursor $[M^{II}(diimine)(CN)_4]^{2-}$ complexes were synthesized according to literature methods.[23,24] $K_2[Ru(flpy)(CN)_4]$ (**Ru-flpy**) was synthesized in a similar manner. Bis(triphenylphosphine)iminium (PPN^+) salts of the anions were prepared by addition of a stoichiometric excess of PPNCl to a warm, aqueous solution of $K_2[M^{II}(diimine)(CN)_4]$, yielding a solid that was collected by filtration. The tetrabutylammonium (TBA^+) salts of selected anions were prepared through metathesis with hydrochloric acid to precipitate $H_2[M^{II}(diimine)(CN)_4]$. Subsequent titration with TBAOH afforded $(TBA)_2[M^{II}(diimine)(CN)_4]$.

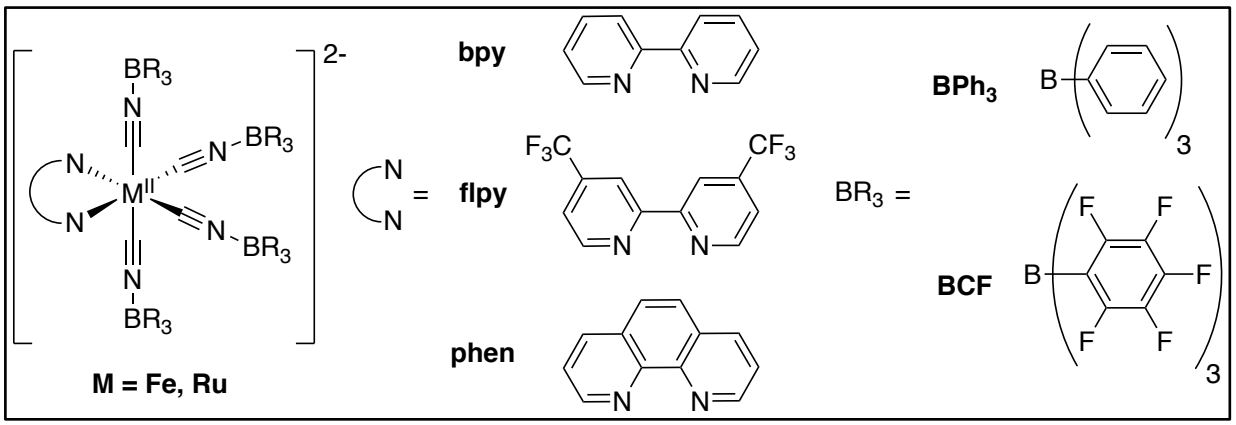

Figure 6.2. General structures of $[M(diimine)(CN\text{-}BR_3)_4]^{2-}$, diimine ligands, and boranes investigated in this work.

To obtain the borane adducts of these species, a slight excess of BPh_3 or BCF was added to a nitrogen-purged dichloromethane solution of the TBA^+ or PPN^+ salts of $[M^{II}(diimine)(CN)_4]^{2-}$ complexes under reflux conditions. Addition of hexanes (excess) to a concentrated solution afforded the following complexes: $(TBA)_2[Fe^{II}(bpy)(CN\text{-}BPh_3)_4]$ (**Fe-bpy-BPh$_3$**), $(TBA)_2[Fe^{II}(bpy)(CN\text{-}B(C_6F_5)_3)_4]$ (**Fe-bpy-BCF**), $(TBA)_2[Fe^{II}(phen)(CN\text{-}BPh_3)_4]$ (**Fe-phen-BPh$_3$**), $(TBA)_2[Fe^{II}(phen)(CN\text{-}B(C_6F_5)_3)_4]$ (**Fe-phen-BCF**), $(TBA)_2[Ru^{II}(bpy)(CN\text{-}BPh_3)_4]$ (**Ru-bpy-BPh$_3$**), $(TBA)_2[Ru^{II}(bpy)(CN\text{-}B(C_6F_5)_3)_4]$ (**Ru-bpy-BCF**), and $(PPN)_2[Ru(flpy)(CN\text{-}B(C_6F_5)_3)_4]$ (**Ru-flpy-BCF**). Characterization by ^1H NMR, ^{11}B NMR and, when applicable, ^{19}F NMR, confirmed that all compounds were pure. All compounds also were characterized by elemental analysis or mass spectrometry, IR spectroscopy, voltammetry, and UV-visible spectroscopy. General structures of species investigated in these studies are depicted in **Figure 6.2**.

Growth of X-ray quality crystals proved challenging for these complexes due to their tendency to form oils. However, we were able to obtain four crystal structures: **Ru-flpy**, **Ru-flpy-BCF**, **Fe-phen-BPh$_3$**, and **Fe-phen-BCF**. Comparing **Ru-flpy** and **Ru-flpy-BCF**, we observe a negligible change in

the average C-N bond length and a minor shortening (ca. 0.05 Å) of the average Ru-C bond length. These small structural changes are consistent with work on boronated hexacyanoferrates.[19,28]

Infrared, UV-Visible, and Luminescence Spectroscopy

IR stretching frequencies, MLCT absorbance maxima (and extinction coefficients) for the parent complexes and heteroleptic isocyanoborates are set out in **Table 6.1**. Only one MLCT transition is reported for **Fe-phen-BCF** and **Fe-phen-BPh$_3$** due to overlap with the first π-π* absorption of the phenanthroline ligand. The blueshifts in CN stretching frequencies indicate strengthening of the CN bond due to coordination of borane to the nitrogen lone pair.[12,25] The IR stretching frequencies for **Ru-flpy-BCF** are very slightly blueshifted from those of **Ru-bpy-BCF**, consistent with a slight decrease in π back donation due to electron withdrawal by the flpy trifluoromethyl groups. NMR and IR spectra are shown in the experimental section (**Figures 6.10-6.40**).

Table 6.1. Vibrational and metal-to-ligand charge transfer data for [M(diimine)(CN)$_4$]$^{2-}$ and [M(diimine)(CN-BR$_3$)$_4$]$^{2-}$ in MeCN.

Species	ν_{CN} (cm^{-1})	λ_{MLCT} (nm)	ε (M^{-1} cm^{-1})
Fe-bpy[a,b]	2047, 2077	654, 440	---
Fe-bpy-BPh$_3$	2145, 2181	465, 333	1670, 1940
Fe-bpy-BCF	2170, 2207	413, 309	2360, 4170
Fe-phen	2045, 2074	615	---
Fe-phen-BPh$_3$	2146, 2182	439	2610
Fe-phen-BCF	2169, 2206	394	3160
Ru-bpy[c]	2051, 2082	535, 374	---
Ru-bpy-BPh$_3$	2140, 2188	391, 309	2950, 5000
Ru-bpy-BCF	2168, 2216	357	3000
Ru-flpy	2062, 2090	589, 413	3850, 6130
Ru-flpy-BCF	2171, 2218	390, 320	3830, 4560

[a]Reference 26.
[b]Reference 27.
[c]Reference 28

The absorption and luminescence spectra of $[Ru(bpy)(CN)_4]^{2-}$ are extremely sensitive to the polarity and presence of protons in the solvent.[10,29] **Figure 6.3** displays the UV-vis spectra for all newly reported species. It is well known that Fe and Ru diimine complexes exhibit well-defined MLCT transitions in the visible/near-UV region that are strongly solvatochromic.[30] Substituents on the diimine ligand further perturb the spectra: electron-donating groups ($-CH_3$) produce a blue shift; electron-withdrawing groups ($-C_6H_5$, $-C_6F_5$, $-COO^-$) produce red shifts.[18] Thus, it is not surprising that **Ru-flpy** MLCT transitions red shift by 5500 cm^{-1} when the solvent is changed from water to acetonitrile.[31] This shift is expected in view of the much larger Gutmann-Beckett acceptor number of H_2O compared to MeCN.[11] The trifluoromethyl group is a much more effective electron withdrawing group than the substituents examined previously, and consequently the absorption and luminescence maxima of $[Ru(flpy)(CN)_4]^{2-}$ are dramatically red-shifted relative to those of the parent dianion. Although the trifluoromethyl groups should render the cyanide ligands somewhat less basic, removal of solvent protons nevertheless induces a 0.70-eV red-shift of the $[Ru(flpy)(CN)_4]^{2-}$ MLCT absorption maximum from its value in aqueous solution. This red-shift is only slightly smaller than that found with $[Ru(bpy)(CN)_4]^{2-}$ (0.75 eV)[29,32] and $[Ru(4,4'\text{-Me-bpy})(CN)_4]^{2-}$ (0.82 eV).[22] Luminescence from $[Ru(flpy)(CN)_4]^{2-}$ in aqueous solution exhibits a maximum at 706 nm. In the solid state, $(PPN)_2[Ru(flpy)(CN)_4]$ displays a luminescence maximum at 880 nm. These spectra are shown in **Figure 6.4**.

In contrast to the dramatic shifts observed in MLCT transitions, the π-π^* absorption shifts only slightly (550 cm^{-1}), indicating that solvent interactions and, by extension MCN-B bonding, minimally perturb diimine orbital energies.

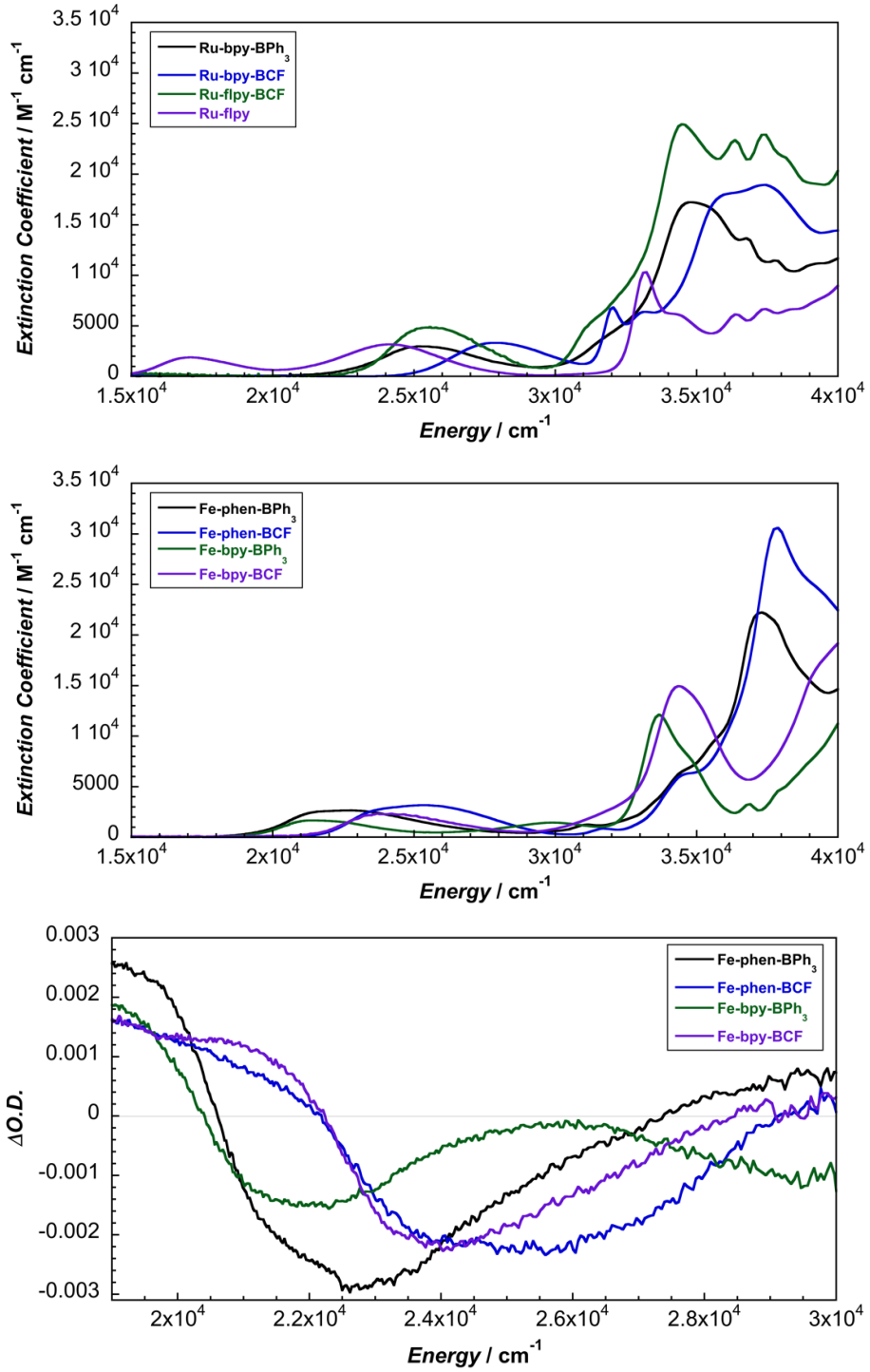

Figure 6.3. (**Top**) UV-visible absorption spectra of $[Ru(diimine)(CN)_4]^{2-}$ and (**Middle**) $[Fe(diimine)(CN\text{-}BR_3)_4]^{2-}$ in MeCN solution. (**Bottom**) Transient absorption spectra of $[Fe(diimine)(CN\text{-}BR_3)_4]^{2-}$ in MeCN solution at 1 ps after 34,500 cm^{-1} (290 nm) excitation.

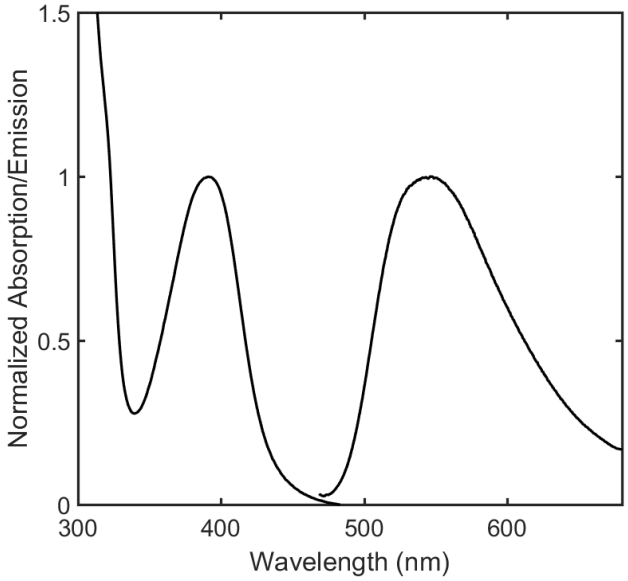

Figure 6.4. UV-visible absorption (left) and luminescence (right) spectra for $(PPN)_2[Ru(flpy)(CN\text{-}B(C_6F_5)_3)_4]$ in MeCN at room temperature.

Boronation produces a dramatic change in the electronic properties of cyanide ligands: they become weaker σ donors and stronger π acceptors.[19] Notably, boronation of $[Ru(bpy)(CN)_4]^{2-}$ greatly blue shifts the MLCT absorption ($CN\text{-}B(C_6H_5)_3$, 0.85 eV; $CN\text{-}B(C_6F_5)_3$, 1.15 eV) and luminescence (0.74, 0.91 eV) bands. These large blue shifts are accompanied by substantial increases in excited-state lifetimes. Part of this increase may be attributed to energy-gap effects,[33] but protection of the cyanide ligands from solvent interactions likely is the main contributor. It is interesting to compare the effects of boronation and methylation in $[Ru(bpy)(CN)_4]^{2-}$. The lowest energy MLCT absorption maximum in $[Ru(bpy)(CN\text{-}CH_3)_4]^{2+}$ is blueshifted so far that it is obscured by bpy ligand centered absorptions. Moreover, the luminescence observed in this complex appears to be ligand centered.[20] The MLCT bands of BCF adducts are blueshifted to a greater extent than those of BPh_3**,** likely owing to the stronger Lewis acidity of BCF. We observe greater MLCT blue shifts than those reported for $Fe(bpy)_2(CN\text{-}BPh_3)_2$, $Os(bpy)_2(CN\text{-}BPh_3)_2$, and $Os(bpy)_2(CN\text{-}BCF)_2$,[7,34] likely due to the greater ligand

field stabilization of occupied d orbitals upon boronation of the tetracyano complexes.[2] Additionally, BCF steric hindrance attenuates the MLCT energy dependence on solvent. **Table 6.2** summarizes and delineates the absorbance and luminescence data for ruthenium-based heteroleptic cyanometallates.

Table 6.2. UV-vis absorption and luminescence properties of $[Ru(diimine)(CN)_4]^{2-}$ and $[Ru(diimine)(CN\text{-}BR_3)_4]^{2-}$.

Complex	Solvent	$^{abs}\nu_{max}$, cm^{-1} ($^{abs}\lambda_{max}$, nm)	$^{lum}\nu_{max}$, cm^{-1} ($^{lum}\lambda_{max}$, nm)	ϕ_{lum}	τ_{lum}, ns
$K_2[Ru(bpy)(CN)_4]$	H_2O	24,750 (404)[a]	16,030 (624)[a]	0.0076[b]	120[b]
$(TBA)_2[Ru(bpy)(CN)_4]$	CH_3CN	18,690 (535)[c]	12,660 (790)[c]	0.0003[c]	7[c]
$K_2[Ru(flpy)(CN)_4]$	H_2O	22,570 (443)	14,160 (706)	---	---
$(PPN)_2[Ru(flpy)(CN)_4]$	CH_3CN	16,980 (589)		---	---
$(TBA)_2[Ru(bpy)(CN\text{-}BPh_3)_4]$	CH_3CN	25,570 (391)	18,620 (537)	---	810
$(TBA)_2[Ru(bpy)(CN\text{-}B(C_6F_5)_3)_4]$	CH_3CN	28,010 (357)	19,960 (501)	---	210
$(PPN)_2[Ru(flpy)(CN\text{-}B(C_6F_5)_3)_4]$	CH_3CN	25,640 (390)	18,350 (545)	0.14	3400

[a]Reference 32.
[b]Reference 18.
[c]Reference 29.

We also investigated the low temperature (77 K) luminescence of $[Ru(bpy)(CN\text{-}BPh_3)_4]^{2-}$ in frozen butyronitrile solution is shown in **Figure 6.5**. For both $[Ru(bpy)(CN\text{-}B(C_6F_5)_3)_4]^{2-}$ and $[Ru(bpy)(CN\text{-}BPh_3)_4]^{2-}$, vibronic coupling to a bipyridine stretching mode is observed (ν_{avg} = 1,287 cm^{-1} for $[Ru(bpy)(CN\text{-}BPh_3)_4]^{2-}$, ν_{avg} = 1,278 cm^{-1} for $Ru(bpy)(CN\text{-}B(C_6F_5)_3)_4]^{2-}$, consistent with other studies on heteroleptic cyanometallates and homoleptic tris(bipyridine) complexes.[20,35] Previous studies have shown that the vibronic coupling of the emission band is dependent on whether the emission is ligand-centered (LC) or ligand-to-metal charge transfer-centered (LMCT).[20] The vibronic progressions for both of these species are consistent with LMCT phosphorescence, with the sharp, narrow features from diimine emission absent. The blueshifted emission, greater number of vibrational components, and small decrease in vibrational coupling frequency observed for $[Ru(bpy)(CN\text{-}B(C_6F_5)_3)_4]^{2-}$ suggest

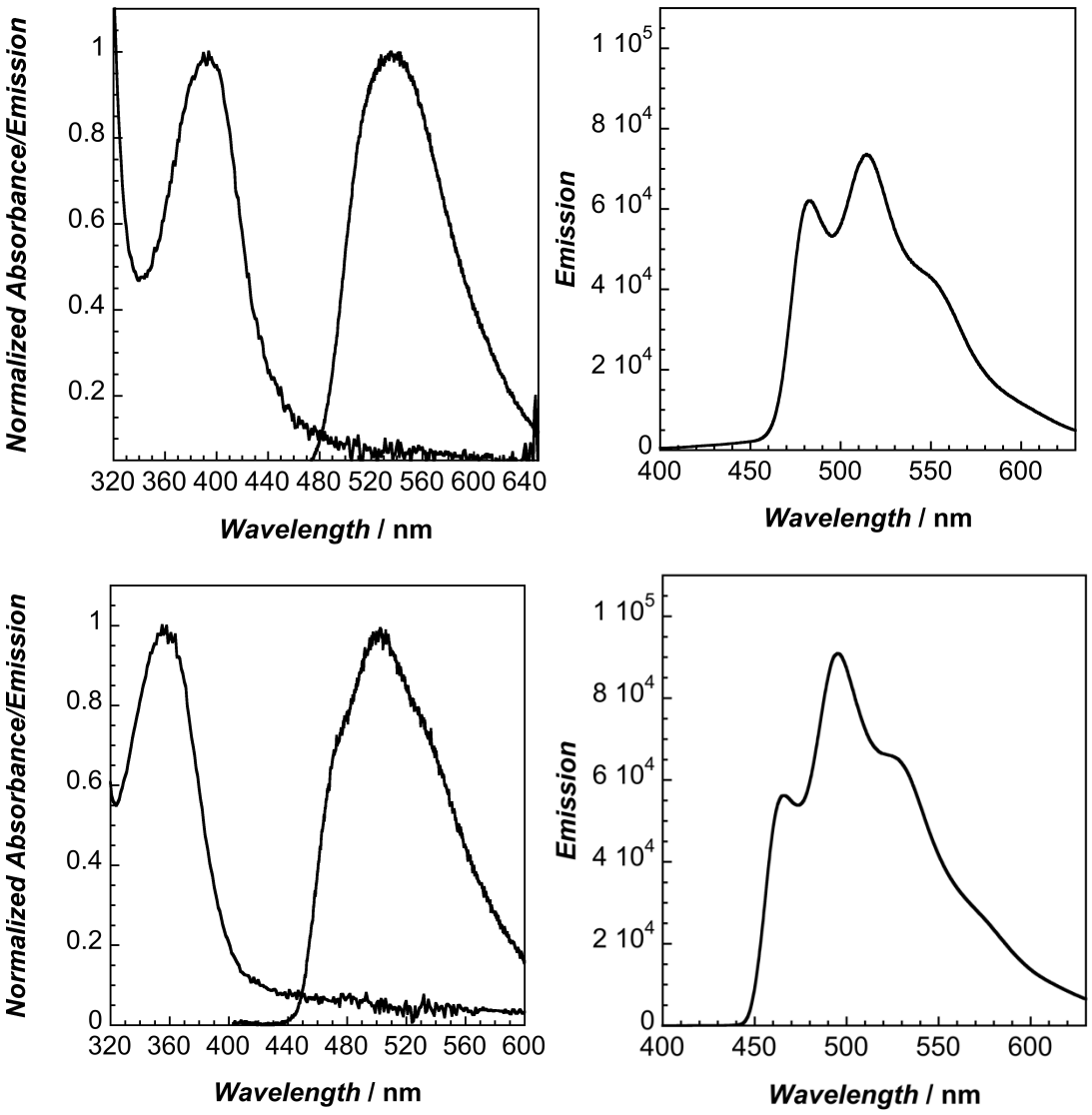

Figure 6.5. (**Upper Left**) Normalized absorbance and emission for $(TBA)_2[Ru(bpy)(CN\text{-}BPh_3)_4]$ in MeCN at room temperature. (**Upper Right**). 77 K emission spectrum for $(TBA)_2[Ru(bpy)(CN\text{-}BPh_3)_4$ in butyronitrile. (**Lower Left**) Normalized absorbance and emission for $(TBA)_2[Ru(bpy)(CN\text{-}B(C_6F_5)_3)_4]$ in MeCN at room temperature. (**Lower Right**). 16.5 K emission spectrum for $(TBA)_2[Ru(bpy)(CN\text{-}B(C_6F_5)_3)_4]$ in butyronitrile.

a greater amount of distortion in the excited state and, possibly, a greater amount of charge transferred to the diimine ligand.[20] We attempted to observe further vibronic coupling down to 16.5 K in the solid

state, as shown for $[Ru(bpy)(CN\text{-}B(C_6F_5)_3)_4]^{2-}$ at 16.5 K in **Figure 6.5**; however, lowering the temperature did nothing to resolve additional fine structure in the emission spectra.

The foregoing data demonstrate that trifluoromethyl substituents on bpy and cyanide boronation have countervailing effects on the absorption and luminescence spectra of $[Ru(bpy)(CN)_4]^{2-}$. When both modifications are introduced it is clear that boronation dominates: the absorption and luminescence maxima of $[Ru(flpy)(CN\text{-}B(C_6F_5)_3)_4]^{2-}$ are markedly blue-shifted (0.86 and 0.71 eV, respectively) from those of $[Ru(bpy)(CN)_4]^{2-}$. The effects on the excited-state lifetime and quantum yield are even more dramatic, with both quantities increasing by a factor of nearly 500. Interestingly, the lowest energy MLCT transition linearly correlates with the difference between the formal potentials for one-electron oxidations and reductions, as shown in **Figure 6.6** for ruthenium-based

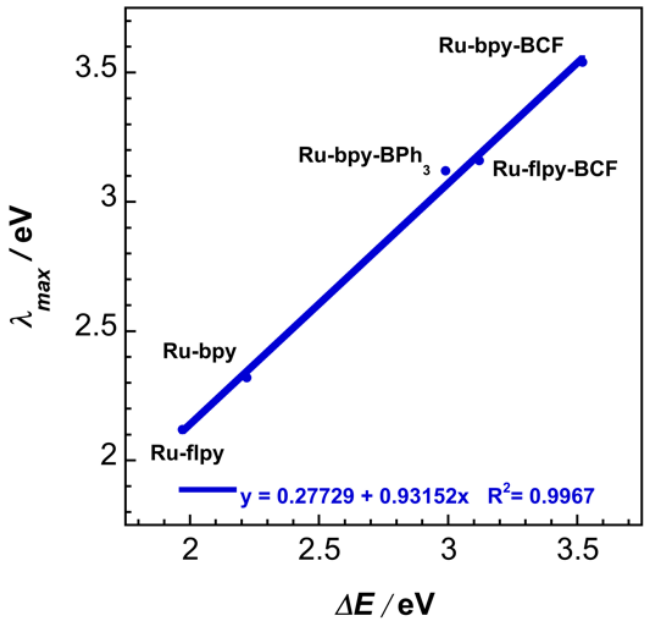

Figure 6.6. MLCT absorbance maximum versus difference in formal potential for heteroleptic ruthenium complexes. All spectra and voltammetry acquired in MeCN.

compounds. As the process is electrochemically irreversible, the **Ru-bpy-BPh$_3$** formal potential was estimated from the inflection potential of a 100 mV s^{-1} cyclic voltammogram.[36]

Transient Absorption

Excited-state lifetimes of **Fe-bpy-BPh$_3$**, **Fe-phen-BPh$_3$**, **Fe-bpy-BCF**, and **Fe-phen-BCF** were investigated using ultrafast transient absorption (TA) spectroscopy. 0.33-0.35 mM samples in MeCN were prepared under a N_2 atmosphere. A 2 mm path length cuvette was used for all spectra, which corresponds to approximately 1 a.u. optical density at the excitation wavelength. The differential absorption spectra of the four **Fe** complexes obtained 1 ps after excitation are shown in the bottom panel of **Figure 6.3**. Each complex displays concomitant ground state bleach (GSB) and excited-state absorption (ESA) features upon irradiation, with **Fe-bpy-BCF** and **Fe-phen-BCF** exhibiting a ~1500 cm^{-1} blueshift in isosbestic point versus **Fe-bpy-BPh$_3$** and **Fe-phen-BPh$_3$** (**Figure 6.52** and **6.56** versus **Figures 6.54** and **6.58**). A sharp ESA feature at 27,000/24,000 cm^{-1} and a broad GSB system at 19,000/16,000 cm^{-1} corresponding to the bpy/phen radical anion were not observed, suggesting that the transient feature before relaxation is not attributable to a charge transfer state.[37,38] Instead, the spectral features likely originate from a LF state that preferentially forms due to the high energy of the MLCT state. The excited- state kinetics and spectral features for these species are consistent with those previously assigned as LF (^{3}MC or ^{5}MC) in related work on **Fe-bpy** in coordinating solvents.[2,39,40] The ESA observed around 20,000/22,000 cm^{-1} supports this interpretation, since the absorption likely is due to a lower energy MLCT transition coming from a relaxed LF excited state.[26]

Based on previous research regarding the solvatochromatic behavior of the excited state profile of **Fe-bpy**, the excited state lifetimes and transient absorption (TA) spectra of **Fe-bpy-BPh$_3$**, **Fe-phen-**

BPh_3, **Fe-bpy-BCF**, and **Fe-phen-BCF** were investigated using ultrafast TA spectroscopy. 0.33-0.35 mM samples in MeCN were prepared under a N_2 atmosphere. A 2 mm path length cuvette was used for all spectra, which corresponds to approximately 1 a.u. optical density at the excitation

Table 6.3. Kinetic lifetimes for $[Fe(diimine)(CN)_4]^{2-}$ and $[Fe(diimine)(CN\text{-}BR_3)_4]^{2-}$ in MeCN. Spectra fit using SVD/global analysis.

Species	τ (ps)
Fe-bpy	18.1 ps[26]
Fe-bpy-BPh_3	18.5 ± 2.1 ps
Fe-bpy-BCF	22.4 ± 2.3 ps
Fe-phen	19.5 ± 1.3 ps
Fe-phen-BPh_3	17.9 ± 1.7 ps
Fe-phen-BCF	25.1 ± 2.3 ps

As a control, we also measured the TA spectrum of **Fe-phen** in MeCN. Previous studies on **Fe-bpy** in solvents with low Gutmann-Beckett acceptor numbers (AN = 19.3 for MeCN; AN = 19.3 for dimethyl sulfoxide; AN = 12.5 for acetone)[41] demonstrated that the **Fe-bpy** MLCT is much longer-lived (picoseconds versus hundreds of femtoseconds)[2,26,40]. Consistent with these studies, the TA spectrum for **Fe-phen** displays a sharp ESA around 27,000 cm^{-1} and a broad GSB around 17,000 cm^{-1}, corresponding to population of a transient MLCT state involving phenanthroline that preferentially forms over the MC transient state (**Figure 6.49**).

Table 6.3 lists the excited-state lifetimes for the heteroleptic cyanoferrates. While excited-state lifetimes for BPh_3 adducts are virtually identical with those of the parents, both **Fe-bpy-BCF** (22.4 ± 2.3 ps) and **Fe-phen-BCF** (25.1 ± 2.3 ps) exhibit slight increases, presumably due to diminished solvent-based non-radiative decay pathways.[31] **Figures 6.49-6.64** provide additional time-dependent TA data and first-order exponential decay fits.

Density Functional Theory (DFT) and CASSCF+NEVPT2 Calculations

Optimizations and CASSCF+NEVPT2 calculations were performed for the heteroleptic cyanoruthenates. Previous *ab initio* theoretical work on both homoleptic and heteroleptic cyanometallates predicted both LF and charge transfer transitions with high accuracy, provided an appropriate active space was chosen.[42,43,44] In calculations of the boronated complexes, trihydridoborane (BH_3) was used as a mimic for BCF to decrease computational cost; arguably, the results should be valid, as the two boranes are both strong Lewis acids [Gutmann-Beckett acceptor numbers: BH_3 (75.8); BCF (78.9)].[45]

All calculations were performed in ORCA 4.2.1.[46] All DFT structural optimizations used the PBE0 functional, the def2-QZVPP basis set for Ru, and the def2-TZVP basis set for all other atoms. The conductor-like polarizable continuum model (CPCM) was used to account for solvation in acetonitrile ($\varepsilon = 36.64$). X-ray crystal structures of **Ru-flpy, Ru-bpy** and **Ru-flpy-BCF** were used as initial guesses for structural optimization. X-ray crystal structure bond lengths along with those obtained from ground-state optimizations are set out in **Table 6.4**. In all cases, the bond lengths obtained from theory are in good agreement with those obtained from X-ray crystallography.

All CASSCF calculations were state averaged, with one quintet, nine triplets, and ten singlets included. The coordinates of all complexes were aligned such that the dimine ligand was coincident with the *xy* plane. For all complexes, the active space consisted of three metal t_{2g} π-bonding orbitals, two metal σ* orbitals, two CN σ bonding orbitals, three CN π* + Ru 5d orbitals, one diimine π orbital, and two diimine π* orbitals, giving twelve electrons in thirteen orbitals (CAS(12,13)). **Figure 6.7** depicts the active space orbitals for **Ru-flpy**. We reduced the number of π bonding orbitals given the negligible

change in MLCT transition energies that resulted from inclusion of the HOMO – 1 for bpy or flpy. NEVPT2 was used to account for dynamical correlation of active-space electrons.[43]

Table 6.4. Experimental and DFT-optimized bond lengths for heteroleptic cyanometallates.

Bond / Length (Optimized/Experimental)	Ru-flpy (Å)	Ru-flpy-BCF (Å)	Ru-bpy[a] (Å)
M-CN (Axial)	1.9705 / 2.0090(19)	2.0114 / 2.0167(16)	2.0268 / 2.070
M-CN (Axial)	2.0294 / 2.063(2)	2.0112 / 2.0137(16)	2.02683 / 2.063
M-CN (Equatorial)	1.9707 / 2.017(2)	1.9537 / 1.9687(16)	1.96714 / 2.011
M-CN (Equatorial)	2.0296 / 2.059(2)	1.9537 / 1.9640(16)	1.96676 / 1.989
M-N_1	2.1024 / 2.0880(15)	2.1141 / 2.1052(14)	2.11414 / 2.115
M-N_2	2.1024 / 2.0816(16)	2.1143 / 2.1043(14)	2.11434 / 2.100
C≡N_1	1.1683 / 1.160(3)	1.1575 / 1.1494(19)	1.16946 / 1.128
C≡N_2	1.1683 / 1.161(3)	1.1593 / 1.155(2)	1.16943 / 1.162
C≡N_3	1.1664 / 1.158(3)	1.1593 / 1.1553(19)	1.16724 / 1.125
C≡N_4	1.1663 / 1.162(3)	1.1575 / 1.150(2)	1.16728 / 1.139

[a]Reference 8

DFT optimization input files and the active space orbital depictions for **Ru-flpy**, **Ru-bpy-BCF**, and **Ru-flpy-BCF** are given in the supporting information (**Figures 6.77-6.79**).

Calculated energies of MLCT and LF transitions for heteroleptic cyanometallates are given in **Table 6.5** and **Table 6.6**. The calculations for all four complexes are in excellent agreement with the two experimental MLCT maxima for each species, with higher MLCT energies for both boronated complexes and higher MLCT energies for **Ru-bpy-BH_3** compared to **Ru-flpy-BH_3**.

CASSCF+NEVPT2 also correctly predicted moderate blueshifts of LF excited states upon boronation of ruthenates. We therefore suggest that the Gutmann-Beckett acceptor number is a useful parameter in estimating the relative excited-state energies of boronated complexes.[47]

Table 6.5. Experimental and calculated singlet MLCT transition energies for heteroleptic cyanoruthenates.

Complex	Orbital Transition	MLCT Energy, Experimental (cm^{-1})	MLCT Energy, NEVPT2 (cm^{-1})	Oscillator Strength
Ru-bpy	$d_{yz} \rightarrow \pi^*_1$	---	16,870	0.00126
	$d_{x^2-y^2} \rightarrow \pi^*_1$	---	17,540	0.0000155
	$d_{xz} \rightarrow \pi^*_1$	18,690	19,150	0.231
	$d_{yz} \rightarrow \pi^*_2$	---	23,880	0.00925
	$d_{x^2-y^2} \rightarrow \pi^*_2$	---	24,530	0.0000379
	$d_{xz} \rightarrow \pi^*_2$	26,738	25,620	0.0848
Ru-flpy	$d_{yz} \rightarrow \pi^*_1$	---	14,490	0.00197
	$d_{x^2-y^2} \rightarrow \pi^*_1$	---	15,230	0.0000276
	$d_{xz} \rightarrow \pi^*_1$	17,120	17,550	0.271
	$d_{yz} \rightarrow \pi^*_2$	---	21,950	0.00802
	$d_{x^2-y^2} \rightarrow \pi^*_2$	---	22,680	0.0000239
	$d_{xz} \rightarrow \pi^*_2$	24,210	23,810	0.0819
Ru-bpy-BH_3	$d_{yz} \rightarrow \pi^*_1$	---	23,940	0.000245
	$d_{x^2-y^2} \rightarrow \pi^*_1$	---	24,420	0.00000899
	$d_{xz} \rightarrow \pi^*_1$	28,570	25,720	0.204
	$d_{yz} \rightarrow \pi^*_2$	---	31,290	0.0113
	$d_{x^2-y^2} \rightarrow \pi^*_2$	---	31,840	0.0000831
	$d_{xz} \rightarrow \pi^*_2$	---	32,700	0.0624
Ru-flpy-BH_3	$d_{yz} \rightarrow \pi^*_1$	---	21,150	0.00113
	$d_{x^2-y^2} \rightarrow \pi^*_1$	---	21,640	0.0000139
	$d_{xz} \rightarrow \pi^*_1$	25,510	23,240	0.238
	$d_{yz} \rightarrow \pi^*_2$	---	29,020	0.00927
	$d_{x^2-y^2} \rightarrow \pi^*_2$	---	29,600	0.0000517
	$d_{xz} \rightarrow \pi^*_2$	31,250	30,500	0.0579

Table 6.6. Calculated singlet LF transition energies for heteroleptic cyanoruthenates.

Complex	Orbital Transition	Transition Energy, NEVPT2 (cm^{-1})	Oscillator Strength
Ru-bpy	$d_{x^2-y^2} \rightarrow d_{xy}$	39,210	0.00313
	$d_{yz} \rightarrow d_{xy}$	42,270	0.00954
	$d_{xz} \rightarrow d_{xy}$	43,480	0.0000112
Ru-flpy	$d_{x^2-y^2} \rightarrow d_{xy}$	39,580	0.00272
	$d_{yz} \rightarrow d_{xy}$	42,700	0.00893
	$d_{xz} \rightarrow d_{xy}$	44,160	0.00000423
Ru-bpy-BH_3	$d_{x^2-y^2} \rightarrow d_{xy}$	42,990	0.00381
	$d_{yz} \rightarrow d_{xy}$	47,600	0.0132
	$d_{xz} \rightarrow d_{xy}$	48,250	0.00000160
Ru-flpy-BH_3	$d_{x^2-y^2} \rightarrow d_{xy}$	40,470	0.00290
	$d_{yz} \rightarrow d_{xy}$	43,590	0.0119
	$d_{xz} \rightarrow d_{xy}$	44,570	0.0000131

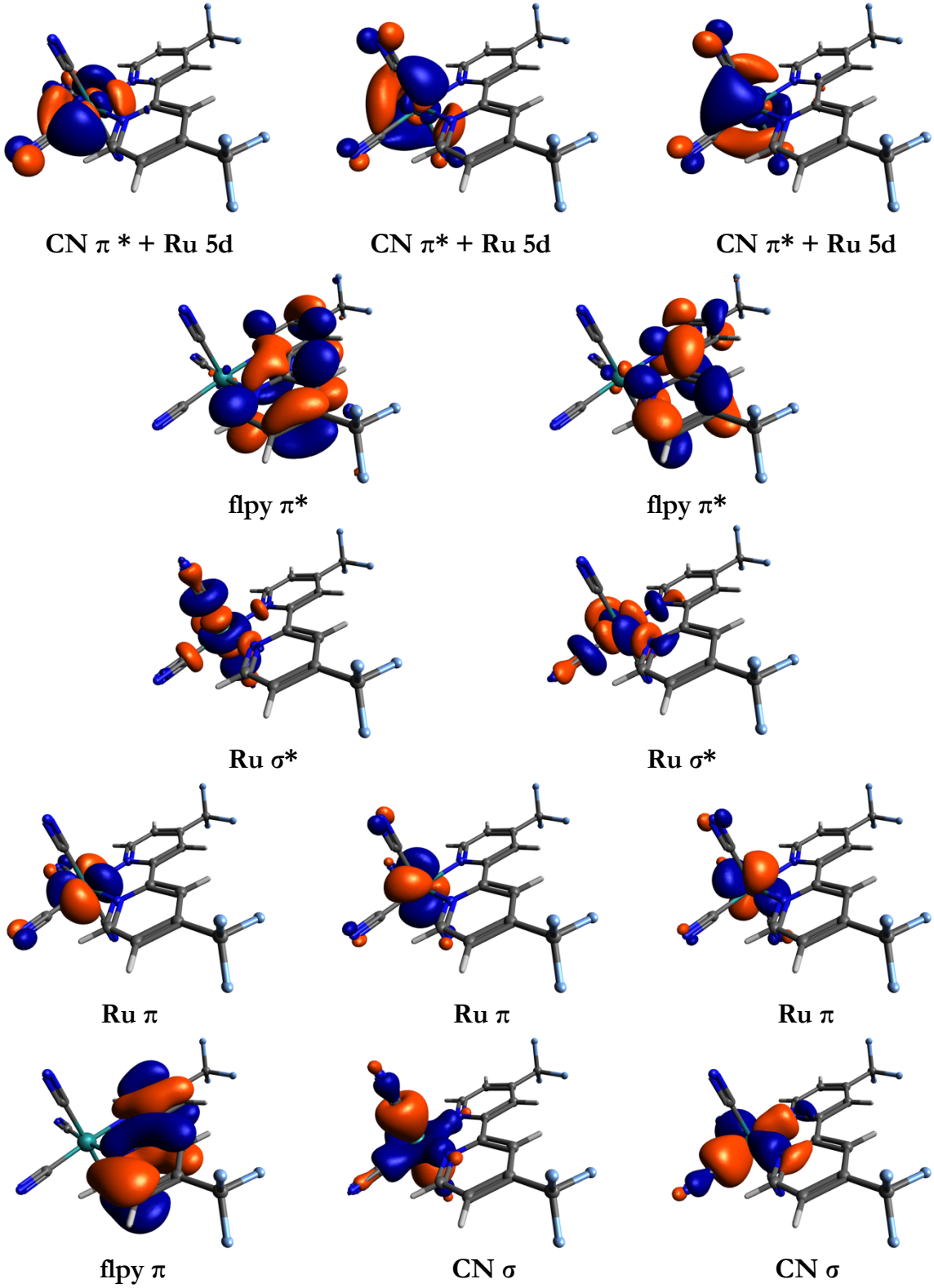

Figure 6.7. Active space molecular orbitals for state-averaged CAS(12,13) of $[Ru(flpy)(CN)_4]^{2-}$. Isosurface values set to 0.04

Electrochemistry

Cyclic voltammetry was conducted in a nitrogen-filled glove box in either MeCN or THF with 0.1-0.2 M $TBAPF_6$ as supporting electrolyte. Formal potentials (or peak potentials in electrochemically irreversible cases), peak current ratios ($i_{p,a}/i_{p,c}$), and diffusion coefficients (D_0) are summarized in **Table 6.7**. **Figure 6.8** displays the voltammetry of five of the heteroleptic tetracyanometallates.

Diffusion coefficients were calculated from linear fits of peak current versus the square root of the scan rate (Randles-Sevcik equation), **Equation 6.1**

$$i_p = 0.4463 C_0 nFA\left(\frac{nFvD}{RT}\right)^{1/2} \quad (6.1)$$

where C_0 is the bulk concentration of redox active species, n is the number of electrons transferred in each redox process (one in this case), F is Faraday's constant, A is the surface area of the electrode, v is the scan rate, R is the ideal gas constant, and T is the temperature.[48] All complexes exhibit diffusion coefficients on the order of 10^{-6} cm^2 s^{-1}, suggesting that boronation does not significantly affect the diffusional properties of these complexes. We note that most of the boronated species exhibit somewhat smaller diffusion coefficients compared to the bare species, as expected from viscoelastic considerations, though the minimal decrease is likely a result of differences in ion-pairing or solvent interactions between bare versus boronated species.

Given the anodic formal potentials for these species, peak current ratios were calculated using an empirical formula that deconvolutes the current at the reversal potential from the redox event, **Equation 6.2**,

$$\frac{i_{p,c}}{i_{p,a}} = \frac{i_{p,c,0}}{i_{p,a,0}} + \frac{i_{p,c,0}}{i_{sp}} + 0.0486 \quad (6.2)$$

where $i_{p,c}/i_{p,a}$ is the corrected peak current ratio, $i_{p,c,0}/i_{p,a,0}$ is the peak current ratio relative to zero current, and $i_{p,c,0}/i_{sp}$ is the ratio of the uncorrected peak cathodic current and the current at the switching potential.[49]

The cyclic voltammetry of all parent complexes and their tris(pentafluorophenyl)borane adducts are nearly or fully electrochemically reversible for both ligand-centered reduction and metal-centered oxidation. Bare bipyridine complexes are reduced through an ECE mechanism, where electron transfer results in bipyridine dissociation followed by additional reduction.[50] In contrast, decomposition was not observed for reduction of BCF and BPh_3 adducts of all species. This behavior likely stems from the slight anodic shift in potential for diimine reduction, thus stabilizing the diimine radical on the time scale of voltammetry.

We previously demonstrated that $[Fe(CN\text{-}BPh_3)_6]^{4-}$ oxidation is electrochemically irreversible, as a result of coupling to an irreversible chemical follow up reaction.[19] As evidenced by both chemical and electrochemical methods, oxidation results in dissociation of one or more boranes, and the BPh_3 adducts of heteroleptic complexes exhibit similar voltammetry. Additionally, the smaller peak current ratio for **Ru-flpy-BCF** oxidation in MeCN could be due to the redox event being close to the solvent window of MeCN.

Table 6.7. Electrochemical data for $[M(diimine)(CN)_4]^{2-}$ and $[M(diimine)(CN\text{-}BR_3)_4]^{2-}$. Formal potentials or peak potentials, potential separations, and peak current ratios are for 100 mV s^{-1} scan rates (0.1 - 0.2 M $TBAPF_6$ electrolyte).

Solvent	Species	$E^{III/II}$ (V vs. $Fc^{+/0}$)	$E^{0/\bullet-}$ (V vs. $Fc^{+/0}$)	ΔE_{ox} (mV)	ΔE_{red} (mV)	$i_{p,a}/i_{p,c}$ (ox)	$i_{p,a}/i_{p,c}$ (red)	D_0 (cm^2 s^{-1})
MeCN	Fe-bpy	–0.64	–2.54[b]	76	---	0.99	---	5.9 x 10^{-6} (ox.)
	Fe-bpy-BPh_3	0.66[a]	–2.19	---	95	---	0.98	4.8 x 10^{-6} (red.)
	Fe-bpy-BCF	1.00	–2.17	87	110	1.04	0.84	---
	Fe-phen	–0.62	–2.46	75	88	0.99	0.73	8.2 x 10^{-6} (ox.); 5.8 x 10^{-6} (red.)
	Fe-phen-BPh_3	0.43[a]	–2.11	---	290	---	1.05	---
	Fe-phen-BCF	1.02	–2.17	87	97	0.99	0.70	4.7 x 10^{-6} (ox.); 5.1 x 10^{-6} (red.)
	Ru-bpy	–0.17	–2.39	80	80	1.01	0.72	2.6 x 10^{-6} (ox.)
	Ru-bpy-BPh_3	0.90[a]	–2.13	---	100	---	0.92	2.1 x 10^{-6} (red.)
	Ru-bpy-BCF	1.43	–2.09	85	85	1.00	1.00	5.0 x 10^{-6} (ox.); 4.2 x 10^{-6} (red.)
	Ru-flpy	0.05	–1.92	76	84	0.94	0.93	5.2 x 10^{-6} (ox.); 6.1 x 10^{-6} (red.)
	Ru-flpy-BCF	1.63	–1.56	95	115	0.75	0.97	7.4 x 10^{-6} (ox.); 2.2 x 10^{-6} (red.)
THF	Fe-bpy-BCF	0.91	–2.36	100	100	1.00	0.99	2.9 x 10^{-6} (ox.); 2.8 x 10^{-6} (red.)

[a]Peak anodic potential.
[b]Peak cathodic potential.

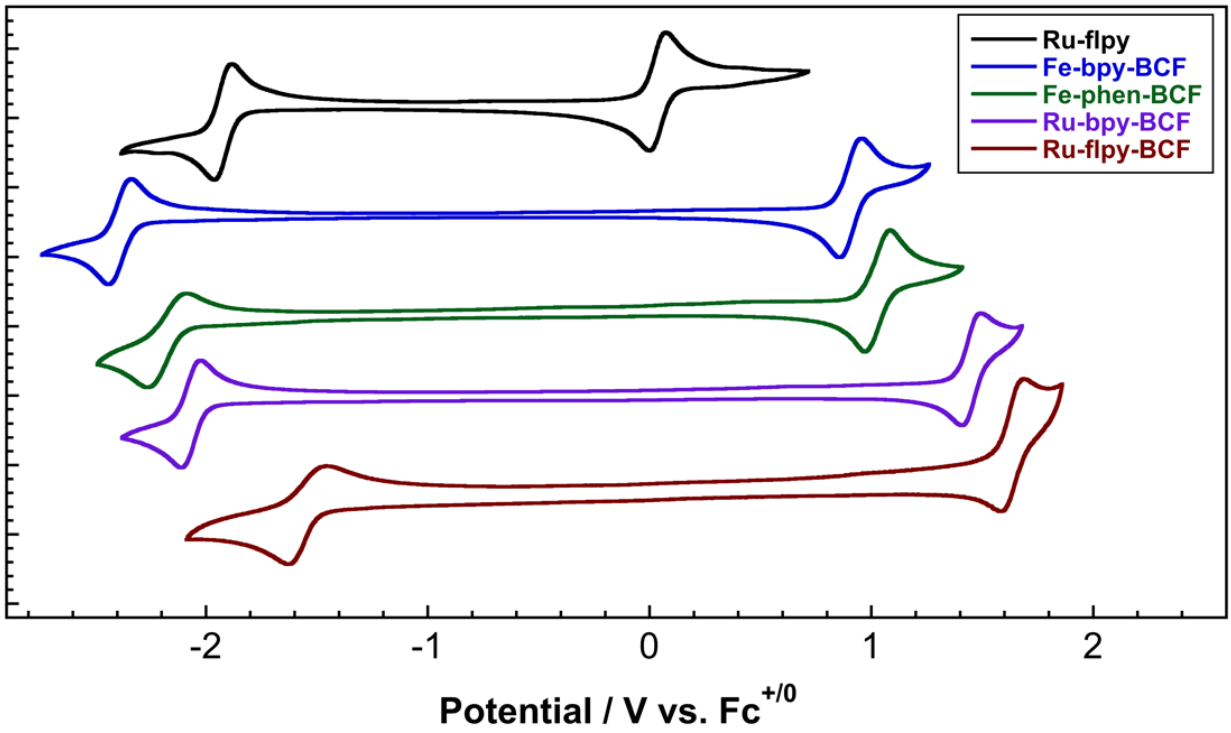

Figure 6.8. Voltammetry of parent and boronated $[M(diimine)(CN)_4]^{2-}$ complexes. Voltammetry of **Fe-bpy-BCF** was acquired in THF. All other voltammetry was acquired in MeCN. The supporting electrolyte was 0.1-0.2 M $TBAPF_6$ with electronic compensation for 85% of the uncompensated resistance. All potentials referenced to $Fc^{+/0}$.

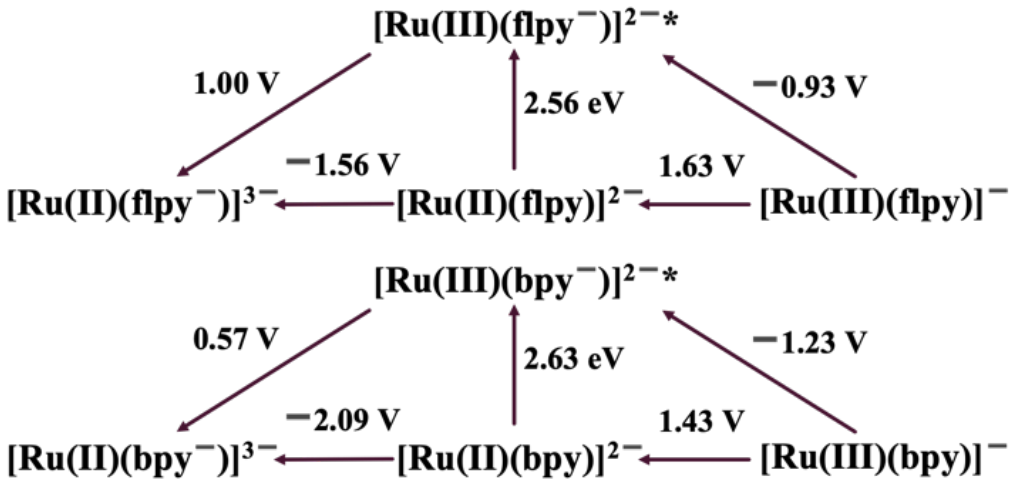

Figure 6.9. Modified Latimer diagrams: **Ru-flpy-BCF** (upper); **Ru-bpy-BCF** (lower). Potentials referenced versus $Fc^{+/0}$.

The separation in formal potentials for these species are among the highest ever reported.[1,20] To our knowledge, only heteroleptic species with alkyl isocyanides exhibit greater formal potential separations (potential separation for $[Ru(bpy)(CN\text{-}Me)_4]^{2+}$ is 3.70 V).[20] As two of the boronated complexes have greatly separated potentials [**Ru-flpy-BCF** (3.19 V); **Ru-bpy-BCF** (3.52 V)] and long excited-state lifetimes, they likely will be useful photooxidants and photoreductants. **Figure 6.9** depicts the modified Latimer diagrams for both Ru-flpy-BCF and Ru-bpy-BCF, where all potentials are relative to $Fc^{+/0}$.

6.4 Concluding Remarks

We have extended investigations of boronated cyanometallates to include heteroleptic species with a variety of diimine ligands. We demonstrated that the formal potentials of heteroleptic iron and ruthenium complexes can be tuned with boranes while preserving or improving the solubilities, stabilities, and electronic properties.

The 1.4 eV energy range over which MLCT absorption and luminescence can be modulated through solvent variations, diimine substitution, and cyanide boronation of the basic $[Ru(diimine)(CN)_4]^{2-}$ platform is remarkable. With relatively minor alterations in the complex and solvent, luminescence can be transformed from green to deep red. Importantly, we have shed new light on the factors that control Lewis-acid-tuning of both formal potentials and MLCT energies using both experimental and theoretical studies, which should aid the development of vapochromic sensors, photoredox catalysts, and electrolytes for symmetric, non-aqueous redox flow batteries.[51]

6.5 Synthesis and Experimental

General

$K_2[Fe(bpy)(CN)_4]$[23], $K_2[Fe(phen)(CN)_4]$[23], $K_4[Ru(CN)_6]$[52], and $K_2[Ru(bpy)(CN)_4]$[53] were all prepared using previously reported procedures. Tetrabutylammonium hydroxide (TBAOH) (Sigma Aldrich), bis(triphenylphosphine)iminium chloride (PPNCl) (Sigma Aldrich), 2,2'-bipyridine (bpy) (Sigma Aldrich), and 1,10-phenanthroline (phen) (Sigma Aldrich) were used as received. Triphenylborane (BPh_3) (Sigma Aldrich) and tris(pentafluorophenyl)borane ($B(C_6F_5)_3$/BCF) (TCI Chemicals) were purified from dry diethyl ether and hexanes, respectively. All solvents were dried, degassed, and stored over 3 Å molecular sieves.

All boronation reactions were performed in a nitrogen-filled glove box. Electrochemical experiments were performed in a standard three electrode cell with a glassy carbon working electrode (3 mm diameter), a $Ag^{+/0}$ in MeCN quasireference electrode, and a platinum counter electrode. A Gamry Reference 600 potentiostat was used for all room temperature voltammetry. All NMR spectra were collected on a Varian 500 MHz spectrometer or Bruker 400 MHz spectrometer (δ in ppm, m: multiplet, s: singlet, d: doublet, t: triplet, pt: pseudo- triplet). ^{19}F NMR spectra were externally referenced to neat $CFCl_3$, and ^{11}B NMR were internally referenced to 15% $BF_3{\cdot}Et_2O$. UV−vis spectroscopy was performed in MeCN using a Varian Cary 50 Bio or Cary 500 spectrophotometer. Infrared spectra were acquired on a Thermo Scientific Nicolet iS5 FTIR Spectrometer with an iD5 diamond ATR accessory. High resolution mass spectrometry was performed using a Waters LCT Premiere XE mass spectrometer (ESI-TOF, negative ion mode). Luminescence spectra were recorded using a Fluorolog-3 (Jobin-Yvon Horiba) instrument modified to use two overlapping (300-684 nm, 550-928 nm) QE Pro High Performance Spectrometers (Ocean Optics) with back-thinned, TE-cooled

CCD detectors. The instrument is controlled using software developed in MATLAB (Mathworks, Inc). Luminescence from solid state, $K_2[Ru(flpy)(CN)_4]$ was recorded using an Andor spectrometer (Kymera 193i spectrograph; iDus CCD detector). Luminescence decay kinetics were recorded using 355 nm 8 ns excitation pulses from the third harmonic of a Q-switched Nd:YAG laser (Spectra Physics Quanta-Ray Pro). Luminescence was collected using reflective optics, focused onto the entrance slit of a DH-10 double 100 mm spectrophotometer (Jobin Yvon), and detected using an R928 photomultiplier tube (Hamamatsu). The photomultiplier current was amplified and recorded using a Compuscope 85G transient digitizer (Gage Applied Inc) controlled with Labview software (National Instruments).

Ultrafast Transient Absorption Spectroscopy

Transient absorption measurements were collected using a pump-probe spectrometer (Helios, Ultrafast Systems) with detection in the ultraviolet region (800 nm/12,500 cm^{-1} to 320 nm/31,250 cm^{-1}). This system delivers 5 mJ, 35 fs pulses at 800 nm with a 1 kHz repetition rate obtained from an amplified $Ti:Al_2O_3$ laser (Coherent brand Astrella) with some output pumped into a commercial two-stage noncollinear optical parametric amplifier (Coherent OPerA Solo kHz). The pump wavelengths used in this study, 290 nm (34,500 cm^{-1}) and 700 nm (14,300 cm^{-1}), were obtained from the second and fourth harmonic of the signal beam. The probe beam was aligned with a computer-controlled program and focused on a 2 mm sapphire plate to generate a white light continuum. Some of the samples were also measured at longer wavelengths (approximately 390 nm); with no changes in TA spectra.

Samples were stirred by rotating a magnetic stirrer; insignificant sample degradation was observed over the time scale of the experiments as monitored by UV-vis absorption. The white probe light overlapped

the pump beam in the sample holder, and the change in absorbance was measured with a charge-coupled detector. The pump pulse energy was 0.3 mW. The instrument response function for this setup was determined to be 90 fs. Transient absorption data were collected −10 ps before pump overlap. Over five scans, 500 steps were collected with an initial step of 0.01 ps, totaling 2500 points per spectrum. Scans were collected in an exponential stepping mode out to 1 ns. In the diimine complexes, a residual signal persisted following 290 nm excitation, corresponding to the solvated dimer anion of MeCN, which is in equilibrium with the solvated free electron, at time scales greater than 70 ps.[54] To eliminate confluence of this residual signal with measured kinetics, two component singular value decomposition and global analysis of transient spectra were performed according to literature procedures with the Surface Xplorer Data Analysis Program (Ultrafast Systems). Each spectrum was fit over the region 16,000-28,000 cm^{-1} (**Fe-phen**) and 18,000-29,000 cm^{-1} (**Fe-bpy-BPh$_3$, Fe-phen-BPh$_3$, Fe-bpy-BCF**, and **Fe-phen-BCF**) to a single exponential.[55,56]

Synthesis

$(TBA)_2[Fe(bpy)(CN\text{-}BPh_3)_4]$ (Fe-bpy-BPh$_3$)

$(TBA)_2[Fe(bpy)(CN)_4]$ (50.8 mg, 0.0634 mmol) dissolved in DCM was added to a solution of 5.1 equivalents of BPh_3 (78.6 mg, 0.325 mmol) in 5 mL of DCM. An immediate color change from dark green to orange was observed. The solution was refluxed overnight. The solution was allowed to cool to room temperature, and the solvent was removed *in vacuo* until a minimal volume of DCM remained. 50 mL of hexanes were then added, and the solution was shaken. The solvent was decanted, and the precipitate was dissolved in minimal DCM. 50 mL of hexanes were again added. The solvent was decanted, and the precipitate was dried *in vacuo* overnight, yielding the product as an orange solid (0.0559 mmol, 88% yield). ^{1}H NMR (500 MHz, CD_2Cl_2) δ ^{1}H NMR (500 MHz, Methylene Chloride-

d$_2$) δ 8.75 (d, *J* = 5.8, 2H), 7.72 – 7.54 (m, 16H), 7.05 – 6.91 (m, 50H), 2.59 – 2.45 (m, 16H), 1.29 – 1.12 (m, 32H), 0.87 (t, *J* = 7.0 Hz, 24H). ^{11}B NMR (128 MHz, CD_3CN) δ -3.62. TOF MS—ES-: m/z = 1,526.8151 (calc'd for (TBA)[Fe(bpy)(CN-BPh_3)$_4$]$^-$: m/z = 1,526.8126). Selected IR data (ATR, 4,000−600 cm^{-1}) ν / cm^{-1}: 2,181, 2,145 (ν_{CN}). Elem. Anal. (for TBA salt) (%) found (calc'd): C, 80.09 (78.97); H, 7.97 (7.41); N, 6.33 (5.98).

(TBA)$_2$[Fe(bpy)(CN-B(C_6F_5)$_3$)$_4$] (Fe-bpy-BCF)

(TBA)$_2$[Fe(bpy)(CN)$_4$] (111 mg, 0.139 mmol) was dissolved in 10 mL DCM and added to a solution of 5.0 equivalents of B(C_6F_5)$_3$ (358 mg, 0.699 mmol) in 15 mL of DCM. An immediate color change from dark green to yellow was observed. The solution was refluxed overnight, and the reaction vessel was allowed to cool to room temperature. The solvent was removed *in vacuo* until a minimal volume of DCM remained. 50 mL of hexanes were added, and the solvent was decanted. The resulting solid was then dissolved in minimal DCM, and 50 mL of hexanes was added. The solvent was decanted, and the precipitate was dried *in vacuo*, yielding the product as a yellow solid (0.133 mmol, 96% yield). ^{1}H NMR (400 MHz, CD_3CN) 8.57 (m, 2H), 7.75 (m, 2H), 7.63 (m, 2H), 6.96 (m, 2H), 2.79 (m, 16H), 1.31 (m, 16H), 1.05 (m, 16H), 0.65 (m, 24H). ^{11}B NMR (128 MHz, CD_3CN) δ -14.44. ^{19}F NMR (376 MHz, CD_3CN) δ -134.64 (d, *J* = 21.9 Hz), -135.09 (d, *J* = 22.7 Hz), -162.55 (t, *J* = 18.9 Hz), -162.82 (t, *J* = 18.5 Hz), -167.80 (d, *J* = 21.4 Hz), -168.07 (d, *J* = 20.7 Hz). TOF MS—ES-: m/z = 1,181.9811 (calc'd for [Fe(bpy)(CN-B(C_6F_5)$_3$)$_4$]$^{2-}$: m/z = 1,181.9810). Selected IR data (ATR, 4,000−600 cm^{-1}) ν / cm^{-1}: 2,207, 2,170 (ν_{CN}). Elem. Anal. (for TBA salt) (%) found (calc'd): C, 49.75 (49.38); H, 2.83 (2.76); N, 3.93 (3.70).

(TBA)$_2$[Fe(phen)(CN-BPh$_3$)$_4$] (Fe-phen-BPh$_3$)

The general procedure used to form **Fe-bpy-BPh$_3$** was followed, starting instead with (TBA)$_2$[Fe(phen)(CN)$_4$] to obtain the product as an orange powder (89% yield). ^{1}H NMR (500 MHz, CD_2Cl_2) δ 8.88 (dd, J = 5.8, 1.5 Hz, 2H), 8.09 (dd, J = 8.2, 1.3 Hz, 2H), 7.71 (s, 2H), 7.69 – 7.65 (m, 12H), 7.08 (dd, J = 8.2, 5.2 Hz, 2H), 7.04 (dd, J = 7.9, 6.6 Hz, 12H), 7.00 – 6.94 (m, 6H), 6.83 – 6.76 (m, 12H), 6.76 – 6.71 (m, 6H), 6.70 – 6.64 (m, 12H), 2.45 (t, 16H), 1.25 – 1.09 (m, 32H), 0.86 (t, J = 7.0 Hz, 24H). ^{11}B NMR (128 MHz, CD_3CN) δ -3.61. TOF MS—ES-: m/z = 1550.8112 (calc'd for (TBA)$_2$[Fe(phen)(CN-BPh$_3$)$_4$]$^-$: m/z = 1,550.8126Selected IR data (ATR, 4,000−600 cm^{-1}) ν / cm^{-1}: 2,182, 2,146 (ν_{CN}). Elem. Anal. (for TBA salt) (%) found (calc'd): C, 80.36 (79.07); H, 7.87 (7.88); N, 6.25 (5.82).

(TBA)$_2$[Fe(phen)(CN-B(C$_6$F$_5$)$_3$)$_4$] (Fe-phen-BCF)

The general procedure used to form **Fe-bpy-BCF** was followed, starting instead with (TBA)$_2$[Fe(phen)(CN)$_4$] to obtain the product as a yellow powder (94% yield). ^{1}H NMR (500 MHz, CD_2Cl_2) δ 9.14 (d, J = 5.2 Hz, 2H), 8.34 (dd, J = 8.2 Hz, 2H), 7.84 (s, 2H), 7.56 (dd, J = 8.1, 5.2 Hz, 2H), 3.08 (t, 16H, CH_{but}, J_{HH} = 8.2 Hz), 1.60 (pquint, 16H, CH_{but}), 1.35 (psextet, 16H, CH_{but}), 0.95 (t, 12H, CH_{but}, J_{HH} = 7.3 Hz). ^{11}B NMR (128 MHz, CD_3CN) δ -14.54. ^{19}F NMR (376 MHz, CD_3CN) δ -134.74 (d, J = 22.0 Hz), -135.53 (d, J = 22.5 Hz), -162.57 (t, J = 19.3 Hz), -162.79 (t, J = 19.1 Hz), -167.85 (pt, J = 19.8 Hz), -168.14 (pt, J = 19.3 Hz). TOF MS—ES-: m/z = 1,193.9819 (calc'd for [Fe(phen)(CN-B(C$_6$F$_5$)$_3$)$_4$]$^{2-}$: m/z = 1,193.9810). Selected IR data (ATR, 4,000−600 cm^{-1}) ν / cm^{-1}: 2206, 2169 (ν_{CN}). Elem. Anal. (for TBA salt) (%) found (calc'd): C, 50.17 (48.97); H, 2.81 (2.61); N, 3.90 (3.34).

(TEA)$_2$[Ru(bpy)(CN-BPh$_3$)$_4$] (Ru-bpy-BPh$_3$)

The general procedure used to form **Fe-bpy-BPh$_3$** was followed, starting instead with (TEA)$_2$[Ru(bpy)(CN)$_4$] to obtain the product as a yellow powder (79% yield). ^{1}H NMR (400 MHz, CD_3CN) δ 8.90 (dd, *J* = 5.5, 1.6 Hz, 2H), 8.21 (d, *J* = 8.2 Hz, 2H), 7.95 (td, *J* = 7.9, 1.6 Hz, 2H), 7.49 (dt, *J* = 7.8, 1.7 Hz, 12H), 7.18 (ddd, *J* = 7.7, 5.5, 1.3 Hz, 2H), 7.04 – 6.89 (m, 12H), 6.87 – 6.76 (m, 18H), 3.05 (q, *J* = 7.3 Hz, 16H), 1.13 (tt, *J* = 1.9, 7.3 Hz, 24H). ^{11}B NMR (128 MHz, CD_3CN) δ -5.19. TOF MS—ES-: m/z = 1,460.6587 (calc'd for (TEA)[Ru(bpy)(CN-BPh$_3$)$_4$]$^-$: m/z = 1,460.6578). Selected IR data (ATR, 4,000−600 cm^{-1}) ν / cm^{-1}: 2,188, 2,140 (ν_{CN}). Elem. Anal. (for TEA salt) (%) found (calc'd): C, 39.57 (39.93); H, 2.22 (2.06); N, 6.81 (7.16).

(TBA)$_2$[Ru(bpy)(CN-B(C$_6$F$_5$)$_3$)$_4$] (Ru-bpy-BCF)

The general procedure used to form **Fe-bpy-BCF** was followed, starting instead with (TBA)$_2$[Ru(bpy)(CN)$_4$] to obtain the product as a colorless powder (99% yield). ^{1}H NMR (400 MHz, CD_3CN) δ 8.79 (dd, *J* = 5.6, 1.5 Hz, 2H), 8.16 (d, *J* = 8.2 Hz, 2H), 7.99 (dd, *J* = 7.9, 1.6 Hz, 2H), 7.34 (d, *J* = 7.4, 5.6 Hz, 2H), 3.07 (t, 16H, CH_{but}, J_{HH} = 8.6 Hz), 1.59 (pquint, 16H, CH_{but}), 1.34 (psextet, 16H, CH_{but}), 0.95 (t, 12H, CH_{but}, J_{HH} = 7.3 Hz); ^{11}B NMR (128 MHz, CD_2Cl_2) δ -14.19; ^{19}F NMR (376 MHz, CD_2Cl_2) δ -134.28 (d, *J* = 16.0 Hz), -134.57 (d, *J* = 15.4 Hz), -162.19 (t, *J* = 20.2 Hz), -162.60 (t, *J* = 20.0 Hz), -167.25 (pt, *J* = 18.2 Hz), -167.56 (pt, *J* = 18.3 Hz). TOF MS—ES-: m/z = 1,204.9670 (calc'd for [Ru(bpy)(CN-B(C$_6$F$_5$)$_3$)$_4$]$^{2-}$: m/z = 1204.9663). Selected IR data (ATR, 4,000−600 cm^{-1}) ν / cm^{-1}: 2216, 2168 (ν_{CN}). Elem. Anal. (for TBA salt) (%) found (calc'd): C, 48.97 (48.47); H, 2.79 (2.70); N, 3.87 (3.87).

$(PPN)_2[Ru(flpy)(CN)_4]$ (**Ru-flpy**)

$K_2Ru(flpy)(CN)_4$ was synthesized with a modified literature procedure.[53] To a boiling solution of $K_4Ru(CN)_6$ (400 mg, 0.908 mmol) and flpy (305 mg, 1.04 mmol) in 50 mL 1:1 methanol:water was added 400 μL 3.6 N H_2SO_4 (pH = 4). The solution was refluxed for 24 h, over which time it slowly turned red, then cooled to room temperature and neutralized. Excess flpy was removed by filtration, and the solvent was removed. The remaining solid was purified by gel-filtration chromatography on a Sephadex G-15 column. Elution with water gave an orange band free of excess $K_4Ru(CN)_6$. The main fraction was dried under vacuum to give $K_2Ru(flpy)(CN)_4$ (30% yield). The cation was exchanged by precipitation from concentrated aqueous solution with a saturated solution of PPNCl (307 mg, 0.535 mmol) dissolved in 20 mL water. The resulting red precipitate was collected by filtration and dried in a desiccator or under vacuum until it turned green (326 mg, 25% yield). Single crystals suitable for X-ray diffraction analysis were grown by slow evaporation from DCM solution. ^{1}H NMR (400 MHz, CD_2Cl_2): δ 9.97 (d, J = 8 Hz, 2H, 6,6'-H), 8.14 (s, 2H, 3,3'-H), 7.71-7.65 (m, 24H, (PPN)), 7.54-7.46 (m, 36H, (PPN)), 7.44 (d, J = 8 Hz, 2H, 5,5'-H). ^{19}F NMR (CD_2Cl_2): δ -64.70. Selected IR data (ATR, 4,000−600 cm^{-1}) ν / cm^{-1}: 2,062, 2,090 (ν_{CN}). Elem. Anal. (for PPN salt) (%) found (calc'd): C, 67.13 (64.21); H, 4.23 (4.28); N, 7.12 (5.55).

$(PPN)_2[Ru(flpy)(CN\text{-}BCF)_4]$ (**Ru-flpy-BCF**)

$(PPN)_2Ru(flpy)(CN)_4$ (100. mg, 0.0637 mmol) and excess $B(C_6F_5)_3$ (133 mg, 0.261 mmol) were dissolved in minimal DCM. The two solutions were combined, and an immediate color change from green to red to yellow was observed. The solution was refluxed for 1 h, then dried under vacuum. The resulting yellow solid was washed 3 x 10 mL hexanes, then dried under vacuum. The resulting yellow solid was further purified by flash chromatography on silica gel (eluent gradient from 100% hexanes to 90%

dichloromethane in hexanes), resulting in 131 mg yellow product (0.0362 mmol, 56% yield). Single crystals suitable for X-ray diffraction analysis were grown from a saturated ethanol solution at –25 °C. ^{1}H NMR (400 MHz, CD_2Cl_2): δ 9.22 (d, J = 4 Hz, 2H, 6,6'-H), 8.29 (s, 2H, 3,3'-H), 7.65-7.59 (m, 14H, (PPN) + 5,5'-H), 7.51-7.40 (m, 48H, (PPN)). ^{19}F NMR (CD_2Cl_2): δ -65.48 (s, 6F, CF_3), -134.52 (dd, 12F, *o*-F), -134.99 (dd, 12F, *o*-F), -161.56 (t, 6F, *p*-F), -162.03 (t, 6F, *p*-F), -167.01 (td, 12F, *m*-F), -167.29 (td, 12F, *m*-F). ^{11}B NMR (CD_2Cl_2): δ -14.05. Selected IR data (ATR, 4,000−600 cm^{-1}) ν / cm^{-1}: 2,171, 2,216 (ν_{CN}). Elem. Anal. (for PPN salt) (%) found (calc'd): C, 53.05 (51.69); H, 1.84 (2.09); N, 3.09 (2.76).

Electrochemistry

Electrochemical experiments were performed using a standard three electrode cell with a glassy carbon working electrode (3 mm diameter), a $Ag^{+/0}$ in MeCN quasireference electrode, and a platinum counter electrode. Voltammograms were collected in a nitrogen-filled glove box on complexes in either MeCN or THF with 0.1-0.2 M $TBAPF_6$ as supporting electrolyte. A Gamry Reference 600 potentiostat was used for all room temperature voltammetry. All voltammograms were electronically compensated using positive-feedback iR-compensation for 85% of the R_u, as measured by potentiostatic electrochemical impedance spectroscopy.

NMR Spectra:

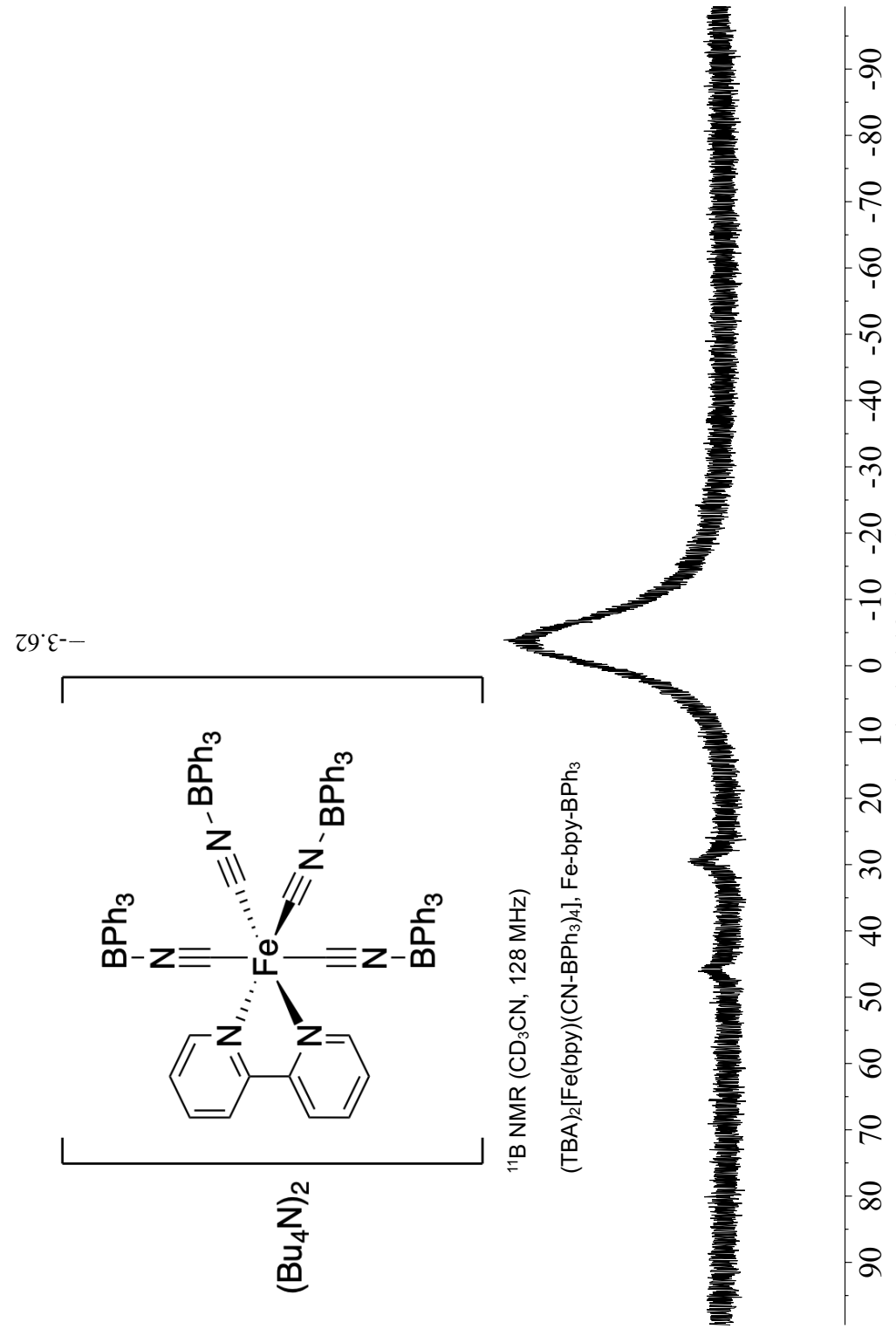

Figure 6.10. ^{11}B NMR spectrum of $(TBA)_2[Fe(bpy)(CN\text{-}BPh_3)_4]$ (**Fe-bpy-BPh$_3$**) in CD_3CN.

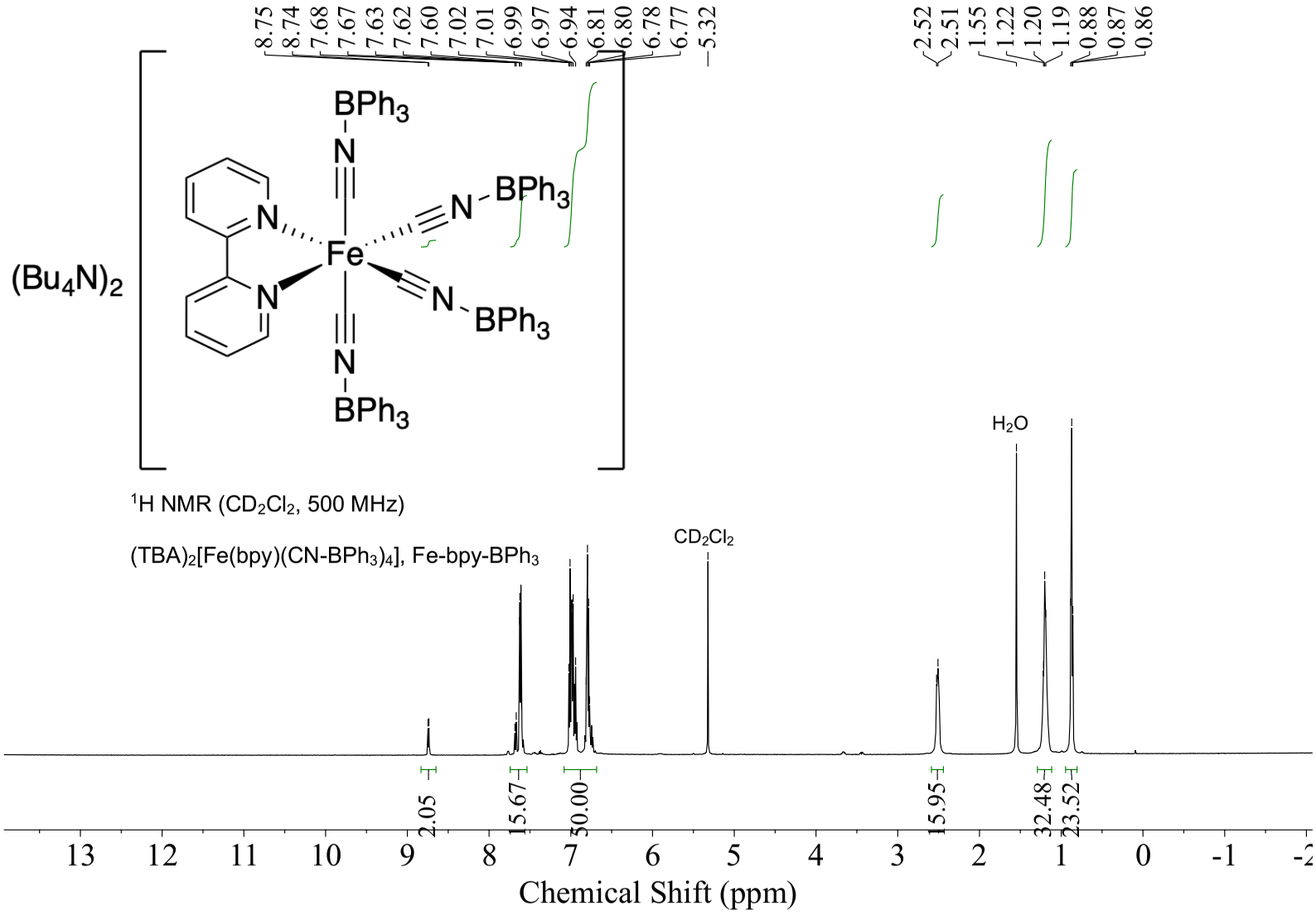

Figure 6.11. ^{1}H NMR spectrum of $(TBA)_2[Fe(bpy)(CN\text{-}BPh_3)_4]$ (**Fe-bpy-BPh$_3$**) in CD_2Cl_2.

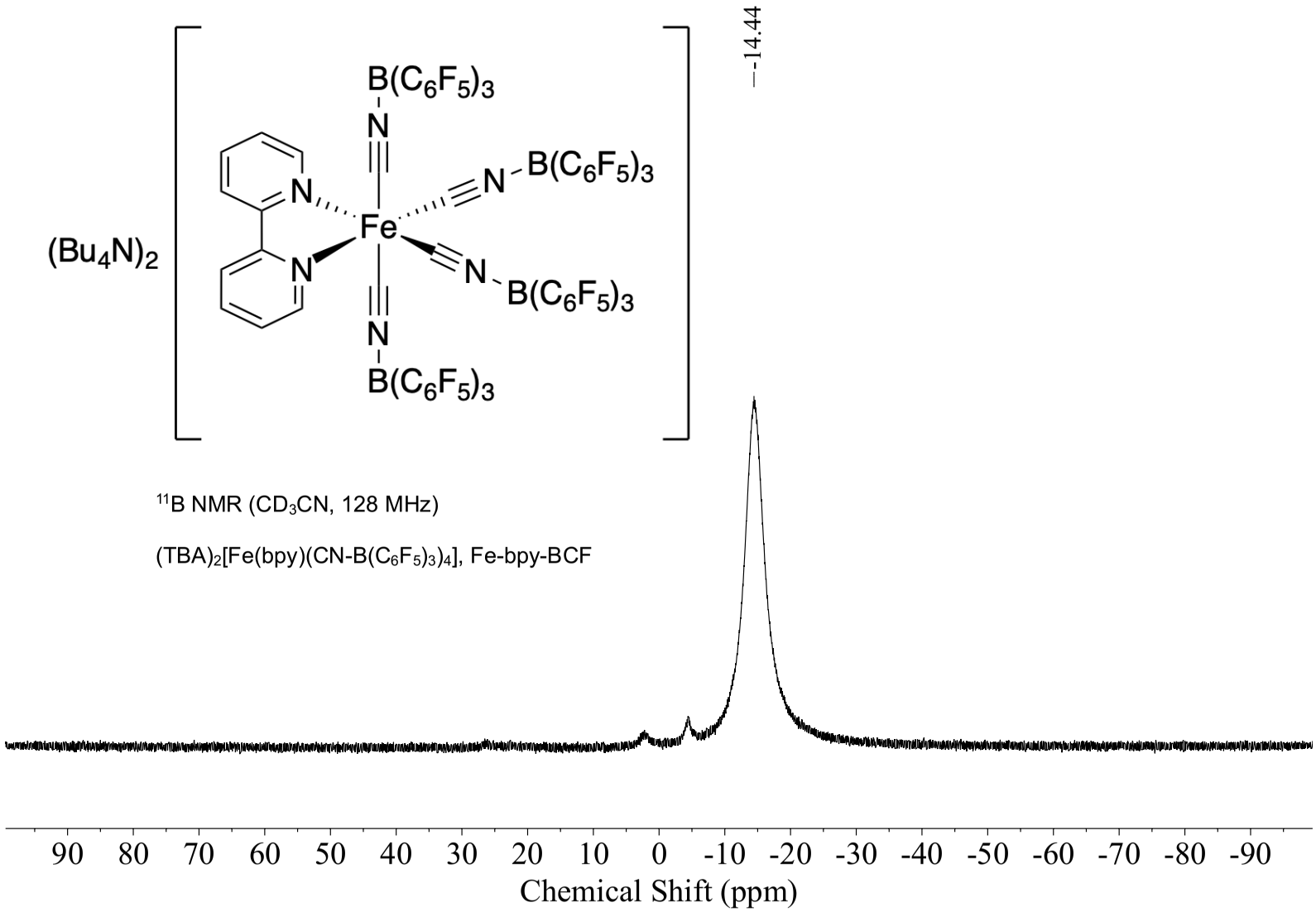

Figure 6.12. ^{11}B NMR spectrum of $(TBA)_2[Fe(bpy)(CN\text{-}B(C_6F_5)_3)_4]$ (**Fe-bpy-BCF**) in CD_3CN.

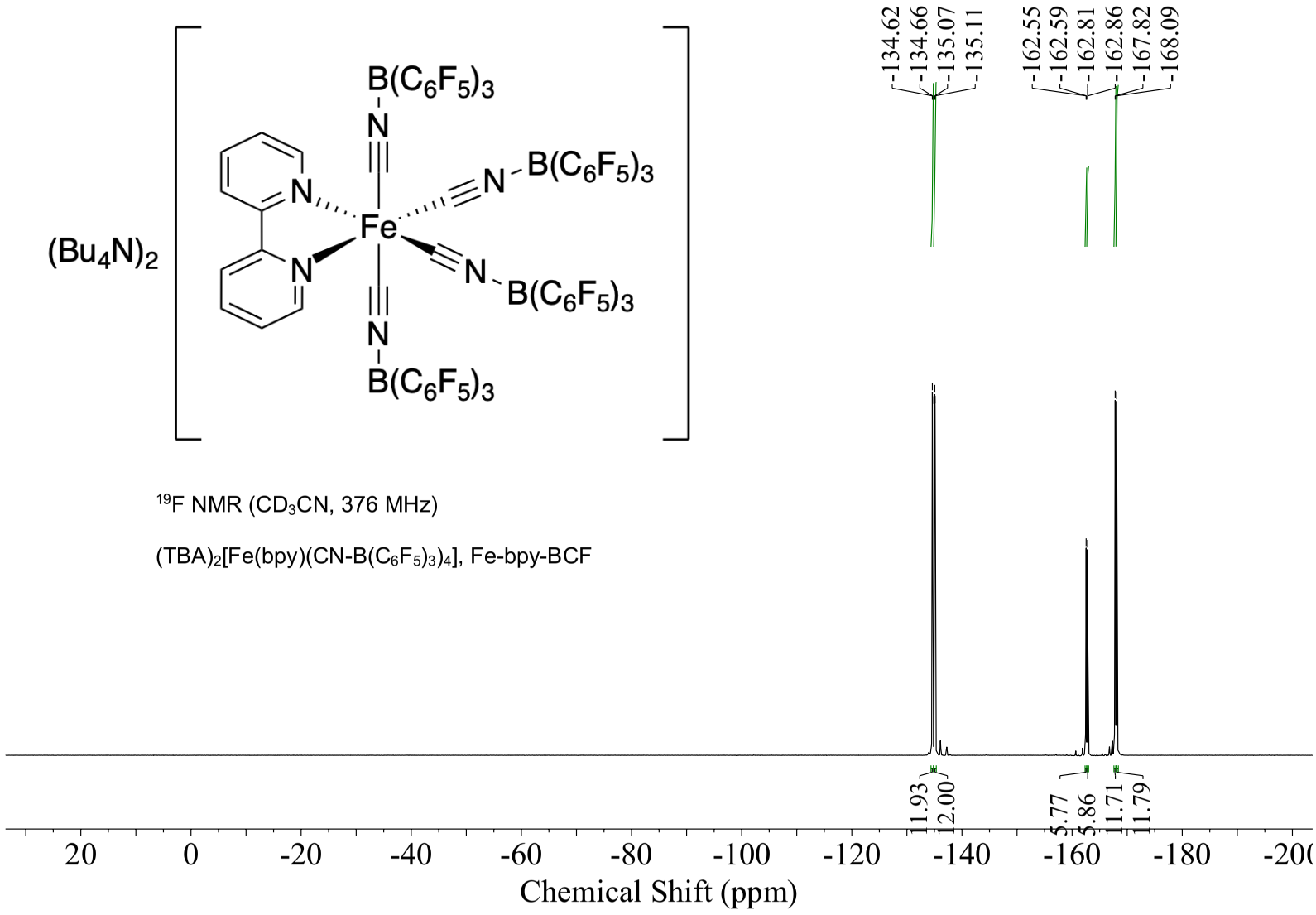

Figure 6.13. ^{19}F NMR spectrum of $(TBA)_2[Fe(bpy)(CN\text{-}B(C_6F_5)_3)_4]$ (**Fe-bpy-BCF**) in CD_3CN.

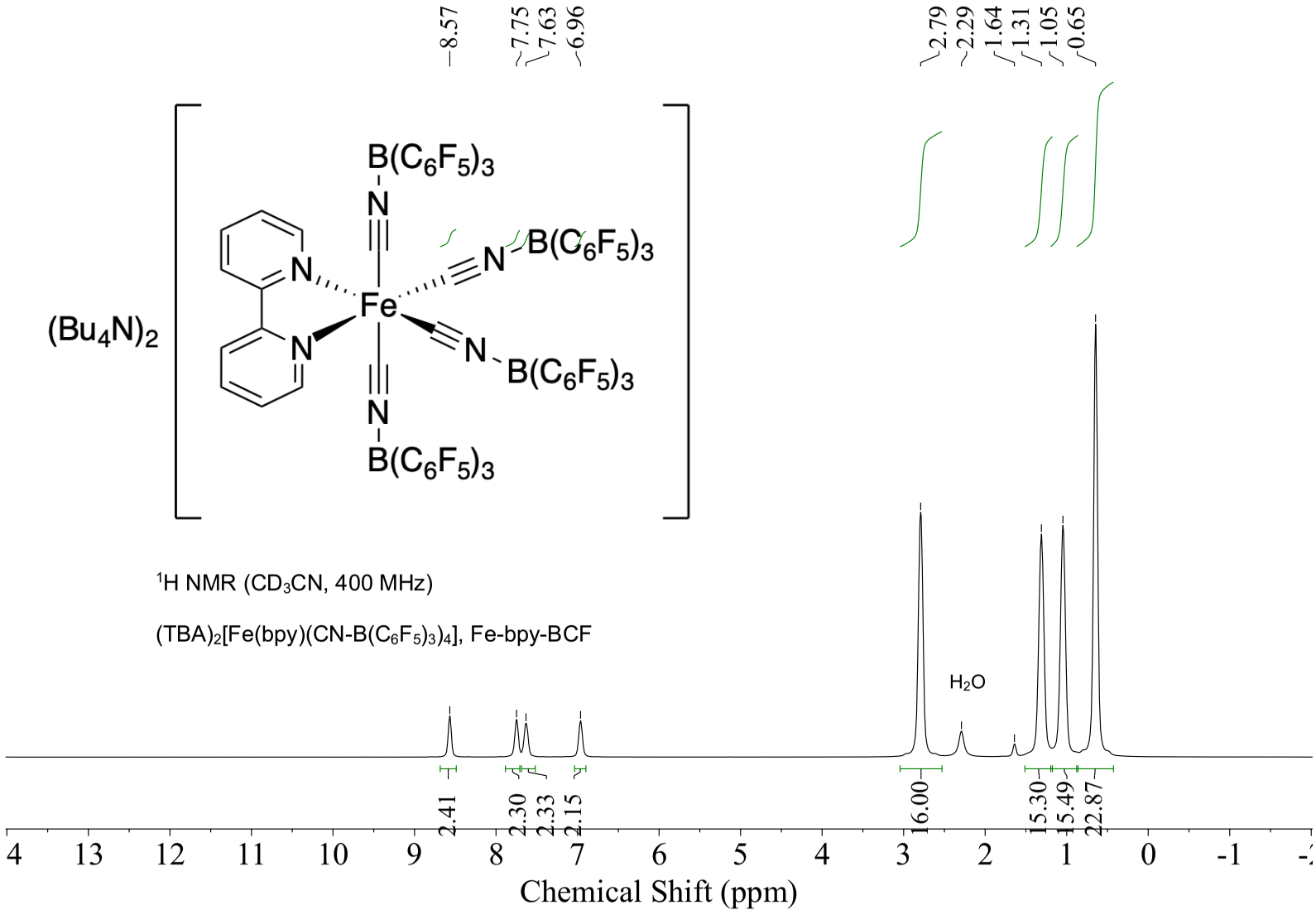

Figure 6.14. ^{1}H NMR spectrum of $(TBA)_2[Fe(bpy)(CN\text{-}B(C_6F_5)_3)_4]$ (**Fe-bpy-BCF**) in CD_3CN.

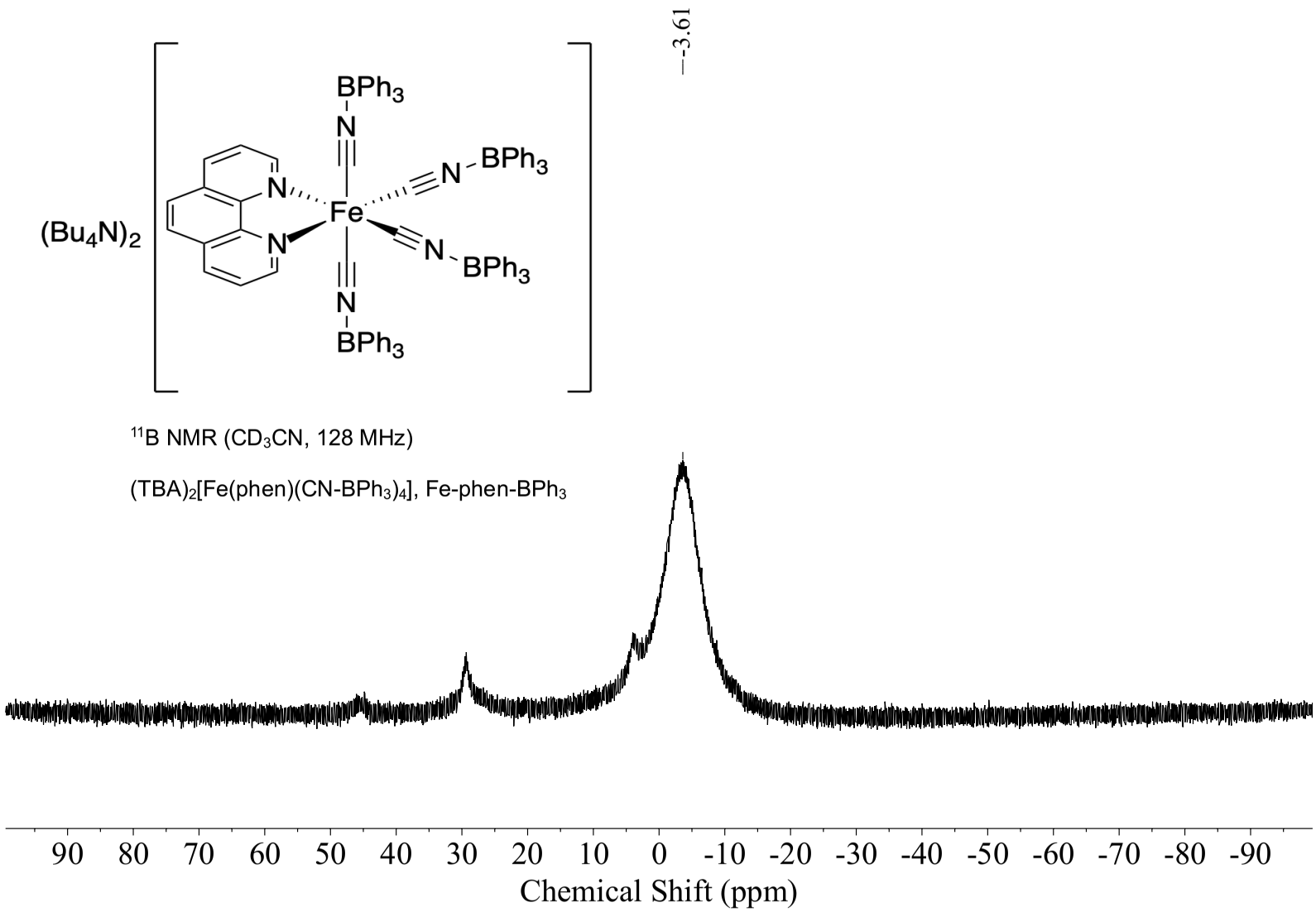

Figure 6.15. ^{11}B NMR spectrum of $(TBA)_2[Fe(phen)(CN\text{-}BPh_3)_4]$ (**Fe-phen-BPh$_3$**) in CD_3CN.

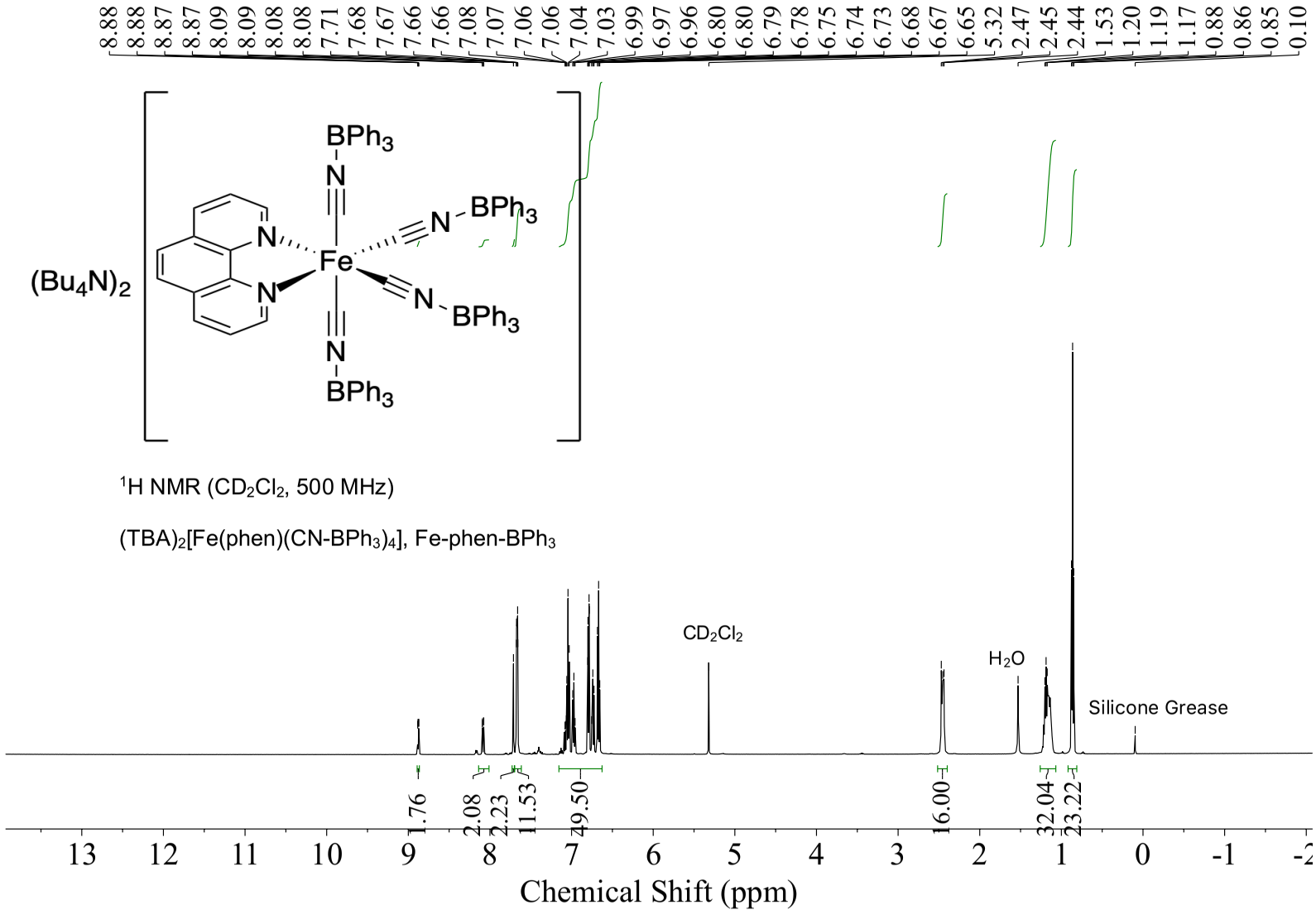

Figure 6.16. ^{1}H NMR spectrum of (TBA)$_2$[Fe(phen)(CN-BPh$_3$)$_4$] (**Fe-phen-BPh$_3$**) in CD$_3$CN.

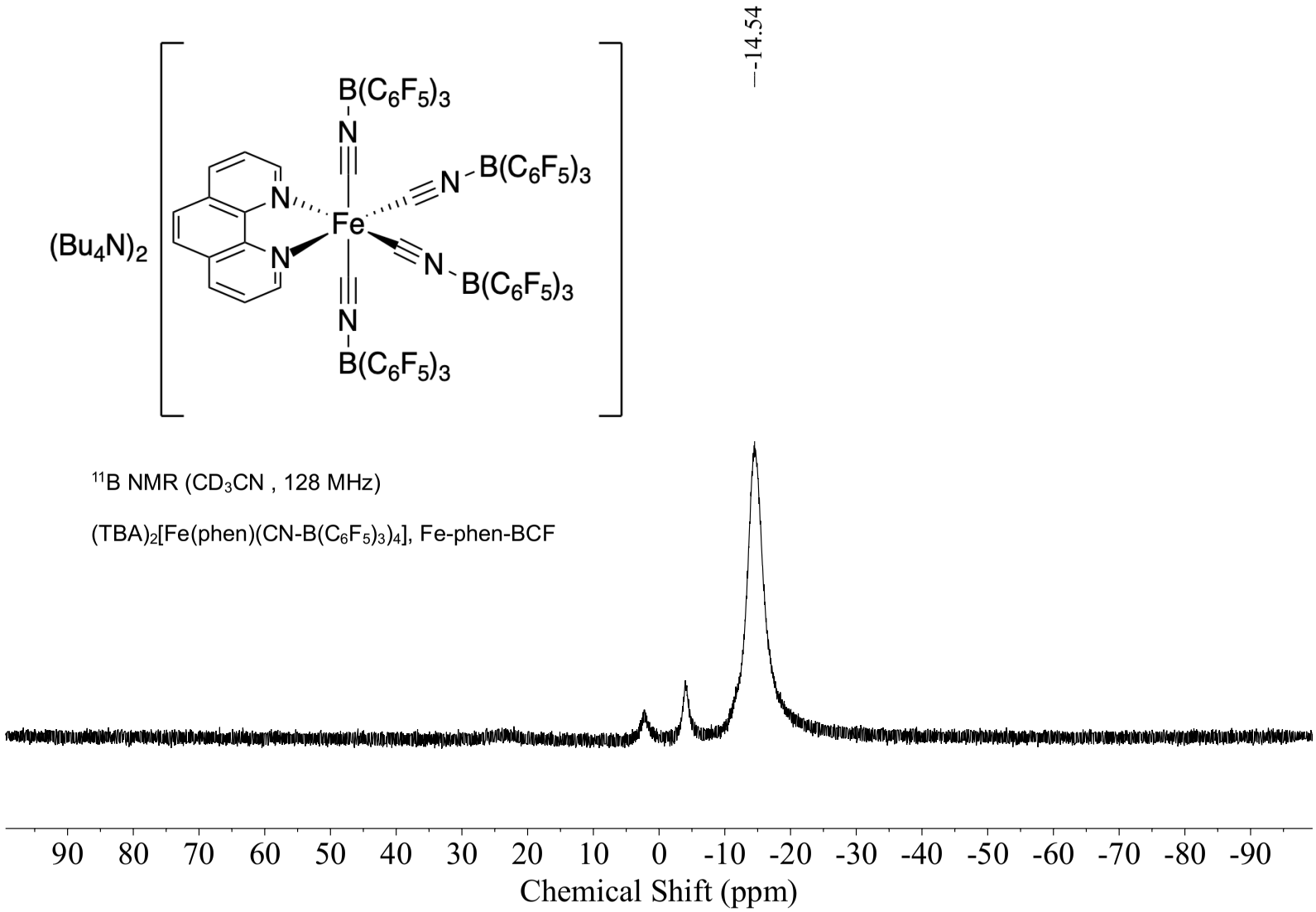

Figure 6.17. ^{11}B NMR spectrum of $(TBA)_2[Fe(phen)(CN\text{-}B(C_6F_5)_3)_4]$ (**Fe-phen-BCF**) in CD_3CN.

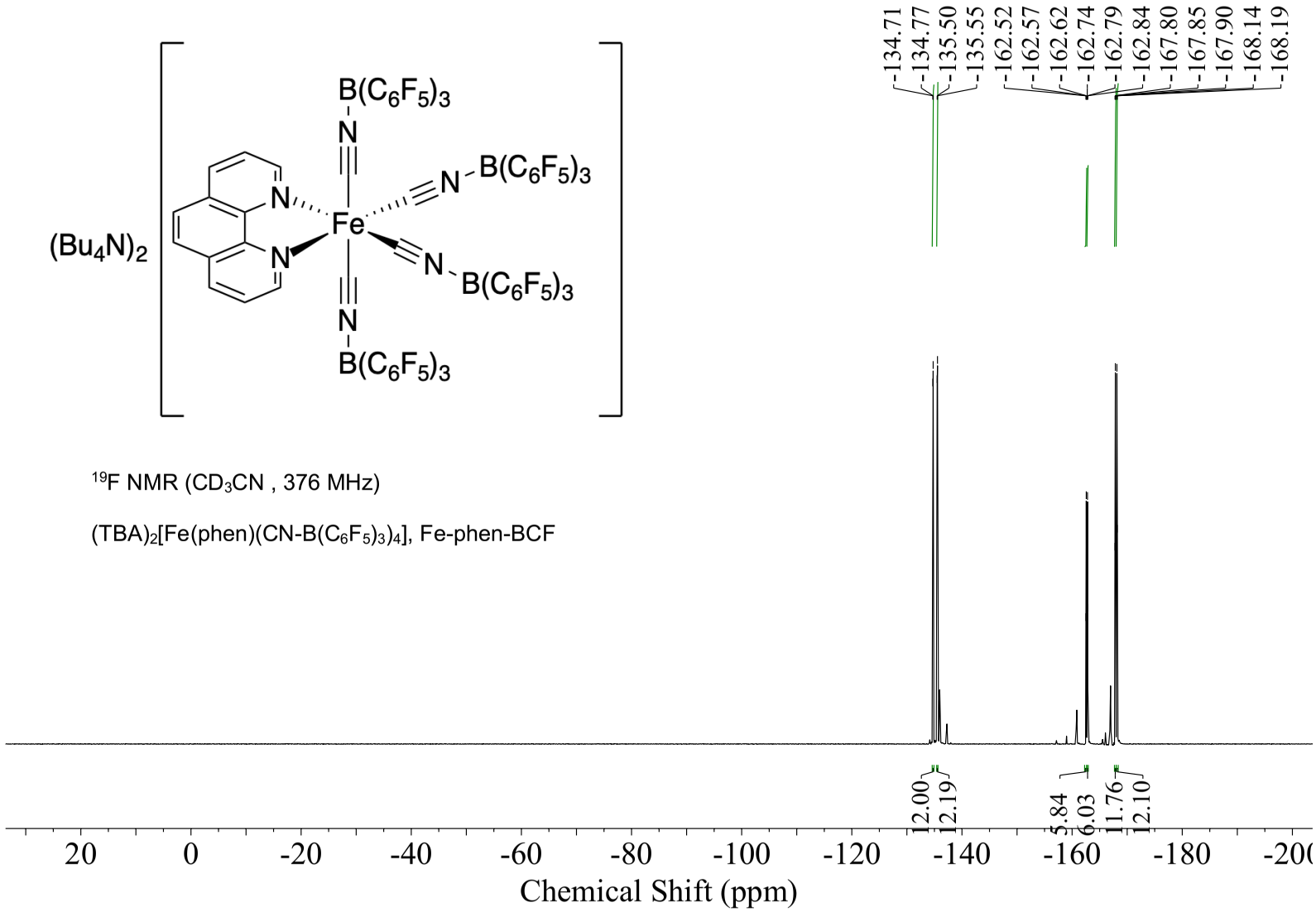

Figure 6.18. ^{19}F NMR spectrum of (TBA)$_2$[Fe(phen)(CN-B(C$_6$F$_5$)$_3$)$_4$] (**Fe-phen-BCF**) in CD$_3$CN.

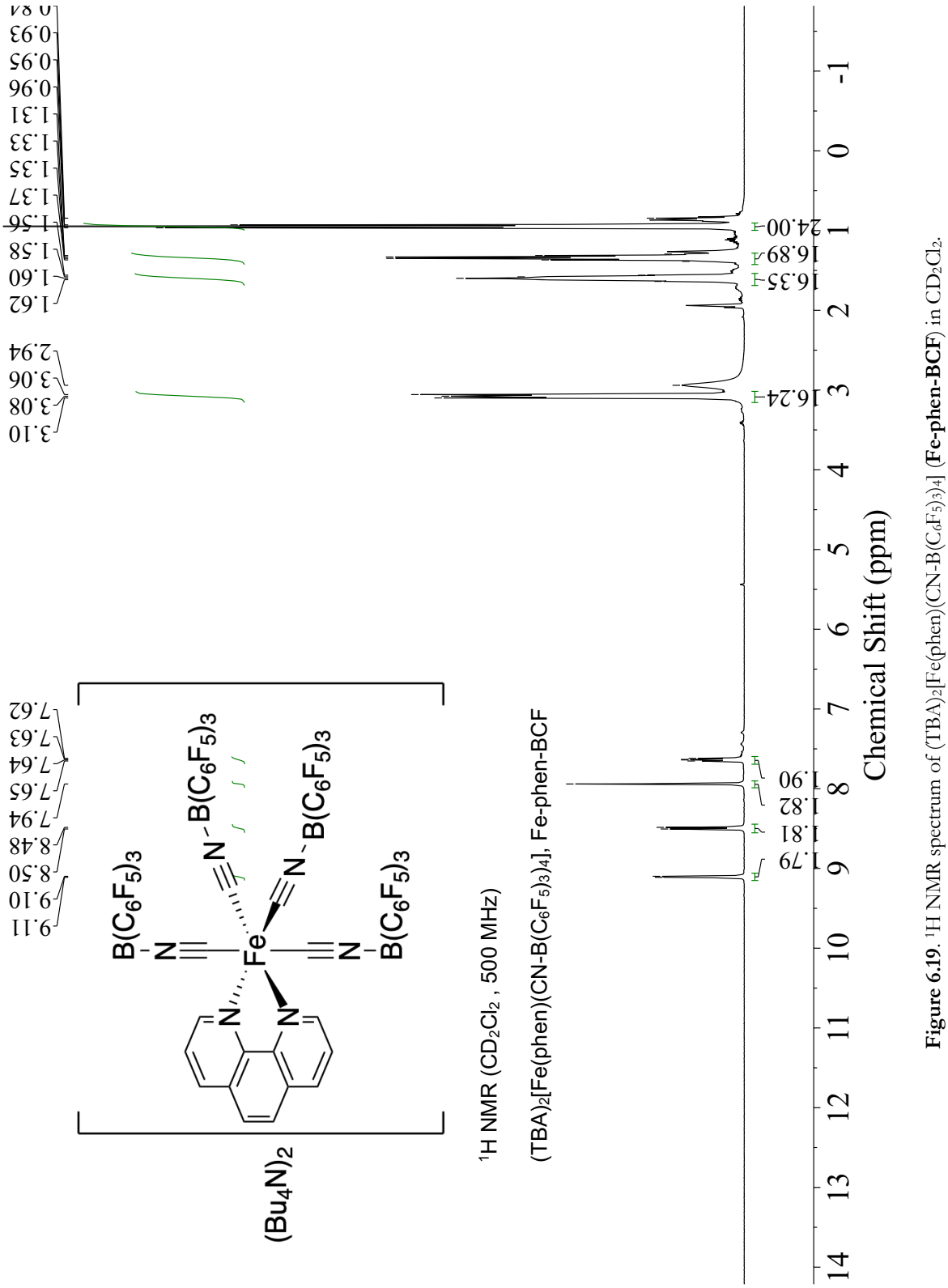

Figure 6.19. ^{1}H NMR spectrum of $(TBA)_2[Fe(phen)(CN\text{-}B(C_6F_5)_3)_4]$ (**Fe-phen-BCF**) in CD_2Cl_2.

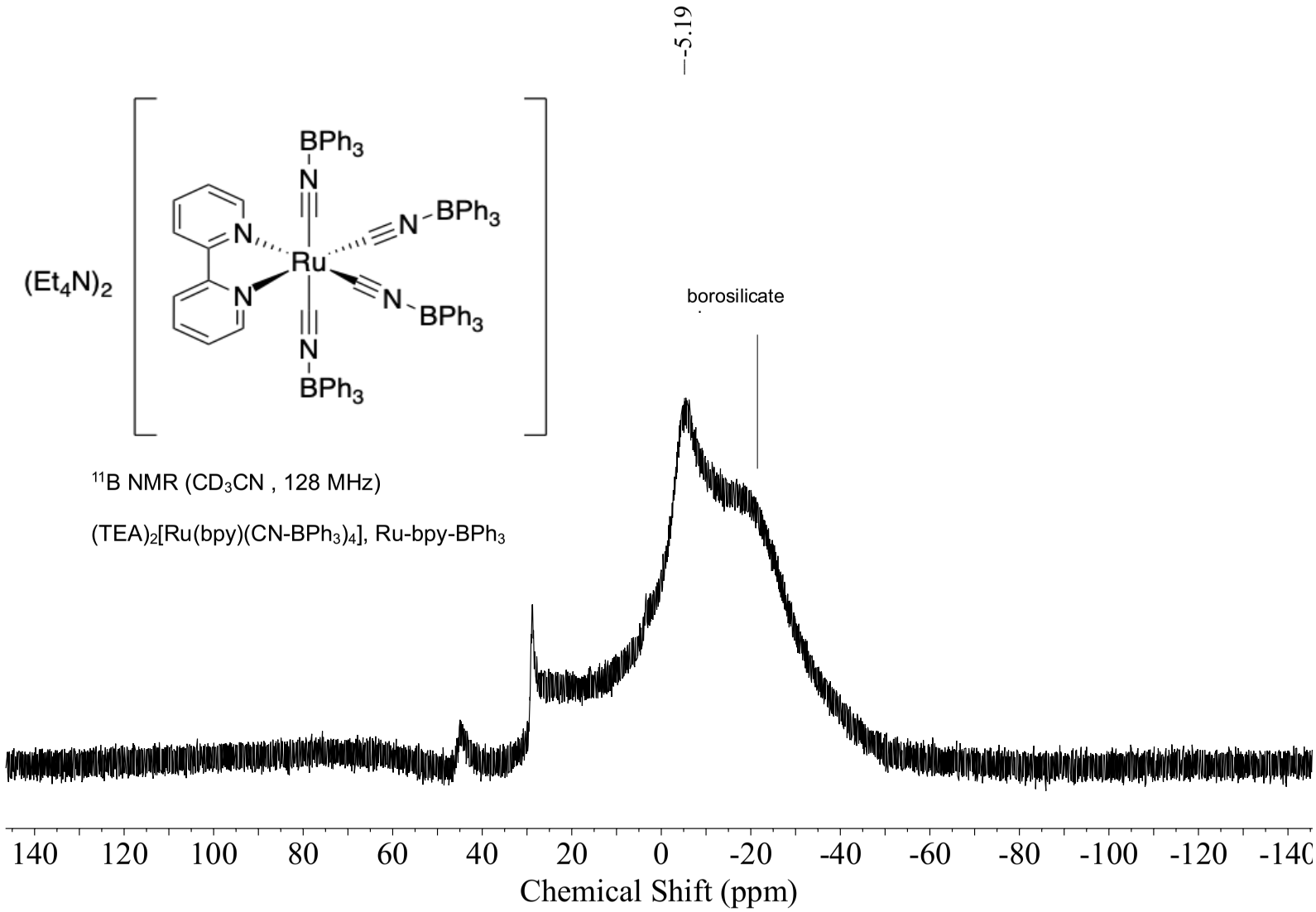

Figure 6.20. ^{11}B NMR spectrum of $(TEA)_2[Ru(bpy)(CN\text{-}BPh_3)_4]$ (**Ru-bpy-BPh$_3$**) in CD_3CN.

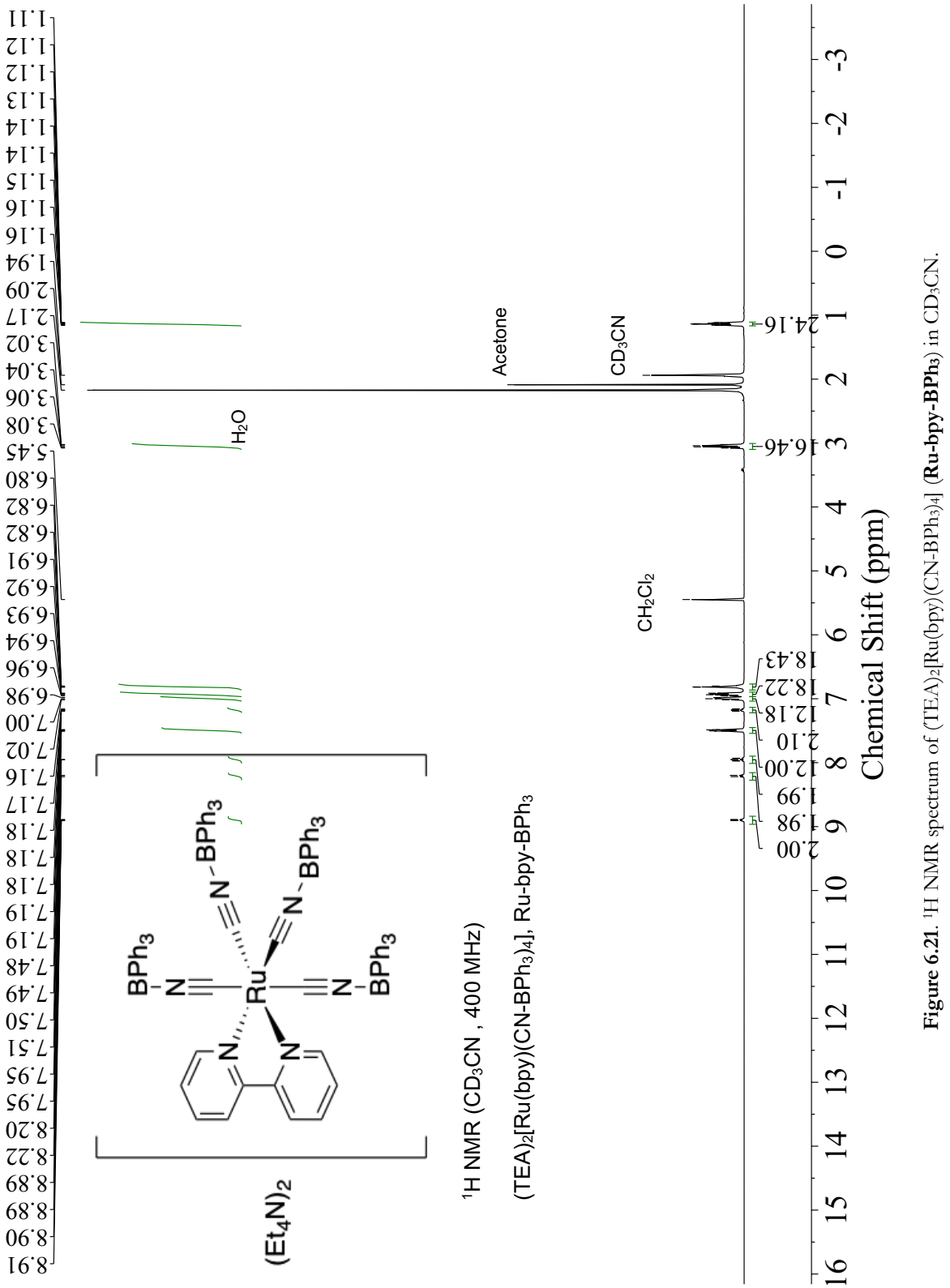

Figure 6.21. ^1H NMR spectrum of $(TEA)_2[Ru(bpy)(CN\text{-}BPh_3)_4]$ (**Ru-bpy-BPh$_3$**) in CD_3CN.

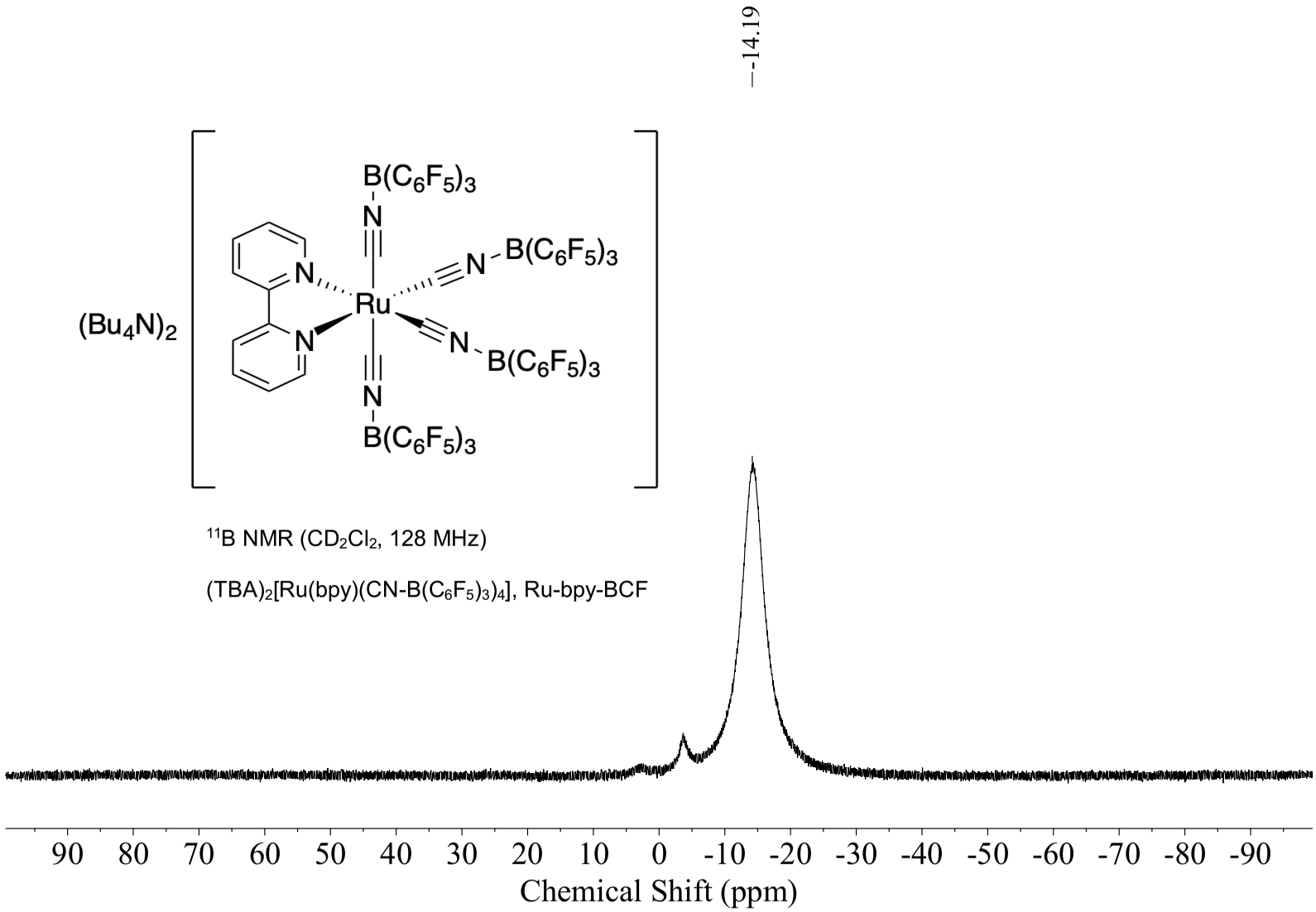

Figure 6.22. ^{11}B NMR spectrum of $(TBA)_2[Ru(bpy)(CN\text{-}B(C_6F_5)_3)_4]$ (**Ru-bpy-BCF**) in CD_2Cl_2.

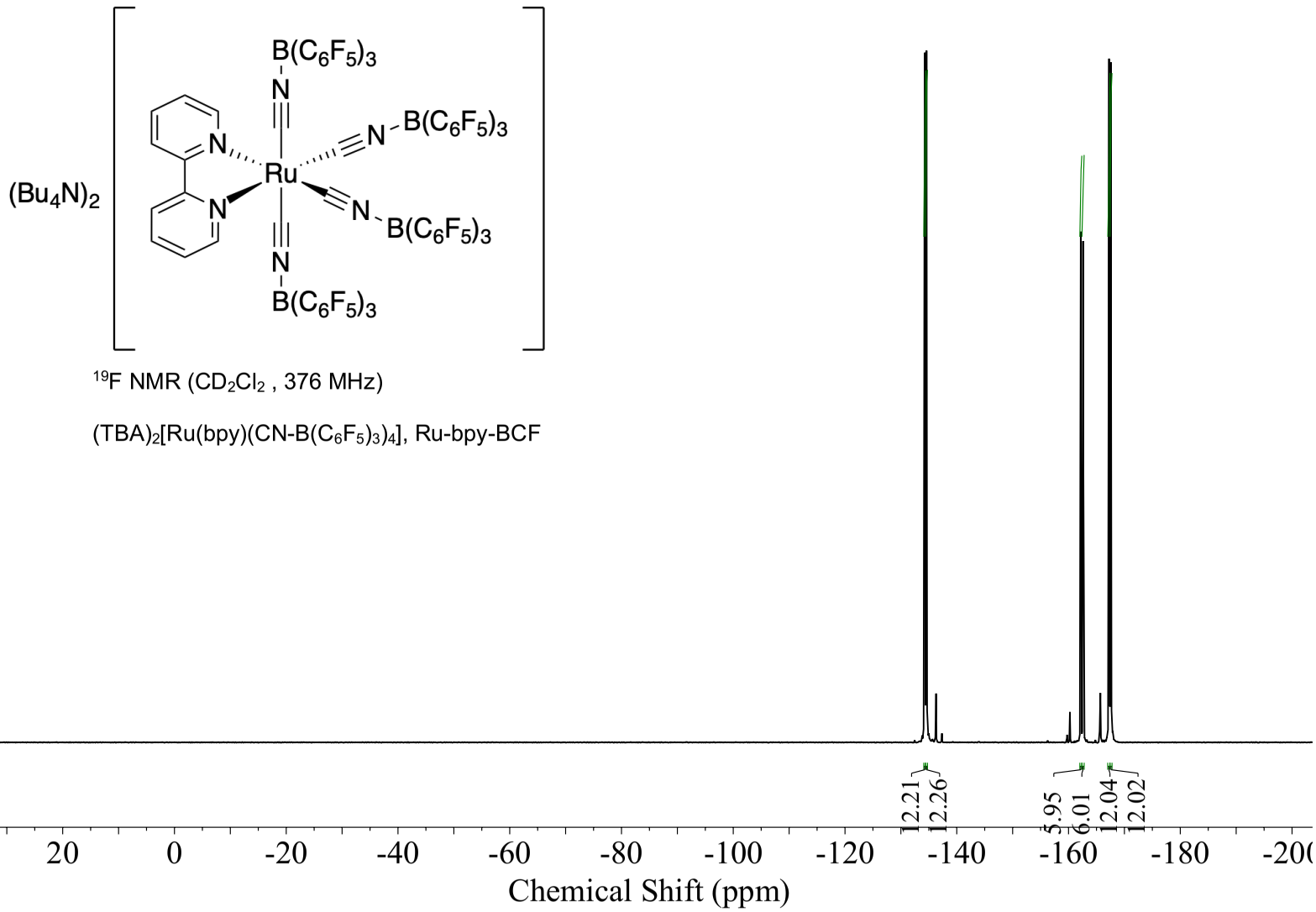

Figure 6.23. ^{19}F NMR spectrum of $(TBA)_2[Ru(bpy)(CN\text{-}B(C_6F_5)_3)_4]$ (**Ru-bpy-BCF**) in CD_2Cl_2.

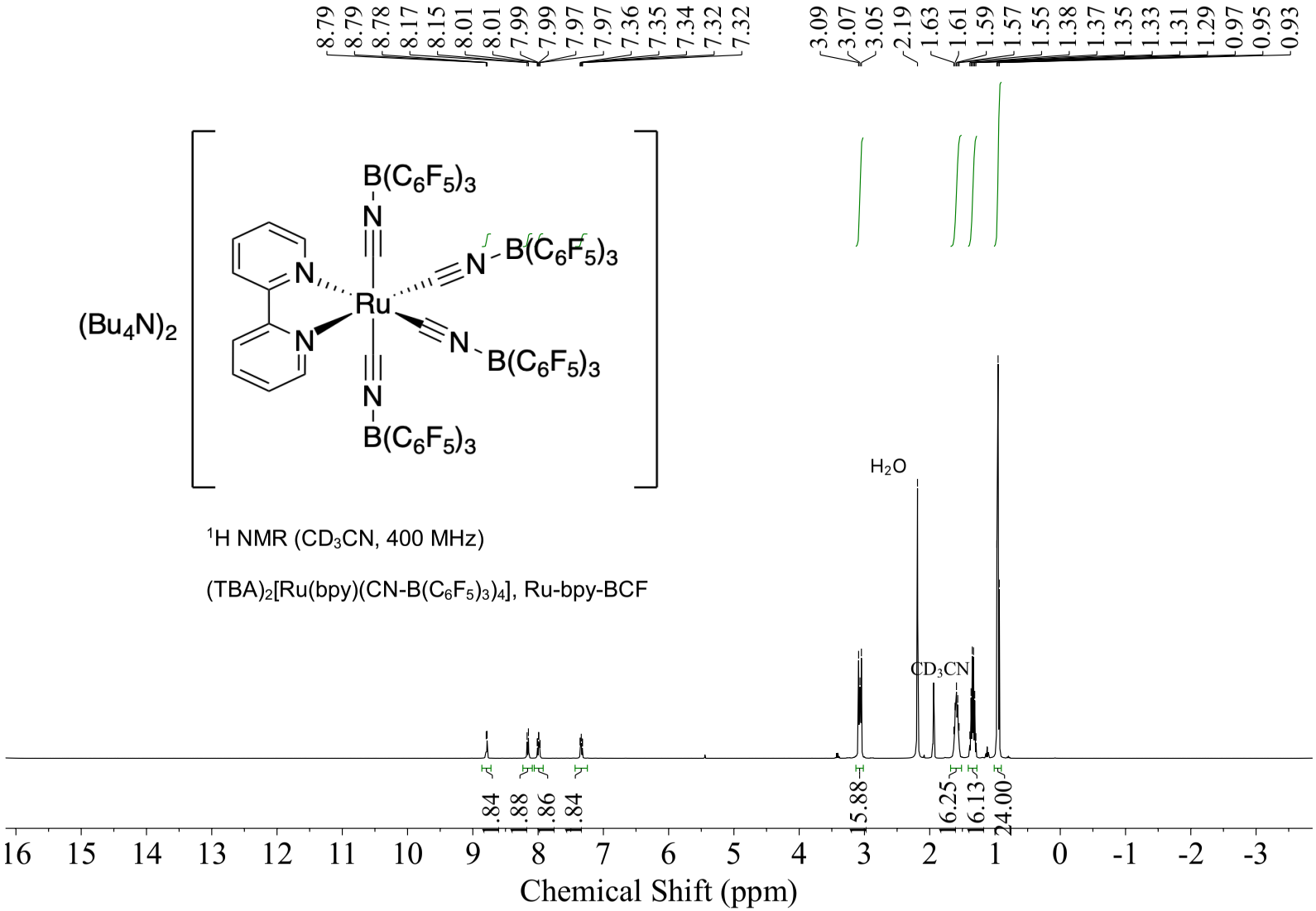

^{1}H NMR (CD_3CN, 400 MHz)

$(TBA)_2[Ru(bpy)(CN\text{-}B(C_6F_5)_3)_4]$, Ru-bpy-BCF

Figure 6.24. ^{1}H NMR spectrum of $(TBA)_2[Ru(bpy)(CN\text{-}B(C_6F_5)_3)_4]$ (**Ru-bpy-BCF**) in CD_3CN.

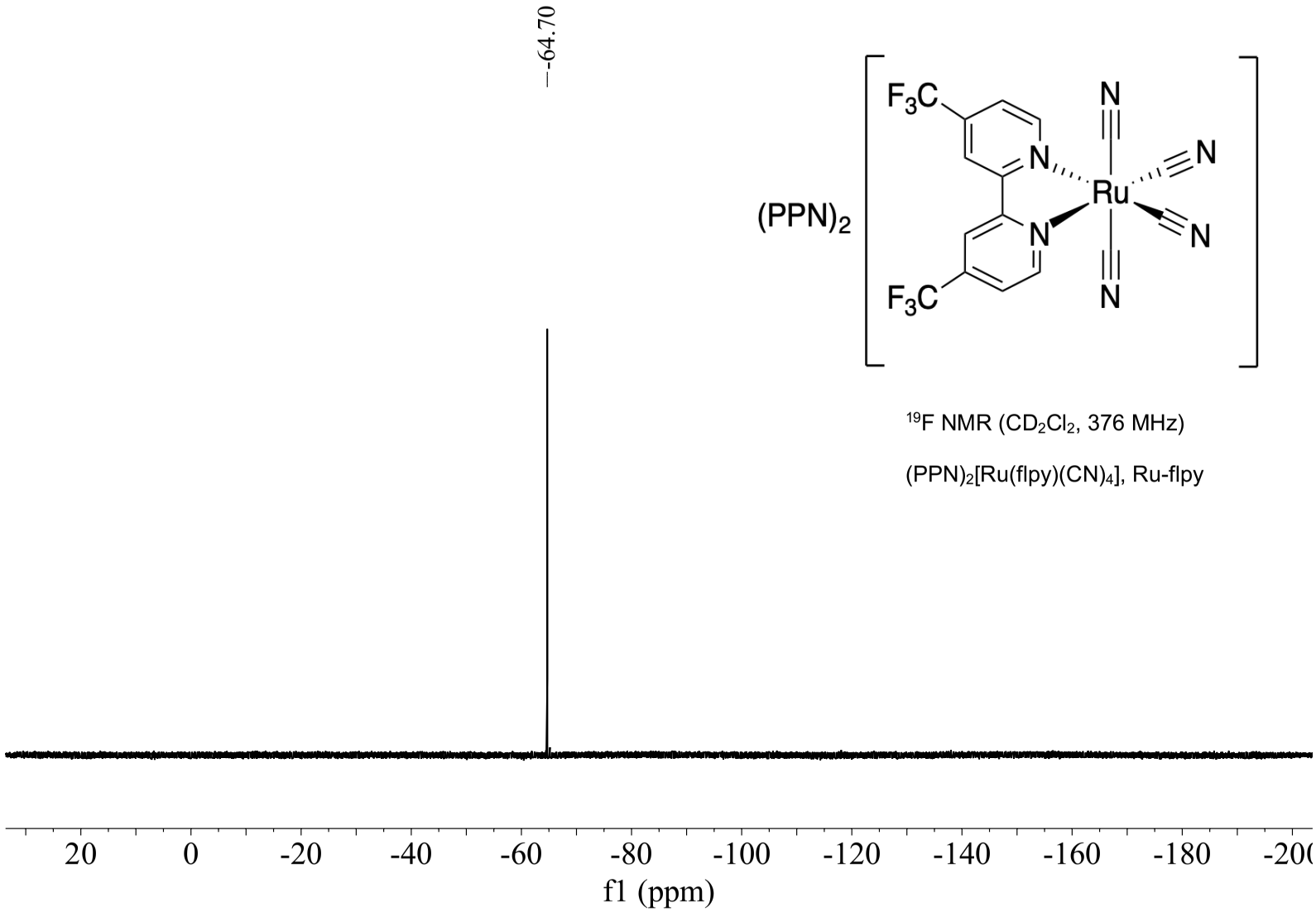

Figure 6.25. ^{19}F NMR spectrum of $(PPN)_2[Ru(flpy)(CN)_4]$ (**Ru-flpy**) in CD_2Cl_2.

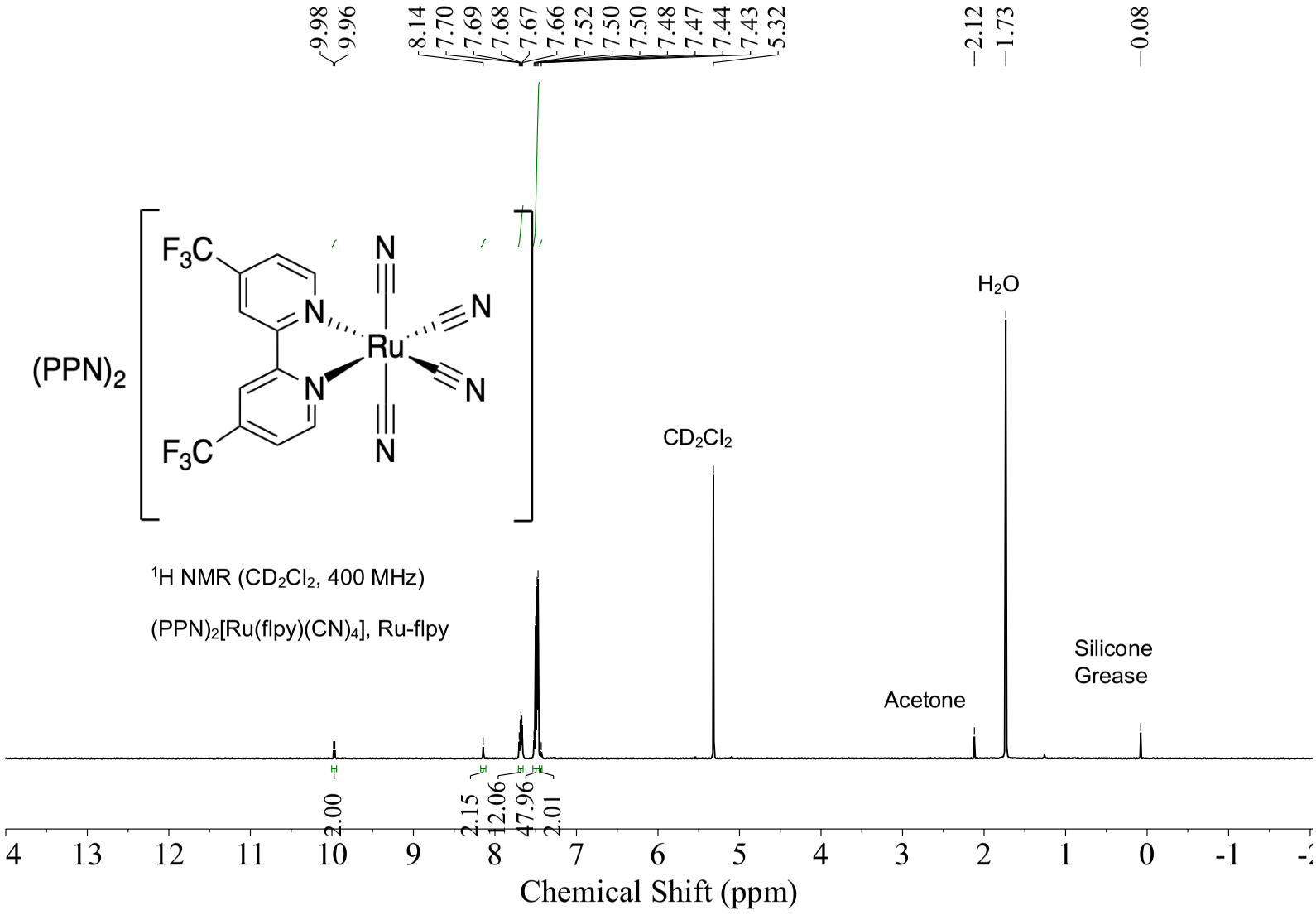

Figure 6.26. ^{1}H NMR spectrum of $(PPN)_2[Ru(flpy)(CN)_4]$ (**Ru-flpy**) in CD_2Cl_2.

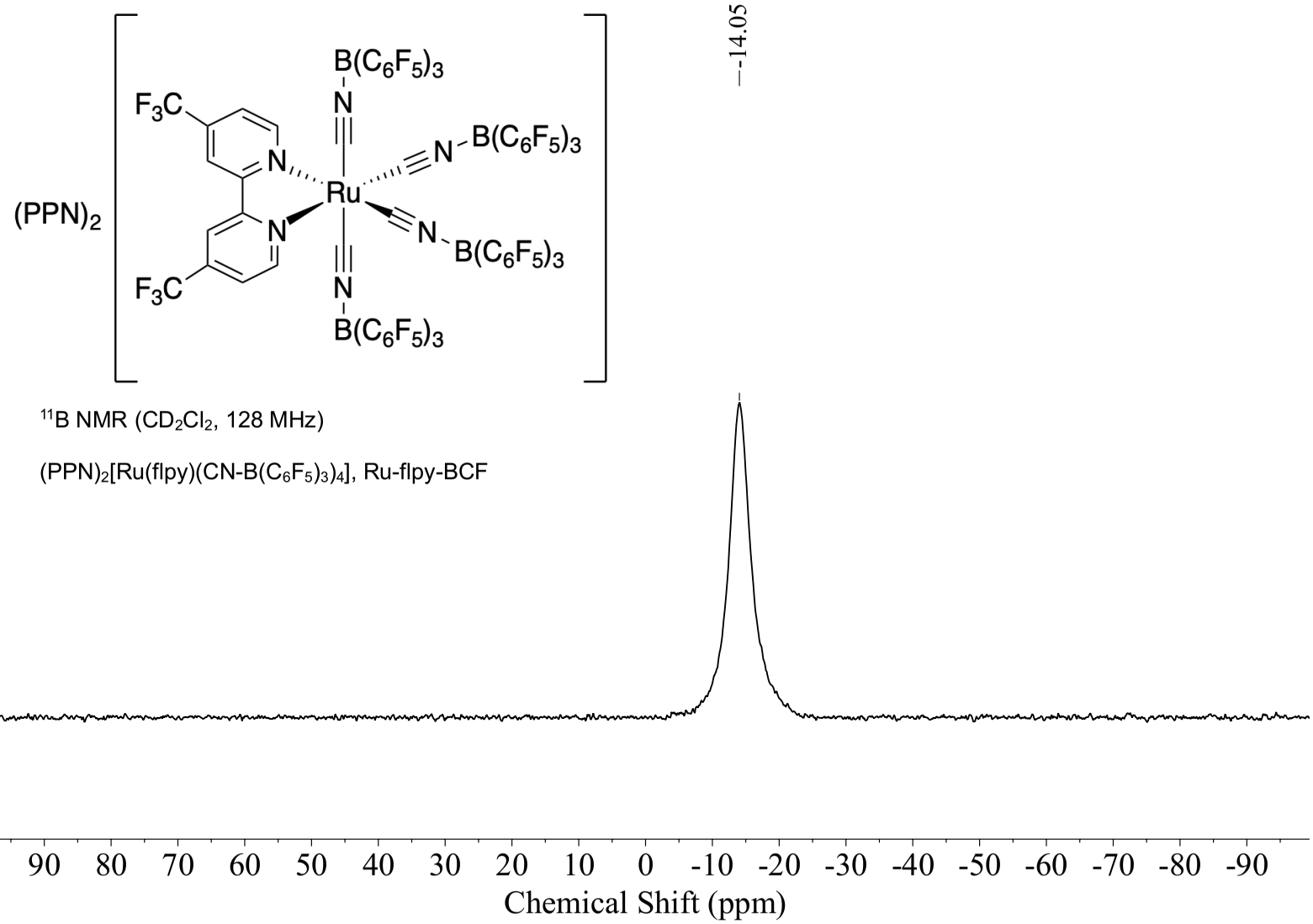

Figure 6.27. ^{11}B NMR spectrum of $(PPN)_2[Ru(flpy)(CN\text{-}B(C_6F_5)_3)_4]$ (**Ru-flpy-BCF**) in CD_2Cl_2.

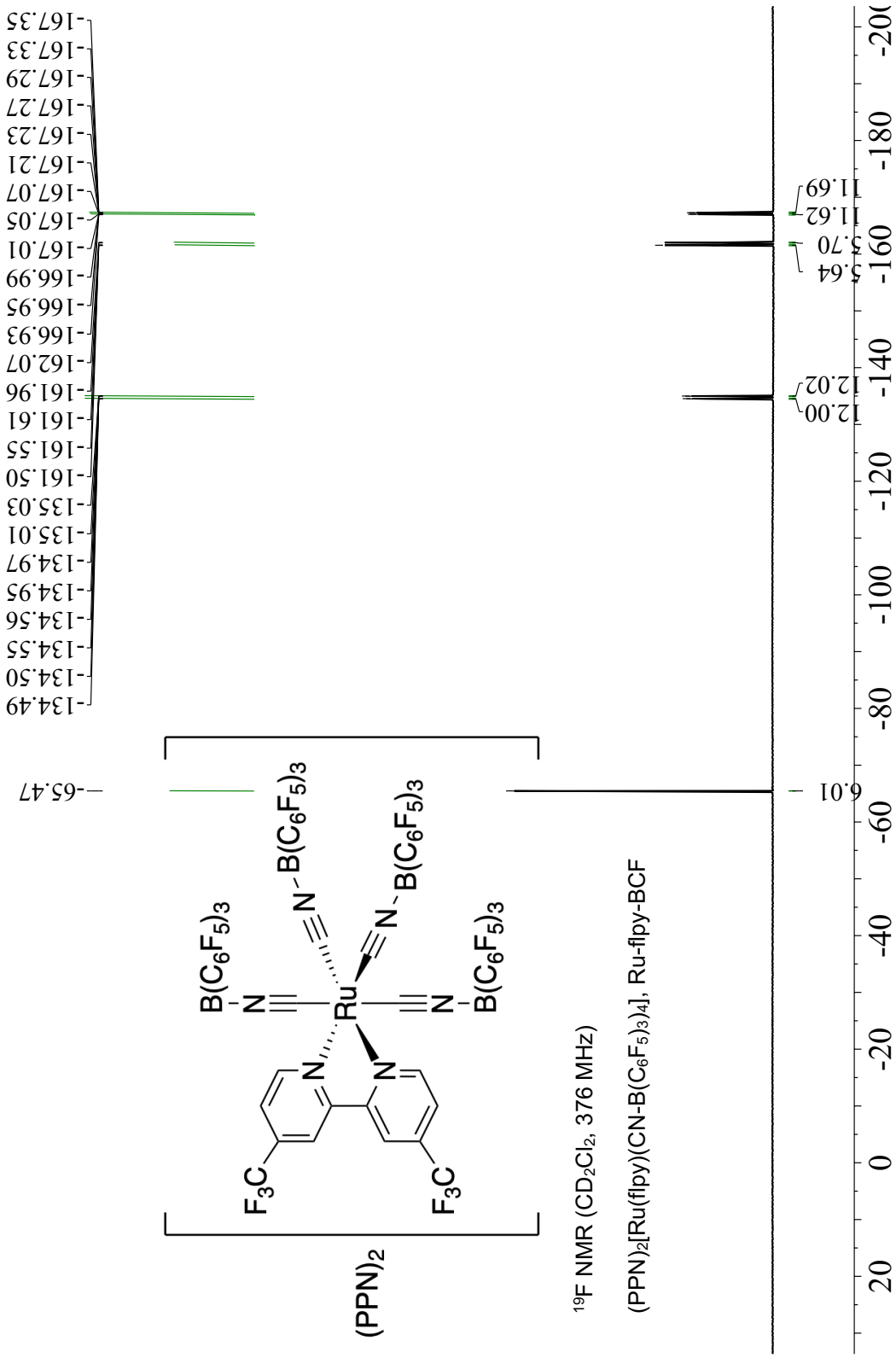

Figure 6.28. ^{19}F NMR spectrum of $(PPN)_2[Ru(flpy)(CN\text{-}B(C_6F_5)_3)_4]$ (**Ru-flpy-BCF**) in CD_2Cl_2.

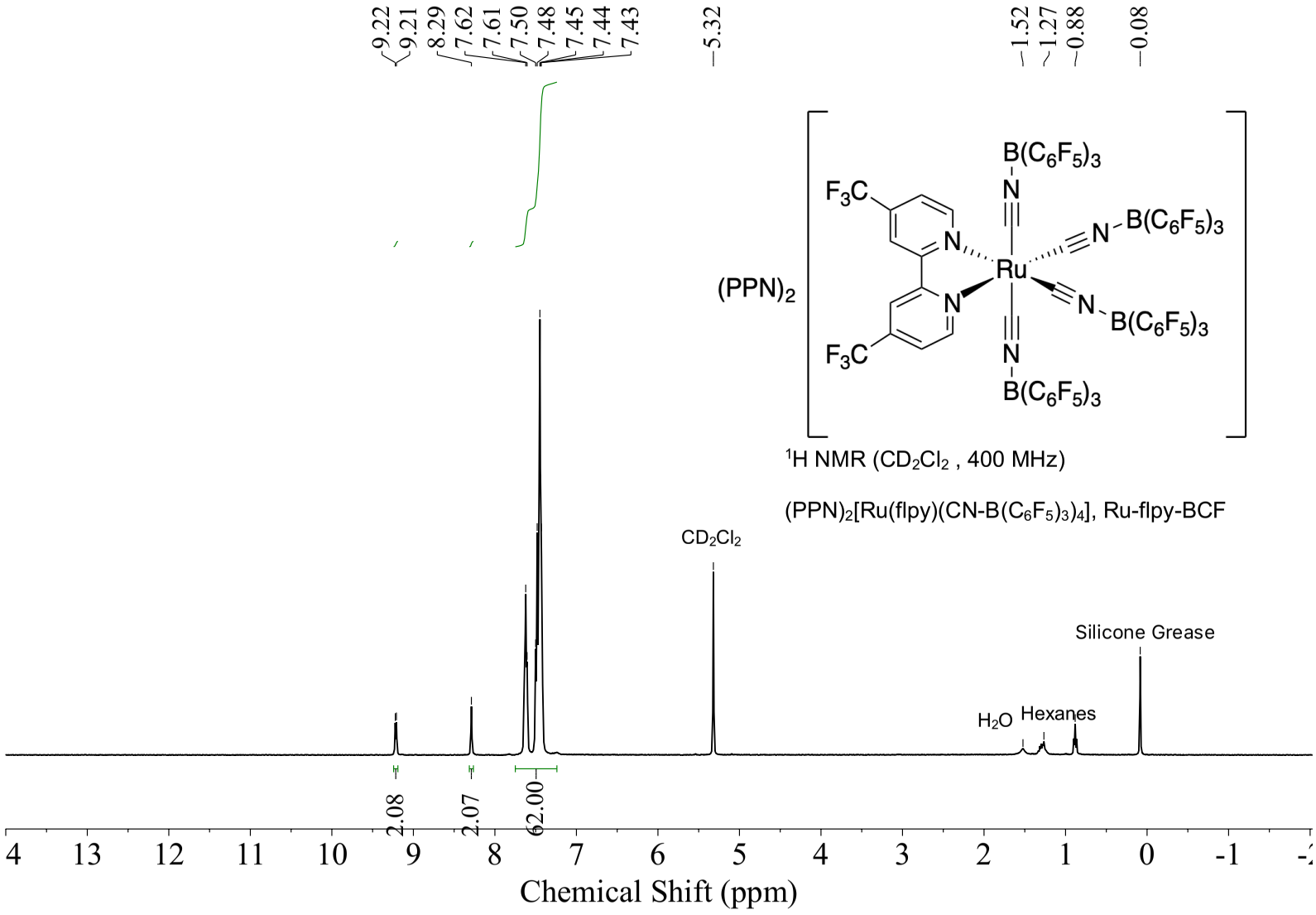

Figure 6.29. ^{1}H NMR spectrum of $(PPN)_2[Ru(flpy)(CN\text{-}B(C_6F_5)_3)_4]$ (**Ru-flpy-BCF**) in CD_2Cl_2.

Solid-State ATR-IR Spectra

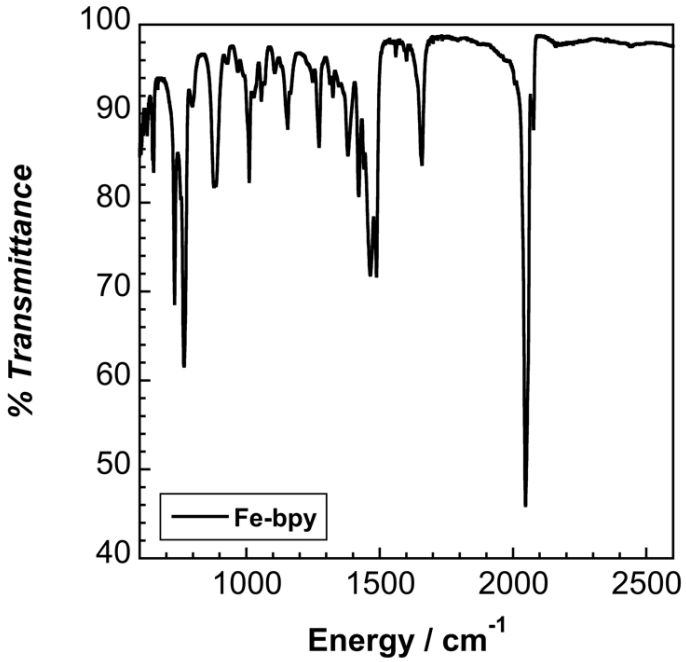

Figure 6.30. ATR-IR spectrum of **Fe-bpy**.

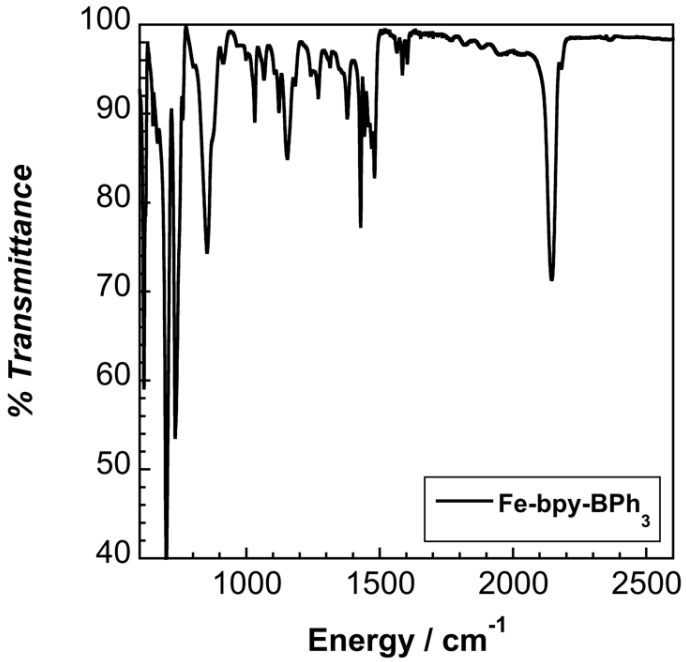

Figure 6.31. ATR-IR spectrum of **Fe-bpy-BPh$_3$**.

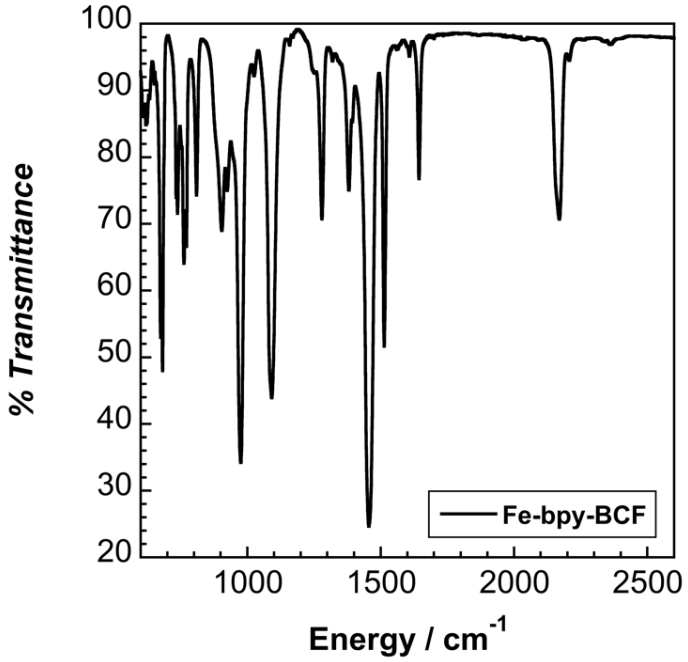

Figure 6.32. ATR-IR spectrum of **Fe-bpy-BCF**.

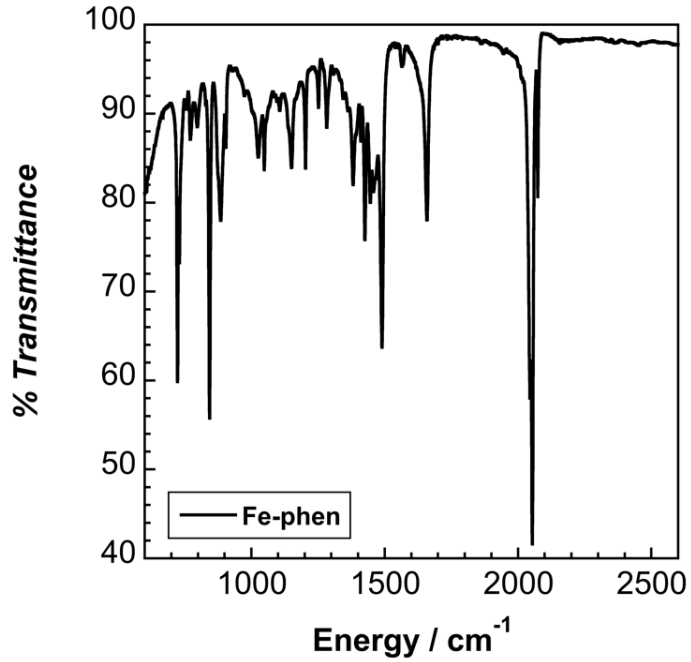

Figure 6.33. ATR-IR spectrum of **Fe-phen**.

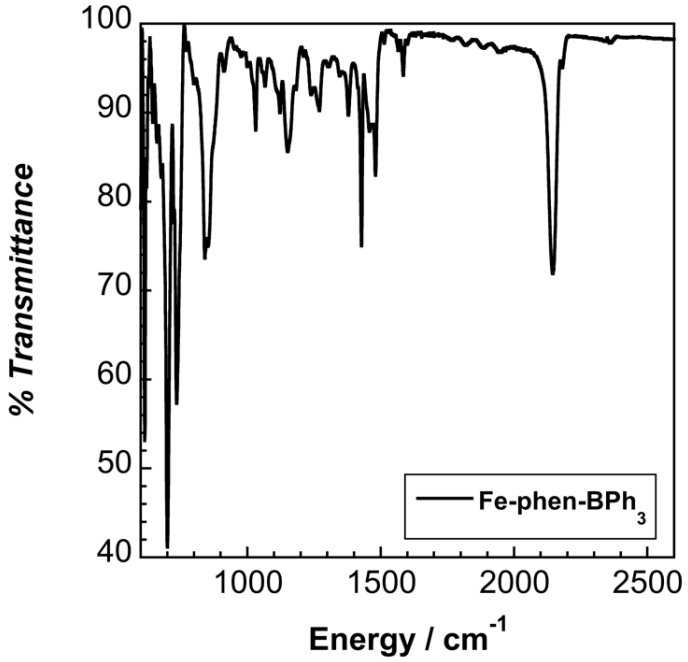

Figure 6.34. ATR-IR spectrum of **Fe-phen-BPh$_3$**.

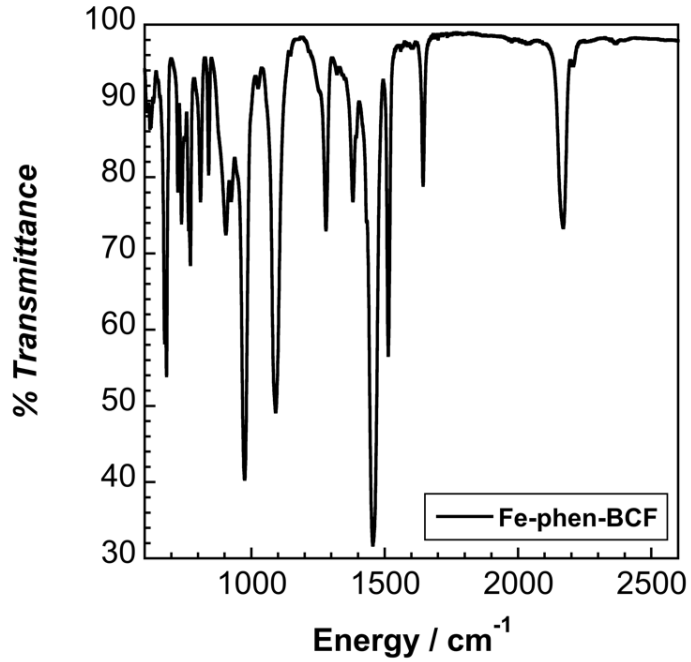

Figure 6.35. ATR-IR spectrum of **Fe-phen-BCF**.

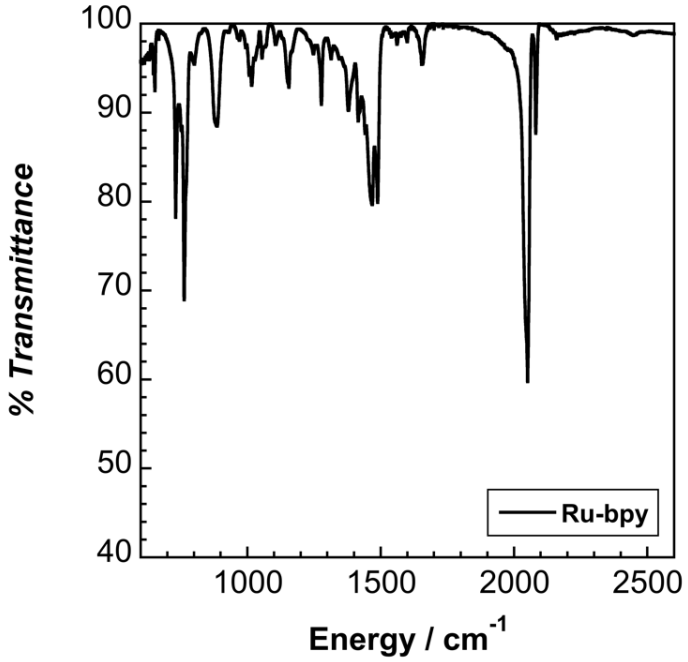

Figure 6.36. ATR-IR spectrum of **Ru-bpy**.

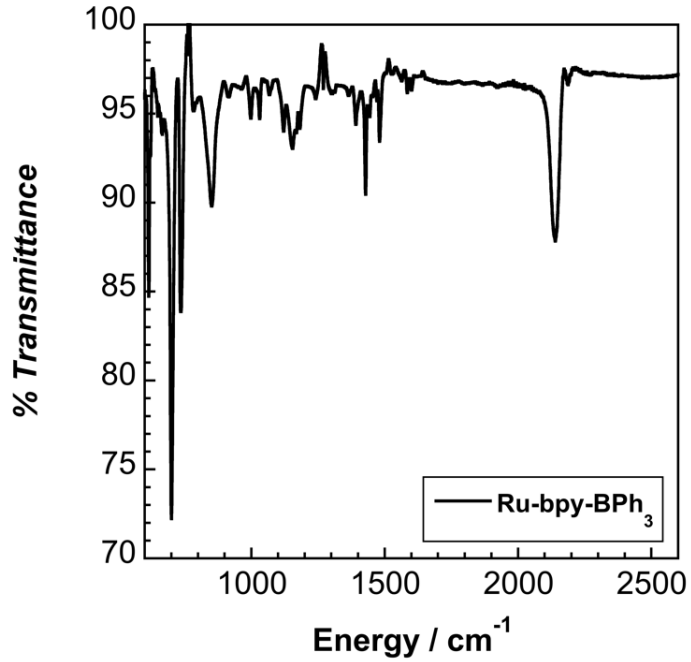

Figure 6.37. ATR-IR spectrum of **Ru-bpy-BPh$_3$**.

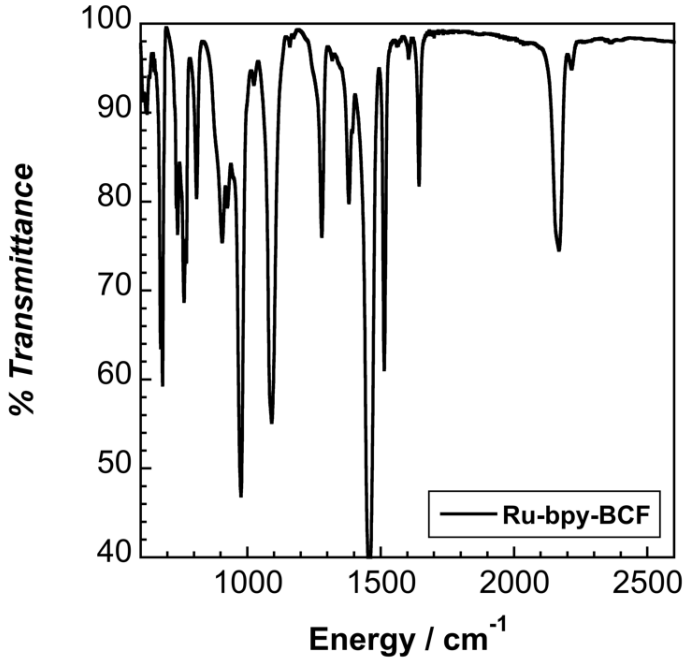

Figure 6.38. ATR-IR spectrum of **Ru-bpy-BCF**.

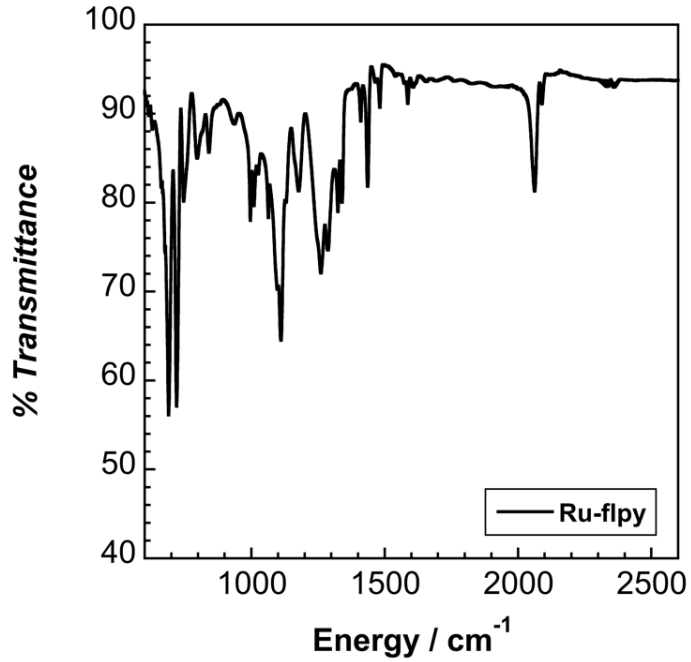

Figure 6.39. ATR-IR spectrum of **Ru-flpy**.

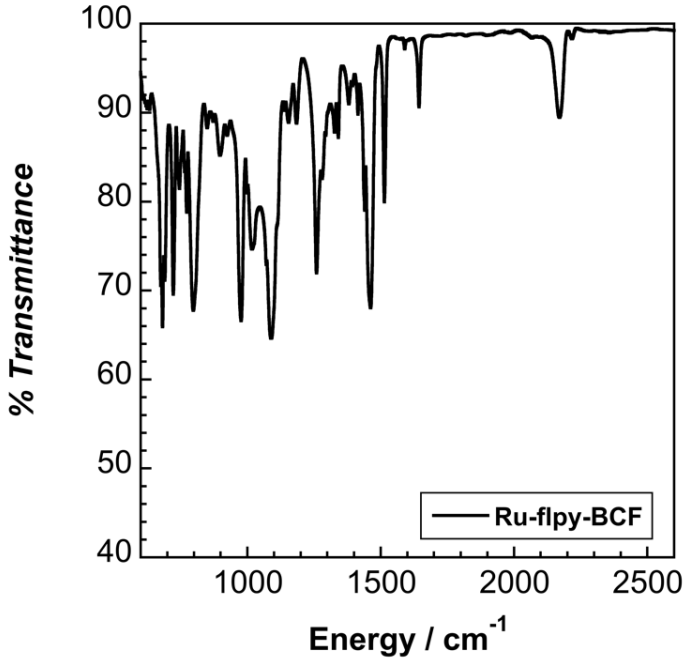

Figure 6.40. ATR-IR spectrum of **Ru-flpy-BCF**.

UV-Visible Spectroscopy and Transient Absorption Spectroscopy:

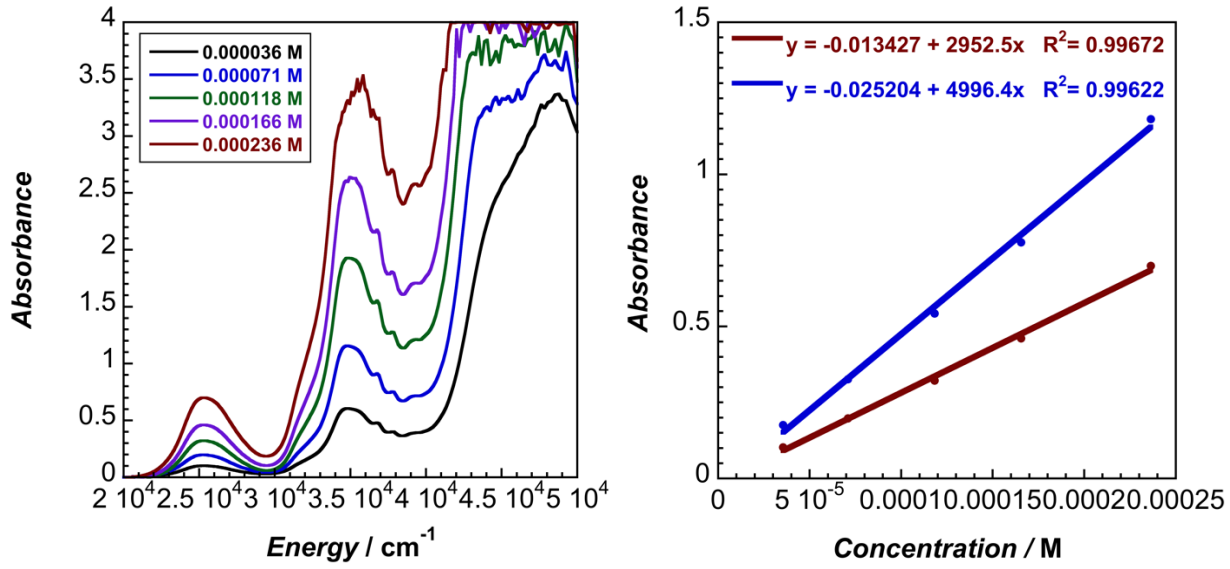

Figure 6.41. UV-visible absorption spectra and metal-to-ligand charge transfer linear fits for **Ru-bpy-BPh$_3$** in MeCN using a 1 cm path length cuvette.

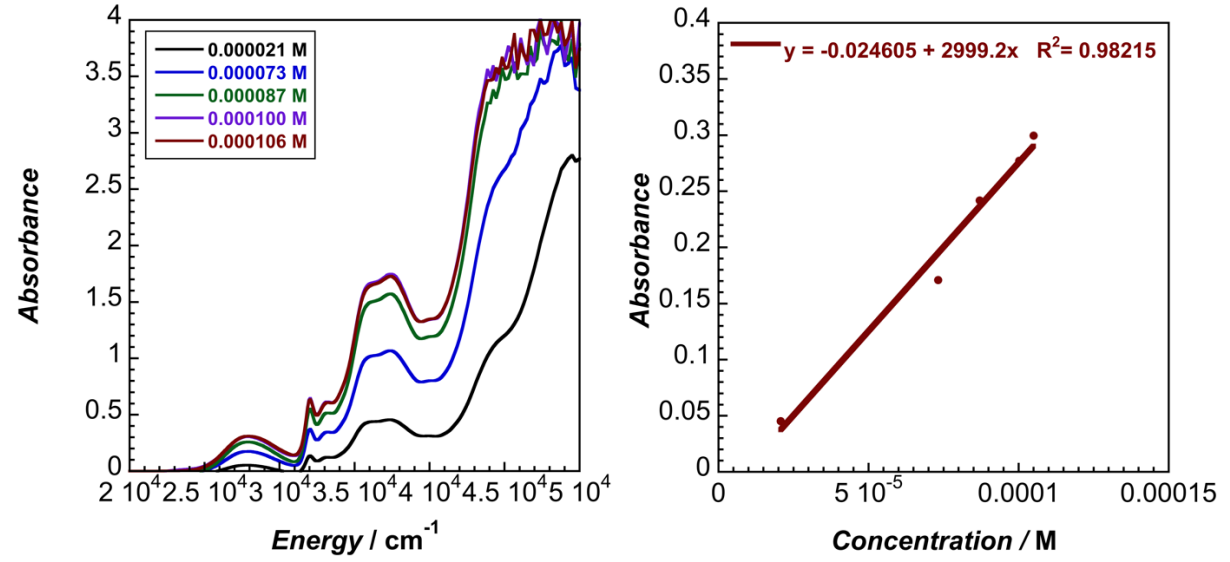

Figure 6.42. UV-visible absorption spectra and metal-to-ligand charge transfer linear fit for **Ru-bpy-BCF** in MeCN using a 1 cm path length cuvette.

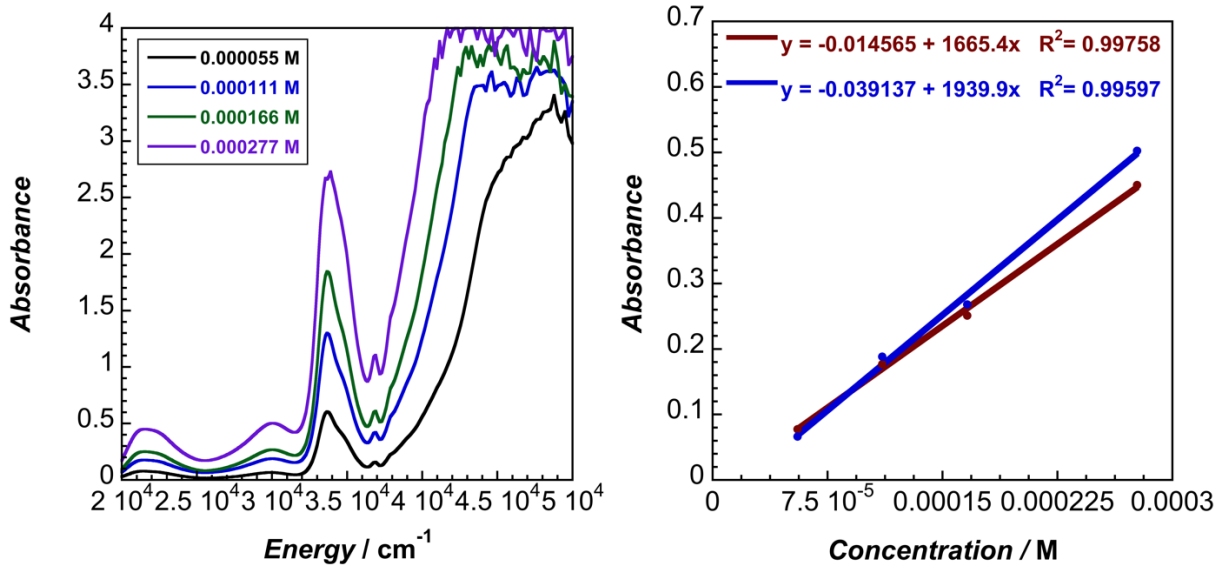

Figure 6.43. UV-visible absorption spectra and metal-to-ligand charge transfer linear fit for **Fe-bpy-BPh$_3$** in MeCN using a 1 cm path length cuvette.

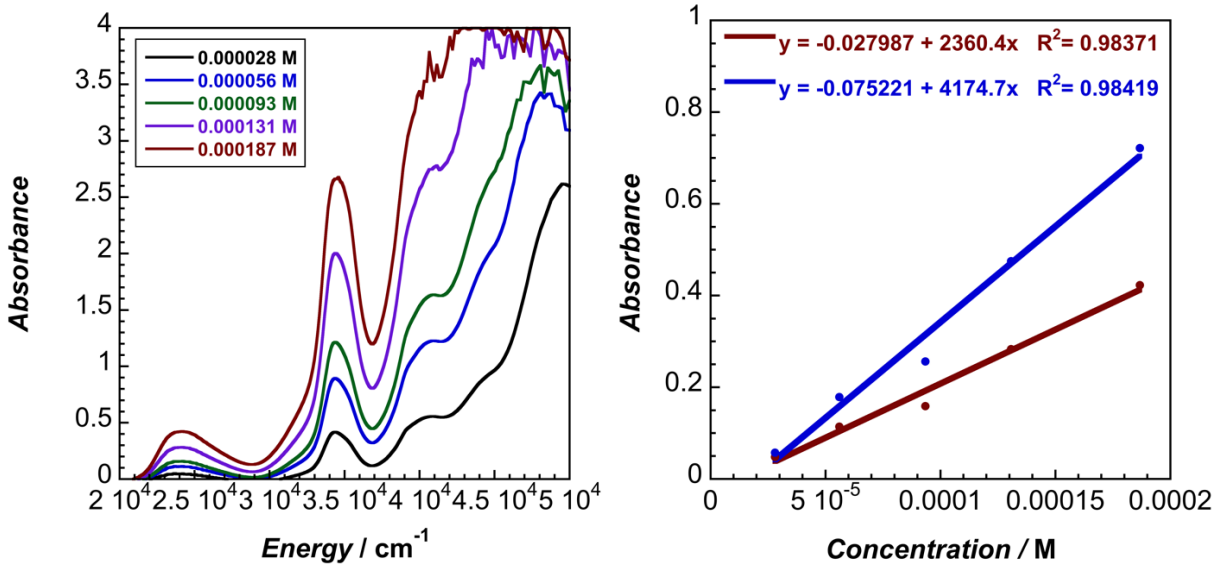

Figure 6.44. UV-visible absorption spectra and metal-to-ligand charge transfer linear fit for **Fe-bpy-BCF** in MeCN using a 1 cm path length cuvette.

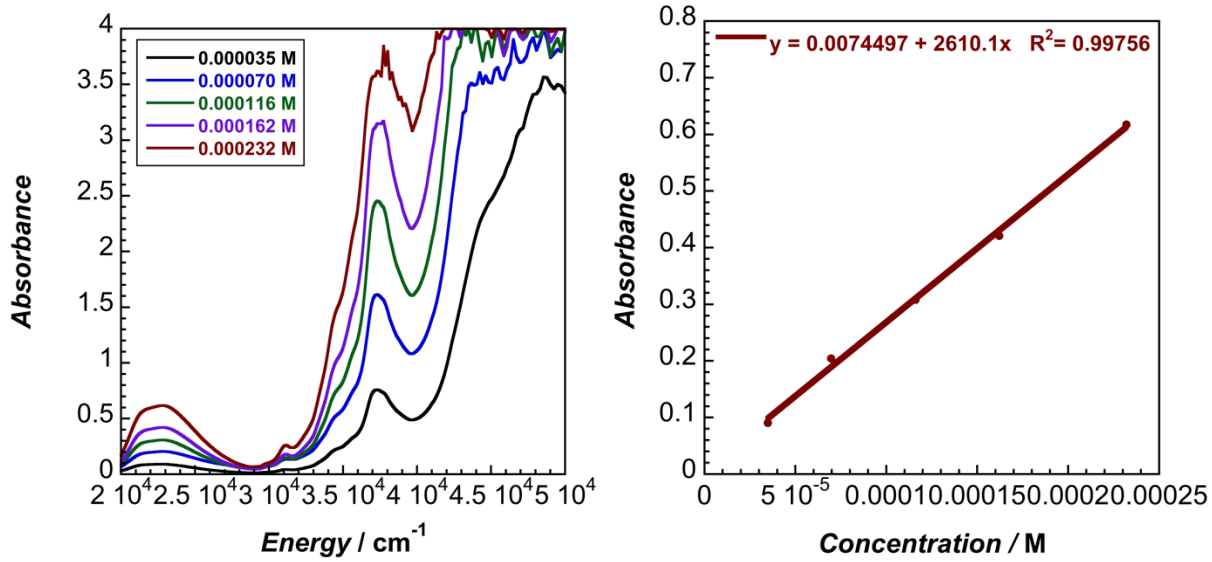

Figure 6.45. UV-visible absorption spectra and metal-to-ligand charge transfer linear fit for **Fe-phen-BPh$_3$** in MeCN using a 1 cm path length cuvette.

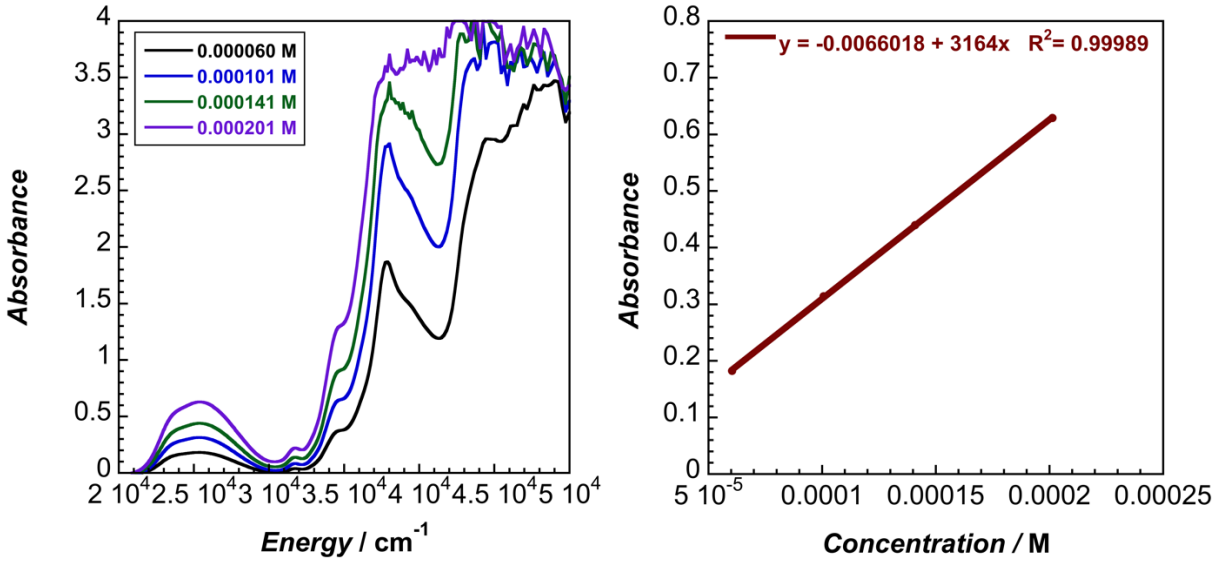

Figure 6.46. UV-visible absorption spectra and metal-to-ligand charge transfer linear fit for **Fe-phen-BCF** in MeCN using a 1 cm path length cuvette.

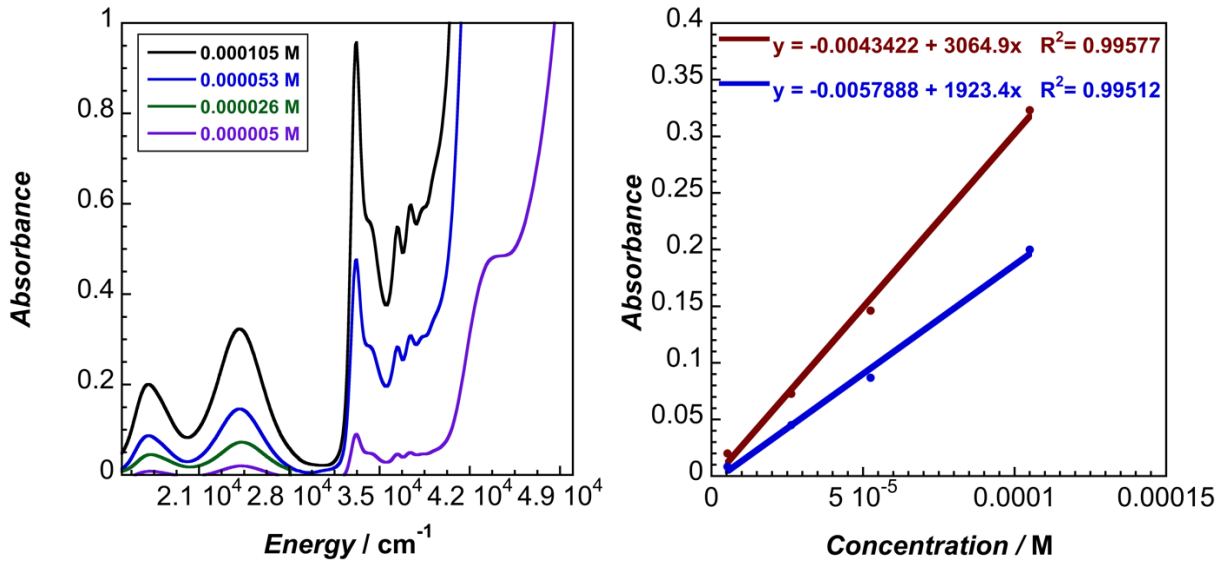

Figure 6.47. UV-visible absorption spectra and metal-to-ligand charge transfer linear fit for **Ru-flpy** in MeCN using a 0.5 cm path length cuvette.

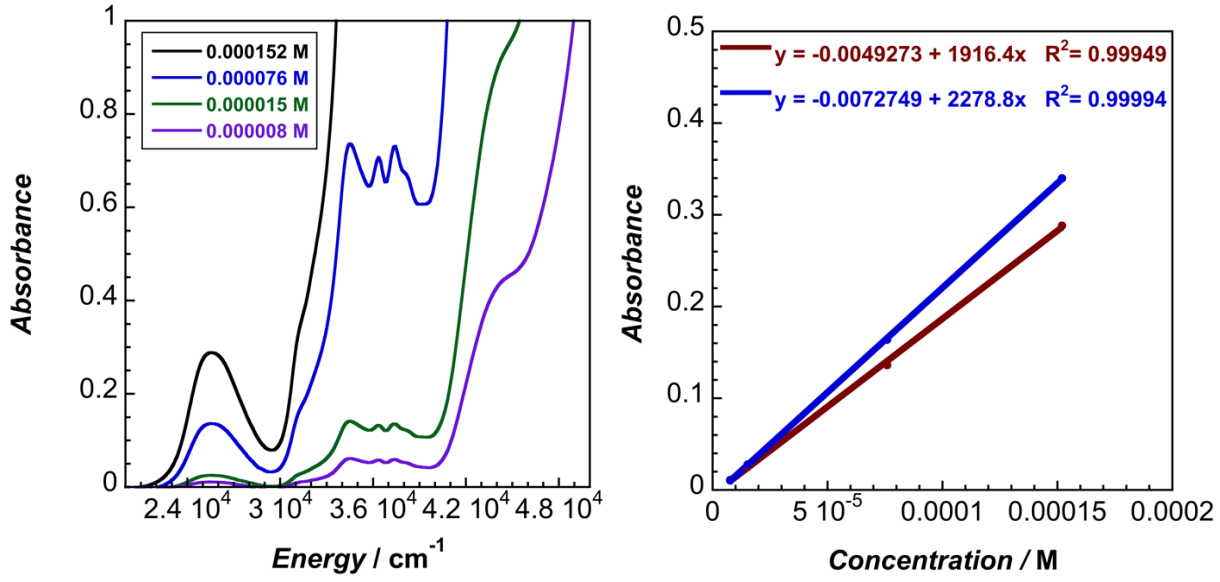

Figure 6.48. UV-visible absorption spectra and metal-to-ligand charge transfer linear fit for **Ru-flpy-BCF** in MeCN using a 0.5 cm path length cuvette.

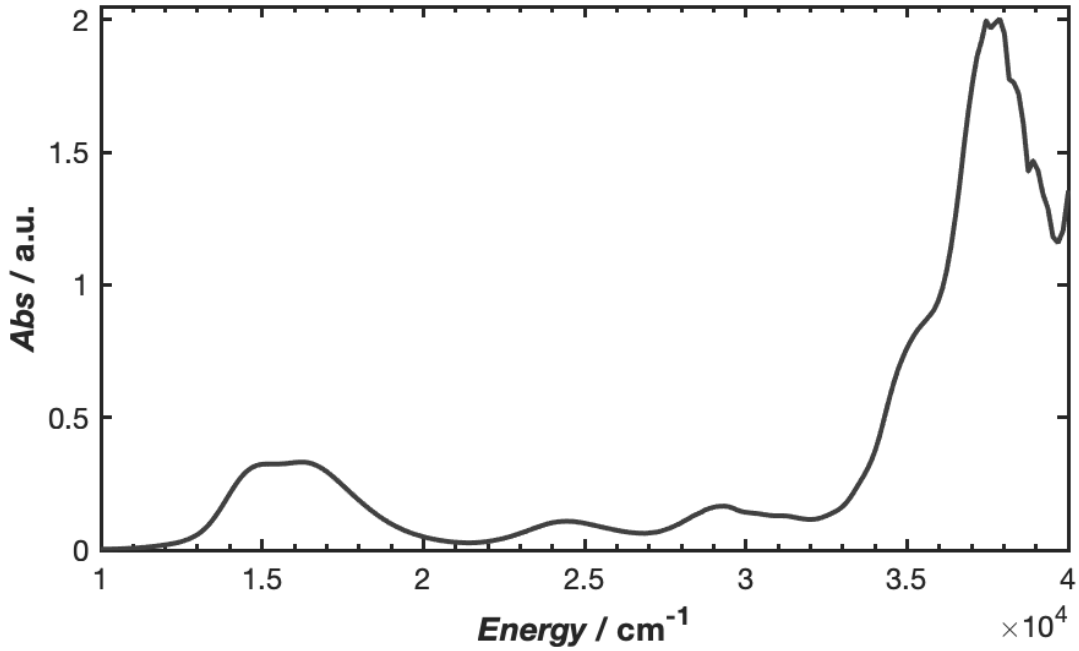

Figure 6.49. UV-visible absorption spectrum of 0.34 mM **Fe-phen** in MeCN. Spectrum recorded in a 2 mm path length cuvette. For this sample, the optical density is 0.25 a.u. at the intended excitation wavelength.

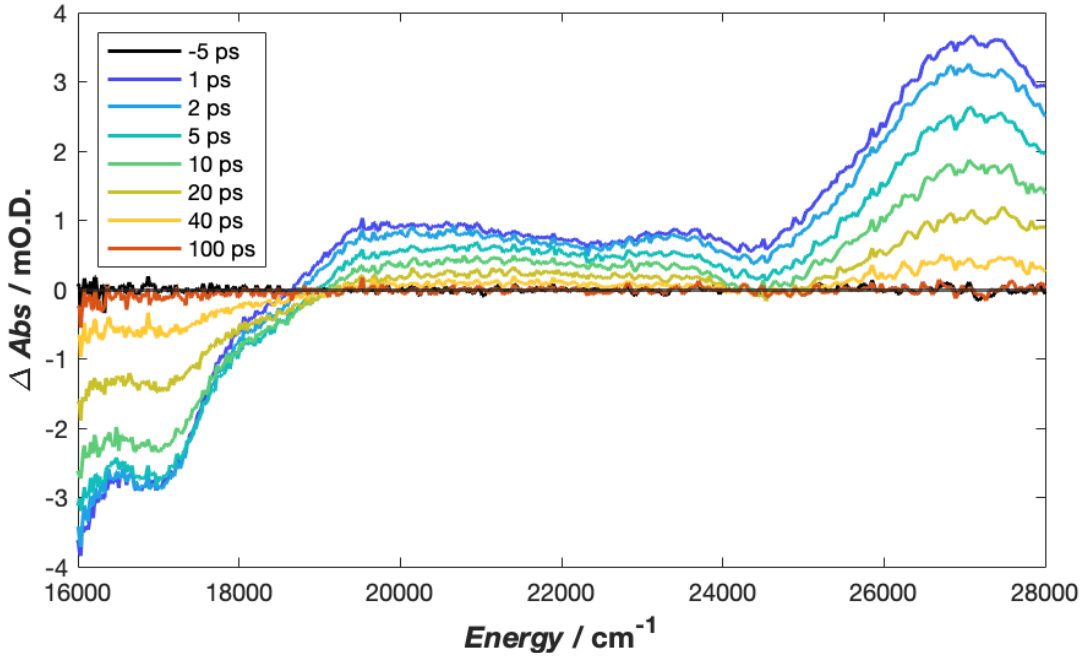

Figure 6.50. Transient absorption spectra of **Fe-phen** in MeCN after 700 nm / 14,300 cm^{-1} excitation, depicting traces from −5 to 100 ps time delay.

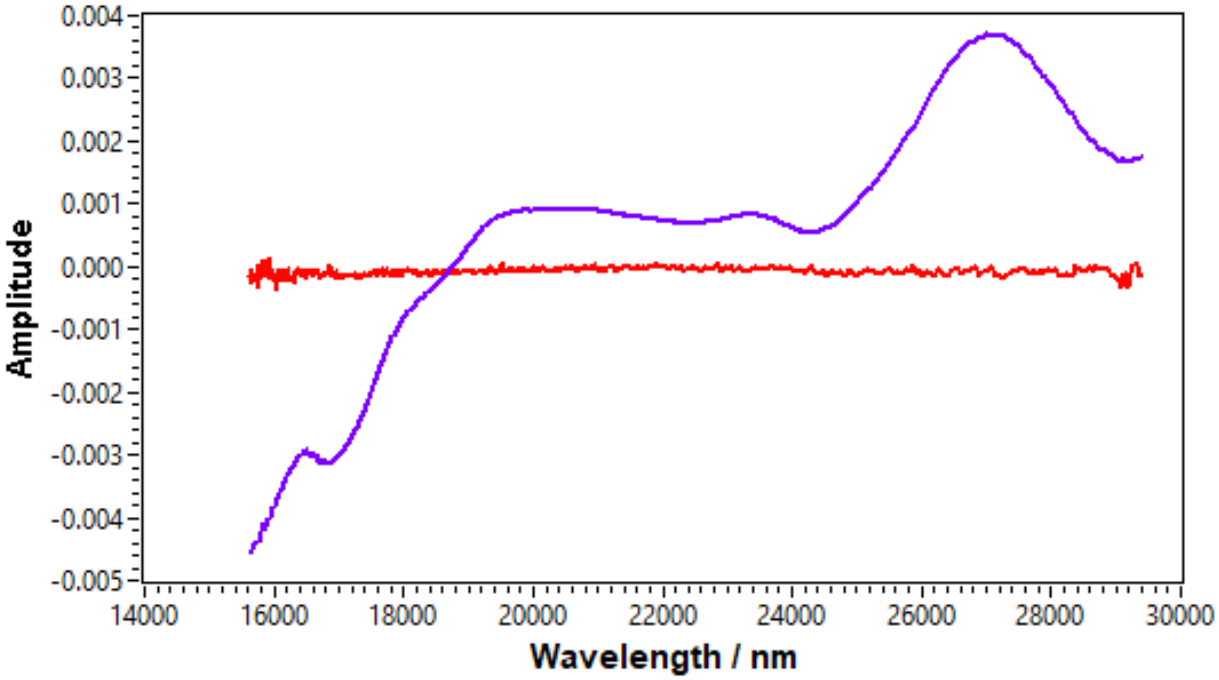

Figure 6.51. Principal components from a global analysis of the transient absorption data for **Fe-phen**. The red trace, associated with instrument noise, has an infinite lifetime. Single exponent decay kinetics of the purple trace are reported.

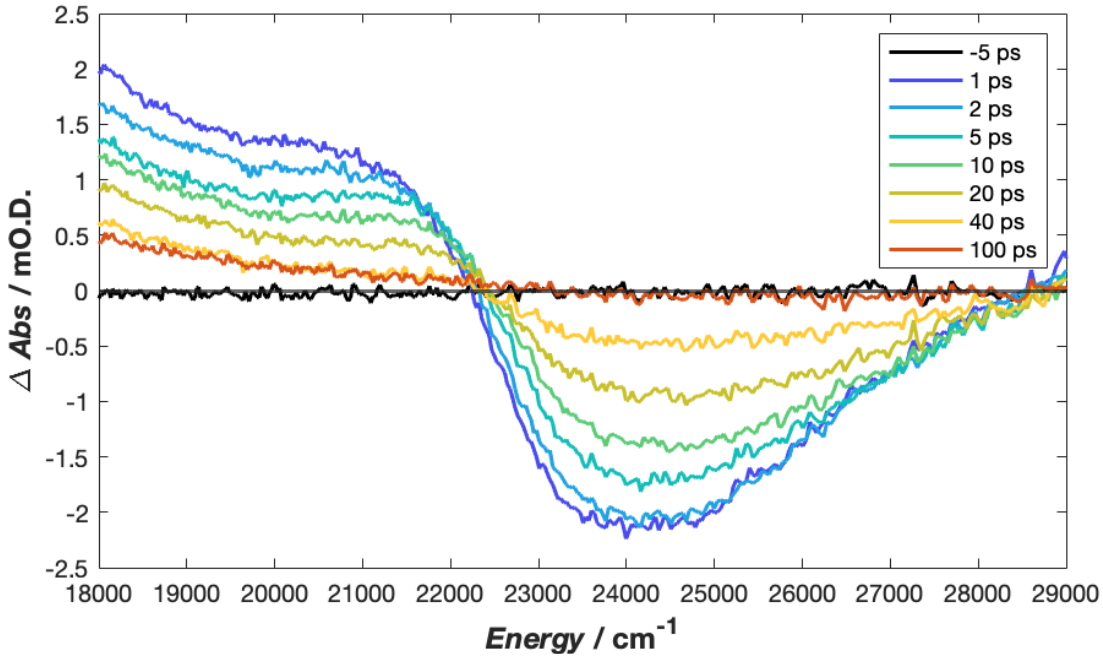

Figure 6.52. Transient absorption spectra of **Fe-bpy-BCF** after 290 nm / 34,500 cm^{-1} excitation, depicting traces at -5 ps to 100 ps time delay.

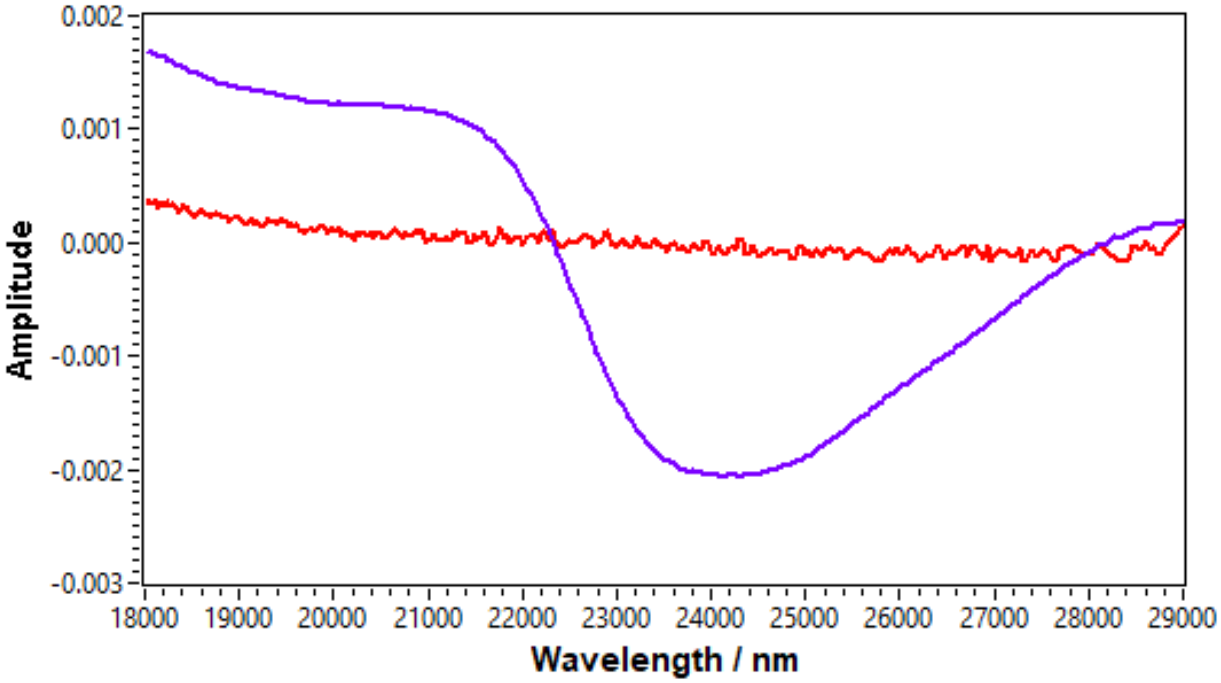

Figure 6.53. Principal components from a global analysis of the transient absorption data for **Fe-bpy-BCF**. The red trace corresponding to generation of $[(MeCN)_2]^-$ in solution has an infinite lifetime over the experimental time scale. Single exponent decay kinetics of the purple trace are reported.

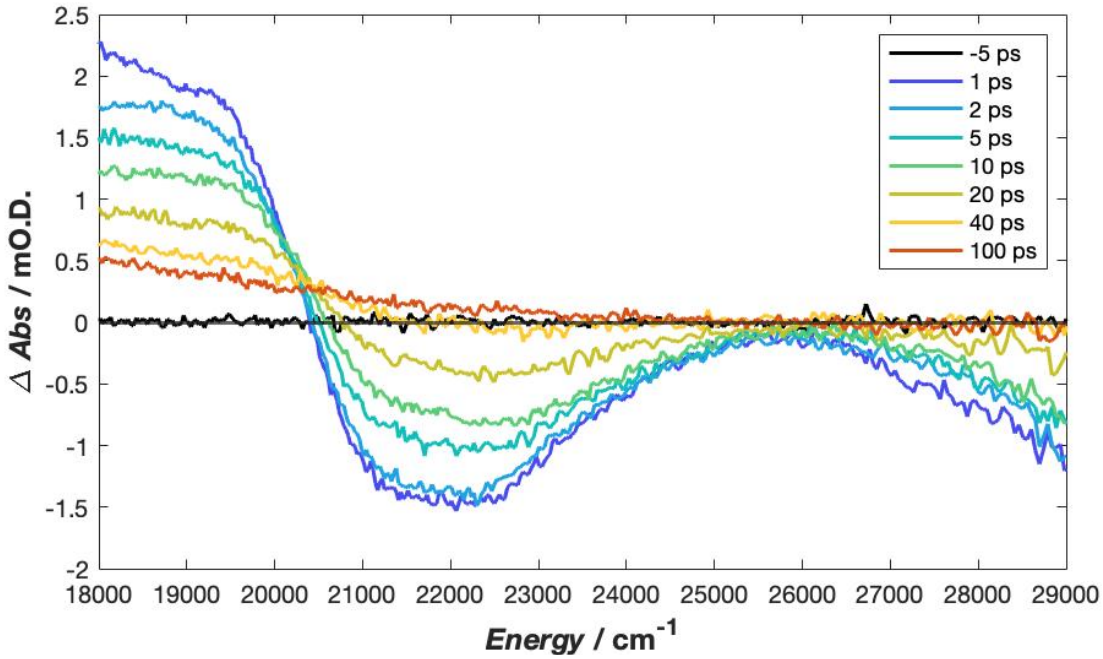

Figure 6.54. Transient absorption spectra of **Fe-bpy-BPh$_3$** after 290 nm / 34,500 cm^{-1} excitation, depicting traces at -5 ps to 100 ps time delay.

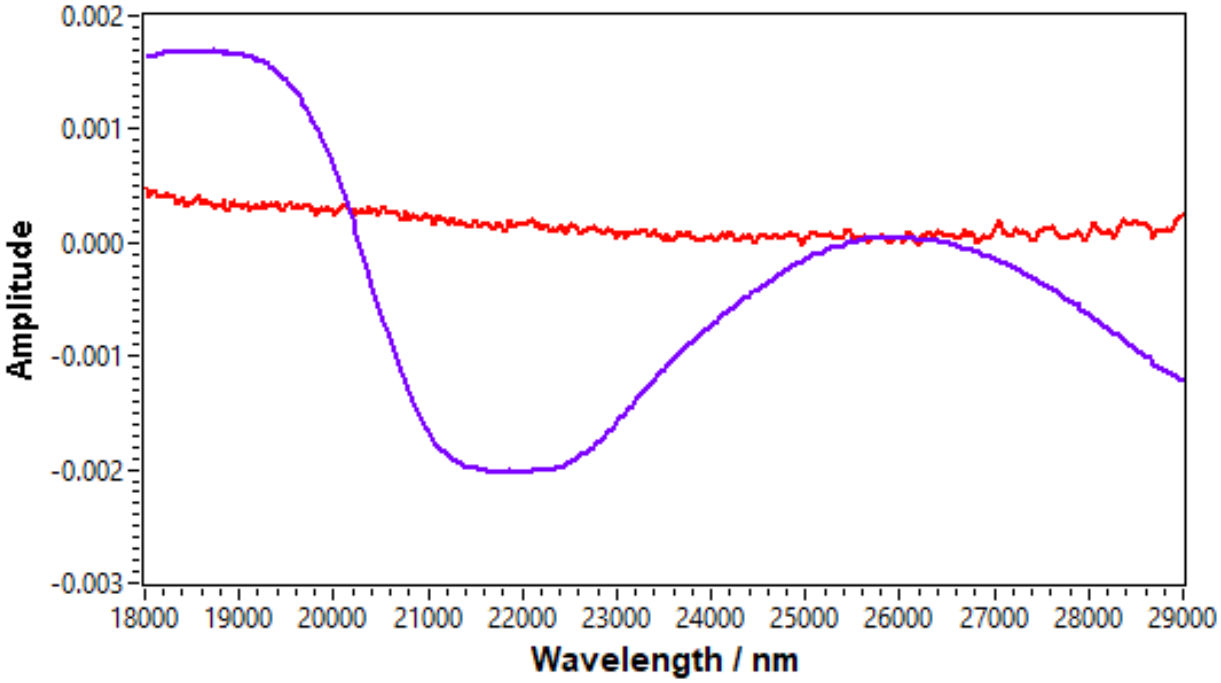

Figure 6.55. Principal components from a global analysis of the transient absorption data for **Fe-bpy-BPh$_3$**. The red trace corresponding to generation of $[(MeCN)_2]^-$ in solution has an infinite lifetime over the experimental time scale. Single exponent decay kinetics of the purple trace are reported.

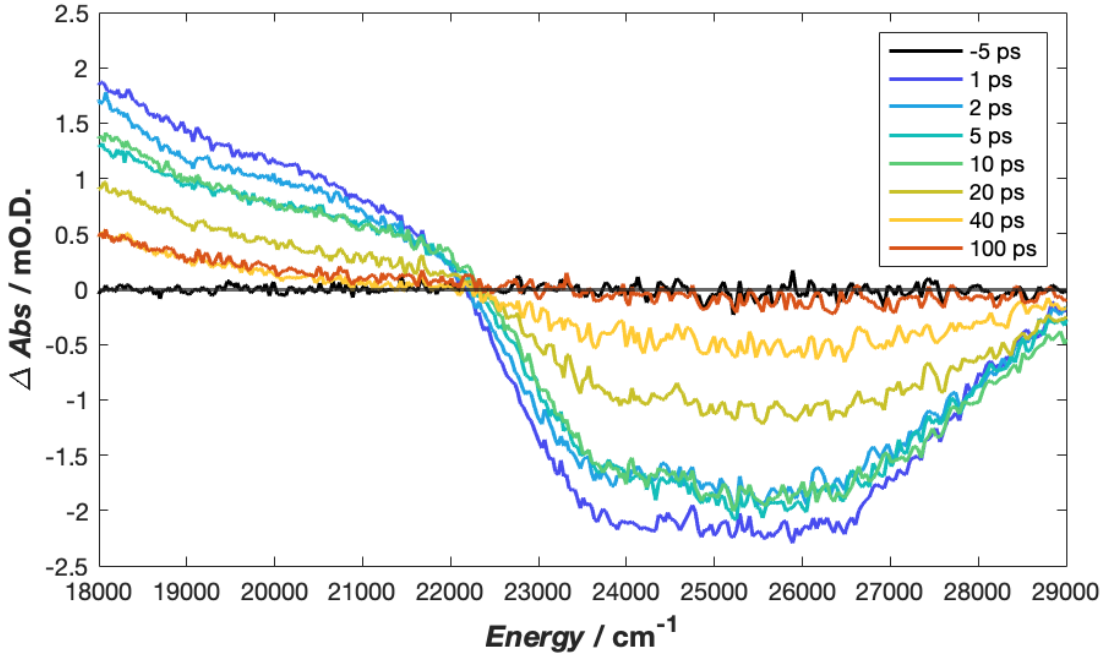

Figure 6.56. Transient absorption spectra of **Fe-phen-BCF** after 290 nm / 34,500 cm^{-1}, depicting traces at -5 ps to 100 ps time delay.

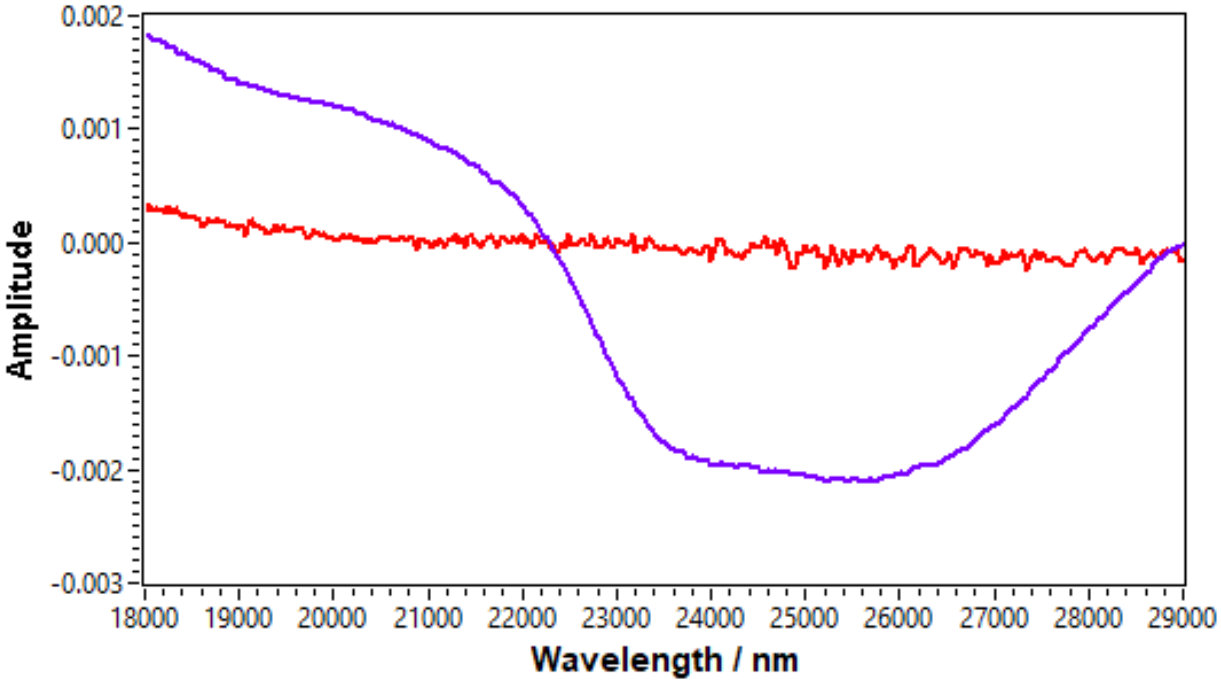

Figure 6.57. Principal components from a global analysis of the transient absorption data for **Fe-phen-BCF**. The red trace corresponding to $[(MeCN)_2]^-$ in solution has an infinite lifetime over the experimental time scale. Single exponent decay kinetics of the purple trace are reported.

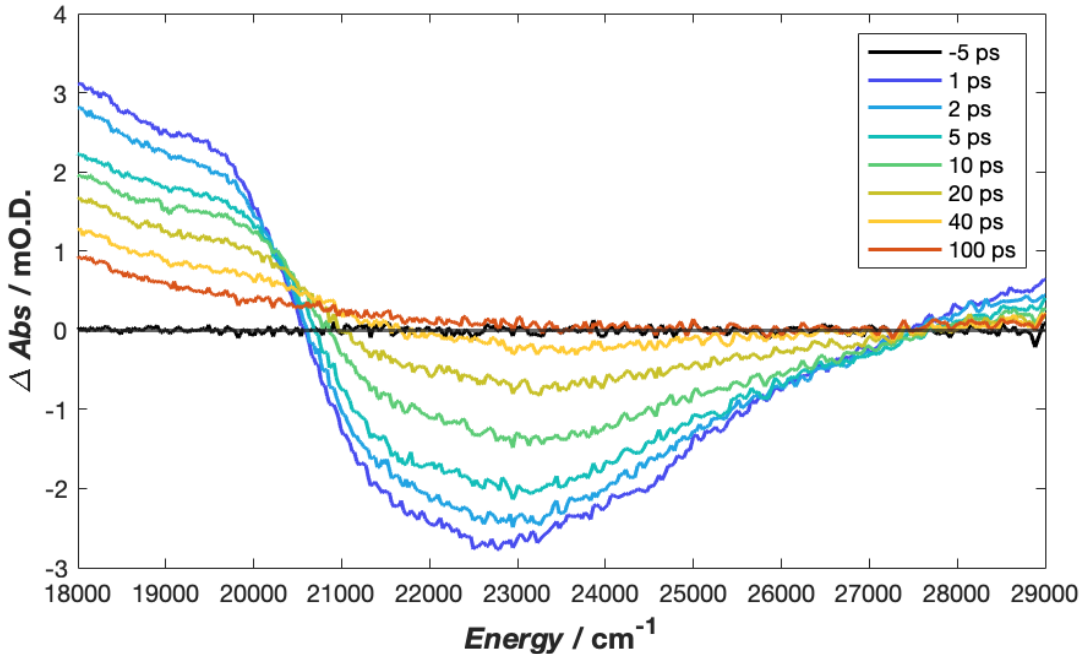

Figure 6.58. Transient absorption spectra of **Fe-phen-BPh$_3$** after 290 nm / 34,500 cm^{-1}, depicting traces at -5 ps to 100 ps time delay.

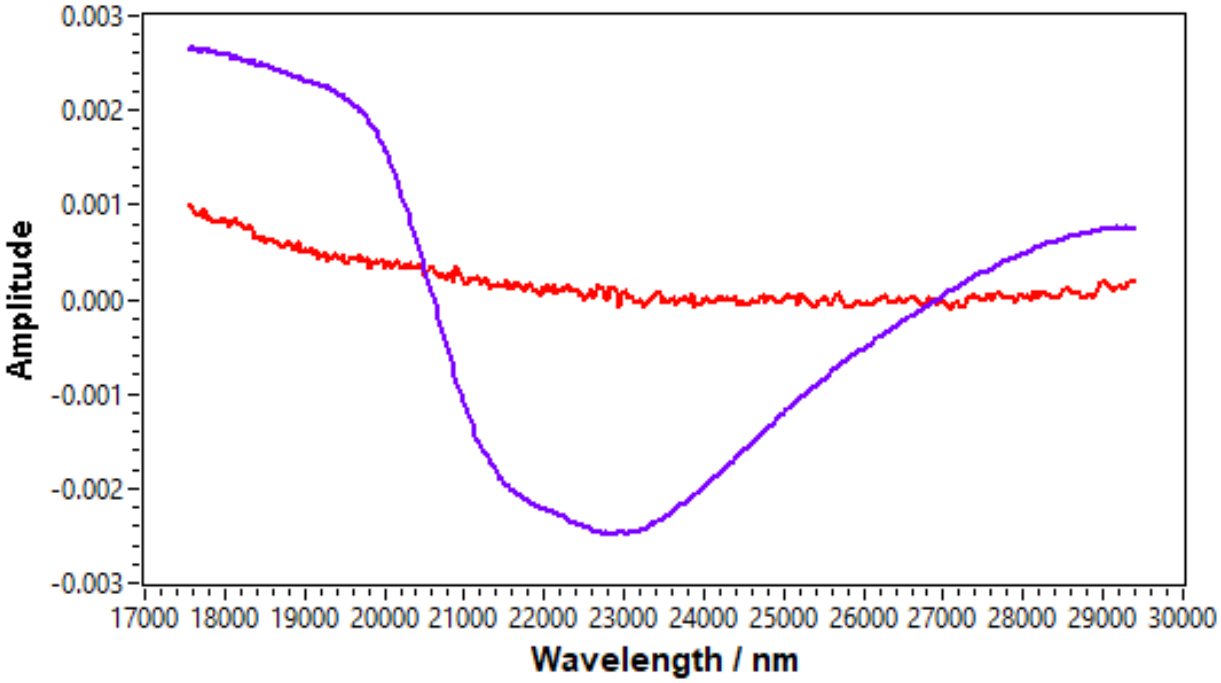

Figure 6.59. Principal components from a global analysis of the transient absorption data for **Fe-phen-BPh$_3$**. The red trace corresponding to $[(MeCN)_2]^-$ in solution has an infinite lifetime over the experimental time scale. Single exponent decay kinetics of the purple trace are reported.

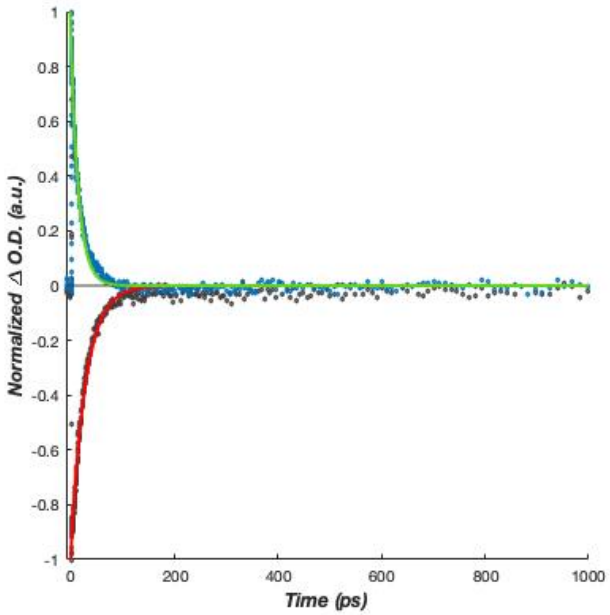

Figure 6.60. Exponential decay fits for the ESA and GSB of **Fe-phen** excited at 290 nm. **ESA**: 588 nm / 17,000 cm^{-1}, **GSB**: 370 nm / 27,000 cm^{-1}.

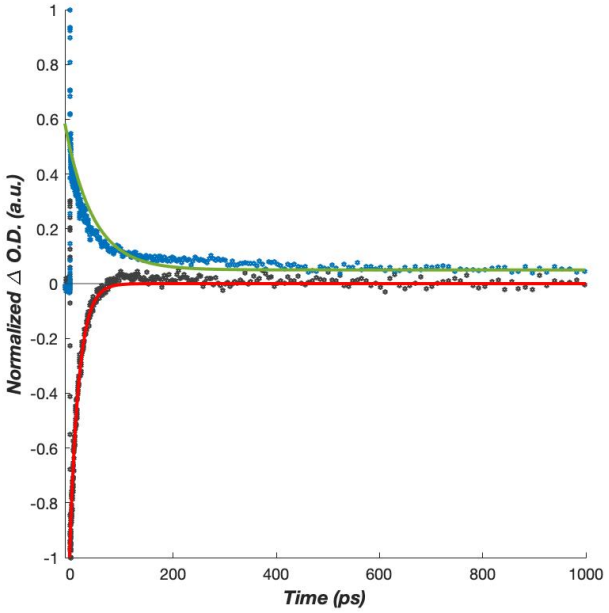

Figure 6.61. Exponential decay fits for the ESA and GSB of **Fe-phen-BPh$_3$** excited at 290 nm. **ESA**: 500 nm / 20,000 cm^{-1}, **GSB**: 435 nm / 23,000 cm^{-1}.

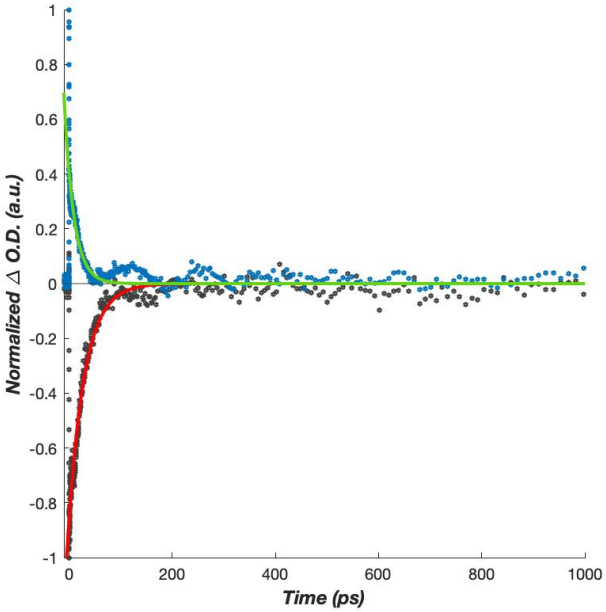

Figure 6.62. Exponential decay fits for the ESA and GSB of **Fe-phen-BCF** excited at 290 nm. **ESA**: 477 nm / 21,000 cm^{-1}, **GSB**: 400 nm / 25,000 cm^{-1}.

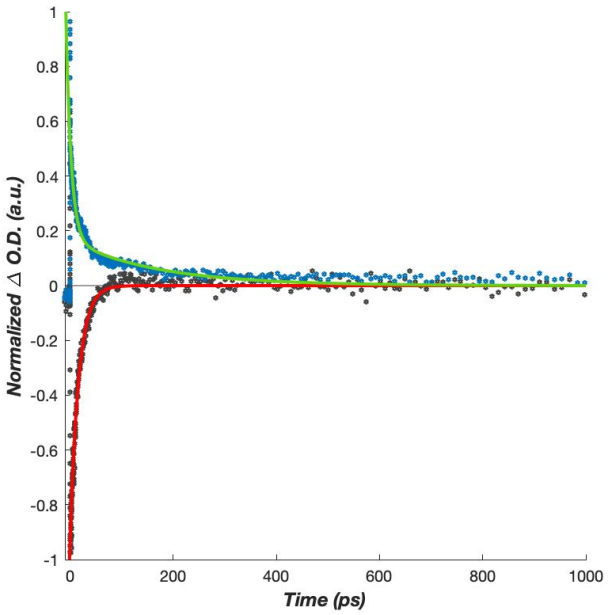

Figure 6.63. Exponential decay fits for the ESA and GSB of **Fe-bpy-BPh$_3$** excited at 290 nm. **ESA**: 515 nm / 19,500 cm^{-1}, **GSB**: 435 nm / 23,000 cm^{-1}.

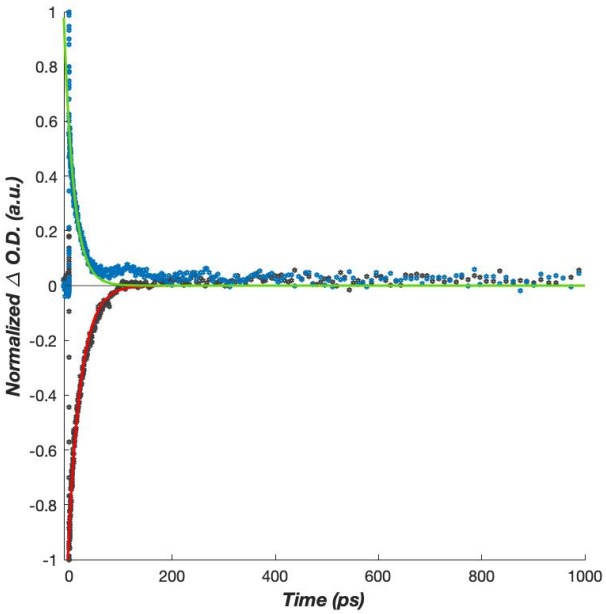

Figure 6.64. Exponential decay fits for the ESA and GSB of **Fe-bpy-BCF** excited at 290 nm. **ESA**: 477 nm / 21,000 cm^{-1}, **GSB**: 417 nm / 24,000 cm^{-1}.

Additional Electrochemistry Data

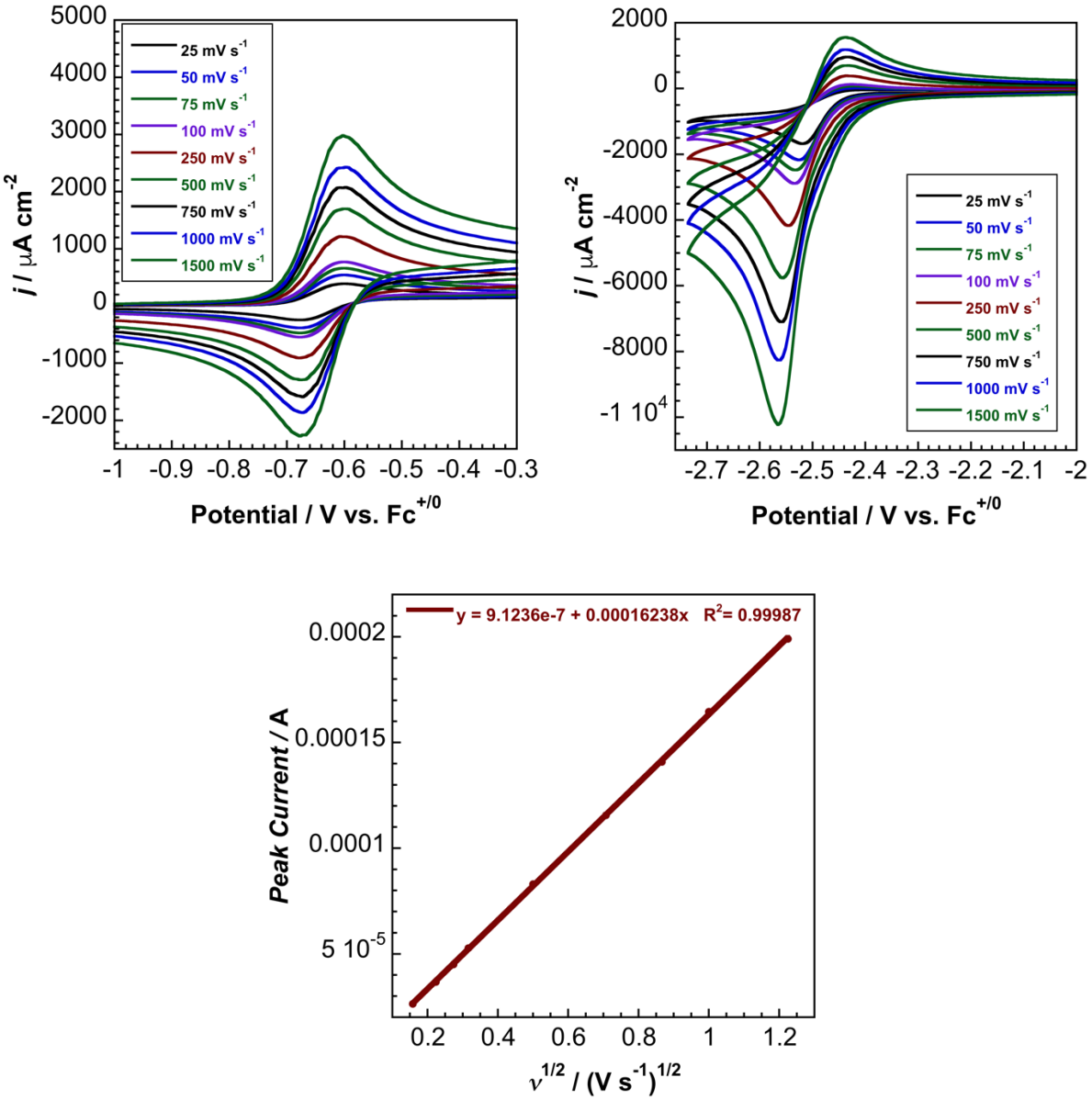

Figure 6.65. Scan rate dependence and oxidation Randles-Sevcik plot for 3.5 mM $(PPN)_2[Fe(bpy)(CN)_4]$ (**Fe-bpy**) in MeCN with 0.2 M $TBAPF_6$ electrolyte.

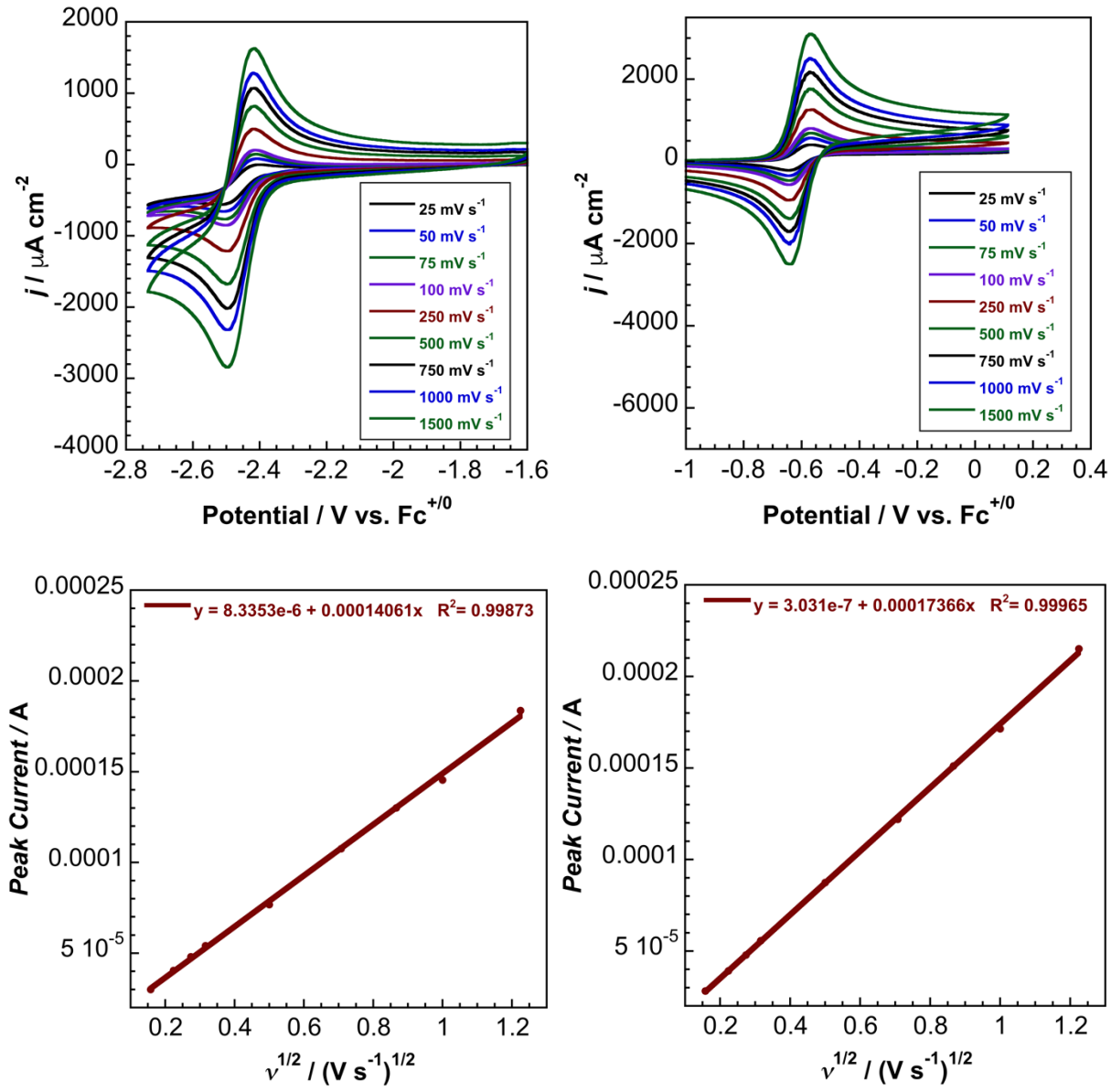

Figure 6.67. Scan rate dependence and Randles-Sevcik plots for 3.1 (reduction)/3.2 (oxidation) mM $(TBA)_2[Fe(phen)(CN)_4]$ (**Fe-phen**) in MeCN with 0.2 M $TBAPF_6$ electrolyte.

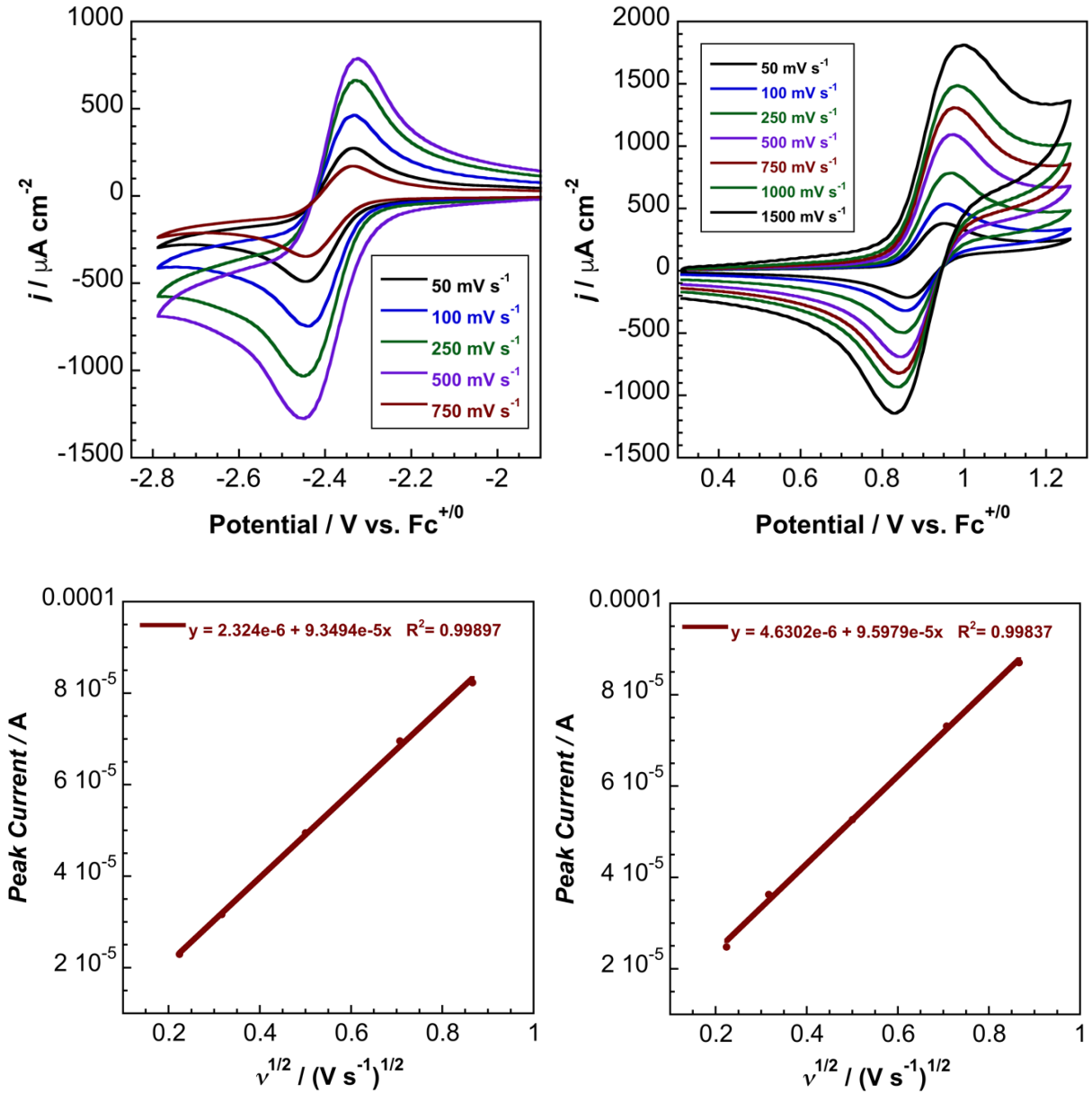

Figure 6.68. Scan rate dependence and Randles-Sevcik plots for 2.9 mM $(TBA)_2[Fe(bpy)(CN\text{-}B(C_6F_5)_3)_4]$ (**Fe-bpy-BCF**) in THF with 0.2 M $TBAPF_6$ electrolyte.

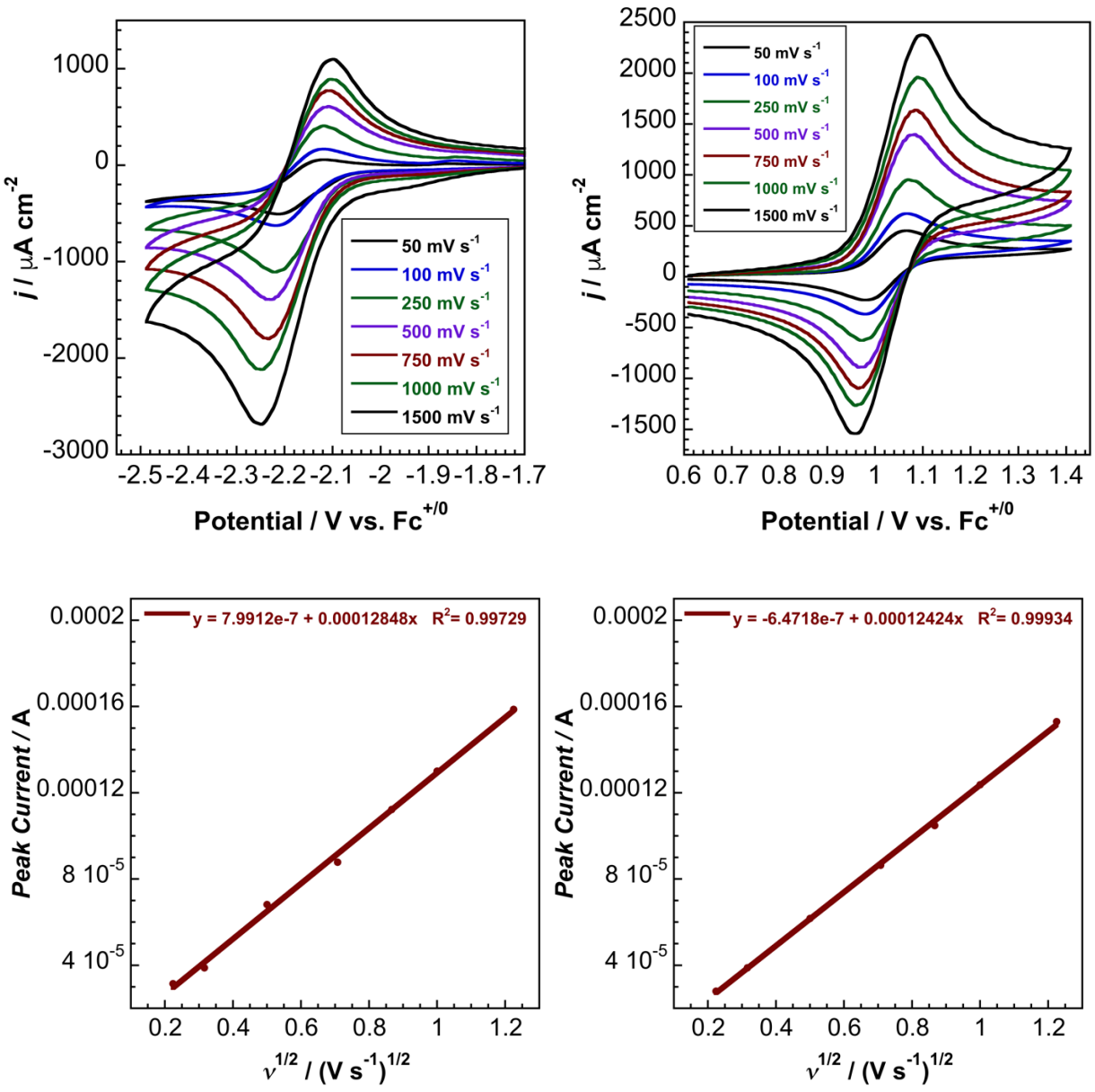

Figure 6.69. Scan rate dependence and Randles-Sevcik plots for 3.0 mM $(TBA)_2[Fe(phen)(CN\text{-}B(C_6F_5)_3)_4]$ (**Fe-phen-BCF**) in MeCN with 0.1 M $TBAPF_6$ electrolyte.

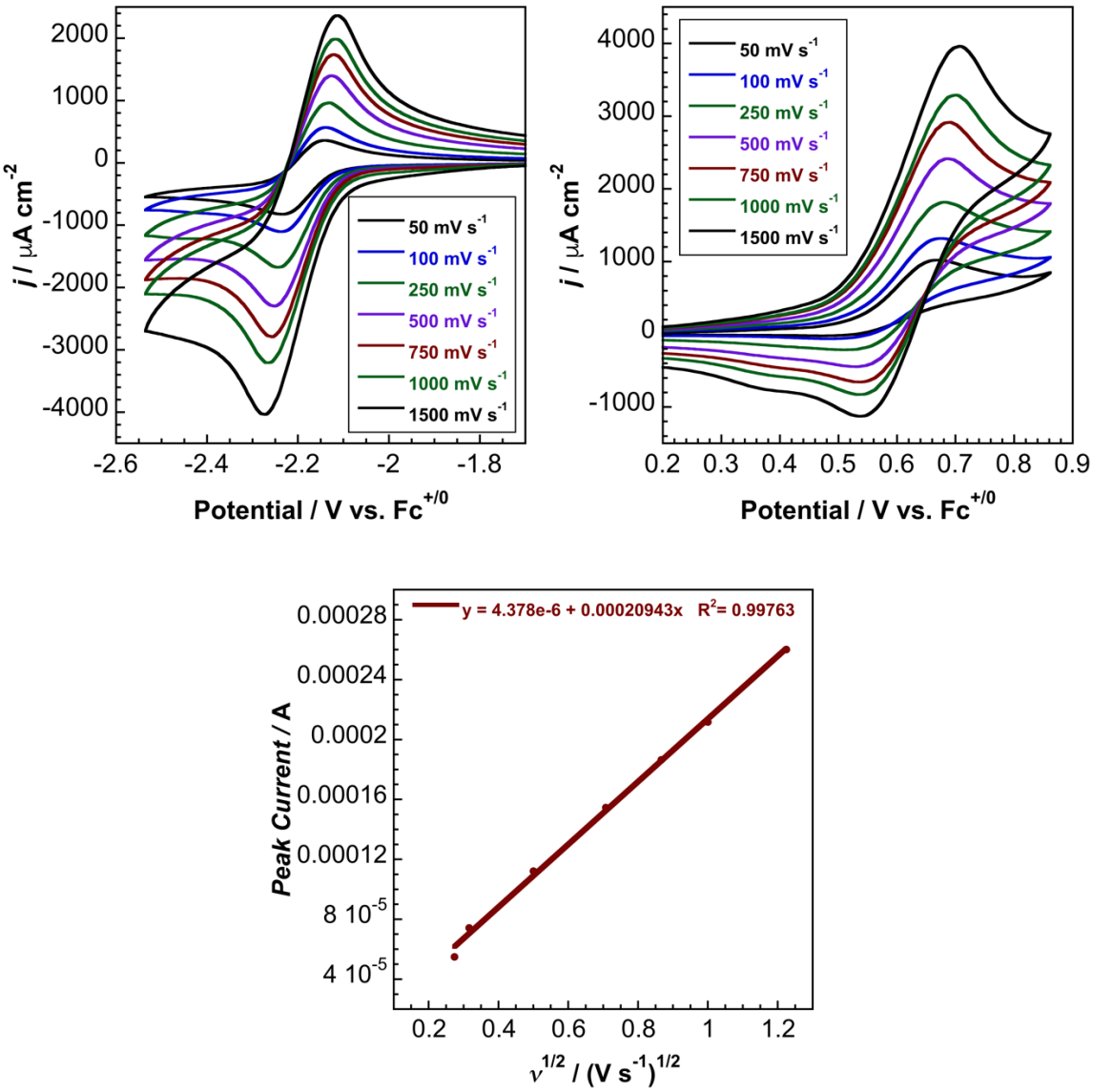

Figure 6.70. Scan rate dependence and reduction Randles-Sevcik plot for 5.0 mM $(TBA)_2[Fe(bpy)(CN\text{-}BPh_3)_4]$ (**Fe-bpy-BPh$_3$**) in MeCN with 0.1 M $TBAPF_6$ electrolyte.

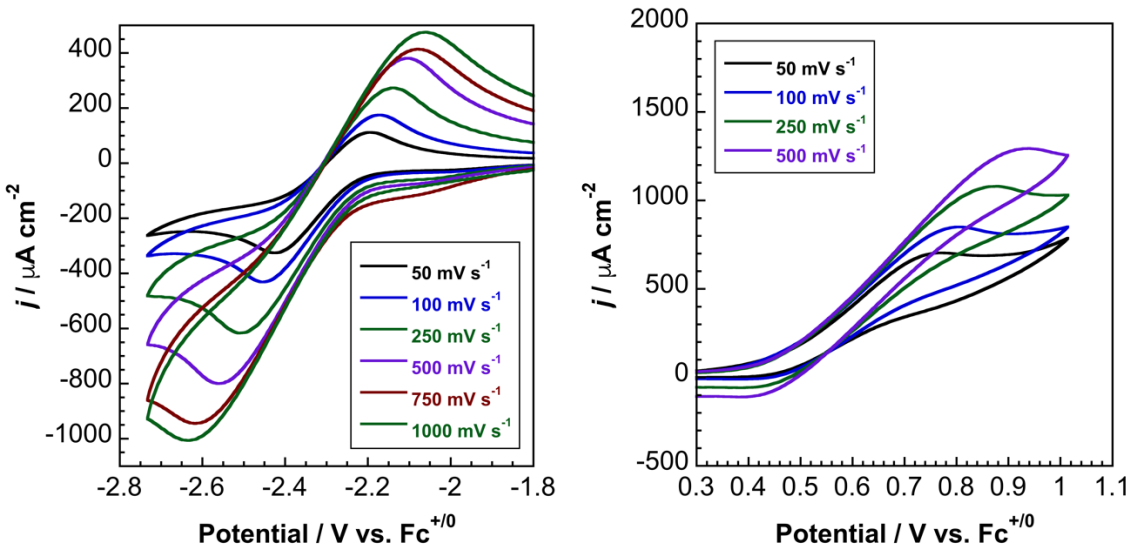

Figure 6.71. Scan rate dependence for 3.9 mM $(TBA)_2[Fe(phen)(CN\text{-}BPh_3)_4]$ (**Fe-phen-BPh$_3$**) in MeCN with 0.1 M $TBAPF_6$ electrolyte.

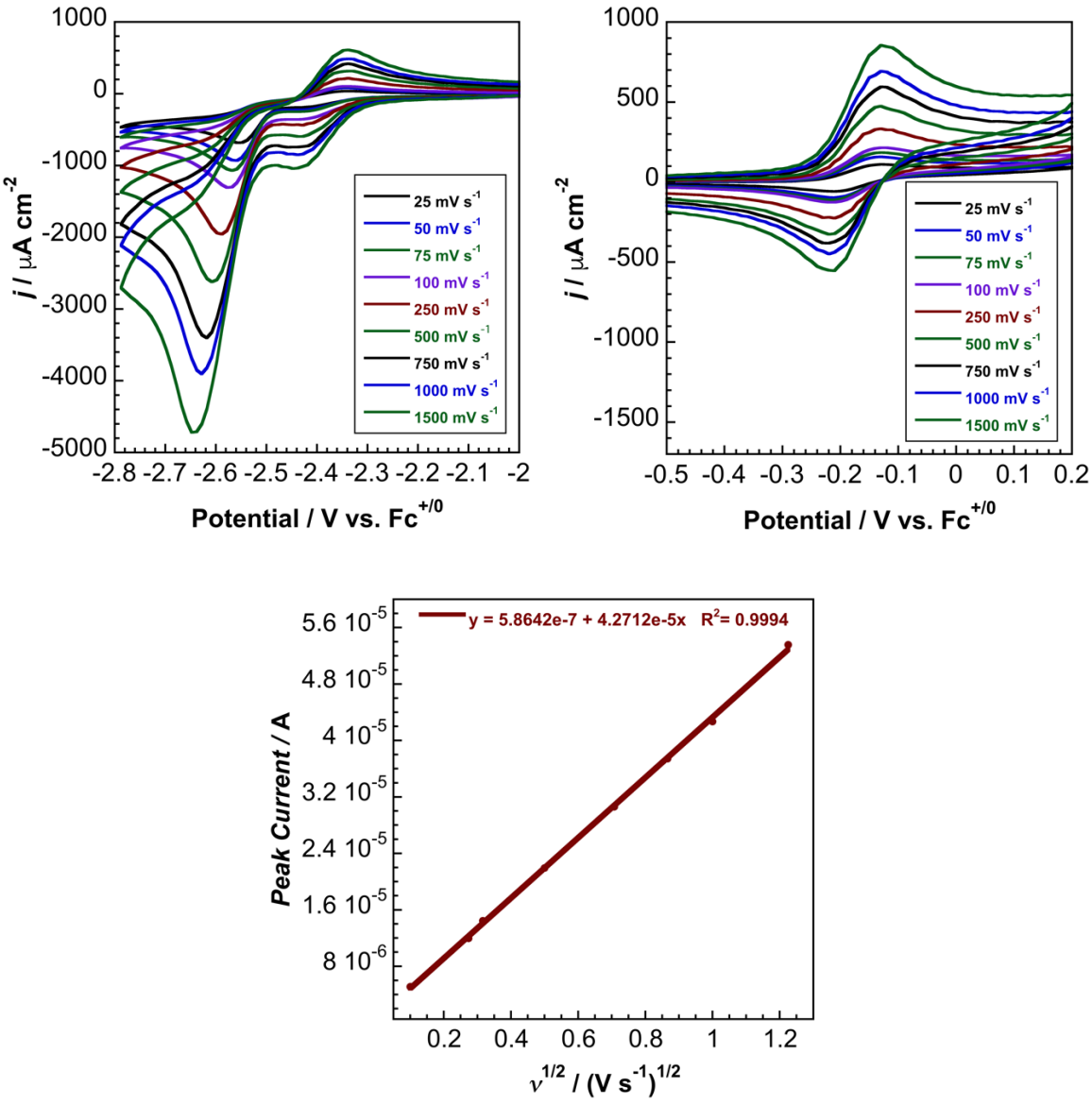

Figure 6.72. Scan rate dependence and oxidation Randles-Sevcik plot for 1.4 mM $(PPN)_2[Ru(bpy)(CN)_4]$ (**Ru-bpy**) in MeCN with 0.1 M $TBAPF_6$ electrolyte.

X-Ray Crystallography

Collection and Refinement Details for $(PPN)_2[Fe(phen)(CN\text{-}BPh_3)_4]$

Low-temperature diffraction data (ϕ- and ω-scans) were collected on a Bruker AXS D8 VENTURE KAPPA diffractometer coupled to a PHOTON II CPAD detector or Cu K_α radiation (λ = 1.54178 Å) from an IμS micro-source for the structure of compound $(PPN)_2[Fe(phen)(CN\text{-}BPh_3)_4]$. The structure was solved by direct methods using SHELXS[57] and refined against F^2 on all data by full-matrix least squares with SHELXL-2017[58] using established refinement techniques.[59] All non-hydrogen atoms were refined anisotropically. All hydrogen atoms were included into the model at geometrically calculated positions and refined using a riding model. The isotropic displacement parameters of all hydrogen atoms were fixed to 1.2 times the U value of the atoms they are linked to (1.5 times for methyl groups). All disordered atoms were refined with the help of similarity restraints on the 1,2- and 1,3-distances.

$(PPN)_2[Fe(phen)(CN\text{-}B(C_6F_5)_3)_4]$ crystallizes in the monoclinic space group $C2c$ with half a molecule in the asymmetric unit along with half a molecule of dichloromethane. The dichloromethane molecule is located near a crystallographic symmetry element and disordered appropriately. One of the chlorine atoms was disordered over two additional positions.

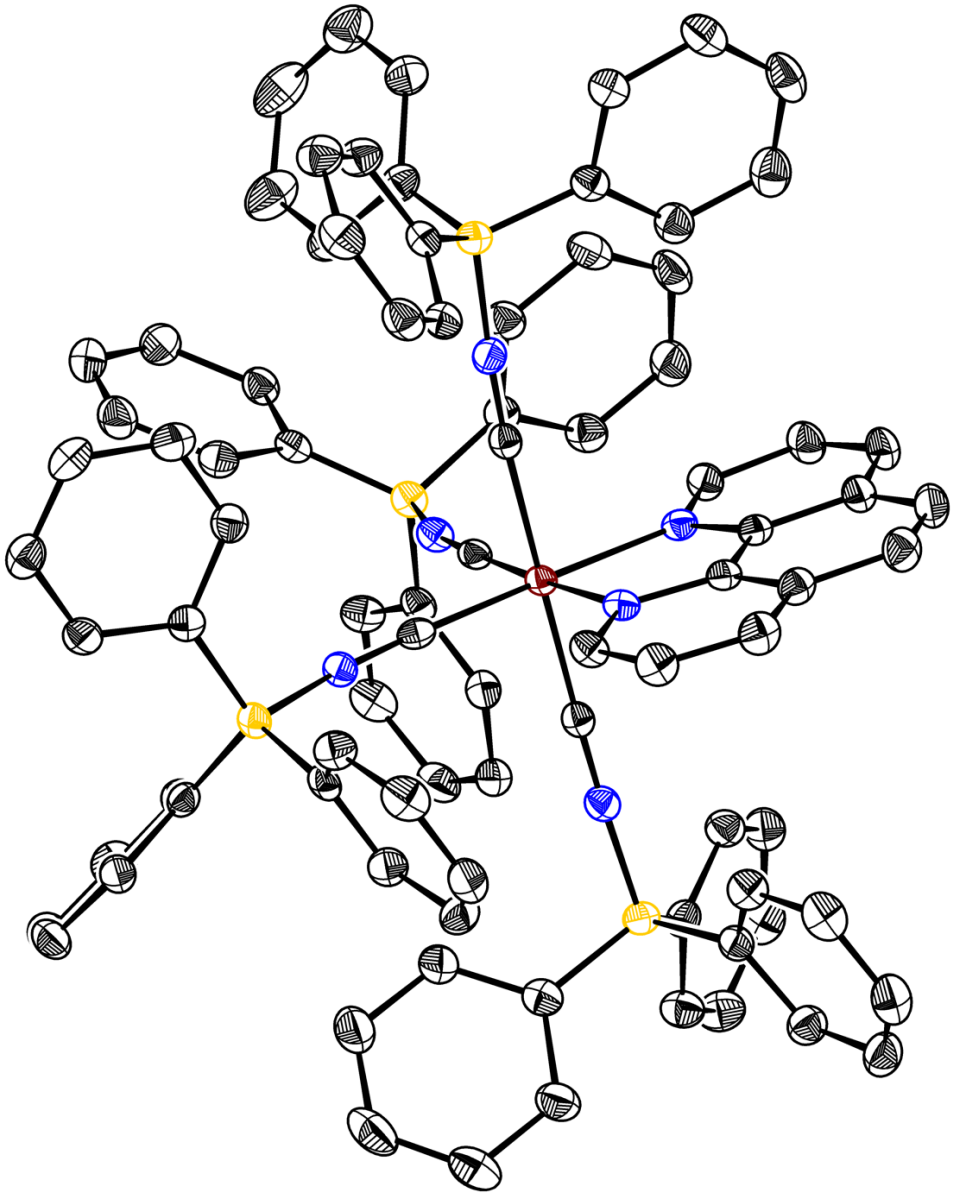

Figure 6.73. Crystal structure of $(PPN)_2[Fe(phen)(CN\text{-}BPh_3)_4]$ (solvent, protons, and cations are omitted for clarity). Thermal ellipsoids set at 50% probability.

Table 6.8. Crystal data and structure refinement for **$(PPN)_2[Fe(phen)(CN\text{-}BPh_3)_4]$**.

Empirical formula	C161 H130 B4 Cl2 Fe N8 P4	
Formula weight	2470.59	
Temperature	100(2) K	
Wavelength	1.54178 Å	
Crystal system	Monoclinic	
Space group	C2/c	
Unit cell dimensions	a = 21.782(2) Å	a= 90°.
	b = 17.4783(19) Å	b= 94.841(7)°.
	c = 35.354(5) Å	g = 90°.
Volume	13412(3) $Å^3$	
Z	4	
Density (calculated)	1.224 Mg/m^3	
Absorption coefficient	2.151 mm^{-1}	
F(000)	5168	
Crystal size	0.300 x 0.200 x 0.050 mm^3	
Theta range for data collection	3.246 to 74.772°.	
Index ranges	$-27 \leq h \leq 26$, $-21 \leq k \leq 21$, $-44 \leq l \leq 43$	
Reflections collected	112475	
Independent reflections	13749 [R(int) = 0.0780]	
Completeness to theta = 67.679°	100.0 %	
Absorption correction	Semi-empirical from equivalents	
Max. and min. transmission	1.0000 and 0.7510	
Refinement method	Full-matrix least-squares on F^2	
Data / restraints / parameters	13749 / 1 / 836	
Goodness-of-fit on F^2	1.021	
Final R indices [I>2sigma(I)]	R1 = 0.0558, wR2 = 0.1393	
R indices (all data)	R1 = 0.0695, wR2 = 0.1502	
Extinction coefficient	n/a	
Largest diff. peak and hole	1.411 and -0.708 $e.Å^{-3}$	

Collection and Refinement Details for $(PPN)_2[Ru(flpy)(CN\text{-}B(C_6F_5)_3)_4]$

Low-temperature diffraction data (ϕ- and ω-scans) were collected on a Bruker AXS KAPPA APEX II diffractometer coupled to an PHOTON 100 CMOS detector with graphite monochromated Mo K_α radiation (λ = 0.71073 Å) for the structure of compound $(PPN)_2[Ru(flpy)(CN\text{-}B(C_6F_5)_3)_4]$. The structure was solved by direct methods using SHELXS[57] and refined against F^2 on all data by full-matrix least squares with SHELXL-2017[58] using established refinement techniques.[59] All non-hydrogen atoms were refined anisotropically. All hydrogen atoms were included into the model at geometrically calculated positions and refined using a riding model. The isotropic displacement parameters of all hydrogen atoms were fixed to 1.2 times the U value of the atoms they are linked to (1.5 times for methyl groups). All disordered atoms were refined with the help of similarity restraints on the 1,2- and 1,3-distances and displacement parameters as well as enhanced rigid bond restraints for anisotropic displacement parameters.

$(PPN)_2[Ru(flpy)(CN\text{-}B(C_6F_5)_3)_4]$ crystallizes in the triclinic space group P-1 with one molecule in the asymmetric unit along with half a molecule of ethanol. One phenyl and two pentafluorophenyl groups were disordered over two positions. All disordered aromatic rings were restrained to be flat. The ethanol is located near a crystallographic inversion center and disordered over six positions, three of which are pairwise related to the other three by the inversion center. The O-C and C-C distances in the disordered ethanol were restrained to be 1.43(2) Å and 1.54(2) Å respectively.

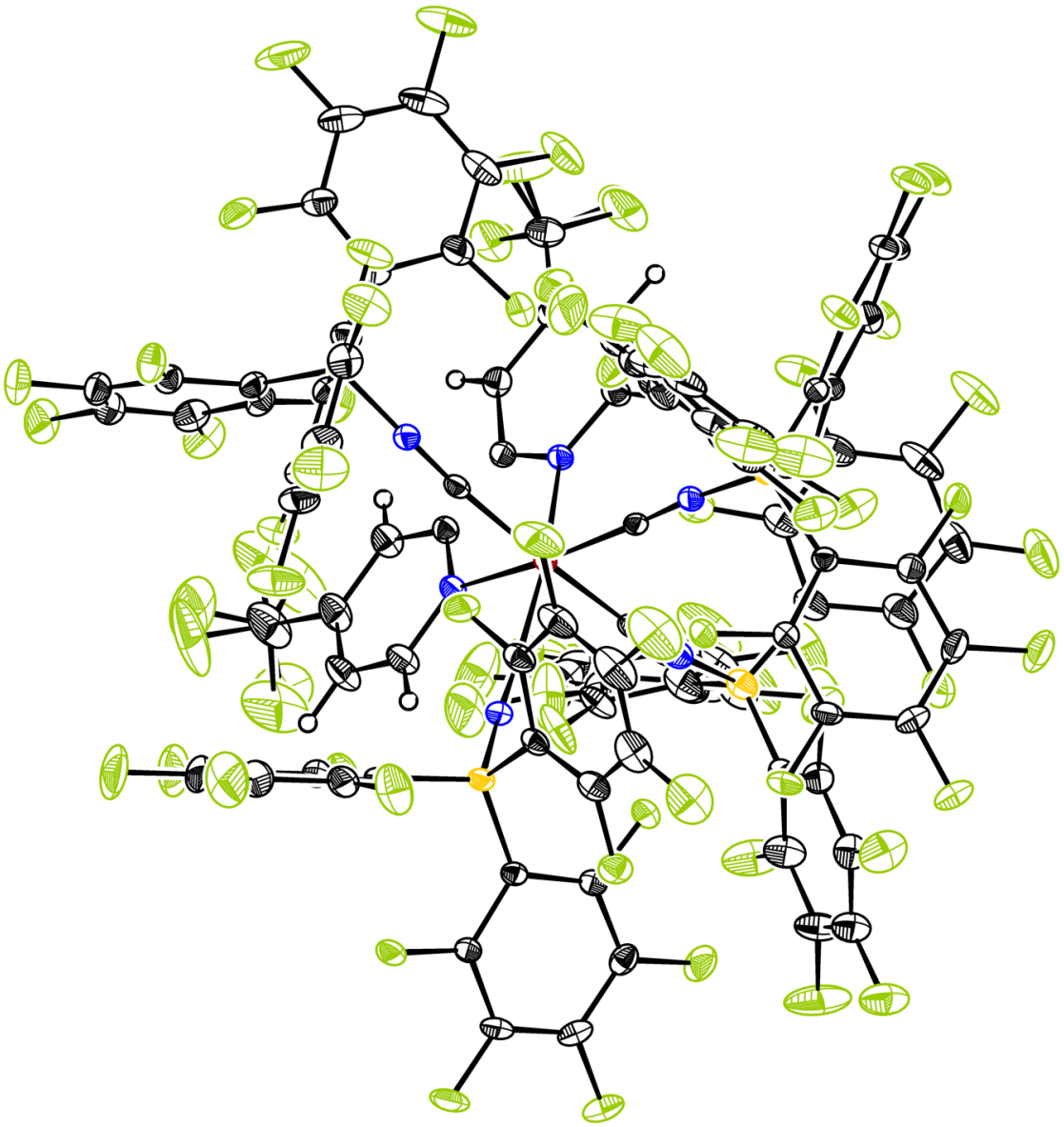

Figure 6.74. Crystal structure of **$(PPN)_2$[Ru(flpy)(CN-$B(C_6F_5)_3)_4$]** (solvent and cations are omitted for clarity). Thermal ellipsoids set at 50% probability.

Table 6.9. Crystal data and structure refinement for **$(PPN)_2[Ru(flpy)(CN\text{-}B(C_6F_5)_3)_4]$**.

Empirical formula	C161 H69 B4 F66 N8 O0.50 P4 Ru	
Formula weight	3645.43	
Temperature	100(2) K	
Wavelength	0.71073 Å	
Crystal system	Triclinic	
Space group	P-1	
Unit cell dimensions	a = 16.024(6) Å	a= 73.248(14)°.
	b = 21.220(6) Å	b= 76.541(18)°.
	c = 23.585(10) Å	g = 79.114(12)°.
Volume	7404(5) $Å^3$	
Z	2	
Density (calculated)	1.635 Mg/m^3	
Absorption coefficient	0.291 mm^{-1}	
F(000)	3626	
Crystal size	0.300 x 0.250 x 0.150 mm^3	
Theta range for data collection	1.523 to 30.508°.	
Index ranges	$-22 \leq h \leq 22$, $-29 \leq k \leq 30$, $-33 \leq l \leq 33$	
Reflections collected	246908	
Independent reflections	44916 [R(int) = 0.0493]	
Completeness to theta = 25.242°	99.9 %	
Absorption correction	Semi-empirical from equivalents	
Max. and min. transmission	1.0000 and 0.9509	
Refinement method	Full-matrix least-squares on F^2	
Data / restraints / parameters	44916 / 2373 / 2588	
Goodness-of-fit on F^2	1.011	
Final R indices [I>2sigma(I)]	R1 = 0.0395, wR2 = 0.0858	
R indices (all data)	R1 = 0.0588, wR2 = 0.0936	
Extinction coefficient	n/a	
Largest diff. peak and hole		
0.577 and -0.980 $e.Å^{-3}$		

Collection and Refinement Details for $(PPN)_2[Ru(flpy)(CN)_4]$

A crystal was mounted on a polyimide MiTeGen loop with STP Oil Treatment and placed under a nitrogen stream. Low temperature (100K) X-ray data were collected with a Bruker AXS D8 VENTURE KAPPA diffractometer running at 50 kV and 1mA (Cu K_α = 1.54178 Å; PHOTON II CPAD detector and Helios focusing multilayer mirror optics). All diffractometer manipulations, including data collection, integration, and scaling, were carried out using the Bruker APEX3 software. An absorption correction was applied using SADABS. The space group was determined, and the structure was solved by intrinsic phasing using XT. Refinement was full-matrix least squares on F^2 using XL. All non-hydrogen atoms were refined using anisotropic displacement parameters. Hydrogen atoms were placed in idealized positions and the coordinates refined. The isotropic displacement parameters of all hydrogen atoms were fixed at 1.2 times the U_{eq} value of the bonded atom.

$(PPN)_2[Ru(flpy)(CN)_4]$ crystallizes in the triclinic space group P-1 (# 2) with one ruthenium anion, two PPN cations, and 2.2 CH_2Cl_2 in the asymmetric unit.

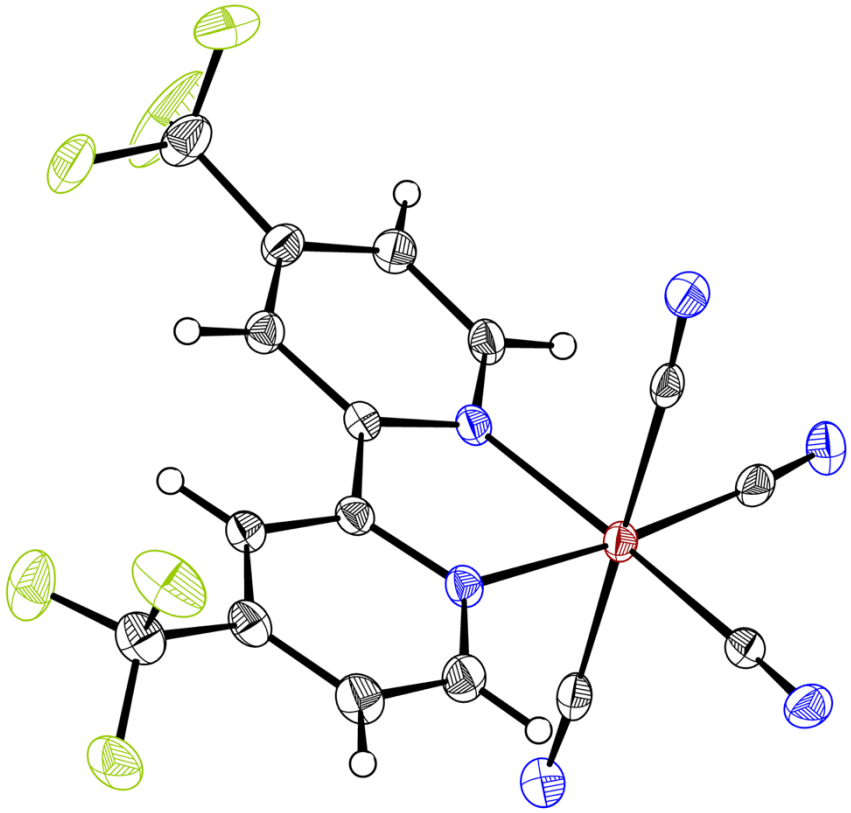

Figure 6.75. Crystal structure of **$(PPN)_2[Ru(flpy)(CN)_4]$** (solvent and cations are omitted for clarity). Thermal ellipsoids set at 50% probability.

Table 6.10. Crystal data and structure refinement for **$(PPN)_2[Ru(flpy)(CN)_4]$**.

Empirical formula	C90.22 H70.45 Cl4.45 F6 N8 P4 Ru	
Formula weight	1763.39	
Temperature	100 K	
Wavelength	1.54178 Å	
Crystal system	Triclinic	
Space group	P-1 (# 2)	
Unit cell dimensions	a = 14.4673(16) Å	a= 104.706(6)°
	b = 14.6282(16) Å	b= 101.091(7)°
	c = 21.314(2) Å	g = 105.094(6)°
Volume	4047.9(8) $Å^3$	
Z	2	
Density (calculated)	1.447 g/cm^3	
Absorption coefficient	4.215 mm^{-1}	
F(000)	1803	
Crystal size	0.07 x 0.23 x 0.26 mm^3	
Theta range for data collection	3.29 to 79.44°	
Index ranges	$-18 \leq h \leq 18, -18 \leq k \leq 18, -27 \leq l \leq 25$	
Reflections collected	196088	
Independent reflections	16799 [R(int) = 0.0435]	
Completeness to theta = 67.679°	99.6 %	
Absorption correction	Semi-empirical from equivalents	
Max. and min. transmission	1.0000 and 0.6999	
Refinement method	Full-matrix least-squares on F^2	
Data / restraints / parameters	16799 / 3 / 1075	
Goodness-of-fit on F^2	1.082	
Final R indices [I>2sigma(I)]	R1 = 0.0339, wR2 = 0.0783	
R indices (all data)	R1 = 0.0373, wR2 = 0.0816	
Extinction coefficient	n/a	
Largest diff. peak and hole	0.74 and -0.94 $e.Å^{-3}$	

Collection and Refinement Details for (TBA)(Ph_4As)[Fe(phen)(CN-B(C_6F_5)$_3$)$_4$]

A crystal was mounted on a polyimide MiTeGen loop with STP Oil Treatment and placed under a nitrogen stream. Low temperature (100K) X-ray data were collected with a Bruker AXS D8 VENTURE KAPPA diffractometer running at 50 kV and 1mA (Cu K_α = 1.54178 Å; PHOTON II CPAD detector and Helios focusing multilayer mirror optics). All diffractometer manipulations, including data collection, integration, and scaling, were carried out using the Bruker APEX3 software. An absorption correction was applied using SADABS. The space group was determined and the structure solved by intrinsic phasing using XT. Refinement was full-matrix least squares on F^2 using XL. All non-hydrogen atoms were refined using anisotropic displacement parameters. Hydrogen atoms were placed in idealized positions and the coordinates refined. The isotropic displacement parameters of all hydrogen atoms were fixed at 1.2 times the U_{eq} value of the bonded atom.

(TBA)(Ph_4As)[Fe(phen)(CN-B(C_6F_5)$_3$)$_4$] crystallizes in the triclinic space group P-1 (# 2) with one Fe anion, one Ph_4As cation, and one TBA cation in the asymmetric unit.

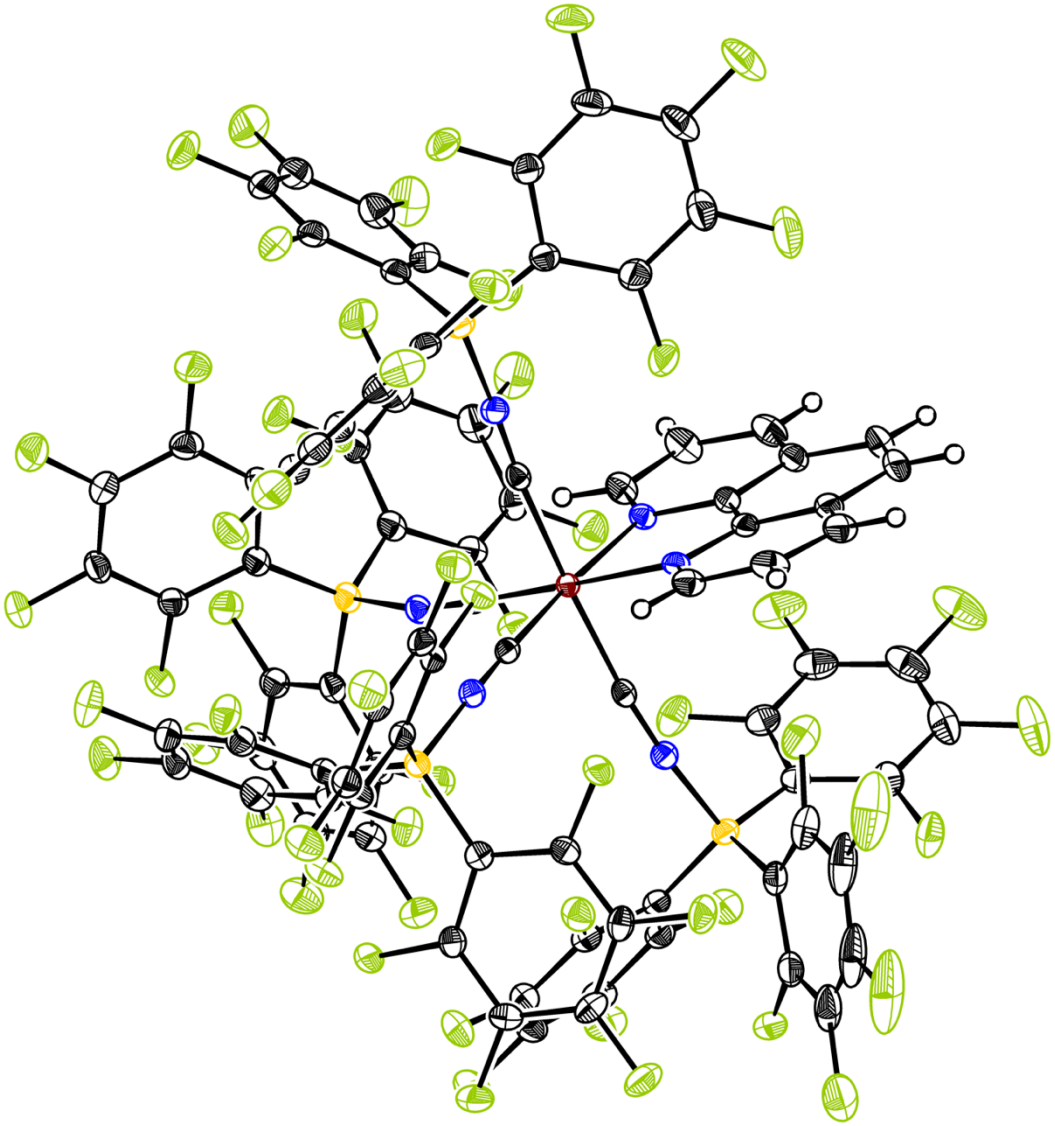

Figure 6.76. Crystal structure of (TBA)(Ph_4As)[Fe(phen)(CN-$B(C_6F_5)_3)_4$]. Thermal ellipsoids set at 50% probability. Solvent and cations are omitted for clarity.

Table 6.11. Crystal data and structure refinement for **(TBA)(Ph$_4$As)[Fe(phen)(CN-B(C$_6$F$_5$)$_3$)$_4$]**.

Empirical formula	C128 H64 As B4 F60 Fe N7	
Formula weight	3013.87	
Temperature	100 K	
Wavelength	1.54178 Å	
Crystal system	Triclinic	
Space group	P-1 (# 2)	
Unit cell dimensions	a = 14.1069(12) Å	a= 95.150(6)°
	b = 15.1484(12) Å	b= 92.682(7)°
	c = 31.623(3) Å	g = 117.453(4)°
Volume	5942.8(9) Å^3	
Z	2	
Density (calculated)	1.684 g/cm^3	
Absorption coefficient	2.696 mm^{-1}	
F(000)	3000	
Crystal size	0.05 x 0.13 x 0.22 mm^3	
Theta range for data collection	2.82 to 80.01°	
Index ranges	-17 ≤ h ≤ 17, -18 ≤ k ≤ 19, -40 ≤ l ≤ 40	
Reflections collected	179819	
Independent reflections	24417 [R(int) = 0.0419]	
Completeness to theta = 67.679°	98.3 %	
Absorption correction	Semi-empirical from equivalents	
Max. and min. transmission	1.0000 and 0.7915	
Refinement method	Full-matrix least-squares on F^2	
Data / restraints / parameters	24417 / 0 / 1814	
Goodness-of-fit on F^2	1.072	
Final R indices [I>2sigma(I)]	R1 = 0.0338, wR2 = 0.0763	
R indices (all data)	R1 = 0.0367, wR2 = 0.0776	
Extinction coefficient	n/a	
Largest diff. peak and hole.	0.46 and -0.50 e.Å^{-3}	

Theoretical Calculations

Below are sample input files for structural optimizations and CASSCF+NEVPT2 calculations. **Figures 6.X-6.X** depict the active space orbitals for CASSCF+NEVPT2 calculations.

Structural Optimization for Ru-bpy-BH_3

```
! PBE0 def2-TZVP Opt TightSCF LargePrint printbasis
!Grid4 FinalGrid6
!CPCM(Acetonitrile)

%basis
NewGTO Ru "def2-QZVPP" end
end

%pal
   nprocs 16
end

%scf
maxiter 2000
end

%maxcore 12000

* xyzfile -2 1 Ru_bpy_XRay.xyz
```

CASSCF-NEVPT2 Calculation for Ru-bpy-BH_3

```
! RI DKH DKH-def2-tzvp SARC/J RIJK AutoAux CONV NEVPT2 CPCM(Acetonitrile) MOREAD
LargePrint
! NoFrozenCore

%basis
NewGTO Ru "old-DKH-TZVP" end
end

%moinp "Ru_bpy_BH3_CASSCF5_12.gbw"

%rel method DKH picturechange 2 end

%casscf
trafostep ri
nel 12
norb 13
MaxIter 200
Mult 5,3,1
NRoots 1,9,10 end

%pal
nprocs 6
end

* xyzfile -2 1 Ru_bpy_BH3_Aligned.xyz
```

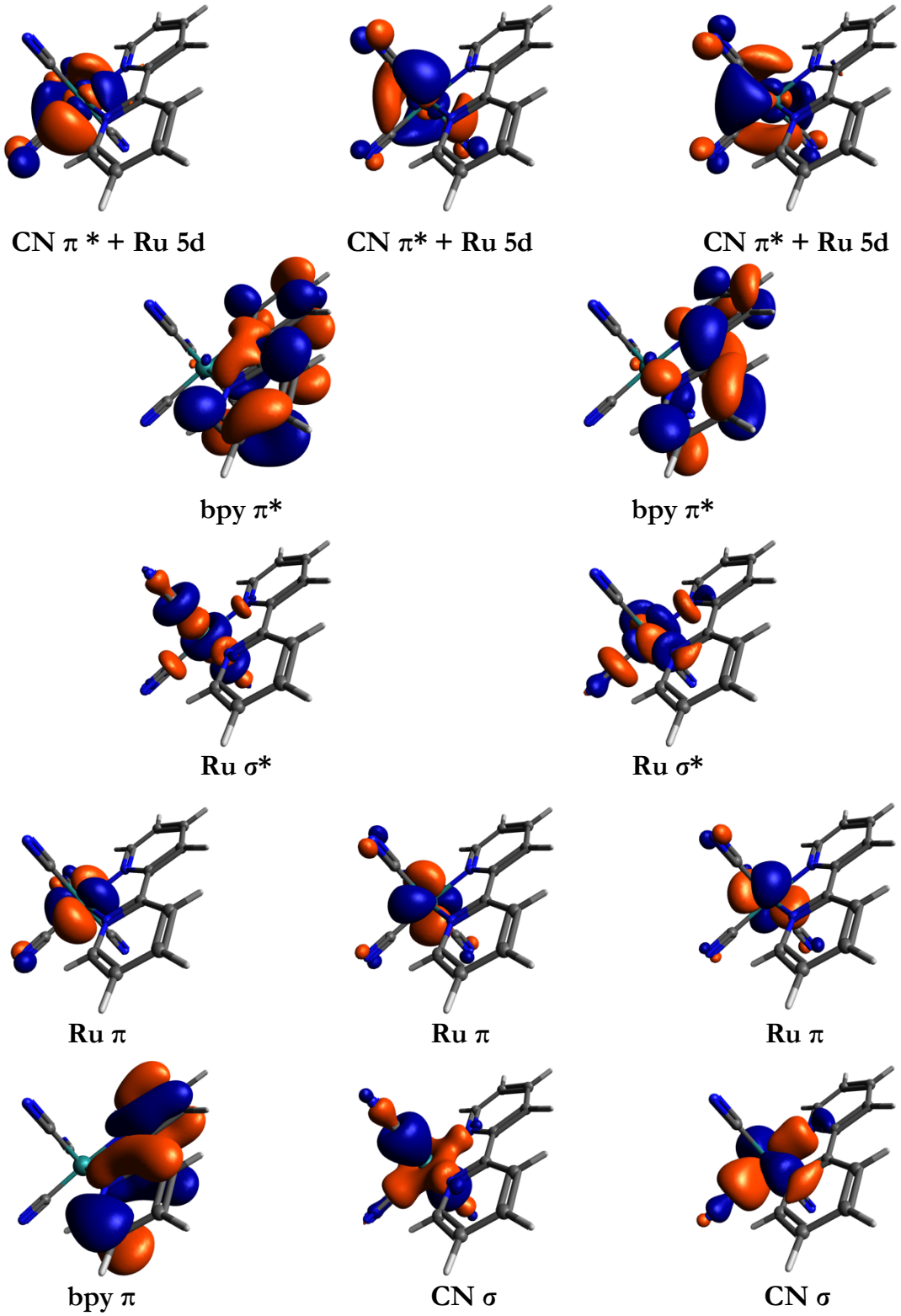

Figure 6.77. Active space molecular orbitals for the state-averaged CAS(12,13) of $[Ru(bpy)(CN)_4]^{2-}$. Isosurface values set to 0.04.

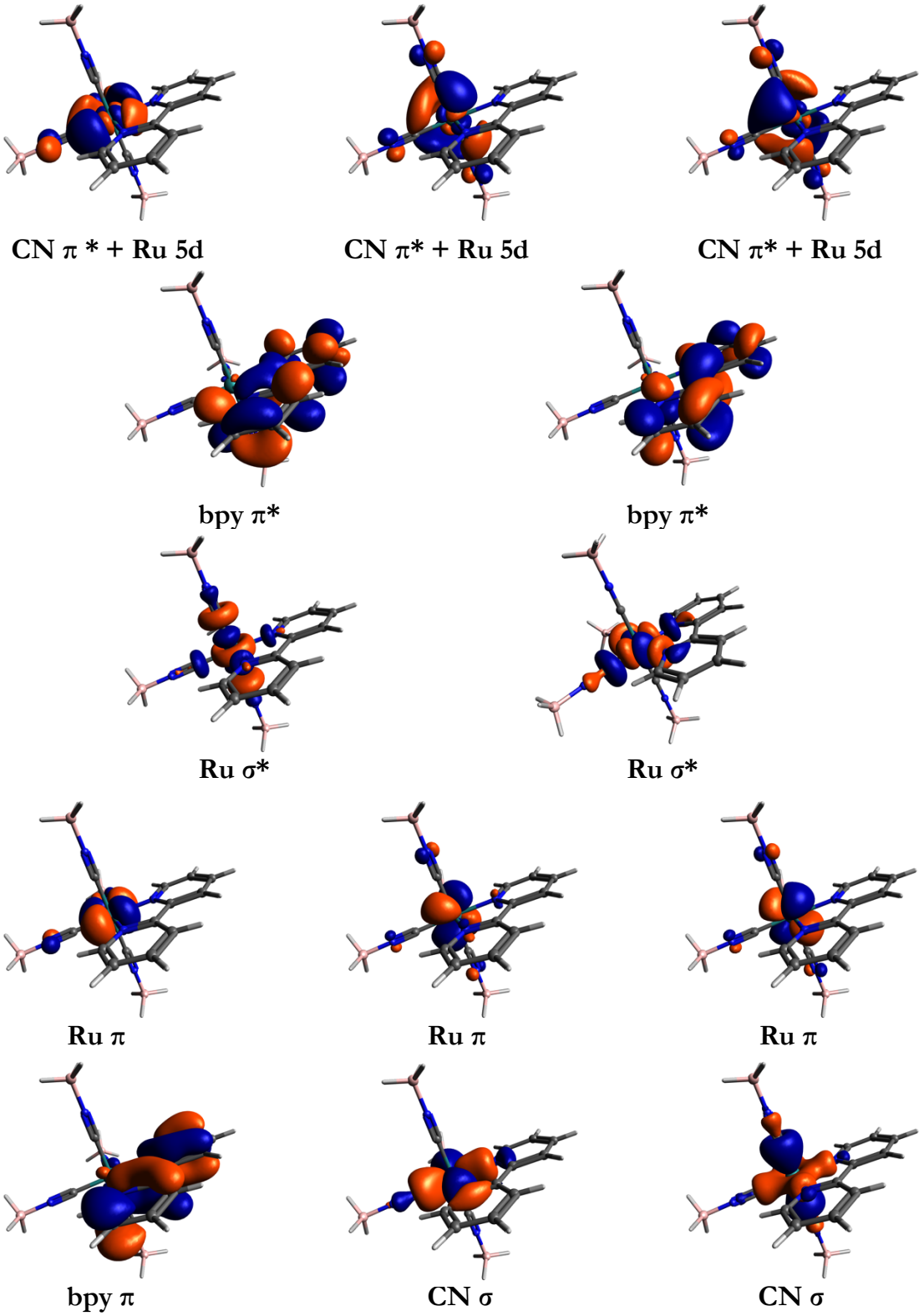

Figure 6.78. Active space molecular orbitals for the state-averaged CAS(12,13) of $[Ru(bpy)(CN\text{-}BH_3)_4]^{2-}$. Isosurface values set to 0.04

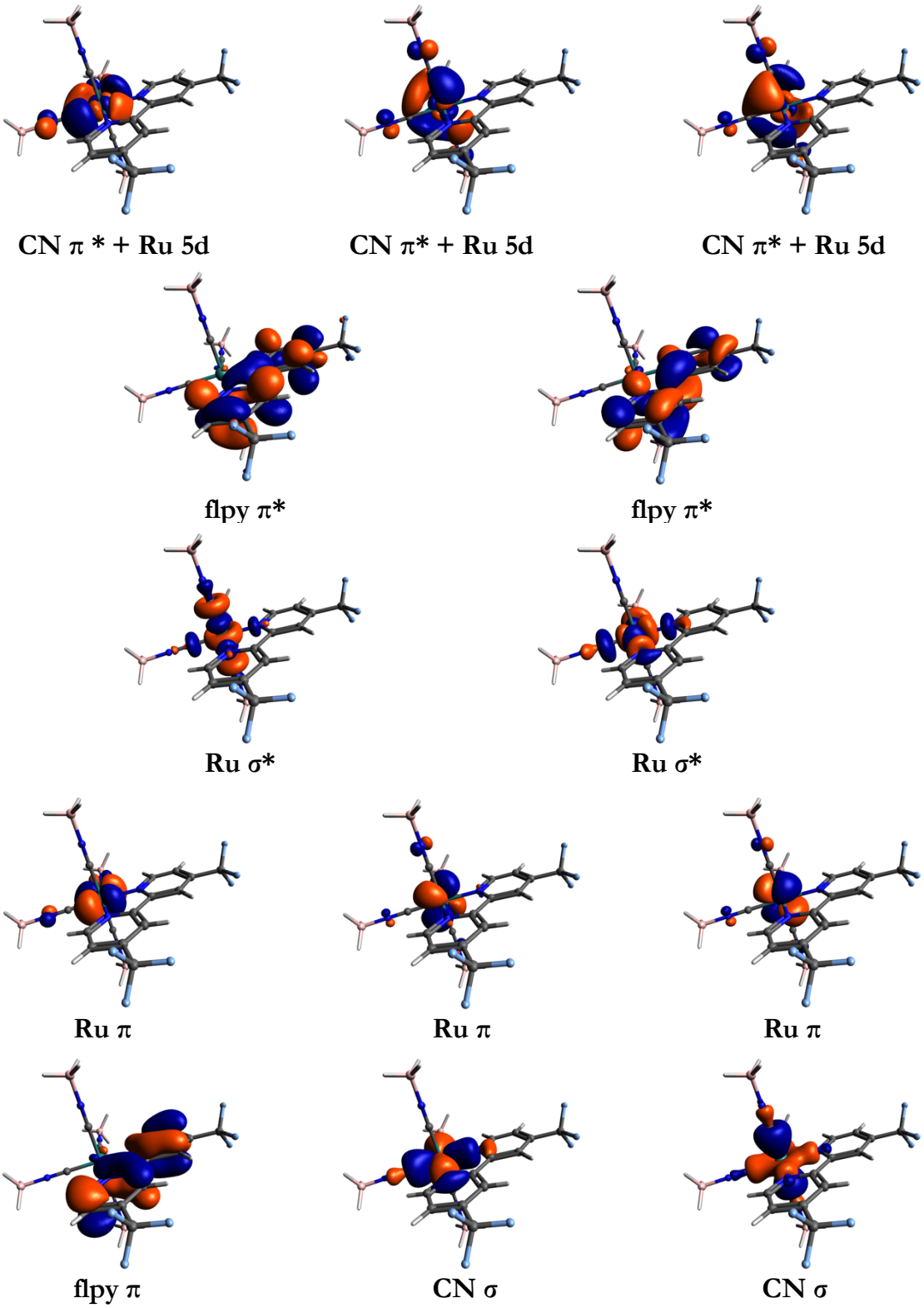

Figure 6.79. Active space molecular orbitals for the state-averaged CAS(12,13) of $[Ru(flpy)(CN\text{-}BH_3)_4]^{2-}$. Isosurface values set to 0.04.

6.6 References

(1) Garcia Posse, M. E.; Katz, N. E.; Baraldo, L. M.; Polonuer, D. D.; Colombano, C. G.; Olabe, J. A. Comparative Bonding and Photophysical Properties of 2,2'-Bipyridine and 2,2'-Bipyrazine in Tetracyano Complexes Containing Ruthenium and Osmium. *Inorg. Chem.* **1995**, *34* (7), 1830–1835. https://doi.org/10.1021/ic00111a034.

(2) Winkler, J. R.; Creutz, C.; Sutin, N. Solvent Tuning of the Excited-State Properties of (2,2'-Bipyridine)Tetracyanoferrate(II): Direct Observation of a Metal-to-Ligand Charge-Transfer Excited State of Iron(II). *J. Am. Chem. Soc.* **1987**, *109* (11), 3470–3471. https://doi.org/10.1021/ja00245a053.

(3) Chan, K.-C.; Cheng, S.-C.; Lo, L. T.-L.; Yiu, S.-M.; Ko, C.-C. Luminescent Charge-Neutral Copper(I) Phenanthroline Complexes with Isocyanoborate Ligand: Luminescent Charge-Neutral Copper(I) Phenanthroline Complexes with Isocyanoborate Ligand. *Eur. J. Inorg. Chem.* **2018**, *2018* (7), 897–903. https://doi.org/10.1002/ejic.201701205.

(4) Chan, K.-C.; Chu, W.-K.; Yiu, S.-M.; Ko, C.-C. Synthesis, Characterization, Photophysics and Electrochemical Study of Luminescent Iridium(III) Complexes with Isocyanoborate Ligands. *Dalton Trans.* **2015**, *44* (34), 15135–15144. https://doi.org/10.1039/C5DT00904A.

(5) Chu, W.-K.; Ko, C.-C.; Chan, K.-C.; Yiu, S.-M.; Wong, F.-L.; Lee, C.-S.; Roy, V. A. L. A Simple Design for Strongly Emissive Sky-Blue Phosphorescent Neutral Rhenium Complexes: Synthesis, Photophysics, and Electroluminescent Devices. *Chem. Mater.* **2014**, *26* (8), 2544–2550. https://doi.org/10.1021/cm4038654.

(6) Ahrens, M. J.; Bertin, P. A.; Gaustad, A. G.; Georganopoulou, D.; Wunder, M.; Blackburn, G. F.; Gray, H. B.; Meade, T. J. Spectroscopic and Redox Properties of Amine-Functionalized $K_2[Os^{II}(bpy)(CN)_4]$ Complexes. *Dalton Trans.* **2011**, *40* (8), 1732. https://doi.org/10.1039/c0dt01478h.

(7) Chu, W.-K.; Yiu, S.-M.; Ko, C.-C. Neutral Luminescent Bis(Bipyridyl) Osmium(II) Complexes with Improved Phosphorescent Properties. *Organometallics* **2014**, *33* (23), 6771–6777. https://doi.org/10.1021/om500630c.

(8) Evju, J. K.; Mann, K. R. Synthesis and Spectroscopic Investigations of a Crystalline Humidity Sensor: Bis(Triphenylphosphine)Iminium 2,2'-Bipyridyltetracyanoruthenate. *Chem. Mater.* **1999**, *11* (6), 1425–1433. https://doi.org/10.1021/cm980323i.

(9) Chu, W.-K.; Wei, X.-G.; Yiu, S.-M.; Ko, C.-C.; Lau, K.-C. Strongly Phosphorescent Neutral Rhenium(I) Isocyanoborato Complexes: Synthesis, Characterization, and Photophysical, Electrochemical, and Computational Studies. *Chem. - Eur. J.* **2015**, *21* (6), 2603–2612. https://doi.org/10.1002/chem.201405291.

(10) Bignozzi, C. A.; Chiorboli, C.; Indelli, M. T.; Rampi Scandola, M. A.; Varani, G.; Scandola, F. Simple Poly(Pyridine)Ruthenium(II) Photosensitizer: (2,2'-Bipyridine)Tetracyanoruthenate(II). *J. Am. Chem. Soc.* **1986**, *108* (24), 7872–7873. https://doi.org/10.1021/ja00284a084.

(11) Gutmann, V.; Gritzner, G.; Danksagmoller, K. Solvent Effects on the Redox Potential of Hexacyanoferrate(III)-Hexacyanoferrate(II) *Inorganica Chim. Acta* **1976**, *17*, 81-86.

(12) Shriver, D. F.; Posner, J. Bridge Addition Compounds. III. The Influence of Boron-Containing Lewis Acids on Electronic Spectra, Vibrational Spectra, and Oxidation Potentials of Some Iron-Cynanide Complexes. *J. Am. Chem. Soc.* **1966**, *88* (8), 1672–1677. https://doi.org/10.1021/ja00960a018.

(13) Shriver, D. F.; Swanson, B. Nature of the Donor-Acceptor Interaction in Boron Trihalide Complexes. Vibrational Spectra and Vibrational Analysis of Acetonitrile-Boron Trichloride and Acetonitrile-Boron Tribromide. *Inorg. Chem.* **1971**, *10* (7), 1354–1365. https://doi.org/10.1021/ic50101a008.

(14) Shriver, D. F.; Shriver, S. A.; Anderson, S. E. Ligand Field Strength of the Nitrogen End of Cyanide and Structures of Cubic Cyanide Polymers. *Inorg. Chem.* **1965**, *4* (5), 725–730. https://doi.org/10.1021/ic50027a028.

(15) Kovács, M.; Horváth, A. Temperature Dependence Study on Photophysics of RuL(CN)42− Complexes: Effects of Diimine Ligand and Solvent Deuteration. *Inorganica Chim. Acta* **2002**, *335*, 69–76. https://doi.org/10.1016/S0020-1693(02)00814-9.

(16) Scandola, F.; Indelli, M. T. Second Sphere Donor Acceptor Interactions in Excited States of Coordination Compounds. Ruthenium(II)Bipyridine Cyano Complexes. *Pure & Appl. Chem.* **1988**, *60* (7), 973-980.

(17) Kovács, M.; Horváth, A. The Effect of H/D-Bond Solute–Solvent Interaction on Deactivation Channels of MLCT Excited State of $[Ru(bpy)(CN)_4]^{2-}$. *J. Photochem. Photobiol. Chem.* **2004**, *163* (1–2), 13–19. https://doi.org/10.1016/S1010-6030(03)00400-3.

(18) Kovács, M.; Ronayne, K. L.; Browne, W. R.; Henry, W.; Vos, J. G.; McGarvey, J. J.; Horváth, A. The Effects of Ligand Substitution and Deuteriation on the Spectroscopic and Photophysical

Properties of $[Ru(LL)(CN)_4]^{2-}$ Complexes. *Photochem. Photobiol. Sci.* **2007**, *6* (4), 444–453. https://doi.org/10.1039/B611825A.

(19) McNicholas, B. J.; Grubbs, R. H.; Winkler, J. R.; Gray, H. B.; Despagnet-Ayoub, E. Tuning the Formal Potential of Ferrocyanide over a 2.1 V Range. *Chem. Sci.* **2019**, *10* (12), 3623–3626. https://doi.org/10.1039/C8SC04972F.

(20) Indelli, M. Teresa.; Bignozzi, C. Alberto.; Marconi, Anna.; Scandola, Franco. Ruthenium(II) 2,2'-Bipyridine Complexes Containing Methyl Isocyanide Ligands. Extreme Effects of Nonchromophoric Ligands on Excited-State Properties. *J. Am. Chem. Soc.* **1988**, *110* (22), 7381–7386. https://doi.org/10.1021/ja00230a018.

(21) Bignozzi, C. A.; Indelli, M. T.; Scandola, F. Bis(2,2'-Bipyridine)Ruthenium(II)-Hexacyanochromate(III) Chromophore-Luminophore Complexes. Intramolecular Energy Transfer, Excited-State Intervalence Transfer, and Doublet-Doublet Annihilation. *J. Am. Chem. Soc.* **1989**, *111* (14), 5192–5198. https://doi.org/10.1021/ja00196a028.

(22) Indelli, M. T.; Ghirotti, M.; Prodi, A.; Chiorboli, C.; Scandola, F.; McClenaghan, N. D.; Puntoriero, F.; Campagna, S. Solvent Switching of Intramolecular Energy Transfer in Bichromophoric Systems: Photophysics of (2,2'-Bipyridine)Tetracyanoruthenate(II)/Pyrenyl Complexes. *Inorg. Chem.* **2003**, *42* (18), 5489–5497. https://doi.org/10.1021/ic034185x.

(23) Schilt, A. A. Mixed Ligand Complexes of Iron(II) and (III) with Cyanide and Aromatic Di-Imines. *J. Am. Chem. Soc.* **1960**, *82* (12), 3000–3005. https://doi.org/10.1021/ja01497a007.

(24) Changes Associated with Intramolecular Electron Transfer during MLCT State Formation. Time-Resolved Optoacoustic Studies of Ruthenium Cyano Complexes.

(25) Shriver D.F. (1966) The ambident nature of cyanide. In: Structure And Bonding. Structure and Bonding, vol 1. Springer, Berlin, Heidelberg

(26) Kjær, K. S.; Kunnus, K.; Harlang, T. C. B.; Van Driel, T. B.; Ledbetter, K.; Hartsock, R. W.; Reinhard, M. E.; Koroidov, S.; Li, L.; Laursen, M. G.; Biasin, E.; Hansen, F. B.; Vester, P.; Christensen, M.; Haldrup, K.; Nielsen, M. M.; Chabera, P.; Liu, Y.; Tatsuno, H.; Timm, C.; Uhlig, J.; Sundstöm, V.; Németh, Z.; Szemes, D. S.; Bajnóczi, É.; Vankó, G.; Alonso-Mori, R.; Glownia, J. M.; Nelson, S.; Sikorski, M.; Sokaras, D.; Lemke, H. T.; Canton, S. E.; Wärnmark, K.; Persson, P.; Cordones, A. A.; Gaffney, K. J. Solvent Control of Charge Transfer Excited State Relaxation Pathways in $[Fe(2,2'\text{-Bipyridine})(CN)_4]^{2-}$. *Phys. Chem. Chem. Phys.* **2018**, *20* (6), 4238–4249. https://doi.org/10.1039/C7CP07838B.

(27) Toma, H.E., Takasugi, M.S. Spectroscopic studies of preferential and asymmetric solvation in substituted cyanoiron(II) complexes. *J. Solution Chem.* **1983**, *12*, 547–561. https://doi.org/10.1007/BF01150847

(28) Timpson, C. J.; Bignozzi, C. A.; Sullivan, B. P.; Kober, E. M.; Meyer, T. J. Influence of Solvent on the Spectroscopic Properties of Cyano Complexes of Ruthenium(II). *J. Phys. Chem.* **1996**, *100* (8), 2915–2925. https://doi.org/10.1021/jp953179m.

(29) Rampi, M. A.; Indelli, M. T.; Scandola, F.; Pina, F.; Parola, A. J. Photophysics of Supercomplexes. Adduct between $Ru(Bpy)(CN)_4^{2-}$ and the [32]Ane-$N_8H_8^{8+}$ Polyaza Macrocycle. *Inorg. Chem.* **1996**, *35* (11), 3355–3361. https://doi.org/10.1021/ic951590i.

(30) Ward, M. D. $[Ru(bipy)(CN)_4]^{2-}$ and Its Derivatives: Photophysical Properties and Its Use in Photoactive Supramolecular Assemblies. *Coord. Chem. Rev.* **2006**, *250* (23–24), 3128–3141. https://doi.org/10.1016/j.ccr.2006.02.012.

(31) Ngo, D.; Del Ciello, S. A.; McNicholas, B. J.; Sanders, B. C.; Fajardo Jr., J.; Gray, H. B.; Winkler, J. R. Cyano-Ambivalence: Spectroscopy and Photophysics of $[Ru(diimine)(CN\text{-}BR_3)_4]^{2-}$ *Polyhedron* **2020**, submitted for publication.

(32) Simpson, N. R. M.; Ward, M. D.; Morales, A. F.; Barigelletti, F. Solvatochromism as a Mechanism for Controlling Intercomponent Photoinduced Processes in a Bichromophoric Complex Containing [Ru(Bpy)3]2+ and [Ru(Bpy)(CN)4]2– Units. *J. Chem. Soc. Dalton Trans.* **2002**, No. 12, 2449–2454. https://doi.org/10.1039/b201597h.

(33) Englman, R.; Jortner, J. The Energy Gap Law for Radiationless Transitions in Large Molecules. *Mol. Phys.* **1970**, *18* (2), 145–164. https://doi.org/10.1080/00268977000100171.

(34) Zhou, Y.; Xiao, H.-P.; Kang, L.-C.; Zuo, J.-L.; Li, C.-H.; You, X.-Z. Synthesis and Characterization of Neutral Iron(Ii) and Ruthenium(Ii) Complexes with the Isocyanotriphenylborate Ligand. *Dalton Trans.* **2009**, No. 46, 10256. https://doi.org/10.1039/b914262b.

(35) *Photochemistry and Photophysics of Coordination Compounds*; Yersin, H., Vogler, A., Eds.; Springer-Verlag: Berlin ; New York, 1987.

(36) Espinoza, E. M.; Clark, J. A.; Soliman, J.; Derr, J. B.; Morales, M.; Vullev, V. I. Practical Aspects of Cyclic Voltammetry: How to Estimate Reduction Potentials When Irreversibility Prevails. *J. Electrochem. Soc.* **2019**, *166* (5), H3175–H3187. https://doi.org/10.1149/2.0241905jes.

(37) Creutz, C. Bipyridine Radical Ions *Comment. Inorg. Chem.* **1982**, *1* (5), 293-311.

(38) Kato, T.; Shida, T. Electronic Structures of Ion Radicals of Nitrogen-Heteroaromatic Hydrocarbons as Studied by ESR and Optical Spectroscopy. *J. Am. Chem. Soc.* **1979**, *101* (23), 6869–6876. https://doi.org/10.1021/ja00517a014.

(39) Liu, Y.; Kjaer, K. S.; Fredin, L. A.; Chábera, P.; Harlang, T.; Canton, S. E.; Lidin, S.; Zhang, J.; Lomoth, R.; Bergquist, K.-E.; Persson, P.; Wärnmark, K.; Sundström, V. A Heteroleptic Ferrous Complex with Mesoionic Bis(1,2,3-Triazol-5-Ylidene) Ligands: Taming the MLCT Excited State of Iron(II). *Chem. - Eur. J.* **2015**, *21* (9), 3628–3639. https://doi.org/10.1002/chem.201405184.

(40) Zhang, W.; Kjær, K. S.; Alonso-Mori, R.; Bergmann, U.; Chollet, M.; Fredin, L. A.; Hadt, R. G.; Hartsock, R. W.; Harlang, T.; Kroll, T.; Kubiček, K.; Lemke, H. T.; Liang, H. W.; Liu, Y.; Nielsen, M. M.; Persson, P.; Robinson, J. S.; Solomon, E. I.; Sun, Z.; Sokaras, D.; van Driel, T. B.; Weng, T.-C.; Zhu, D.; Wärnmark, K.; Sundström, V.; Gaffney, K. J. Manipulating Charge Transfer Excited State Relaxation and Spin Crossover in Iron Coordination Complexes with Ligand Substitution. *Chem. Sci.* **2017**, *8* (1), 515–523. https://doi.org/10.1039/C6SC03070J.

(41) Kolling, O. W. Comparisons between Hydrogen Bond Donor-Acceptor Parameters and Solvatochromic Red Shifts. *Anal. Chem.* **1978**, *50* (2), 212–215. https://doi.org/10.1021/ac50024a013.

(42) Pierloot, K.; Van Praet, E.; Vanquickenborne, L. G.; Roos, B. O. Systematic Ab Initio Study of the Ligand Field Spectra of Hexacyanometalate Complexes. *J. Phys. Chem.* **1993**, *97* (47), 12220–12228. https://doi.org/10.1021/j100149a021.

(43) Hahn, A. W.; Van Kuiken, B. E.; Chilkuri, V. G.; Levin, N.; Bill, E.; Weyhermüller, T.; Nicolaou, A.; Miyawaki, J.; Harada, Y.; DeBeer, S. Probing the Valence Electronic Structure of Low-Spin Ferrous and Ferric Complexes Using 2p3d Resonant Inelastic X-Ray Scattering (RIXS). *Inorg. Chem.* **2018**, *57* (15), 9515–9530. https://doi.org/10.1021/acs.inorgchem.8b01550.

(44) Formiga, A. L. B.; Vancoillie, S.; Pierloot, K. Electronic Spectra of *N*-Heterocyclic Pentacyanoferrate(II) Complexes in Different Solvents, Studied by Multiconfigurational Perturbation Theory. *Inorg. Chem.* **2013**, *52* (18), 10653–10663. https://doi.org/10.1021/ic401704r.

(45) Jakubczyk, M.; Adamczyk-Woźniak, A.; Sporzyński, A. Acceptor Number of Organoboron Molecules - Quantitative Determination of Lewis Acidity. In *Molecular Receptors*. Rybachenko, V. I., Ed.; East Publisher House, 2011

(46) Neese, F. The ORCA Program System. Wiley Interdisciplinary Reviews: Computational Molecular Science 2012, 2 (1), 73−78.

(47) Mayer, U., Gutmann, V.; Gerger, W. The acceptor number — A quantitative empirical parameter for the electrophilic properties of solvents. *Monatshefte für Chemie* **1975**, *106*, 1235–1257. https://doi.org/10.1007/BF00913599.

(48) Bard, A. J.; Faulkner, L. R. Electrochemical Methods; Wiley: New York, 2000

(49) Nicholson, R. S. Semiempirical Procedure for Measuring with Stationary Electrode Polarography Rates of Chemical Reactions Involving the Product of Electron Transfer. *Anal. Chem.* **1966**, 38, 10, 1406

(50) Roffia, S.; Ciano, M. Electrochemical behaviour of dicyanobis(2,2'-bipyridine) ruthenium(II) and dicyanobis(1,10-phenanthroline) ruthenium(II) complexes. J Electroanal. Chem. **1977**, *77* (3), 349-359.

(51) Potash, R. A.; McKone, J. R.; Conte, S.; Abruña, H. D. On the Benefits of a Symmetric Redox Flow Battery. *J. Electrochem. Soc.* **2016**, *163* (3), A338–A344. https://doi.org/10.1149/2.0971602jes.

(52) Krause, R. A.; Violette, C. An Improved Synthesis of Potassium Hexacyanoruthenate(II). Inorganica Chim. Acta **1986**, *113* (2), 161-162.

(53) Jiwan, J. L. H.; Wegewijs, B.; Indelli, M. T.; Scandola, F.; Braslavsky, S. E. Volume Changes Associated with Intramolecular Electron Transfer during MLCT State Formation. Time-Resolved Optoacoustic Studies of Ruthenium Cyano Complexes. *Recl. Trav. Chim. Pays-Bas-J. R. Neth. Chem. Soc.* **1995**, *114* (11–12), 542-.

(54) Doan, S. C.; Schwartz, B. J. Ultrafast Studies of Excess Electrons in Liquid Acetonitrile: Revisiting the Solvated Electron/Solvent Dimer Anion Equilibrium. *J. Phys. Chem. B* **2013**, *117* (16), 4216–4221. https://doi.org/10.1021/jp303591h.

(55) *Surface Xplorer*; Ultrafast Systems LLC: Sarasota, Fl, 2012.

(56) Gawelda, W.; Cannizzo, A.; Pham, V.-T.; van Mourik, F.; Bressler, C.; Chergui, M. Ultrafast Nonadiabatic Dynamics of $[Fe^{II}(Bpy)_3]^{2+}$ in Solution. *J. Am. Chem. Soc.* **2007**, *129* (26), 8199–8206. https://doi.org/10.1021/ja070454x.

(57) Sheldrick, G. M. Phase annealing in *SHELX*-90: Direct Methods for Larger Structures. *Acta Crystallogr.* **1990**, *A46*, 467–473.

(58) Sheldrick, G. M. Crystal Structure Refinement with SHELXL. *Acta Crystallogr.* **2015**, *C71*, 3–8.

(59) Müller, P. Practical Suggestions for Better Crystal Structures. *Crystallogr. Rev.* **2009**, *15*, 57–83.

Chapter VII

COBALT(II) AND COBALT(III) BORONATED CYANOMETALLATES: SYNTHESIS, REACTIVITY, AND EPR SPECTROSCOPY

7.1. Summary

We report the synthesis and characterization of Co(III) and Co(II) boronated cyanometallates. Boronation of $[Co(CN)_6]^{3-}$ to generate $[Co(CN\text{-}B(C_6F_5)_3)_6]^{3-}$ (**1**) shifts the peak cathodic potential of the species quite positive. Based on inflection potential for **1** and comparison to other formal potentials, we estimate $E_0' = -1.62$ V vs. NHE for aqueous $[Co(CN)_6]^{3-}$. Chemical reduction of **1** with cobaltocene affords $(C)_2(CoCp_2)[Co(CN\text{-}B(C_6F_5)_3)_5]$ (C = PPN^+, TBA^+), which has been characterized by ^1H, ^{11}B, ^{19}F, and ^{13}C NMR, EA, X-ray crystallography, UV-visible-NIR spectroscopy, and continuous wave and (for the first time) pulsed EPR techniques. The $^2A_1 \rightarrow {}^2E$ NIR transition shifts from 9,260 cm^{-1} (for $[Co(CN)_5]^{3-}$ in MeCN) to 11,190 cm^{-1} (for $(TBA)_2(CoCp_2)[Co(CN\text{-}B(C_6F_5)_3)_5]$ in MeCN). CASSCF-NEVPT2 calculations on both $[Co(CN)_5]^{3-}$ and $[Co(CN\text{-}BH_3)_5]^{3-}$ correctly predict transition energies for ligand field transitions and EPR properties. The $^2A_1 \rightarrow {}^2B_1$ energy increases less than the $^2A_1 \rightarrow {}^2E$ and $^2A_2$ transitions. These data demonstrate the greater ligand field strength of isocyanoborates relative to cyanide for Co species and correctly predict the relative lowering and raising of electronic transitions based on σ-donation of the borane and π-backdonation of the metal center.

7.2. Introduction

Jack Halpern published the seminal studies on the reactivity of pentacyanocobaltate as a strong reductant for the cleavage of alkyl halide bonds and the activation of dihydrogen.[1,2,3] Aside from practical and synthetic applications, pentacyanocobaltate's rich spectroscopy of has contributed in

large part to the staggering number of CW electron paramagnetic resonance, UV-visible, infrared, and Raman studies on its salts and isostructures (such as nitrile species).[4,5,6,7,8]

Hexacyanocobaltate has been used as a component of Prussian blue analogues for detection of biologically relevant molecules, for potassium- and lithium-ion batteries, as a heterogeneous oxygen evolution catalyst, as a dilution agent for magnetic molecular systems, and as a long-lived phosphor.[9,10,11,12,13] For example, Prussian blue analogues employing Co(II) and Co(III) linkages exhibit high photocatalytic activity for water oxidation in tandem with $[Ru(bpy)_3]^{2+}$ and persulfate as a photosensitizer.[14] Another study used cobaltate coupled with Nd(III) and Yb(III) to demonstrate effective sensitization of the NIR luminescence of heavy metals by the long-lived excited state of $[Co(CN)_6]^{3-}$.[15] Despite these promising applications, the fundamental reactivity and electrochemistry of the constituent complexes as a result of nitrogen-based modification are understudied.

7.3 Results and Discussion

Bis(triphenylphosphine)iminium hexacyanocobaltate ($(PPN)_3[Co(CN)_6]$) was synthesized by combining a stoichiometric excess of PPNCl with potassium hexacyanocobaltate. The salt was characterized by ^{1}H, ^{13}C, and ^{31}P NMR, IR, UV-vis, and elemental analysis. The ^{13}C NMR for cyanometallates is particularly enlightening.[16,17] For $(PPN)_3[Co(CN)_6]$, a characteristic octet of doublets pattern centered at δ 127.9 ppm is present. This splitting corresponds to the coupling of the ^{59}Co nucleus to the ^{13}C nucleus, with a further doublet splitting by each ^{14}N nucleus (**Figure 7.11**).[18,19] This shift is upfield by nearly δ 7.6 ppm from previously reported ^{13}C shifts of hexacyanocobaltate. This upfield shift could be due to complete removal of water, which hydrogen bonds to the cyanide nitrogens. Facile removal of water results from utilization of the lipophilic PPN^+ cation. Alternatively,

the upfield shift could result from decreased cation-cyanide interaction due to the bulkiness of the PPN cation. To rationalize this behavior, we characterized $(TBA)_3[Co(CN)_6]$ by ^{13}C and ^{1}H NMR and found that an anhydrous salt of this species exhibited a ^{13}C octet at 137.5 ppm. The discrepancy in shift is then likely the result of decreased ion-dipole interactions for PPN^+ versus TBA^+, increasing the shielding of the cyanide carbon.[20]

$(TBA)_3[Co(CN\text{-}B(C_6F_5)_3)_6]$ or $(PPN)_3[Co(CN\text{-}B(C_6F_5)_3)_6]$ was synthesized by combining excess $B(C_6F_5)_3$ with $(C)_3[Co(CN)_6]$ (C = TBA^+, PPN^+) in dichloromethane (DCM) and was confirmed pure and characterized by NMR, X-ray crystallography, Raman, IR, UV-vis, room- and low-temperature voltammetry, and low-temperature luminescence.

The bond length range for $(TBA)_3[Co(CN\text{-}B(C_6F_5)_3)_6]$, 1.8876(18)-1.890(2) Å, indicates a near perfect O_h coordination environment for the complex. These values are consistent with respect to bond lengths for $[Co(CN)_6]^{3-}$, with even less contraction upon boronation relative to $[Fe(CN)_6]^{4-}$.[21] The diminished contraction likely results from the smaller ionic radius of Co^{3+} relative to Fe^{2+}.

Analogous to the isoelectronic species $[Fe(CN\text{-}B(C_6F_5)_3)_6]^{4-}$, the lowest energy absorption band observed in $(TBA)_3[Co(CN\text{-}B(C_6F_5)_3)_6]$ is a spin-allowed $^1A_{1g} \rightarrow {}^1T_{1g}$ (ε = 195 M^{-1} cm^{-1}, based on Gaussian deconvolution) ligand field transition with λ_{max} = 32,100 cm^{-1}.[22,23] Since borane transitions at approximately 38,000 cm^{-1} and 45,000 cm^{-1} convolute the ligand field transition, we were unable to observe the $^1A_{1g} \rightarrow {}^1T_{2g}$ ligand field transition. The solid-state emission of $(PPN)_3[Co(CN\text{-}B(C_6F_5)_3)_6]$ (**Figure 7.1**), (λ_{max} = 14,320 cm^{-1}) is known to result from $^3T_{1g} \rightarrow {}^1A_{1g}$ phosphorescence, and the band maximum is known to depend on secondary sphere interactions with solvent or cations.[24,22,25]

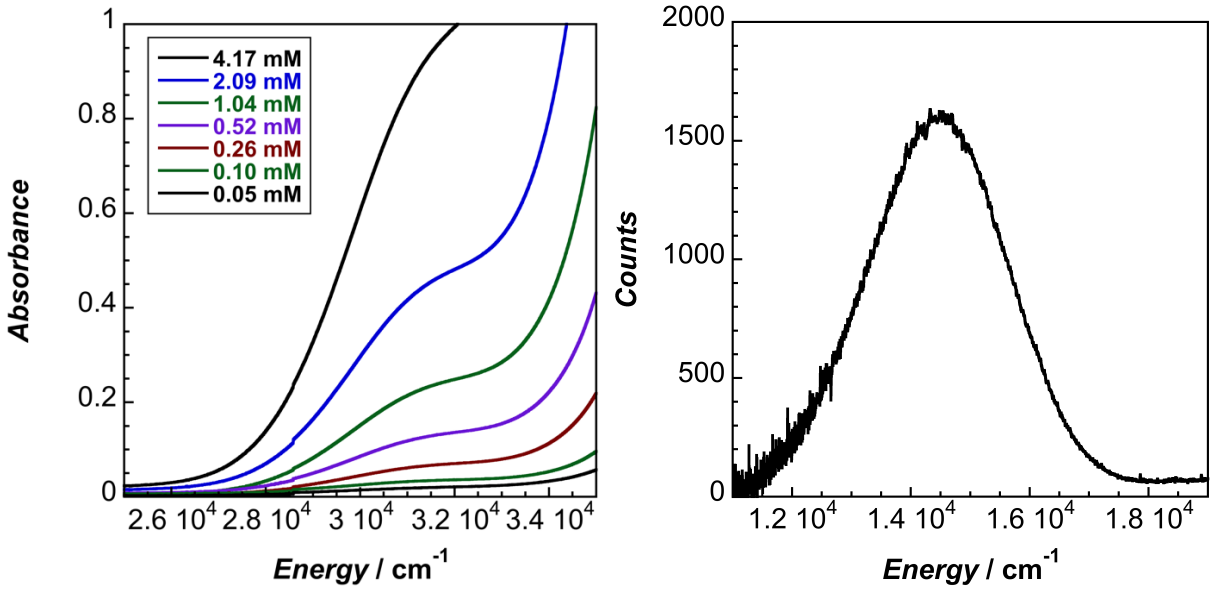

Figure 7.1. UV-visible absorption spectrum in MeCN (Left) and 12.6 K powder emission spectrum (Right) of $(TBA)_3[Co(CN\text{-}B(C_6F_5)_3)_6]$.

For $(TBA)_3[Co(CN)_6]$, the emission maximum is at 13,250 cm^{-1} in a glass of ethanol-isopentane-diethyl ether,[24] a redshift of 1050 cm^{-1} in energy, consistent with isocyanoborate ligands exerting a stronger ligand field in O_h metal complexes. This shift would be even greater if the emission were measured for the base compound in an aprotic solvent. Additionally, as pointed out previously,[24] many of the reported $^3T_{1g} \rightarrow {}^1A_{1g}$ emission maxima for hexacyanocobaltate are spurious due to not correcting for the wavelength-dependent response of the detector.[26,23,27] We were unable to observe vibrational fine structure for $(TBA)_3[Co(CN\text{-}B(C_6F_5)_3)_6]$, which has been shown previously to correspond to Co-C stretching frequencies (for $K_3[Co(CN)_6]$, $\nu_{Co\text{-}C}$ = 420 cm^{-1}). However, the fine structure for our species is likely obscured in the solid state due to inhomogeneous broadening. We attempted to observe the emission for $(TBA)_3[Co(CN)_6]$ in the solid state; however, consistent with previous reports, the compound does not emit as a powder.[28]

We also obtained an emission lifetime for the phosphorescence of $(TBA)_3[Co(CN\text{-}B(C_6F_5)_3)_6]$ in a frozen solution of butyronitrile at 77 K. The emission curve fits nicely to a single exponential, consistent with previous reports of the first-order decay mechanism for $[Co(CN)_6]^{3-}$.[24,29] The lifetime for this emission is 0.21 ms, slightly lower than, but consistent with the 0.56 ms lifetime for $[Co(CN)_6]^{3-}$ in aqueous solution at 77 K and 0.68 ms for $K_3[Co(CN)_6]$ in a single crystal reported previously.[23,22]

To obtain a meaningful comparison of the Co-C bond strength in cyanometallates versus metal isocyanoborates, we conducted solid-state Raman spectroscopy on $(PPN)_3[Co(CN)_6]$, $(TBA)_3[Co(CN)_6]$, and both the PPN and TBA salts of **1**. For both $(PPN)_3[Co(CN)_6]$ and $(TBA)_3[Co(CN)_6]$, sharp resonances are observed at 389 cm^{-1} and 390 cm^{-1}, respectively, and are ascribed to the a_{1g} symmetric Co-C stretch. These values are red shifted relative to values obtained for alkali metal salts and aqueous solutions of $[Co(CN)_6]^{3-}$, consistent with their greater donation or electrostatics with nitrogen lone pairs. The boronated species exhibits an a_{1g} symmetric Co-C stretch at 409 cm^{-1}, consistent with simultaneous weakening and strengthening of the M-C bond from Lewis acid coordination.

The electrochemistry of $K_3[Co(CN)_6]$ in aqueous solution exhibits an electrochemically irreversible reduction that has conflicting estimates for formal potential reported in literature ranging anywhere from −0.80 V to −1.80 V vs. NHE.[10,30,31] For **1**, we were able to observe the $Co^{III/II}$ reduction. To experimentally observe a formal potential for the Co(III/II) reduction, we attempted to increase reversibility by using rapid scan rates and by taking the voltammetry of the complex at −25 °C

(**Figures 7.22** and **7.23**); however, we were unable to observe appreciable anodic current, consistent with a fast, irreversible chemical follow-up reaction (E_rC_i mechanism). Despite this limitation, we can estimate the formal potential of this process based on the potential at the inflection point of the voltammogram (E_i = −1.65 V vs. $Fc^{+/0}$).[32] As previously shown, inflection potentials are superior to peak potentials for estimating the formal potentials of electrochemically irreversible processes since both peak potentials and the potential at half of the peak current ($E_{p/2}$) tend to vary with scan rate.[32] This formal potential aligns relatively well with the entire series of boronated, homoleptic cyanometallates and their respective LMCT transition energies. However, we are still in the process of identifying the position of the CN(π) → dσ* LMCT transition in $(TBA)_3[Co(CN\text{-}B(C_6F_5)_3)_6]$ as a result of obfuscation by the second π → π* transition of $B(C_6F_5)_3$.[33] Given shifts in one-electron energy levels of $[Fe(CN)_6]^{4-}$ and the linear fit for boronated cyanometallates, CN(π) → dσ* should lie at approximately 44,000 cm^{-1}. At a concentration of 0.05 mM at 45,000 cm^{-1}, the molar absorptivity of the solution is over 60,000 M^{-1} cm^{-1}. Given the extinction coefficient of the borane transition, the presence of the LMCT transition in this envelope is likely.

Given our studies on $[Fe(CN\text{-}B(C_6F_5)_3)_6]^{4-}$, the potential shift as a result of boronation, and the excitation energy of the $^1A_{1g} \rightarrow {}^1T_{1g}$ transition for both $[Fe(CN)_6]^{3-}$ and $[Fe(CN\text{-}B(C_6F_5)_3)_6]^{4-}$, we can approximate the formal potential for the first reduction (E_rC_i) process of $[Co(CN)_6]^{3-}$ in MeCN as −3.48 V vs. $Fc^{+/0}$. Based on the formal potential for $[Fe(CN)_6]^{3-}$, the potential difference between the $Fe^{III/II}$ and $Co^{III/II}$ couples is 2.03 V. Solvation for two different redox couples should not affect the potential difference between the couples. Given this constant potential separation, we predict the unboronated formal potential of $[Co(CN)_6]^{3-}$ to lie at −1.62 V vs. NHE. This value is very near to,

but more anodic than, a poorly resolved wave observed at a dropping mercury electrode that was ascribed to the $Co^{III/II}$ reduction in aqueous solution (−1.66 V vs. NHE).[30] However, as evidenced by the electrochemical reversibility at fast scan rates and depressed temperatures, this value is not simply the formal potential for population of the e_g set; rather, it is a convolution of the equilibrium for dissociation of an isocyanoborate ligand coupled to the simultaneous reduction of the metal center. One of the observed return oxidations occurs at a potential that is consistent with the voltammetry observed for boronated pentacyanocobaltate.

Based on the potential at the foot of the reduction wave for $(TBA)_3[Co(CN\text{-}B(C_6F_5)_3)_6]$, cobaltocene ($E_{1/2}$ = −1.33 V vs. $Fc^{+/0}$) was selected as a reductant. Addition of a stoichiometric excess yielded a bright yellow solution, which was filtered, washed with diethyl ether (Et_2O), and recrystallized from DCM to yield $(TBA)_2(CoCp_2)[Co(CN\text{-}B(C_6F_5)_3)_5]$, a d^7, Co(II) species that is isoelectronic to previously studied pentacyanocobaltate and isostructural to isocyanide derivatives.[6] The complex was characterized by IR spectroscopy, solution and solid phase UV-vis-NIR spectroscopy, voltammetry, and continuous-wave (CW) and pulse electron paramagnetic resonance (EPR) spectroscopy. In this case, the species is greatly stabilized relative to the base complex as a result of stabilizing the unpaired electron in the d_z^2 antibonding orbital by at least 0.2 eV, the approximate anodic energy shift resulting from addition of $B(C_6F_5)_3$ to a ligand that is colinear with a sigma antibonding orbital. This behavior allowed facile characterization of the structure and spectroscopy of this species relative to the unboronated complex.

Examination of the crystal structure of $(TBA)_2(CoCp_2)[Co(CN\text{-}B(C_6F_5)_3)_5]$ (**Figure 7.3**) reveals equatorial bond lengths which range from 1.8542(10)-1.8632(10) Å and an axial bond length equal to

1.9239(10) Å. The axial cyanide bond length, 1.1485(13) Å, is slightly shorter than the equatorial cyanide bond lengths (1.1504(13)-1.1522(13) Å), consistent with greater π backbonding in the equatorial plane.

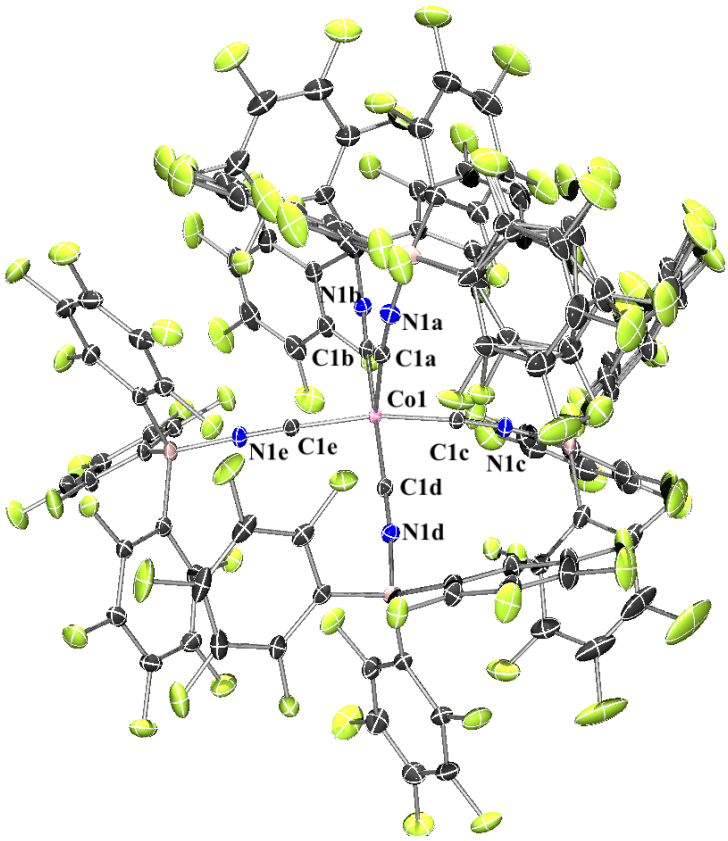

Figure 7.2. Molecular structure of $[Co(CN\text{-}B(C_6F_5)_3)_5]^{3-}$. Cations and solvent molecules omitted for clarity. Thermal ellipsoids set at 50% probability.

Relative to $[Co(CN)_5]^{3-}$, the axial bond length decreases by nearly 0.1 Å, a large contraction that is consistent with lowering cyanide molecular orbital energies upon borane binding. The equatorial Co-C bond lengths are incredibly short for an anionic Co(II) species, with bond lengths comparable to a

cationic Co(II) isocyanide species, $[Co(CN\text{-}C_6H_5)_5]^{2+}$.[34,35,36] IR CN stretches at 2202 cm^{-1}, 2217 cm^{-1}, and 2242 cm^{-1} are consistent with the stretching pattern for a C_{4v} molecular geometry.

The electronic structure of $[Co(CN)_5]^{3-}$ and its derivatives have been previously studied by UV-vis-NIR, infrared, and electron paramagnetic resonance spectroscopy.[37,7,38] A combination of absorbance and EPR spectroscopy was used to suggest the square pyramidal geometry of the species prior to X-ray crystallographic analysis.[37,39,40]

Despite all one-electron molecular orbital energy levels being lowered in energy, the separation among all energy levels increases, resulting in blueshifted energies for all electronic transitions. Spectra for $[Co(CN)_5]^{3-}$ in a variety of solvents and with a variety of countercations have been reported in the literature.[41,40,39,42] There has been some discussion of the assignment of the NIR transition in pentacyanocobaltate.[41,40,39,42] Originally assigned to the $^2A_1 \rightarrow {}^2B_1$ transition, consideration of a decrease in spin-orbit coupling due to electron delocalization onto the cyanide ligands results in a z^2 – (xz,yz) splitting that is close in energy to the NIR transition, assigning the lowest-energy band to $^2A_1 \rightarrow {}^2E$.[37,43] The UV-vis spectrum of $(TBA)_2(CoCp_2)[Co(CN\text{-}B(C_6F_5)_3)_5]$ (**Figure 7.3**) is characterized by blue shifts in the energy of all electronic transitions relative to the base complex. However, as evidenced by X-ray structural analysis, the presence of $CoCp_2^+$ (which exhibits absorbance maxima at 24,690 cm^{-1} and 33,113 cm^{-1} with comparable extinction coefficients) precludes detailed position and intensity assignments for higher energy bands of $[Co(CN\text{-}B(C_6F_5)_3)_5]^{3-}$. However, based on the asymmetry of the envelopes and positions of bands in bare pentacyanocobaltate, we are confident that multiple bands are present near these values. Greater resolution of bands will be achieved by

characterizing the species in a poly(methyl methacrylate) film at low temperature and/or using a UV-silent reductant.

Table 7.1. Ligand field transitions for pentacyanocobaltate in various solvents and $(TBA)_2(CoCp_2)[Co(CN\text{-}B(C_6F_5)_3)_5]$ in MeCN. Assignments based on a combination of literature and theoretical calculations.

State	Orbital Transition	H_2O[a] (cm^{-1})	DMSO[b] (cm^{-1})	MeCN[c] (cm^{-1})	$B(C_6F_5)_3$ (cm^{-1})
^2E	$e(xz,yz) \rightarrow a_1(z^2)$	10,350	9,010	9,260	11,190
$^4A_2,^4E$	$b_2(xy), e(xz,yz) \rightarrow b_1(x^2-y^2)$	16,200	---	15,290	17,700
$^2B_1,^2B_2$	$a_1(z^2) \rightarrow b_1(x^2-y^2)$	23,420	25,250	23,420	24,600
$^2A_2,^2E$	$b_2(xy), e(xz,yz) \rightarrow b_1(x^2-y^2)$	31,700	28,090	30,120	33,100

[a]Reference 39.
[b]Reference 42.
[c]Reference 41.

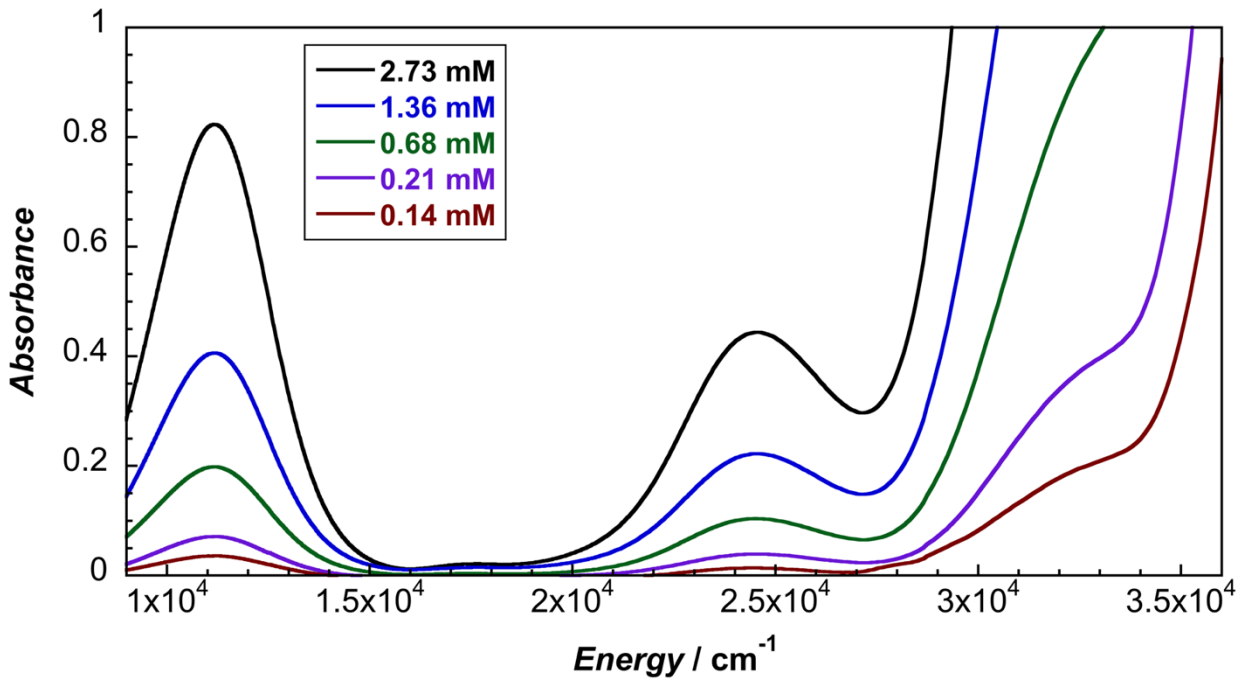

Figure 7.3. UV-visible spectroscopy of $(TBA)_2(CoCp_2)[Co(CN\text{-}B(C_6F_5)_3)_5]$ in MeCN.

EPR Studies of $[Co(CN\text{-}B(C_6F_5)_3)_5]^{3-}$

In order to further probe the electronic structure and spin distribution of complex 2, we turned to characterization of the S = ½ ground state via CW and pulse EPR spectroscopies at X- and Q-band frequencies, respectively. Consistent with its d_z^2 SOMO parentage, complex 2 exhibits an X-band CW-EPR spectrum (**Figure 7.4**) with approximately axial symmetry with $g_{x,y,z}$ = [2.152, 2.141, 2.003], and exhibits resolved splittings from hyperfine coupling to the ^{59}Co nucleus (I = 7/2, 100% natural abundance) which is well simulated using $|A(^{59}Co)|$ = [104, 80, 260] MHz. When measured at Q-band ($\nu \approx 34$ GHz) using the analogous field-swept pulse EPR technique, electron spin echo-detected EPR (ESE-EPR), the ~ 4-fold higher excitation frequency and associated magnetic fields utilized allow significant enhancement of resolution of the g-anisotropy of the species (**Figure 7.4**), with a well isolated ^{59}Co octet splitting observed centered at 1215 mT corresponding to g_z.

While these field-swept EPR spectra provide reasonable resolution of the g-values and magnitude of ^{59}Co hyperfine within the paramagnetic species, smaller hyperfine couplings to the ^{14}N, ^{11}B, and ^{19}F nuclei of the $^{-}CN\text{-}B(C_6F_5)_3$ ligands are obscured within the inhomogeneously broadened EPR lineshape. In order to measure these ligand hyperfine couplings, we turned to a combination of electron nuclear double resonance (ENDOR) and hyperfine sublevel correlation (HYSCORE) pulse EPR spectroscopies.

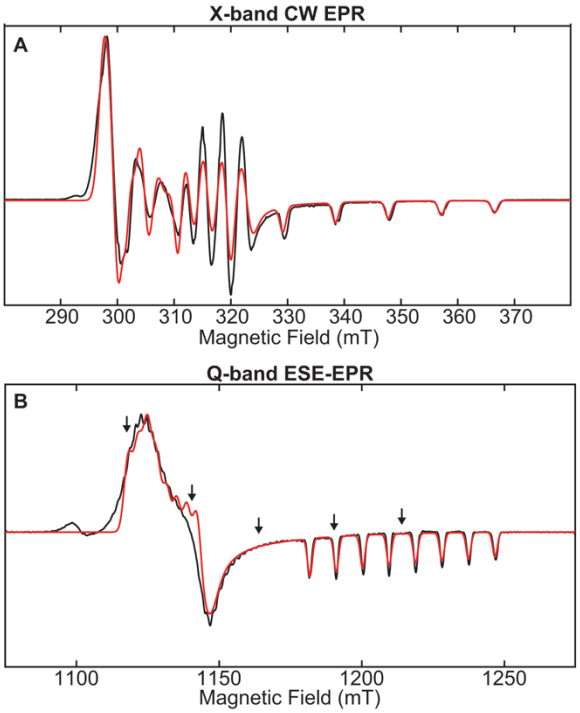

Figure 7.4. (**A**) X-band CW-EPR spectrum (black) of frozen solution of complex **2** prepared in 2Me-THF with simulation overlaid in red. Acquisition parameters: temperature = 77 K; MW freq. = 9.381 GHz; MW power = 2 mW; modulation amplitude = 0.2 mT; conversion time = 40 ms.
(**B**) Pseudomodulated Q-band echo-detected EPR spectrum (black) of complex **2** prepared in 2Me-THF with simulation overlaid in red. Black arrows indicate field positions at which pulse EPR spectra in Figs. 4,5 were acquired (vide infra). Acquisition parameters: temperature = 15 K; MW freq. = 34.046 GHz; MW pulse length ($\pi/2$, π) = 80 ns, 160 ns; τ = 300 ns; shot repetition time (srt) = 2 ms.
Simulation parameters: g = [2.152, 2.141, 2.003]; A(^{59}Co) = [-104, -80, 260] MHz; H-strain = [60, 40, 30] MHz; g-strain = [0.005, 0.01, 0.0025] MHz.

Q-band Davies ENDOR was acquired at five magnetic fields across the envelope of the EPR spectrum (**Figure 7.5**) using two different RF frequency ranges: relatively wide ENDOR scans from 25-200 MHz which targeted detection of hyperfine couplings to ^{19}F and ^{59}Co (**Figure 7.5**), and lower frequency scans from 0.5-25 MHz targeting ^{14}N and ^{11}B (**Figure 7.6**).

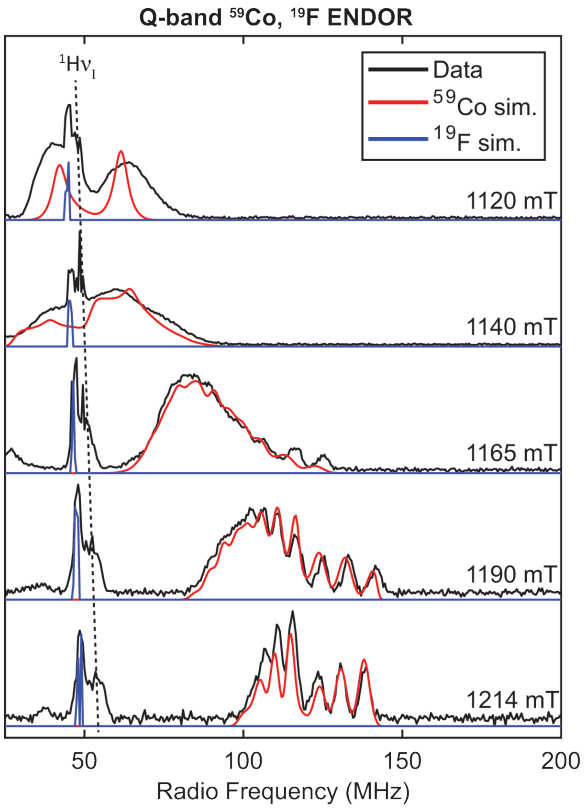

Figure 7.5. Field-dependent Q-band Davies ENDOR spectra (black) of complex **2** with simulations of features arising from hyperfine interactions with ^{59}Co (red) and ^{19}F (blue) overlaid. Acquisition parameters: T = 15 K; MW frequency = 34.046 GHz; MW pulse length ($\pi/2$, π) = 40 ns, 80 ns; RF pulse length = 15 μs; τ = 240 ns; shot repetition time (srt) = 2 ms. Simulation parameters: g = [2.152, 2.141, 2.003]; A(^{59}Co) = [-104, -80, 260] MHz; A(^{19}F) = [-0.8, -0.8, 1.6] MHz.

In the higher frequency ENDOR spectra, relatively broad features are observed from the same ^{59}Co hyperfine coupling resolved in the field-swept EPR. In contrast to the field swept EPR spectra, which is insensitive to the relative sign of the individual components of hyperfine tensors, satisfactory simulations of the spectral lineshapes of these ENDOR features required the use of an extremely anisotropic hyperfine tensor, with $A(^{59}\text{Co}) = [-104, -80, 260]$. The approximate axial symmetry of this tensor, with the largest component oriented along the molecular z-axis, is consistent with the majority of spin density at Co being localized in an orbital of d_{z^2} parentage. This tensor can be decomposed into its constituent isotropic and anisotropic terms, with $a_{iso}(^{59}\text{Co}) = 25.3$ MHz, and

$T(^{59}\text{Co})$ = [−105.3, −129.3, 234.7], which can be compared to calculated values for ^{59}Co hyperfine coupling to unit spin density in Co 4s (a_{iso}^0 = 5947 MHz) and $3d_{z^2}$ ($T_{dz^2}^0$ = [−241.5, −241.5, 483.0] MHz) orbitals[44] to yield spin density estimates of $\rho_{4s} \approx 0.004$ e$^-$ and $\rho_{dz^2} \leq 0.485$ e$^-$, respectively. This estimate for ρ_{dz^2} is expressed as an upward bound, as orbital mixing with the symmetry-related $3p_z$ orbital would account for a larger portion of the observed hyperfine due to lower orbital angular momentum. In addition, very sharp features centered at the ^{19}F Larmor frequency are observed at each field, just below features from weakly coupled ^{1}H nuclei from solvent molecules ($\gamma(^{19}\text{F})/\gamma(^1\text{H})$ = 0.94). These ^{19}F features are consistent with extremely weak hyperfine couplings of approximately $A(^{19}\text{F})$ = [−0.8, −0.8, 1.6] MHz, likely corresponding to a purely through-space dipolar magnetic interaction between most of the ^{19}F nuclei in the $^-$CN-B(C_6F_5)$_3$ ligands and spin density localized at cobalt. This indicates a lack of significant spin density delocalized into the pi-system of the C_6F_5 groups, as this would transfer significant spin density to the ^{19}F nuclei through the fluorine p_z orbital(s), as has been observed in fluorinated tyrosine radicals.[45]

In the lower frequency ENDOR spectra (**Figure 7.6**), features from hyperfine couplings to a single class of ^{14}N nucleus, denoted $^{14}N_a$, are evident near 9 MHz at all magnetic fields which are well simulated with hyperfine parameters $A(^{14}N_a)$ = [9.2, 9.2, 12] MHz. At the magnetic fields at which these experiments were conducted, this nucleus is in the strong coupling limit where $A > 2\nu_I$, in which ENDOR peaks for a given nucleus generally manifest as a pair of peaks split by the $2\nu_I$ and centered about half the hyperfine coupling. However, in this case, the lower frequency ENDOR peaks are not observed, likely due to very low ENDOR efficiency at frequencies below 2 MHz or significant nuclear spin polarization from the hyperfine interaction. An additional splitting in the ^{14}N ENDOR is induced by the electric interaction of the I = 1 ^{14}N nuclear quadrupole with the inhomogeneous

electric field produced by electron density in p-orbitals at the nucleus. This interaction is parameterized by the nuclear quadrupole coupling constant ($^{14}N_a$ e^2qQ/h = 1.2) and the electric field gradient (EFG) asymmetry ($^{14}N_a$ η = 0). The low magnitude of e^2qQ/h and negligible EFG rhombicity indicates nearly spherical charge density about this class of CN-B(C_6F_5)$_3$ ligand.

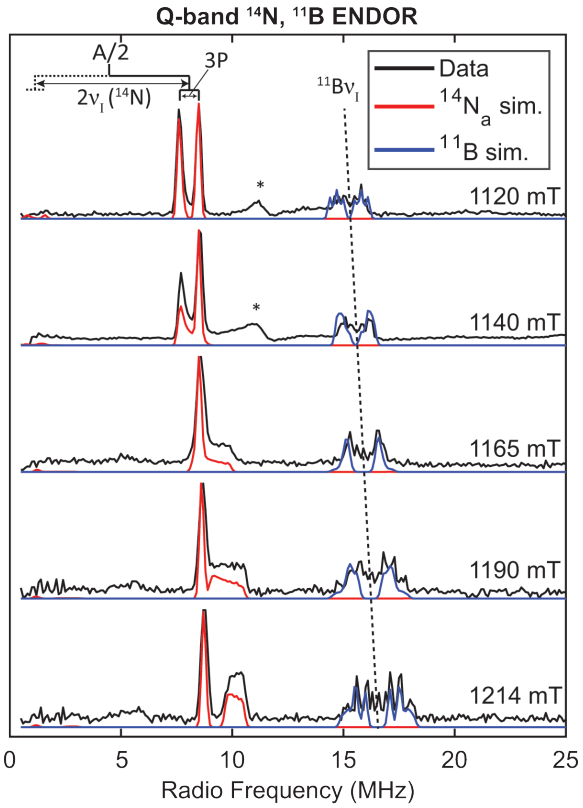

Figure 7.6. Low-frequency field-dependent Q-band Davies ENDOR spectra (black) of complex **2** with simulations of features arising from hyperfine interactions with $^{14}N_a$ (red) and ^{11}B (blue) overlaid. Asterisks above peaks in ENDOR near 12 MHz indicate the presence of RF artifacts arising from the 3rd harmonic of ^{59}Co ENDOR signals. Note: P is the quadrupole coupling tensor, and related to e^2qQ/h and η by $\frac{e^2Qq}{h} = 2I(2I-1)P_z$ and $\eta = \frac{P_x - P_y}{P_z}$, respectively. Acquisition parameters: temperature = 15 K; MW freq. = 34.046 GHz; MW pulse length ($\pi/2$, π) = 40 ns, 80 ns; RF pulse length = 15 μs; τ = 240 ns; shot repetition time (srt) = 2 ms. Simulation parameters: A($^{14}N_a$) = [9.2, 9.2, 12] MHz, e^2qQ/h($^{14}N_a$) = 1.2 MHz, η($^{14}N_a$) = 0; A(^{11}B) = [1.1, 1.1, 2.2] MHz, e^2qQ/h(^{11}B) = 1.2 MHz, η(^{11}B) = 0.

Moreover, features from a single class of ^{11}B with a small hyperfine coupling of $A(^{11}\text{B})$ = [1.1, 1.1, 2.2] MHz are resolved at all fields, which manifest as pairs of peaks centered at the ^{11}B Larmor frequency and split by the hyperfine coupling. Particularly in the ENDOR acquired at the high field edge corresponding to the molecular z-orientation, additional fine structure from the ^{11}B I = 3/2 nuclear quadrupole is also resolved and simulated with $e^2qQ/h(^{11}\text{B})$ = 1.2 MHz, $\eta(^{11}\text{B})$ = 0, indicating an axially symmetric (e.g. C_3) bonding environment at B.

In addition to the above ENDOR characterization, we performed Q-band HYSCORE experiments in order to more thoroughly evaluate couplings from ^{14}N and determine if couplings to the axial and equatorial ligands could be differentiated. HYSCORE is generally quite sensitive to highly anisotropic hyperfine couplings and quadrupolar nuclei and offers equivalent information on these couplings to that provided by ENDOR without some of the technical limitations at very low frequencies. The 2D nature of the FT spectra of this technique also separates features from strongly coupled and weakly coupled nuclei which would be overlapping in the 1D ENDOR data. A representative HYSCORE spectrum acquired at a field corresponding to the maximum of the EPR spectrum is presented in **Figure 7.7**. Other spectra and simulations at other fields are given in **Figures 7.24-7.28**.

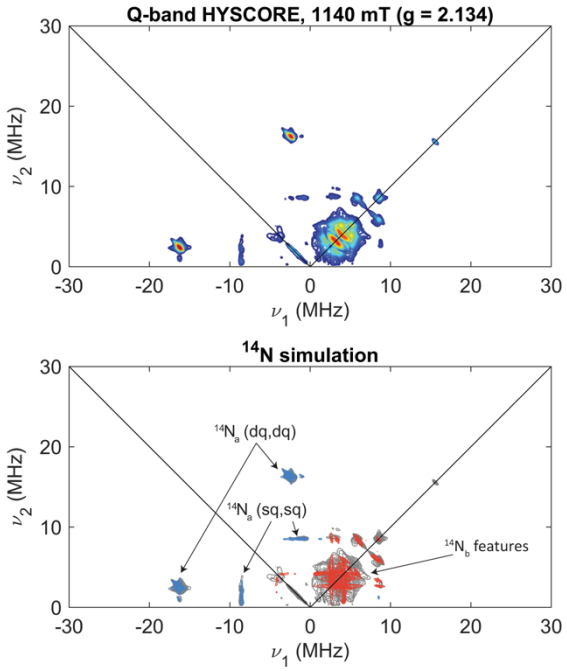

Figure 7.7. Q-band Hyperfine sublevel correlation (HYSCORE) spectrum of complex **2** acquired at 1140 mT (g = 2.134). The experimental data is plotted in color in the top panel, ranging from dark blue to red in increasing intensity. This same data is plotted in grey in the bottom panel, with simulations of a single coupling of class $^{14}N_a$ (blue) and coupling to four equivalent $^{14}N_b$ nuclei (red) overlaid. Acquisition parameters: temperature = 15 K; MW freq. = 34.046 GHz; MW pulse length ($\pi/2$, π) = 12 ns, 24 ns; τ = 100 ns; t_1 = t_2 = 100 ns; Δt_1 = Δt_2 = 16 ns; shot repetition time (srt) = 2 ms. Simulation parameters: A($^{14}N_a$) = [9.2, 9.2, 12] MHz, e^2qQ/h($^{14}N_a$) = 1.2 MHz, η($^{14}N_a$) = 0; A($^{14}N_b$) = [0.5, 0.5, 4] MHz, e^2qQ/h($^{14}N_b$) = 1.2 MHz, η($^{14}N_b$) = 0

Gratifyingly, the HYSCORE spectra at all fields exhibit features from a strongly coupled ^{14}N in the (−,+) quadrant which are well simulated using the same parameters as the $^{14}N_a$ class detected in the ENDOR, but also reveal additional intense features in the (+,+) quadrant from a highly anisotropic, relatively weakly coupled class of nitrogen with $A(^{14}N_b)$ = [0.5, 0.5, 4] MHz and nuclear quadrupole coupling parameters $e^2qQ/h(^{14}N_b)$ = 1.2 MHz, $\eta(^{14}N_b)$ = 0. Simulation of the HYSCORE data using different numbers of equivalent $^{14}N_a$ and $^{14}N_b$ required the use of 1($^{14}N_a$):4($^{14}N_b$) to reproduce the relative intensities of the distinct features arising from these two nitrogen classes (**Figures 7.24-7.28**), which allows assignment of $^{14}N_a$ and $^{14}N_b$ to the axial and equatorial $^{-}$CN-B(C_6F_5)$_3$ ligands, respectively.

Decomposition of the hyperfine tensors of these two classes of ^{14}N couplings yields $a_{iso}(^{14}N_a)$ = 10.1 MHz, $T(^{14}N_a)$ = [−0.9, −0.9, 1.8] MHz, and $a_{iso}(^{14}N_b)$ = 1.67 MHz, $T(^{14}N_b)$ = [−1.17, −1.17, 2.33] MHz. Using the same method used for estimation of the spin density at Co with calculated unit spin density in ^{14}N 2s (a_{iso}^0 = 1811 MHz) and $2p_z$ ($T_{2p_z}^0$ = [−63.6, −63.6, 127.2] MHz) orbitals[44] indicate that there is very little spin density localized at either class of nitrogen, with estimates for $^{14}N_a$ of ρ_{2s} ≈ 0.006 e^- and $\rho_{2p_z} \leq 0.014$ e^-, and $^{14}N_b$ of $\rho_{2s} \approx 0.001$ e^- and $\rho_{2p_z} \leq 0.018$ e^-. In this case, the estimates of ^{14}N $2p_z$ spin density represent upward bounds, as the through space dipolar hyperfine interaction with spin density localized at Co and C nuclei of the CN ligands certainly contributes significantly, and we have no experimental handle on the spin density at C in this complex. Given the relatively low estimate of spin density at Co ($\rho_{Co} \leq 0.489$ e^-) and dearth of other strongly coupled nuclei, it seems likely that a significant portion of spin is localized at C in all of the CN ligands.

CASSCF+NEVPT2 Calculations

To further probe effects on ligand field states, orbital compositions, and spin densities upon boronation, we performed CASSCF+NEVPT2 calculations on DFT-optimized structures of both $[Co(CN)_5]^{3-}$ and $[Co(CN\text{-}BH_3)_5]^{3-}$. Our previous work on both homoleptic and heteroleptic cyanometallates demonstrate the efficacy of BH_3 in mimicking the Lewis acidity and subsequent increase in ligand field strength afforded by $B(C_6F_5)_3$. Additionally, previous studies have demonstrated the accuracy of CASSCF+NEVPT2 in predicting the ligand field and charge transfer states of cyanometallates.[46] DFT optimizations were performed using the PBE0 functional and DKH-def2-TZVP basis set. All calculations utilized the approximate C_{4v} symmetry of the complexes, with the axial cyanide or isocyanoborate ligand coincident with the z-axis. Sample output files for both DFT optimizations and CASSCF-NEVPT2 calculations are given on page SX. For $[Co(CN)_5]^{3-}$, the equatorial M-C bond lengths

were well-reproduced. However, despite continuum solvation in MeCN, the axial M-C bond length was approximately 0.1 Å shorter than that reported for $[NEt_2(i\text{-}Pr)_2]_3[Co(CN)_5]$.[34] Therefore, the apical M-C bond length was constrained to the experimental distance to accurately reproduce excitation energies and ground state magnetic properties.

For both complexes, the CASSCF calculations considered all 10 quartets and 35 out of 40 doublets. The chosen active space consisted of the metal-based π-bonding orbitals ($e + b_2$), the metal-based σ-antibonding orbitals ($a_1 + b_1$), the ligand-based σ-bonding orbitals ($a_1 + b_1$), and the Co "double-shell" ($a_1 + e + b_2 + b_1$), giving a configuration of 11 electrons in 12 orbitals, CAS(11,12). The active space molecular orbitals for the ground state of both species are depicted in **Figure 7.8** and **Figure 7.9**, and ground state orbital percent compositions, occupancy numbers, and energies are given in **Table 7.2** and **Table 7.3**.

The quartet and doublet ligand field transitions and their oscillator strengths predicted by CASSCF+NEVPT2 are detailed in **Table 7.4** and **Table 7.5**. Deviations from experimental values for the boronated species likely stems from small variations in Lewis acidity for BH_3 versus $B(C_6F_5)_3$ and possibly, small effects from cation-Co interactions in the open apical position.[47] However, the deviations for both species are similar in magnitude, so the variations could stem from the uniquely high dependence of the electronic transitions of cyanometallates on both the MC and CN bond lengths.

Table 7.2. Ground state orbital occupancy numbers, energies, and percent compositions for $[Co(CN)_5]^{3-}$.

Orbital	Energy (eV)	Occupancy Number	% Co	% CN
CN σ (a_1)	−13.942	1.99245	29.4	70.6
CN σ (b_1)	−13.456	1.96026	49.4	50.6
M π (b_2)	−13.113	1.96617	90.1	9.9
M π (e)	−12.816	1.96624	92.5	7.5
M π (e)	−12.813	1.96622	92.5	7.5
M σ* (a_1)	−1.651	0.99329	85.7	14.3
M σ* (b_1)	9.946	0.05264	77.4	22.6
CN σ* + Co 4d (a_1)	23.485	0.03151	60.9	39.1
CN π* + Co 4d (b_2)	25.620	0.01555	72.8	27.2
CN π* + Co 4d (e)	27.103	0.02739	68.0	32.0
CN π* + Co 4d (e)	27.112	0.02738	68.0	32.0
CN σ* + Co 4d (b_1)	66.405	0.00090	71.5	28.5

Table 7.3. Ground state orbital occupancy numbers, energies, and percent compositions for $[Co(CN\text{-}BH_3)_5]^{3-}$.

Orbital	Energy (eV)	Occupancy Number	% Co	% CN-BH_3
CN σ (a_1)	−15.656	1.99126	30.8	69.2
CN σ (b_1)	−15.213	1.96087	49.3	50.7
M π (b_2)	−14.542	1.96541	89.5	10.5
M π (e)	−14.205	1.96538	91.6	8.4
M π (e)	−14.201	1.96356	91.5	8.5
M σ* (a_1)	−2.941	0.99377	83.8	16.2
M σ* (b_1)	8.672	0.05142	77.3	22.7
CN π* + Co 4d (b_2)	21.407	0.03237	59.5	40.5
CN σ* + Co 4d (a_1)	23.828	0.01604	70.4	29.6
CN π* + Co 4d (e)	24.547	0.02864	65.4	34.6
CN π* + Co 4d (e)	24.566	0.02862	65.4	34.6
CN σ* + Co 4d (b_1)	65.201	0.00086	70.8	29.2

CASSCF+NEVPT2 calculations properly predict blueshifted transitions for excitations involving orbitals of e symmetry as a result of enhanced π-backbonding upon Lewis acid coordination. Additionally, calculations predict the redshifted absorbance of the $^2A_1 \rightarrow {}^2B_1$ transition as a result of depressing the d_{x2-y2} to a greater extent relative to the d_{z2}. We observe a smaller blueshift in this transition. However, this could be due to ion pairing in the apical position or differential solvation between the BH_3 and $B(C_6F_5)$ adducts.

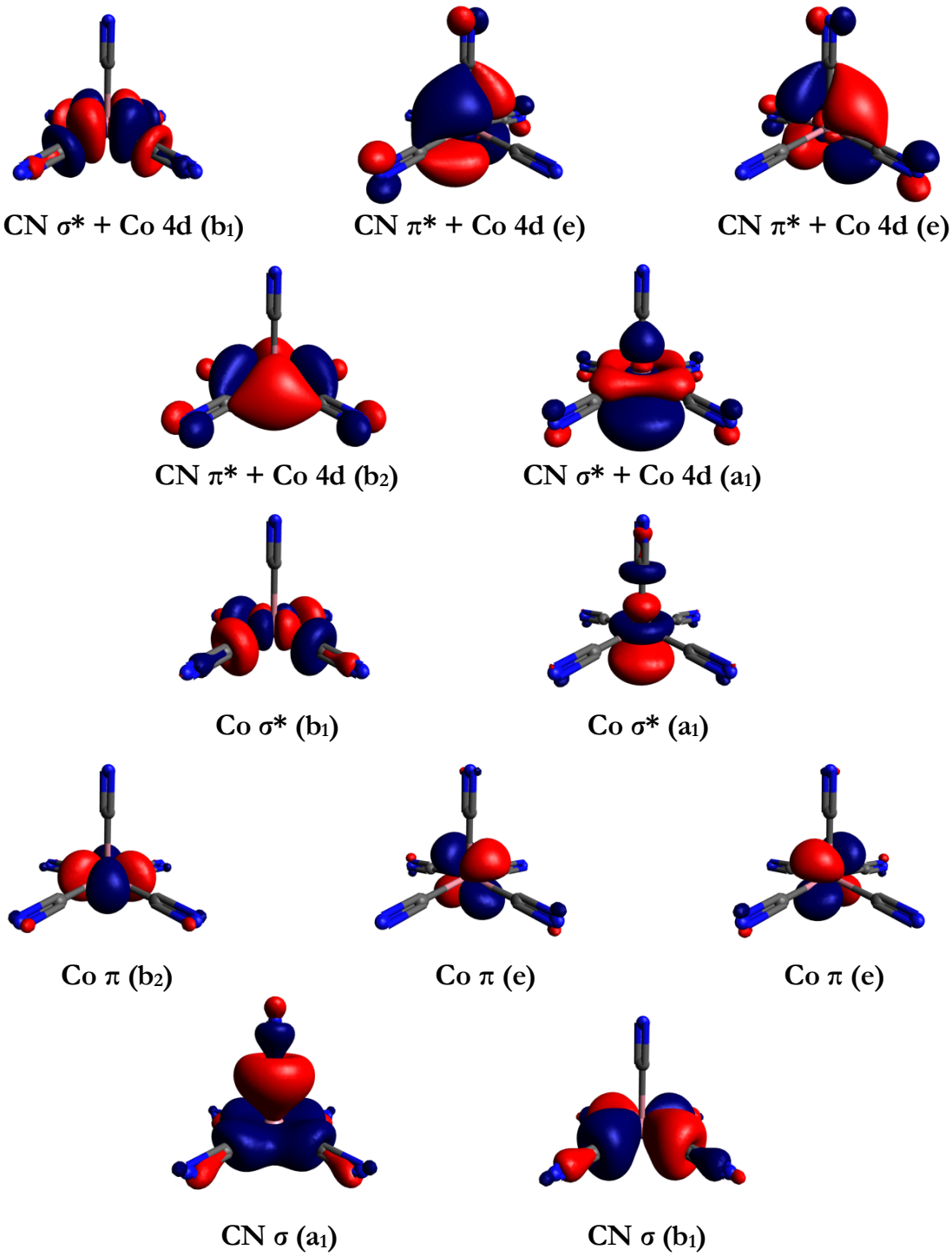

Figure 7.8. Active space molecular orbitals for CAS(11,12) of the doublet ground state of $[Co(CN)_5]^{3-}$. Calculations employed continuum solvation in MeCN.

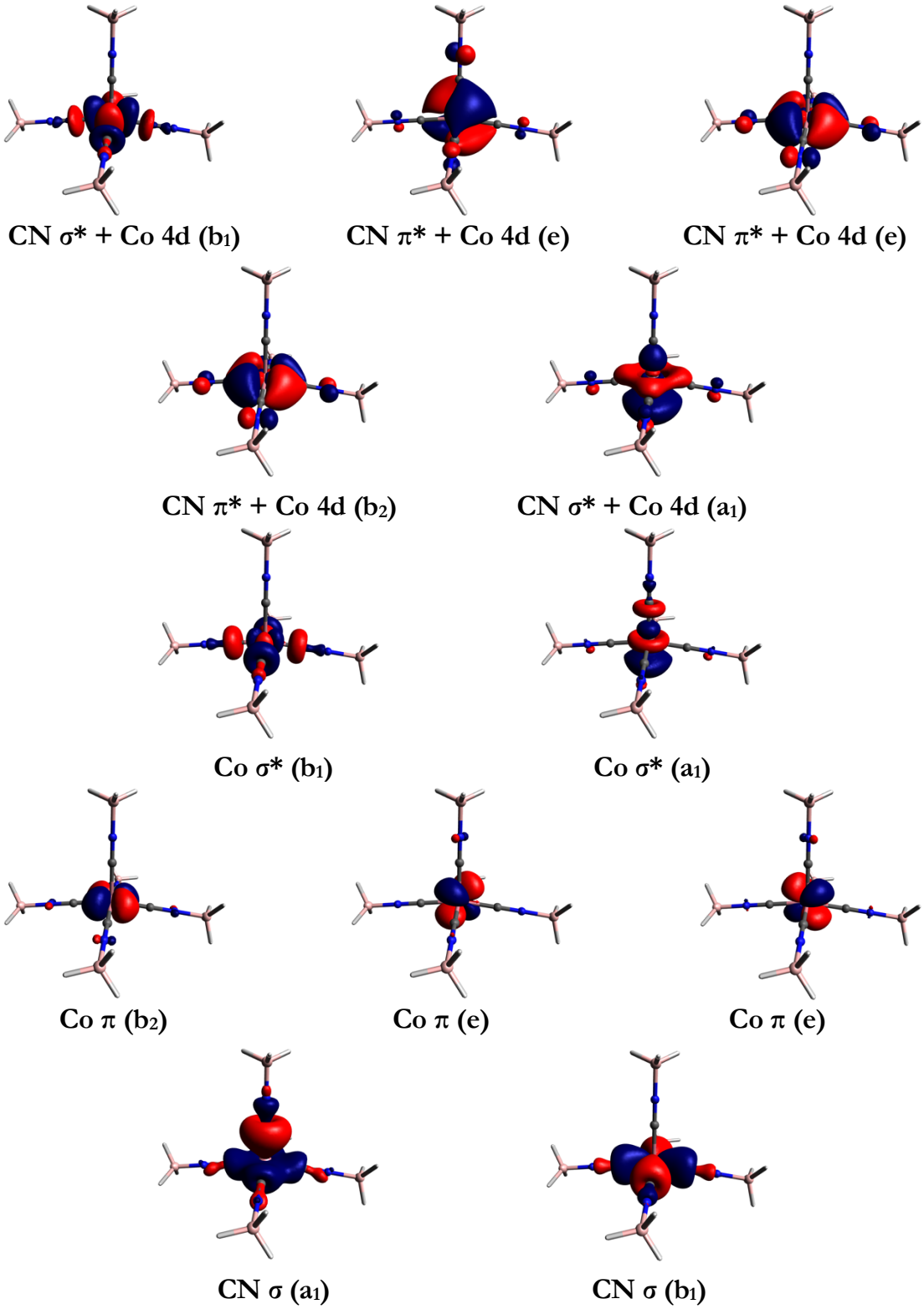

Figure 7.9. Active space molecular orbitals for CAS(11,12) of the doublet ground state of $[Co(CN\text{-}BH_3)_5]^{3-}$. Calculations employed continuum solvation in MeCN.

Table 7.4. State energies, principal transitions, and oscillator strengths of CASSCF+NEVPT2 calculations on $[Co(CN)_5]^{3-}$.

State	Principal Orbital Transition	Experiment [a] (cm^{-1})	CASSCF+ NEVPT2 (cm^{-1})	Oscillator Strength	Multiplicity
$^2A_1 \rightarrow {}^2E(a)$	$e(xz,yz) \rightarrow a_1(z^2)$	9,260	8,371.6	0.002067	2
$^2A_1 \rightarrow {}^2E(a)$	$e(xz,yz) \rightarrow a_1(z^2)$	---	8,387.6	0.00207	2
$^2A_1 \rightarrow {}^2B_2$	$b_2(xy) \rightarrow a_1(z^2)$		16,438.1	0.000000013	2
$^2A_1 \rightarrow {}^4E$	$e(xz,yz) \rightarrow b_1(x^2-y^2)$	15,290	18,878.5	---	4
$^2A_1 \rightarrow {}^4E$	$e(xz,yz) \rightarrow b_1(x^2-y^2)$	---	18,886.0	---	4
$^2A_1 \rightarrow {}^4A_2$	$b_2(xy) \rightarrow b_1(x^2-y^2)$	---	19,497.6	---	4
$^2A_1 \rightarrow {}^4B_2$ [b]	---	---	24,438.2	---	4
$^2A_1 \rightarrow {}^2B_1$	$a_1(z^2) \rightarrow b_1(x^2-y^2)$	23,419	26,355.0	0.000000944	2
$^2A_1 \rightarrow {}^4E$ [b]	---	---	30,223.2	---	4
$^2A_1 \rightarrow {}^4E$ [b]	---	---	30,257.4	---	4
$^2A_1 \rightarrow {}^2A_2$	$b_2(xy) \rightarrow b_1(x^2-y^2)$	---	31,664.0	0.000000134	2
$^2A_1 \rightarrow {}^2E(b)$	$e(xz,yz) \rightarrow b_1(x^2-y^2)$	30,120	33,391.9	0.0000654	2
$^2A_1 \rightarrow {}^2E(b)$	$e(xz,yz) \rightarrow b_1(x^2-y^2)$	---	33,392.6	0.0000656	2
$^2A_1 \rightarrow {}^2E(c)$	$e(xz,yz) \rightarrow b_1(x^2-y^2)$	---	33,679.6	0.00184	2
$^2A_1 \rightarrow {}^2E(c)$	$e(xz,yz) \rightarrow b_1(x^2-y^2)$	---	33,688.4	0.00179	2

[a]Reference 41

[b]Denotes double excitation to produce the quartet excited state

Table 7.5. State energies, principal transitions, and oscillator strengths from CASSCF+NEVPT2 calculations on $[Co(CN\text{-}BH_3)_5]^{3-}$.

State	Principal Orbital Transition	Experiment (cm^{-1})	CASSCF+ NEVPT2 (cm^{-1})	Oscillator Strength	Multiplicity
$^2A_1 \rightarrow {}^2E(a)$	$e(xz,yz) \rightarrow a_1(z^2)$	11,190	11,990.0	0.00184	2
$^2A_1 \rightarrow {}^2E(a)$	$e(xz,yz) \rightarrow a_1(z^2)$	---	12,024.8	0.00187	2
$^2A_1 \rightarrow {}^4E$	$e(xz,yz) \rightarrow b_1(x^2-y^2)$	17,700	19,597.3	---	4
$^2A_1 \rightarrow {}^4E$	$e(xz,yz) \rightarrow b_1(x^2-y^2)$	---	19,611.8	---	4
$^2A_1 \rightarrow {}^4A_2$	$b_2(xy) \rightarrow b_1(x^2-y^2)$	---	20,268.7	---	4
$^2A_1 \rightarrow {}^2B_2$	$b_2(xy) \rightarrow a_1(z^2)$	---	21,688.7	0.000000498	2
$^2A_1 \rightarrow {}^2B_1$	$a(z^2) \rightarrow b_1(x^2-y^2)$	24,600	23,974.0	0.000000105	2
$^2A_1 \rightarrow {}^4B_2$[a]	---	---	28,100.7	---	4
$^2A_1 \rightarrow {}^2A_2$	$b_2(xy) \rightarrow b_1(x^2-y^2)$	---	32,674.4	0.000000049	2
$^2A_1 \rightarrow {}^2E(b)$	$e(xz,yz) \rightarrow b_1(x^2-y^2)$	33,100	34,129.4	0.0000161	2
$^2A_1 \rightarrow {}^2E(b)$	$e(xz,yz) \rightarrow b_1(x^2-y^2)$	---	34,147.5	0.0000156	2
$^2A_1 \rightarrow {}^4E$[a]	---	---	34,290.3	---	4
$^2A_1 \rightarrow {}^4E$[a]	---	---	34,327.1	---	4
$^2A_1 \rightarrow {}^2E(c)$	$e(xz,yz) \rightarrow b_1(x^2-y^2)$	---	35,131.8	0.000547	2
$^2A_1 \rightarrow {}^2E(c)$	$e(xz,yz) \rightarrow b_1(x^2-y^2)$	---	35,137.4	0.000539	2

[a]Denotes double excitation to produce the quartet excited state

The EPR properties of both systems are reproduced accurately by SOC CASSCF+NEVPT2 calculations. Assuming 10 quartets and 35 doublets, the theoretical g tensor for $[Co(CN\text{-}BH_3)_5]^{3-}$ is g = [2.182, 2.183, 2.001]. This compares favorably to the experimental g-tensor for $[Co(CN\text{-}B(C_6F_5)_3)_5]^{3-}$, g = [2.152, 2.141, 2.003]. EPR parameters for the $[Co(CN)_5]^{3-}$ are also consistent, with g = [2.233, 2.234, 1.998] and g = [2.172, 2.172, 2.004] (the discrepancy for $g_{x,y}$ likely stems from measurements being conducted on the potassium salt of the complex or in aqueous solution).[7]

7.4. Conclusions

We have performed a systematic investigation of the effects of boronation on cobalt cyanide derivatives. Unlike isocyanide derivatives, isocyanoborates will allow researchers to effect predicted changes to the electronic structure of complexes while maintaining their formal charge, providing an avenue for meaningful comparisons in the electronic structures of isostructural species. Additionally, the opportunity to predictably alter the electronic structure of cobalt cyanide complexes provides a pathway for improving materials for cobalt-based sodium ion batteries, improving sensory materials for biologically relevant molecules, and structurally and electronically stabilizing otherwise difficult-to-isolate species. Additionally, the ability to predictably shift voltages for coordinating ligands allows researchers to estimate thermodynamic quantities that were previously inaccessible, as we have demonstrated with reliably estimating the $Co^{III/II}$ formal potential. To our knowledge, this is the first example of pulsed EPR analysis of a pentacyanocobaltate derivative, where HYSCORE spectroscopy demonstrates differential spin delocalization for axial versus equatorial ^{14}N, with greater spin density residing on the axial N. DFT optimizations coupled with CASSCF+NEVPT2 calculations reliably predict the effects of Lewis acid coordination on the ligand field transitions and ground-state magnetic properties for both the base and boronated species.

7.5. Experimental

General

Potassium hexacyanocobaltate(III) ($K_3[Co(CN)_6]$) (Sigma-Aldrich), bis(triphenylphosphine)iminium chloride (PPNCl) (Sigma-Aldrich), and cobaltocene (Sigma-Aldrich) were used as received. Deuterated solvents were dried and stored over 3 A molecular sieves in a nitrogen-filled glove box. Tetrabutylammonium hexacyanocobaltate and bis(triphenylphosphine)iminium hexacyanocobaltate were synthesized according to literature precedent.[48,49] All NMR spectra were collected on a Varian 400 MHz spectrometer or Bruker 400 MHz spectrometer (δ in ppm, m: multiplet, s: singlet, d: doublet, t: triplet, pt: pseudo- triplet). NMR spectra were collected on either a Varian 400 MHz spectrometer or Bruker 400 MHz spectrometer (δ in ppm, m: multiplet, s: singlet, d: doublet, t: triplet, pt: pseudo-triplet). ^{13}C NMR and ^{31}P NMR were ^{1}H decoupled. ^{11}B NMR spectra were externally referenced to 85% H_3PO_4, ^{19}F NMR spectra were externally referenced to neat $CFCl_3$, and ^{11}B NMR were internally referenced to 15% $BF_3{\cdot}Et_2O$. UV-visible-NIR spectra were recorded on either a Cary 500 UV-Vis-NIR or HP 8453 spectrophotometer. Infrared spectra were recorded on a Thermo Scientific Nicolet iS5 FT-IR spectrometer with an iD5 ATR diamond. Low temperature luminescence spectra were recorded on a Melles-Griot 13 FOS 200 spectrometer coupled to a fiber optic cable which collected sample luminescence. Samples were excited with a 365 nm Thorlabs, Inc. UV LED (M365L1) and Thorlabs, Inc. LED driver (LEDD1). A 475 nm long pass filter was used to isolate the luminescence signal. An Edwards T-Station turbo vacuum pump was used to evacuate samples. Samples were cooled using a CTI-Cryogenics Model 22 refrigerator. Voltammograms were recorded on a Gamry 600 Reference potentiostat with a glassy carbon working electrode, an $Ag^{+/0}$ quasireference electrode, and a platinum counter electrode. Electrochemical impedance spectroscopy was used to determine the internal cell resistance, and 85% of the internal cell resistance was compensated for using electronic

compensation. Solid-state Raman spectra were collected using either a coherent Innova argon ion laser with a 488 nm line, a Spex 0.75 m spectrograph, and a Horiba thermoelectrically cooled CCD detector or an Ar-ion laser with a 457.9 nm excitation line. $CHCl_3$ was used as a calibration standard for the low energy Raman shift region, and CH_3CN was used as a calibration standard for the cyanide stretching region.

Luminescence decay kinetics were recorded using 266 nm 8 ns excitation pulses from the fourth harmonic of a Q-switched Nd:YAG laser (Spectra Physics Quanta-Ray Pro). Luminescence was collected using reflective optics, focused onto the entrance slit of a DH-10 double 100 mm spectrophotometer (Jobin Yvon), and detected using an R928 photomultiplier tube (Hamamatsu). The photomultiplier current was amplified and recorded using a Compuscope 85G transient digitizer (Gage Applied Inc) controlled with Labview software (National Instruments).

Electron Paramagnetic Resonance Spectroscopy

Continuous wave X-band EPR spectra were obtained on a Bruker EMX spectrometer on 2-2.7 mM solutions prepared as frozen glasses in 2-MeTHF. Pulse EPR spectroscopy: All pulse Q-band (~34 GHz) EPR, electron nuclear double resonance (ENDOR), and hyperfine sublevel correlation spectroscopy (HYSCORE) experiments were acquired using a Bruker ELEXSYS E580 pulse EPR spectrometer and a Bruker D2 pulse ENDOR resonator. Temperature control was achieved using an ER 4118HV-CF5-L Flexline Cryogen-Free VT cryostat manufactured by ColdEdge equipped with an Oxford Instruments Mercury ITC temperature controller.

Pulse ENDOR spectra were acquired using the Davies pulse sequence ($\pi - T_{RF} - \pi_{RF} - t_{RF} - \pi/2 - \tau - \pi -$ echo), where t_{RF} is the delay between mw pulses and RF pulses, π_{RF} is the length of the RF pulse

and the RF frequency is randomly sampled during each pulse sequence. For all ENDOR scans the same t_{RF} of 2 μs was used, all other acquisition parameters are detailed in the caption for each ENDOR figure. For Q-band ^{14}N, ^{11}B ENDOR experiments in the range from 0-25 MHz, an LP-2500 low-pass filter (Vectronics, Starkville, MS) with a cutoff frequency of 35 MHz was attached in-line with the RF amplifier and ENDOR coils in order to eliminate contributions from ^{1}H harmonics in the RF region of interest.

Pulse HYSCORE spectra were acquired using the 4-pulse sequence ($\pi/2-\tau-\pi/2-t_1-\pi-t_2-\pi/2$ − echo), where τ is a fixed delay, while t_1 and t_2 are independently incremented by Δ_{t_1} and Δ_{t_2}, respectively. The time domain data was baseline-corrected (third-order polynomial) to eliminate the exponential decay in the echo intensity, apodized with a Hamming window function, zero-filled to eight-fold points, and fast Fourier-transformed to yield the 2-dimensional frequency domain.

In general, the ENDOR spectrum for a given nucleus with spin I= 1⁄2 (^{19}F) coupled to the S = 1⁄2 electron spin exhibits a doublet at frequencies,

$$\nu_{\pm} = \left|\frac{A}{2} \pm \nu_N\right| \tag{7.1}$$

where $\nu_{\pm}$ is the nuclear Larmor frequency and A is the hyperfine coupling. For nuclei with $I \geq 1$ (^{14}N, ^{11}B), an additional splitting of the $\nu_{\pm}$ manifolds is produced by the nuclear quadrupole interaction (P).

$$\nu_{\pm,m_I} = \left|\nu_N \pm \frac{3P(2m_I-1)}{2}\right| \tag{7.2}$$

In HYSCORE spectra, these signals manifest as cross-peaks or ridges in the 2-D frequency spectrum which are generally symmetric about the diagonal of a given quadrant. This technique allows hyperfine

levels corresponding to the same electron-nuclear submanifold to be differentiated, as well as separating features from hyperfine couplings in the weak-coupling regime ($|A| < 2|\nu_I|$) in the (+,+) quadrant from those in the strong coupling regime ($|A| > 2|\nu_I|$) in the (−,+) quadrant. The (−,−) and (+,−) quadrants of these frequency spectra are symmetric to the (+,+) and (−,+) quadrants, thus typically only two of the quadrants are typically displayed in literature. For systems with appreciable hyperfine anisotropy in frozen solutions or solids, HYSCORE spectra typically do not exhibit sharp cross peaks, but show ridges that represent the sum of cross peaks from selected orientations at the magnetic field position at which the spectrum is collected. The length and curvature of these correlation ridges allow for the separation and estimation of the magnitude of the isotropic and dipolar components of the hyperfine tensor, as shown in **Figure 7.10**.

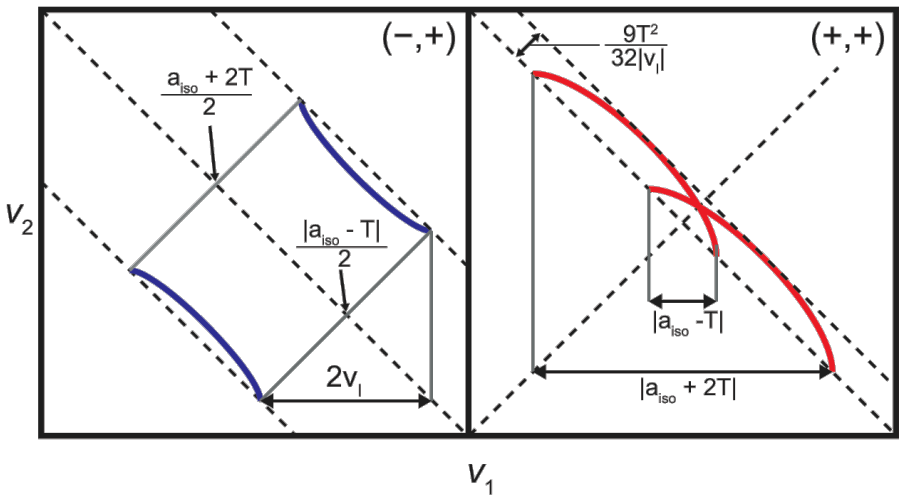

Figure 7.10. HYSCORE patterns for an $S = 1/2$, $I = 1/2$ spin system with an axial hyperfine tensor which contains isotropic (a_{iso}) and dipolar (T) contributions. Blue correlation ridges represent the strong coupling case; red correlation ridges represent the weak coupling case.

For systems coupled to nuclei with $I = 1$, such as ^{14}N, the double-quantum (dq) peaks are often the most intense feature. These cross-peaks are defined by the following equations,

$$\nu_\alpha = \pm 2\sqrt{(\upsilon_I + A/2)^2 + K^2(3+\eta^2)}$$
$$\nu_\beta = \pm 2\sqrt{(\upsilon_I - A/2)^2 + K^2(3+\eta^2)} \quad (7.3)$$

where $K = e^2qQ/4\hbar$. For weakly coupled nuclei ($A < 2\upsilon_I$) ν_α and ν_β are both positive, appearing in the (+,+) quadrant, while for strongly coupled nuclei ($A < 2\upsilon_I$) they will show up in the (−,+) quadrant. In the intermediate coupling regime where $A \approx 2\upsilon_I$, peaks will often appear in both the (+,+) and (−,+) quadrants of the HYSCORE spectrum.

All EPR spectra (CW, ENDOR, HYSCORE) were simulated using the EasySpin simulation toolbox (version 5.2.28)[50] with Matlab 2019 using the following Hamiltonian,

$$\hat{H} = \mu_B \vec{B}_0 g \hat{S} + \mu_N g_N \vec{B}_0 \hat{I} + h\hat{S} \cdot \boldsymbol{A} \cdot \hat{I} + h\hat{I} \cdot \boldsymbol{P} \cdot \hat{I} \quad (7.4)$$

n this expression, the first term corresponds to the electron Zeeman interaction term where μ_B is the Bohr magneton, g is the electron spin g-value matrix with principle components g = [gxx gyy gzz], and $\hat{S}$ is the electron spin operator; the second term corresponds to the nuclear Zeeman interaction term where μ_N is the nuclear magneton, g_N is the characteristic nuclear g-value for each nucleus (e.g. ^{19}F, ^{14}N, ^{11}B) and $\hat{I}$ is the nuclear spin operator; the third term corresponds to the electron-nuclear hyperfine term, where $\boldsymbol{A}$ is the hyperfine coupling tensor with principle components $\boldsymbol{A}$ = [Axx, Ayy, Azz]; and for nuclei with $I \geq 1$, the final term corresponds to the nuclear quadrupole (NQI) term which arises from the interaction of the nuclear quadrupole moment with the local electric field gradient (efg) at the nucleus, where $\boldsymbol{P}$ is the quadrupole coupling tensor. In the principle axis system (PAS), $\boldsymbol{P}$ is traceless and parametrized by the quadrupole coupling constant $e^2Qq/$h and the asymmetry parameter η such that,

$$\boldsymbol{P} = \begin{pmatrix} P_{xx} & 0 & 0 \\ 0 & P_{yy} & 0 \\ 0 & 0 & P_{zz} \end{pmatrix} = \frac{e^2Qq/h}{4I(2I-1)} \begin{pmatrix} -(1-\eta) & 0 & 0 \\ 0 & -(1+\eta) & 0 \\ 0 & 0 & 2 \end{pmatrix} \quad (7.5)$$

where $\frac{e^2Qq}{h} = 2I(2I-1)P_{zz}$ and $\eta = \frac{P_{xx}-P_{yy}}{P_{zz}}$. The asymmetry parameter may have values between 0 and 1, with 0 corresponding to an electric field gradient with axial symmetry and 1 corresponding to a fully rhombic efg.

The orientations between the hyperfine and NQI tensor principle axis systems and the g- matrix reference frame are defined by the Euler angles (α, β, γ), with rotations performed within the zyz convention where α rotates xyz counterclockwise about the z-axis to give x'y'z', β rotates x'y'z counterclockwise about the y'-axis to give x",y",z", γ rotates xyz counterclockwise about the z"- axis to give the final frame orientation.

Synthesis:

Bis(triphenylphosphine)iminium hexacyanocobaltate(III) $(PPN)_3[Co(CN)_6]$

A solution of bis(triphenylphosphine)iminium chloride (5.20 g, 0.009 mol) was added to a solution of potassium hexacyanocobaltate $K_3[Co(CN)_6]$ (1.00 g, 0.003 mol). A colorless precipitate immediately formed. The mixture was stirred for one hour, after which it was filtered. The solid was washed extensively with water followed by diethyl ether. The compound was then dried in vacuo overnight to yield a colorless powder (4.394 g, 79.8%). Elem. Anal. (%) found (calc'd) for $C_{114}H_{90}N_9P_6$ ($(PPN)_3[Co(CN)_6]$): C, 73.20 (74.79); H, 5.00 (4.96); N, 6.71 (6.89). ^{1}H NMR (400 MHz, CD_3CN) δ 7.44-7.67 (m, 30H, CH_{Ph}); ^{31}P NMR (162 MHz, CD_3CN) δ 20.8; ^{13}C NMR (100 MHz, CD_3CN).

Tetrabutylammonium/Bis(triphenylphosphine)iminium hexakisisocyanotris(pentafluorophenyl)boratocobaltate(III) (TBA/PPN)$_3$[Co(CN-B(C_6F_5)$_3$)$_6$]:

A solution of (TBA)$_3$[Co(CN)$_6$] (0.102 g, 0.11 mmol) in DCM was added dropwise to a solution of 6.2 equivalents of B(C_6F_5)$_3$ (0.350 g, 0.68 mmol) in DCM (about five mL total). The solution was allowed to crystallize overnight at −20 °C to yield colorless crystals. The solution was decanted to isolate the solid, and another 5 mL of DCM was added. This solution was shaken and placed in the freezer for one hour. The solution was decanted, and the resulting solid was washed with Et_2O (3 x 5 mL). The solid was then washed with hexanes (10 mL) and dried *in vacuo* to yield a colorless powder. The PPN salt of this compound was synthesized using the same procedure. Elem. Anal. (for TBA salt) (%) found (calc'd) for $C_{162}H_{108}B_6F_{90}N_9Co$ ((TBA)$_3$[Co(CN-B(C_6F_5)$_3$)$_6$]): C, 47.99 (48.47); H, 2.56 (2.71); N, 3.09 (3.14). ^{11}B NMR (128 MHz, CD_3CN) δ -12.0; ^{19}F NMR (376 MHz, CD_3CN) δ -133.4 (d, J_{FF} = 16.9 Hz), -161.9 (pt, J_{FF} = 19.6 Hz), -167.5 (pt, J_{FF} = 17.7 Hz); ^{1}H NMR (400 MHz, CD_3CN) δ 3.07 (t, 2H, CH_{but}, J_{HH} = 8.7 Hz), 1.59 (pquint, 2H, CH_{but}), 1.34 (psextet, 2H, CH_{but}), 0.95 (t, 3H, CH_{but}, J_{HH} = 7.3 Hz).

Bis(tetrabutylammonium/PPN)cobaltocenium pentakisisocyanotris(pentafluorophenyl)boratocobaltate(II) (TBA/PPN)$_2$($CoCp_2$)[Co(CN-B(C_6F_5)$_3$)$_5$]:

(PPN)$_3$[Co(CN-B(C_6F_5)$_3$)$_6$] (0.441 g, 0.09 mmol) was combined with cobaltocene (0.017 g, 0.09 mmol) in DCM. An immediate color change from colorless to yellow was observed. After fifteen minutes, the solution was evaporated, the resulting solid was washed with 3 x 5 mL of diethyl ether, and dried in vacuo to yield (PPN)$_2$($CoCp_2$)[Co(CN-B(C_6F_5)$_3$)$_5$)] (0.27 g, 75.5%). Elem. Anal. (%) found (calc'd) for $C_{137}H_{82}B_5F_{75}Co_2N_7$ ((TBA)$_2$($CoCp_2$)[Co(CN-B(C_6F_5)$_5$)$_6$]): C, 47.83 (48.07); H, 2.29 (2.41); N, 2.90 (2.86).

NMR Spectra

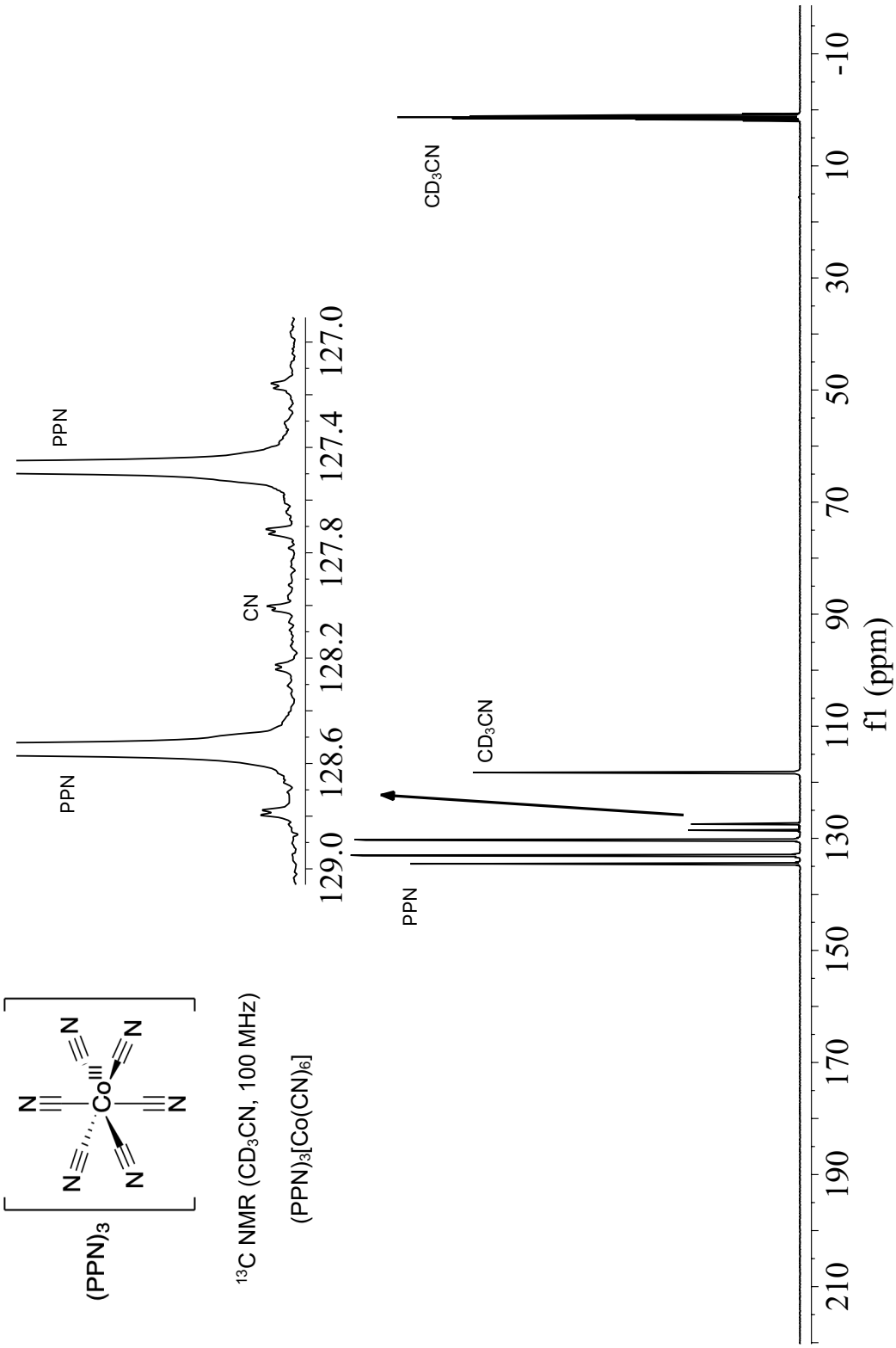

Figure 7.11. ^{13}C NMR spectrum of $(PPN)_3[Co(CN)_6]$ in CD_3CN.

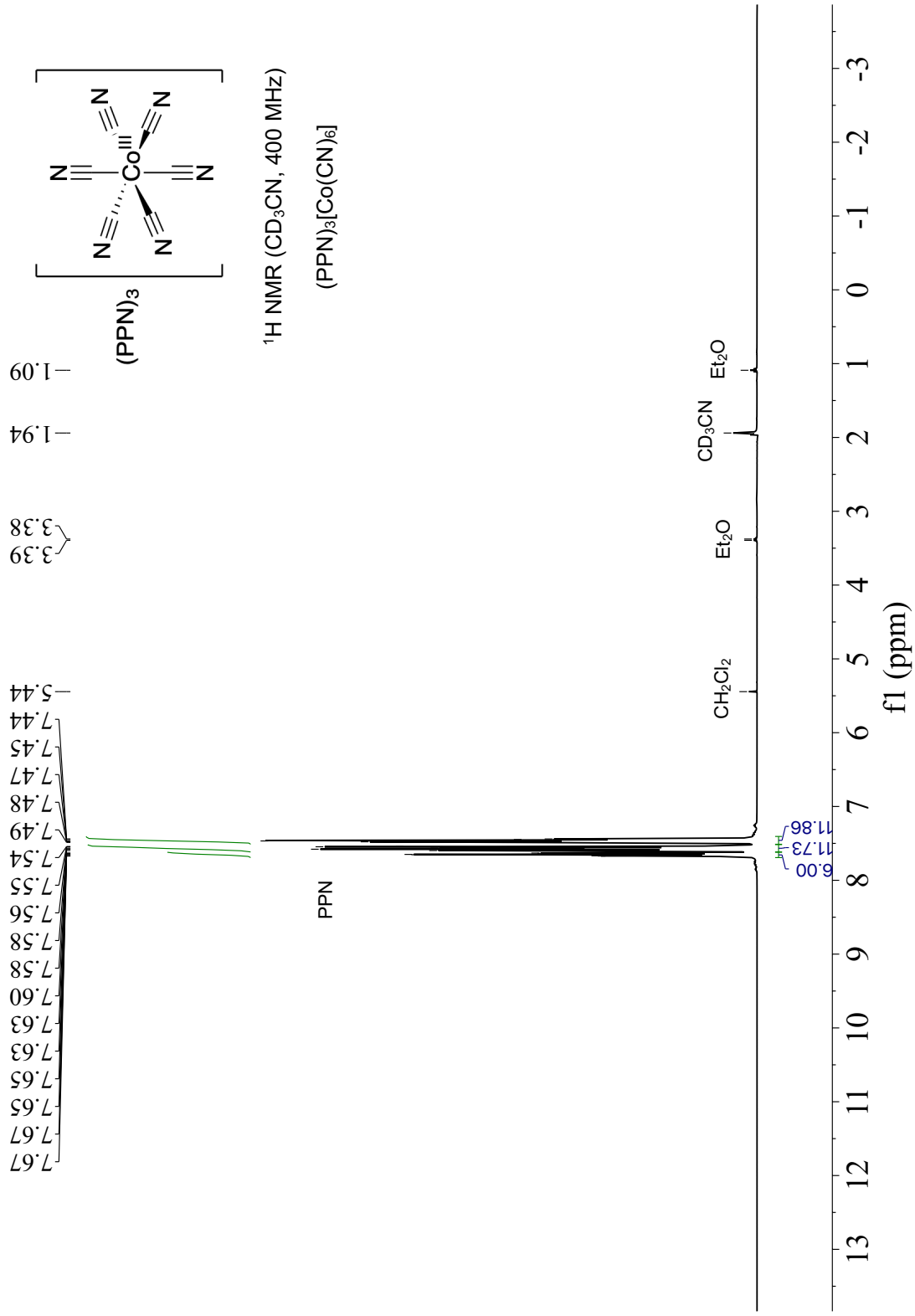

Figure 7.12. ^{1}H NMR spectrum of $(PPN)_3[Co(CN)_6]$ in CD_3CN.

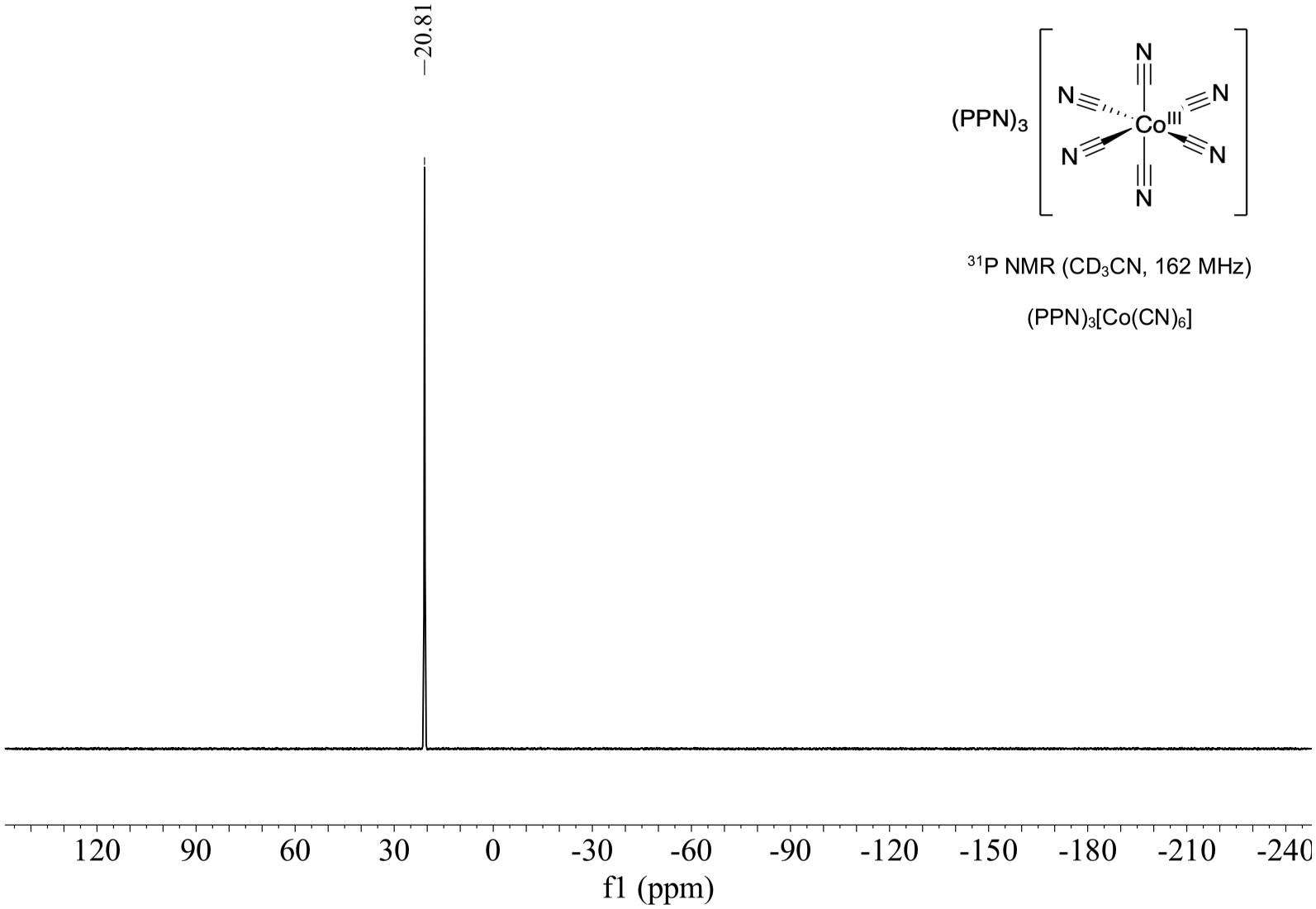

Figure 7.13. ^{31}P NMR spectrum of $(PPN)_3[Co(CN)_6]$ in CD_3CN.

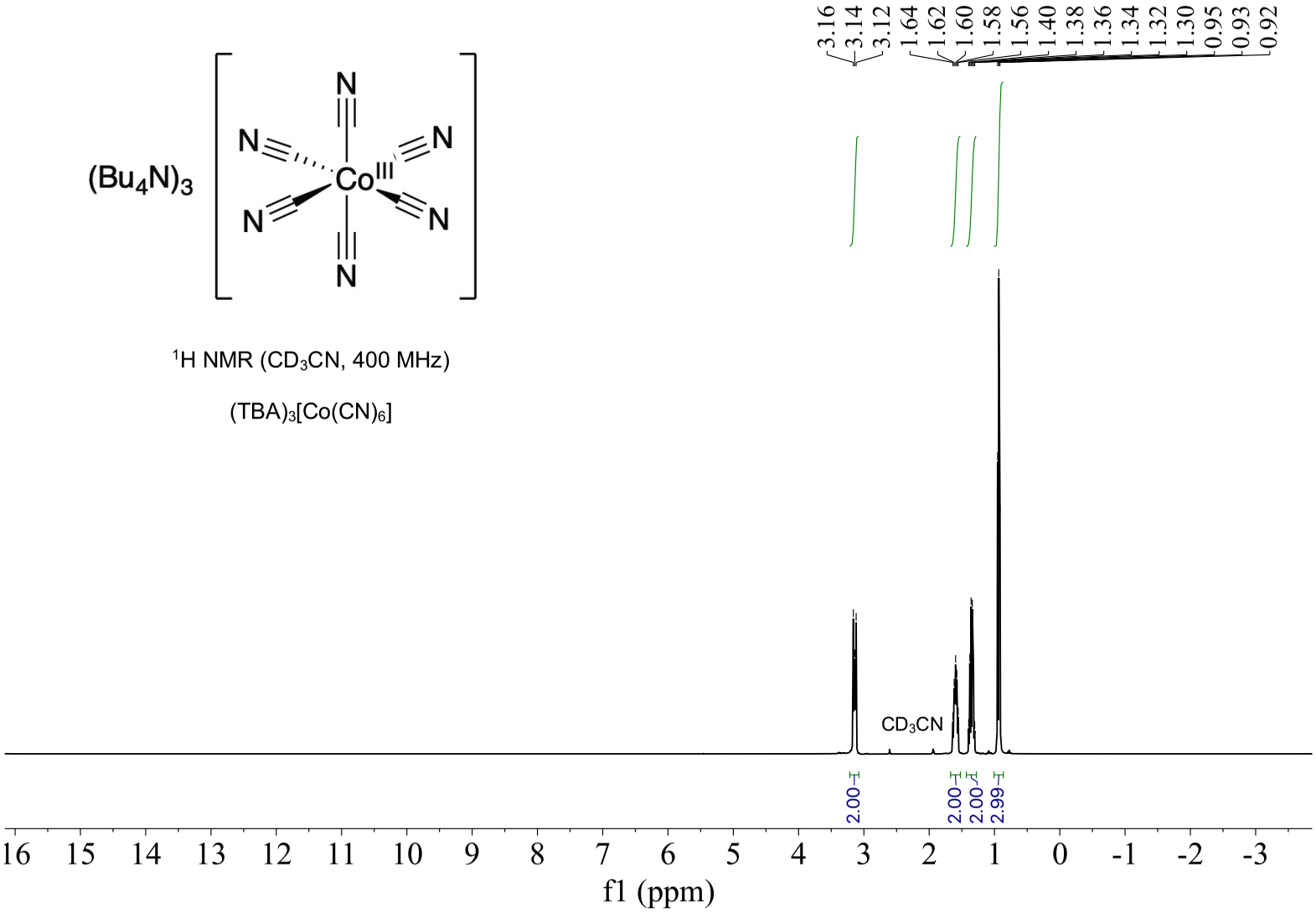

Figure 7.14. ^{1}H NMR spectrum of $(TBA)_3[Co(CN)_6]$ in CD_3CN.

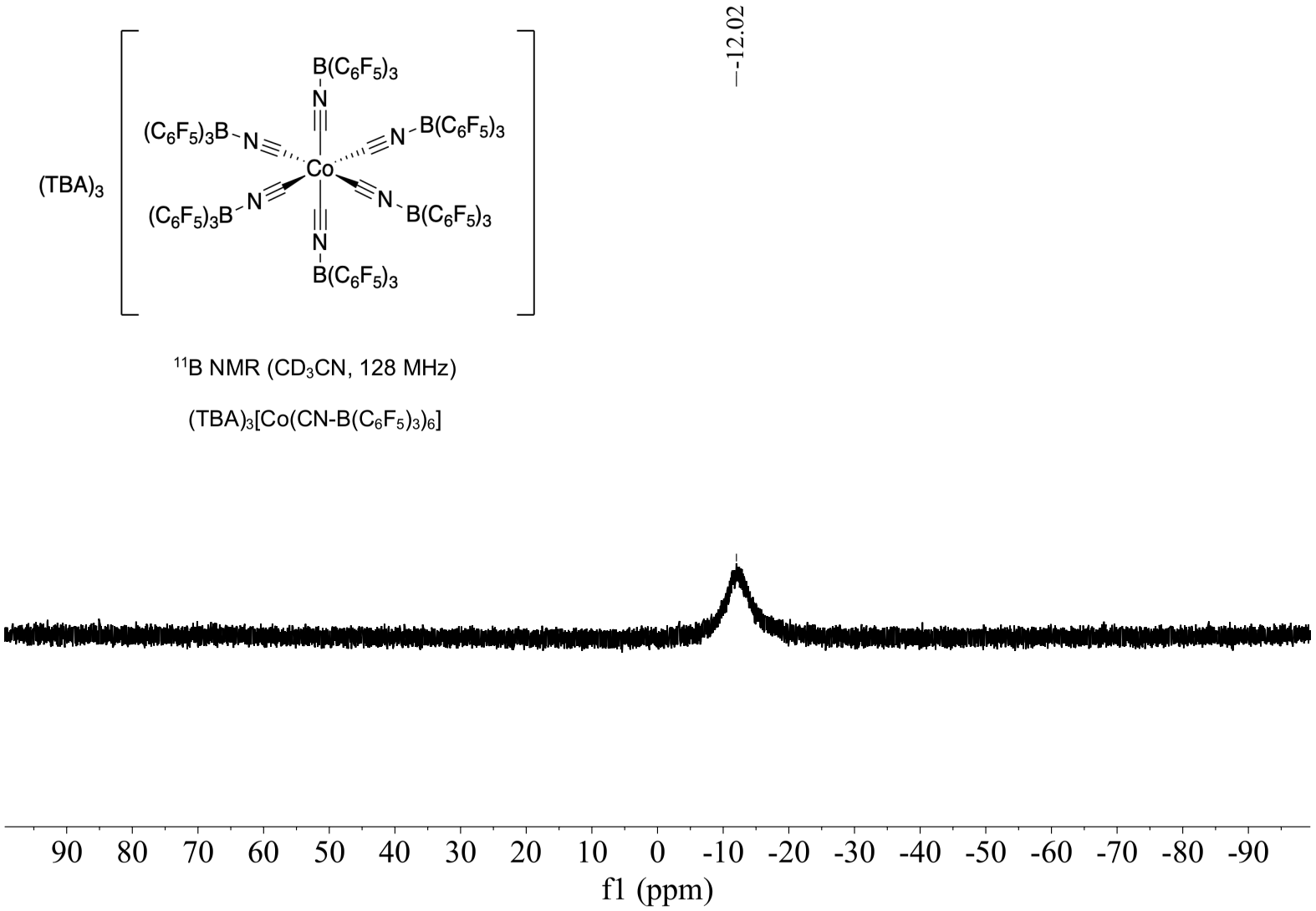

Figure 7.15. ^{11}B NMR spectrum of $(TBA)_3[Co(CN\text{-}B(C_6F_5)_3)_6]$ in CD_3CN.

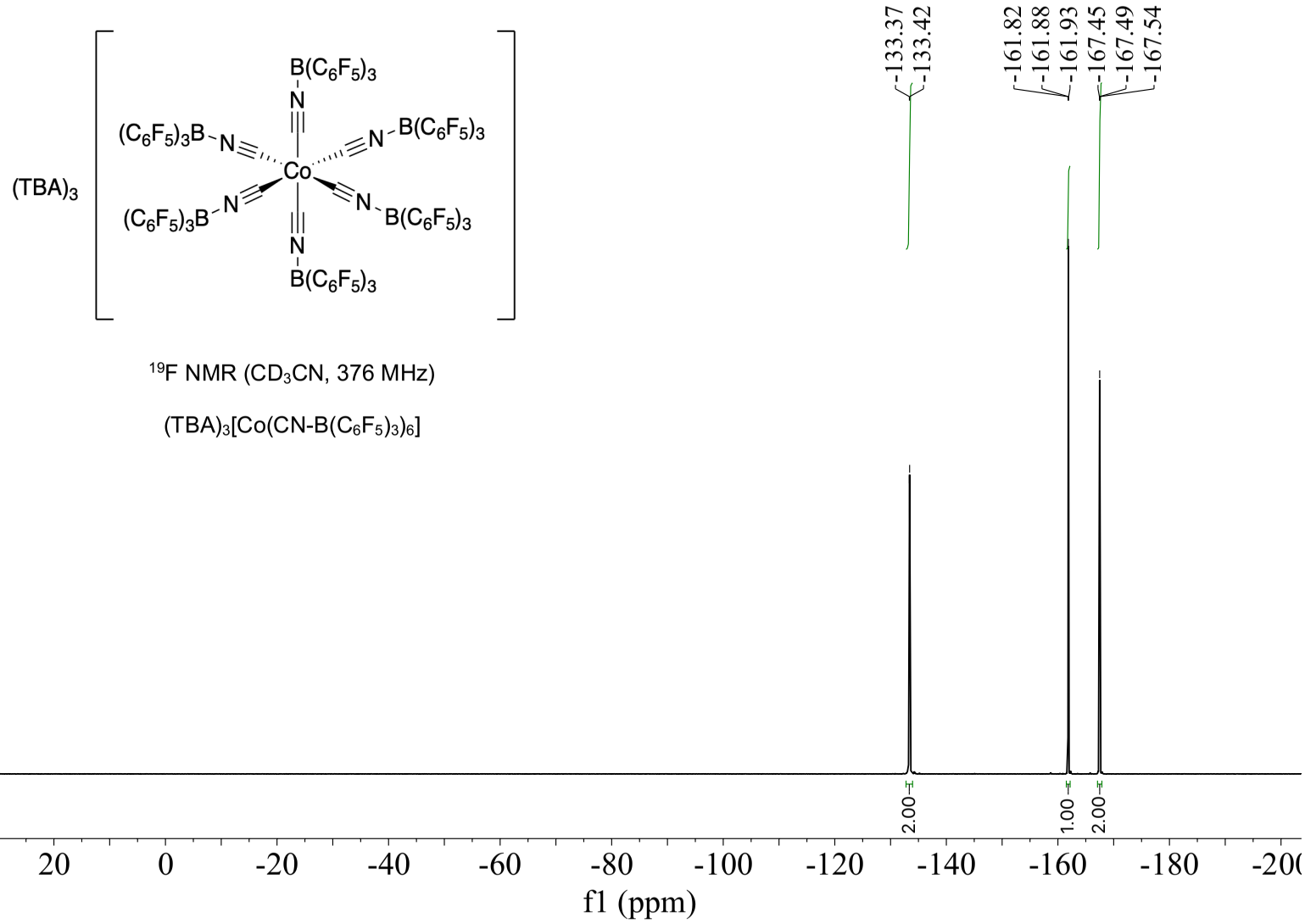

Figure 7.16. ^{19}F NMR spectrum of $(TBA)_3[Co(CN\text{-}B(C_6F_5)_3)_6]$ in CD_3CN.

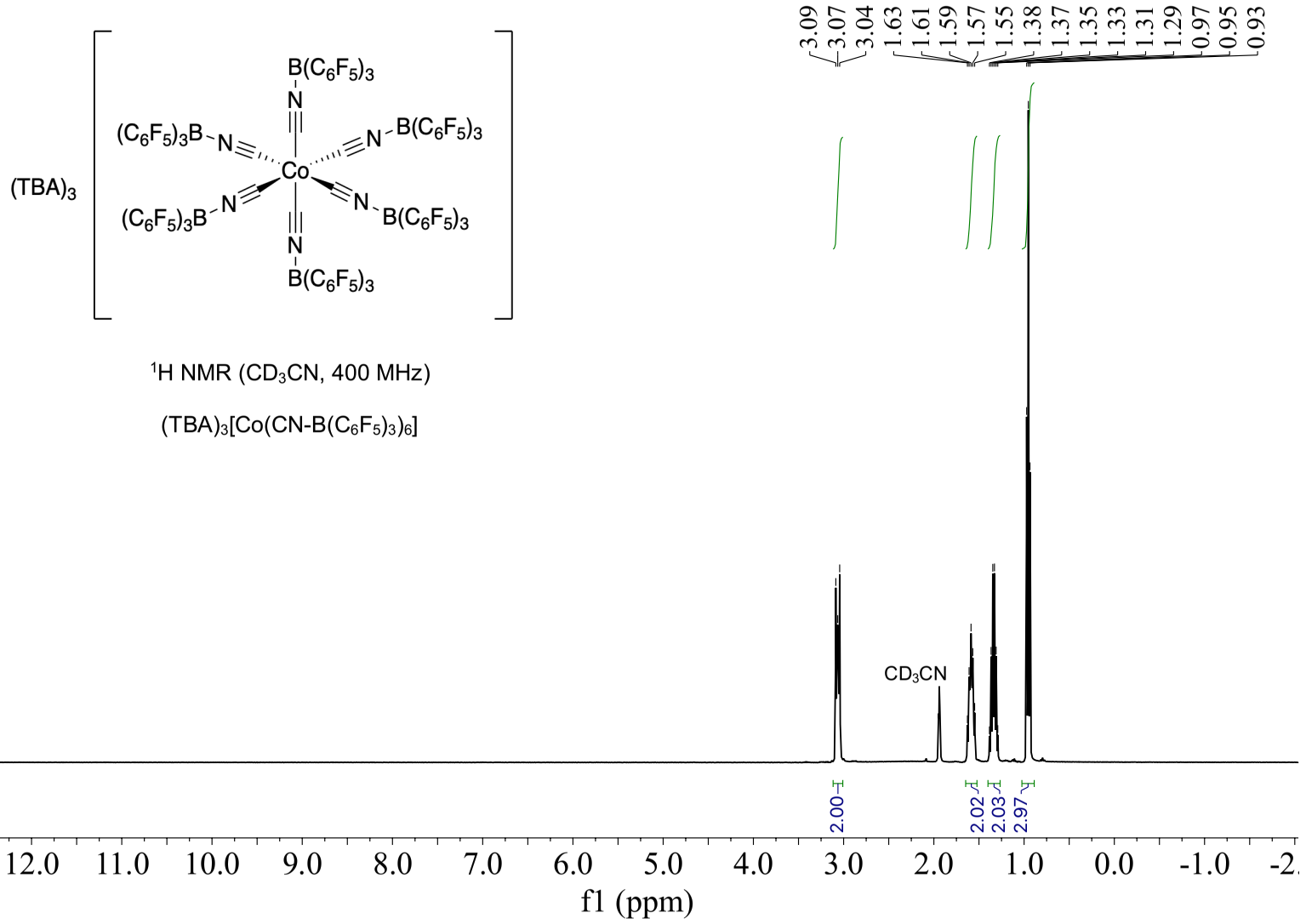

Figure 7.17. ^{1}H NMR spectrum of $(TBA)_3[Co(CN\text{-}B(C_6F_5)_3)_6]$ in CD_3CN.

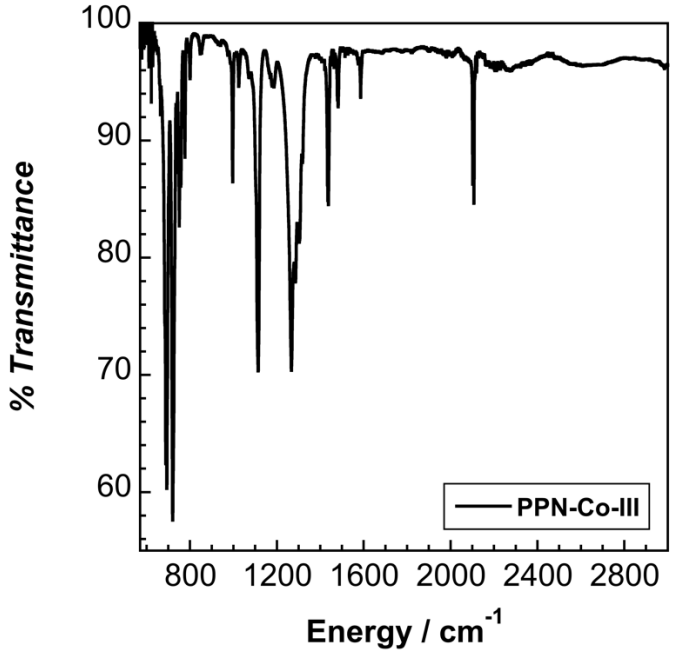

Figure 7.18. Solid state ATR-IR spectrum of $(PPN)_3[Co(CN)_6]$.

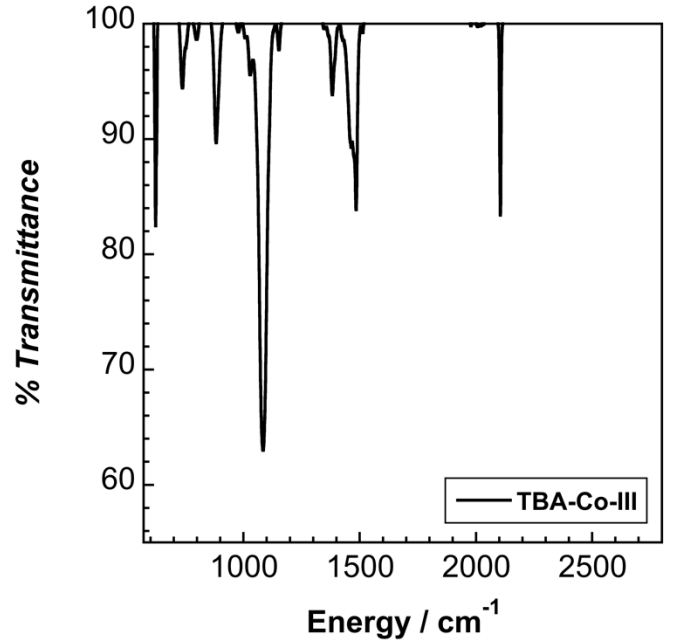

Figure 7.19. Solid state ATR-IR spectrum of $(TBA)_3[Co(CN)_6]$.

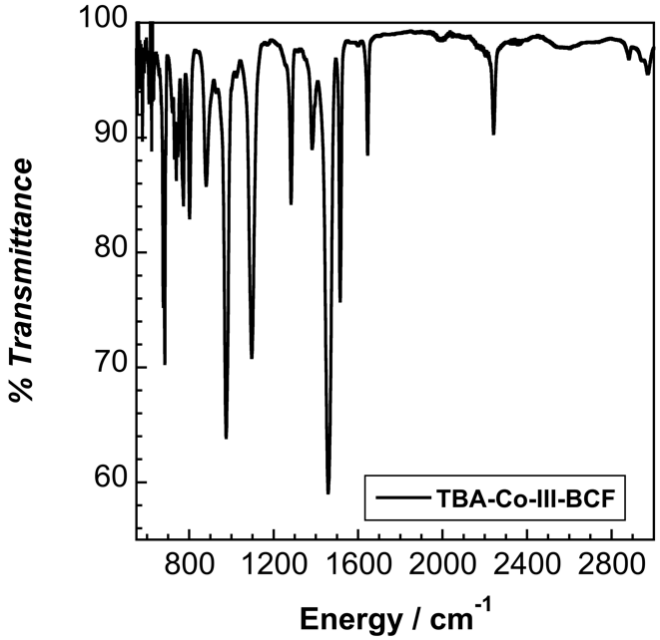

Figure 7.20. Solid state ATR-IR spectrum of $(TBA)_3[Co(CN\text{-}B(C_6F_5)_3)_6]$

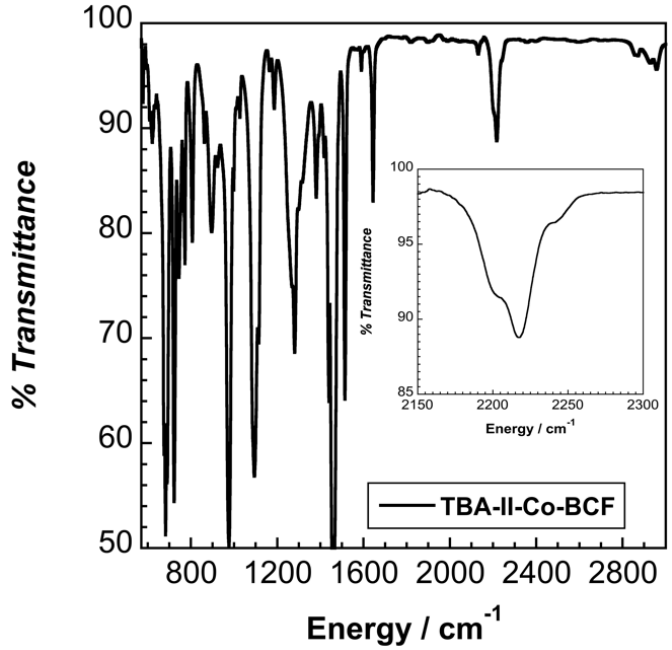

Figure 7.21. Solid state ATR-IR spectrum of $(PPN)_2(CoCp_2)[Co(CN\text{-}B(C_6F_5)_3)_5]$.

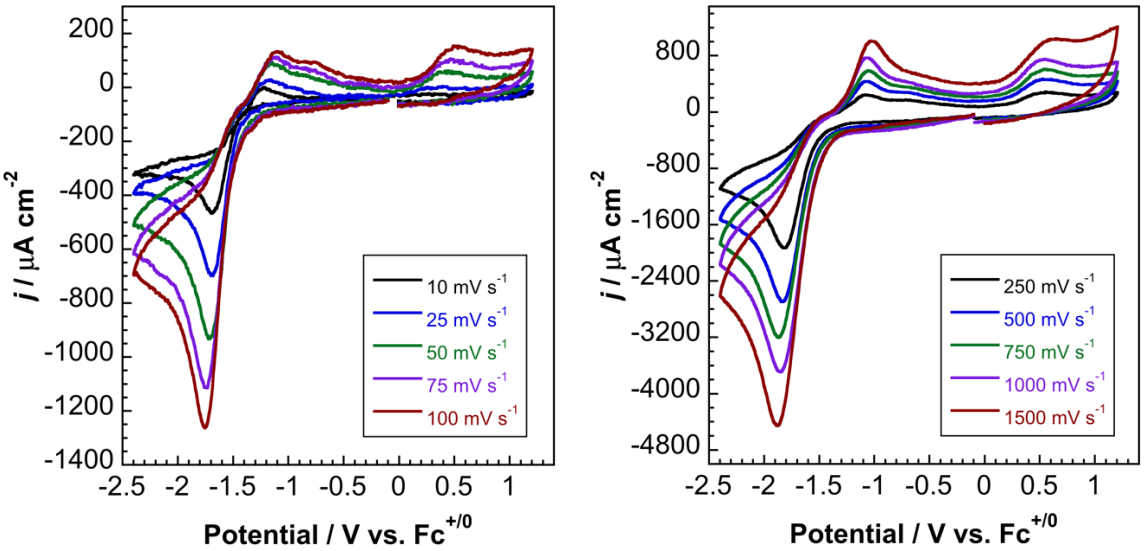

Figure 7.22. Scan rate dependence data for the $Co^{III/II}$ reduction of $(TBA)_3[Co(CN\text{-}B(C_6F_5)_3)_6]$ in MeCN with 0.1 M $TBAPF_6$.

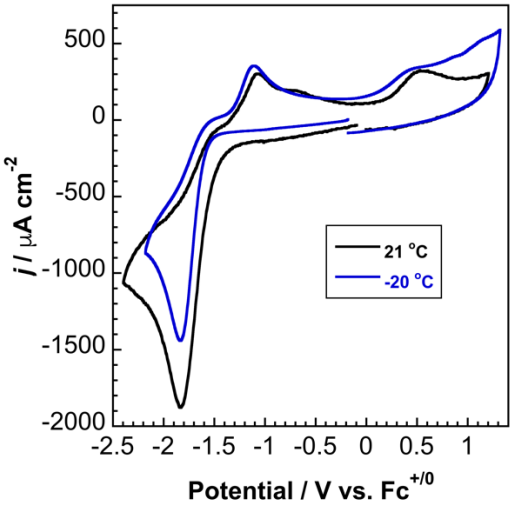

Figure 7.23. Comparison of room temperature and low temperature voltammetry for $(TBA)_3[Co(CN\text{-}B(C_6F_5)_3)_6]$ in MeCN with 0.1 M $TBAPF_6$.

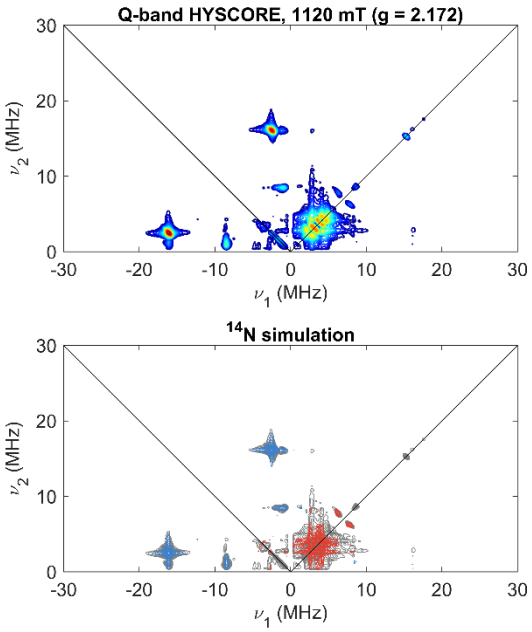

Figure 7.24. Q-band Hyperfine sublevel correlation (HYSCORE) spectrum of complex **2** acquired at 1120 mT (g = 2.172). The experimental data is plotted in color in the top panel, ranging from dark blue to red in increasing intensity. This same data is plotted in grey in the bottom panel, with simulations of a single coupling of class $^{14}N_a$ (blue) and coupling to four equivalent $^{14}N_b$ nuclei (red) overlaid. Acquisition parameters: temperature = 15 K; MW freq. = 34.046 GHz; MW pulse length ($\pi/2$, π) = 12 ns, 24 ns; τ = 100 ns; $t_1 = t_2$ = 100 ns; $\Delta t_1 = \Delta t_2$ = 16 ns; shot repetition time (srt) = 2 ms. Simulation parameters: $A(^{14}N_a)$ = [9.2, 9.2, 12] MHz, $e^2qQ/h(^{14}N_a)$ = 1.2 MHz, $\eta(^{14}N_a)$ = 0; $A(^{14}N_b)$ = [0.5, 0.5, 4] MHz, $e^2qQ/h(^{14}N_b)$ = 1.2 MHz, $\eta(^{14}N_b)$ = 0.

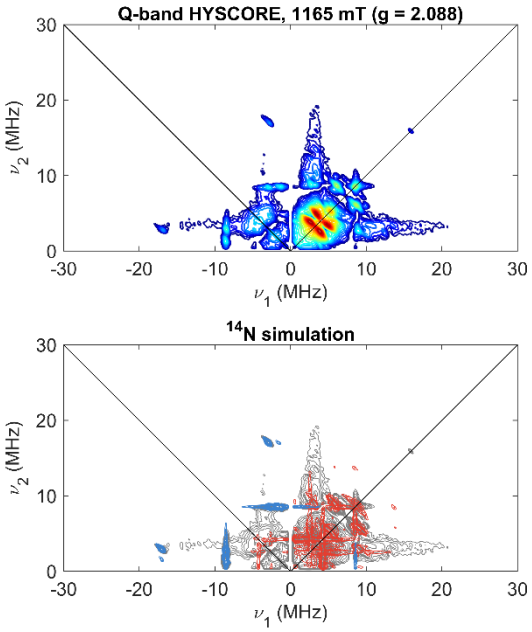

Figure 7.25. Q-band Hyperfine sublevel correlation (HYSCORE) spectrum of complex **2** acquired at 1165 mT (g = 2.088). The experimental data is plotted in color in the top panel, ranging from dark blue to red in increasing intensity. This same data is plotted in grey in the bottom panel, with simulations of a single coupling of class $^{14}N_a$ (blue) and coupling to four equivalent $^{14}N_b$ nuclei (red) overlaid. Acquisition parameters: temperature = 15 K; MW freq. = 34.046 GHz; MW pulse length ($\pi/2$, π) = 12 ns, 24 ns; τ = 100 ns; $t_1 = t_2$ = 100 ns; $\Delta t_1 = \Delta t_2$ = 16 ns; shot repetition time (srt) = 2 ms. Simulation parameters: $A(^{14}N_a)$ = [9.2, 9.2, 12] MHz, $e^2qQ/h(^{14}N_a)$ = 1.2 MHz, $\eta(^{14}N_a)$ = 0; $A(^{14}N_b)$ = [0.5, 0.5, 4] MHz, $e^2qQ/h(^{14}N_b)$ = 1.2 MHz, $\eta(^{14}N_b)$ = 0.

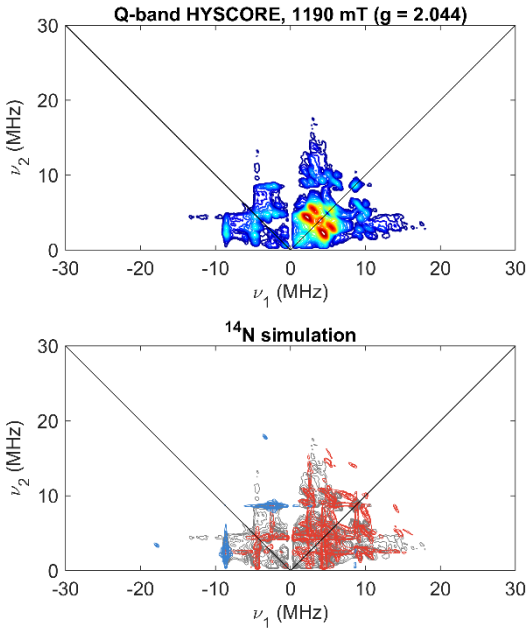

Figure 7.26. Q-band Hyperfine sublevel correlation (HYSCORE) spectrum of complex **2** acquired at 1190 mT (g = 2.044). The experimental data is plotted in color in the top panel, ranging from dark blue to red in increasing intensity. This same data is plotted in grey in the bottom panel, with simulations of a single coupling of class $^{14}N_a$ (blue) and coupling to four equivalent $^{14}N_b$ nuclei (red) overlaid. Acquisition parameters: temperature = 15 K; MW freq. = 34.046 GHz; MW pulse length ($\pi/2$, π) = 12 ns, 24 ns; τ = 100 ns; $t_1 = t_2$ = 100 ns; $\Delta t_1 = \Delta t_2$ = 16 ns; shot repetition time (srt) = 2 ms. Simulation parameters: $A(^{14}N_a)$ = [9.2, 9.2, 12] MHz, $e^2qQ/h(^{14}N_a)$ = 1.2 MHz, $\eta(^{14}N_a)$ = 0; $A(^{14}N_b)$ = [0.5, 0.5, 4] MHz, $e^2qQ/h(^{14}N_b)$ = 1.2 MHz, $\eta(^{14}N_b)$ = 0.

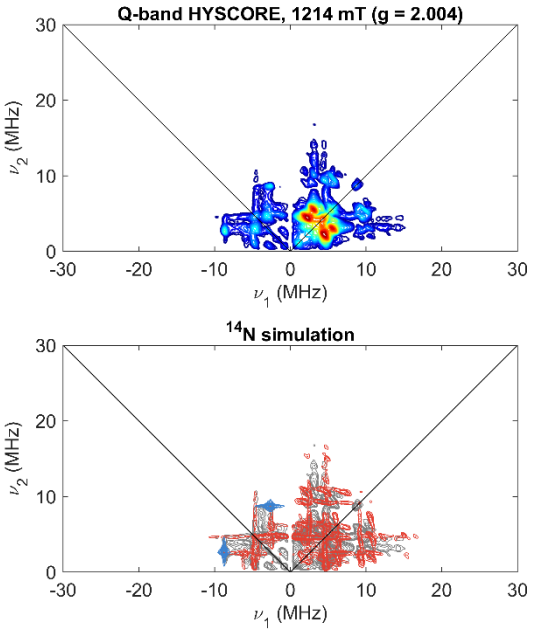

Figure 7.27. Q-band Hyperfine sublevel correlation (HYSCORE) spectrum of complex **2** acquired at 1214 mT (g = 2.004). The experimental data is plotted in color in the top panel, ranging from dark blue to red in increasing intensity. This same data is plotted in grey in the bottom panel, with simulations of a single coupling of class $^{14}N_a$ (blue) and coupling to four equivalent $^{14}N_b$ nuclei (red) overlaid. Acquisition parameters: temperature = 15 K; MW freq. = 34.046 GHz; MW pulse length ($\pi/2$, π) = 12 ns, 24 ns; τ = 100 ns; $t_1 = t_2$ = 100 ns; $\Delta t_1 = \Delta t_2$ = 16 ns; shot repetition time (srt) = 2 ms. Simulation parameters: $A(^{14}N_a)$ = [9.2, 9.2, 12] MHz, $e^2qQ/h(^{14}N_a)$ = 1.2 MHz, $\eta(^{14}N_a)$ = 0; $A(^{14}N_b)$ = [0.5, 0.5, 4] MHz, $e^2qQ/h(^{14}N_b)$ = 1.2 MHz, $\eta(^{14}N_b)$ = 0.

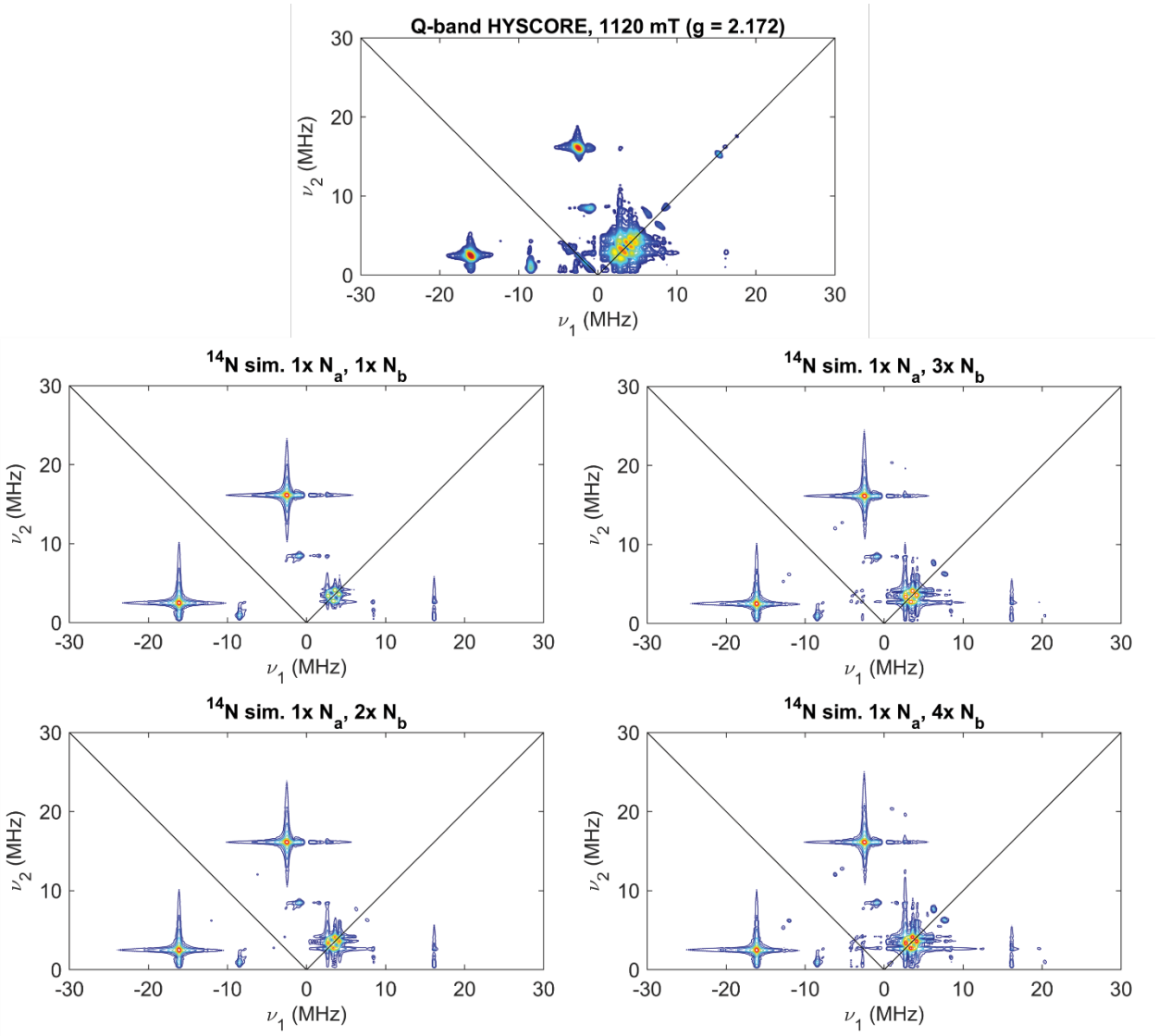

Figure 7.28. Q-band Hyperfine sublevel correlation (HYSCORE) spectrum of complex **2** acquired at 1120 mT (g = 2.134), with comparisons to simulations of 14N HYSCORE features with differing numbers of the more weakly coupled class of ^{14}N hyperfine coupling (N_b). For this comparison, experimental data and simulations are both plotted in color, ranging from dark blue to red in increasing intensity. Acquisition parameters: temperature = 15 K; MW freq. = 34.046 GHz; MW pulse length ($\pi/2$, π) = 12 ns, 24 ns; τ = 100 ns; $t_1 = t_2$ = 100 ns; $\Delta t_1 = \Delta t_2$ = 16 ns; shot repetition time (srt) = 2 ms. Simulation parameters: A($^{14}N_a$) = [9.2, 9.2, 12] MHz, $e^2qQ/h(^{14}N_a)$ = 1.2 MHz, $\eta(^{14}N_a)$ = 0; A($^{14}N_b$) = [0.5, 0.5, 4] MHz, $e^2qQ/h(^{14}N_b)$ = 1.2 MHz, $\eta(^{14}N_b)$ = 0.

X-Ray Crystallographic Data

Collection and Refinement of $(PPN)_3[Co(CN\text{-}B(C_6F_5)_3)_6]$

A crystal was mounted on a polyimide MiTeGen loop with STP Oil Treatment and placed under a nitrogen stream. Low temperature (100K) X-ray data were collected with a Bruker AXS D8 VENTURE KAPPA diffractometer running at 50 kV and 1 mA (Mo K_α = 0.71073 Å; PHOTON II CPAD detector and Helios focusing multilayer mirror optics). All diffractometer manipulations, including data collection, integration, and scaling were carried out using the Bruker APEX3 software. An absorption correction was applied using SADABS. The space group was determined and the structure solved by intrinsic phasing using XT. Refinement was full-matrix least squares on F^2 using XL. All non-hydrogen atoms were refined using anisotropic displacement parameters. Hydrogen atoms were placed in idealized positions and refined using a riding model. The isotropic displacement parameters of all hydrogen atoms were fixed at 1.2 times (1.5 times for methyl groups) the U_{eq} value of the bonded atom.

$(PPN)_3[Co(CN\text{-}B(C_6F_5)_3)_6]$ crystallizes in the triclinic space group *P-1* (#2) with the asymmetric unit consisting of two half anions on inversion centers, three PPN (bis(triphenylphosphine)iminium) cations, along with 4.93 dichloromethanes and 0.80 diethyl ether in a disordered solvent region.

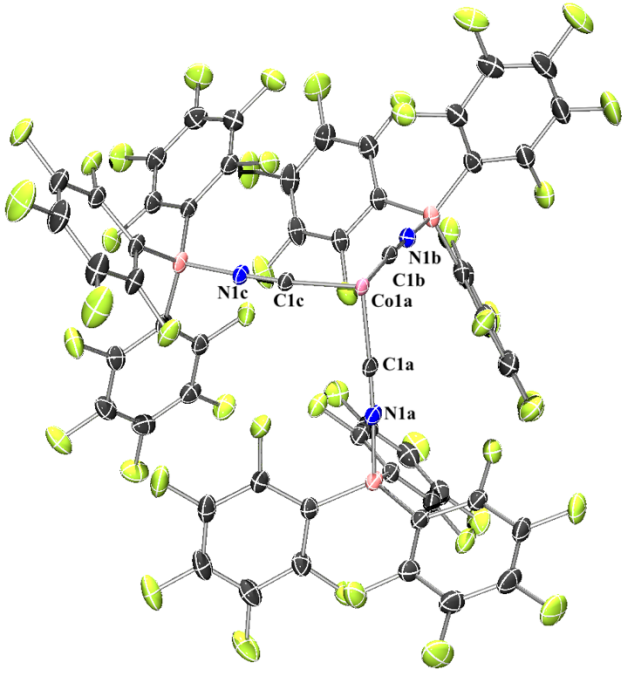

Figure 7.29. Crystal structure of the asymmetric unit of $[Co(CN\text{-}B(C_6F_5)_3)_6]^{3-}$ (solvent and cations are omitted for clarity). Thermal ellipsoids set at 50% probability.

Table 7.6. Crystal data and structure refinement for $(PPN)_3[Co(CN\text{-}B(C_6F_5)_3)_6]$

Empirical formula	C230.14 H107.86 B6 Cl9.87 Co F90 N9 O0.80 P6	
Formula weight	5380.86	
Temperature	100 K	
Wavelength	0.71073 Å	
Crystal system	Triclinic	
Space group	P-1	
Unit cell dimensions	a = 19.085(4) Å	a= 85.597(5)°
	b = 20.186(5) Å	b= 80.402(7)°
	c = 31.587(7) Å	g = 67.806(13)°
Volume	11109(5) $Å^3$	
Z	2	
Density (calculated)	1.609 g/cm^3	
Absorption coefficient	0.374 mm^{-1}	
F(000)	5366	
Crystal size	0.27 x 0.18 x 0.11 mm^3	
Theta range for data collection	2.230 to 34.207°.	
Index ranges	$-30 \le h \le 30$, $-30 \le k \le 31$, $-49 \le l \le 49$	
Reflections collected	327924	
Independent reflections	80338 [R(int) = 0.0389]	
Completeness to theta = 25.242°	99.9 %	
Absorption correction	Semi-empirical from equivalents	
Max. and min. transmission	1.0000 and 0.9484	
Refinement method	Full-matrix least-squares on F^2	
Data / restraints / parameters	80338 / 231 / 3327	
Goodness-of-fit on F^2	1.041	
Final R indices [I>2sigma(I)]	R1 = 0.0645, wR2 = 0.1612	
R indices (all data)	R1 = 0.0914, wR2 = 0.1764	
Extinction coefficient	n/a	
Largest diff. peak and hole	1.760 and -1.068 e.$Å^{-3}$	

Collection and Refinement of $(TBA)_2(CoCp_2)[Co(CN\text{-}B(C_6F_5)_3)_5]$

A crystal was mounted on a polyimide MiTeGen loop with STP Oil Treatment and placed under a nitrogen stream. Low temperature (100K) X-ray data were collected with a Bruker AXS D8 VENTURE KAPPA diffractometer running at 50 kV and 1 mA (Mo K_α = 0.71073 Å; PHOTON II CPAD detector and Helios focusing multilayer mirror optics). All diffractometer manipulations, including data collection, integration, and scaling were carried out using the Bruker APEX3 software. An absorption correction was applied using SADABS. The space group was determined and the structure solved by intrinsic phasing using XT. Refinement was full-matrix least squares on F^2 using XL. All non-hydrogen atoms were refined using anisotropic displacement parameters. Hydrogen atoms were placed in idealized positions and refined using a riding model. The isotropic displacement parameters of all hydrogen atoms were fixed at 1.2 times (1.5 times for methyl groups) the U_{eq} value of the bonded atom.

$(TBA)_2(CoCp_2)[Co(CN\text{-}B(C_6F_5)_3)_5]$ crystallizes in the triclinic space group *P-1* (#2) with the asymmetric unit consisting of one anion, one cobaltocenium and two TBA (tetrabutylammonium) cations, along with two diethyl ethers. Modelled disorder includes three pentafluorophenyl groups (55;45, 51:49, and 51:49 with two nearby carbons constrained to have the same displacement parameters), the two terminal carbons of a butyl (62:38), the terminal carbons of two butyl groups (55:45 and 56:44), and one diethyl ether (53:47).

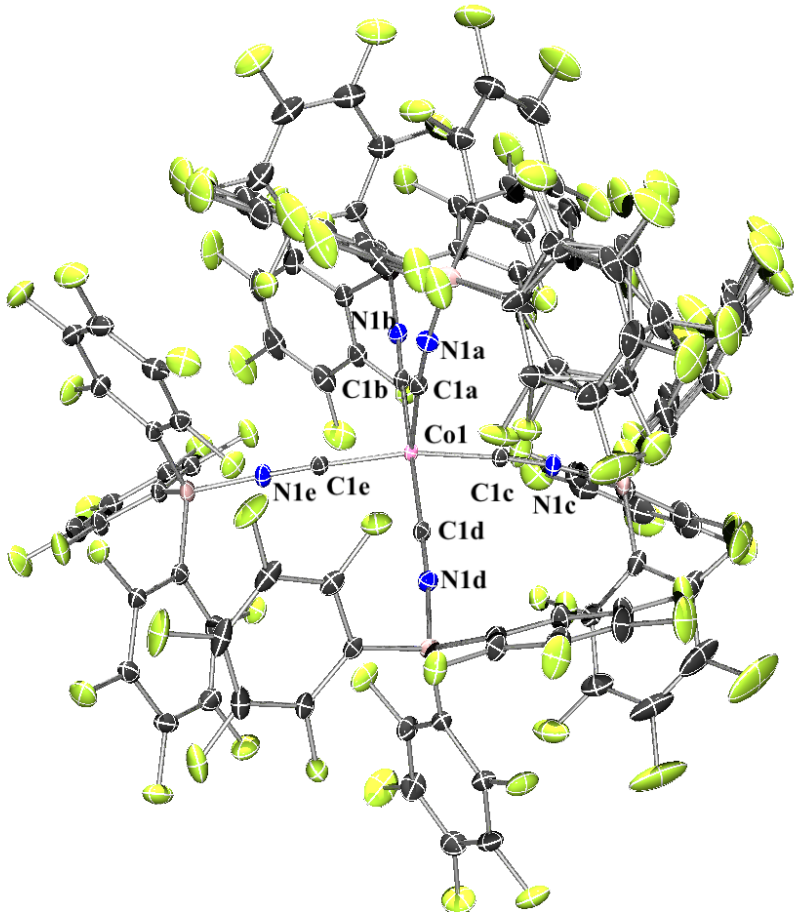

Figure 7.30. Crystal structure of $[Co(CN\text{-}B(C_6F_5)_3)_5]^{3-}$ (**2**) (solvent and cations are omitted for clarity). Thermal ellipsoids set at 50% probability.

Table 7.7. Crystal data and structure refinement for $(TBA)_2(CoCp_2)[Co(CN\text{-}B(C_6F_5)_3)_5]$

Empirical formula	C145 H102 B5 Co2 F75 N7 O2	
Formula weight	3571.24	
Temperature	100 K	
Wavelength	0.71073 Å	
Crystal system	Triclinic	
Space group	P-1	
Unit cell dimensions	a = 16.0829(6) Å	a= 83.8399(14)°
	b = 16.3015(6) Å	b= 87.4031(15)°
	c = 27.9243(11) Å	g = 85.8490(15)°
Volume	7254.5(5) $Å^3$	
Z	2	
Density (calculated)	1.635 g/cm^3	
Absorption coefficient	0.382 mm^{-1}	
F(000)	3582	
Crystal size	0.21 x 0.20 x 0.16 mm^3	
Theta range for data collection	2.308 to 37.466°.	
Index ranges	$-27 \le h \le 27$, $-27 \le k \le 27$, $-47 \le l \le 46$	
Reflections collected	517177	
Independent reflections	71979 [R(int) = 0.0501]	
Completeness to theta = 25.242°	99.9 %	
Absorption correction	Semi-empirical from equivalents	
Max. and min. transmission	0.9947 and 0.9706	
Refinement method	Full-matrix least-squares on F^2	
Data / restraints / parameters	71979 / 0 / 2521	
Goodness-of-fit on F^2	1.027	
Final R indices [I>2sigma(I)]	R1 = 0.0473, wR2 = 0.1188	
R indices (all data)	R1 = 0.0701, wR2 = 0.1329	
Extinction coefficient	n/a	
Largest diff. peak and hole	1.542 and -0.879 $e.Å^{-3}$	

DFT Input Parameters

CASSCF+NEVPT2 and Relativistic Calculations for $[Co(CN\text{-}BH_3)_5]^{3-}$

```
! DKH DKH-def2-tzvp AutoAux RIJK CONV CPCM(Acetonitrile) NEVPT2 MOREAD LargePrint
! NoFrozenCore
%moinp "Co_II_BH3_CASSCF6.gbw"
%rel method DKH picturechange 2 end
%casscf
trafostep ri
nel 11
norb 12
Mult 4,2
NRoots 10,35
rel
printlevel 3
dosoc true
gtensor true
dtensor true end
end
%pal
nprocs 7
end
%maxcore 27000
* xyzfile -3 2 Co_II_BH3.xyz
```

7.6 References

(1) Halpern, J.; Maher, J. P. Kinetics of the Reactions of Pentacyanocobaltate(II) with Organic Halides. *J. Am. Chem. Soc.* **1965**, *87* (23), 5361–5366. https://doi.org/10.1021/ja00951a018.

(2) Halpern, J.; Pribanic, M. Hydrogenation of Pentacyanocobaltate(II) at High Pressures. *Inorg. Chem.* **1970**, *9* (11), 2616–2618. https://doi.org/10.1021/ic50093a057.

(3) Halpern, J. Mechanism of the Splitting of Dihydrogen by Pentacyanocobaltate(II). A Reappraisal. *Inorganica Chim. Acta* **1983**, *77*, L105–L106. https://doi.org/10.1016/S0020-1693(00)82581-5.

(4) Lin, W. C.; McDowell, C. A.; Ward, D. J. Electron Paramagnetic Resonance of X-Ray-Irradiated Single Crystals of Potassium Cobalticyanide, $K_3Co(CN)_6$. *J. Chem. Phys.* **1968**, *49* (7), 2883–2886. https://doi.org/10.1063/1.1670522.

(5) Jain, S. C.; Reddy, K. V.; Reddy, T. Rs. EPR of Low Spin d^7 Fe^+, Co^{2+}, and Ni^{3+} Cyanide Complexes in NaCl and KCl. *J. Chem. Phys.* **1975**, *62* (11), 4366–4372. https://doi.org/10.1063/1.430336.

(6) Kimball, M. E.; Pratt, D. W.; Kaska, W. C. Pentacoordinate Complexes. II. Electron Spin Resonance Spectrum of Pentakis(Methyl Isocyanide)Cobalt(II) and a Comparison with Pentacyanocobaltate(II). *Inorg. Chem.* **1968**, *7* (10), 2006–2009. https://doi.org/10.1021/ic50068a009.

(7) Symons, R. Electron Spin Resonance Studies of the Pentacyanocobaltate(II) Ion in Various Host Lattices. *J Chem Soc. A.* **1971**, *0*, 2069-2074.

(8) Birk, J. P.; Halpern, Jack. Electron-Transfer Reactions of Pentacyanocobaltate(II) with Various Pentacyanocobaltate(III) Complexes. *J. Am. Chem. Soc.* **1968**, *90* (2), 305–309. https://doi.org/10.1021/ja01004a017.

(9) Pinkowicz, D.; Southerland, H. I.; Avendaño, C.; Prosvirin, A.; Sanders, C.; Wernsdorfer, W.; Pedersen, K. S.; Dreiser, J.; Clérac, R.; Nehrkorn, J.; Simeoni, G. G.; Schnegg, A.; Holldack, K.; Dunbar, K. R. Cyanide Single-Molecule Magnets Exhibiting Solvent Dependent Reversible "On" and "Off" Exchange Bias Behavior. *J. Am. Chem. Soc.* **2015**, *137* (45), 14406–14422. https://doi.org/10.1021/jacs.5b09378.

(10) Juris, A.; Manfrin, M. F.; Maestri, M.; Serpone, N. Luminescence Quenching of Tris(2,2'-Bipyridine) Complexes of Chromium(III), Ruthenium(II), and Osmium(II) by Cyanide Complexes. *Inorg. Chem.* **1978**, *17* (8), 2258–2261. https://doi.org/10.1021/ic50186a049.

(11) Taylor, R. J.; Drago, R. S.; Hage, J. P. A Reversible Molecular Oxygen Binding System: $Co(CN)_5^{3-}$ inside Zeolite Y. *Inorg. Chem.* **1992**, *31* (2), 253–258. https://doi.org/10.1021/ic00028a024.

(12) Deng, L.; Yang, Z.; Tan, L.; Zeng, L.; Zhu, Y.; Guo, L. Investigation of the Prussian Blue Analog $Co_3[Co(CN)_6]_2$ as an Anode Material for Nonaqueous Potassium-Ion Batteries. *Adv. Mater.* **2018**, *30* (31), 1802510. https://doi.org/10.1002/adma.201802510.

(13) Zhang, K.; Lee, T. H.; Cha, J. H.; Varma, R. S.; Choi, J.-W.; Jang, H. W.; Shokouhimehr, M. Cerium Hexacyanocobaltate: A Lanthanide-Compliant Prussian Blue Analogue for Li-Ion Storage. *ACS Omega* **2019**, *4* (25), 21410–21416. https://doi.org/10.1021/acsomega.9b03104.

(14) Goberna-Ferrón, S.; Hernández, W. Y.; Rodríguez-García, B.; Galán-Mascarós, J. R. Light-Driven Water Oxidation with Metal Hexacyanometallate Heterogeneous Catalysts. *ACS Catal.* **2014**, *4* (6), 1637–1641. https://doi.org/10.1021/cs500298e.

(15) Lazarides, T.; Davies, G. M.; Adams, H.; Sabatini, C.; Barigelletti, F.; Barbieri, A.; Pope, S. J. A.; Faulkner, S.; Ward, M. D. Ligand-Field Excited States of Hexacyanochromate and Hexacyanocobaltate as Sensitisers for near-Infrared Luminescence from Nd(III) and Yb(III) in Cyanide-Bridged d–f Assemblies. *Photochem. Photobiol. Sci.* **2007**, *6* (11), 1152. https://doi.org/10.1039/b708683k.

(16) Kirby, C. W.; Puranda, C. M.; Power, W. P. Cobalt-59 Nuclear Magnetic Relaxation Studies of Aqueous Octahedral Cobalt(III) Complexes. *J. Phys. Chem.* **1996**, *100* (35), 14618–14624. https://doi.org/10.1021/jp9614254.

(17) Delville, A.; Laszlo, P.; Stockis, A. Cobalt-59 NMR as a Sensitive Probe into Hydrophobic Effects. *J. Am. Chem. Soc.* **1981**, *103* (20), 5991–5998. https://doi.org/10.1021/ja00410a001.

(18) Taura, T. Solvent Influence on UV, ^{59}Co, and ^{13}C NMR of $[Co(CN)_6]^{3-}$ and Its Solvation Site. *Bull. Chem. Soc. Jpn.* **1990**, *63*, 1105-1110.

(19) Dykes, D.; Huckerby, T. N.; Oldham, C. ^{13}C N.M.R. of Two Octahedral d^6 Transition Metal Cyanide Complexes. *Inorg. Nucl. Chem. Lett.* **1977**, *13* (1), 63–64. https://doi.org/10.1016/0020-1650(77)80014-7.

(20) Bramley, R.; Brorson, M.; Sargeson, A. M.; Schaeffer, C. E. Cobalt-59 NMR Chemical Shifts of Cobalt(III) Complexes; Correlations with Parameters Calculated from Ligand-Field Spectra. *J. Am. Chem. Soc.* **1985**, *107* (9), 2780–2787. https://doi.org/10.1021/ja00295a034.

(21) McNicholas, B. J.; Grubbs, R. H.; Winkler, J. R.; Gray, H. B.; Despagnet-Ayoub, E. Tuning the Formal Potential of Ferrocyanide over a 2.1 V Range. *Chem. Sci.* **2019**, *10* (12), 3623–3626. https://doi.org/10.1039/C8SC04972F.

(22) Milder, S. J.; Gray, H. B.; Miskowski, V. M. Photochemistry of Hexacyanocobaltate(III) in Haloalkanes. *J. Am. Chem. Soc.* **1984**, *106* (13), 3764–3767. https://doi.org/10.1021/ja00325a009.

(23) Mingardi, M. A. P. Luminescence and Absorption Spectra of Some d^6 Complexes. Ph.D. Dissertation, The University of British Columbia, Vancouver, Canada, 1969.

(24) Viaene, L.; D'Olieslager, J. Luminescence from and Absorption by the 3T1g Level of the Hexacyanocobaltate(III) Ion. *Inorg. Chem.* **1987**, *26* (6), 960–962. https://doi.org/10.1021/ic00253a039.

(25) Mazur, Ursula.; Hipps, K. W. The Role of the Crystal Lattice in the Electronic Spectra of the Hexacyanocobaltate Ion. 1. Luminescence Spectra, Decay Times, and Relative Quantum Yields. *J. Phys. Chem.* **1979**, *83* (14), 1884–1889. https://doi.org/10.1021/j100477a019.

(26) Fujita, J.; Shimura, Y. The Absorption Spectra of Cobalt(III) Complexes. III. The Spin-Forbidden Bands. *Bull. Chem. Soc. Jpn.* **1963**, *36* (10), 1281–1285. https://doi.org/10.1246/bcsj.36.1281.

(27) Kataoka, H. Emission Spectrum of Hexamminechromium Hexacyanocobaltate. *Bull. Chem. Soc. Jpn.* **1973**, *46*, 2078-2086.

(28) Miskowski, V. M.; Gray, H. B.; Wilson, R. B.; Solomon, E. I. Position of the $^3T_{1g} \leftarrow {}^1A_{1g}$ Transition in Hexacyanocobaltate(III). Analysis of Absorption and Emission Results. *Inorg. Chem.* **1979**, *18* (5), 1410-1412.

(29) Viaene, L.; D'Olieslager, J.; Ceulemans, A.; Vanquickenborne, L. G. Excited-State Spectroscopy of Hexacyanocobaltate(III). *J. Am. Chem. Soc.* **1979**, *101* (6), 1405–1409. https://doi.org/10.1021/ja00500a009.

(30) Kotov, V. Yu.; Nazmutdinov, R. R.; Botukhova, G. N.; Tsirlina, G. A.; Petrii, O. A. Hard-to-Detect Co^{III}/Co^{II} Reduction in a Hexacyanocobaltate. *Mendeleev Commun.* **2004**, *14* (3), 113–115. https://doi.org/10.1070/MC2004v014n03ABEH001884.

(31) Hume, D. N.; Kolthoff, I. M. A Polarographic Study of Cobalt Cyanide Complexes. *J. Am. Chem. Soc.* **1949**, *71* (3), 867-869.

(32) Espinoza, E. M.; Clark, J. A.; Soliman, J.; Derr, J. B.; Morales, M.; Vullev, V. I. Practical Aspects of Cyclic Voltammetry: How to Estimate Reduction Potentials When Irreversibility Prevails. *J. Electrochem. Soc.* **2019**, *166* (5), H3175–H3187. https://doi.org/10.1149/2.0241905jes.

(33) Miskowski, V. M.; Gray, H. B. Charge Transfer Energies of Metal Complexes. Nature of the Lowest Charge Transfer Excited State of Hexacyanocobaltate(1ll). *Comments Inorg. Chem.* **1985**, *4* (6), 323–327. https://doi.org/10.1080/02603598508072270.

(34) Brown, L. D.; Raymond, K. N. Structural Characterization of the Pentacyanocobaltate(II) Anion in the Salt Tris(Diethyldiisopropylammonium) Pentacyanocobaltate(II). *Inorg. Chem.* **1975**, *14* (11), 2590–2594. https://doi.org/10.1021/ic50153a002.

(35) Brown, L. D.; Raymond, K. N. ..Sigma.-Bonded Dioxygen Adduct of the Pentacyanocobaltate(II) Anion. Crystal Structure of Tris(Tetraethylammonium)Dioxopentacyanocobaltate(II) Pentahydrate. *Inorg. Chem.* **1975**, *14* (11), 2595–2601. https://doi.org/10.1021/ic50153a003.

(36) Shriver D.F. (1966) The ambident nature of cyanide. In: Structure And Bonding. Structure and Bonding, vol 1. Springer, Berlin, Heidelberg

(37) Tsay, F.; Gray, H. B.; Danon, J. Electron Paramagnetic Resonance and Optical Spectra of Pentacyanocobaltate(II). *J. Chem. Phys.* **1971**, *54* (9), 3760–3769. https://doi.org/10.1063/1.1675426.

(38) White, D. A.; Solodar, A. J.; Baizer, M. M. Tetraalkylammonium Pentacyanocobaltates. Their Preparation, Properties, and Reactivity. *Inorg. Chem.* **1972**, *11* (9), 2160–2167. https://doi.org/10.1021/ic50115a034.

(39) Caulton, K. G. Analysis of the Ligand Field Spectrum of Pentacyanocobaltate(II). *Inorg. Chem.* **1968**, *7* (2), 392–394. https://doi.org/10.1021/ic50060a050.

(40) Alexander, J. J.; Gray, H. B. Molecular and Electronic Structure of Pentacyanocobaltate. *J. Am. Chem. Soc.* **1967**, *89* (13), 3356–3357. https://doi.org/10.1021/ja00989a050.

(41) Carter, S. J.; Foxman, B. M.; Stuhl, L. S. Cobalt(II) Cyanides in Aprotic Media: Effect of Varying Counterion and Solvent. *Inorg. Chem.* **1986**, *25* (16), 2888–2894. https://doi.org/10.1021/ic00236a046.

(42) King, N. K.; Winfield, M. E. The Liquid Phase Hydrogenation of Cyanocobaltate(II). *J. Am. Chem. Soc.* **1961**, *83* (16), 3366–3373. https://doi.org/10.1021/ja01477a003.

(43) Caride, A. O.; Panepucci, H.; Zanette, S. I. Analysis of the Ligand Field Spectra of Some Low Spin Pentacoordinate Co^{2+} Complexes. *J. Chem. Phys.* **1971**, *55* (8), 3651–3654. https://doi.org/10.1063/1.1676643.

(44) Morton, J. R.; Preston, K. F. Atomic Parameters for Paramagnetic Resonance Data. *J. Magn. Reson.* **1978**, *30* (3), 577–582. https://doi.org/10.1016/0022-2364(78)90284-6.

(45) Oyala, P. H.; Ravichandran, K. R.; Funk, M. A.; Stucky, P. A.; Stich, T. A.; Drennan, C. L.; Britt, R. D.; Stubbe, J. Biophysical Characterization of Fluorotyrosine Probes Site-Specifically Incorporated into Enzymes: *E. Coli* Ribonucleotide Reductase As an Example. *J. Am. Chem. Soc.* **2016**, *138* (25), 7951–7964. https://doi.org/10.1021/jacs.6b03605.

(46) Pierloot, K.; Van Praet, E.; Vanquickenborne, L. G.; Roos, B. O. Systematic Ab Initio Study of the Ligand Field Spectra of Hexacyanometalate Complexes. *J. Phys. Chem.* **1993**, *97* (47), 12220–12228. https://doi.org/10.1021/j100149a021.

(47) Jakubczyk, M.; Adamczyk-Woźniak, A.; Sporzyński, A. Acceptor Number of Organoboron Molecules - Quantitative Determination of Lewis Acidity. In *Molecular Receptors*. Rybachenko, V. I., Ed.; East Publisher House, 2011.

(48) Alexander, J. J.; Gray, H. B. Electronic Structures of Hexacyanometalate Complexes. *J. Am. Chem. Soc.* **1968**, *90* (16), 4260–4271. https://doi.org/10.1021/ja01018a013.

(49) Jaselskis, B.; Diehl, H. Preparation and Properties of Tetraalkylammonium Hexacyanocobaltates(III) and Hexacyanoferrates(III). *J. Am. Chem. Soc.* **1958**, *80* (16), 4197–4198. https://doi.org/10.1021/ja01549a020.

(50) Stoll, S.; Schweiger, A. EasySpin, a Comprehensive Software Package for Spectral Simulation and Analysis in EPR. *J. Magn. Reson.* **2006**, *178* (1), 42–55. https://doi.org/10.1016/j.jmr.2005.08.013.